

INFORMATION TO USERS

This manuscript has been reproduced from the microfilm master. UMI films the text directly from the original or copy submitted. Thus, some thesis and dissertation copies are in typewriter face, while others may be from any type of computer printer.

The quality of this reproduction is dependent upon the quality of the copy submitted. Broken or indistinct print, colored or poor quality illustrations and photographs, print bleedthrough, substandard margins, and improper alignment can adversely affect reproduction.

In the unlikely event that the author did not send UMI a complete manuscript and there are missing pages, these will be noted. Also, if unauthorized copyright material had to be removed, a note will indicate the deletion.

Oversize materials (e.g., maps, drawings, charts) are reproduced by sectioning the original, beginning at the upper left-hand corner and continuing from left to right in equal sections with small overlaps. Each original is also photographed in one exposure and is included in reduced form at the back of the book.

Photographs included in the original manuscript have been reproduced xerographically in this copy. Higher quality 6" x 9" black and white photographic prints are available for any photographs or illustrations appearing in this copy for an additional charge. Contact UMI directly to order.

UMI

A Bell & Howell Information Company
300 North Zeeb Road, Ann Arbor MI 48106-1346 USA
313/761-4700 800/521-0600

NOTE TO USERS

The original manuscript received by UMI contains pages with indistinct print. Pages were microfilmed as received.

This reproduction is the best copy available

UMI

FINE ASH MORPHOLOGY AND AEROSOL
FORMATION - A COMPARISON OF COAL
AND BIOMASS FUELS

by

Blake Charles Chenevert

A dissertation submitted in partial fulfillment of the
requirements for the degree of

Doctor of Philosophy

University of Washington

1998

Approved by



Chairperson of Supervisory Committee

Program Authorized
to Offer Degree

Department of Mechanical Engineering

Date

December 15, 1998

UMI Number: 9916633

**Copyright 1998 by
Chenevert, Blake Charles**

All rights reserved.

**UMI Microform 9916633
Copyright 1999, by UMI Company. All rights reserved.**

**This microform edition is protected against unauthorized
copying under Title 17, United States Code.**

UMI
300 North Zeeb Road
Ann Arbor, MI 48103

© Copyright 1998
Blake Charles Chenevert

Doctoral Dissertation

In presenting this dissertation in partial fulfillment of the requirements for the Doctoral degree at the University of Washington, I agree that the Library shall make its copies freely available for inspection. I further agree that extensive copying of this dissertation is allowable only for scholarly purposes, consistent with "fair use" as prescribed in the U.S. Copyright Law. Requests for copying or reproduction of this dissertation may be referred to University Microfilms, 1490 Eisenhower Place, P.O. Box 975, Ann Arbor, MI 48106, to whom the author has granted "the right to reproduce and sell (a) copies of the manuscript in microform and/or (b) printed copies of the manuscript made from microform."

Signature Blake Chenevert
Date 12/15/98

University of Washington

Abstract

**FINE ASH MORPHOLOGY AND AEROSOL
FORMATION - A COMPARISON OF COAL
AND BIOMASS FUELS**

by Blake Charles Chenevert

Chairperson of the Supervisory Committee: Professor John C. Kramlich
Department of Mechanical Engineering

Modeling and experimental methods were used to investigate ash formation mechanisms of four industrially significant high-alkali biomass (sawdust/sanderdust) fuels. Alkali minerals tend to vaporize and recondense to form sub-micron aerosol, which poses health risks and causes special operational problems for industrial combustors.

Sawdust/sanderdust was burned in a 15 kW natural gas-fired tunnel furnace. The resulting ash was collected by a water-cooled probe, and size sorted by cascade impaction and Electrical Aerosol Size Analysis. Scanning Electron Microscopy and Energy Dispersive X-Ray Spectroscopy techniques were used to determine morphology and composition by size cut. Three ash modes were present:

- 1) A residual mode composed primarily of porous calcium structures with a scale length of 8 microns and larger. This mode was likely the result of direct oxide and carbonate formation.
- 2) A secondary residual mode near 2 microns composed of fluxed and fragmented calcium, but also containing significant amounts of Si, Fe, Mn and Al. This mode appeared to be composed of eutectic melts separated from the parent ash particle.
- 3) An aerosol mode composed of Na and K with Cl anion, or sulfate anion when Cl was not present. The aerosol mode diameter was found to be a function of initial nucleate number density and coagulation time. Long coagulation time or high initial number density resulted in an aerosol mode diameter near 0.1 micron.

Modeling was composed of three elements: 1) Equilibrium modeling - These calculations validated experimental evidence for alkali vaporization and condensation, predicting all alkali to enter the vapor phase as NaCl or KCl when Cl is available, or NaOH and KOH otherwise. 2) Condensation modeling - This model was used to determine the partitioning of alkali metal between homogeneous particulate matter formation (self-nucleation) and deposition on existing residual particles. It was shown that vaporized alkali can be collected on the residual particulate matter by controlling the time/temperature history just prior to self-nucleation. 3) Coagulation modeling - This code determined the ultimate diameter of nucleated aerosol particulate. Results agreed well with experimental data, showing a clear relationship between coagulation time, initial number density, and ultimate particle diameter.

TABLE OF CONTENTS

LIST OF FIGURES	iv
LIST OF TABLES	xi
LIST OF VARIABLES.....	xvi
CHAPTER 1: INTRODUCTION	1
CHAPTER 2: MECHANISMS OF MINERAL TRANSFORMATIONS IN COAL AND BIOMASS FUELS.....	4
2.1 Sources and Form of Mineral Matter in Coal and Biomass Fuels.....	4
2.1.1 Pulverized Coal Composition and Structure	5
2.1.2 Biomass Composition and Structure	8
2.1.3 Summary of Coal and Biomass Properties.....	10
2.2 Combustion of Pulverized or Finely-Divided Solid Fuel.....	10
2.2.1 Drying and Devolatilization	11
2.2.2 Char Combustion and Burnout.....	12
2.3 Fate of Mineral Matter in Combustion.....	14
2.3.1 Vaporized Mineral Matter and Capture Mechanisms.....	15
2.3.2 Residual Ash Mechanism	19
CHAPTER 3: FOCUS AND OBJECTIVES.....	29
CHAPTER 4: TECHNICAL APPROACH AND EXPERIMENT APPARATUS.....	32
4.1 Facility Description - Tunnel Furnace	33
4.2 Pulverized Coal Experiments - Setup and Procedures.....	34
4.2.1 Pulverized Coal Feed System.....	35
4.2.2 Pulverized Coal - Ash Collection and Size Sorting	36
4.2.3 Cascade Impactor Modifications and Preparation	36
4.3 Pulverized Artificial Char Experiments.....	39
4.4 Screened Sawdust/Sanderdust Experiments	40
4.5 Milled Sawdust/Sanderdust Experiments	41
4.5.1 Ash Collection and Size Sorting.....	42
4.5.1.1 Isokinetic Sampling Probe	42
4.5.1.2 Electrical Aerosol Size Analyzer - Particle Sizing	43
4.5.1.3 Cascade Impactor Modifications and Preparation	44
4.5.2 Determination of Isokinetic Conditions.....	44
4.5.3 Data Acquisition System	45

4.6 Furnace Temperature Profiling - High Velocity Thermocouple	45
CHAPTER 5: INFLUENCE OF COAL TREATMENT AND MINERAL CONTACT	
ON AEROSOL YIELDS.....	57
5.1 Pulverized Coal Experiments	57
5.1.1 Coal Characterization	57
5.1.2 Pulverized Coal Test Matrix	60
5.1.3 Pulverized Coal Horizontal Probe Tests - Results	62
5.1.4 Pulverized Coal Vertical Probe Tests - Results.....	67
5.1.5 Summary of Pulverized Coal Results.....	70
5.2 Pulverized Artificial Char Experiments.....	70
5.2.1 Artificial Char Characterization.....	71
5.2.2 Artificial Char Test Matrix	71
5.2.3 Artificial Char Results	72
5.2.4 Discussion of Artificial Char Results	75
CHAPTER 6: MINERAL BEHAVIOR IN SAWDUST/SANDERDUST	
COMBUSTION	109
6.1 Fuel Properties and Preparation	109
6.1.1 Sawdust/sanderdust Characterization.....	109
6.1.2 Fuel Preparation for Screened Sawdust/sanderdust Experiments	111
6.1.3 Fuel Preparation for Milled Sawdust/sanderdust Experiments	111
6.2 Screened Sawdust/sanderdust Experiments.....	112
6.2.1 Screened Sawdust/sanderdust Test Matrix and Conditions	112
6.2.2 Screened Sawdust/sanderdust Results.....	113
6.2.2.1 Ash Size Distribution and Morphology.....	113
6.2.2.2 Ash Composition as a Function of Ash Size.....	115
6.2.3 Discussion of Screened Sawdust/sanderdust Results.....	121
6.3 Milled Sawdust/sanderdust Experiments.....	131
6.3.1 Milled Sawdust/sanderdust Test Matrix and Conditions	131
6.3.2 Milled Sawdust/sanderdust Results.....	135
6.3.3 Discussion of Milled Sawdust/sanderdust Results	137
CHAPTER 7: MODELING.....	187
7.1 Modeling Parameters	187
7.2 Equilibrium	189
7.2.1 Fuel 1 Equilibrium at Laboratory Conditions.....	189
7.2.2 Fuel 1 Equilibrium at Industrial Conditions.....	190

7.2.3 Fuel 2 Equilibrium.....	192
7.2.4 Fuel 3 Equilibrium.....	193
7.2.5 Fuel 4 Equilibrium.....	194
7.2.6 Summary of Equilibrium Findings.....	194
7.3 Homogeneous and Heterogeneous Condensation Modeling.....	197
7.3.1 Homogeneous and Heterogeneous Modeling Method.....	197
7.3.2 Homogeneous and Heterogeneous Condensation Model Results.....	201
7.3.3 Summary of Homogeneous and Heterogeneous Modeling Findings.....	205
7.4 Coagulation Modeling.....	206
7.4.1 Coagulation Modeling for Fuel 1 Ash.....	206
7.4.2 Summary of Coagulation Modeling.....	209
CHAPTER 8: CONCLUSIONS AND SUMMARY.....	232
BIBLIOGRAPHY	240
APPENDIX A: SIMPLIFIED RESIDUAL SIZE DISTRIBUTION.....	248
APPENDIX B: AIR, WATER AND NATURAL GAS SCHEMATICS, AND SUMMARY OF LABORATORY MODIFICATIONS	256
APPENDIX C: SAMPLING EFFICIENCY USING A SIMPLE WATER-COOLED PROBE AT NON-ISOKINETIC CONDITIONS	260
APPENDIX D: NATURAL GAS COMPOSITION	264
APPENDIX E: SCREENED SAWDUST/SANDERDUST CASCADE IMPACTOR TEST SUMMARIES.....	265
APPENDIX F: MILLED SAWDUST/SANDERDUST ELECTRICAL AEROSOL ANALYZER TEST SUMMARIES	279
APPENDIX G: PULVERIZED COAL CASCADE IMPACTOR TEST SUMMARIES	322
APPENDIX H: ARTIFICIAL CHAR CASCADE IMPACTOR TEST SUMMARIES	366
APPENDIX I: HOMOGENEOUS AND HETEROGENEOUS CONDENSATION COMPETITION MODEL	393

LIST OF FIGURES

Figure 2.1: Two-film model for diffusion controlled char particle combustion (adapted from Saxena, 1990)	28
Figure 4.1: Natural gas-fired tunnel furnace (modified from Hoffman, 1994)	47
Figure 4.2: Tunnel furnace cross sections (from Hoffman, 1994).....	48
Figure 4.3: Pulverized coal feed system.....	48
Figure 4.4: Sampling in horizontal orientation.....	49
Figure 4.5: Sampling in vertical orientation.....	50
Figure 4.6: Artificial char syringe drive	51
Figure 4.7: Sawdust/sanderdust feed system, modifications of existing coal feed system.....	52
Figure 4.8: Milled sawdust/sanderdust isokinetic sampling probe, cascade impactor and EAA setup (continued next page).....	53
Figure 4.8 (cont.): Milled sawdust/sanderdust isokinetic sampling probe, cascade impactor and EAA setup	54
Figure 4.9: Isokinetic sampling probe schematic.....	55
Figure 4.10: Schematic of Water-Cooled High Velocity Thermocouple.....	56
Figure 5.1: Coal mineral composition as a function of discrete mineral inclusion diameter, as measured by CCSEM (Compiled from data in Boni et al., 1990, Table 4.4).....	80
Figure 5.2: Ash size distributions of Upper Freeport, Kentucky #11 and Illinois #6 coals as measured with the horizontal sampling probe.....	82
Figure 5.3: Ash size distributions of Upper Freeport, Kentucky #11 and Illinois #6 coals as measured with the horizontal sampling probe, normalized to total mass collected.....	83
Figure 5.4: Ash size distributions of Upper Freeport, Kentucky #11 and Illinois #6 coals as measured with the horizontal sampling probe, in terms of $\Delta\text{Mass}/\Delta\log D$	84
Figure 5.5: Upper Freeport ash size distribution using a horizontal sampling probe, $\Delta\text{Mass}/\Delta\log D$ as a function of particle diameter.....	85
Figure 5.6: Upper Freeport ash size distribution using a horizontal sampling probe, mass percent adjusted for total fraction of original coal.....	85

Figure 5.7: Upper Freeport cumulative ash size distribution using a horizontal sampling probe, mass percent as a function of cascade impactor size cut	86
Figure 5.8: Upper Freeport cumulative ash size distribution using a horizontal sampling probe, mass percent adjusted for total fraction of original coal.....	86
Figure 5.9: Kentucky #11, ash mass distribution using a horizontal sampling probe	87
Figure 5.10: Kentucky #11, cumulative mass distribution using a horizontal sampling probe	87
Figure 5.11: Illinois #6, ash size distribution using a horizontal sampling probe	88
Figure 5.12: Illinois #6, cumulative mass distribution using a horizontal sampling probe	88
Figure 5.13: Three coals, ash collected as a function of impactor stage for 1.8 furnace equivalence ratio	89
Figure 5.14: Three coals, ash collected expressed as $\Delta\text{Mass\%}/\Delta\log D$ for 1.8 furnace equivalence ratio	90
Figure 5.15: Three coals, ash collected expressed as cumulative mass for 1.8 furnace equivalence ratio	90
Figure 5.16: Kentucky #11, the effect of furnace stoichiometry on ash yield	91
Figure 5.17: Kentucky #11, ash collected expressed as cumulative mass.....	92
Figure 5.18: All Upper Freeport tests conducted with the vertical probe.....	93
Figure 5.19: All Upper Freeport test with the vertical probe with ash yield expressed as $\Delta\text{Mass\%}/\Delta\log D$	94
Figure 5.20: All Upper Freeport test with the vertical probe with ash yield expressed as cumulative mass	95
Figure 5.21: Upper Freeport tests scaled by coal fraction, expressed as $\Delta\text{Mass\%}/\Delta\log D$ on logarithmic scale	96
Figure 5.22: Upper Freeport tests scaled by coal fraction, expressed as $\Delta\text{Mass\%}/\Delta\log D$	97
Figure 5.23: Upper Freeport raw coal ash distribution compared to the sum of the sized coal, expressed as $\Delta\text{Mass\%}/\Delta\log D$	98
Figure 5.24: Upper Freeport raw coal ash distribution compared to the sum of the sized coal, expressed as cumulative mass	99
Figure 5.25: Upper Freeport, comparison of ash yields between horizontal and vertical probe tests	100
Figure 5.26: Artificial char with sodium doping only, ash mass distribution by cascade impactor stage.....	102

Figure 5.27: Artificial char with sodium doping only, cumulative mass	103
Figure 5.28: Artificial char with bentonite/sodium doping, ash mass distribution by cascade impactor stage	104
Figure 5.29: Artificial char with bentonite/sodium doping, cumulative mass	105
Figure 5.30: Artificial char with calcium/sodium doping, ash mass distribution by cascade impactor stage	106
Figure 5.31: Artificial char with pyrite/sodium doping, ash mass distribution by cascade impactor stage	107
Figure 5.32: Artificial char with pyrite/sodium doping, cumulative mass	108
Figure 6.1: Atomic Absorption analysis of As-Received fuels.....	141
Figure 6.2: As-Received fuels size distribution by cumulative mass.....	142
Figure 6.3: As-Received fuels size distribution.....	142
Figure 6.4: Milled fuel size distribution. Fuel 1 As-Received, Fuels 2, 3, and 4 milled to 0.5 mm diameter exit screen.....	142
Figure 6.5: Temperature as a function of furnace height	144
Figure 6.6: Temperature as a function of calculated residence time for Screened sawdust/sanderdust fuels, based on High Velocity Thermocouple measurements	144
Figure 6.7: Screened sawdust/sanderdust ash size distribution as a function of impactor stage cutoff diameter	145
Figure 6.8: Screened sawdust/sanderdust ash size distribution as a function of cumulative mass	146
Figure 6.9: Screened sawdust/sanderdust ash size distribution as a function of impactor cutoff diameter, excluding ash of greater than 5 μm	147
Figure 6.10: Screened sawdust/sanderdust ash size distribution as a function of cumulative mass, excluding particles of greater than 5 μm	148
Figure 6.11: Fuel 1 Stage 0 Scanning Electron Microscope results.....	149
Figure 6.12: Fuel 1 Stage 1 Scanning Electron Microscope results.....	150
Figure 6.13: Fuel 1 Stage 4 Scanning Electron Microscope results.....	151
Figure 6.14: Fuel 1 Stage 7 Scanning Electron Microscope results.....	152
Figure 6.15: Fuel 1 aerosol filter	153
Figure 6.16: Fuel 2, ash from preseparator.....	154
Figure 6.16 (cont.): Fuel 2, Preseparator	155
Figure 6.17: Fuel 2, Stage 0.....	156
Figure 6.18: Fuel 2, Stage 4.....	157

Figure 6.19: Fuel 2, Stage 4	158
Figure 6.20: Fuel 2, aerosol filter	159
Figure 6.21: Fuel 2 filter, oversize particles	160
Figure 6.22: Fuel 3, aerosol filter	161
Figure 6.23: Fuel 4, aerosol filter	162
Figure 6.24: Clean (unused) and blank (used) aerosol filters.....	163
Figure 6.25: Fuel 1 ash elemental analysis by EDS, composition variation with particulate matter size.....	164
Figure 6.26: Phase diagram for CaOSiO_2 system (American Ceramic Society, 1964) ..	165
Figure 6.27: Phase diagram for $\text{CaOSiO}_2\text{-Na}_2\text{OSiO}_2$ system (American Ceramic Society, 1964)	166
Figure 6.28: Ternary diagram for the high silica end of $\text{CaO-Na}_2\text{O-SiO}_2$ system (American Ceramic Society, 1964).....	167
Figure 6.29: Composition of aerosol collected on filters, determined by correcting EDS results for background signal from the filter substrate	168
Figure 6.30: Ternary diagram for the high silica end of $\text{K}_2\text{O-Na}_2\text{O-SiO}_2$ system (American Ceramic Society, 1964).....	169
Figure 6.31: Transverse temperature profile by High Velocity Thermocouple at maximum temperature/flow rate settings, test number 101796T.....	171
Figure 6.32: Transverse temperature profile by High Velocity Thermocouple at moderate temperature/flow rate settings, test number 112596T.....	171
Figure 6.33: Transverse temperature profile by High Velocity Thermocouple at minimum temperature/flow rate settings, test number 112096T	172
Figure 6.34: Temperature profile as a function of distance from pulverized fuel injection for three different furnace settings	173
Figure 6.35: Temperature and dilution profiles for sawdust/sanderdust experiments....	174
Figure 6.36: Fuel 1 EAA experiments at highest furnace temperature	175
Figure 6.37: Fuel 2 EAA experiments at highest furnace temperature	176
Figure 6.38: Fuel 3 EAA experiments at highest furnace temperature	177
Figure 6.39: Fuel 4 EAA experiments at highest furnace temperature	178
Figure 6.40: Fuel 1 and 4 EAA experiments at moderate temperature	179
Figure 6.41: Fuel 1 EAA experiments at low furnace temperature	180
Figure 6.42: Fuel 2, 3 and 4 EAA experiments at low furnace temperature.....	181
Figure 6.43: Fuels 1, 2, 3 and 4 cascade impactor data at highest furnace temperature .	182
Figure 6.44: Fuels 1 and 4 cascade impactor data at moderate furnace temperature.....	183

Figure 6.45: Fuels 1, 2, 3 and 4 cascade impactor data at low furnace temperature	184
Figure 6.46: Fuel 1 tests with variable delay tank residence times	185
Figure 6.47: Fuel 1 EAA experiments showing the effect of sample inlet temperature on size distribution	186
Figure 7.1: Example configuration of a sawdust/sanderdust burner used for wood chip drying in a strand board production facility	210
Figure 7.2: Fuel 1 equilibrium calculations for tunnel furnace conditions. Excess oxygen is 7.9% by dry volume, $(\text{Fuel 1 flowrate})/(\text{Total flowrate}) = 0.0085$	211
Figure 7.3: Fuel 1 equilibrium calculations for tunnel furnace conditions, alkali species only. Excess oxygen is 7.9% by dry volume, $(\text{Fuel 1 flowrate})/(\text{Totalflowrate}) = 0.0085$	212
Figure 7.4: Fuel 1 equilibrium calculations for industrial burner conditions. Excess oxygen is 9.3% by dry volume, $(\text{Fuel 1 flowrate})/(\text{Total flowrate}) = 0.094$	213
Figure 7.5: Fuel 1 equilibrium calculations for industrial burner conditions in Blend Chamber, with sulfur and carbon included, and with sulfur and carbon not included, $(\text{Fuel 1 flowrate})/(\text{Total flowrate}) = 0.017$	214
Figure 7.6: Fuel 1 equilibrium calculations for industrial burner conditions in Blend Chamber; sulfur, carbon and chlorine not included, $(\text{Fuel 1 flowrate})/(\text{Totalflowrate}) = 0.017$	215
Figure 7.7: Fuel 2 equilibrium calculations for industrial burner conditions, $(\text{Fuel 2flowrate})/(\text{Total flowrate}) = 0.093$	216
Figure 7.8: Fuel 2 equilibrium calculations for laboratory burner conditions, $(\text{Fuel 2flowrate})/(\text{Total flowrate}) = 0.0068$	217
Figure 7.9: Fuel 3 equilibrium calculations for industrial burner conditions, $(\text{Fuel 3flowrate})/(\text{Total flowrate}) = 0.090$	218
Figure 7.10: Fuel 3 equilibrium calculations for laboratory burner conditions, $(\text{Fuel 3flowrate})/(\text{Total flowrate}) = 0.0081$	219
Figure 7.11: Fuel 4 equilibrium calculations for industrial burner conditions, $(\text{Fuel 4flowrate})/(\text{Total flowrate}) = 0.087$	220
Figure 7.12: Fuel 4 equilibrium calculations for laboratory burner conditions, $(\text{Fuel 4flowrate})/(\text{Total flowrate}) = 0.0062$	221

Figure 7.13: Predicted aerosol composition vs. measured aerosol composition. A comparison based on raw fuel composition, aerosol ash composition and equilibrium composition.	222
Figure 7.14: Limit cases of homogeneous condensation and heterogeneous condensation in a super saturated environment.	223
Figure 7.15: Condensation regimes for a system containing NaCl vapor at 14 Pa partial pressure.	224
Figure 7.16: Alkali vapor capture by heterogeneous particles as a function of system quench rate for an initial vapor pressure of 9.62 Pa, Fuel/Total Mass =.094. Heterogeneous particle size and number densities: $dp_1 = 7.16 \mu\text{m}$, $4.74\text{e}9 \text{ \#/kgFuel}$; $dp_2 = .669 \mu\text{m}$, $2.64\text{e}12 \text{ \#/kgFuel}$	225
Figure 7.17: Vapor capture by heterogeneous particles as a function of quench rate for Fuel 1, Fuel/Total Mass =.094. Heterogeneous particle size and number densities: $dp_1 = 7.16 \mu\text{m}$, $4.74\text{e}9 \text{ \#/kgFuel}$; $dp_2 = .669 \mu\text{m}$, $2.64\text{e}12 \text{ \#/kgFuel}$	226
Figure 7.18: Change in Alkali vapor pressure with quench rate, for Fuel 1 in Industrial Blend Chamber and Laboratory Furnace. Heterogeneous particle size and number densities: $dp_1 = 7.16 \mu\text{m}$, $4.74\text{e}9 \text{ \#/kgFuel}$; $dp_2 = .669 \mu\text{m}$, $2.64\text{e}12 \text{ \#/kgFuel}$	227
Figure 7.19: Comparison of heterogeneous collection efficiency as a function of Quench Rate and dilution ratio for Fuel 1. Heterogeneous particle size and number densities: $dp_1 = 7.16 \mu\text{m}$, $4.74\text{e}9 \text{ \#/kgFuel}$; $dp_2 = .669 \mu\text{m}$, $2.64\text{e}12 \text{ \#/kgFuel}$	228
Figure 7.20: Fuel 1 aerosol coagulation in industrial blend chamber at initial conditions	229
Figure 7.21: Fuel 1 aerosol coagulation in industrial blend chamber at 0.02 seconds ...	229
Figure 7.22: Fuel 1 aerosol coagulation in industrial blend chamber at 0.04 seconds ...	229
Figure 7.23: Fuel 1 aerosol coagulation in industrial blend chamber as a function of time.....	229
Figure 7.24: Fuel 1 aerosol coagulation in industrial blend chamber for long residence	230
Figure 7.25: Fuel 1 aerosol coagulation in industrial blend chamber, comparing limit cases of plug flow versus perfect mixing.....	230
Figure 7.26: Fuel 1 aerosol coagulation in the EAA delay tank as calculated by MAEROS2	231

Figure 7.27: Fuel 1 aerosol coagulation in the EAA delay tank as measured experimentally.....	231
Figure A.1: Approximated mass/size distribution for Fuel 1 and Fuel 2 based on experimentally determined size distributions	254
Figure A.2: Approximated mass/size distribution for Fuel 3 and Fuel 4 based on experimentally determined size distributions	255
Figure B.1: Air Supply Schematic	257
Figure B.2: Natural Gas Supply Schematic.....	258
Figure B.3: Water Supply Schematic	259
Figure C.1: Super-Isokinetic sampling efficiency.....	263
Figure C.2: Isokinetic sampling efficiency with instrument error included	263

LIST OF TABLES

Table 2.1: Proximate and ultimate analysis for the recommended standard suite of U.S. research coals (from Smith and Smoot, 1990)	22
Table 2.2: Ash composition of the recommended standard suite of U.S. research coals (from Smith and Smoot, 1990)	23
Table 2.3: Alkali-metal species in low- and high-rank coals(from Raask, 1985, Table 15.5)	24
Table 2.4: Ash composition of typical biomass fuels, expressed as oxides in weight percent (from Osman and Goss, 1983)	25
Table 2.5: Ash chemistry of some typical biomass fuels (from Baxter et al., 1996).....	26
Table 2.6: Fuel properties of eastern Canadian bark (from Bryers, 1996)	27
Table 5.1: Proximate and ultimate analysis of pulverized coals (Adapted from Boni et al., 1990, Table 3-8 (a))	76
Table 5.2: Ash chemistry of pulverized coals (Adapted from Boni et al., 1990, Table 3-8 (b)).....	77
Table 5.3: Conventional analysis and ICP metals analysis of aerodynamically sized Upper Freeport pulverized coal	78
Table 5.4: Conventional analysis and ICP metals analysis with weak acid solution of aerodynamically sized Upper Freeport pulverized coal	79
Table 5.5: Upper Freeport froth floatation cleaning	81
Table 5.6: Pulverized coal test matrix.....	81
Table 5.7: Composition of artificial char	101
Table 5.8: Artificial char test matrix.....	101
Table 6.1: Analysis of As Received sanderdust and sawdust samples.....	140
Table 6.2: Screened sawdust/sanderdust test matrix	143
Table 6.3: Test conditions for Screened sawdust/sanderdust experiments	143
Table 6.4: Comparison of alkali content to potential anion content in unburned fuels and aerosol ash.....	168
Table 6.5: Milled sawdust/sanderdust test matrix	170
Table 7.1: Comparison of typical laboratory conditions to typical industrial burner conditions.....	210
Table 7.2: Simplified residual particle size distributions used for modeling	210

Table 7.3: Saturation Ratio ($S=P_{\text{vap}}/P_{\text{sat}}$) condensation regimes for systems containing only vapor phase, and systems containing foreign particles.....	223
Table A.1: Averages of mass collected on stages for screened sawdust/sanderdust experiments.....	254
Table E.1: Test 08089501.....	266
Table E.2: Test 08099501.....	267
Table E.3: Test 08169501.....	268
Table E.4: Test 08169502.....	269
Table E.5: Test 08169503.....	270
Table E.6: Test 10139501.....	271
Table E.7: Test 10169501T.....	272
Table E.8: Test 10269501.....	273
Table E.9: Test 10269502.....	274
Table E.10: Test 10319501.....	275
Table E.11: Test 11029501.....	276
Table E.12: Test 11079501.....	277
Table E.13: Test 11229501.....	278
Table F.1: Test Log for milled sawdust/sanderdust experiments.....	280
Table F.2: Test 08019601.....	281
Table F.3: Test 08069601.....	282
Table F.4: Test 08129601.....	283
Table F.5: Test 08149601.....	284
Table F.6: Test 09039601.....	285
Table F.7: Test 09099601.....	286
Table F.8: Test 10089601.....	287
Table F.9: Test 10149601.....	288
Table F.10: Test 101796T.....	289
Table F.11: Test 10179602.....	291
Table F.12: Test 10219601.....	292
Table F.13: Test 10229601.....	293
Table F.14: Test 10249601.....	294
Table F.15: Test 11079601.....	295
Table F.16: Test 11129601.....	296
Table F.17: Test 11139601.....	297
Table F.18: Test 11149601.....	298

Table F.19: Test 11149602	299
Table F.20: Test 11159601	300
Table F.21: Test 11169601	301
Table F.22: Test 11169602	302
Table F.23: Test 11179601	303
Table F.24: Test 112096T.....	304
Table F.25: Test 11219601	306
Table F.26: Test 11219602	307
Table F.27: Test 11219601	308
Table F.28: Test 11219606	309
Table F.29: Test 11229601	310
Table F.30: Test 11229602	311
Table F.31: Test 11229603	312
Table F.32: Test 11239601	313
Table F.33: Test 11239602	314
Table F.34: Test 11239603	315
Table F.35: Test 112596T.....	316
Table F.36: Test 11269601	318
Table F.37: Test 11279601	319
Table F.38: Test 11279602	320
Table F.38: Test 11279603	321
Table G.1: Test log for pulverized coal experiments.....	322
Table G.2: Test 05049401	323
Table G.3: Test 05059401	324
Table G.4: Test 05069401	325
Table G.5: Test 05109401	326
Table G.6: Test 05119401	327
Table G.7: Test 05129401	328
Table G.8: Test 05139401	329
Table G.9: Test 05209401	330
Table G.10: Test 05219401.....	331
Table G.11: Test 05239401.....	332
Table G.12: Test 05249401.....	333
Table G.13: Test 05269401.....	334
Table G.14: Test 05269402.....	335

Table G.15: Test 05279401.....	336
Table G.16: Test 05319401.....	337
Table G.17: Test 06019401.....	338
Table G.18: Test 06029401.....	339
Table G.19: Test 09089401.....	340
Table G.20: Test 09099401.....	341
Table G.21: Test 09159401.....	342
Table G.22: Test 09169401.....	343
Table G.23: Test 09219401.....	344
Table G.24: Test 09239401.....	345
Table G.25: Test 10069401.....	346
Table G.26: Test 10079401.....	347
Table G.27: Test 10119401.....	348
Table G.28: Test 10139401.....	349
Table G.29: Test 10149401.....	350
Table G.30: Test 10169401.....	351
Table G.31: Test 10219401.....	352
Table G.32: Test 10259401.....	353
Table G.33: Test 11039401.....	354
Table G.34: Test 11049401.....	355
Table G.35: Test 11079401.....	356
Table G.36: Test 11109401.....	357
Table G.37: Test 11119401.....	358
Table G.38: Test 11149401.....	359
Table G.39: Test 11149402.....	360
Table G.40: Test 11169401.....	361
Table G.41: Test 11219401.....	362
Table G.42: Test 11289401.....	363
Table G.43: Test 12029401.....	364
Table G.44: Test 12079401.....	365
Table H.1: Test log for artificial char experiments	366
Table H.2: Test 02039501	367
Table H.3: Test 02069501	368
Table H.4: Test 02149501	369
Table H.5: Test 02179501	370

Table H.6: Test 02219501	371
Table H.7: Test 02239501	372
Table H.8: Test 02279501	373
Table H.9: Test 03019501	374
Table H.10: Test 03029501.....	375
Table H.11: Test 03039501.....	376
Table H.12: Test 03039502.....	377
Table H.13: Test 03069501.....	378
Table H.14: Test 03069502.....	379
Table H.15: Test 03079501.....	380
Table H.16: Test 03079502.....	381
Table H.17: Test 03129501.....	382
Table H.18: Test 03129502.....	383
Table H.19: Test 03139501.....	384
Table H.20: Test 03149501.....	385
Table H.21: Test 03149502.....	386
Table H.22: Test 03149503.....	387
Table H.23: Test 03169501.....	388
Table H.24: Test 03169503.....	389
Table H.25: Test 03169504.....	390
Table H.26: Test 03179501.....	391
Table H.27: Test 03179502.....	392

LIST OF VARIABLES

p_{sat} = plane surface saturation pressure

p_d = curved surface saturation pressure

\bar{v} = specific volume of liquid

σ = surface tension

T = temperature

\bar{R} = ideal gas constant

p_1 = partial pressure of monomer

n = monomers per volume

m = mass of molecule

k = Boltzmann constant

v_m = monomer volume

s = saturation ratio

ACKNOWLEDGMENTS

The author wishes to sincerely thank Professor John Kramlich for his guidance, wisdom, support and patience. A student could not ask for a finer mentor.

The author would also like to thank George Andexler, Jerry Berg, Tom Collins, Professor Joe Firey, Jean Hamlin, John Lee, Rebecca Sliger, Rob Steele and Travis Stevens. All of these individuals aided the author much more than one could hope for or expect, and for that the author will always be grateful.

This research was generously funded by The Weyerhaeuser Company, and the U.S. Department of Energy.

DEDICATION

To my wife, Jean, who keeps me strong

INTRODUCTION

Coal and biomass fuels contain inorganic material that forms ash when burned. These inorganic components, which may be in the form of clays, sand and mineral nutrients, are transformed physically and chemically during combustion. The resulting ash often leads to significant obstacles for those who endeavor to design efficient, robust, and safe energy conversion facilities.

Some consequences of ash generation include:

- Slagging, fouling, and corrosion. *Slagging* is typically associated with flowing or stationary ash deposits near the primary combustion zone. Deposition is via settling or impaction. *Fouling* is more common in the heat recovery zone and the flue gas pathway. It usually occurs via impaction of gas-borne particulate matter or by thermophoresis. *Corrosion* is often a gas-phase problem, but chemically reactive ash can also lead to degradation of furnace surfaces. All of these issues affect energy conversion efficiency, facility maintenance, and the lifetime of the plant.
- Environmental and health hazards. Uncontrolled or under-controlled emissions result in particulate matter escape from the facility. This leads to various health risks and damage to the environment, depending on the composition and mobility of the particulate matter. In particular, the health risks associated with fine particulate matter has become widely recognized in recent years, and have led to regulations on particulate matter less than 2.5 μm in diameter (*i.e.* PM_{2.5} regulations, EPA, 1997).

Thus, the fate and behavior of the mineral matter associated with solid fuels, particularly coal, has been a topic studied by researchers for decades.

Two general mechanisms of ash production are known: The first is the residual mechanism in which ash is formed as a residue as the char particle burns away. Factors that govern the fate of mineral matter processed through this mechanism include whether the char fragments on burning, the degree to which minerals are released at the char surface during burning, and the level of mineral coalescence and melting that take place. This mechanism normally yields ash particles larger than 0.5 μm (*e.g.* Flagan and Friedlander, 1978). The second mechanism is a vaporization/condensation process. Mineral matter is vaporized in a

high temperature region, and eventually condenses either homogeneously (forming nuclei) or heterogeneously (*i.e.* on a surface). The nuclei will eventually coagulate by Brownian motion to form larger particles, typically agglomerations with diameters on the order of 0.1 μm . Obviously, there is interaction between these general mechanisms, and there are a number of sub-mechanisms that reside within these overall processes.

Modern combustion facilities use pollution control equipment to capture post-combustion ash. Capture of large ash particles can often be accomplished using gravitational settling or cyclones. These methods are less effective as particle diameter (*i.e.* settling velocity) decreases.

Electrostatic precipitators and fabric filter devices are common ways to control fine flue-borne material. Unfortunately, both Electrostatic precipitators and fabric filters have reduced efficiencies (McCain *et al.*, 1975, Friedlander, 1977) in the size range of particles that are very efficiently captured in the alveolar region of the human lung (Morrow, 1964). It has been estimated that 50% of the particles between 0.01 μm and 0.1 μm that enter the pulmonary compartment will be deposited there (Burchard, 1974).

The risks associated with the small particles is compounded because they present condensation surfaces for volatile, toxic metals. Although only a small fraction of the total ash mass may be sub-micron in size, the high surface to volume ratio for these small particles results in large surface areas. Hence, volatile toxic metals, such as arsenic and selenium, are likely to be deposited on these particles upon condensation (Flagan and Friedlander, 1978).

Aerosols have tended to create problems as new and complex pollution control technologies are integrated into industrial plants. An example can be taken from the wood products industry: Sawdust and sanderdust, a by-product of board manufacturing, is sometimes used as a fuel for drying and curing operations. This fuel is combusted in a suspension burner, mixed with forced air to regulate the temperature, and channeled through a wood chip dryer. The hot gas stream dries the chips and picks up moisture and organic vapors in the process. Cyclones and an electrostatic precipitator remove the majority of the ash after the drying operation. The flue gas is then routed through either a catalytic or non-catalytic oxidizer to remove the organic vapors. In some facilities, the particulate matter not captured by the control systems has damaged or degraded these oxidizers. Catalytic system

are deactivated by a physical masking of the catalyst surface. In non-catalytic systems, the ceramic recuperative heat exchange surfaces are destroyed by interaction with the mineral matter. The process is complex, and it appears to include contributions from (1) the ash from the primary flame, (2) reactions between the ash and organic vapors in the curing system, and (3) processes occurring in the electrostatic precipitator.

The underlying mechanisms that give rise to these practical problems obviously depend on the characteristics of the ash generated by these biomass fuels. Sawdust and sanderdust are important fuel sources in the wood products industry and have unique mineral compositions, including very high alkali metal concentrations and an almost complete lack of the aluminosilicate minerals that are so common in coals. The behavior of this combination of minerals during combustion has not been explored in detail. The principal goal of this research is to understand the mechanisms that govern the transformation of these minerals into ash during combustion. These mechanisms provide the means of linking mineral composition, fuel characteristics, and combustion environment with the characteristics of the product ash that are important in the industrial system (*e.g.*, size distribution, and the distribution of the various ash elements across the range of particle sizes).

A secondary goal of this research is the investigation of aerosol formation in coal combustion. Previous research suggests that aerosol yield is enhanced by coal cleaning (Kramlich and Newton, 1994a). Aerodynamically sized coal fractions also exhibit an enhanced aerosol mode (Kramlich and Newton, 1994a). The implication is that coal beneficiation can reduce overall ash yield, but may increase aerosol yield. The coal experiments focus on coal mineral behavior, specifically dealing with certain observations involving the formation of sub-micron aerosols. This portion of the study is undertaken both on its own right, and to serve as a point of comparison for the biomass work.

MECHANISMS OF MINERAL TRANSFORMATIONS IN COAL AND BIOMASS FUELS

Chemical and physical transformations of mineral matter during coal and biomass combustion are of critical concern in practical industrial applications. The minerals in fuels affect the operability of the furnace and contribute to the environmental risk associated with the flue gas. The research community has responded to these technical and environmental challenges with a substantial research output, particularly with respect to mineral transformations in coal combustion. This literature forms the point of departure for the present study, and it is the subject of this chapter.

Section 2.1 describes the sources and form of mineral matter in coal and biomass fuels. Section 2.2 discusses the combustion process, which consists of a series of steps that include drying, devolatilization, char combustion, and burnout. These steps form the background against which the mineral transformations occur. Section 2.3 details the literature on the transformation of various inorganic components during combustion.

2.1 Sources and Form of Mineral Matter in Coal and Biomass Fuels

Coal and biomass are significantly different in their organic composition, and the physical and chemical form of their inorganic constituents. This is a natural and obvious result of the very different histories of these two fuels, and it causes them to generate significantly different ash size distributions and compositions.

An important factor in the ultimate fate of inorganic matter in coal/biomass fuel combustion is the form of the parent inorganic component. Mineral matter can generally be divided into two classifications, *included* (or inherent) and *extraneous* (or excluded, or adventitious).

Included minerals generally refers to inorganic components of the fuel that are contained within the individual organic particles (*i.e.*, the macerals in coal). These are difficult to separate by physical means, and are generally present as small mineral particles (1 to 15 μm) dispersed throughout the organic matrix (Sarofim, 1977). This class also includes minerals that are chemically bound to the organic matter; sometimes referred to as “atomically dispersed” minerals.

Extraneous generally refers to discrete mineral particles (typically on the order of tens of microns or larger in diameter) either loosely bound or physically separated from the macerals. The literature disagrees somewhat on the precise definition of inherent and extraneous minerals, and thus there is not a complete consensus of the exact boundary dividing these two classes (Baxter, 1993; Wall, 1992).

In general, pulverized coal ash research is virtually inseparable from the study of its included and extraneous mineral matter. Biomass ash research, on the other hand, is almost exclusively involved with included minerals, more explicitly the fuel's atomically dispersed inorganic composition, usually in the form of plant nutrients. This is especially true for biomass fuels that are carefully harvested and collected, so that extraneous soil contamination is minimized.

2.1.1 Pulverized Coal Composition and Structure

Detailed information on coal formation mechanisms and on coal composition is covered in a number of sources (for example, Berkowitz, "Introduction to Coal Technology" ; Stach et al, "Stach's Textbook of Coal Petrology"). Only a brief overview of this large literature is presented here.

Coal is formed from biomass in a process taking up to 300 million years, depending on biomass composition, local climate and geological conditions. Diagenesis, the biochemical breakdown of vegetation, is the first phase of coal formation. Although diagenesis occurs over a short period of geologic time, it is during this stage of coal formation that biomass (including its inorganic components) becomes mixed with extraneous minerals via erosion, flooding, wind, and other transport mechanisms. Diagenesis is terminated by the flooding of the organic bed, followed by the deposit of an overlayer of silt that seals the organic material from further microbial activity (Berkowitz, 1994). A common feature of diagenesis is increasing aromaticity and acidity (Berkowitz, 1994). The metamorphic stage, driven by compression from siltation and heat flow from the interior of the earth, increases carbon content at the expense of oxygen, and eventually hydrogen.

The degree of metamorphosis is quantified in various ways, with the ASTM (1966) classification scheme commonly used in North America. The ASTM ranks coal by fixed

carbon content for fixed carbon greater than 69%, and by calorific heating value for fixed carbon less than 69%. Fixed carbon content is defined as:

$$(\text{Fixed Carbon})\% = 100\% - (\text{Moisture})\% - (\text{Volatile Matter})\% - (\text{Ash})\%$$

Moisture, volatile matter, and ash yield are all determined by specific empirical tests using carefully controlled atmospheres, temperatures, and heating rates (ASTM, 1966). In order of increasing rank, classes are lignitic, subbituminous, bituminous, and anthracite (ASTM, 1966). Some researchers also include peat as a classification, considering it to be the lowest rank of coal.

A problem plaguing coal researchers is the wide range of properties exhibited by the various coals. This makes it impossible to choose an “average” coal for research purposes. Instead, a suite of research coals have been proposed that cover the range of properties presented by most of the economically important deposits. Examination of the properties of these coals provides the best opportunity for developing generalizations about coal mineral makeup.

Smith and Smoot (1990) proposed such a set of standard research coals, selected using the following criteria:

“(1) representative of a variety of characteristics, ranks and properties, (2) available analysis of chemical and physical properties with wide property variations among coal types and ranks, (3) availability from major producing seams, (4) future production expected, (5) wide geographical distribution within the U.S., (6) used in previous combustion work, (7) common to existing prominent coal banks, and (8) availability of small, controlled samples.”

Table 2.1 shows the proximate and ultimate analysis for these research coals, as compiled by Smith and Smoot (1990). Most are bituminous coals, as is about 50% of the U.S. demonstrated reserve base (Energy Information Administration, 1982). Note that ash yield varies from 4.1% to 19.4% (as received basis), illustrating the variability of U.S. coals. Table 2.2 shows ash composition of these research coals. Although ash composition varies, note that coal is generally high in silicon, aluminum, calcium and iron - which are, not coincidentally, among the most abundant elements found in the earth’s crust (Lide, 1994).

The most common noncombustible mineral species in coal is aluminosilicate clay, making up 60% to 80% of mineral matter in a typical coal (Mackowsky, in Stach *et al.*, 1982). It can be in the form of finely distributed particles, on the order of a few microns in diameter (Mackowsky, in Stach *et al.*, 1982) to macroscopic scales. Experiments performed by Raask (1985) with milled coals showed mineral enrichment with decreasing coal particle diameter, primarily driven by aluminosilicate concentrated in coal particles below 20 μm . Clay minerals are typically represented by illites (potassium aluminosilicates), kaolinite (aluminosilicate), and montmorillonite ($((1-x)\text{Al}_2\text{O}_3 \cdot x (\text{MgO,NaO}) \cdot 4\text{SiO}_2 \cdot \text{H}_2\text{O})$). (Berkowitz, 1994).

Silica, as quartz, also can be a significant fraction of coal, making up 15% to 20% of the ash yield. (Berkowitz, 1994). Mackowsky (in Stach *et al.*, 1982) notes that quartz usually is present with other finely dispersed minerals, likely from weathering of feldspar and mica.

Together, aluminosilicates and quartz make up 60 to 90% of total mineral matter in coal (Raask, 1985).

Carbonates are generally secondary to clays in abundance (Mackowsky, in Stach *et al.*, 1982). Typical forms are calcite (CaCO_3), siderite (FeCO_3), dolomite ($\text{CaCO}_3 \cdot \text{MgCO}_3$), and ankarite ($2\text{CaCO}_3 \cdot \text{MgCO}_3 \cdot \text{FeCO}_3$). Siderite and dolomite are deposited/formed in the first stage of coalification (Mackowsky, in Stach *et al.*, 1982), implying a fine grain size and inherent association, while calcite and ankarite are more commonly deposited during the metamorphic stage along cracks and seams (Mackowsky, in Stach *et al.*, 1982), implying a coarser and larger grain size.

Sulfur in coal can be found organically combined, or as mineral components. Non-organically bound sulfur is typically in the form of a sulfide - pyrite or marcasite (both approximately FeS_2) (Raask, 1985). It can occur as micron sized crystals, 10 μm to 40 μm framboids, or as boulder sized deposits in unprocessed coal (Calkins, 1994).

Critical to this research is alkali metal content in the parent fuel. The presence of alkali metal species in coal is summarized by Raask (1985), as shown in Table 2.3. Chlorides, sulfates, and nitrates are usually found only in trace quantities. Chlorides present in significant quantities are associated with infiltration from salt deposits. (Mackowsky, in Stach *et al.*, 1982).

2.1.2 Biomass Composition and Structure

Biomass fuel composition and combustion has not been as thoroughly reviewed as coal. Baxter *et al.* (1996) present some comprehensive data concerning the behavior of the inorganic material in biomass when fired under industrial combustor conditions. The reader may also consult Bryers (1996) for a review of the state of the art in biomass ash transformations.

The majority of biomass is composed of cellulose, hemicellulose and lignin, with wood as an obvious example (Theander, 1982). Cellulose and hemicellulose are polysaccharides (long chain carbohydrates) that make up plant cell walls; these make up 60 to 75% of the dry mass in wood (Theander, 1982). Cellulose and hemicellulose are less than 50% carbon and 50% oxygen by weight (Glasser, 1982). Lignin is 20 to 30% dry mass in wood, and provides a plant with structural support, among other properties. Lignin is more than 60% carbon and about 30% oxygen (Glasser, 1982). Hence, biomass overall has a high atomic oxygen to atomic carbon ratio, and a high atomic hydrogen to atomic carbon ratio. Baxter (1993) estimates a hydrogen to carbon ratio of 1.2 to 1.8 and an oxygen to carbon ratio of about 0.4 to 0.8 for biomass fuels. This information supports the view that biomass is composed of reactive functional groups, in contrast to more tightly bound, less reactive aromatic rings in coal.

According to Bryers (1996), 80% of the biomass used for steam generation is wood based, while 20% is agricultural waste (straw, manure, nutshells, and other material). Unlike coal, biomass ash yield is derived primarily from organically bound components, rather than from mineral based inorganics. If clay minerals are present, they are in the form of discrete contaminates, usually acquired during harvest or processing. Inorganic components vary significantly with the type of biomass material and soil conditions (*i.e.* nutrient content), but some general observations are possible.

Biomass fuels generally contain calcium, silicon, and potassium. As pointed out by Bryers (1996), these elements play specific roles in plant nutrition. Grasses and straws are generally high in silica and potassium, and low in calcium, based on the research by Osman and Goss (1983). Bryers analyzed 14 eastern Canadian barks and found these samples to

be rich in calcium (43% to 68% of ash as CaO, 1.4% to 17.8% CaCO₃), silicon (1.5% to 39% as SiO₂) and potassium (2.6% to 10.1% as K₂O).

Other inorganic components that may have significant concentrations are sodium, iron, phosphorous, chlorine, and aluminum. Sodium is toxic to plants, but in low concentrations can substitute for potassium (Bryers, 1996). High sodium concentrations are often caused by salt water intrusion or as a process additive (Bryers, 1996). Aluminum is usually an indicator of fuel contamination by extraneous soil. Iron is usually found in leaves, and participates in transport processes in the plant and is critical for photosynthesis (Baxter *et al.*, 1996). Phosphorous can be about 10% of ash (measured as P₂O₅) in alfalfa, cotton gin trash, barley straw, and corn stalks (Osman and Goss, 1983).

The total ash yield from biomass fuels is variable, ranging from 1.5% for olive pits to 19% for rice straw, based on proximate analysis at 950 C (Bryers, 1996). Ash yields and compositions can be very deceptive when conducted on high alkali content biomass fuels. The low boiling temperatures of some alkali minerals can result in vaporization and loss of some alkali yield if ashing is performed at or above the traditional ASTM ashing temperature of 750 C, as discussed by Bryers (1996).

Elemental composition of some typical biomass fuels are shown on Tables 2.4 and 2.5. Biomass fuels analyzed by Osman and Goss (1983), shown in Table 2.4, were ashed at 575 C prior to elemental analysis. It should be noted that their analysis neglected Al, Cl, Ti, V Cr, Mn, Ni, Cu Br, Ba and Pb, and assumed that all detected elements were in the form of oxides. Hence Osman and Goss did not achieve mass closure (right most column in Table 2.4). Biomass fuels analyzed by Baxter *et al.* (1996), shown in Table 2.5, were ashed at 500 C. Note that mass closure is not complete on these ash samples either, implying that other elements not detected by the test method are present (such as aluminum and chlorine), and the elements are not necessarily in oxide form in the ash.

Ash transformations during sawdust/sanderdust combustion is the focus of this dissertation, so examples of proximate and elemental analysis of similar wood fuels are shown in Table 2.6. Proximate ashing temperature of 950 C is implied by Bryers (1996) for wood bark fuels shown in Table 2.6.

It should be noted that sawdust/sanderdust used in the current research is a byproduct of strand board production. These wood-based fuels will contain an additional inorganic

fraction from binding resins introduced during the manufacturing process. This will be discussed in some detail with the experimental results.

2.1.3. Summary of Coal and Biomass Properties

Comparing biomass and coal directly, some generalizations can be made:

- Coal consists predominantly of carbon in the form of linked aromatic rings, in which oxygen to carbon ratio and hydrogen to carbon ratio decrease with increasing rank (Baxter, 1993). Biomass, with wood as an example, has a high oxygen to carbon ratio and high hydrogen to carbon ratio. These compositions lead to generally higher heating values for coal, and higher organic volatility for biomass fuels.
- Coal inorganic content is dominated by geologic minerals, deposited and homogenized by forces such as erosion, compaction, heating. Hence, it is made up of clays, silica, some carbonates, and pyrites. Alkali metal content is low, and is generally associated with salts and carbonates in low rank coal, and mainly silicates in higher rank coals. Mineral matter content ranges from about 5% to about 20%.
- Biomass inorganic content is mainly comprised of elements necessary for plant growth, assuming a clean (*i.e.* low soil content) source. Well dispersed silicon, calcium and potassium are primary constituents. Alkali metal content can be high, with sodium particularly high in shells, pits and some woods. Mineral matter content ranges from about 1% to 20%.

2.2 Combustion of Pulverized or Finely-Divided Solid Fuel

Much of the research concerning pulverized fuel combustion and mineral matter transformations has focused on coal. Pulverized coal and sawdust/sanderdust combustion have many common features. Thus, we describe the combustion process from a coal perspective, with exceptions and modifications noted for biomass as required. The discussion is also limited to fuel lean combustion of a pulverized or finely-divided fuel in a suspension environment.

Following the review articles by Saxena (1990), Anthony and Howard (1976) and modern interpretations by Niksa (1996), coal can be thought of as a polymer consisting of aromatic ring structures connected by aliphatic linkages and bonds containing O, S, and N. Heating induces a competitive process in which these links are the center of action. The heating either cleaves the bond, tending to release the aromatic “monomer” as a primary tar, or it generates a refractory char link that joins the two aromatic structures together permanently. The latter case is accompanied by the release of noncondensable gases (H_2 , CO, CO_2 , H_2O , and light hydrocarbons), and the residue becomes char. (Char is generally stable to thermal attack, only yielding to oxidation.) The tar is capable of undergoing secondary pyrolysis on the porous surface of the char. Alternately, it is released, where further reactions condense it into soot with a further release of noncondensable gases. This scenario completes the partitioning of the original coal into a refractory char particle, soot, and noncondensable gases (the “volatile matter”). This event is kinetically controlled for small particles (usually $<100\ \mu\text{m}$) and it occurs on the order of tens of milliseconds.

With the above model as our road map, pulverized or finely-divided fuel combustion can be divided into stages: Drying, devolatilization, char combustion, and burnout. These stages are briefly discussed below.

2.2.1 Drying and Devolatilization

Pulverized fuel introduced into a combustion environment undergoes rapid heating. Free water is driven off (drying), and volatile matter is liberated by thermal decomposition (devolatilization). Literature suggests that the devolatilization process does not affect the phase or chemical composition of mineral matter for two reasons: First, devolatilization times are typically short compared to those of char combustion. For coal particles less than $100\ \mu\text{m}$ in diameter (*i.e.* pulverized coal), the total combustion time is on the order of 1 second or less, with a devolatilization time of 0.1 second or less (Howard, 1981). Secondly, the particle temperature is most likely too cool for mineral matter liquification/vaporization. Endothermic cracking and vaporization of the volatile organic species is thought to suppress the particle temperature until devolatilization is complete.

Devolatilization can induce particle breakup (Mitchell and Akanetuk, 1996), resulting in faster burnout of residual carbon. Rapid internal generation of noncondensable volatiles,

coupled with the formation of a plastic metastate is thought to account for devolatilization-induced fragmentation.

Biomass devolatilization has not been as extensively studied as coal devolatilization. Biomass can lose more than 90% of its mass by devolatilization, owing to high hydrogen to carbon ratios, high oxygen to carbon ratios and low aromaticity (Baxter, 1993). A fraction of the inorganic material in biomass may be liberated by convective transport during devolatilization, according to Baxter (1993). Wornat *et al.* (1995) saw very little evidence of inorganic loss during devolatilization in experiments with southern pine wood and switchgrass. Wornat *et al.* (1995) attributed this to the endothermic nature of devolatilization suppressing the particle internal temperature, such that metal vaporization temperatures are not attained during devolatilization.

2.2.2 Char Combustion and Burnout

The fuel particle remaining after devolatilization is referred to as char, and is composed primarily of carbonaceous material and minerals. Review articles by Essenhigh (1981), Mulcahy and Smith (1969) and Saxena (1990) provide details on the char combustion process.

Char combustion is a heterogeneous reaction, which is fundamentally a conversion of bound carbon with freestream oxygen to form CO₂ (*e.g.*, see Glassman (1987)).



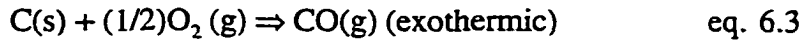
The details of this conversion, as well as the study of simultaneous and competing chemical reactions between other chemical species present, has resulted in very extensive literature.

Char combustion can be diffusion limited or kinetically limited. One diffusion limited hypothesis is known as the two-film model, and is shown in Figure 2.1.

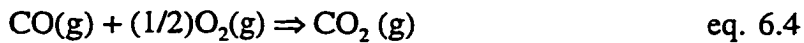
In the two-film model, as described by Saxena (1990), CO is the primary reaction product at the particle surface, via the reaction:



Depending on the diameter of the char particles and the combustion conditions, CO may also be formed by:



CO diffuses outward, where it reacts with O₂ to form CO₂. Hence, the second film is CO oxidation:



One half of the resulting CO₂ diffuses away from the particle and one half diffuses back to the particle surface. The CO₂ is reduced at the particle surface to 2CO, and repeats the cycle again. For large particles at high temperatures, the process becomes diffusionally limited. In this case, little O₂ penetrates to the char surface, and Reaction 6.3 is insignificant. As discussed below, for smaller particles in the kinetically-controlled regime, the clear boundaries between the diffusion zones shown in Figure 2-1 become blurred and O₂ can reach the surface.

Following Mulcahy and Smith (1969), the burning rate of char less than 100 μm in diameter, under oxidizing conditions and heating rates typically found in a pulverized fuel combustor, is a kinetically controlled process. This conclusion is drawn from the comparison of the rates of adsorption/desorption of oxides on the char surface versus the mass diffusion rate for a smooth, solid carbon particle. Mass diffusion varies inversely with particle diameter, while the chemical rate is independent of diameter. This naturally leads to a critical diameter (at a given temperature) for which the control mechanism shifts from kinetic control to mass transfer control.

Variations in particle temperature as a function of furnace wall temperature and particle diameter further complicate burning rate estimates. Shaw and Essenhigh (1991) used a two color optical pyrometer in a pulverized coal flame to observe that particulate matter temperature decreased as radiating particle surface area increased in a hot-walled furnace. They concluded that the temperature difference can be traced to the heat balance of a given particle; heat loss via conduction to the gas and loss via radiation to the walls. Their results showed that smaller particles exchange a larger fraction of their energy radiatively than the larger particles. Shaw and Essenhigh contrast their results with those of Mitchell and

McLean (1982), which show larger particles being cooler than small particles in a cold wall environment.

Char porosity has been shown to have a strong influence on char burning behavior (Glassman, 1987). Porosity is typically divided into macropores and micropores. Under kinetically-limited conditions, oxidizing species are able to penetrate the macropores, but not the micropores. This leads to a situation in which the macropores become enlarged due to oxidation, and become avenues for char fragmentation during burnout. The inability of the oxygen to penetrate the micropores generally leaves these internal surfaces under fuel-rich conditions, even when the overall char oxidation is under kinetic control. This provides opportunities for non-volatile mineral oxides (*e.g.* CaO) to be reduced to suboxide and elemental forms (*e.g.* Ca), with a significant increase in volatility. This introduces a mechanism of vaporization for what would normally be considered non-volatile species, as discussed in the next section. Lower rank coal chars tend to possess more macroporosity, and these tend to fragment most severely during char combustion.

In many cases, the char combustion process is interrupted before completion. In particular, modern low-NO_x combustors delay the oxidation of the char, providing it with a longer “soak” time under high temperature, fuel rich conditions. This causes a thermal annealing of the char, resulting in a more crystalline, less reactive surface (Beeley *et al.*, 1996). This leads to higher levels of unburned carbon in the ash.

Details of biomass char combustion are limited compared to coal char combustion. The high volatile organics content of biomass chars suggests high porosity in biomass chars, so its behavior may be considered to be similar to high porosity coal chars.

Although the pathway to burnout only incrementally affects the total energy yield of a given fuel, it is of great significance relative to ash morphology; this is discussed next.

2.3 Fate of Mineral Matter in Combustion

Elemental components of a mineral matter will follow one of two simple pathways: In the first pathway, the material is vaporized and escapes the char particle. This pathway may include obstacles or dead-ends, such as diffusional resistance and capture by eutectic-forming discrete minerals. This is the preferred pathway of many alkali species.

Ultimately, vapor that escapes the particle will recondense on existing particles or surfaces, homogeneously condense, or chemically recombine to form a condensed species.

In the second pathway, mineral matter that has a low vapor pressure remains in the condensed phase. This mineral matter may stay in a solid form, become somewhat mobile in a melt phase, recombine with other non-volatiles, and/or capture volatile minerals attempting to escape the particle. This pathway is often dominated by alumino-silicate minerals in coal combustion. Although conceptually straight-forward, the details of these pathways are very complex.

Many mechanisms influence the transformations of mineral matter into the various forms of ash. These mechanisms, discussed below, exert a strong influence on both final composition and size distribution. Detailed reviews are also available elsewhere (*e.g.* Wall, 1992; Bryers, 1996).

2.3.1. Vaporized Mineral Matter and Capture Mechanisms

Work by a number of researchers shows that the fate of alkali mineral matter depends on both the original form of the alkali in the fuel, and the nature of the other mineral matter present. The research described in the following paragraphs paints an overall picture in which alkali minerals can either be vaporized, or they can be captured by other minerals. In the latter case, the “capture” is essentially the formation of an alkali-mineral complex within which the vapor pressure of the alkali is suppressed to the point that minimal vaporization occurs. The tendency to form these complexes is governed by both the chemical composition (*e.g.*, the tendency of the minerals to form low melting eutectics) and physical properties (*e.g.*, the dispersion of the mineral inclusions in the char, or over the char surface). This is a very complex problem.

Research by Neville and Sarofim (1985) demonstrates that sodium organically bound in the coal matrix, or as halide (NaCl), is volatile under combustion conditions, while sodium that is bound with silica minerals is much less volatile. Neville and Sarofim burned four coals at 1750K and 20% O₂. Sodium fraction appearing as fume was greatest for coals containing mainly organically bound sodium. Sodium fraction appearing as fume increased with Cl/Na ratio, and decreased with Si content. It was also found that organically bound sodium vaporization decreased with increasing combustion temperature. The latter

observation mirrors the increased mobility of sodium within the silica particles as temperature is increased. This mobility prevents the surface of the silica particles from becoming saturated in sodium, which would prevent further absorption.

Sodium capture appears to be a function of its original form (ion-exchangeable *vs.* organically bound) in the pulverized fuel, as can be seen in research performed by Lindner and Wall (1990). Lindner and Wall used Loy Yang brown coal, acid leached to 0.5% ash, as a baseline fuel. This baseline coal was modified with additives to form ion exchangeable sodium with discrete mineral inclusions (NaCl and quartz doping), and organically bound sodium with discrete mineral inclusions (sodium acetate and quartz doping). The doping material and coal were slurried, blended, dried, pulverized, and size fractionated to 63 -90 μm . The burning of these particles in a drop tube furnace at 1000 C, 1200 C and 1400 C revealed the following trends:

- Complexing of Na with quartz to form a silicate was three to five times greater for acetate doped coal than for NaCl doped coal (Lindner and Wall, 1990). Although Lindner and Wall do not directly explain, it is likely that the sodium chloride vapor is favored by equilibrium in the presence of quartz, reducing the availability of sodium for fluxing of the quartz crystal.
- For the NaCl doped tests, 47 to 66% of the sodium that was not complexed with the silica became submicron (0.2 μm to 0.5 μm) NaCl particles. The balance of the non-silica sodium was found as condensed NaCl species on the residual ash particles (Lindner and Wall, 1990). Although not directly stated by the authors, this appears to lend support to the favored equilibrium of vapor NaCl over silica fluxing.

An interesting secondary investigation by Lindner and Wall (1990) involved a doping a coal with NaCl and kaolin (presumably $\text{Al}_2\text{O}_3 \cdot 2\text{SiO}_2 \cdot 2\text{H}_2\text{O}$). This experiment showed that this alumino-silicate clay captured five to eight times more sodium from NaCl, than an equal mass of quartz. Additional fragmentation of kaolin (such that more reactive surface is available) is suggested by Lindner and Wall as a possible explanation.

Gallagher *et al.* (1996) performed experiments with three different coals in a drop tube furnace to investigate sodium transformations as a function of combustion temperature and the form of the sodium in the parent coal. Sodium occurrence was quantified by the ratio

of acid soluble sodium (expressed as an oxide) to alumino-silicate (expressed as oxides of silicon and aluminum). Specifically,

$$\text{Na-Si ratio} \equiv \text{Na}_2\text{O} / (\text{SiO}_2 + \text{Al}_2\text{O}_3).$$

Ash samples were collected by a cascade impactor and afterfilter, and analyzed by for Na, Si, and Al by size cut.

Gallagher *et al.* (1996) burned Kentucky No. 11, a low sodium coal (Na-Si ratio = 0.003, 0.3% Na₂O ash composition) and found that silica was moderately enriched in the small size cuts (<.65 μm), but sodium was not. Changing the peak combustion temperature from 1380 K to 1530K did not significantly change element partitioning. Gallagher *et al.* (1996) postulated that the small amount of vaporized sodium initially available was quickly scavenged by the abundant alumino-silicates.

Tests by Gallagher *et al.* (1996) with Buelah lignite (Na-Si ratio =.21, 6.1% Na₂O ash composition) showed progressive enrichment of Na as particle diameter decreased, as compared to Si and Al. Enrichment in the sub-micron range was attributed to sodium vaporization and nucleation/condensation. Further, Gallagher *et al.* (1996) noted that increasing the peak combustion temperature from 1400K to 1560K resulted in significant sodium reduction in the smaller (≤0.065 μm) size cuts and slight increase in larger size cuts. It was suggested that higher temperature increased the sodium - silicate reaction rate, resulting in an increase in sodium complexing in larger size cuts.

Tests by Gallagher *et al.* (1996) with Loy Yang 2301, a high sodium coal (Na-Si ratio = 1.7, 30.7% Na₂O ash composition), showed progressive enrichment of Na as particle diameter decreased, like Buelah lignite. Increasing peak temperatures from 1530K to 1610K did not significantly change the sodium fraction in the small particle range. It was concluded by Gallagher *et al.* (1996) that inadequate amounts of silica were available to effectively compete for sodium capture.

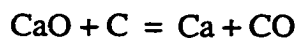
The rate of release of sodium from artificial char has been measured by Srinivasachar *et al.* (1990b). They find that organic Na release, in the absence of other minerals, essentially parallels char burnout. Transport-based models predict that sodium has sufficient diffusivity within the porous char matrix to be fully vaporized before char burnout is

complete (Kramlich *et al.*, 1996). The significantly slower observed vaporization rate has been interpreted as indicating kinetic control. In reality, it appears that sodium is released only as the burning char surface recedes over the site of the sodium. This observation raises issues regarding the physical mechanism of sodium capture by the residual minerals that collect at the surface of the burning char particle, *i.e.*, the proximity of the sodium release to the surface minerals. The issue of whether these conclusions hold true for sodium that is initially NaCl is not known.

Research by Kramlich and Newton (1994a,b) demonstrated that aerosol yield can be influenced by partitioning of the pulverized fuel prior to combustion. Raw pulverized coal was aerodynamically separated into a series of size cuts. Each cut was fired individually and the aerosol yields measured to determine the contribution of each size to the overall aerosol yield of the parent coal. The results showed that each cut generated more aerosol than the parent coal, indicating that the aerosol formation mechanism was modified by the sizing process. It was suggested that the aerodynamic sizing disrupted the contact between the macerals and excluded minerals, leading to a reduction in alkali vapor absorption by the minerals and generating an increased aerosol yield.

In a further series of tests by Kramlich and Newton (1994a,b), the raw coal was divided into a series of fractions by a froth flotation cleaning process. The cleaning process was accomplished in stages, with each stage generating a "float" fraction (the cleaned fuel) and a "sink" fraction (the ash-rich stream). Each new stage used the float fraction from the previous stage, which resulted in one final cleaned fuel, and a series of reject "tailings" from each stage. The combustion of each of the tailings also resulted in an increase in the aerosol yield relative to that of the unmodified coal. The sole exception was the tail from the first stage, which was the richest in mineral matter. This cut showed a significantly lower aerosol yield. Kramlich and Newton (1994a) suggested that this first cut is composed of excluded minerals that suppress the aerosol mode, either through direct absorption of vapor phase minerals or by influencing the char combustion temperature. In summary, a number of factors govern the fate of alkali (capture vs. release). These include the nature of the original bonding, the type of other minerals present, and the proximity of these minerals to the site of alkali release. The temperature also governs the ability of the minerals to absorb alkali into a non-volatile form.

One other mechanism has been proposed to account for the generation of aerosol from non-volatile minerals, such as calcium or aluminum. The fuel-rich interior of a char particle can lead to reactions that reduce refractory oxides to suboxides and elements. An example is:



Elemental calcium will vaporize under char combustion temperatures and escape the particle. Within the boundary layer surrounding the particle the calcium reoxidized to CaO and is instantly in such a high supersaturation that it forms nanoparticles. These grow by Brownian coagulation and generate aerosol particles (Senior and Flagan, 1982; Quann and Sarofim, 1982). This reoxidation/condensation is so fast that a significant fraction of these “short-term” volatile species may be retained at the char interface and become part of the residual ash (Benson *et al.*, 1993). This mechanism was necessary to account for the large number of aerosol particles with refractory oxide cores that were noted in samples from field facilities burning low-alkali coals.

2.3.2 Residual Ash Mechanism

Fragmentation

Minerals that do not vaporize remain with the char particle. Hence, fragmentation of the char particle during combustion is important to establishing the final fate of the minerals. Char break-up separates mineral inclusions that could otherwise interact directly.

Flagan and Friedlander proposed the break-up model (1978) for residual ash formation, in which each coal particle is assumed to produce a fixed number of equal-sized char particles, and each char particle is assumed to burn out leaving its mineral matter as one residual ash particle. Thus, a known original coal size distribution and coal mineral content can be combined with an empirical “breakup number” (*i.e.*, number of char particles per parent coal particle) to derive an expected residual ash size distribution. This simple model has had some success in empirically correlating ash size distributions, but does not address mechanistic issues.

Intensive research into the mechanisms of fragmentation and coal combustion have led to more complex modeling schemes (*e.g.* Miccio and Salatino, 1992). Current research tends to suggest that fragmentation of char is primarily driven by oxidation in macropores of

porous chars (*e.g.* Mitchell and Akanetuk, 1996). Fragmentation of reactive minerals such as pyrite (Baxter, 1990, Srinivasachar *et al.* 1990a) are also a factor.

Fluxing and Coalescence

Residual inorganic material may reach its melting point, or be induced to molten stage by the presence of a fluxing agent. This results in a molten droplet that may collide (and possibly react) with other molten droplets, solid particles or furnace walls. It can also react with volatile species, or solidify in cooler regions of the combustor. Ultimate particle size is usually dependent on original particle size, but can be a complex function of other variables as well, and can result in a size mode larger or smaller than the parent material diameter. Some specific examples are given below.

Helble *et al.* (1990) examined pulverized Kentucky #11 and Illinois #6 coals fired at 7% oxygen and found that agglomeration and coalescence were dominant transformation mechanisms. Coalescence of finely divided illite, kaolinite and quartz resulted in a glassy ash particulate in Kentucky #11, with occasional enrichment with iron and potassium. Some calcite (CaCO_3) fragmentation was evident in the ash size distribution of the calcium carbonate-rich Illinois #6. Almost 90% of the calcite ultimately went to CaO particles, rather than combining with silicate ash particles, in Illinois #6. (Helble *et al.*, 1990).

Experiments with Beulah lignite showed that a high concentration of large ($>40 \mu\text{m}$) pyrite excluded minerals resulted in significant fragmentation, with more pronounced fragmentation as oxygen content was increased from 7% to 21% (Helble *et al.*, 1990). Some limited calcium incorporation into existing kaolinite and other silicates was noted, but calcium did not interact with quartz. San Miguel lignite, a 40% ash coal, showed very little coalescence (Helble *et al.*, 1990). This was attributed to the large mineral inclusion sizes in the parent fuel.

Kramlich and Newton (1994b) investigated the supra-micron ash distribution from pulverized coal, as measured by a cascade impactor and by a laser diffraction size analyzer. The data showed three modes: (1) the aerosol mode ($<0.5 \mu\text{m}$), most likely a result of the vaporization / condensation of volatile species, (2) a residual mode ($>3 \mu\text{m}$), which is a result of coalesced minerals, and (3) a 1-2 μm mode, which was postulated to be liberated mineral inclusions. The basic break-up model (Flagen and Friedlander, 1978) was modified to incorporate measured aerosol formation and a Gaussian size distribution of

break-up particles. The 1-2 μm mode was not predicted by the model, leading Kramlich and Newton (1994b) to conclude that a specific mechanism was responsible. Cleaned coals showed an undiminished 1-2 μm mode, indicating the mode is not from inclusions that can be liberated by grinding. The mode was most prevalent in finely ground coals, suggesting that it is a function of exposed surface area. This suggests that it is caused by shedding of inclusions near the char surface during the initial stages of char burnout.

Zygarlicke *et al.* (1992) used synthetic coal to study Ca-Si-S interactions, particularly as a function of the form of the calcium - inorganic as discrete 10 μm calcite particles, and atomically dispersed as calcium acetate. Experiments at 900 C, 1100 C and 1500 C showed increasing coalescence with temperature in the calcite system. Chemical analysis supports their conclusion that conversion of calcium to calcium silicate increases with temperature. Interestingly, this contrasts with their experiments with Na-Si-S systems, which show decreased sodium silicate interaction as temperature increases and a decrease in coalescence. It was concluded that the calcium remained with the char particle at higher temperatures, to form agglomerating calcium silicate particles, while sodium became more volatile at high temperatures, and escaped the char.

Heat Transfer Surface Deposition

Much of the research associated with residual ash has focused on deposition characteristics on heat transfer surfaces in the form of slag or fouling. Baxter (1992) identifies these mechanisms as inertial deposition, thermophoresis, condensation, and chemical reaction. An in-depth review of heat transfer surface collection mechanisms are beyond the scope of this work. It is worthwhile to note, however, that alkali-silicate interactions can play an important role in the deposition mechanism. For example, thermodynamic calculations by Wibberly and Wall (1981a) show that vapor sodium reacting with silica in the temperature range of 1300 K to 1850 K can form a low viscosity surface layer of sodium silicate on existing silica particles. This surface layer can enhance adhesion of the ash particle upon impact with a heat transfer surface. Below about 1400 K, sulfur reduces the silicate formation. In experiments (Wibberly and Wall, 1981b), formation of a sodium silicate layer on silica particles was verified. This evidence supports the "sticky particle" deposition mechanism. They concluded that a silicate layer of about 1 μm will allow capture of the bulk of impinging fly ash particles.

Table 2.1: Proximate and ultimate analysis for the recommended standard suite of U.S. research coals
(from Smith and Smoot, 1990)

Coal	Source of Data ††	Proximate Analysis *					Ultimate Analysis †						
		Moist rec'd (%)	Ash rec'd (%)	Vol Mat rec'd (%)	F Carbon rec'd (%)	Cal Val rec'd (Btu/lb)	Carbon maf (%)	Hydrogen maf (%)	Nitrogen maf (%)	Sulfur maf (%)	Chlorine maf (%)	Oxygen maf (%)	Cal Val MAF (Btu/lb)
Upper Freeport (MVB)	ANL	1.13	13.03	27.14	58.70	13315	85.50	4.70	1.55	0.74	0.00	7.51	15511
Wyodak (SUBC)	ANL	28.09	6.31	32.17	33.43	8426	75.01	5.35	1.12	0.47	0.03	18.02	12843
Illinois #6 (HVCB)	PSOC 1520	26.69	9.08	40.13	24.10	8277	73.78	2.77	1.11	1.38	0.03	20.95	12868
Pittsburgh (#8) (HVAB)	ANL	7.97	14.25	36.86	40.92	10999	77.67	5.00	1.37	2.38	0.06	13.51	14140
Pocahontas #3 (LVB)	PSOC 1493	9.43	13.74	34.34	42.50	10835	78.07	4.92	1.50	5.87	0.04	9.61	14011
Utah Blind Canyon (HVBB)	ANL	1.65	9.10	37.20	52.05	13404	83.20	5.32	1.64	0.89	0.12	8.83	15018
Upper Kanawha (MVB)	PSOC 1451	2.54	13.32	33.56	50.58	12528	83.26	5.41	1.58	1.58	0.09	8.10	14713
Beulah-Zap (SUBC)	ANL	0.65	4.74	18.48	76.13	14926	91.05	4.44	1.33	0.50	0.20	2.47	15777
Lower Wilcox (LIGA)	PSOC 1508	1.14	7.36	15.52	75.98	14376	91.48	4.38	1.10	0.69	0.06	2.30	15711
Dietz (SUBB)	ANL	4.63	4.49	43.72	47.16	13280	80.69	5.76	1.57	0.37	0.03	11.58	14613
Buck Mountain (AN)	PSOC 1502	8.72	8.20	37.20	45.89	11547	80.04	5.26	1.23	0.56	0.02	12.89	13898
	ANL	2.42	19.36	29.44	48.78	11534	82.58	5.25	1.56	0.65	0.12	9.83	14733
	ANL	32.24	6.59	30.45	30.72	7454	72.94	4.83	1.15	0.70	0.04	20.34	12185
	PSOC 1507	33.57	8.30	27.08	31.06	7060	71.55	5.04	0.95	1.63	0.02	20.81	12144
	PSOC 1443	28.54	15.31	44.17	11.98	7062	72.34	5.21	1.35	0.94	0.07	20.11	12577
	PSOC 1488	23.66	4.08	31.95	40.31	9557	76.00	5.23	0.94	0.53	0.04	17.27	13227
	PSOC 1468	4.51	6.52	3.49	85.48	13128	95.36	1.38	0.84	0.53	0.03	1.86	14772

* Moist = moisture content, Ash = ash content, Vol Mat = volatile matter, F Carbon = fixed carbon content, Cal Val = calorific value, rec'd = analysis on an as-received basis from the mine.

† maf = analysis on a moisture ash free basis, MAF = calorific value on a moisture ash free basis.

†† ANL = data obtained from the Argonne National Laboratory for the PSCP Coals, PSOC = data obtained from the Penn State Coal Data Base for the coal number specified.

Table 2.2: Ash composition of the recommended standard suite of U.S. research coals
(from Smith and Smoot, 1990)

	Upper Freeport (MVB)	Wyodak (SUBC)	Illinois #6 (HVCB)	Pittsburgh #8 (HVAB)	Pocahontas #3 (LVB)	Utah Blind Canyon (HVBB)	Beulah- Zap (SUBC)	Lower Wilcox (LIGA)	Dietz (SUBB)	Buck Mountain (AN)
Source of Data	ANL	ANL	Penn State	Penn State	Penn State	ANL	Penn State	Penn State	Penn State	Penn State
Major & minor elements in ash (%):										
SiO ₂	42.82	32.91	41.20	54.40	46.50	49.60	19.70	47.90	32.50	44.70
Al ₂ O ₃	23.97	17.26	15.70	24.50	24.40	10.50	9.34	22.20	19.60	39.00
CaO	4.60	21.81	7.39	2.97	7.38	17.60	23.20	14.00	16.20	0.58
Fe ₂ O ₃	21.35	6.77	23.90	9.16	8.29	6.04	12.19	3.51	5.33	8.93
SO ₃	1.32	10.69	7.90	2.30	8.40	8.90	20.00	7.00	12.50	0.70
MgO	1.07	5.11	0.90	0.85	1.31	2.25	5.33	2.79	5.62	0.64
Na ₂ O	0.44	2.15	0.40	0.61	1.12	2.38	5.87	0.37	3.17	0.32
TiO ₂	1.02	1.29	0.76	1.14	1.76	0.84	0.37	1.14	1.14	2.30
K ₂ O	2.46	0.33	1.70	2.02	0.53	0.06	0.69	0.55	0.37	1.45
P ₂ O ₅	0.09	1.31	0.26	0.34	0.32	0.35	0.34	0.11	0.24	0.22
BaO	0.05	0.50								
MnO	0.05	0.04								
SrO	0.05	0.42								

Table 2.3: Alkali-metal species in low-and high-rank coals
(from Raask, 1985, Table 15.5)

Fuel Deposits	Sodium and potassium species	Comments
Vegetable matter and flood and ground waters	Organometal salts, chlorides, sulfates, and carbonates	The vegetable matter is rich in potassium, but flood and ground waters can be rich in sodium
Lignites and sub-bituminous coals	Chiefly organometal salts and soluble inorganic salts	Frequently rich in sodium, potassium content is usually low
Low-rank bituminous coals	Chiefly chlorides and silicates	Sodium is present partly as chloride and partly in silicates, potassium has a high affinity to silicates
High-rank bituminous coals and anthracites	Chiefly silicates with some chloride	High-rank, low-porosity coals have a limited capacity to hold chlorides

Table 2.4: Ash composition of typical biomass fuels, expressed as oxides in weight percent
(from Osman and Goss, 1983)

I.D.#		SiO ₂	Fe ₂ O ₃	MgO	CaO	ZnO	K ₂ O	Na ₂ O	SO ₃	P ₂ O ₅	Total
1	Bean Straw (I)	29.90	2.70	0.90	4.67	0.03	22.34	0.52	4.70	2.29	68.05
2	Safflower	20.46	1.20	6.10	10.84	0.03	30.01	0.91	8.36	3.64	81.65
0	Rice Hulls	94.60	0.03	0.02	0.25	0.00	2.40	0.14	2.24	0.46	100.12
3	Alfalfa	7.96	0.51	2.87	11.20	0.13	33.97	3.64	4.64	10.46	75.46
4	Cotton Gin Trash	23.20	1.93	2.87	7.18	0.19	13.00	1.59	4.24	10.00	64.20
5	Barley Straw	44.70	2.60	4.84	3.22	0.13	8.01	5.25	1.80	11.56	81.11
6	Corn Stalks	50.70	3.14	3.08	3.90	0.95	10.30	0.53	11.08	10.00	93.68
7	Rice Straw	75.20	0.58	0.83	0.72	0.00	11.90	0.28	1.51	8.87	99.89
8	Bean Straw (II)	32.70	3.93	3.65	6.30	0.15	25.30	0.82	2.28	7.30	82.43
9	Wood Chips	8.30	10.00	6.22	18.61	0.19	11.80	1.32	9.00	6.87	71.61
10	Corn Fodder	55.30	2.40	3.32	1.05	0.09	9.59	0.73	3.48	2.98	78.95
11	Paper Pellets	57.20	4.29	0.83	0.15	0.31	1.85	5.09	4.00	4.46	78.19
12	Corn Stalks (Ex.)	63.30	4.72	4.78	0.56	0.00	8.37	0.47	7.20	2.06	91.46
13	Almond Shell	22.60	3.77	2.49	12.27	0.05	14.14	5.08	8.00	5.50	73.90
14	Corn Cobs	40.30	4.06	2.49	1.27	0.22	2.04	1.19	8.74	6.87	85.53
15	Manzanita Chips	5.97	2.86	4.94	24.49	0.25	10.96	2.85	6.74	8.20	67.16
16	Tree Pruning	9.95	1.94	8.29	19.87	0.06	12.66	1.48	19.72	4.96	85.93
17	Walnut Shell	13.60	2.44	3.65	7.00	0.44	21.50	1.08	8.48	4.58	62.92
18	Olive Pits	10.50	2.20	3.48	25.89	0.12	3.13	7.60	17.20	7.56	77.74
19	Almond Shells	18.60	3.83	1.99	16.00	0.23	14.70	5.86	17.48	7.79	86.48
20	Corn Stalks	71.70	7.10	2.70	0.46	0.02	10.28	0.33	2.20	0.66	95.45
21	Cotton Stalks	33.00	2.80	6.05	3.56	0.07	21.40	1.37	6.55	6.40	83.57
22	Rice Mix	75.00	0.47	2.50	1.10	0.00	15.85	0.54	1.00	1.10	97.56
23	Wheat + Corn (1:3)	71.70	3.30	8.30	0.95	0.62	14.76	0.54	2.96	1.10	103.64
24	Rice Straw Good Bales	78.30	0.36	2.00	0.70	0.00	13.00	0.43	1.69	0.80	97.78
25	Rice Straw Decayed Bales	78.60	0.44	2.00	0.88	0.00	14.50	0.44	1.83	0.90	99.59

Table 2.5: Ash chemistry of some typical biomass fuels
(from Baxter et al., 1996)

Elemental Composition	Waste Paper	Wheat Straw	80% Wood 20% Wheat Straw	Rice Straw	Almond Hulls	Almond Shells	Olive Pits	Wood Waste/ Almond Shells	Aspen	Chicken Litter
	1	2	3	4	5	6	7	8	9	10
SiO ₂	20.5	55.7	56.8	73.0	4.0	4.9	23.1	49.6	14.9	10.7
Al ₂ O ₃	54.0	1.8	10.9	1.4	1.3	1.5	5.3	11.0	1.2	5.8
TiO ₂	1.5	.	0.5	.	.	.	0.1	0.4	.	.
Fe ₂ O ₃	0.1	0.7	4.9	0.6	0.4	1.3	5.1	4.6	1.2	0.8
CaO	10.2	2.6	10.2	1.9	5.0	6.9	10.9	14.4	65.2	21.4
MgO	1.9	2.4	2.4	1.8	2.9	2.6	3.0	2.7	4.3	6.2
Na ₂ O	1.1	0.9	3.8	0.4	0.2	0.5	29.9	2.4	0.4	3.8
K ₂ O	0.2	22.8	6.7	13.5	50.9	49.6	5.2	7.4	6.5	15.1
SO ₃	2.3	1.7	1.9	0.7	1.2	1.6	2.4	1.4	1.8	7.0
P ₂ O ₅	.	1.2	1.1	1.4	5.5	5.0	2.7	1.5	2.0	30.2
Total Percentage	91.8	89.8	99.2	94.7	71.4	73.9	87.7	95.4	97.5	100.0
TGA Loss on LTA, 500 °C %	8	10	9	15	26	23	20	11	--	--
Ash Fusion Temperatures										
Reducing										
I.T.	2694	2464	2065	2023	2359	1960	2340	2084	--	--
S.T. (Sph.)	2910	2466	2096	2246	2401	1981	2372	2130	--	--
S.T. (Hem.)	2910	2467	2288	2258	2408	2010	2495	2178	--	--
F.T.	2910	2474	2384	2641	2410	2071	2497	2239	--	--
Oxidizing										
I.T.	2619	1911	2084	1965	2558	1897	2448	2072	--	--
S.T. (Sph.)	2632	1913	2105	2158	2801	1899	2449	2096	--	--
S.T. (Hem.)	2910	2238	2322	2496	2818	1911	2487	2175	--	--
F.T.	2910	2316	2499	2582	2820	2348	2704	2262	--	--

* = Nil

Table 2.6: Fuel properties of eastern Canadian bark
(from Bryers, 1996)

	Balsam	Black Spruce	White Spruce	Red Spruce	Jack Pine	Poplar	Birch White	Birch Yellow	Maple Hard	Maple Soft	Elm	Beech	Tamarack	Hemlock
Proximate Analysis														
Volatile	77.4	74.7	72.5	72.9	74.3	78.9	80.3	76.5	75.1	78.1	73.1	75.2	69.5	72.0
Fixed carbon	20.0	22.5	24.0	23.7	23.6	17.2	18.0	21.0	19.9	18.9	18.8	18.9	26.3	25.5
Ash	2.6	2.8	3.5	3.3	2.1	2.2	1.7	2.5	5.0	3.0	0.1	7.9	4.2	2.5
Ultimate Analysis														
Carbon	52.8	52.0	52.4	52.1	53.4	51.8	57.4	54.5	50.4	50.1	46.9	47.5	55.2	53.6
Hydrogen	6.1	5.8	6.4	5.9	5.9	6.5	6.7	6.4	5.9	5.9	5.3	5.5	9.9	5.8
Sulfur	0.0	0.0	0.0	0.0	0.0	0.0	0.0	0.0	0.0	0.0	0.0	0.0	0.0	0.0
Nitrogen	0.2	0.1	0.1	0.1	0.2	0.3	0.3	0.6	0.5	0.3	0.6	0.6	0.7	0.2
Oxygen	38.6	39.7	38.4	38.6	38.9	38.0	33.8	26.2	39.1	40.7	39.1	38.5	31.0	37.9
Ash	2.3	2.4	3.0	2.0	3.1	3.4	1.8	2.3	4.1	3.0	8.1	7.9	4.2	2.5
Ash Analysis														
SiO ₂	24.6	6.4	2.0	7.6	16.0	1.5	3.0	4.1	39.5	6.1	3.6	12.4	7.3	10.0
Al ₂ O ₃	1.8	1.1	0.6	0.0	6.3	0.5	0.6	0.3	3.8	3.1	0.0	0.0	8.4	2.1
TiO ₂	0.2	•	•	0.1	0.2	•	•	•	•	0.1	0.1	•	0.1	•
Fe ₂ O ₃	2.5	1.1	0.7	3.1	5.0	0.6	2.9	0.8	1.7	0.8	0.3	1.1	3.6	1.3
CaO	43.2	67.6	62.9	58.4	51.6	62.3	58.2	54.2	55.5	60.4	67.1	68.3	50.3	53.6
CaCO ₃	7.8	11.2	13.6	11.3	4.9	14.6	13.0	17.8	1.4	16.7	16.3	2.2	4.1	9.7
MgO	2.2	1.7	6.4	4.7	5.5	1.9	4.2	5.4	19.4	2.3	2.0	11.5	8.5	13.1
MnO	2.6	2.2	1.2	2.0	1.6	0.3	4.6	1.3	1.0	0.4	0.1	0.4	3.4	1.2
P ₂ O ₅	4.6	2.2	2.6	2.2	2.8	2.0	2.9	3.8	1.1	0.3	1.3	2.3	4.7	2.1
K ₂ O	10.1	6.2	7.3	5.3	4.1	7.2	6.6	8.0	5.8	6.3	4.4	2.6	5.3	4.6
Na ₂ O	2.5	2.5	0.8	2.0	3.1	3.9	1.3	1.7	2.2	0.9	0.7	0.9	3.2	1.1
SO ₃	2.7	1.4	2.2	1.3	2.6	0.6	3.2	1.3	1.4	2.0	0.8	0.8	2.6	1.9
Fusion Temperatures, °K														
Initial	1838	1760	1755	1627	1616	1744	1760	-	1727	1660	-	1633	1505	1788
Softening	1844	1784	1755	1821	1783	1810	1766	1777	1821	1738	-	1811	1533	1744
Fluid	1849	-	1760	1827	1805	1816	1771	1777	1827	1744	-	1816	1560	1799

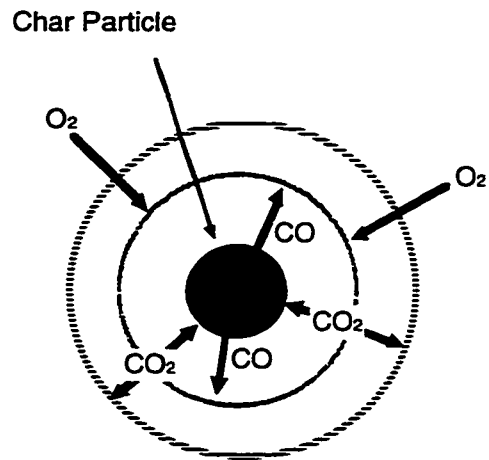


Figure 2.1: Two-film model for diffusion controlled char particle combustion (adapted from Saxena, 1990)

FOCUS AND OBJECTIVES

The principal thrust of the research presented here is modeling and characterization of mineral transformations occurring in sawdust/sanderdust combustion. Emphasis is on sub-micron aerosol production, its magnitude, and composition relative to other ash modes.

Sawdust/sanderdust fuels behave very differently from the coals described in the previous chapter, whose behavior has been much more thoroughly characterized in the literature. One unique feature is a very high alkali mineral content, suggesting very large yields of sub-micron aerosol via the vaporization/condensation mechanism. These fuels also largely lack aluminosilicate minerals, which would normally be active in both absorbing alkali vapors and in fluxing the residual ash. This ash creates unique operational and environmental barriers that must be overcome in order to use these abundant, renewable fuels as an in-plant energy source. The objectives of this work are given below.

OBJECTIVE 1: SAWDUST/SANDERDUST CHARACTERIZATION

A primary objective is to present an accurate physical and chemical characterization of the ash generated by the combustion of practical sawdust/sanderdust fuels. Ash particle morphology and composition measurements of high-alkali biomass fuels is a lightly researched field, but is of critical importance when identifying and quantifying transformation mechanisms. Fulfillment of this objective includes the following:

- Simulation of a wood-fired industrial-scale suspension burner using a laboratory scale (15 kW) tunnel furnace, with accurate measurement of relevant control variables such as temperature/time history, excess oxygen content and residence time.
- Quantitative size distribution measurements of the resulting ash using a cascade impactor for particulate matter greater than 0.4 μm , and an Electrical Aerosol Size Analyzer (EAA) for particulate matter less than 0.4 μm .
- Composition and morphology of ash particulate matter using Scanning Electron Microscopy (SEM) and Energy Dispersive X-ray Analysis (EDAX) techniques.

The output of the work supporting this objective is a physical and chemical “picture” of the state of the output mineral matter after it has been transformed by a realistic, yet well characterized combustion environment.

OBJECTIVE 2: COMPONENT MODELING OF ASH TRANSFORMATIONS

A primary objective is to present a modeling methodology for predicting the properties of the ash (*i.e.*, size distribution and chemical composition *vs.* size) as a function of the initial composition of the fuel and the environment provided by the combustor. This modeling phase is comprised of a number of components rather than a single model entity. It examines critical mechanisms that control ash transformations in the sub-micron particle size range, and is used to bridge the gap between carefully controlled laboratory results and industrial-scale combustor conditions. This objective is accomplished in parts, as listed below.

- Vaporized alkali species have two fates. They can either condense onto existing non-alkali particles, or homogeneously nucleate into an alkali aerosol. Heterogeneous condensation tends to promote formation of large particles with low number density, while homogeneous condensation promotes formation of very fine particles ($d \ll 0.1 \mu\text{m}$) with high mobility and high number density. Hence, the relative contributions of these two mechanisms are examined relative to controllable parameters such as quench rate and fuel firing density.
- Determination of equilibrium concentrations of condensed species is made using CET89, informally known as the NASA equilibrium code (Eddings, 1973). Equilibrium calculations are used to determine the favored anion and condensation temperature of critical vapor-phase species. Due to the high furnace temperatures (and thus fast reaction rates), equilibrium is expected to be a good model for gas-phase mineral chemistry. This information is also critically examined relative to processes that are likely kinetically controlled, such as condensed species formation during rapid quench conditions.
- The ultimate size distribution of sub-micron particles is examined using the coagulation program MAEROS2 (Gelbard, 1996). The coagulation rate of the highly mobile (*i.e.*

diffusionally transported) sub-micron particles is strongly driven by initial particle number density and the residence time of condensed species. MAEROS2 aids in scaling laboratory measurements of number density and residence time to the conditions used in industry.

Other ash formation mechanisms are important, but beyond the scope of this research. These include:

- Alkali-sulfur species are not predicted by equilibrium in the vapor phase, but are favored in solid phase. This observation, and experiments conducted by others, tend to indicate that sulfation is kinetically limited. This potentially extensive research area is not explored in depth.
- Residual ash, defined here as any ash component that does not enter a vapor phase, is typically on the order of 1 μm and larger. Important processes in residual ash formation include particle break-up, melting and fluxing, and aggregation. The focus of the modeling objective is the sub-micron ash yield, hence residual ash formation is only included as it pertains to influencing the sub-micron yield (*e.g.*, heterogeneous condensation surfaces).
- Organic particulate matter formation (*i.e.* sub-micron soot particles) is a well known result of incomplete combustion, but does not significantly influence this research. Factors favoring complete combustion in sanderdust burners are high excess oxygen (about 8% by volume) and long furnace residence time (about 1 second). Compared to coal, this fuel also has high volatile yield (leaving little char). The remaining char has very high porosity, which provides a large surface area for oxidation.

OBJECTIVE 3: PULVERIZED COAL CHARACTERIZATION

A secondary focus of this research is developing a database of ash morphology for a well-characterized set of research coals. This coal database serves as a source of comparison for the sawdust/sanderdust experiments, but also examines the influence of coal cleaning, size segregation and coal composition on aerosol yield.

TECHNICAL APPROACH AND EXPERIMENT APPARATUS

Objectives outlined in Chapter 3 were investigated using procedures and apparatus described below.

A laboratory-scale (15 kW) tunnel furnace was the primary experimental tool. It was designed to provide a combustion environment that is similar to that found in industrial-scale systems, but at the same time to be more idealized. The principal benefit is flexibility. The combustion environment can be directly controlled and easily characterized, allowing the research of fundamental and generic phenomena. Interpretation is eased because the myriad of complications associated with a practical combustor are avoided. A description of this facility is presented in Section 4.1.

Pulverized coal experiments were conducted with three bituminous coals, one cleaned coal, and one sized coal. Ash size distributions were obtained using a water cooled sampling probe and a cascade impactor. Procedural details and equipment are addressed in Section 4.2.

Mechanistically-based experiments were conducted using artificial chars that contain organically-bound sodium and varying amounts of bentonite macerals, calcite macerals, and pyrite macerals, respectively. Ash size distributions were obtained using a water cooled sampling probe and a cascade impactor, similar to the pulverized coal experiments. Procedural details are addressed in Section 4.3.

Sawdust/sanderdust experiments were conducted with fuels from four different sources. Experiments were conducted with the fuels using a water-cooled sampling probe and cascade impactor. Chemical analysis and scanning electron microscopy were also conducted on selected size cuts and aerosol components. These procedures are addressed in Section 4.4.

Further sawdust/sanderdust experiments were conducted with milled samples. An isokinetic sampling probe and an electrical aerosol analyzer were used to determine the size distribution of the resulting ash, as well determine the detailed size distribution of the sub-micron aerosol. These procedures are addressed in Section 4.5.

A description of the design and use of a High Velocity Thermocouple (HVTC) is given in Section 4.6. This instrument was used to conduct detailed temperature profiles at each station of the reactor.

4.1 Facility Description- Tunnel Furnace

Combustion experiments were performed using a tunnel furnace, as shown in cross-section in Figure 4.1. A high temperature refractory (Greencast 97, 1760C max, 1.5 W/m-K thermal conductivity) forms the inner walls of the combustion tunnel, with heat loss to the surroundings minimized by three layers of material with progressively lower thermal conductivity. The furnace refractory is 230 cm tall with a diameter of 91 cm, and is encased in a 6.4 mm steel jacket. To simplify construction, the furnace was cast in five sections, and then stacked. A Kaowool insulation blanket, one inch thick prior to compression, was used as a gasket material between sections. More complete details of the refractory design and construction are available in Hoffman (1994).

Primary combustion occurs at the top of the reactor, where a swirl mixed natural gas/air burner is used to produce a high temperature, oxygen rich environment. Burner design and construction, and the associated electrical safety system, is discussed in Hoffman (1994). The as-designed maximum firing rate is 15 kW (51,000 Btu/hr). Stoichiometry and overall mass flow rate (hence furnace residence time) is controlled by metering the air and natural gas independently, via rotometers. Local natural gas composition tends to be 95% methane, with the a balance of primarily ethane, N₂ and propane, resulting in well characterized combustion products (Riley, 1997, Appendix D). A 35.6 cm long by 10.2 cm diameter combustion zone (prior to the point of coal/biomass fuel injection) helps to stabilize the natural gas flame and leads to complete combustion. An observation port and a sampling port accessing the natural gas combustion zone have been blocked with refractory to limit heat loss.

The finely-divided or pulverized fuel of interest is pneumatically injected into the hot gas stream using a stainless steel, water-cooled injector. A 90° bend at the probe exit allows for fuel injection 2.5 cm above the venturi constriction leading to the reactor tunnel in the lower section. Turbulent flow at the 2.5 cm venturi constriction aids in mixing of the fuel with the oxygen-rich hot gas stream. The combustion tunnel expands from 2.5 cm to 20.3

cm diameter with a half-cone angle of approximately 7 degrees, and is a constant diameter thereafter. The expansion was designed for a uniform transition from turbulent mixing at the throat to laminar flow in the main tunnel.

To provide flexibility in setting the temperature profile, four auxiliary burners are used to internally heat the refractory. The four auxiliary burners are shown in vertical cross section in Figure 4.1. Horizontal cross sections are shown in Figure 4.2. Swirl mixed natural gas and air is burned at the lower (inlet) port of each auxiliary burner channel. This heats the common wall between the main tunnel and the channel, and then exhausts through the upper channel. Note that the stoichiometry of the auxiliary burners does not effect the stoichiometry of the main tunnel because the hot gas streams are separated by the refractory wall. The auxiliary burners are operated in pairs for radial temperature symmetry.

Ten horizontally oriented sampling ports of 2.6 cm diameter are distributed down the length of the reactor. Temperature verses furnace residence time is documented by sampling the tunnel hot gas temperature via these ports.

Schematics of the air, water, and natural gas supply systems are given in Appendix B. A brief overview of furnace and laboratory modifications not directly related to experimental results is included in Appendix B.

4.2 Pulverized Coal Experiments- Setup and Procedures

The tunnel furnace was activated and steady state conditions were achieved. Due to the large thermal inertia of the furnace, about 36 hours of warm-up with natural gas combustion was required to reach steady state. A temperature profile was taken per the procedure in Section 4.6, to verify the desired operating conditions. Repetition of temperature profiling between tests series was not required if combustion conditions were not modified between tests.

A pulverized coal was selected for testing, loaded into the coal feeder hopper, and the feed screw was primed. Equipment and preparation for coal feeding is addressed in Section 4.2.1. The feed system was verified to be ready for activation, but remained in standby until the sampling probe and impactor were in place.

The cascade impactor, sampling probe and vacuum system were prepared for testing according to the procedures outlined in Section 4.2.2. and 4.2.3.

The sampling system vacuum pump and a timer were started simultaneously. The sample flowrate was adjusted to ensure a flow of one cubic foot per minute through the impactor. The coal feeder was activated, and a second timer started. Coal flowrate was terminated after a predetermined time limit had been reached. The vacuum pump was turned off and the elapsed time noted.

The impactor was immediately disassembled, the foil stages and backup filter were placed in their proper petri dishes, and desiccated in a 110 C laboratory oven. The contents of the preseparator was washed with acetone into the earlier prepared foil cup. The connector tube, if used, was also washed into the foil cup. The foil cup and its contents were placed in the 110 C oven after the acetone wash had been evaporated at room temperature. The foil stages, backup filter and foil cup were removed after at least 30 minutes in the laboratory oven.

The foil stages, backup filter and foil cup were reweighed using the same procedures followed prior to testing, as outlined in Section 4.2.3.

4.2.1 Pulverized Coal Feed System

The pulverized coal feed system is shown in Figure 4.3. Typical pulverized coals used for experiments were about 70 μm in diameter with an aspect ratio near unity, resulting in a fuel that was amenable to screw feeding. Pulverized coal was placed in the screw feeder (AccuRate Model 310-83-0017, Whitewater, Wisconsin), with the screw motor set to the appropriate speed for the desired coal flow rate. The fuel was fed by the rotating screw to a tee junction, where the fuel was entrained by a perpendicular air stream. The fuel was conveyed by the airflow through a water cooled injector into the hot gas stream at the throat of the furnace.

Prior to testing, the screw feeder was calibrated for the fuel of interest, as follows: The screw feeder tube was disconnected from the air entrainment line, and the fuel was fed through the screw feeder at a preselected screw turn rate. The mass of coal fed over a

given time was determined by weighing the ejected coal. The procedure was repeated over a range of turn rates in order to produce a calibration curve.

4.2.2 Pulverized Coal - Ash Collection and Size Sorting

Ash collection and particulate size sorting was performed using a watercooled sampling probe and a Mark II Cascade Impactor, combined with a vacuum pump. For initial experiments, the probe was used in the horizontal orientation, along the center line of the horizontal exhaust duct leading from the furnace exit to the exhaust duct. This configuration is shown in Figure 4.4. Accurate positioning of the horizontal probe was difficult, and entrainment of water from the exhaust duct cooling system (a water atomizer), prompted the relocation of the probe to the bottom of the reactor in later tests. This configuration is shown in Figure 4.5. Clearance limitations did not allow this probe to be removed from the furnace when testing was performed with the probe in the vertical position.

4.2.3 Cascade Impactor Modifications and Preparation

A cascade impactor (Andersen Instruments Incorporated, 1 ACFM Non-Viable Ambient Particle Sizing Sampler, Mark II model, Atlanta, GA) was used to sort particles into eight size classes using inertial impaction. The lower limit of a size class is defined by the diameter of a particle having a 50% probability of capture on that stage. Aerosol, which is typically particulate matter on the order of 0.1 μm diameter, was collected on a borosilicate microfiber filter downstream of the final impaction stage. The impactor was also fitted with a preseparator, which is designed to prevent large particulate matter (greater than 10 μm in diameter) from entering the size segregating area of the impactor. The standard impactor was modified for research purposes as follows:

- 1) An adapter for connection of the preseparator inlet to the sample probe was constructed.
- 2) Rubber inter-stage O-rings were replaced by Teflon O-rings. This allowed higher operating temperatures.
- 3) Impactor sealing pressure was increased by replacing the manufacturer's spring loaded stage clamps with a threaded rod clamping system.

4) Aluminum foil disks were used as collection surfaces. These were supported by the manufacturer's stainless steel collection plates. Use of aluminum foil allowed for very small tare weights, increasing the accuracy of the sample mass measurement.

Standard operation of the unit is discussed in detail in the manufacturer's operating manual (Andersen Instruments Incorporated, 1985), including calibration and maintenance. Additional procedures for this test series are as follows:

The cascade impactor was disassembled. All orifice plates were visually inspected for particulate blockage, and cleared with compressed air as necessary. A low lint cloth with acetone was used to wash all components - eight orifice plates, preseparator, cap, backup filter holder, backup filter retaining ring (Teflon), and stainless steel collection plates. An acetone soaked swab was used to clean all Teflon O-rings. Components were air dried. A bore cleaning rod with an acetone soaked low lint cloth was used to clean the inner diameter of sampling probe. A rod and acetone soaked cloth was used to clean probe-to-impactor connection tube, if the tube was required for the test.

Nine aluminum foil collection disks (household Reynolds aluminum foil) were cut to fit collection plates, using a custom designed and built punch. Two foils required an additional center punch, using the custom punch. On a hard surface with a low lint cloth covering, a low lint cloth and acetone was used to smooth and clean the foils. The foils were rinsed with acetone and air dried (this step was critical in minimizing static electricity on the foil stages). Foils were handled with only an acetone-washed forceps for the remainder of the test. Eight foils were reserved for impactor stages. The remaining foil was shaped into a cup approximately 6 cm diameter and one cm deep by compressing the foil between two appropriately sized cups nested together. The foil cup was rinsed with acetone and left to air dry. The impactor was assembled (without the foil collection disks) and stored in clean environment until ready for test.

Ten inert-plastic petri dishes were obtained, and the lids were discarded. Each petri dish was inscribed with identifying labels. Cloth and acetone was used to wash the petri dishes, followed by an acetone rinse and air drying. The rinse step was critical - it minimized static electricity on the petri dishes. The foils and foil cup were placed in individual petri dishes using acetone-washed forceps. One 81 mm glass fiber filter (Glass Microfibre Filter, grade 934-AH, Whatman International Limited, Maidstone, Kent; England) was

removed from clean storage, using acetone-washed forceps, and placed in a petri dish. The petri dishes with foils and glass fiber filter were placed in a 110C laboratory oven to completely dry. After 20 minutes the dishes were removed and immediately placed in dessicator box with approximately 200 g of CaSO₄ (Drierite Indicating Desiccant, 8 mesh, W. A. Hammond Drierite Company, Xenia, OH) in three separate petri dishes. The petri dishes and foils were allowed to cool to room temperature in the dessicator box.

The mass scale (Mettler AE240-S, Mettler Instrument Corporation, Hightstown, NJ) was calibrated per the manufacturers instructions. Acetone washed forceps were used to remove one foil at a time from dessicator box and place it on the balance. After waiting approximately two minutes for scale to stabilize, the mass was recorded. If mass measurement was not stabilized to 0.00001 grams, it was verified that the scale was isolated from drafts and was properly anchored. The foil was carefully removed from balance with forceps, and returned to its labeled petri dish. The experimenter then waited for the scale to re-zero (approximately one minute). If scale did not rezero, it was manually reset to zero, and the foil was reweighed with the new zero. The foil was removed, and the experimenter again waited for the scale to rezero. This reweigh procedure was repeated until scale returned to zero with no load. If rezeroing failed after three attempts, the scale was recalibrated per manufacturers instructions. All (eight) foils, foil cup, and glass fiber filter were weighed. The weighed stages were stored in the dessicator box until ready for use.

The cascade impactor was preheated in a 110 C laboratory oven for approximately 30 minutes. The cascade impactor was removed from the oven and disassembled using insulated gloves. The impactor was carefully reassembled with aluminum foil collection disks placed on inverted stainless steel collection substrates, per the manufacturers instructions. The glass fiber filter was inserted below the final collection substrate, and secured with Teflon retention ring. Acetone-washed forceps were always used to handle foils, glass fiber filter, and the glass fiber filter retaining ring in the cascade impactor. The cascade impactor stack was clamped securely with the threaded rod compression system to prevent leakage. The cascade impactor was returned to the 110 C laboratory oven. The probe-to-impactor connection tube (if required for test) was placed in the oven. The impactor and connection tube were preheated for 30 minutes (minimum) prior to test.

The final assembly of the sampling system depended on the sampling location. Outlined below are procedures for sampling with the probe horizontally oriented in the exhaust duct, and for a vertically oriented probe in the main furnace body.

Horizontal Sampling Test (Figure 4.4): Using insulated gloves, the connection tube and impactor cap were removed from oven and assembled. The connection tube was connected to the sampling probe. The probe was inserted into horizontal sampling port. The probe was verified to be on the centerline of the sampling duct and at the proper insertion depth, and secured in place with a clamp stand adjacent to sampling port. The cascade impactor was removed from the oven and connected to the vacuum line. The impactor was mated to the impactor cap.

Vertical Sampling Test (Figure 4.5): Using insulated gloves, the impactor cap was removed from the oven and slid over the exit tube of the sample probe. The cascade impactor was removed from the oven and the vacuum line was secured. The impactor was placed beneath the sample probe and cap, which required the cap to be slid up the sample probe to provide clearance for the impactor. Once the impactor was positioned, the cap was lowered and sealed.

4.3 Pulverized Artificial Char Experiments

Artificial char experiments were performed following procedures identical to the pulverized coal experiments described in Section 4.2, with two notable exceptions:

- 1) All artificial char experiments were conducted with the sampling probe in the vertical orientation (See Section 4.2.3 and Figure 4.5).
- 2) The limited amount of artificial char available required that a low volume char feed system be used, as described below.

The coal screw feeder was not used for artificial char testing because the supply of artificial char was insufficient for proper operation of the screw feeder. A syringe delivery system, shown in Figure 4.6, was designed and built to replace the screw feeder.

Artificial char was loaded into three plastic 30 cc syringes, which were cut such that the syringe exit diameter was the same as the syringe body diameter. Frequent tapping of the

syringe support with a metallic rod promoted uniform syringe loading. Following loading, each syringe was inserted into the syringe block. The syringe block was milled from Plexiglas, so that artificial char feeding could be visually monitored. The air entrainment bypass was opened during syringe/char loading, and air entrainment valves to and from the syringe block were maintained closed. The syringe drive rate, corresponding to the desired feed rate, was verified.

To operate the char feeder, the air entrainment valve downstream of the syringe block was opened. The upstream entrainment valve was then opened while simultaneously activating the syringe drive. The bypass air entrainment inlet and outlet valves were then shut, respectively. At the conclusion of an experiment, the valve sequencing was reversed.

4.4 Screened Sawdust/Sanderdust Experiments

Screened Sawdust/sanderdust experiments followed procedures identical to the pulverized coal experiments described in Section 4.2, with the following important exceptions:

- 1) Sawdust/sanderdust experiments were conducted with the sampling probe in the vertical orientation.
- 2) Following collection of sized particulate matter on the cascade impactor stages and aerosol filter, some collected ash was further analyzed by Scanning Electron Microscopy and Energy Dispersive X-ray techniques.
- 3) Sawdust/sanderdust particle size variations and low density required a different fuel feed system, as described below:

Some changes to the existing pulverized fuel feed system were required to feed sawdust/sanderdust into the reactor, as shown Figure 4.7. Significant particle size and shape variation (in a single fuel type as well as from fuel to fuel) and low solid density of the wood led to bridging problems in the screw feeder hopper. This was moderated by increasing the screw size and hopper agitation. Frequent manual stirring of the hopper (approximately once per minute) also helped to prevent bridging.

A vertical drop was added from the screw feed exit to the air mixing area to prevent clogging. A venturi was added to the entrainment air system in order to prevent blowback

into the hopper by lowering the back pressure at the wood screw exit. Additionally, a 1/16" ID air tube was positioned at the screw exit such that compacted sawdust and sanderdust was dispersed prior to entrainment.

A new water cooled injector was built with a larger bore diameter to prevent clogging with oversized particles. A smooth turn at the exit rather than an abrupt 90 degree angle was incorporated to lower clogging susceptibility and to allow bore cleaning nearly to the tip of the injector.

Prior to testing, the screw feeder was calibrated for the fuel of interest. The screw feeder tube was disconnected from the air entrainment line, and the fuel was fed through the screw feeder at a preselected screw turn rate. The mass of fuel fed over a given time was measured. The procedure was repeated in order to produce a calibration curve for flow as a function of screw feed rate.

Due to the presence of oversized materials in some of the feed materials, jamming of the feed system was possible. For these experiments, this was avoided by prescreening the feed materials to remove these oversized wood chips. This is discussed later in conjunction with the experimental results. Prescreening, however, had the disadvantage of removing a portion of the feed material. Premilling of each of the feeds to a uniform size, as discussed in the next section, was used to avoid this problem.

4.5 Milled Sawdust/sanderdust Experiments

Experiments were conducted with milled samples of the four sawdust/ sanderdust fuels. The "As Received" sawdust was milled in a Thomas-Wiley laboratory mill to pass through a 0.5 mm diameter screen. This allowed complete use of the available fuel, aided in dispersion of the fuel at the injection point, and promoted complete combustion of char particles.

Particulate sizing of sub-micron ash particles for these tests was performed using an isokinetic sampling probe, cascade impactor and an Electrical Aerosol Analyzer (EAA), configured as shown in Figure 4.8. The cascade impactor was used primarily for removal of particles greater than the particle size of interest. To that end, stages 6 and 7 were removed for milled fuel testing. A delay tank was also added prior to the EAA to attenuate

fluctuations in sampling rate. By varying the size of the delay tank, different delay times for aerosol coagulation was also achieved.

Procedure:

The tunnel furnace was activated and steady state conditions were achieved. Due to the large thermal inertia of the furnace, about 36 hours of warm-up with natural gas combustion was required to reach steady state conditions. A temperature profile was taken to verify the desired operating conditions, per the procedure in Section 4.6. Repetition of temperature profiling between tests series was not required if combustion conditions were not modified between tests.

The feed system shown in Figure 4.7 (described in Section 4.4.1) was used to feed milled sawdust/ sanderdust. The feed system was verified to be ready for activation, but remained in standby until the impactor was in place.

The isokinetic sampling probe (described in Section 4.5.1.1), Electrical Aerosol Analyzer (described in Section 4.5.1.2) , and the cascade impactor were assembled per the schematic in Figure 4.8.

The sampling system was activated and isokinetic conditions were achieved, per the procedure described in Section 4.5.2.

The data acquisition system, described in Section 4.5.3, was activated.

The fuel feeder was started simultaneously with a timer. Fuel in the feeder hopper was continuously manually agitated with a stainless steel rod during testing. This prevented bridging of the fuel in the hopper and promoted a uniform fuel feed rate. (Minor fluctuations in the fuel feed rate could have led to significant fluctuations in Electrical Aerosol Analyzer signal). The fuel feeder was turned off after the desired test duration. The data acquisition system was turned off, and the isokinetic sampling system was turned off.

The impactor was immediately disassembled, the foil stages were placed in their proper petri dishes, and desiccated in a 110 C laboratory oven. The contents of the preseperator was washed with acetone into the earlier prepared foil cup. The foil cup and its contents were placed in the 110 C oven after the acetone wash had been evaporated at room

temperature. The foil stages and foil cup were removed after at least 30 minutes in the laboratory oven.

The foil stages and foil cup were reweighed using the same weighing procedures followed prior to testing, as outlined in Section 4.5.1.3.

4.5.1 Ash Collection and Size Sorting

4.5.1.1 Isokinetic Sampling Probe

Ash samples were collected through a water-cooled sampling probe, with a porous inner wall for dilution air addition. See Figure 4.9. This design significantly improved representative sampling in three ways: 1) isokinetic sampling was realized by metering the dilution flowrate appropriately, 2) thermophoresis was minimized by the radial dilution flow through a porous stainless-steel inner wall, and 3) the cascade impactor inlet temperature was reduced significantly. The CO₂ content of the undiluted and diluted gas streams was used as a tracer to verify isokinetic conditions.

4.5.1.2 Electrical Aerosol Size Analyzer - Particle Sizing

An Electrical Aerosol Size Analyzer (Model 3030, Thermo-Systems Incorporated, St. Paul, MN) was used to determine the size distribution of particles less than one micron in diameter. The device works on the principle that dispersion charging of sub-micron particles is a monotonically decreasing function of the particle size. In brief, aerosol particles are electrically charged by exposing the sample stream to unipolar positive ions via corona discharge. The charged particles then enter a flow tube with a negatively charged center rod. Small particles (*i.e.* high electrical mobility) migrate to the rod, and become electrically neutral. Larger particles that do not migrate fast enough to reach the rod before leaving the chamber are collected on a grounded filter. The large particles impart a current as they become grounded at the filter; this current is measured. By increasing the charge of the center rod in the main chamber, the rod collects all particles of a incrementally larger diameter, as well as the previous size of particles. The number of particles in a given size range can then be determined from the difference of the currents measured.

Theory of operation is discussed in detail in Lui *et al.* (1974) and Lui and Pui (1975), as well as the operators manual (Thermo-Systems Incorporated, undated).

4.5.1.3 Cascade Impactor Modifications and Preparation

The cascade impactor was used as a preseparator to remove residual ash particles in this test series. The residual ash was of lesser interest in the EAA experiments, and inhibited the accuracy of the EAA if it was not removed. The impactor was used as described in Section 4.2.3, except for the following modifications to the impactor and procedure:

- 1) The cascade impactor was operated without stages 6 and 7 and without an aerosol filter. Preparation of the two aluminum foil substrates associated with these stages and preparation of a borosilicate fiber filter was unnecessary.
- 2) A thermocouple was added to the impactor cap such that the impactor inlet temperature can be monitored.
- 3) Preheating of the cascade impactor prior to testing was not required. Dilution of the hot gas stream resulted in a dew point well below ambient conditions.

4.5.2 Determination of Isokinetic Conditions

The overall furnace mass flow rate was determined by summing the contribution from the main air and natural gas burner, and the entrainment air flowrate. Stoichiometry was calculated and then verified by measurement of CO₂ content (see Figure 4.8) of the combusted gas using a Horiba Model PIR-2000 Infrared Gas Analyzer. The analyzer was calibrated with 99.998% by volume N₂ (for zero calibration) and with 6.96% CO₂ span (for range calibration) prior to testing.

Isokinetic probe inlet flowrate was calculated, based on the cross sectional area of the probe inlet and tunnel furnace, and the total furnace flowrate. The diluent air flowrate required to achieve isokinetic conditions was calculated, based on the required flowrate of the EAA and the gas analyzer. The expected CO₂ concentration at the exit of the sample probe was calculated, based on the previously measured CO₂ concentration and the diluent air flowrate.

The CO₂ analyzer was recalibrated with 99.998% by volume N₂ (for zero calibration) and with 0.502% CO₂ span (for range calibration). The CO₂ analyzer was returned to monitor mode, and the secondary vacuum pump flowrate was adjusted until the measured CO₂ concentration indicated isokinetic conditions were achieved. The EAA, gas analyzer, and secondary vacuum pump flowrates were adjusted as necessary to meet the manufacturers flowrate requirements, while still maintaining isokinetic conditions. Steady state conditions were verified after ten minutes of operation.

4.5.3 Data Acquisition System

A Fluke 2625A Hydra Data Logger (Fluke Corporation, Everett, WA) was used to convert analog signals from the EAA, CO₂ analyzer, and cascade impactor thermocouple data to digital format. A read event was triggered automatically by the EAA using a voltage limit signal. The digital information gathered at the data logger was sent to a Zenith Z-386/AT Series Workstation where it was labeled and stored in ASCII format. A completed test was transferred to disk, and saved on a Power Macintosh 7500/100. The file was translated into Microsoft Excel format, followed by conversion of the digital voltage measurements into a size distribution.

4.6 Furnace Temperature Profiling - High Velocity Thermocouple

Furnace temperature profiling was conducted with a high velocity thermocouple (HVTC). This custom device is shown schematically in Figure 4.10. Accurate measurement of combustion product temperature was challenging because of thermal radiation exchange between the tunnel walls and bare thermocouple. A high velocity thermocouple suppresses the radiative influence by using suction to pull hot gas over the thermocouple, in combination with a ceramic shield (also heated by the convective gas stream) to limit radiative heat transfer. A HVTC is typically used in the coal industry for hot gas temperature measurements in large boilers (*e.g.*, Babcock and Wilcox, 1994) The HVTC used for these experiments is a custom designed and constructed device.

The High Velocity Thermocouple is operated as follows:

Connect air line to 90 psi air source, water inlet line to 70 to 90 psi laboratory water source, thermocouple lead to Omega DP460 thermocouple display, and water exit line to laboratory

drain. Open water flow valve at source to full. Open HVTC water valve to full. Water flow at the exit line should be at least one gallon per minute and flowing continuously. Close vacuum valve, open 90 psi air source, and verify at least 20 inHg vacuum at the eductor vacuum gauge. Maintain vacuum valve in closed position whenever the probe tip is not in the hot gas stream.

Remove 1" NPT pipe cap from port K (lowest horizontal sampling port on the tunnel furnace). Examine inner diameter of sampling port for loose ceramic. Clear port by pushing inaccessible debris with a 3/4" diameter stainless steel tube into the tunnel furnace. Slowly (2.5 cm per second or less) insert HVTC until the probe tip reaches the tunnel furnace center line. Seal the gap between the sample port tube and the HVTC tube by wrapping the junction with aluminum foil.

Slowly open the vacuum valve until the vacuum gauge indicates 15 inHg. Monitor the thermocouple temperature until a stable measurement is achieved (typically 5 minutes) and record. Multiple measurements at various insertion depths can be made in order to obtain a temperature profile at that sampling port.

Close the vacuum valve prior to removing the probe tip from the hot gas stream. Slowly back the probe tip out of the hot gas flow until it is approximately 25 cm from the hot gas zone. Hold the probe in this location until the thermocouple is below 450 C, in order to prevent thermally shocking the ceramic probe tip.

Remove the pipe cap from port J, slowly withdraw the probe from port K, and slowly insert into port J. Do not expose the ceramic tip to ambient conditions more than is necessary while the tip is hot. Repeat the procedure described above at each port. At the conclusion of testing, remove the probe from the tunnel furnace completely, and let the probe tip cool to ambient conditions. After cooling is complete, disconnect water, air, and thermocouple lines.

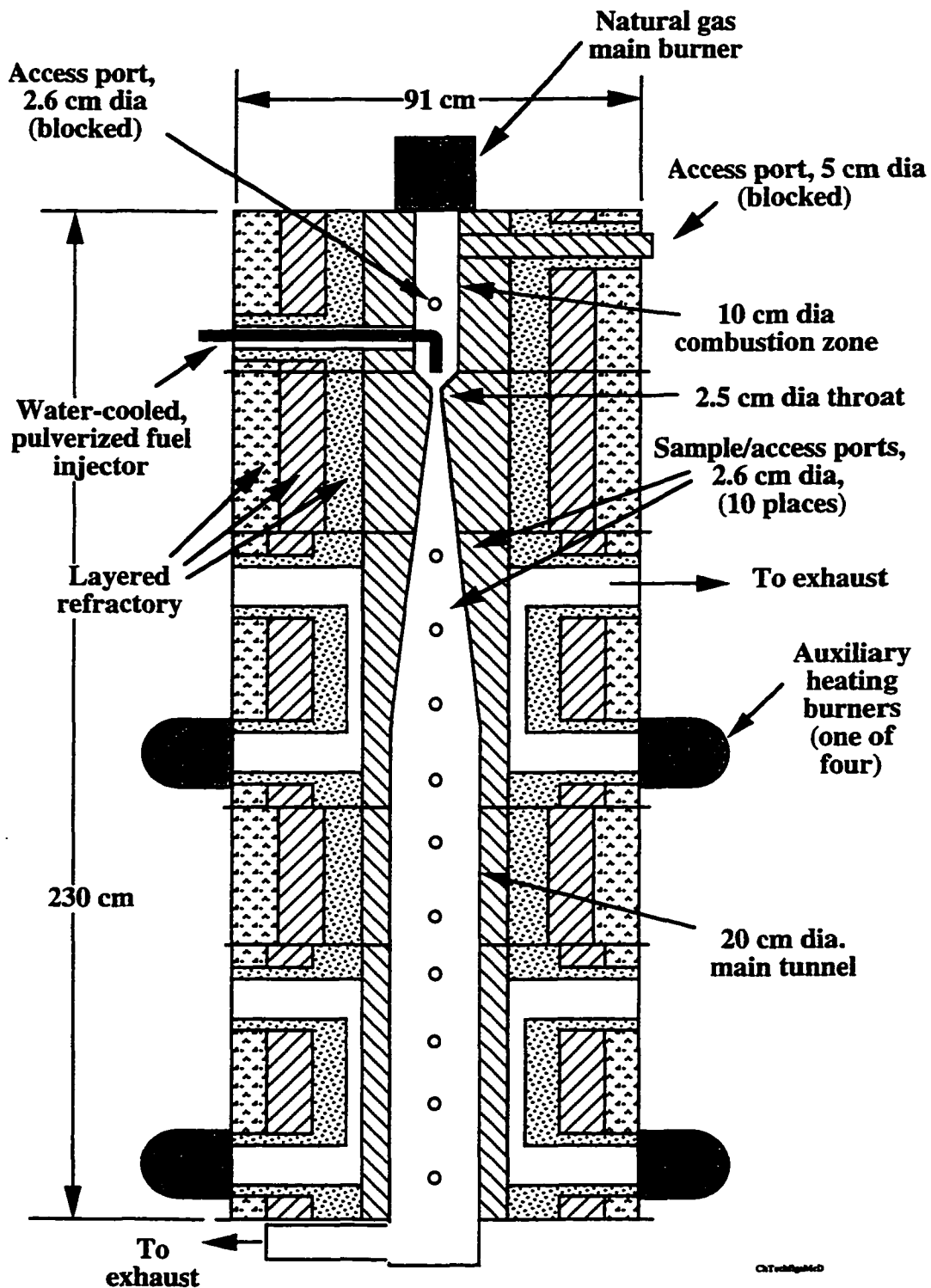
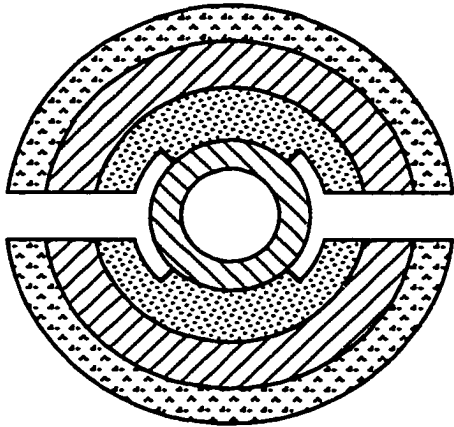
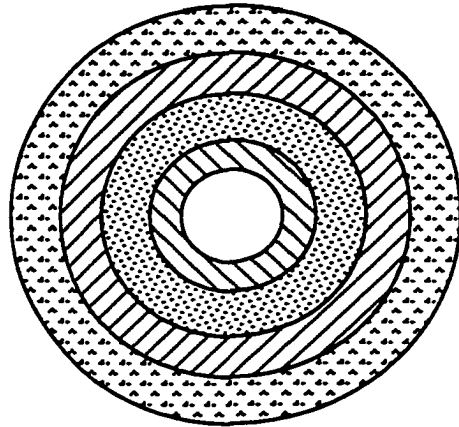


Figure 4.1: Natural gas-fired tunnel furnace (modified from Hoffman, 1994)

Profile through backfire section

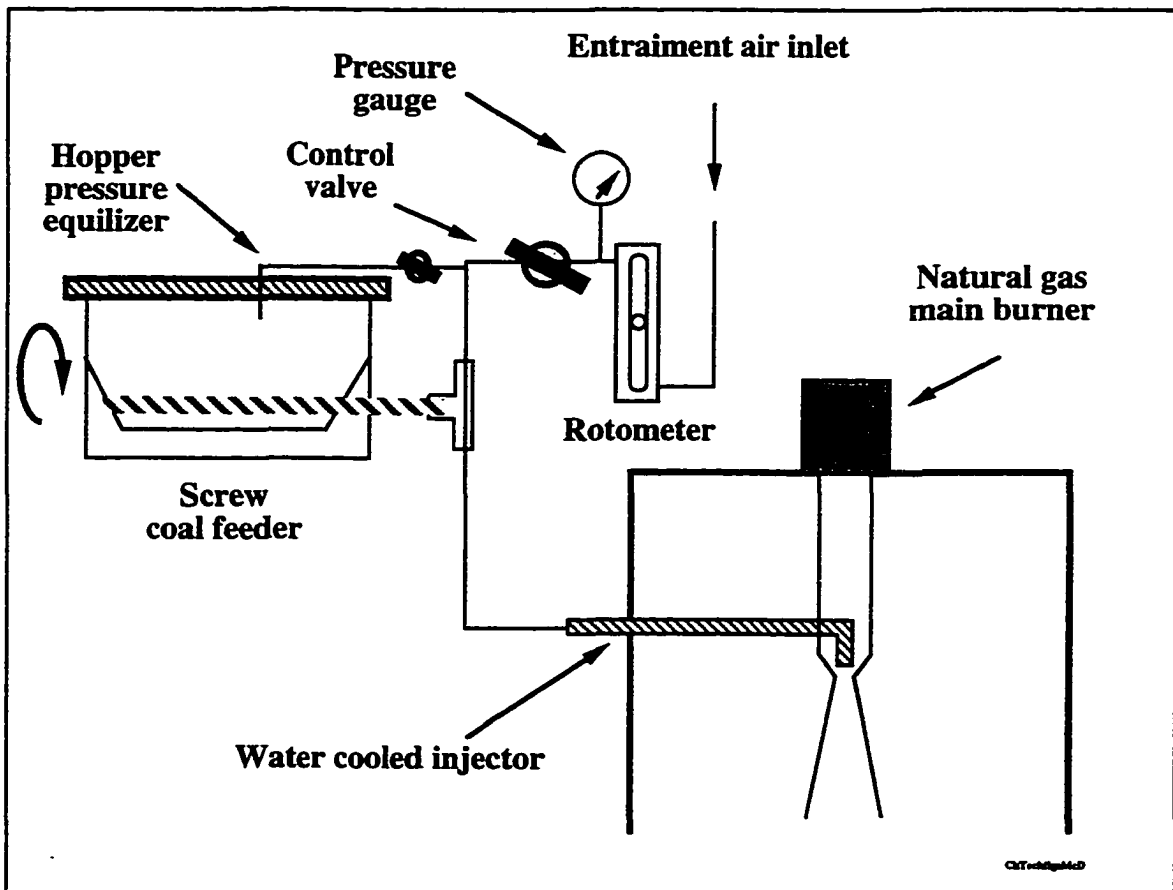


Profile through non-backfire section



CCT-48p44D

Figure 4.2: Tunnel furnace cross sections
(from Hoffman, 1994)



CCT-48p44D

Figure 4.3: Pulverized coal feed system

Tunnel furnace

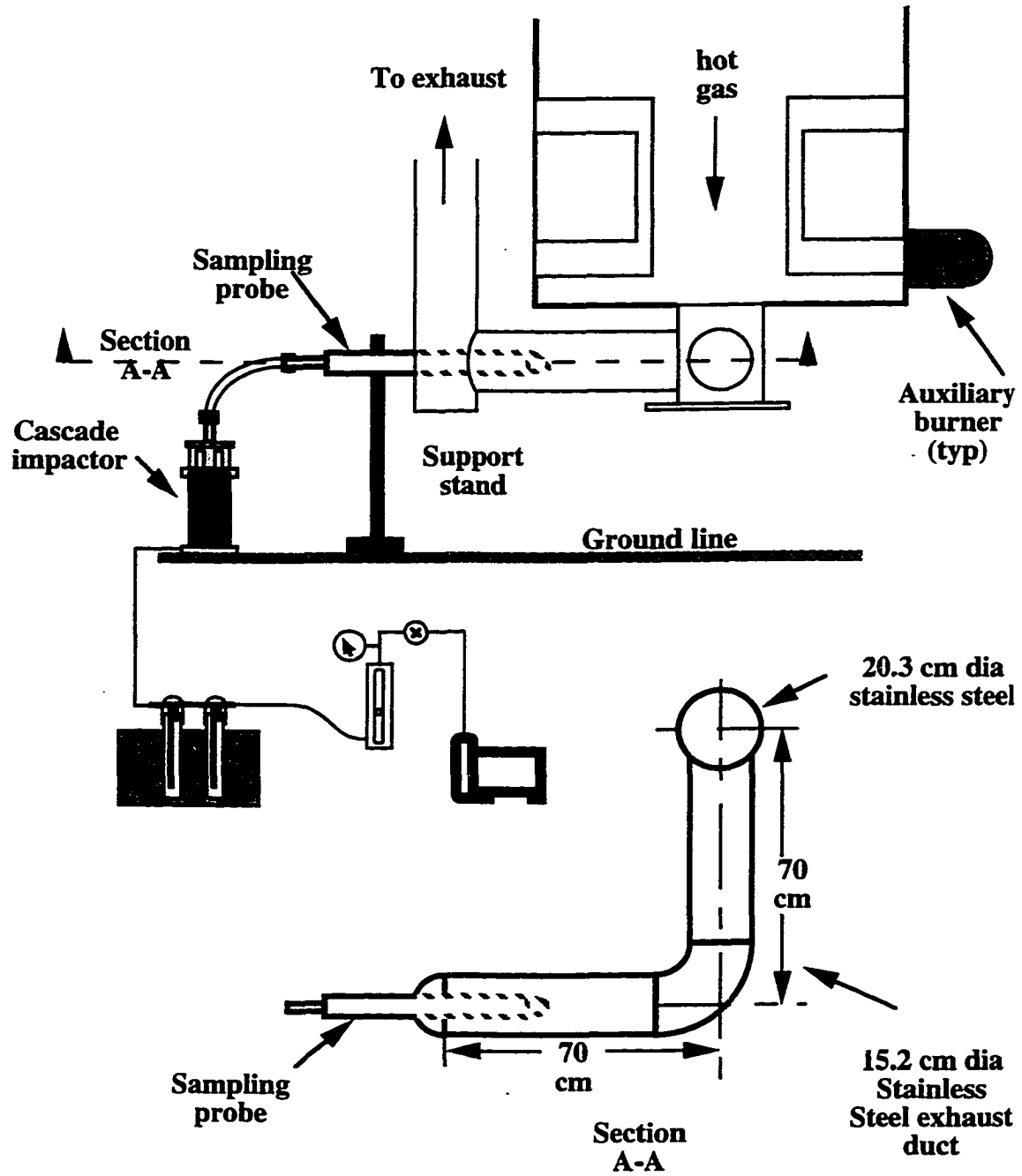


Figure 4.4: Sampling in horizontal orientation

CTC/04/04/00

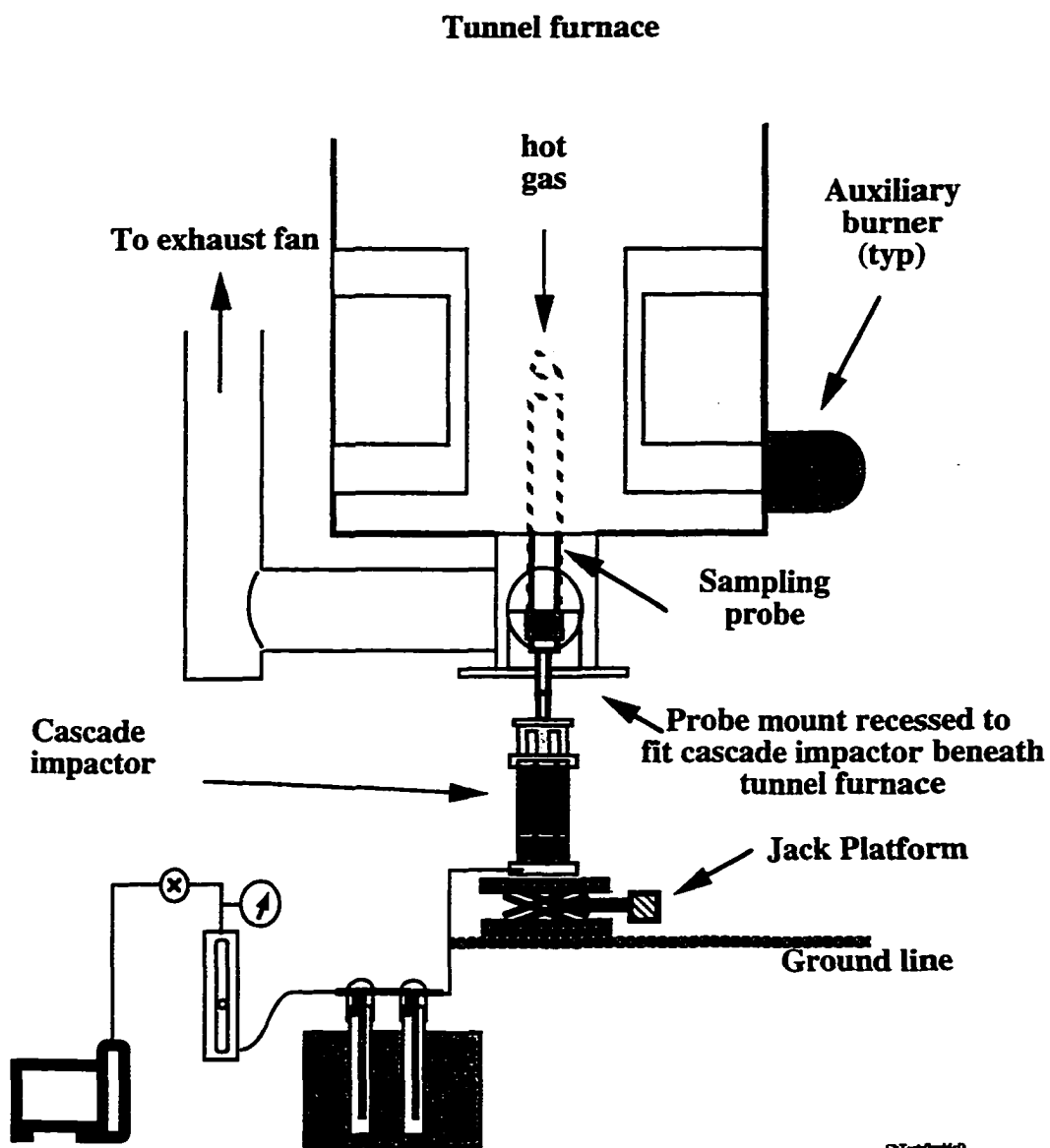


Figure 4.5: Sampling in vertical orientation

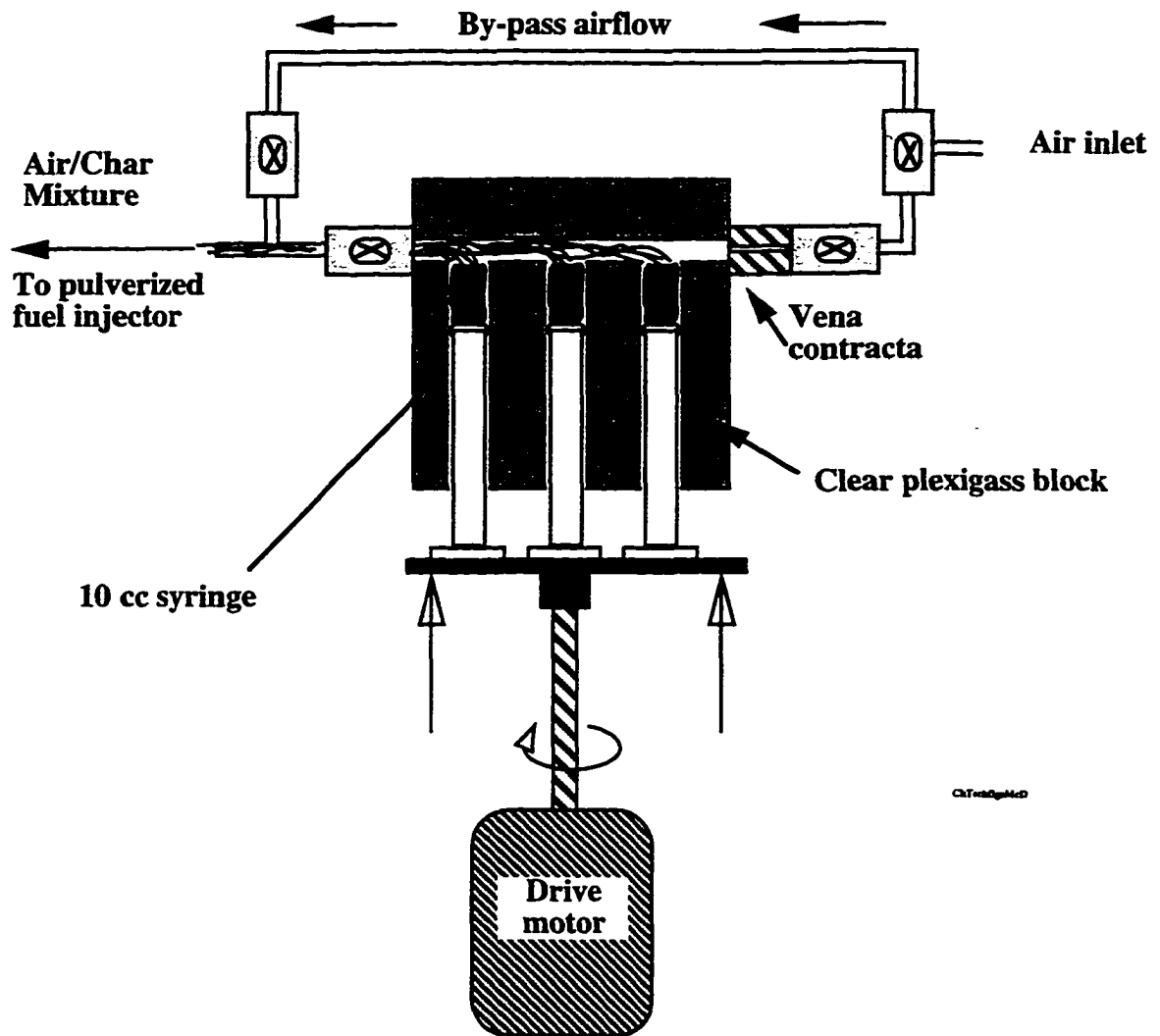


Figure 4.6: Artificial char syringe drive

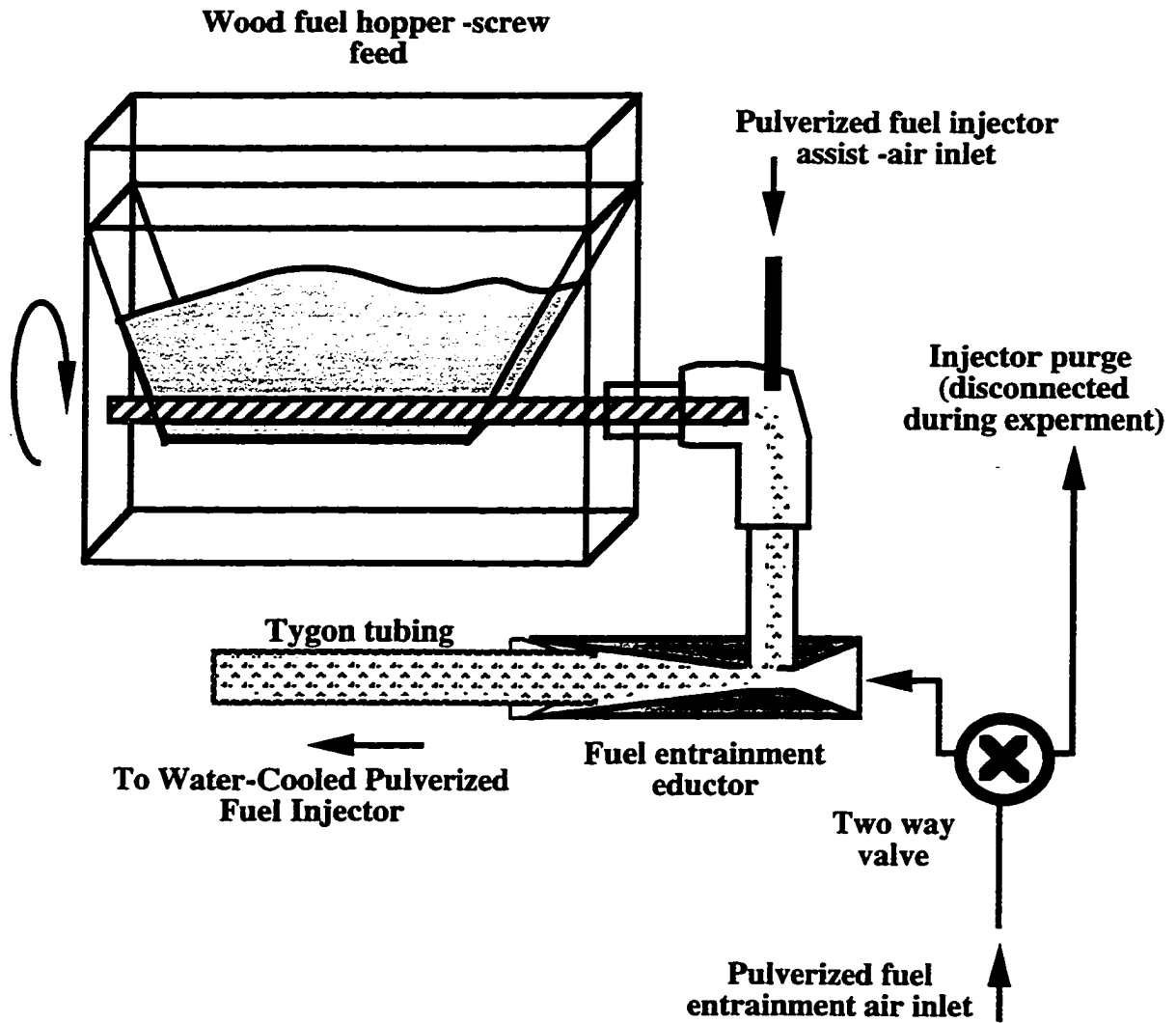


Figure 4.7: Sawdust/sanderdust feed system, modifications of existing coal feed system

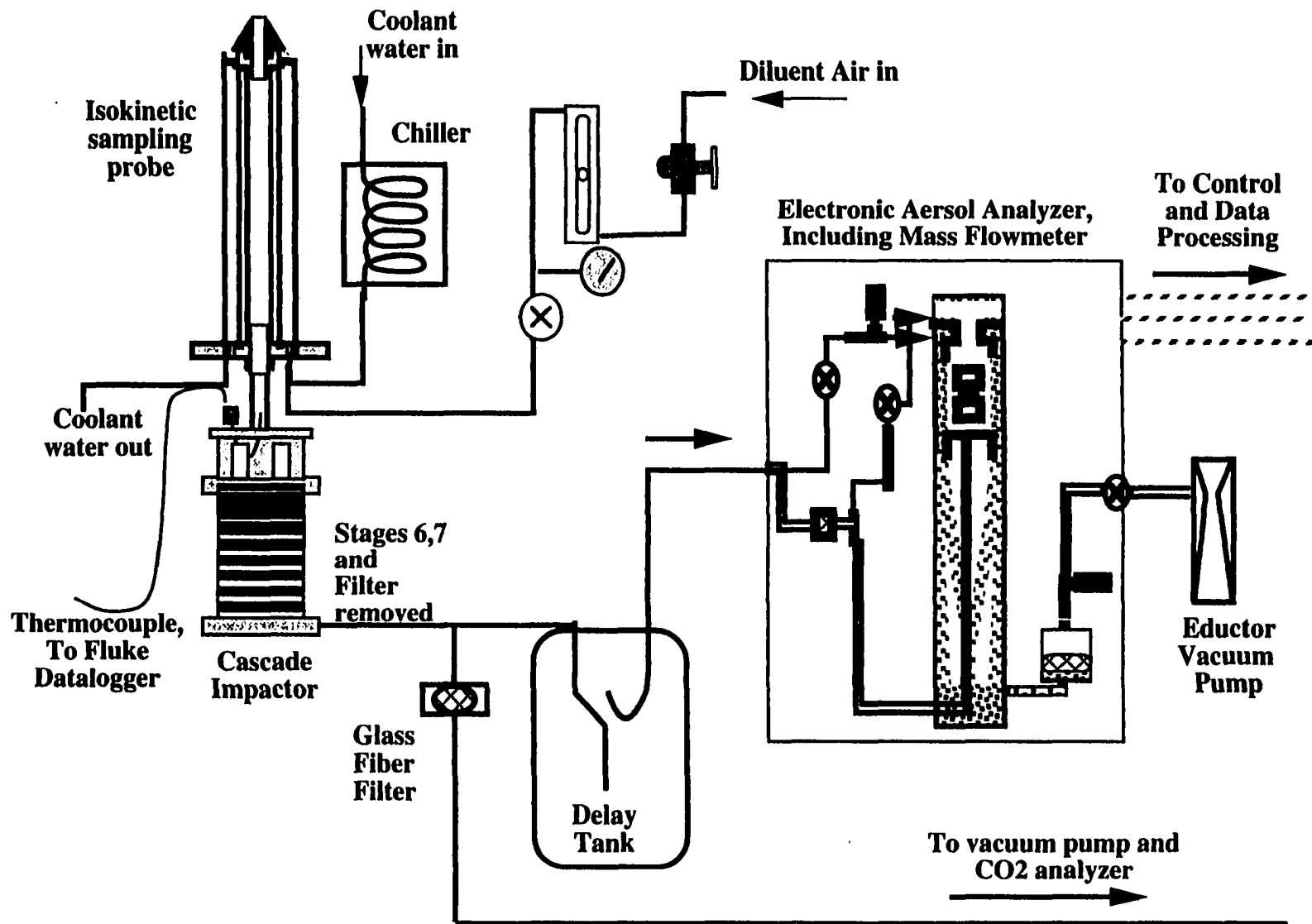


Figure 4.8: Milled sawdust/sanderdust isokinetic sampling probe, cascade impactor and EAA setup (continued next page)

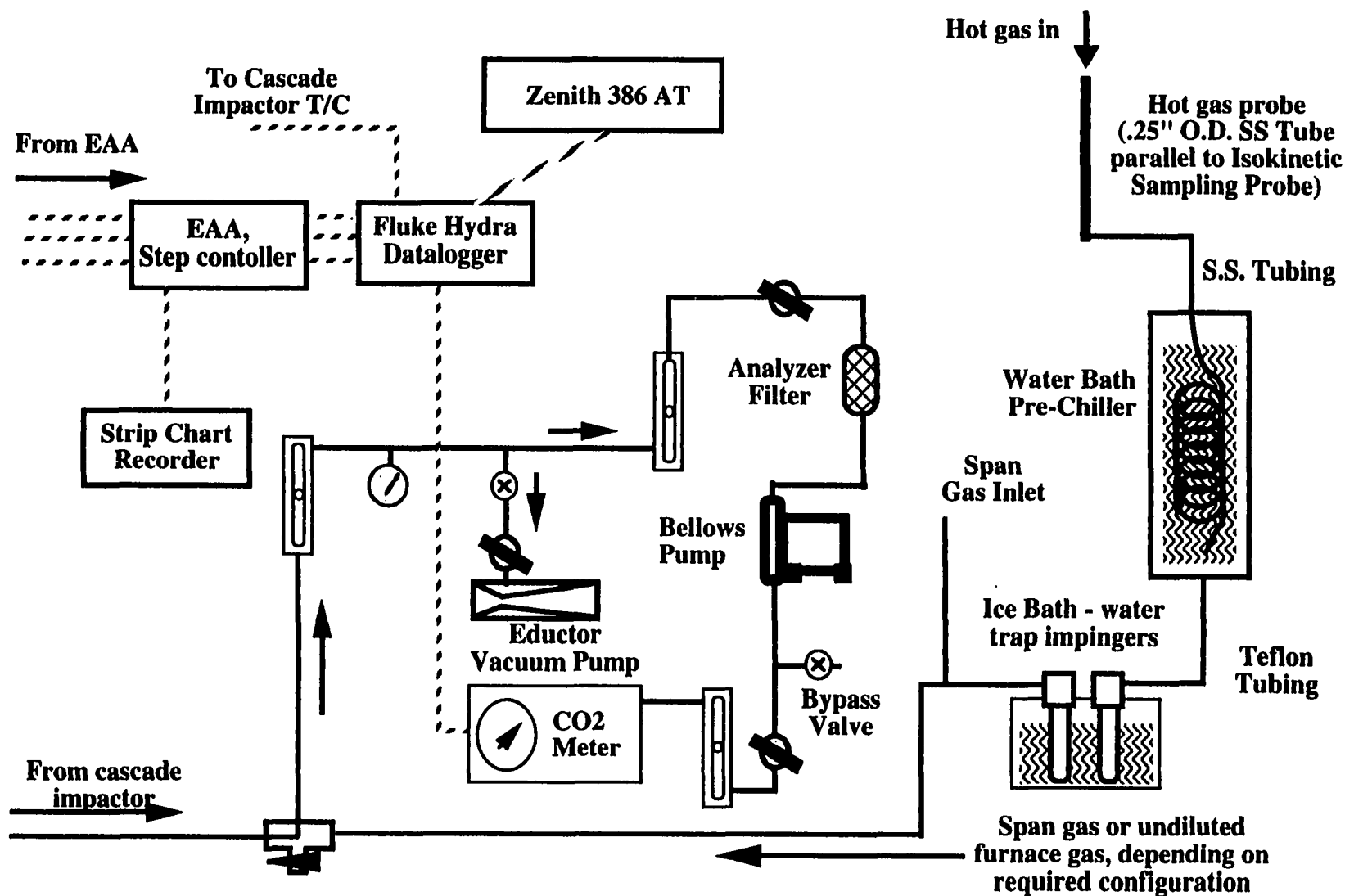


Figure 4.8 (continued): Milled sawdust/sanderdust isokinetic sampling probe, cascade impactor and EAA setup

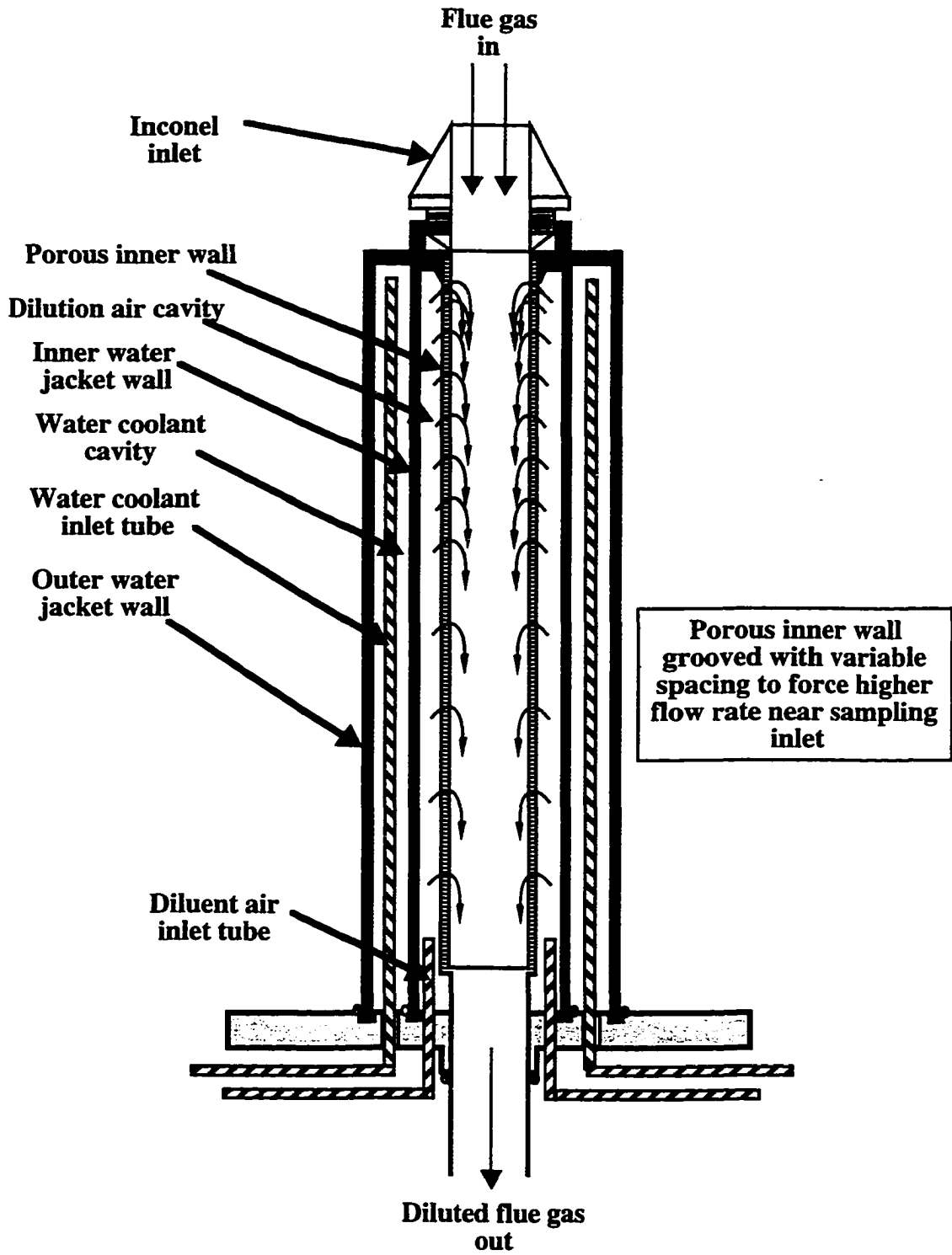


Figure 4.9: Isokinetic sampling probe schematic

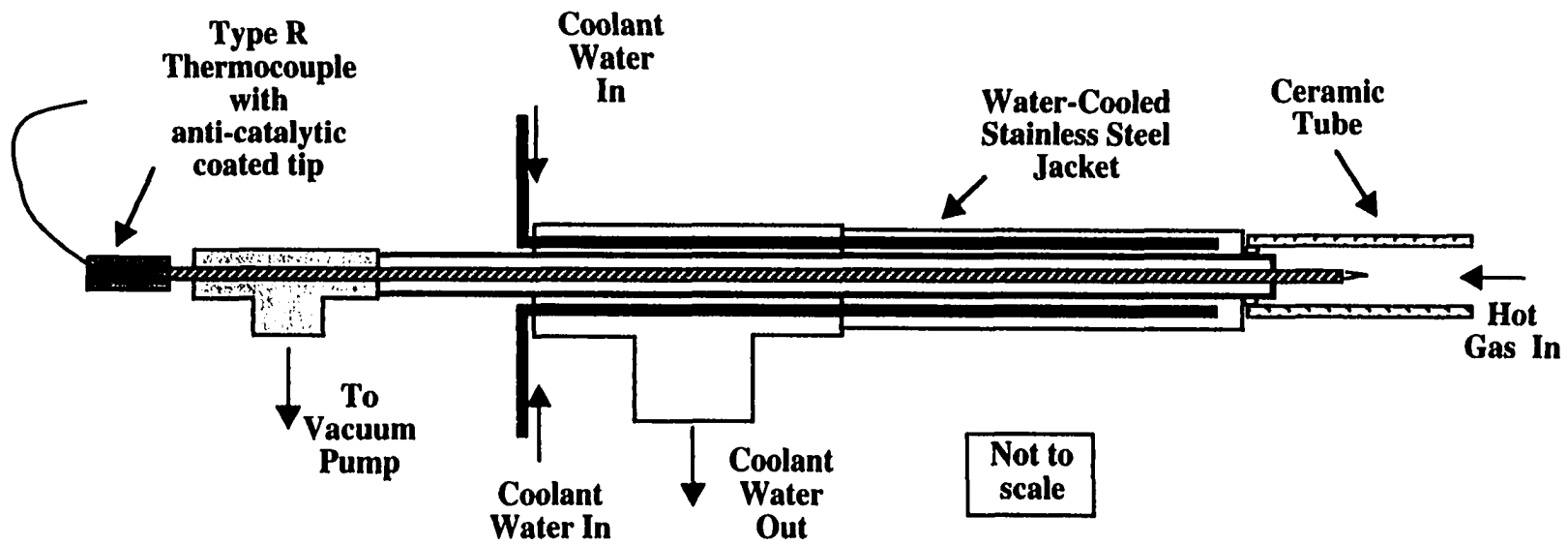


Figure 4.10: Schematic of Water-Cooled High Velocity Thermocouple

INFLUENCE OF COAL TREATMENT AND MINERAL CONTACT ON AEROSOL YIELDS

Mechanical and chemical processing of pulverized coals are known to modify the aerosol yield. This chapter presents coal and artificial char experiments conducted in order to investigate the effects of coal cleaning, pre-combustion size segregation, and coal composition on aerosol yield. The first test series involves well-characterized coals from the Department of Energy database. The second series involves the combustion of artificial chars that allow the original mineral content (including inclusion size distributions) to be preselected.

5.1 Pulverized Coal Experiments

Discrete silicon-based minerals have been shown to reduce alkali metal aerosol formation, as discussed in the Mechanisms chapter. The implications of this phenomena are investigated with three well-characterized bituminous coals - Upper Freeport, Kentucky #11, and Illinois #6. Comparisons of aerosol yield are made between the three coals, burned under similar conditions, in order to investigate variation based on fuel properties. Combustion temperature was also varied in order to examine its effect on aerosol yield.

Upper Freeport pulverized coal was further investigated by aerodynamic size-fractionating the unburned fuel and burning the resulting fractions individually. The behavior of the ash resulting from a weighed sum of the results from the individual fractions (*i.e.*, size distribution, aerosol yield) is compared with the characteristics of the ash from the unfractionated coal. This allows a determination of whether the ash characteristics are simply additive over the individual fractions, or whether interactions yield non-linear behavior (*e.g.*, the sum of the aerosol yield from the individual fractions differs from that of the unfractionated coal).

5.1.1 Coal Characterization

The three bituminous coals selected for investigation are described below. These coals were chosen to complement similar research conducted with higher sodium coals (Kramlich and Newton, 1994a, 1994b), as well as for their history of use in the Department of

Energy coal suite database. The descriptions of the fuel properties have been summarized from work by Boni *et al.* (1990). All fuels were pulverized such that 70% of the fuel mass is able to pass through 200 mesh (74 μm particle diameter). Fuel preparation was done by the Foster Wheeler Company.

Upper Freeport: This is a Appalachian Basin bituminous coal which is relatively low in sodium (0.3% as Na_2O in ash), with a moderate amount of potassium (3.1% as K_2O in ash). It contains a substantial quantity of quartz, coarse pyrite particles (FeS_2), illite (a potassium-containing aluminosilicate), and kaolinite (aluminosilicate).

Kentucky #11: This Appalachian Basin bituminous coal is similar to Upper Freeport in alkalis (0.3% as Na_2O in ash, 2.2% as K_2O in ash). It contains fine pyrite particles, which are not easily removed from the fuel matrix, as well as finely divided quartz and illite.

Illinois # 6: This Illinois Basin bituminous coal is relatively high in sodium (1.3% as Na_2O in ash), as feldspar, and moderate in potassium (2.1% as K_2O in ash). Quartz, dolomite ($[\text{Ca}, \text{Mg}]\text{CO}_3$) and kaolinite are significant, while illite and pyrite are low.

Table 5.1 shows the Proximate analysis and Ultimate analysis of the three coals tested, along with heating value, form of sulfur, and acid soluble alkalis (acid not specified), as determined by Boni *et al.* (1990). Acid soluble sodium is six times higher for Illinois #6 coal than Upper Freeport and Kentucky #11. Note that acid solubility can be a measure of the amount of inorganically-bound sodium. The implication is that sodium is more likely to become mobile if it is organically or ionically bound, rather than tightly bound as an oxide or silicate. Table 5.2 shows the ash composition as oxides and the ash fusion temperatures. As mentioned previously, sodium content is high in Illinois #6. Fusion temperatures were obtained from Gallagher (1992).

Figure 5.1 is a summary of Computer Controlled Scanning Electron Microscopy (CCSEM) results, created from tabulated data available in Boni *et al.* (1990). Pulverized coal particles were mounted in epoxy, sectioned and polished, and examined under SEM to determine mineral inclusion sizes and discrete compositions (Boni, *et al.*, 1990). The dependent variable is the mean diameter of the inclusion. The category adjacent to the inclusion diameter, labeled "baseline", is the average mineral distribution for the whole coal, as determined by summing the inclusions. Hence, the enrichment or depletion of an

individual mineral in a mineral inclusion size range can be directly compared to the mineral content of the sum of all mineral inclusions.

Examining Figure 5.1, Upper Freeport has a significant fraction of its mineral content in the form of mineral inclusions greater than 40 μm in diameter. This size cut is enriched in illite and pyrite, and depleted in quartz and mixed silicates, compared to the average composition of the ash (*i.e.* baseline). Quartz depletion in the largest size cut is balanced by an quartz enrichment in inclusions below 40 μm .

Over 50% of the mineral mass in Kentucky #11 is in inclusions less than 10 μm in diameter, as shown in Figure 5.1. Illite is enriched in these cuts and depleted in larger size cuts. Pyrite is slightly enriched in inclusions greater than 20 μm , and depleted below 10 μm .

Illinois #6 mineral inclusions are predominately less than 40 μm in diameter. Pyrite is depleted below 10 μm , and enriched above 10 μm . Quartz, in the form of fine inclusions, and pyrite, in the form of 40 to 10 μm inclusions are a significant fraction of the total mineral mass in this coal.

A portion of the pulverized Upper Freeport coal was aerodynamically sorted by size into four cuts of <18 μm , 18 to 37 μm , 37 to 85 μm , and >85 μm . Size sorting was conducted by Vortec Products Company of Long Beach, California using a Vortec Model C-1 Particle Classifier. Conventional and Inductively Coupled Plasma analysis (AM Test, Redmond, WA) of each sized fraction is shown in Table 5.3. The largest size cut (>85 μm) has the highest ash percentage by weight. It also has about twice the Fe and S of the other size cuts. This is obviously the result of the large pyrite inclusions observed by Boni et al (1990), as discussed relative to Figure 5.1.

Acid leaching of coals is a common means of extracting the minerals for analysis. Stronger acid solutions (*e.g.*, including HF) may extract more minerals than weak acid solutions. Differences in mineral recovery are often interpreted as a means of measuring the degree of bonding strength of various mineral in the coal.

The ash composition of Upper Freeport size fractions using a strong acid (Table 5.3) and composition using a weak acid (Table 5.4) show significant differences. Most notably, silicon is two orders of magnitude lower in the weak acid-digested sample. This is no

doubt an under-reporting condition due to the strong silica bonds. ICP testing of the sized coals was originally conducted by HNO₃/HCl digestion (EPA method 3050), which is known to under-report aluminum, barium, chromium, potassium, silicon, iron, magnesium, and vanadium. Although HNO₃/HCl digestion a standard analysis technique, silica matrices are not dissolved. The analysis using HF digestion more accurately measures total ash composition. By comparing these two analysis, one may infer the bond strength (and mobility at combustion temperature) of the alkali metals. It appears that about half of the sodium and half of the potassium is tightly bound with the silicates, in all size cuts.

A limited number of tests were conducted with cleaned Upper Freeport coal. Froth floatation cleaning was performed by Hazen Research, Inc of Golden, Colorado. The cleaning process is accomplished in stages, with each stage generating a "float" fraction (the cleaned fuel) and a "sink" fraction (the ash rich stream). The first sink fraction removed is the "rougher tailing", which typically has the highest mineral content of all fractions. Each new stage uses the float fraction from the previous stage, which results in one final cleaned fuel, and a series of reject "tailings" from each stage. A summary of cleaning results are given in Table 5.5. This four stage process is usually only effective at removing excluded mineral matter.

5.1.2 Pulverized Coal Test Matrix

A series of experiments were conducted to explore the effect of coal treatment and mineral contact on aerosol yields. The test matrix is shown in Table 5.6, with individual tests detailed in Appendix G. Most experiments were run for 15 minutes sampling time. Some tests were run with shorter sampling times to prevent overloading of the cascade impactor stages. All tests were conducted with the same volumetric coal flow rate, as controlled by a screw feeder. Assuming the densities of the coal fuels are approximately the same, this corresponds to a dry fuel flow rate of 1.1 grams/minute.

A series of tests were performed with the sampling probe in the horizontal position, as described in section 4.2 and shown in Figure 4.4. This probe location is downstream of a 90 degree vertical-to-horizontal bend in the main furnace, which probably results in loss of some larger ash particulate matter. Furnace free oxygen and air to fuel ratio were maintained relatively constant during this test series, with two exceptions: Test 05069401

(Kentucky #11) was conducted with the Upper Auxiliary burner near stoichiometric, in order to explore the effect of an increase in the overall tunnel temperature, and test 06029401 was conducted with the auxiliary burner off.

A series of tests were also performed with the sampling probe in the vertical position, as shown in Figure 4.5. This probe position allows sampling of the hot gas/particulate prior to bends in the furnace exit duct. This leads to a more representative ash sampling. The Upper Freeport series was conducted with size sorted fuel cuts, as well as with the as-received fuel. Two Upper Freeport tests were conducted with leaner stoichiometry, for comparison to similar tests with Kentucky #11 and Illinois #6.

Two tests each of Kentucky #11 were conducted at three different stoichiometries, to explore the effect of furnace temperature. One blank test was conducted to help determine the uncertainty of measured ash yields.

Temperature profiling in the reactor was limited to three measurements per test with a bare thermocouple at available ports. The column labeled "Upper Temp" on Table 5.6 refers to the temperature as measured at a port 43 cm from the solid fuel injection point, which is the first accessible port. The column labeled "Lower Temp" refers to the temperature as measured at the last port on the furnace, which is 185 cm from the solid fuel injection point. The column labeled "Sample Temp" is the temperature measured at the inlet of the sampling probe. For horizontal tests, this location is in the furnace exhaust duct, as shown in Figure 4.4, so it is cooler than either of the furnace temperatures. For vertical tests, the sample probe tip is two ports above the lowest port on the furnace, 155 cm from the injection point. This is shown schematically in Figure 4.5. Hence, the temperature at this location is slightly higher than the "Lower Temp" measurement.

There is an increase in reactor temperature of about 100 degrees between horizontal testing and vertical testing. This is primarily due to insulation improvements in the main burner and main combustion chamber.

Results of cascade impactor tests are reported below. Most figures are mass distributions, and are based on the following assumptions: 1) The particles are spherical, and 2) the particle density is unity (1 g/cc). Applying these assumptions is a common convention in the literature. The resulting normalized particle diameter is usually referred to as the aerodynamic diameter (*e.g.*, Friedlander, 1977). While the results are not strongly

sensitive to assumed particle density, the shape and porosity of the particles can influence capture. The lower size limit of particles captured on a particular stage is usually quantified by the D_{50} diameter, which is the diameter of a particle that has a 50% probability of capture. The upper size limit of capture is set by the D_{50} diameter of the stage directly before it.

The mass distribution is usually presented as ($\Delta\text{Mass}/\Delta\log \text{Diameter}$), with the independent variable expressed as the logarithm of the particle diameter. Thus, the mass over a set range of diameters is proportional to the area under the curve in that size range. This does lead to some difficulty with the tails of the size distribution (*i.e.* the preseparator and aerosol filter), since there is no clear cut-off diameter for either end of the size distribution.

Material captured on the filter stage is nominally considered to be a log-normal distribution centered at 0.1 μm , which is typically the mode location of particles formed by vaporization/ condensation (Damle, 1982).

A preseparator was used to remove particles larger than 10 μm . This material was not reliably weighed for the horizontal probe tests, and therefore is not included here. Preseparator material collected during vertical probe tests was weighed with reasonable accuracy, and is presented when appropriate. Although the preseparator is not strictly considered a size cut (Andersen Instruments, Inc., 1985), it is plotted at a D_{50} diameter 10 μm .

5.1.3 Pulverized Coal Horizontal Probe Tests - Results

Horizontal Probe Tests, Unmodified Coals:

Figure 5.2 shows a summary of tests of Upper Freeport, Kentucky #11, and Illinois #6 raw coals. The mass collected on each stage of the cascade impactor is plotted relative to the D_{50} size cut of that particular stage. Repeatability is very good for this test series.

Test 05069401 was conducted with the auxiliary burner operating near stoichiometric, resulting in a furnace exit temperature of 688 C, which is 50 degrees higher than comparable tests. The elevated temperature does not seem to significantly change the ash size distribution. This change in temperature may be too small to warrant a change in ash formation mechanisms. Kramlich and Newton (1994a) noted in their experiments that ash yield was not significantly effected by moderate changes in combustion temperature.

Differences in total ash yield are expected to be a direct consequence of differences in ash content of the raw fuels. The table associated with Figure 5.2 shows this trend. The average mass of ash collected for a coal is compared to the other two coals, in terms of ash yield normalized to the ash yield of Upper Freeport. The collected ash yield is compared to the ash content of the coal as obtained from ASTM proximate analysis (see Table 5.1). Agreement is reasonably good, considering that material collected in the preseperator is not included, and all ash collected is not expected to be in the form of elemental oxides.

Detailed mass closure for this system is not practical, primarily due to anisokinetic sampling and loss of large particulate minerals at the first bend prior to the horizontal exhaust duct. Losses relating to super-isokinetic sampling is addressed in Appendix C. Approximately 90% of particulate matter with a diameter below 10 μm is expected to be captured. Above 10 μm the capture efficiency drops significantly, resulting in under-representation of the largest residual particles. Since behavior of mineral matter below 10 μm is of more importance in this investigation, failing to fully capture the largest size fraction is not detrimental.

Figure 5.2 also illustrates the inherent difficulties of interpreting cascade impactor data. The amount of ash collected on a particular stage is not only a function of the true particle size distribution, but also a function of cut-off diameter spacing. Hence, if a stage only catches a narrow range of particle diameters, it will capture less material than if the stage covered a wider range of diameters. With this in mind, it is clear that the area under the mass curve is not proportional to the mass over a size range, unless the D_{50} size cuts of the stages happen to be equally spaced on a logarithmic scale. This can be seen more clearly by comparing Figures 5.3 and 5.4, discussed next, where the apparent dip near 4 μm is partly due to close impactor stage spacing.

In Figure 5.3, the ash distribution has been normalized to the total ash collected for each coal, excluding the ash collected in the preseperator. Preseperator ash was not quantified. Note that the overall ash size distribution is very similar between all tests. All tests show an aerosol mode, a 3 μm mode, and a larger residual mode. Upper Freeport shows a reduced aerosol mode, and a proportionately increased large residual mode. As was shown in Figure 5.1, the average mineral inclusion size in the unburned Upper Freeport is greater than the other two coals. Hence, an enhanced residual size fraction is expected.

Test 05049401 deviates from the family of curves in Figure 5.3. This run was conducted without preheating the cascade impactor prior to test, resulting in condensation of combustion water in the impactor. After drying the stages and filter, the ash yield at $D_{50}=1.1 \mu\text{m}$ is low compared to the other tests. Ash yield at $D_{50}=3.3 \mu\text{m}$ is slightly high. It is possible that condensation on ash particles increased the average aerodynamic diameter of the resulting ash. This phenomenon is exploited in industry by the use of a humidifier prior to a “wet” Electrostatic Precipitator, since the larger, wet particles are more easily charged and captured.

Figure 5.4 shows the same data as Figure 5.3, except replotted as a function of $(\Delta\text{Mass}/\Delta\log D)$. Presented in this form, mass over a particular particle diameter range is proportional to the area under the curve, as discussed earlier. Note the presence of a large residual mode and $3 \mu\text{m}$ mode, similar to Figure 5.3, and the attenuation of the mass distribution dip near $4 \mu\text{m}$. The aerosol mode is not so apparent, which is more an artifact of this method of data presentation than lack of aerosol mode. Expressed in log-log form (lower graph in Figure 5.4) the reduced ash yield around $1 \mu\text{m}$ on test 05049401 is noticeable. As mentioned previously, this is probably a result of condensation in the impactor and subsequent particulate diameter growth.

Upper Freeport Horizontal Probe Tests:

Figure 5.5 shows ash size distribution for as-received Upper Freeport pulverized coal (raw), Upper Freeport cleaned coal, and Upper Freeport coal particles between 37 and $85 \mu\text{m}$. As a percentage of total collected ash, the sized fuel shows a significantly enhanced yield of large particles ($D_{50} = 9 \mu\text{m}$), at the expense of the $\approx 3 \mu\text{m}$ mode. Test 06019401 (Upper Freeport 37 - $85 \mu\text{m}$) had a dark filter, possibly indicative of incomplete char combustion and/or large particle bounce-through. The aerosol measurement for this test should be viewed with this in mind.

These data from Figure 5.5 are shown in normalized form in Figure 5.6. Normalizing consists of adjusting the total ash yield of each fractionated coal such that the yield is proportional to the ratio of the cleaned (or sized) coal mass to the as-received coal mass:

$$\text{measured ash mass} \times \text{fraction of total coal mass} = \text{scaled ash mass}$$

For example, the percentage of cleaned coal derived from a given mass of raw coal is shown in Table 5.5 to be 75.5%. Hence, the cleaned coal total ash yield was reduced to 75.5% of the measured yield, since cleaning removed 24.5% of the total mass from the parent pulverized fuel, as shown in Figure 5.6. Of course, the cleaning process is designed to remove mineral matter, so ash yield is most likely less than 75.5% of the uncleaned coal. Total mineral matter content by proximate analysis for this cleaned coal is not known, but may be determined in the future.

Scaling the 37 to 85 μm cut to 29.2% of its original ash yield (Figure 5.6), shows that a significant fraction of the residual is probably made up of mineral inclusions that have coalesced, or residual ash unchanged since breakup of the original fuel particle. This ash distribution implies that most of the 3 μm mode must be from smaller (<37 μm) coal size cuts. This will be discussed in more detail for tests performed on all size cuts, with the vertical sampling probe.

Aerosol yield is best presented by a cumulative ash yield plot. Figures 5.7 and 5.8 show ash yield as measured, and scaled proportionate to the fraction of original coal, respectively. Material collected on the aerosol filter for the 37-85 μm Upper Freeport test appeared dark, possibly because of incomplete burnout or particle bounce-through, as mentioned earlier. If this is the case, the aerosol yield will be artificially high. Nonetheless, it should be noted that the sized coal aerosol yield is about the same as the raw coal and cleaned coals. If aerosol yield were proportional to the fraction of sized coal to raw coal, one would expect the aerosol yield to be about one-third the aerosol yield of the raw coal.

One cleaned coal test appears to show a very low aerosol yield. No abnormalities were observed during this test that would lead one to expect a low aerosol yield.

Kentucky #11 Horizontal Probe Tests:

Figure 5.9 shows four Kentucky #11 tests. The sized coal test (06029401) is shown twice, once with the ash yield as measured, and secondly with the ash yield scaled to the ratio of sized coal mass to unsized coal mass. For Kentucky #11, 26.6% of the mass of the raw coal is between 37 and 85 μm in diameter, hence the scaling factor was .266. Like the Upper Freeport, the 37 to 85 μm size cut contributes a significant amount to the large (> 9 μm) particle mode, and very little to the 3 μm mode.

It should be noted that test 06029401 was conducted with the auxiliary burner off, possibly resulting in a lower overall tunnel temperature. The temperature measured near the top of the furnace (43 cm from the coal injection port), and at the bottom of the furnace (185 cm from the coal injection port) were 1060 C and 637 C, respectively, which is typical for this test series. The auxiliary burner had failed unexpectedly just prior to testing, so a change in the furnace temperature profile was probably delayed by the low heat dissipation rate of the refractory walls. Burn-out for this test appeared good.

Ash yields for the Kentucky #11 coals are expressed in terms of cumulative mass in Figure 5.10. Test 05049401 had condensation evident in the cascade impactor, making this test questionable, as was discussed earlier in conjunction with Figure 5.3. As can be seen in Figure 5.10, the 37 - 85 μm Kentucky #11 coal ash produces approximately three times the ash of the whole coal, when measured as a percentage of total ash yield. When the ash yield of the 37 -85 μm coal is scaled as before, the aerosol yield is about the same as the raw coal.

Illinois #6 Horizontal Probe Tests:

Tests performed using the horizontal probe with Illinois #6 coal is shown in Figure 5.11. Test 05319401 is shown "as measured" as well as proportionately scaled. The ratio of 37 to 85 μm coal to unsized coal for Illinois #6 is 0.294. Test 05129401 is highlighted because a significant amount of water was found in the preseparator post-test. The likely source is coolant water from the exhaust duct water atomizer. If the probe tip is angled slightly downward, it is possible that condensed water could run down the outside of the probe to the tip, and be pulled into the impactor. The largest size cut seemed to be most significantly effected, most likely from large particle capture by the standing water in the preseparator.

The ash distribution for the 37 to 85 μm coal is very similar to the ash distribution of the unsized coal. The 3 μm mode is apparent for this coal size cut, unlike the sized cuts of Upper Freeport and Kentucky #11. Re-examining Figure 5.1, it can be seen that the average inclusion size of Illinois #6 coal is significantly less than the average inclusion size of Upper Freeport, and moderately less than Kentucky #11. The implication is that Illinois #6 37 - 85 μm coal has many small inclusions, while Upper Freeport 37-85 μm is probably predominantly larger inclusions, and that these modes ultimately carry over to the ash size distribution.

5.1.4 Pulverized Coal Vertical Probe Tests - Results

With the sampling probe in the vertical position, large particles were more efficiently captured in the preseperator, and an improved method of preseperator material weighing was employed. Preseperator mass measurements are provided as appropriate.

Vertical Probe Tests, Unmodified Coals:

Figure 5.13 shows ash mass collected as a function of the cutoff diameter of the capturing stage for each of the three coals tested at a furnace equivalence ratio of 1.8. Recall that furnace equivalence ratio is set by the natural gas and air flow rates, which is about 500 times the flow rate of the solid fuel. Hence, equivalence ratio is primarily a control of the furnace temperature.

Each mass measurement at a particular diameter in Figure 5.13 corresponds the mass collected from the D_{50} diameter indicated, up to the D_{50} diameter of the previous stage. Test to test repeatability is very good. The two Kentucky #11 tests were slightly overloaded in the larger size cuts, and the aerosol filter had some particle bounce-through. The Upper Freeport coals produced dark ash, which may indicate incomplete combustion. The Illinois #6 appeared to have a good ash distribution and burn-out.

As was the case for the horizontal probe tests, Illinois #6 total ash yield is lower than Upper Freeport and Kentucky #11. This is expected, since ASTM ashing shows Illinois #6 to have about half the ash content of Kentucky #11 or Upper Freeport.

If the mass distribution is expressed as $\Delta\text{Mass}\%/\Delta\log D_{50}$ versus the aerodynamic diameter on a logarithmic scale, the area under the curve between two aerodynamic diameters is proportionate to the mass in that size range. This is shown in Figure 5.14 for the three coals tested. All three coals show a similar mass distribution.

Figure 5.15 is the cumulative mass plotted with respect to the cut-off diameter of the capturing stage. Normalized to the total ash collected, including the mass found in the preseperator, the aerosol yield of the Illinois #6 is about 1.5% of the total ash. This contrasts with Kentucky #11 and Upper Freeport, which have less than 0.3% of their ash in the aerosol size range. Tests with the horizontal probe showed only slightly higher aerosol yield for Illinois #6 compared to Upper Freeport and Kentucky #11, as can be seen

in Figure 5.4. Neglecting the mass in the preseparator in the vertical tests does not account for the difference.

Kentucky #11, Vertical Probe Tests with Variable Stoichiometry:

A series of tests using Kentucky #11 with variable air/natural gas stoichiometries were conducted, at air/fuel equivalence ratios of 1.7, 1.8, and 2.0, as shown in Figure 5.16. Maximum furnace temperature measured for each stoichiometry was 1250 C, 1190 C, and 1125 C, as detected by a bare thermocouple at the port closest to the point of solid fuel injection. The bare thermocouple was not a particularly reliable measure of furnace temperature, and accuracy deteriorated with the age of the thermocouple. Thermocouple degradation is documented in the data record sheets of the appropriate tests, but will not be discussed in detail here.

Coal flow rate was maintained at about 1.1 g/minute for all tests, compared to the overall hot gas flow rate of about 515 g/minute, hence the coal flow rate did not significantly influence the overall stoichiometry. The range in stoichiometry resulted in a range of dry O₂ after fuel combustion from 8.6 to 10.9%.

In terms of cumulative mass, the aerosol yield appears to be slightly lower for an equivalence ratio of 1.8, as shown in Figure 5.17. Although this is not the leanest test of this series, Table 5.6 does show that the temperature at the sample port is lower than the temperature for the leaner tests (10079401 and 10119401). One would expect the exit temperature to be cooler for the leaner tests. This may warrant closer scrutiny of the temperature data (*e.g.* reliability of bare thermocouple measurements). It is possible the differences in aerosol yield between these tests are within the error of the data.

Upper Freeport, Vertical Probe Tests:

All vertical probe tests with Upper Freeport coal are shown in Figure 5.18. Two tests (09159401, 09169401) were conducted with the unmodified coal at a stoichiometry of 1.8. These two tests were compared to Kentucky #11 and Illinois #6 in Figure 5.8, with the same stoichiometry. All other tests in Figure 5.18 are at a stoichiometry of 1.7. Tests 10169401, 10219401, and 10259401, are baseline tests, while the remaining tests are the ash distributions for sized fractions of the parent pulverized fuel. It is clear that the size cut of the coal is a factor in the ultimate ash yield. The larger size cuts of coal tend to produce a larger residual ash mode, at the expense of the 3 μm mode, while the smaller sized cut coal

shows a greater 3 μm mode. Note also that the largest size cut of coal produced proportionately the greatest aerosol yield.

Also shown on Figure 5.18 is run 11149401. This is an imperfect test which is included to show the effect of impactor overload. The combination of long sampling time coupled with a possible feeder jam clearing in a single burst, caused an overload of the impactor. The filter was black, most likely from unburned carbon (soot), and stages showed signs of particle blow-by. Blow-by was also a problem with the largest size cut coal. Sampling time was reduced for tests 11289401 and 12029401 to five minutes in order to minimize overload, while tests 12079401 was limited to one minute sampling time.

Figure 5.19 shows the same tests as Figure 5.18, but with a linear independent variable axis. Presented in this way, the area under the curve between two aerodynamic diameters is proportional to the mass between the diameters. As noted before, the smallest size cut is a significant contributor the 3 μm mode.

Aerosol yield is greatest for the coal particles greater than 85 μm , as seen in Figure 5.20. All other size cuts and the raw coal had less than 1% aerosol mass, with the exception of tests 11149401, which was an overloaded test discussed with Figure 5.18.

The ash yield of each size cut was reduced in proportion to the mass of that size cut in the raw (*i.e.* unsized) coal. In this way, the sum of the ash from the sized coals could be compared to the raw coal. The size cut coals, in scaled form, are compared to the raw coal in Figure 5.21. Note that aerosol yield of each sized coal comparable to the aerosol of the unsized coal. Test 11149401, a test with impactor overload, is also shown for comparison. Test 12079401 appears to be moderately inconsistent, compared to other >85 μm tests. This was a one minute test, while the other >85 μm tests were five minute tests.

Figure 5.22 shows the same information as Figure 5.21, but with a linear vertical scale. In this form, it is clear that the residual mode greater than 9 μm is a sum of the size cuts, while the 3 μm mode is mostly from the <18 μm size cut coal.

Summing the fractions of ash from the sized coals produces the ash distribution shown in Figure 5.23. This figure indicates that the residual mass greater than 9 μm is nearly the sum of the large residual mass from the sized coals, but the 3 μm mode is somewhat reduced. Examined in terms of cumulative mass (Figure 5.24), the mass missing from the

3 μm mode appears to be in the aerosol mode. Aerosol yield from the sum of the size-cut coals is about double the aerosol yield of the whole coal. Tests of raw Upper Freeport with the sampling probe in the horizontal position and the vertical position are compared in Figure 5.25. Preseparator mass is not included, since it was not measured for horizontal tests. Mass distributions are very similar. Vertical probe testing shows slightly improved collection of the residual mode, as is expected.

5.1.5 Summary of Pulverized Coal Results

The experiments with pulverized coals support the following observations:

- Experiments with unmodified coals show similar ash size distributions for all three coals tested: A sub-micron aerosol mode, a 3 μm mode, and a >9 μm mode. The aerosol is most likely formed from condensed and coagulated vapors, while the 3 μm and ≥ 9 μm modes are fragmented and coalesced residual ash.
- The sum of aerosol from individually burned aerodynamically-sized coal fractions is greater than the aerosol yield of the whole coal. This is demonstrated with Upper Freeport coal, in which the aerosol yield was about 0.25% of the total ash for the whole coal, compared to 0.75% of the total ash for the summed coal fractions. This lends support to the conclusion that alkali vapor release is attenuated by close association of mineral inclusions.
- Ash size distribution is not identical for all aerodynamically-sized coal fractions. Sized Upper Freeport of <18 μm contributes as much mass to the 4 μm mode as all other size cuts combined. Ash from size cuts greater than 18 μm are predominantly greater than 9 μm in diameter. The obvious implication is incomplete fragmenting of larger mineral inclusions.

5.2 Pulverized Artificial Char Experiments

The complex composition of natural coal makes investigating fundamental properties of a natural coal very challenging. An artificial char is used in this test series to investigate vaporization and/or capture of sodium in the presence of three common minerals. Artificial

char for the current investigation was produced by Park (1995), and the described experiments were conducted with his cooperation.

5.2.1 Artificial Char Characterization

Artificial char is produced using the sucrose pyrolysis technique, following the procedures of Neville *et al.*(1981). A detailed description of the preparation of the artificial char used in this investigation is available in Park (1995). In summary, high purity sucrose, pulverized carbon black, organic alkali salts and discrete mineral inclusions are combined in distilled water to form a paste. The mixture is placed in an nitrogen purged oven at 600 C until a char is formed, in which the pyrolyzed sucrose acts as a binder. Microporosity of the char is controlled by relative proportions of sucrose to carbon black, with higher microporosity associated with higher carbon black content. During pyrolysis, approximately 50% of the sucrose/carbon black dry weight is lost (Park, 1995). After cooling to room temperature in a nitrogen environment, the residual char is pulverized in a ball mill to approximately 50 to 70 μm .

Table 5.7 summarizes the properties of the components used in artificial char preparation, as well as the compositions of the chars prior to pyrolysis. Pyrite, bentonite, and calcite were selected as representative discrete mineral inclusions. Park (1995) chose the ratio of total mineral mass to char mass to be similar to coals studied by Boni *et al.*(1990). Bentonite, chosen as a representative clay mineral, is source variant, and the exact composition of the bentonite used for this study is not certain. A chemical analysis of the remaining bentonite may be warranted.

Sodium oxalate ($\text{Na}_2\text{C}_2\text{O}_4$, decomposition at 270 C) was used as the source of atomically dispersed sodium. The ratio of sodium to char mass was chosen to be representative of a typical western coal of low rank, which is normally high in sodium compared to other coal types (Park, 1995).

5.2.2 Artificial Char Test Matrix

Table 5.8 is a summary of artificial char experiments performed. These tests were performed in cooperation with Park (1995). Individual tests are detailed in Appendix H. All tests were conducted at a furnace air to fuel ratio near 1.45 in order to assure good

burnout, with the exception of test 02069501. This test was conducted at a leaner stoichiometry, which resulted in incomplete burnout.

The very limited supply of artificial char prevented use of the standard screw-type feeder. Instead, a syringe drive system with a premeasured char load was used, as described in the Technical Approach and Experimental Apparatus chapter. Run to run variations with this char feeder is common, so accurate measurement of the total char feed is not readily available. Most tests were conducted with 18 cc (10.8 g) of char over a 10 to 15 minute test period.

5.2.3 Artificial Char Results

When compared to the experiments conducted with pulverized coal and with sawdust/sanderdust (discussed in other sections), it is clear that run to run variability is much greater for the artificial char tests. This is most likely attributable to the char feed system, and compositional variations of the char itself. Char burnout was not complete for all tests, as will be discussed as appropriate.

Artificial Char with Sodium Doping Only:

Figure 5.26 shows all tests using an artificial char composed of only sucrose, carbon black, and dispersed sodium. The higher microporosity char is Suc50/50, as discussed earlier. Results on this figure are given in terms of mass collected on each stage, which is the most fundamental representation of the collected data. All tests have significant aerosol yield, as is indicated by the mass collected on the Backup Filter, and significant residual yield indicated by the mass retrieved from the preseperator. If sodium vaporization and char burnout were complete, one would expect no large residual mode. Test 03169503 is marked for particularly poor burnout, which was manifest as dark ash in the large size cuts. Poor burnout of this nature was usually accompanied by a artificial char feeder jam that was cleared suddenly. No jam was noted on this test, but that is not assurance that one did not occur.

The furnace temperature, as measured by a bare thermocouple in the hot gas stream 43 cm from the point of solid fuel injection, is labeled on the graph. It should be mentioned that furnace temperature is always measured without pulverized fuel flow. Note that the cooler furnace temperature results in higher residual mode compared to the aerosol mode.

These same tests are shown in Figure 5.27, plotted as cumulative mass as a function of D_{50} diameter of the collecting stage. As mentioned previously, run to run variability seems high for artificial char experiments. Aerosol yield for the Suc50/C50 experiments is about 25% to 35% of the total ash collected. The one Suc50/C50 experiment conducted with a cooler furnace temperature yielded 17% aerosol by mass, indicative of incomplete char burnout. This is also evident in the Suc75/C25 test with dark ash, although it appears to have more particulate in the 4 to 5 μm range.

Artificial Char Aerosol Suppression with Bentonite:

All tests conducted with bentonite and sodium doping are shown in Figure 5.28. Two tests with sodium doping, conducted at identical furnace settings as the bentonite tests, are also presented for comparison. It is immediately clear that the bentonite contributes to the residual mode, both in the largest size cut (the preseperator, roughly 10 μm diameter and larger), and intermediate size cuts prior to the aerosol filter. Thus, it is assumed that the particles captured on stages 0 through 7 are primarily residual bentonite particles and a small amount of residual sodium/char that has not been consumed.

Test 03019501 is called out because the char feeder jammed during testing. In the course of clearing it, a large batch of char was sent through the furnace suddenly. This resulted in incomplete combustion and the distorted ash size distribution for that test as shown.

Figure 5.29 shows the same data in terms of the cumulative ash yield, normalized to the total ash. The general trend of a reduction in aerosol yield as a fraction of total ash mass seems clear. Recognizing that burn-out was not necessarily complete, it is difficult to determine if this correlates with sodium absorption by the bentonite or is an artifact of measurement. In particular, increasing the bentonite content from 3.75 g to 5.00 g results in a slightly greater aerosol yield, when the general trend is a reduction in aerosol percentage as bentonite increases. Appropriate scaling factors such that sodium absorption can be quantified is an area worthy of further study in the future.

Artificial Char Aerosol Suppression with Calcite:

Calcite/sodium doped experiments are summarized in Figure 5.30. Tests with sodium doping alone are also shown for comparison. The calcite inclusions do not appear to have fragmented significantly upon firing. The size distribution after the preseperator (about 10 μm and below) is essentially the same for all tests; the majority of the residual ash is captured in the preseperator for all tests. Interestingly, the char with the lowest calcite

content (0.25g) gave the largest preseperator yield. This mass was associated with one large particle that was found in the preseperator and 3 other slightly smaller particles. The test with Cal 0.50 g also had one large particle. These large particles are unusual in that coalescence of this magnitude would be very unlikely. The other calcite tests did not have large particles in the preseperator.

Note that aerosol yield is very similar for all tests. This is likely due to two factors. The small surface to volume ratio of the large (15 to 17 μm) calcite particles offer very little surface area for heterogeneous reaction with the available sodium. Secondly, calcite undergoes calcination to CaO at about 900C, which is a crystalline structure. Melting of CaO does not occur until 2580C, well above practical furnace temperatures. In its crystalline form, it is doubtful CaO would be reactive enough to complex sodium, even with additional surface area.

Artificial Char Aerosol Suppression with Pyrite:

The pyrite series is shown in Figure 5.31. Like the bentonite, the addition of mineral matter generally results in an increase in residual ash. The exception in this case is a higher residual ash yield for char doped with 2.78 grams of pyrite compared to char doped with 3.70 grams. It is very likely that the 2.78 gram tests are distorted by an undetected feeder jam/clear, or other anomaly. An indicator is a dark or black backup filter, usually a sign of impactor overloading due to incomplete char combustion.

All tests show an increase in preseperator yield with addition of pyrite, as well as an enhanced yield in the size range between the preseperator and the backup filter (roughly 0.4 μm to 10 μm). This is significant in that it appears the pyrite has fragmented from its original 9 to 10 μm size. Pyrite fragmentation has been observed by other researchers as well (Srinivasachar *et al.*, 1990, Baxter, 1990). This contrasts with the calcite, which did not show significant fragmentation, and compares well with the bentonite series, which has a 1 to 2 μm inclusion size prior to combustion.

Figure 5.32 shows cumulative mass for this series. Although the general trend is for the percentage of aerosol to be lower as pyrite is increased, it is not clear that this is a result of a reduction in aerosol or is solely an increase in residual mass.

5.2.4 Discussion of Artificial Char Results

The artificial char experiments require further interpretation, particularly in determining the true aerosol change as a function of mineral composition. This information is difficult to directly extract from the tests, because of the affects of incomplete burn-out, possible compositional variations in the unburned artificial char, and run-to-run anomalies that can occur with physical experiments. Nonetheless, some observations may be made:

- Aerosol yield generally decreases with increasing bentonite, although the affect of incomplete burnout and experimental uncertainty cannot be ignored. Suppression of aerosol fraction is most likely alkali metal absorption by bentonite inclusions as the surface of the char particle recedes during combustion, as has been noted by other researchers
- Calcite fragmentation is limited, with most mass remaining in the large ($>9 \mu\text{m}$) particle range. This results in very little surface area for sodium interaction. Sodium and calcite interaction is also probably limited because of the high melting temperature of CaO, which is the favored species above 900 C.
- Pyrite minerals exhibited significant fragmentation, as has been observed by other researchers. Like bentonite, the pyrite generally shows a reduction in aerosol yield with increased mineral content, although it remains to be determined if this is a result of sodium/pyrite interaction or is an experimental artifact.

Table 5.1: Proximate and ultimate analysis of pulverized coals
(Adapted from Boni et. al., 1990, Table 3-8(a))

	Upper Freeport	Kentucky #11	Illinois #6
Proximate Analysis (As Recieved, mass %)			
Fixed Carbon	52.27	41.96	42.15
Volatile Matter	23.99	33.24	35.92
Ash	23.23	20.96	8.62
Moisture	0.51	3.84	13.31
Ultimate Analysis (As Recieved, mass %)			
Carbon	64.57	57.73	59.87
Hydrogen	4.07	4.42	4.55
Oxygen	3.92	7.64	8.52
Nitrogen	1.63	1.29	1.37
Sulfur	2.07	4.22	3.76
Ash	23.23	20.96	8.62
Moisture	0.51	3.84	13.31
Heating Value and Sulfur Form (As Recieved)			
HHV, Btu/lb	11395	--	10693
Sulfate S	0%	0%	0%
Pyrite S	1.41%	2.55%	1.11%
Organic S	0.66%	1.67%	2.65%
Acid Soluble Alkalies (ppm, mass)			
Na	360	371	2258
K	2350	3448	2380
Ca	3700	4875	5811
Mg	1200	1009	1766

Coal Composition for Data

Table 5.2: Ash chemistry of pulverized coals
(Adapted from Boni et. al., 1990, Table 3-8(b))

	Upper Freeport	Kentucky #11	Illinois #6
Ash Chemistry			
SiO ₂	50.6	46.7	46.1
Al ₂ O ₃	24.6	19.4	18.0
TiO ₂	1.2	0.9	0.9
Fe ₂ O ₃	13.5	20.0	20.5
CaO	2.2	4.4	5.3
MgO	1.4	0.9	0.6
Na ₂ O	0.3	0.3	1.3
K ₂ O	3.1	2.2	2.1
SO ₃	2.4	5.0	4.4
P ₂ O ₅	0.1	0.2	0.1
Ash Fusion Temperatures (ASTM)			
* Reducing (°C):			
Initial Deformation	1192	1256	1238
Softening Temperature (Sph.)	1235	1260	1260
Softening Temperature (Hem.)	1271	1278	1268
Fluid Temperature	1298	1289	1349
Oxidizing (°C):			
Initial Deformation	1321	1261	1238
Softening Temperature (Sph.)	1369	1293	1216
Softening Temperature (Hem.)	1381	1316	1277
Fluid Temperature	1391	1333	1368

* From Gallagher, 1992

Coal Conversion to Gas

Table 5.3: Conventional analysis and ICP metals analysis of aerodynamically sized Upper Freeport pulverized coal

	Upper Freeport size cuts			
	<18 μm	18 to 37 μm	37 to 85 μm	> 85 μm
<small>Coal Composite for Data</small>				
Fraction of Unsized fuel	31.0%	26.2%	29.2%	13.7%
Carbon, Volatiles, Ash (Mass %, as received basis)				
Total Carbon%	56.01	57.00	56.85	49.41
Total Solids %	98.45	98.51	98.89	98.64
Volatile Solids %	22.70	23.38	24.14	24.65
Ash %	19.74	18.15	17.90	24.58
Dry-Loss %	1.55	1.49	1.11	1.36
*ICP Metals by EPA method 6010 ($\mu\text{g/g}$ as received fuel)				
Aluminum	24000	19000	20000	25000
Arsenic	28	14	23	23
Barium	110	77	82	100
Calcium	2300	2300	3500	5300
Cadmium				
Cobalt				
Chromium	24	84	18	22
Copper	13	33	20	33
Iron	9800	13000	17000	35000
Potassium	5400	4200	4000	4700
Lithium	30	30	19	25
Magnesium	1400	880	1000	1300
Manganese	56	66	57	97
Sodium	500	550	400	440
Nickel	21	57	14	29
Phosphorus	170	900	180	190
Lead			15	
Sulfur	7300	10000	14000	28000
Silicon	130000	110000	100000	140000
Strontium	65	59	69	85
Titanium	1200	1000	970	1100
Vanadium	50	41	39	46
Yttrium	6.7	5.4	6.6	6
Zinc	45	51	52	79
Elements below detection limits: Sb <7.3, B <36, Be <2.6, Cd <0.73, Hg <3.6, Mo <3.6, Se <11, Ag <3.6, Sn <7.3, Tl <11 $\mu\text{g/g}$ as received fuel				

*Acid digestion of fuel with HNO_3 , HCl , HF

Table 5.4: Conventional analysis and ICP metals analysis with weak acid solution of aerodynamically sized Upper Freeport pulverized coal

	Upper Freeport size cuts			
	<18 μm	18 to 37 μm	37 to 85 μm	> 85 μm
<small>Coal Complain to One</small>				
Fraction of Unsized fuel	31.0%	26.2%	29.2%	13.7%
Carbon, Volatiles, Ash (Mass %, as recieved basis)				
Total Carbon%	56.01	57.00	56.85	49.41
Total Solids %	98.45	98.51	98.89	98.64
Volatile Solids %	22.70	23.38	24.14	24.65
Ash %	19.74	18.15	17.90	24.58
Dry-Loss %	1.55	1.49	1.11	1.36
*ICP Metals by EPA method 6010 ($\mu\text{g/g}$ as recieved fuel)				
Aluminum	13000	8900	5900	7800
Arsenic	12	14		26
Barium	73	53	46	65
Calcium	2900	3400	4400	6500
Cadmium			1.2	1.6
Cobalt	3.2	3.6	3.5	4.6
Chromium	23	16	9.7	12
Copper	19	19	22	31
Iron	11000	15000	20000	39000
Potassium	3200	2400	1800	2000
Lithium	17	10		16
Magnesium	1200	910	750	950
Manganese	62	58	64	99
Sodium	350	260	< 240	250
Nickel	9.6	12	5.5	22
Phosphorus	170	150	120	120
Lead	17	14		24
Sulfur	10000	13000	18000	34000
Silicon	760	740	610	480
Strontium	64	59	53	68
Titanium	160	120	76	76
Vanadium	30	26	22	22
Yttrium	7.9	6.9	4.9	6.8
Zinc	41	44	58	75
Elements below detection limits: Sb <7.3, B <36, Be <2.6, Cd <0.73, Hg <3.6, Mo <3.6, Se <11, Ag <3.6, Sn <7.3, Tl <11 $\mu\text{g/g}$ as recieved fuel				

*Acid digestion of fuel with 1 part HNO₃, 1 part HCl, as 5% solution

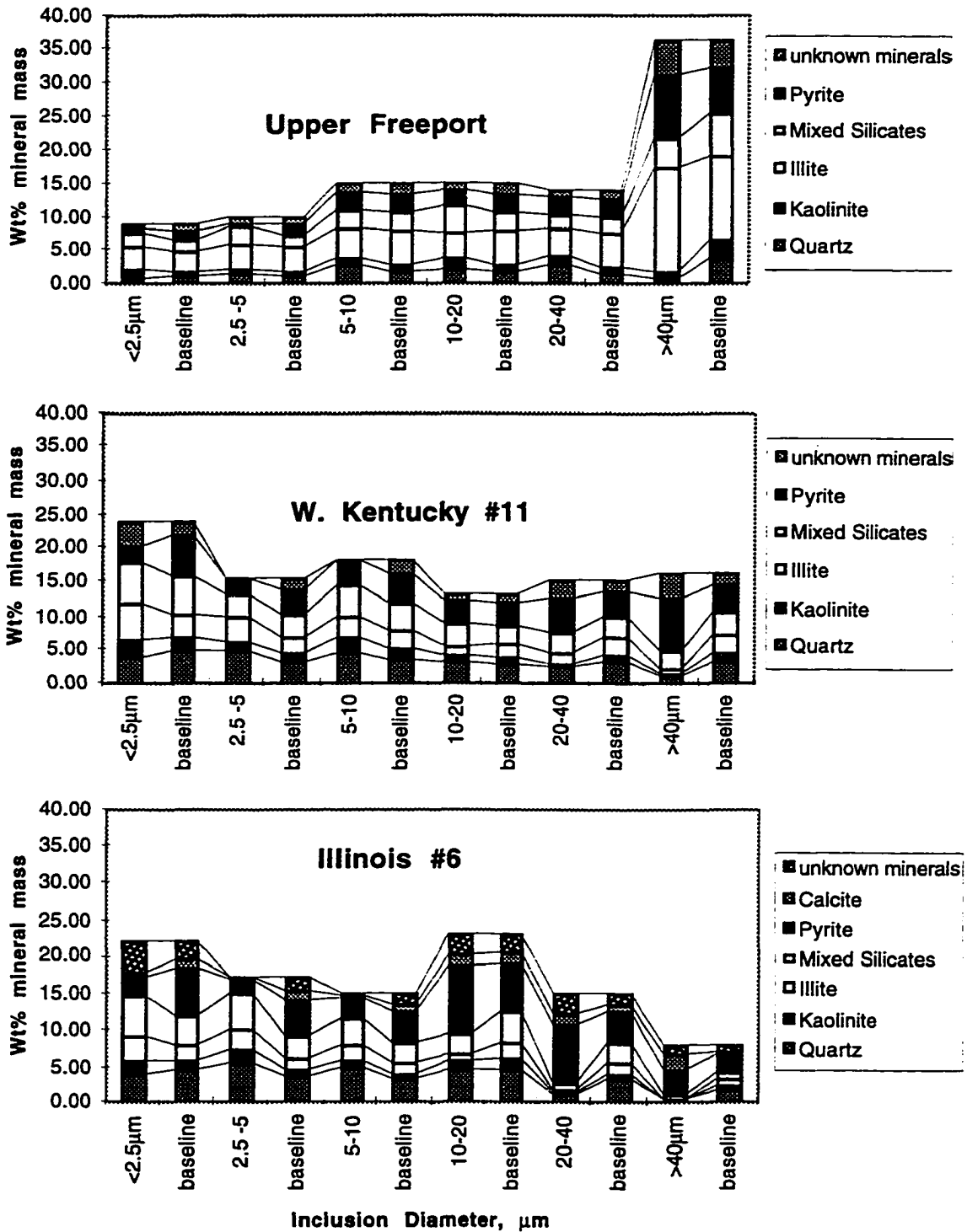


Figure 5.1: Coal mineral composition as a function of discrete mineral inclusion diameter, as measured by CCSEM (Compiled from data in Boni et. al., 1990, Table 4.4)

Table 5.5: Upper Freeport froth floatation cleaning

Froth Floatation cleaning results		
Pulverized Fuel, grams	1991.7	100.0%
Cleaner Froth #3, grams	1503.3	75.5%
Cleaner Tailing #3, grams	110.4	5.5%
Cleaner Tailing #2, grams	130.4	6.5%
Cleaner Tailing #1, grams	136.0	6.8%
Rougher Tailing, grams	111.6	5.6%

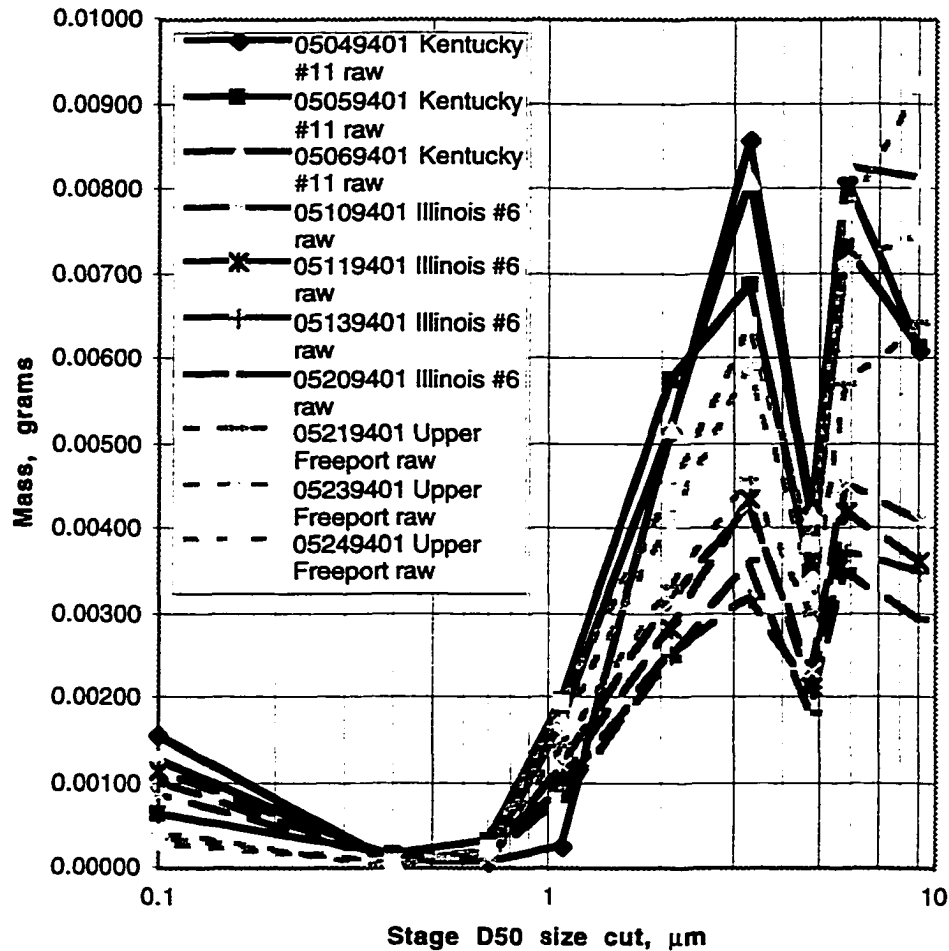
Coal Completion to One

Table 5.6: Pulverized coal test matrix

Test Number	Fuel	Solid Fuel Modification	Furnace Flowrate, g/m (no solid fuel)	A/F equiv	Upper Aux A/F equiv	Dry O2%, no fuel	Dry O2%, w/fuel	Upper Temp, C	Lower Temp, C	Sample Temp, C	Sample Time, min
Horizontal Probe Tests											
05219401	Upper Freeport	raw	489.0	1.7	1.6	9.2	8.8	1058	621	350	15
05239401	Upper Freeport	raw	492.3	1.7	1.5	9.2	8.8	1057	625	325	15
05249401	Upper Freeport	raw	492.3	1.7	1.5	9.2	8.8	1045	624	325	15
05269401	Upper Freeport	cleaned	492.0	1.7	1.6	9.4	9.0	1063	628	360	15
05269402	Upper Freeport	cleaned	492.0	1.7	1.5	9.4	9.0	1058	623	365	15
05279401	Upper Freeport	cleaned	483.5	1.7	1.6	9.2	8.7	1075	623	350	15
06019401	Upper Freeport	37 - 85 μ m	492.1	1.7	1.5	9.3	9.3	1058	642	330	15
05049401	Kentucky #11	raw	494.7	1.7	1.6	9.5	9.1	1060	612	308	15
05059401	Kentucky #11	raw	494.7	1.7	1.6	9.5	9.5	1060	612	308	15
05069401	Kentucky #11	raw	494.7	1.7	1.0	9.5	9.5	1060	688	375	15
06029401	Kentucky #11	37 - 85 μ m	492.0	1.7	Off	9.4	9.0	1068	637	350	15
05109401	Illinois #6	raw	488.9	1.7	1.6	9.3	8.9	1058	603	325	15
05119401	Illinois #6	raw	483.0	1.7	1.6	9.2	8.8	1050	634	350	15
05129401	Illinois #6	raw	494.7	1.7	1.6	9.5	9.1	1063	632	350	15
05139401	Illinois #6	raw	488.9	1.7	1.6	9.3	8.9	1050	632	350	15
05209401	Illinois #6	raw	494.8	1.7	1.6	9.4	9.0	1065	623	372	15
05319401	Illinois #6	37 - 85 μ m	492.0	1.7	1.5	9.4	9.0	1068	630	330	15
Vertical Probe Tests											
09159401	Upper Freeport	raw	507.6	1.8	1.7	9.8	9.4	1190	575	700	15
09169401	Upper Freeport	raw	516.2	1.8	1.7	10.0	9.6	1180	575	700	15
10169401	Upper Freeport	raw	517.6	1.7	1.7	9.0	8.6	1245	660	813	15
10219401	Upper Freeport	raw	519.2	1.7	1.7	9.1	8.7	1243	662	807	15
10259401	Upper Freeport	raw	519.8	1.7	1.7	9.0	8.6	1245	663	805	15
11149401	Upper Freeport	< 18 μ m	518.9	1.7	1.7	9.2	8.8	1246	649	798	15
11149402	Upper Freeport	< 18 μ m	518.9	1.7	1.7	9.2	8.8	1246	649	798	15
11169401	Upper Freeport	< 18 μ m	519.1	1.7	1.7	9.1	8.7	1238	633	777	5
11219401	Upper Freeport	< 18 μ m	519.1	1.7	1.7	9.1	8.7	1244	646	798	5
11079401	Upper Freeport	18 - 37 μ m	518.7	1.7	1.7	9.0	8.6	1243	650	798	15
11109401	Upper Freeport	18 - 37 μ m	521.7	1.7	1.7	9.1	8.7	1250	656	800	15
11119401	Upper Freeport	18 - 37 μ m	519.2	1.7	1.7	9.1	8.7	1239	649	798	15
11039401	Upper Freeport	37 - 85 μ m	517.5	1.7	1.7	9.1	8.7	1254	650	800	15
11049401	Upper Freeport	37 - 85 μ m	519.2	1.7	1.7	9.0	8.6	1245	661	800	15
11289401	Upper Freeport	> 85 μ m	517.6	1.7	1.7	9.0	8.6	1249	646	795	5
12029401	Upper Freeport	> 85 μ m	520.5	1.7	1.7	9.0	8.5	1245	647	791	5
12079401	Upper Freeport	> 85 μ m	519.3	1.7	1.6	9.0	8.6	1250	648	793	1
10139401	Kentucky #11	raw	519.2	1.7	1.7	9.0	8.6	1249	663	813	15
10149401	Kentucky #11	raw	519.8	1.7	1.7	9.0	8.7	1250	662	817	15
09089401	Kentucky #11	raw	517.8	1.8	1.6	10.1	9.7	1190	560	655	15
09099401	Kentucky #11	raw	516.2	1.8	1.6	10.0	9.6	1180	560	680	15
10079401	Kentucky #11	raw	514.7	2.0	1.7	11.1	10.8	1125	628	759	15
10119401	Kentucky #11	raw	514.5	2.0	1.7	11.2	10.9	1118	623	744	15
09219401	Illinois #6	raw	516.4	1.8	1.7	9.9	9.5	1180	580	700	15
09239401	Illinois #6	raw	516.4	1.8	1.7	9.9	9.5	1185	595	725	15
10069401	Blank	-	512.9	1.9	1.7	10.5	10.5	1173	635	770	15

All tests were conducted with pulverized fuel flow rate of 1.1 g/min

Horizontal Probe, All Unmodified Coal Tests, as measured



	Upper Freeport	Illinois #6	Kentucky #11
Average Total Ash collected by horizontal probe, grams	0.02972	0.01845	0.03455
Average Total Ash collected normalized to Upper Freeport, %	100	62	116
Ash in raw coal, (grams ash/ grams as received coal), %	23.2	8.6	21.0
Ash in raw coal, normalized to Upper Freeport, %	100	37	90

Figure 5.2: Ash size distributions of Upper Freeport, Kentucky #11 and Illinois #6 coals as measured with the horizontal sampling probe

Coal Commission for Ohio

Horizontal Probe, All Unmodified Coal Tests, Mass % Basis

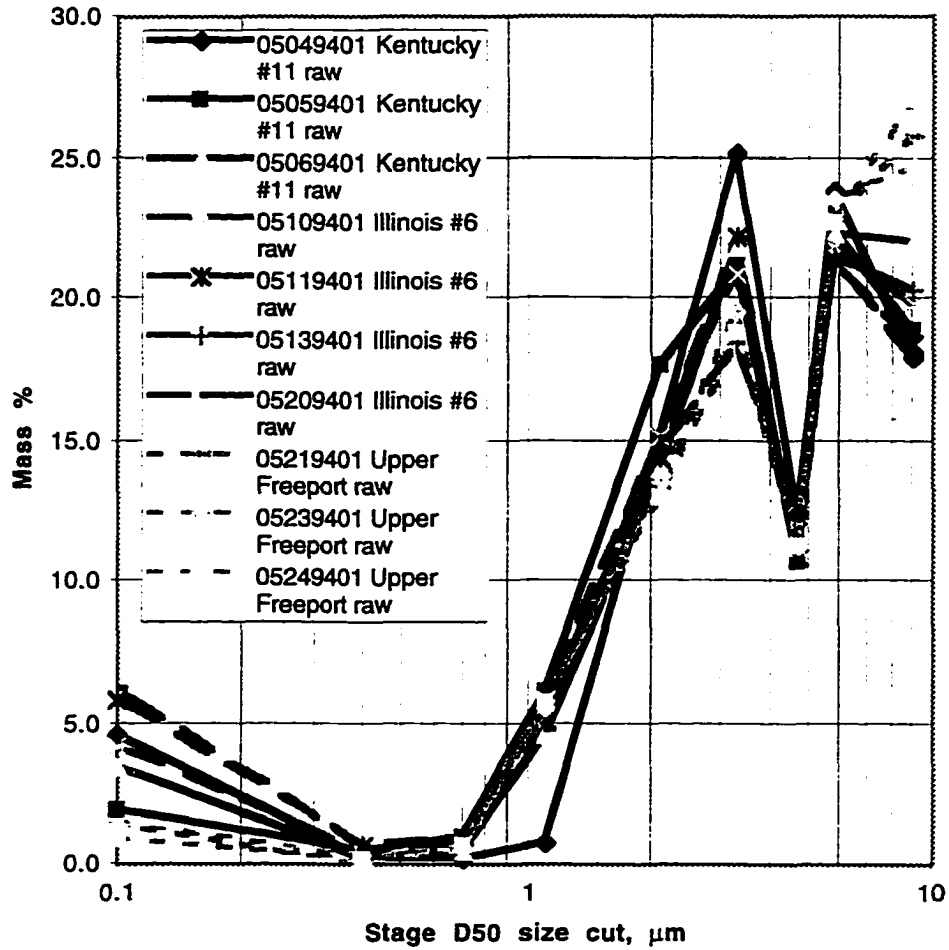


Figure 5.3: Ash size distributions of Upper Freeport, Kentucky #11 and Illinois #6 coals as measured with the horizontal sampling probe, normalized to total mass collected

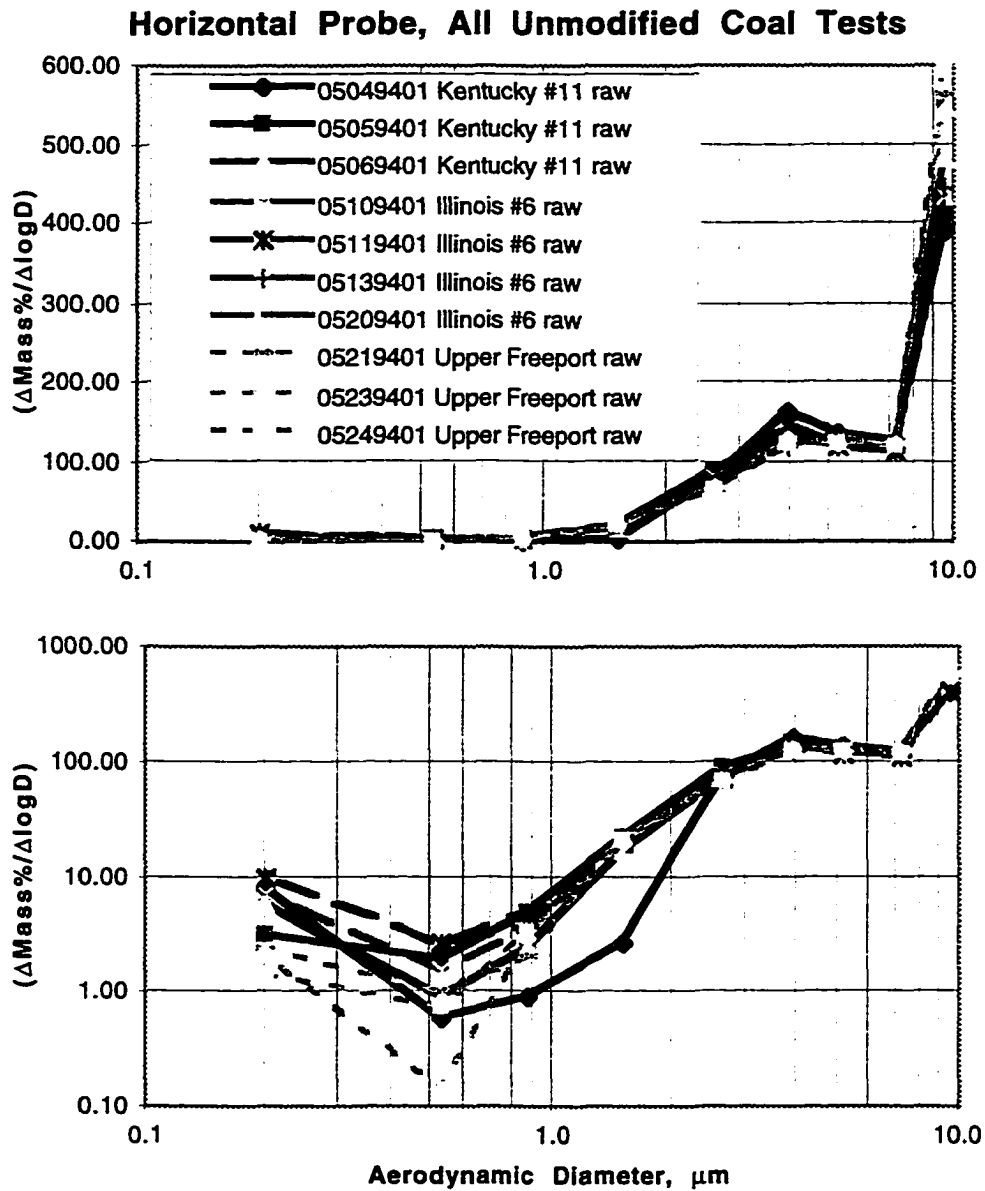


Figure 5.4: Ash size distributions of Upper Freeport, Kentucky #11 and Illinois #6 coals as measured with the horizontal sampling probe, in terms of $\Delta\text{Mass}/\Delta\log\text{D}$

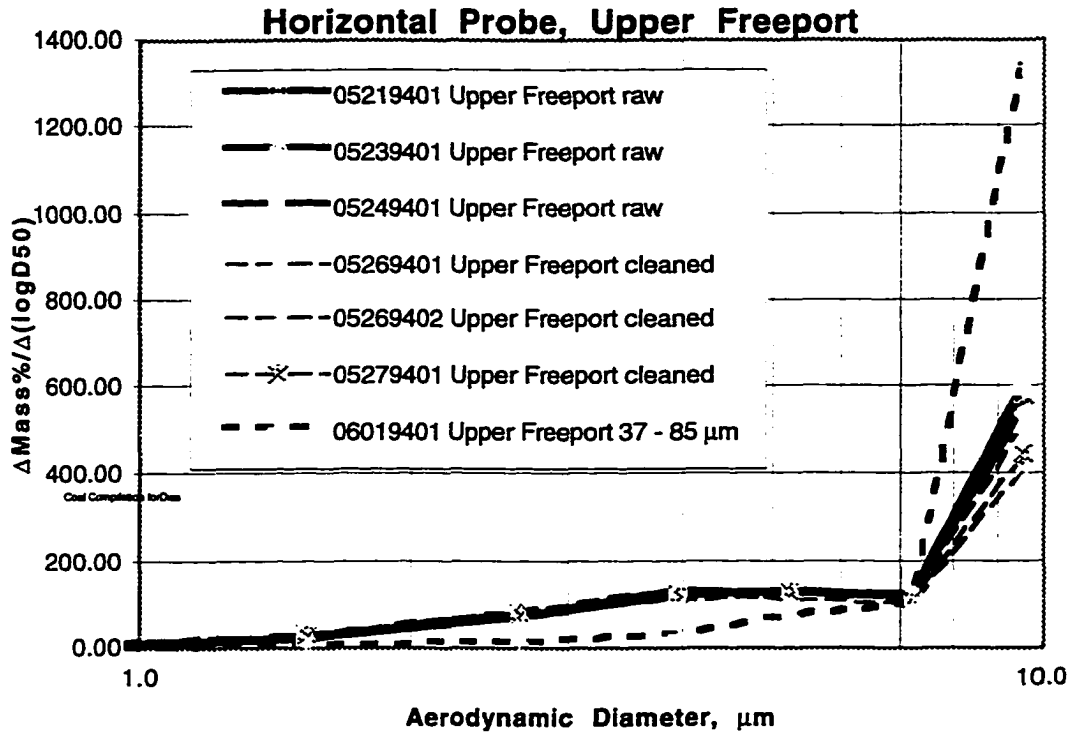


Figure 5.5: Upper Freeport ash size distribution using a horizontal sampling probe, $\Delta\text{Mass}/\Delta\log D$ as a function of particle diameter

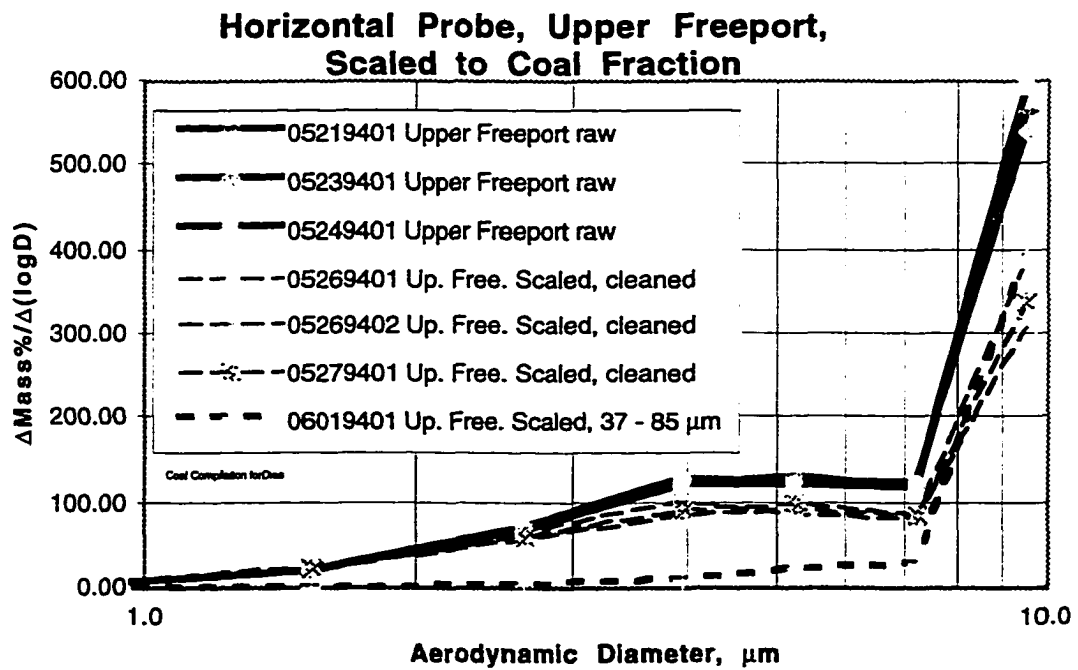


Figure 5.6: Upper Freeport ash size distribution using a horizontal sampling probe, mass percent adjusted for total fraction of original coal

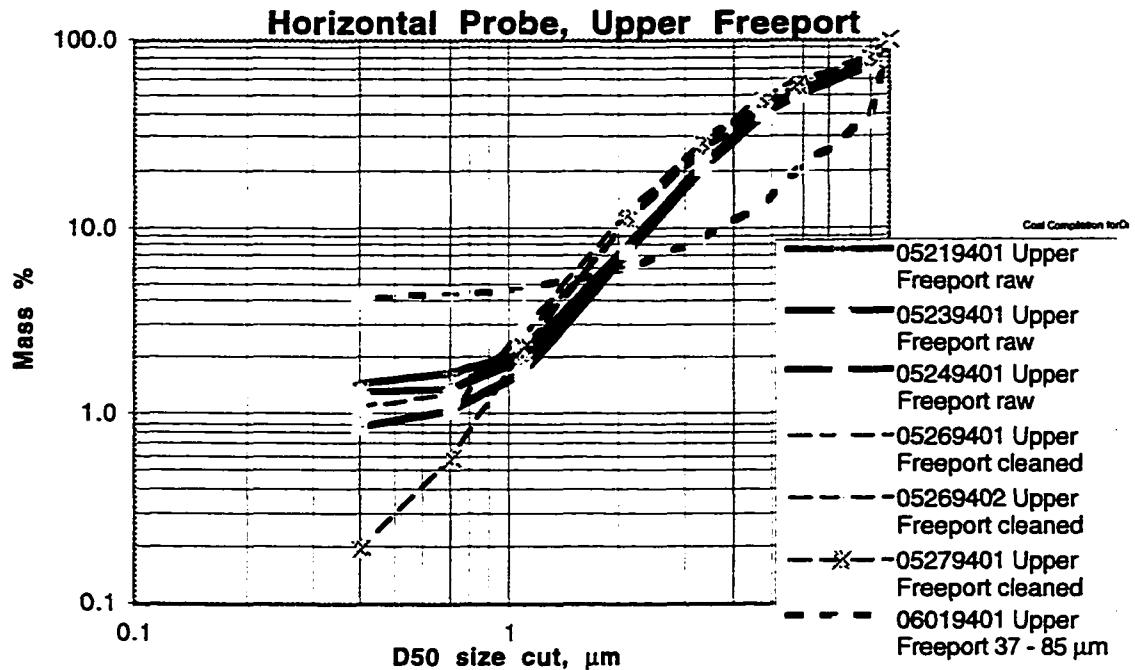


Figure 5.7: Upper Freeport cumulative ash size distribution using a horizontal sampling probe, mass percent as a function of cascade impactor size cut

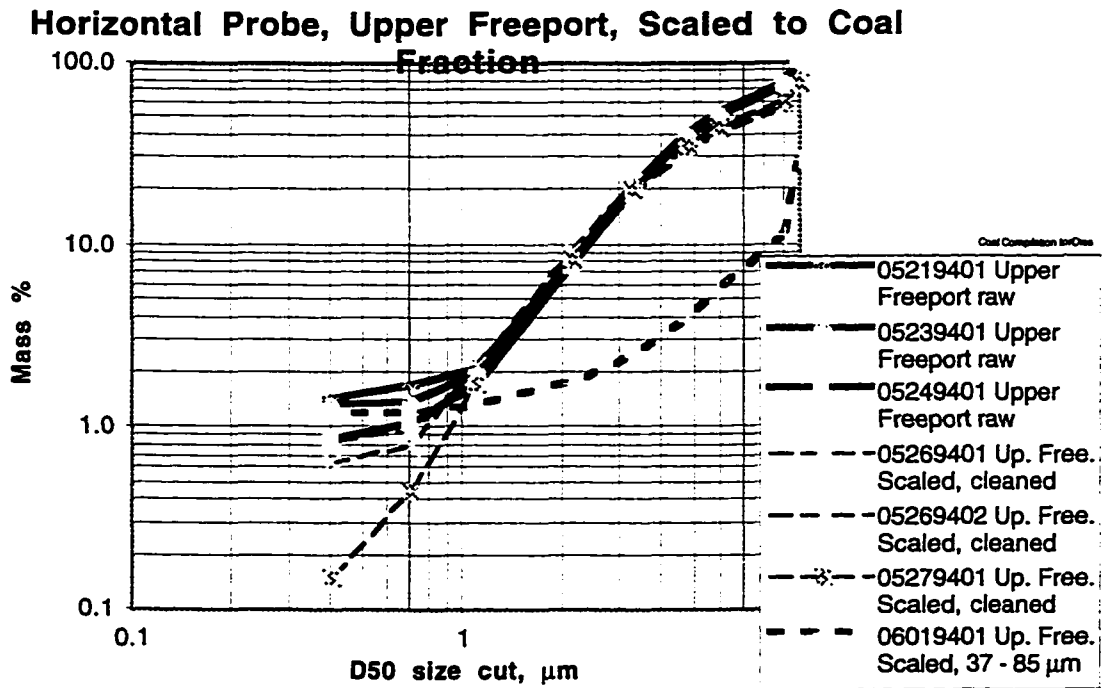


Figure 5.8: Upper Freeport cumulative ash size distribution using a horizontal sampling probe, mass percent adjusted for total fraction of original coal

Horizontal Probe, Kentucky #11

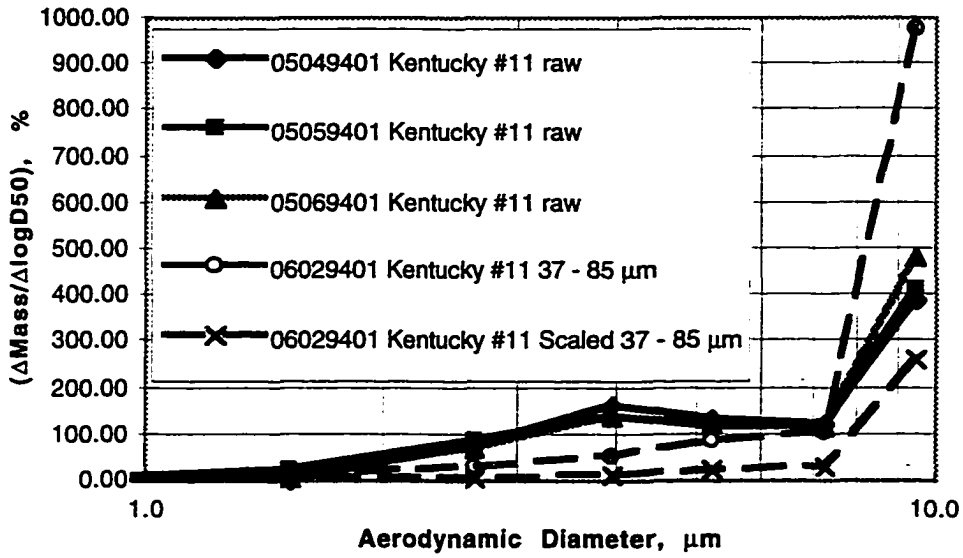


Figure 5.9: Kentucky #11, ash mass distribution using a horizontal sampling probe

Horizontal Probe, Kentucky #11

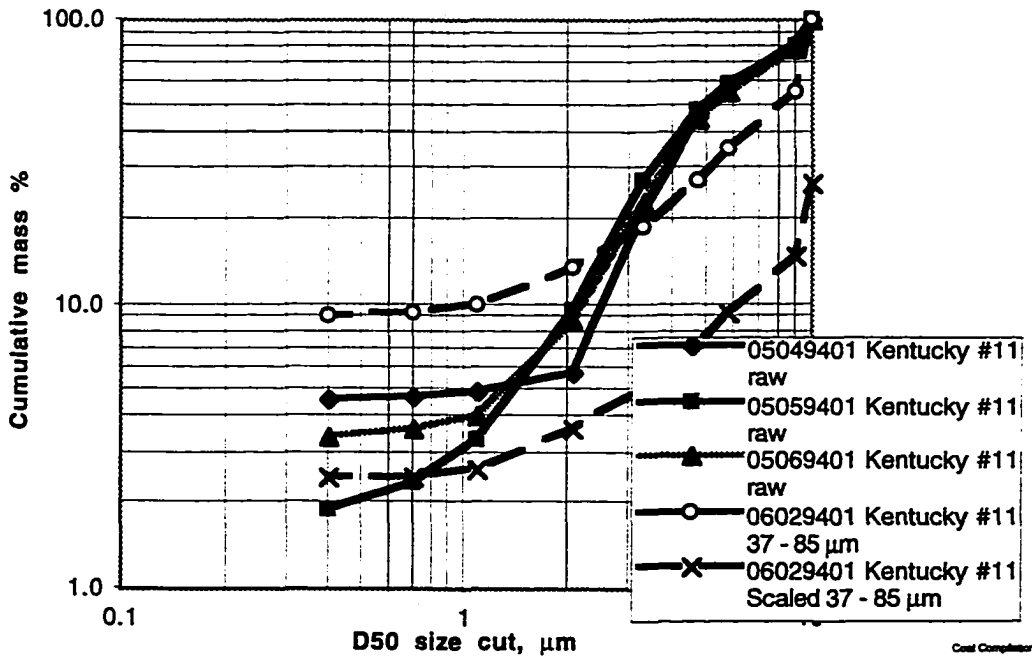


Figure 5.10: Kentucky #11, cumulative mass distribution using a horizontal sampling probe

Horizontal Probe, Illinois #6

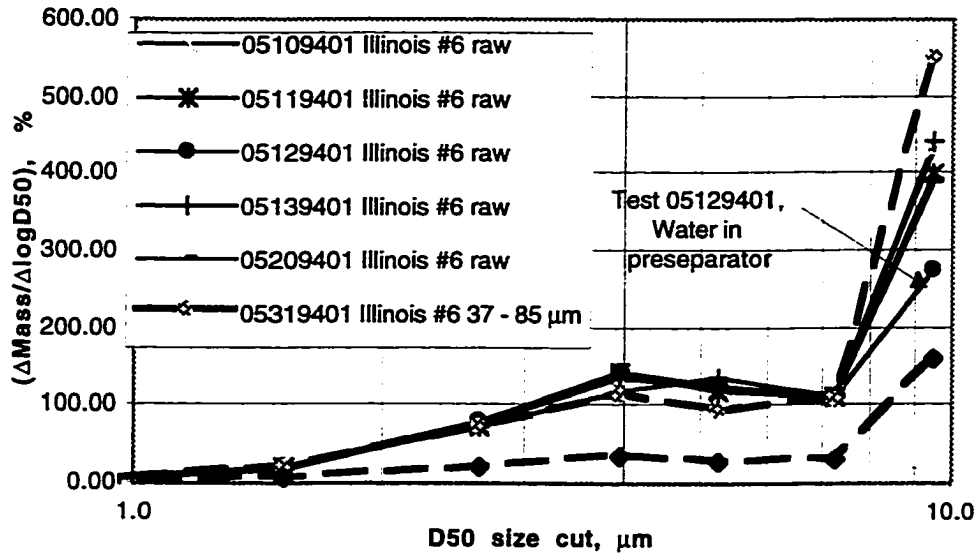


Figure 5.11: Illinois #6, ash size distribution using a horizontal sampling probe

Horizontal Probe, Illinois #6

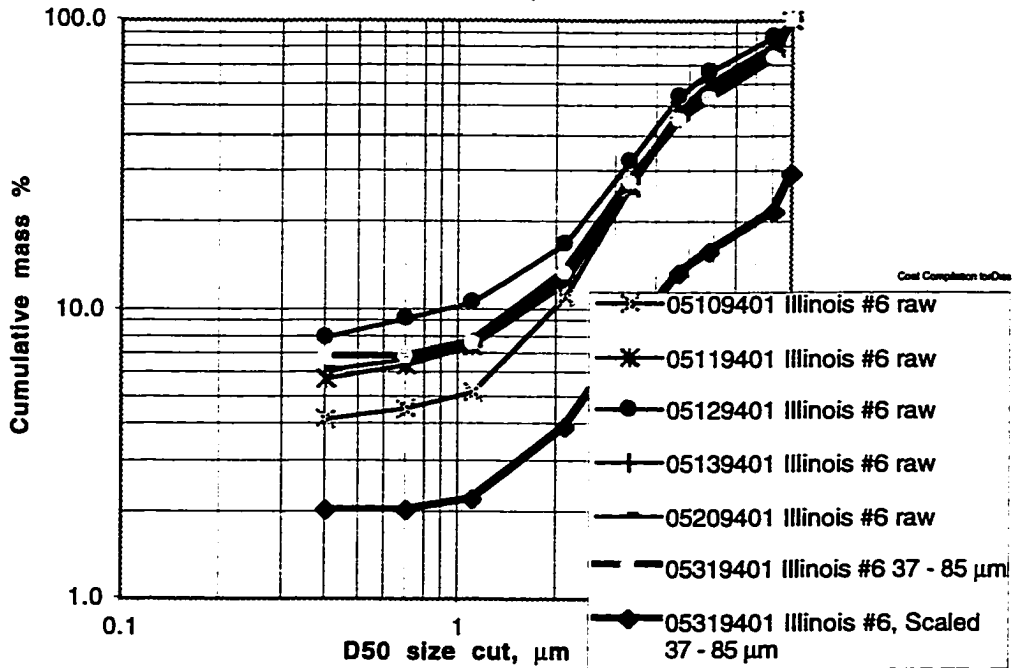


Figure 5.12: Illinois #6, cumulative mass distribution using a horizontal sampling probe

Vertical Probe, 1.8 Equivalence Ratio

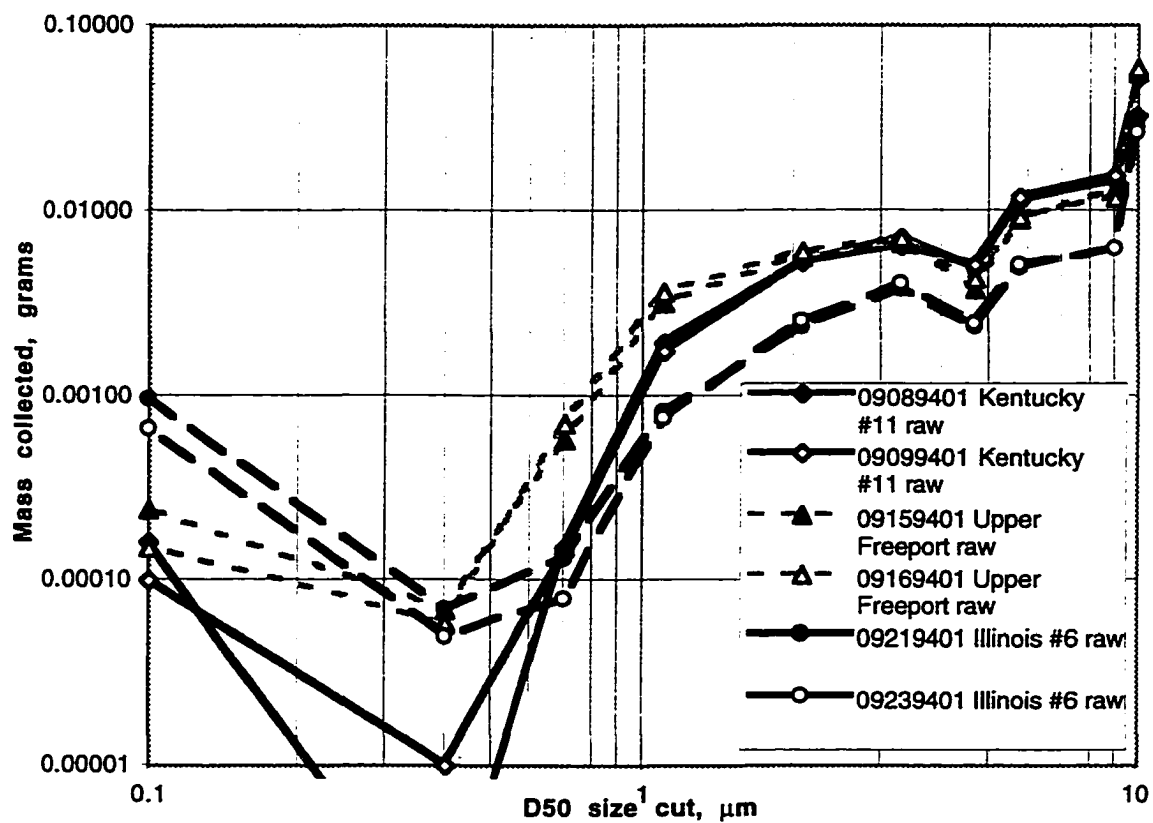


Figure 5.13: Three coals, ash collected as a function of impactor stage for 1.8 furnace equivalence ratio

Vertical Probe, 1.8 Equivalence Ratio

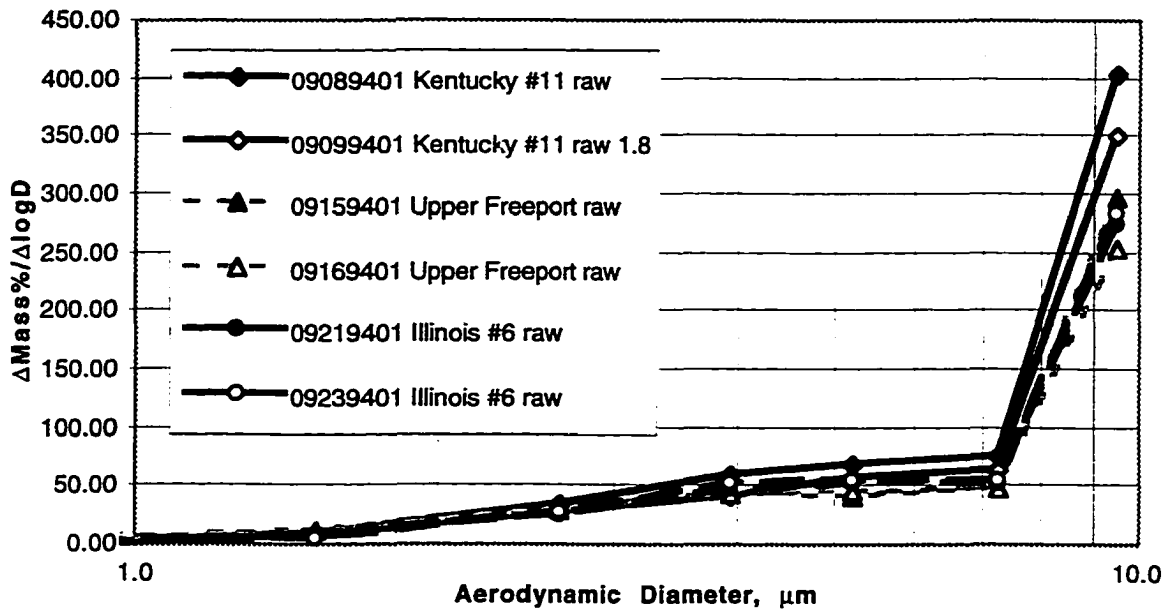


Figure 5.14: Three coals, ash collected expressed as $\Delta\text{Mass\%}/\Delta\log D$ for 1.8 furnace equivalence ratio

Vertical Probe, 1.8 Equivalence Ratio

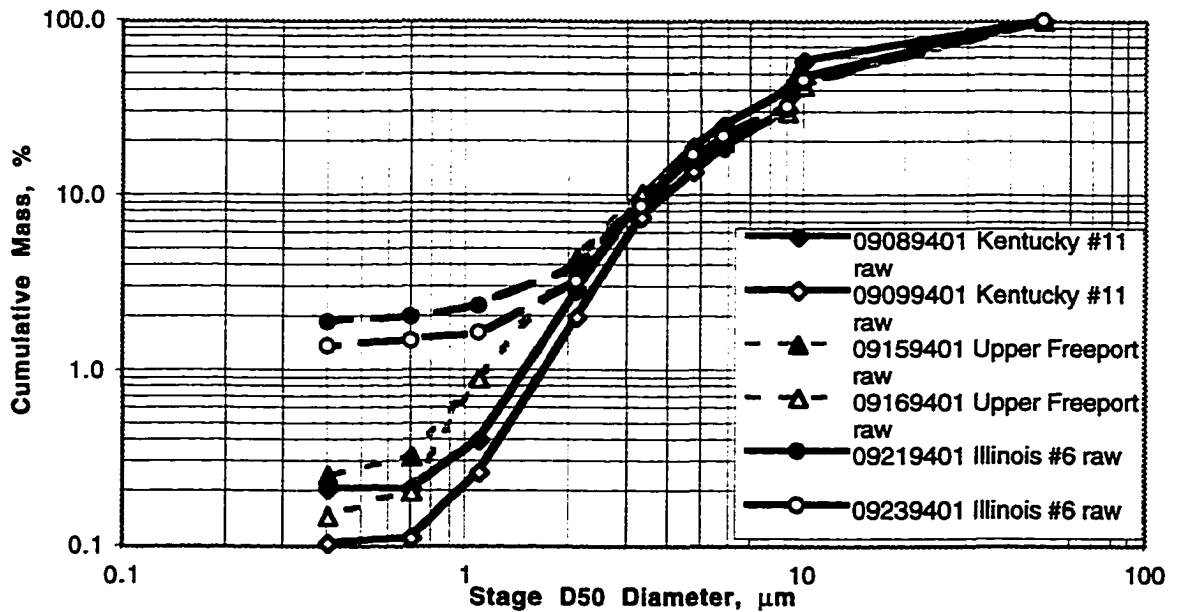


Figure 5.15: Three coals, ash collected expressed as cumulative mass for 1.8 furnace equivalence ratio

Vertical Probe, Kentucky #11, Variable Stoichiometry

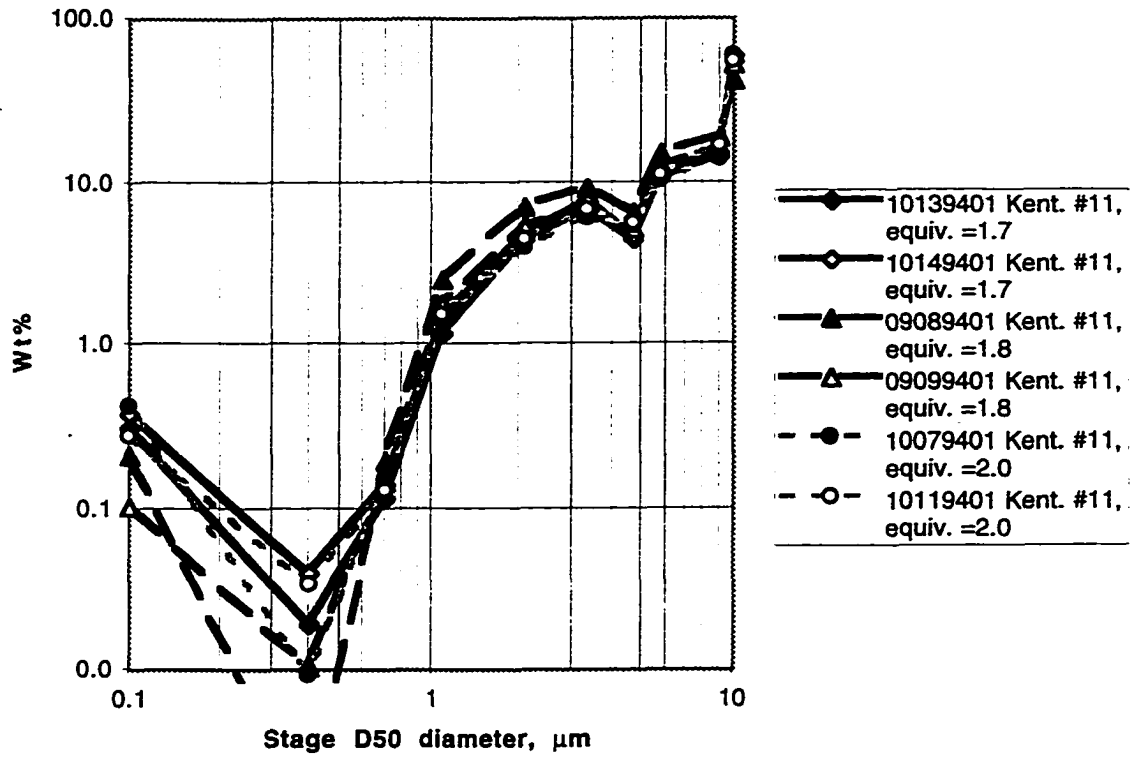


Figure 5.16: Kentucky #11, the effect of furnace stoichiometry on ash yield

Vertical Probe, Kentucky #11, Variable Stoichiometry

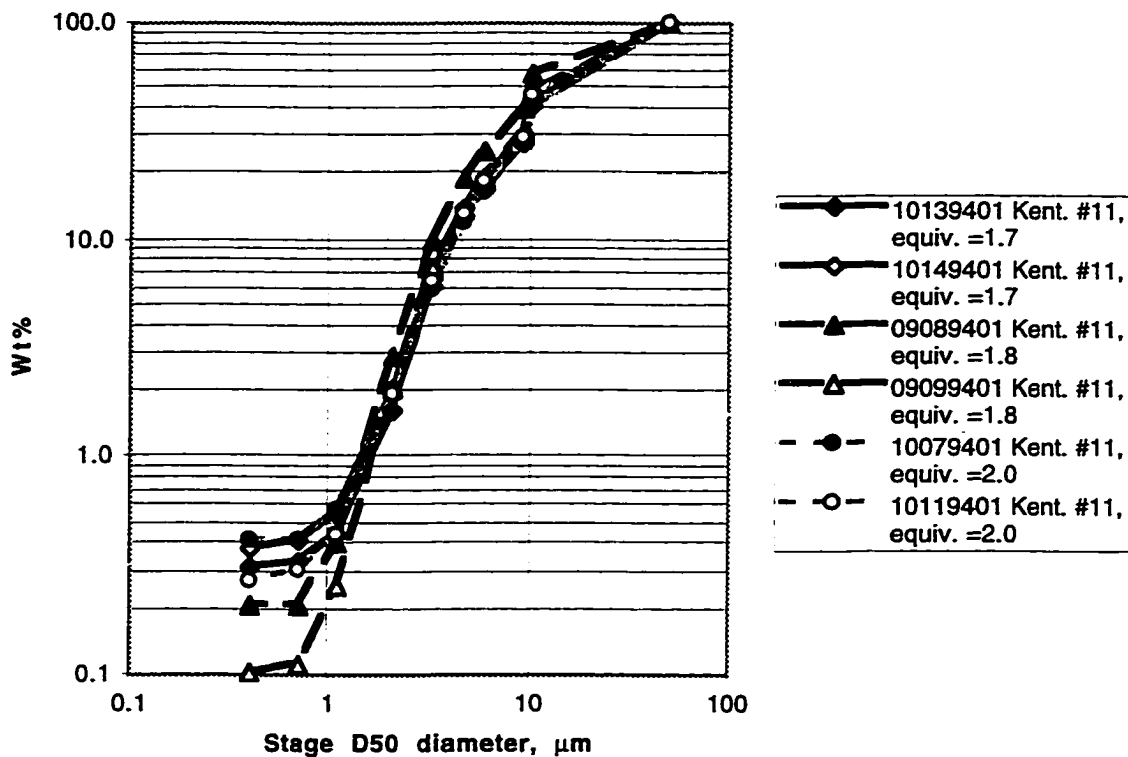
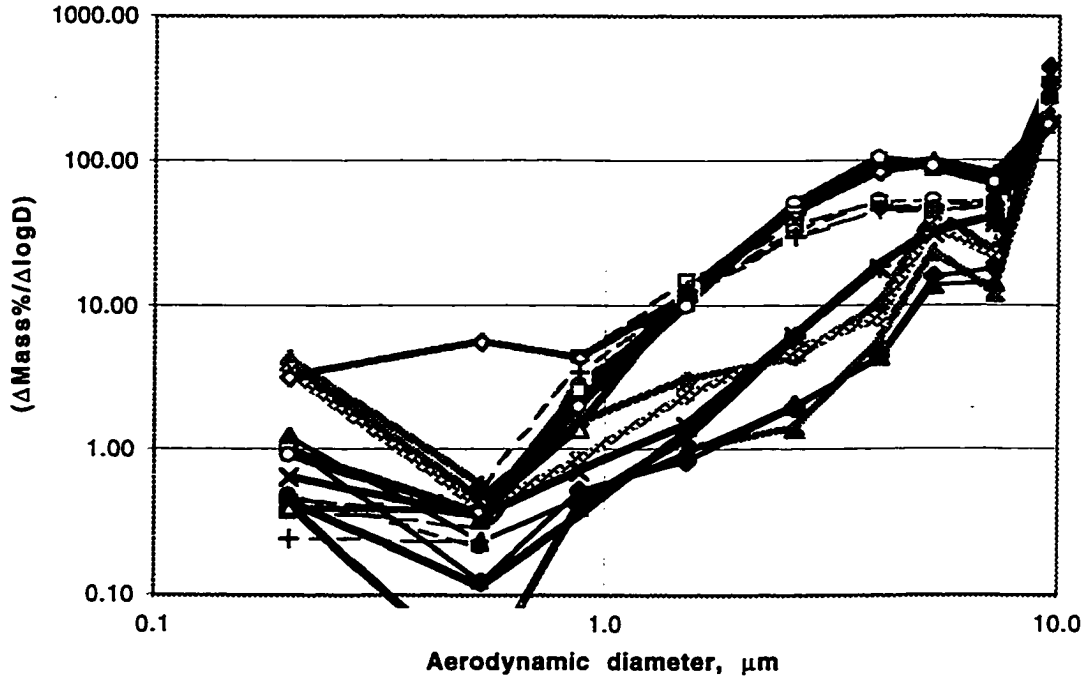


Figure 5.17: Kentucky #11, ash collected expressed as cumulative mass

Vertical Probe, Upper Freeport



—●— -09159401 Upper Freeport raw	—+— -09169401 Upper Freeport raw
—○— -10169401 Upper Freeport raw	—◇— -10219401 Upper Freeport raw
—□— -10259401 Upper Freeport raw	—▲— -12079401 Upper Freeport > 85 μm
—◆— -12029401 Upper Freeport > 85 μm	—⊗— -11289401 Upper Freeport > 85 μm
—▲— -11039401 Upper Freeport 37 - 85 μm	—◆— -11049401 Upper Freeport 37 - 85 μm
—×— -11079401 Upper Freeport 18 - 37 μm	—*— -11109401 Upper Freeport 18 - 37 μm
—■— -11119401 Upper Freeport 18 - 37 μm	—△— -11149401 Upper Freeport < 18 μm
—◇— -11149402 Upper Freeport < 18 μm	—□— -11169401 Upper Freeport < 18 μm
—○— -11219401 Upper Freeport < 18 μm	

Figure 5.18: All Upper Freeport tests conducted with the vertical probe

Vertical Probe, Upper Freeport

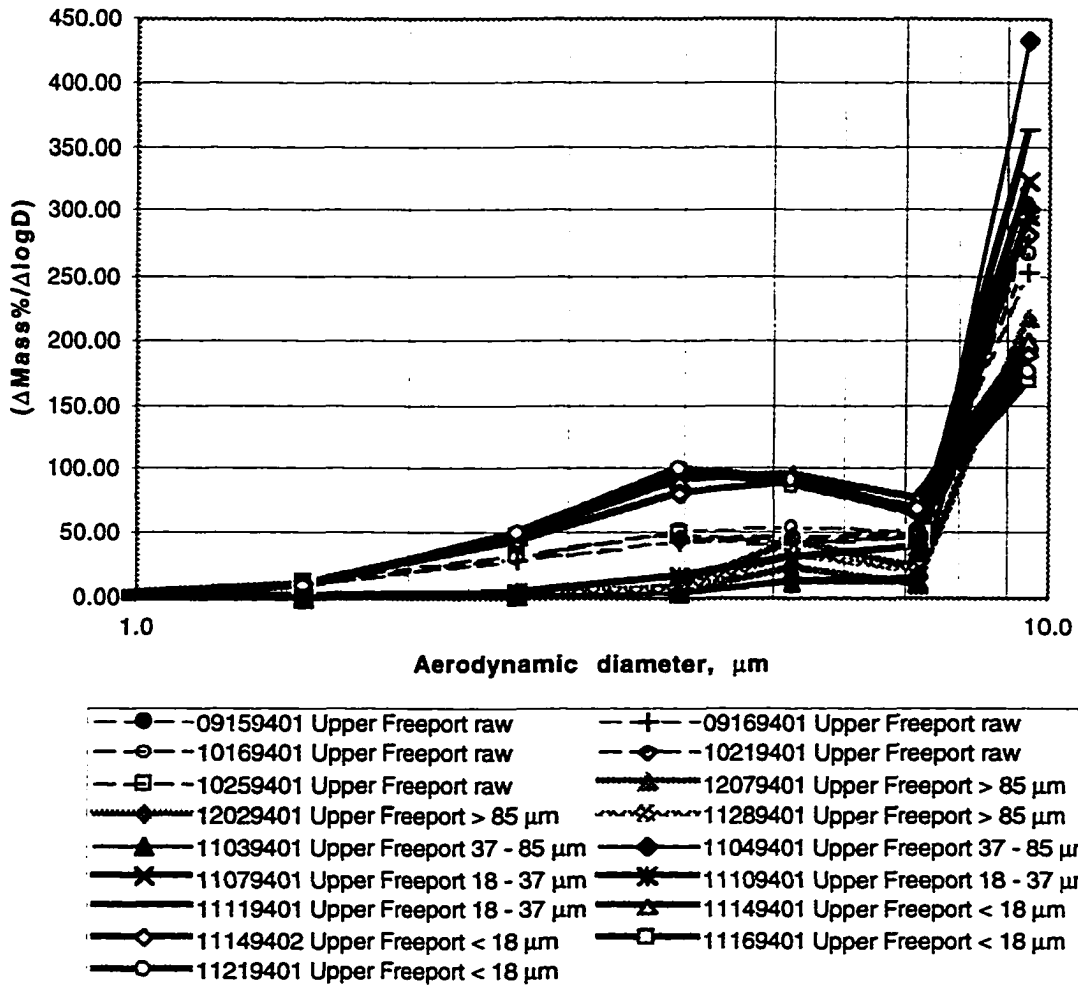


Figure 5.19: All Upper Freeport test with the vertical probe with ash yield expressed as $\Delta\text{Mass\%}/d\log D$

Vertical Probe, Upper Freeport

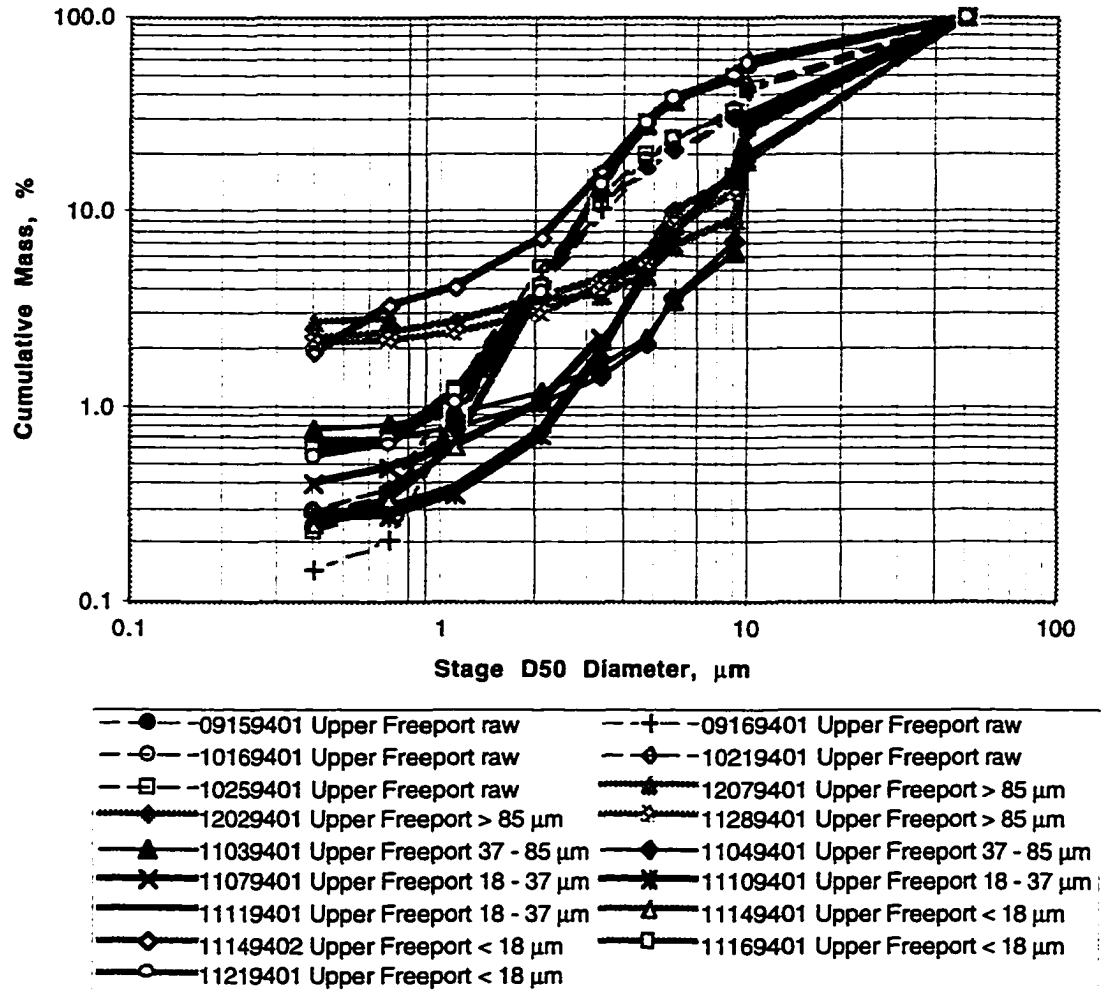


Figure 5.20: All Upper Freeport test with the vertical probe with ash yield expressed as cumulative mass

**Vertical Probe, Upper Freeport
Scaled by coal fraction**

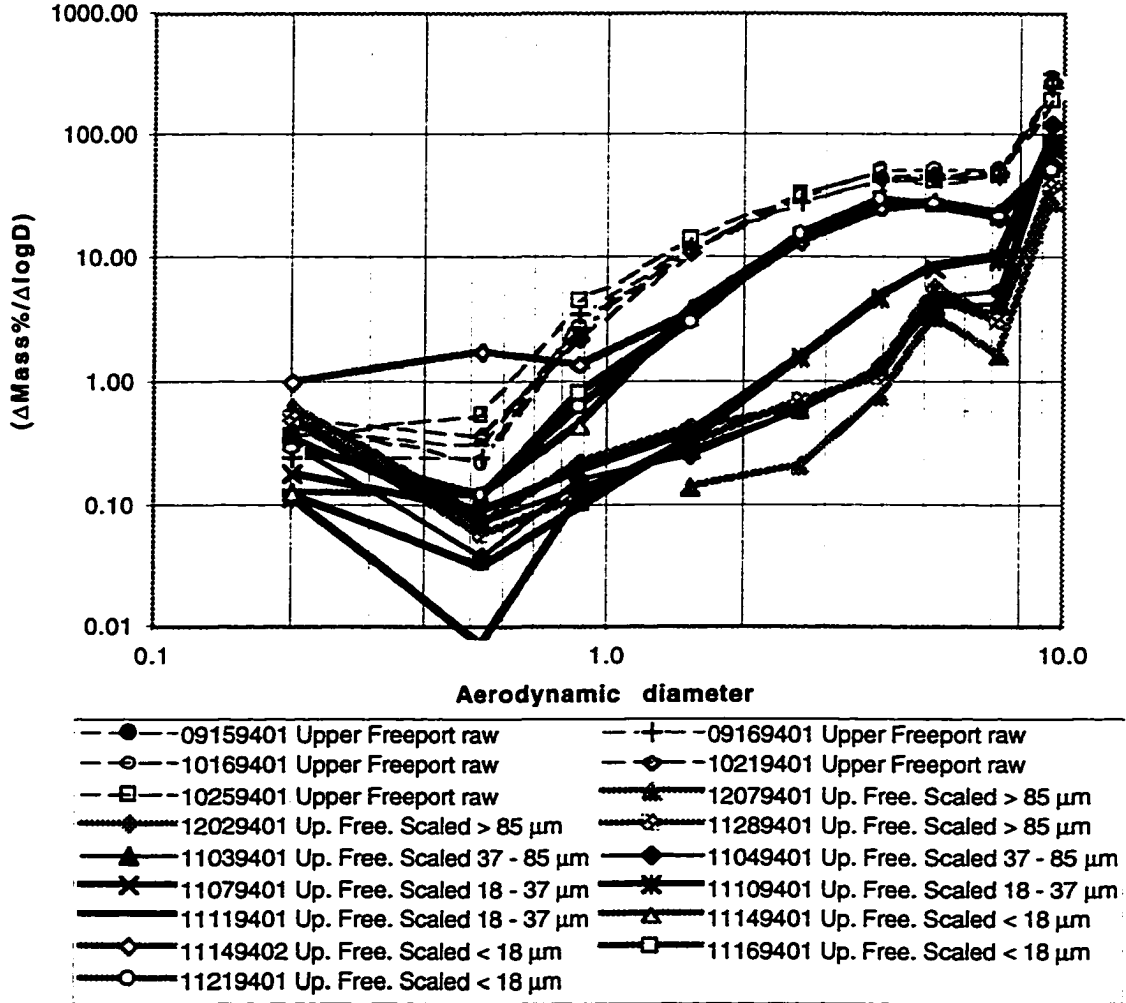


Figure 5.21: Upper Freeport tests scaled by coal fraction, expressed as $\Delta\text{Mass\%}/d\log D$ on logarithmic scale

Vertical Probe, Upper Freeport Scaled by coal fraction

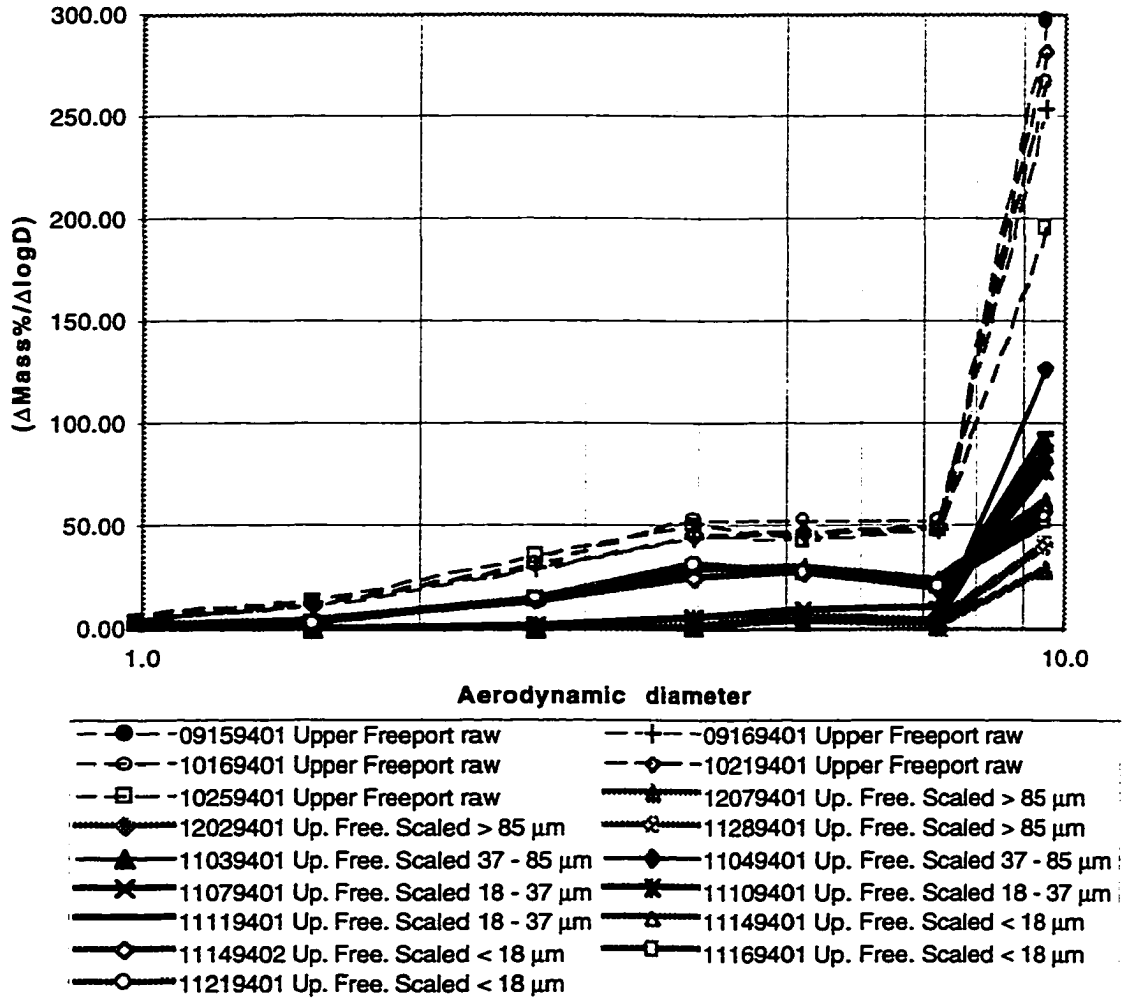


Figure 5.22: Upper Freeport tests scaled by coal fraction, expressed as $\Delta\text{Mass\%}/d\log D$

Vertical Probe, Upper Freeport and composite of coal fractions

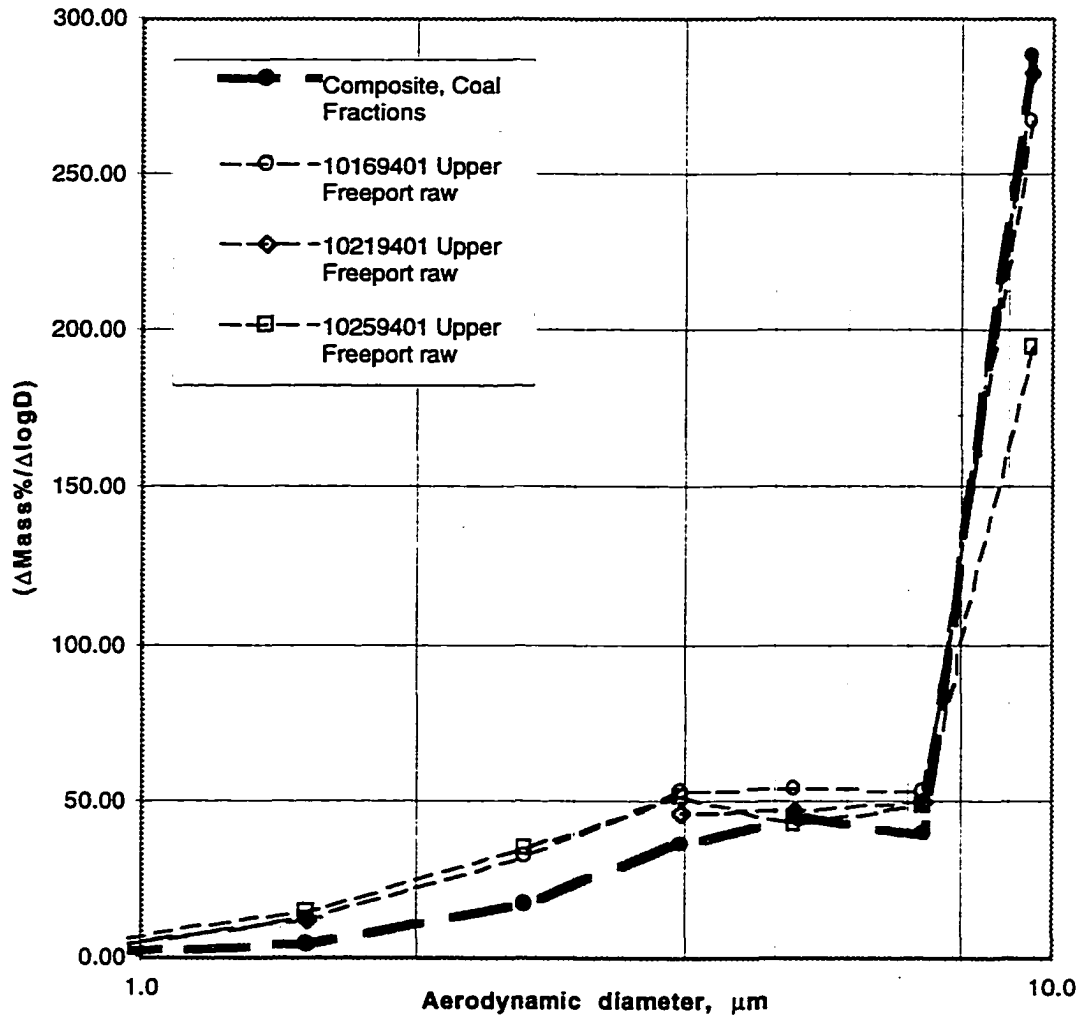


Figure 5.23: Upper Freeport raw coal ash distribution compared to the sum of the sized coal, expressed as $\Delta\text{Mass}\%/\text{dlog}D$

Vertical Probe, Upper Freeport and composite of coal fractions

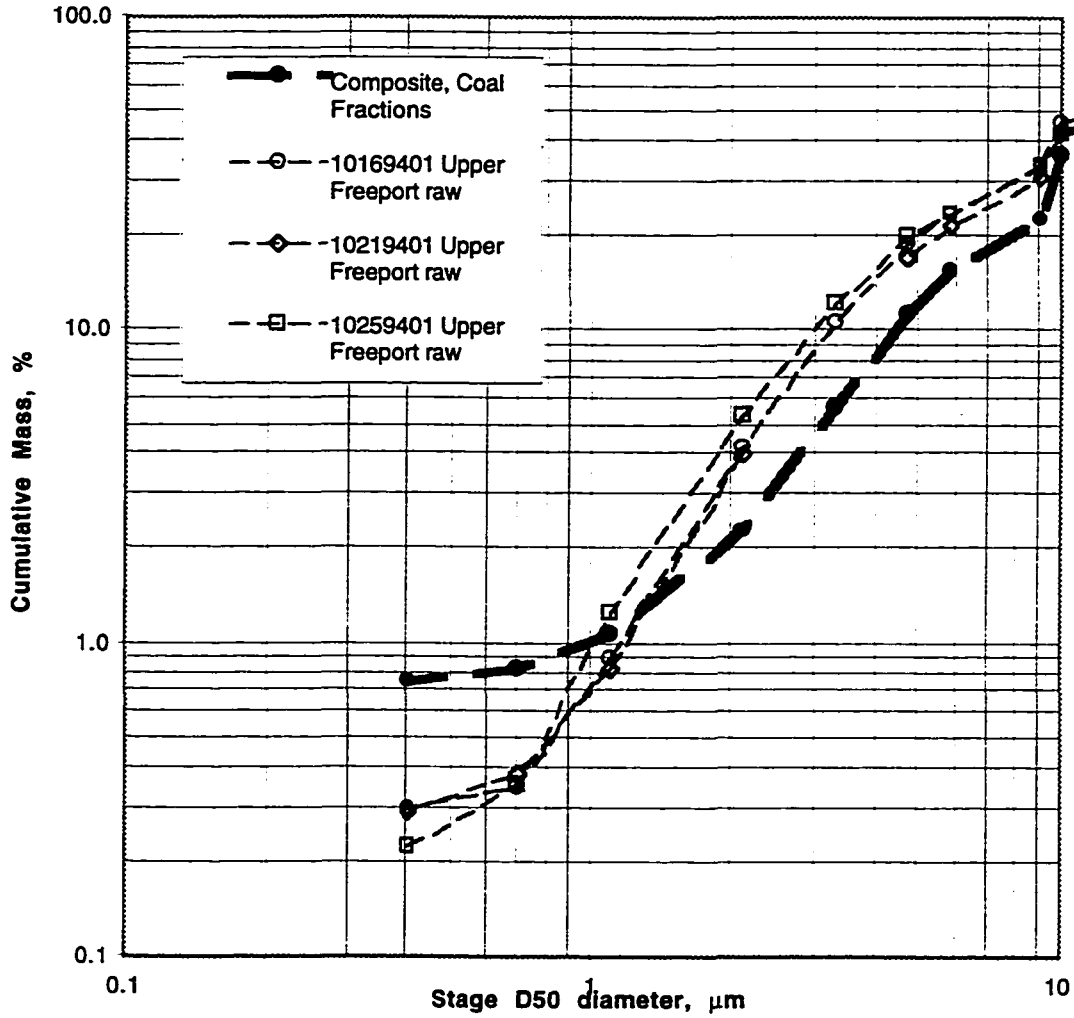


Figure 5.24: Upper Freeport raw coal ash distribution compared to the sum of the sized coal, expressed as cumulative mass

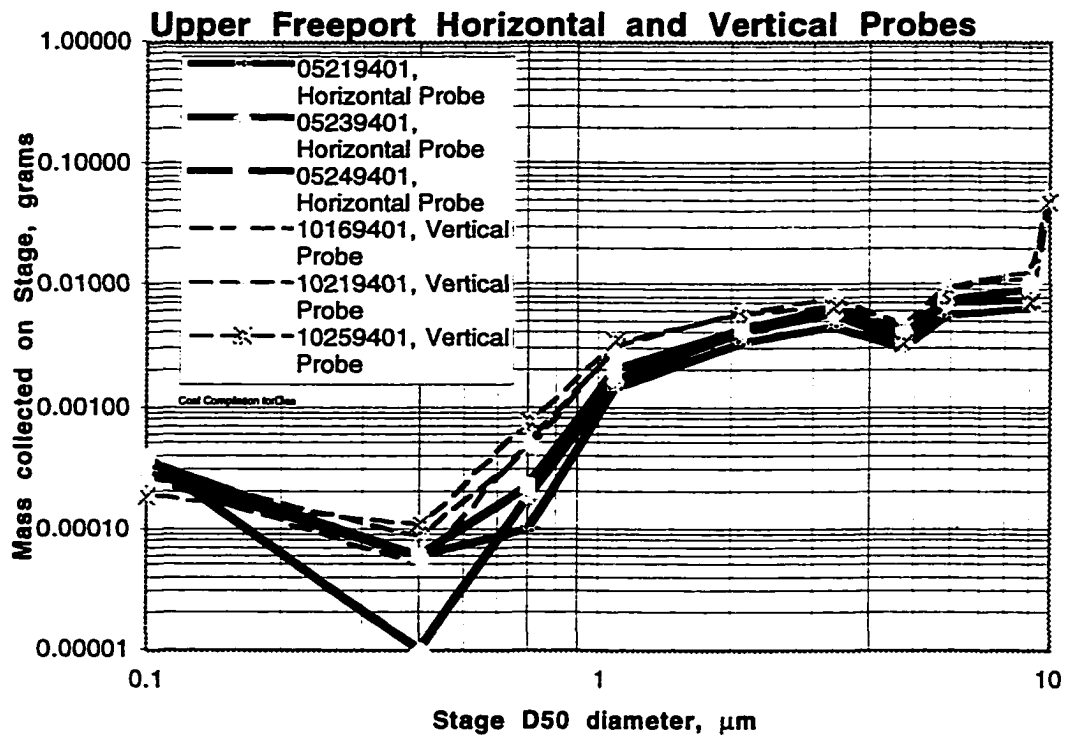


Figure 5.25: Upper Freeport, comparison of ash yields between horizontal and vertical probe tests

Table 5.7: Composition of artificial char

Component:	Sucrose	Carbon Black	Sodium	Pyrite	Bentonite	Calcite
Chemical Formula:	$C_{12}H_{22}O_{11}$	C	$Na_2C_2O_4$	FeS_2	*see note	$CaCO_3$
Average particle diameter, μm :	soluble	0.04 to 0.06 μm	soluble	9 to 10 μm	0.9 to 1 μm	15 to 17 μm
Char Name	grams	grams	grams	grams	grams	grams
Suc50/C50	50	50	0.5			
Suc75/C25	75	25	0.5			
Pyr 0.93 g	50	50	0.5	0.925		
Pyr 1.85 g	50	50	0.5	1.85		
Pyr 2.78 g	50	50	0.5	2.775		
Pyr 3.70 g	50	50	0.5	3.7		
Ben 1.25 g	50	50	0.5		1.25	
Ben 2.50 g	50	50	0.5		2.5	
Ben 3.75 g	50	50	0.5		3.75	
Ben 5.00 g	50	50	0.5		5	
Cal 0.25 g	50	50	0.5			0.25
Cal 0.50 g	50	50	0.5			0.5
Cal 0.75 g	50	50	0.5			0.75
Cal 1.00 g	50	50	0.5			1
* Bentonite is mainly montmorillonite ($((1-x)Al_2O_3 \cdot x(MgO,Na_2O) \cdot 4SiO_2 \cdot H_2O)$)						

Table 5.8: Artificial char test matrix

Test Number	Char Name	A/F Equiv. (w/o char)	Furnace Flow Rate, grams	Dry O ₂ , % (w/o char)
03019501	Ben 1.25 g	1.47	634	7.7
03139501	Ben 1.25 g	1.47	631	7.8
03029501	Ben 2.50 g	1.45	621	7.5
03149501	Ben 2.50 g	1.47	627	7.8
03039501	Ben 3.75 g	1.44	625	7.5
03149502	Ben 3.75 g	1.48	627	7.9
02279501	Ben 5.00 g	1.44	621	7.4
03149503	Ben 5.00 g	1.46	628	7.7
03129501	Cal 0.25 g	1.46	630	7.7
03079502	Cal 0.50 g	1.45	629	7.6
03079501	Cal 0.75 g	1.46	631	7.7
03069502	Cal 1.00 g	1.46	630	7.7
02219501	Pyr 0.93 g	1.44	625	7.5
03179502	Pyr 0.93 g	1.42	617	7.3
03039502	Pyr 1.85 g	1.44	625	7.5
03179501	Pyr 1.85 g	1.46	628	7.7
03069501	Pyr 2.78 g	1.46	630	7.7
03169501	Pyr 2.78 g	1.47	631	7.8
03169504	Pyr 3.70 g	1.47	627	7.8
02239501	Pyr 3.70 g	1.44	622	7.5
02149501	Suc50/C50	1.42	617	7.3
03129502	Suc50/C50	1.43	618	7.4
02069501	Suc50/C50	1.63	521	8.9
02179501	Suc75/C25	1.44	622	7.5
03169503	Suc75/C25	1.45	628	7.6

Sodium only series, including preseparator

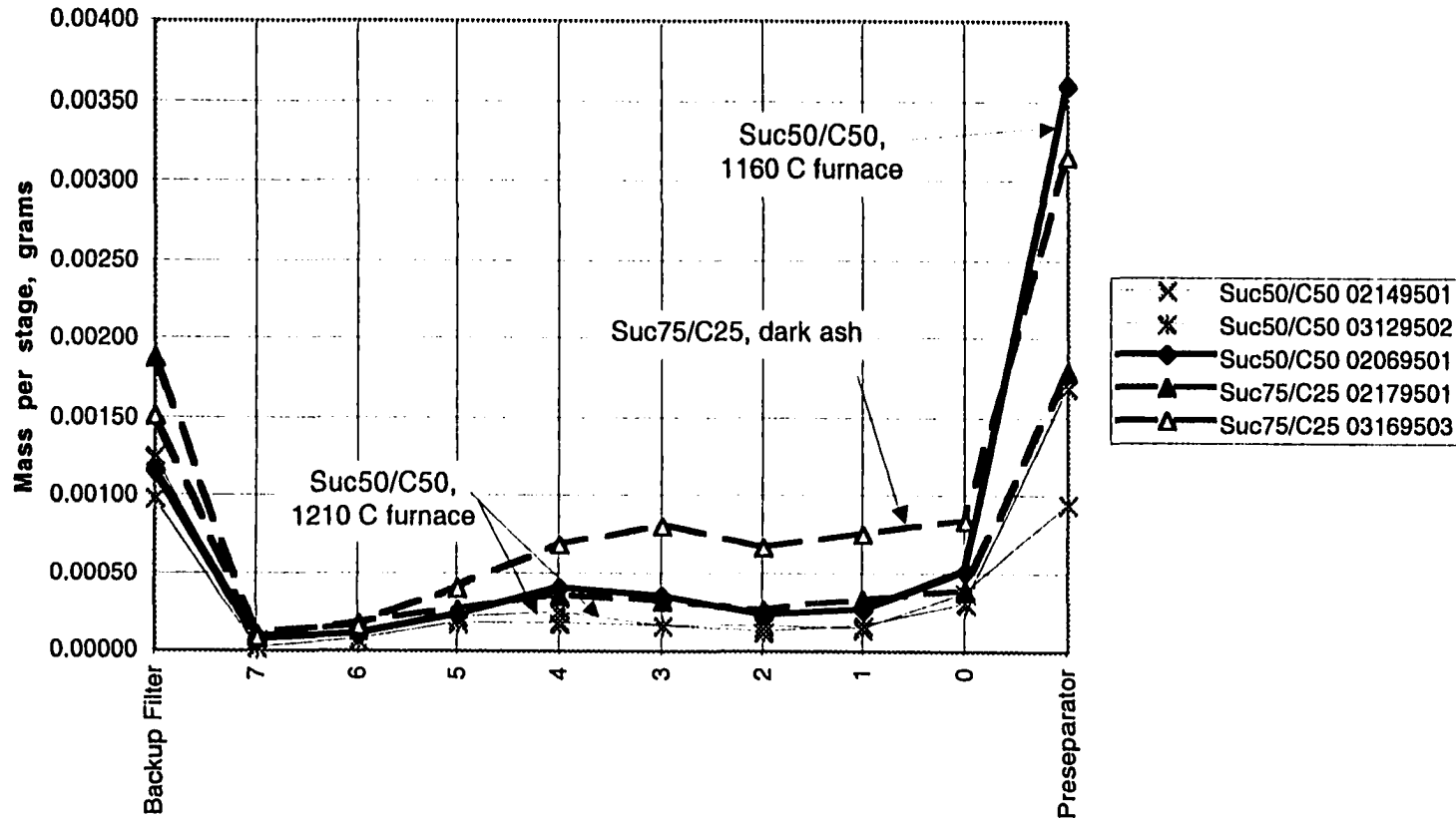


Figure 5.26: Artificial char with sodium doping only, ash mass distribution by cascade impactor stage

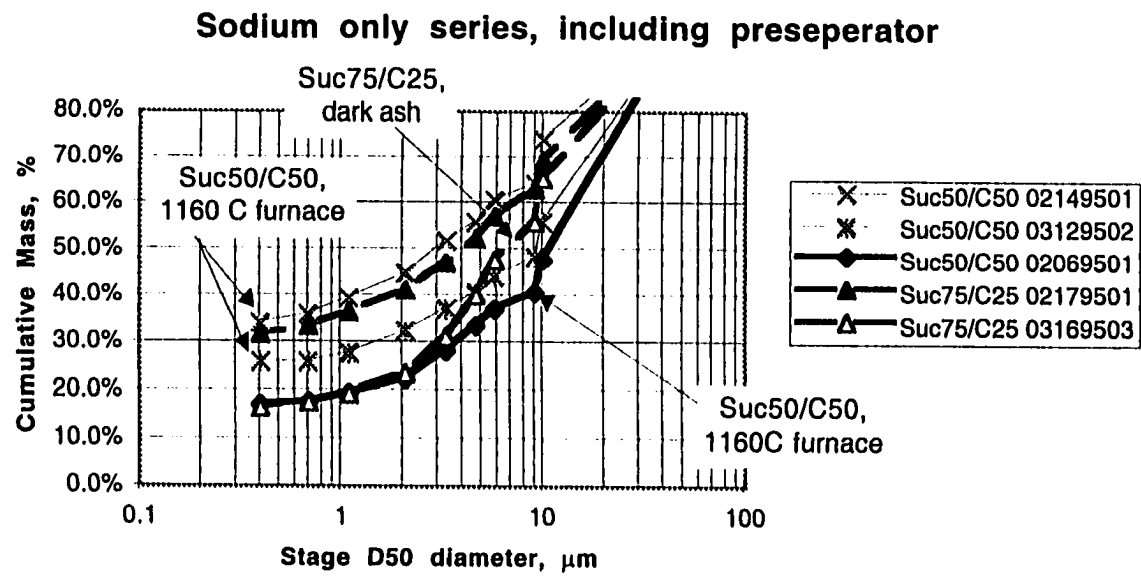


Figure 5.27: Artificial char with sodium doping only, cumulative mass

Bentonite series, including preseparator

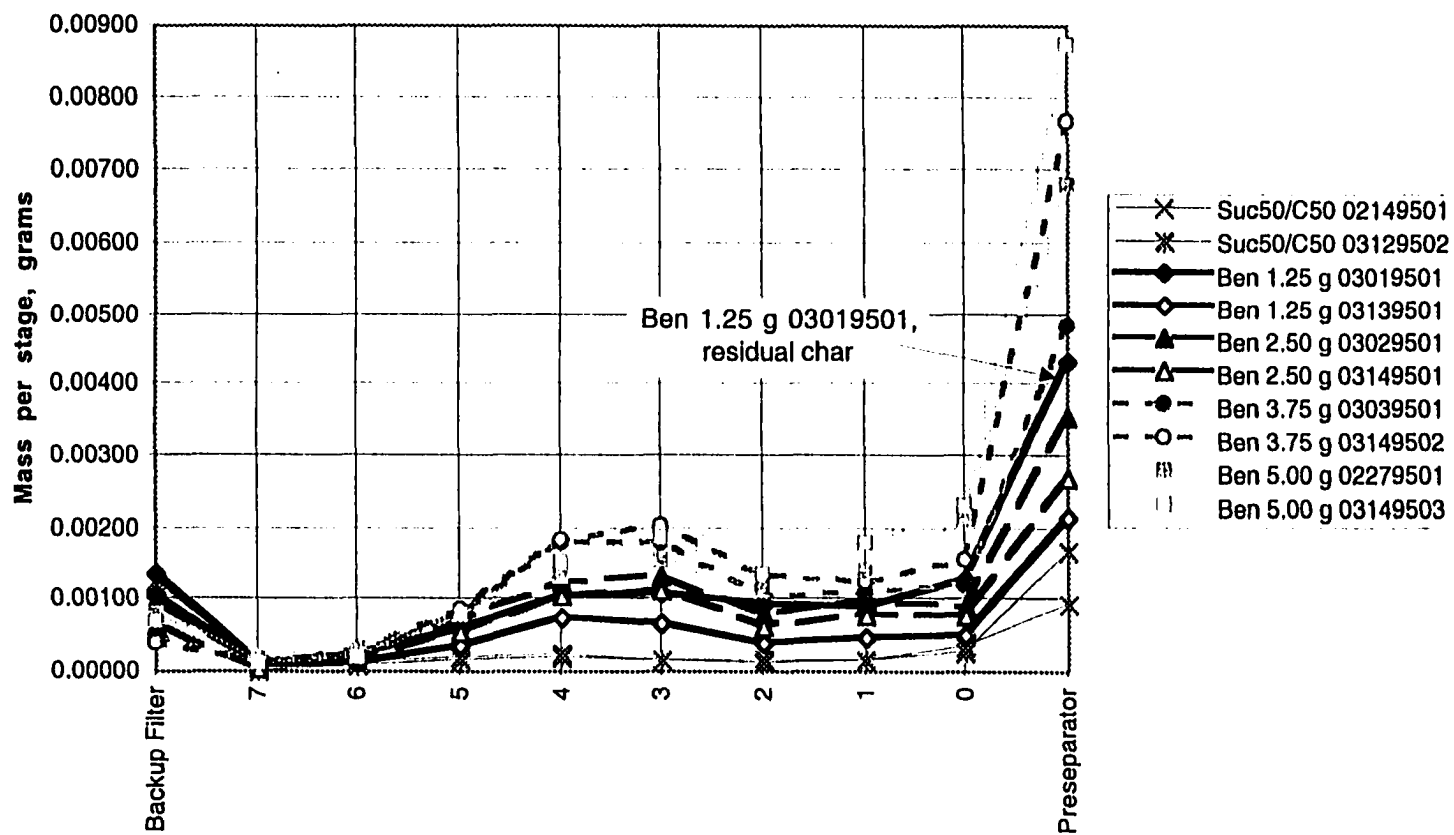


Figure 5.28: Artificial char with bentonite/sodium doping, ash mass distribution by cascade impactor stage

Bentonite series, Including Preseparator

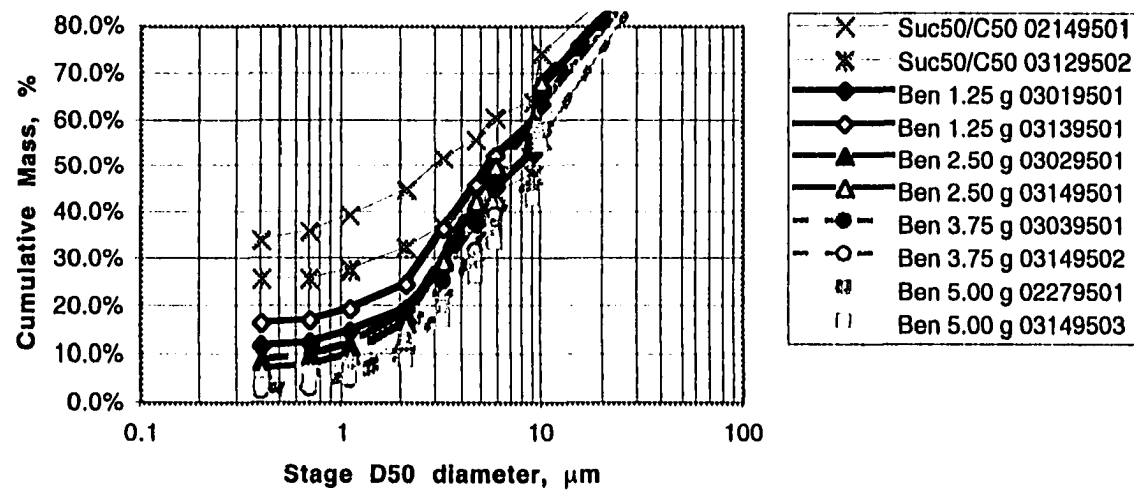


Figure 5.29: Artificial char with bentonite/sodium doping, cumulative mass

Calcite series, including preseparator

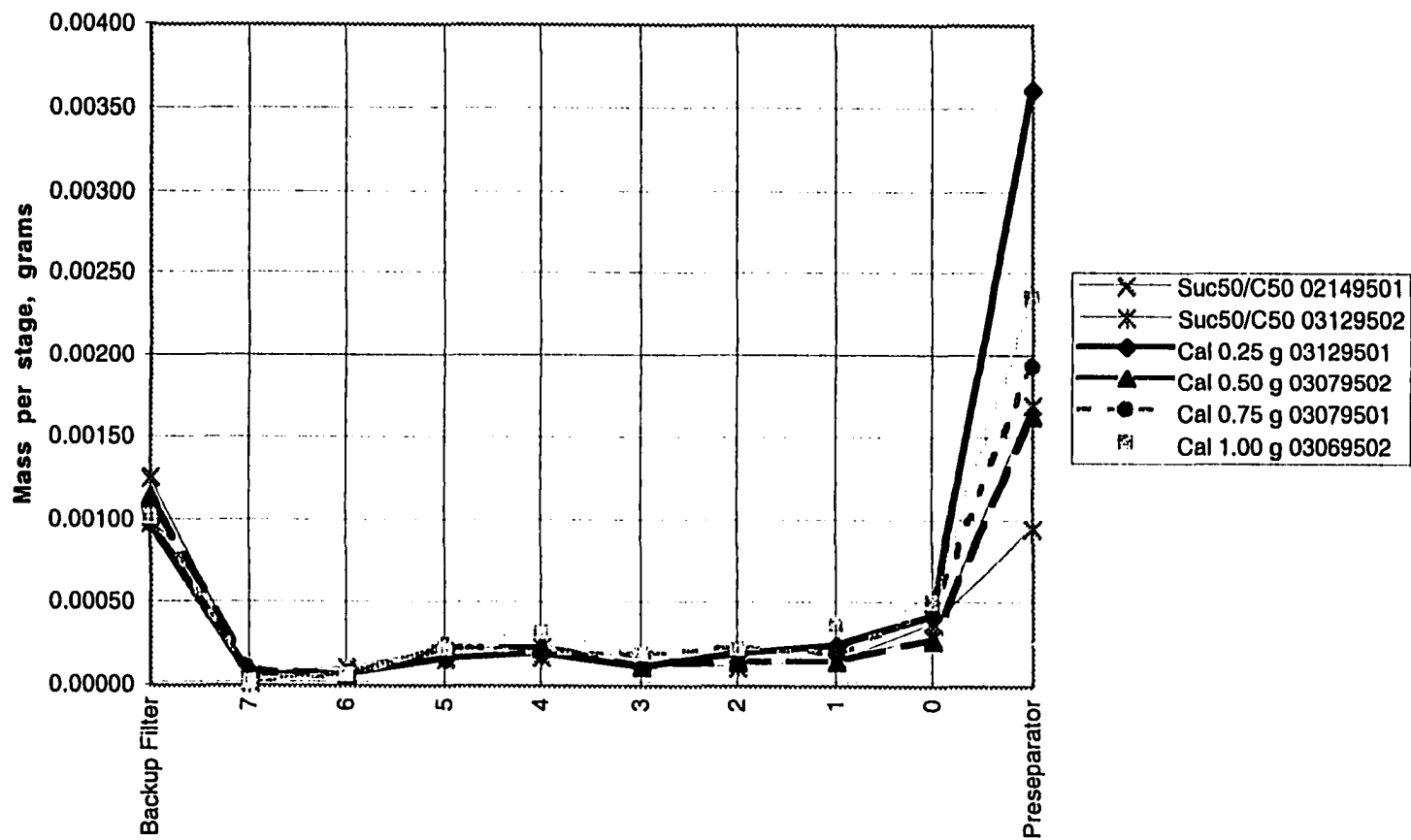


Figure 5.30: Artificial char with calcium/sodium doping, ash mass distribution by cascade impactor stage

Pyrite Series, including preseparator

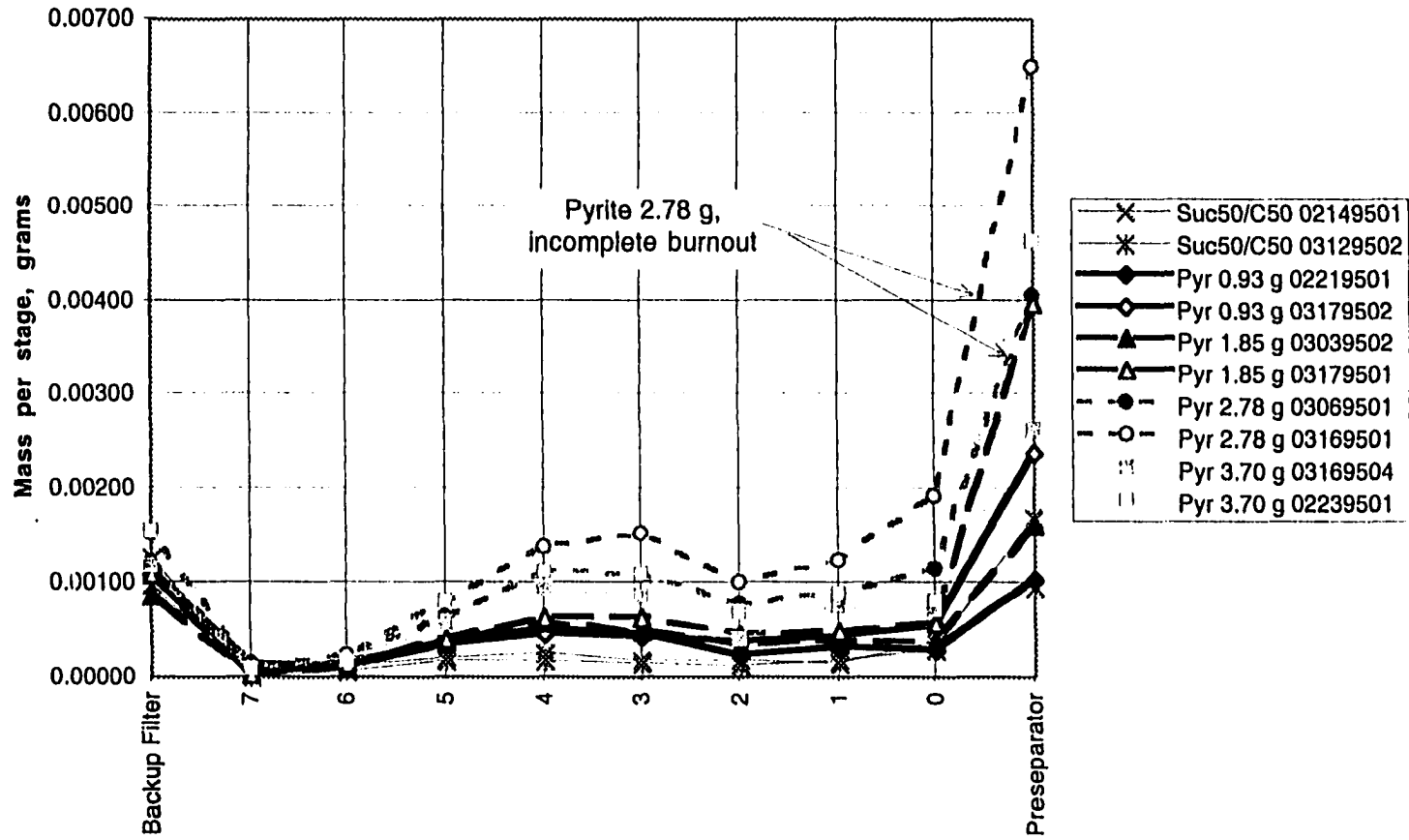


Figure 5.31: Artificial char with pyrite/sodium doping, ash mass distribution by cascade impactor stage

Pyrite Series, including preseparator

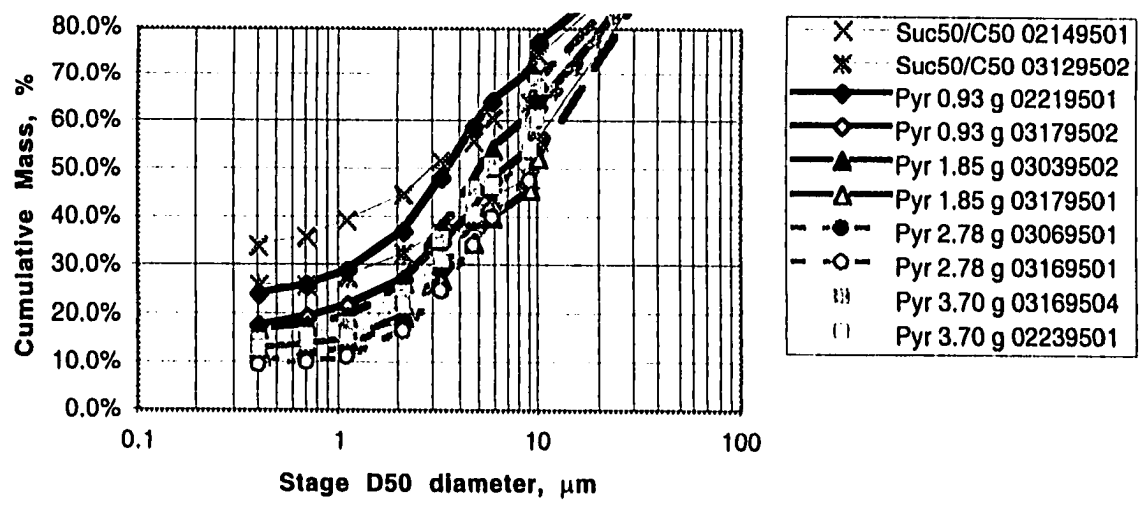


Figure 5.32: Artificial char with pryrite/sodium doping, cumulative mass

MINERAL BEHAVIOR IN SAWDUST/SANDERDUST COMBUSTION

Sawdust and sanderdust are byproducts of particle board and strand board manufacture. Rather than landfill this resource, efficient facilities use this material as fuel for some plant operations, such as chip drying. Unfortunately, experience has shown that the resulting ash plays a role in the fouling of downstream equipment, resulting in high maintenance for particulate matter collection devices (*e.g.* ESPs), and volatile organic compound removal devices (*e.g.* thermal oxidizers).

In this chapter, we examine the ash size distributions and chemical compositions resulting from the firing of these sawdust and sanderdust fuels in a laboratory scale furnace.

6.1 Fuel Properties and Preparation

6.1.1 Sawdust/sanderdust Characterization

The present research examines four sanderdust/sawdust fuels. Various wood-products manufacturing facilities supplied the samples, which were selected to be representative of typical fuels used in suspension burners at the given facility. Ultimate analyses, mineral elemental analyses via atomic absorption, and total halogens analyses were performed by an independent laboratory and are summarized in Table 6.1. The alkaline earth element calcium and the alkali elements sodium and potassium were the primary metals detected. Note that Fuels 1 and 2 have an order of magnitude larger halogen content than Fuels 3 and 4. Significant differences in nitrogen, alkali and halogen content between the fuels are likely the result of manufacturing additives (*i.e.* urea formaldehyde, phenol formaldehyde, and MDI-isocyanide based binding resins), parent wood variety, and/or other processing sources. Research by Miles (1998, personal communication) has shown that binding resins can contain sufficient alkali to cause ash-related problems in industrial burners.

Analysis of Kentucky #11, a pulverized sub-bituminous coal, is also shown on Table 6.1 for comparison. Note that ash yield is significantly higher for coal. Si, Fe and Al are primary elements present in the coal ash, all of which are not readily vaporized in their original mineral forms. Ash-forming components are shown in Figure 6.1, expressed in

terms of mass. Sulfur content is included because it is capable of joining the ash material in the form of a sulfate, as discussed in detail later.

Brief descriptions of the physical properties of the four fuels tested are given below, including their "As-Received" size distributions. The fuels were size classified using US Standard sieve sizes in a column with manual agitation. A cumulative size distribution for each fuel is shown in Figure 6.2. Figure 6.3 shows the size distribution in the form of $\Delta\text{mass } \%/ \Delta(\log D)$ vs. $\log D$. Expressed in this way, the area under the curve between two particle diameters is proportional to the mass in that diameter range.

Fuel 1: This fuel is primarily composed of pine from the southeast United States. The fuel was obtained directly from the sanderdust silo at a particle board production facility. According to the site engineer, it is milled prior to combustion, and is "a mixture of mainly UF (Urea Formaldehyde) resinated sanderdust mixed with other fine waste material from our various pneumatic conveying systems". The sample received was uniformly fine in texture, with an unburned particle size centered at 250 μm and aspect ratios near unity. Sieving of Fuel 1 through standard mesh screens showed that the particle size distribution was log-normal as shown in Figure 6.3. No significant wood chips or slivers were evident. Urea formaldehyde resin, used as a binder in particle board production, is the source of the unusually high nitrogen content (see Table 6.1).

Fuel 2: This fuel was obtained from a sanderdust silo at a medium density fiberboard facility. It is a mixture of sanderdust and other material from pneumatic systems at the facility, all of which contain UF resin. Like Fuel 1 sanderdust, the UF resin is the source of the high nitrogen content. The fuel is not milled prior to pneumatic injection into the burners. It was reported to be "50% hard -oak, hickory, etc. & 50% soft -gum, beech, etc." by the site engineer.

The sample received was a mixture of fine particles and very high aspect ratio fibers. The fibrous nature of this fuel is unique compared to the other fuels tested. Sieving this fuel produced cotton-like material on sieves with a minimum opening of 710 μm and greater, and powdery material on sieves with openings of 180 μm and less. Figure 6.3 indicates that most of the fuel was on the order of 250 μm . A secondary mode near 700 μm was associated with the long fibers.

Fuel 3: This material was mostly sanderdust (phenol formaldehyde and methyl Diisocyanate resinated) and board trim waste from strand board. It consists of 60% Virginia pine, 30% poplar, and 10% miscellaneous hardwoods. A small amount of wax (parafins) is also added to the board, but is not believed to significantly affect the composition or properties of the sanderdust/board trim fuel.

Visual inspection of the Fuel 3 revealed a moderately coarse texture and a diverse size distribution. Fine particles appeared to be on the order of 250 μm in diameter. Larger particles were on the order of 10 mm in the longest dimension, with high aspect ratios (slivers). Sieving showed a broad size range, with a median size near 400 μm , as shown in Figure 6.3

Fuel 4: This fuel is from a strand board plant, and includes the dryer fines which are sieved out of the raw material before resin is added, and the strand board trim. It is likely low in UF resin or other additives. The environmental engineer on site described the fuel as 65% aspen, 20% mixed hardwoods such as maple, and 15% red or jack pine.

Visual inspection of Fuel 4 showed a generally coarser texture than the bulk of the Fuel 3 sample. Qualitatively, particle aspect ratios were lower than Fuel 3. Figure 6.3 shows a size mode near 1 mm, with a secondary distribution centered near 0.3 mm. Note that the majority of Fuel 4 was of larger particle size than Fuels 1, 2 or 3.

6.1.2 Fuel Preparation for Screened Sawdust/sanderdust Experiments

Removal of oversized fuel particles from the "As Received" sawdust and sanderdust samples was required for smooth, repeatable operation of the fuel injection system. Two layers of 1.6 mm by 1.6 mm screen (opening size), separated by approximately 4 mm, were used to remove large particles. To aid in the removal of high aspect ratio particles, the second screen grid was oriented at 45 degrees to the first screen grid. Sieving with the double screen removed 0% of Fuel 1, 10% of Fuel 2, 18% of Fuel 3, and 31% of Fuel 4, as noted in Table 6.1. Composition of the screened product may, thus, be somewhat different from the total compositional analysis shown in Table 6.1.

6.1.3 Fuel Preparation for Milled Sawdust/sanderdust Experiments

For milled sawdust/sanderdust experiments, Fuels 2, 3 and 4 were processed in a Thomas-Wiley laboratory mill with a 0.5 mm diameter exit screen. Fuel 1 was received in a milled state. Milling allowed complete use of the available fuel, aided in dispersion of the fuel at the tunnel furnace injection point, and promoted complete combustion of char particles. It also allowed a more direct comparison between fuels by allowing their ashing properties to be evaluated on a common-size basis. Figure 6.4 shows the size distributions of the four fuels after milling. Note that Fuel 4 has a slightly higher average particle diameter, which can be traced back to the larger mean size of the unmilled Fuel 4 shown in Figure 6.2.

6.2 Screened Sawdust/sanderdust Experiments

6.2.1 Screened Sawdust/sanderdust Test Matrix and Conditions

The experiments specified in Table 6.2 were performed with the Screened sawdust/sanderdust samples. In summary, these tests entailed burning the sawdust/ sanderdust in a natural gas-fired tunnel furnace and collecting the resulting ash using a water-cooled sampling probe coupled with a cascade impactor. Detailed experimental procedures are presented in Section 4.4 and individual test summaries are in Appendix E. Additional tests were performed to verify correct operation of the combustion and sampling apparatus.

Operational settings are summarized in Table 6.3. Some of the fuels required a slightly higher air entrainment flow rate for smooth operation of the injection system. This resulted in a slight variation in the total mass flow and dry O₂ content from test-to-test. Note that tests were conducted in a fuel-lean environment, and the wood fuel flow rate did not significantly deplete the free oxygen content.

Residence time is based on the integration of the inverse of the gas velocity, as calculated from the measured temperature gradient in the reactor and the total mass flow rate. The calculated standard deviation of the residence time is based on the variation in mass flow rate between tests.

Temperature profiling was accomplished using the High Velocity Thermocouple (HVTC) described in Section 4.6. Figure 6.5 shows the gas temperature in the reactor as measured via the sample ports distributed down the height of the reactor. Also included is the

temperature measured with a bare type-K thermocouple (not corrected for radiative heat loss) and the reactor wall temperature measured using a Leeds and Northrop optical pyrometer (Cat. No. 8621-C). The upper auxiliary burners were operated near the same stoichiometry as the main burners, resulting in nearly isothermal wall, thermocouple, and HVTC measurement at sample ports 43.2 cm, 58.4 cm and 73.7 cm from the injection port. The cooler wall temperature measured at 88.9 cm was somewhat surprising, since it is very near the auxiliary burner heat zone. Conductive and radiative heat loss to the unheated section directly below the auxiliary burner must be significant.

Figure 6.6 shows a curve fit of the temperature as measured by the HVTC in terms of the residence time rather than distance from the injection point. The furnace quench rate was about 150 K per second.

6.2.2 Screened Sawdust/sanderdust Results

6.2.2.1 Ash Size Distribution and Morphology

Figures 6.7 through 6.10 present size distribution data for the four wood products tested. The following plots are mass size distributions, and are based on these two assumptions: (1) that the particles are solid spheres, and (2) that the particle density is the same as that of CaCO_3 (2.7 g/cc). While the results are not strongly sensitive to assumed particle density, the shape and porosity of the particles can significantly influence the stage upon which capture occurs. The mass collected on a given stage is normalized to the total mass collected, including the material deposited in the preseparator.

A simple water-cooled sampling probe was used in this test series. The ratio of probe inlet velocity to the free stream velocity was approximately 7 to 1, which is anisokinetic sampling (*e.g.* Hinds, 1982, page 187). A calculation of sampling efficiency for this configuration showed that particles with diameters of 10 μm or less are captured with 90% or better efficiency, as shown in Appendix C. Essentially all particles below 4 μm were expected to be captured. Above 10 μm , the capture efficiency drops significantly, resulting in an under-representation of the largest residual particles.

Mass closure for Fuel 1 and 2, which exhibited very good burn-out, indicated that the collected ash was 20% to 55% less than expected, based on probe flow rate. This is

similar to the results of Gallagher (1992). The capture efficiency calculations (Appendix C) indicate that this missing ash is in the large size mode. As is discussed in detail in the Modeling chapter, it is clear that particulate matter greater than 10 μm does not play a significant role in alkali capture mechanisms, so its under-representation here is of little consequence.

Figure 6.7 is a plot of mass collected on each stage, as well as the mass collected on the aerosol filter. Mass collected on a particular stage is plotted at the diameter of a particle with 50% probability of capture on that particular stage, commonly referred to as D_{50} . The mass of material collected on the aerosol filter is nominally plotted at 0.1 μm . Although not strictly a plot of $d(\text{mass}\%)/d(\log D)$ vs. $\log D$, which is usually used to show mass distribution, this plot is useful in that stage spacing is approximately proportional to $\log D$ for stages between the aerosol filter and the preseparator stage. All four wood-based fuels have three clear modes: An aerosol mode in the sub-micron range, a secondary residual mode at about 1 to 3 μm , and a primary residual mode consisting of the material 8 μm and greater.

The ash size distribution for a typical pulverized coal (Kentucky 11), fired under similar conditions, is also shown in Figure 6.7. Note that all of the wood fuels yield much more aerosol than this typical bituminous coal, no doubt due to the much higher alkali content. Additionally, coal usually has a high clay content (46.7% SiO_2 , 19.4% Al_2O_3 in terms of oxides in ash, for Kentucky 11). These aluminosilicate clays tend to compete with alkali vaporization by complexing alkali metals during char combustion (Gallagher, 1992). This further reduces sub-micron aerosol yields.

Figure 6.8 shows cumulative mass relative to D_{50} of each impactor stage. Fuel 1 and 2 have a high conversion of parent fuel to aerosol. Aerosol yield is also significant for Fuels 3 and 4, making up about 6% of the total mass collected.

The filter stage is typically light brown, possibly indicating some soot or organic tar formation from incomplete combustion. Evidence indicates that the *majority* of the mass collected on the filter stage is non-organic in nature. Energy Dispersive X-ray Spectroscopy performed on the filter stages of the four wood products tested show high alkali content. This suggests that the aerosol was produced by vaporized alkalies, which

condense to form sub-micron particulate matter. This is expected, in light of the high alkali content of the parent fuel.

For Fuel 3 and Fuel 4, the bulk of the mass in the preseparator appears to be char particles too large to burn within the available residence time (about one second). A mass closure calculation indicates that 2 to 4 times more material was captured by the impactor than one would expect from complete combustion. Fuels 1 and 2, being much finer fuels, exhibited better burnout and hence left less organic mass in the preseparator. Burnout at size cuts less than about five microns for all fuels appeared excellent, based on ash color.

The unburned carbon appears to be confined to particles 5 microns and above. Thus, Figure 6.9 attempts to remove the effect of the unburned carbon by renormalizing the size distributions by excluding particles above 5 μm . This attenuates the effect of incomplete char combustion for the Fuel 3 and Fuel 4 samples. Note that the representative coal ash aerosol yield remains significantly lower than the high alkali wood ash. Two distinct families of size distributions are evident in the wood ash. Fuel 1 and Fuel 2 show a significantly lower aerosol yield than the Fuel 3 and Fuel 4, as seen in Figure 6.10. as well as a higher 1.5 micron mode, as seen in Figure 6.9. The reason for the different yields is not clear, although the uncertainty associated with the exclusion of the unburned carbon argues against drawing conclusions at this point.

6.2.2.2 Ash Composition as a Function of Ash Size

Scanning Electron Microscopy (SEM) and Energy Dispersive X-ray Spectroscopy (EDS) were used to gain insight into the morphology and composition of the ash particles. A flat, smooth specimen is ideal. Since particulate matter is far from an ideal flat surface, the elemental analysis presented should be viewed as semi-quantitative. Other limitations of EDS are (1) it cannot directly detect the form of bonding, (2) it cannot detect elements below atomic number 11, (3) composition can vary from particle to particle, and (4) the method is surface composition sensitive rather than volume composition sensitive. This last limitation is a problem if a composition gradient exists, such as a particle with a condensed species on its surface.

The following figures (Figures 6.11a through 6.23) show typical particulate matter collected on selected impactor stages and on the aerosol filter for the four fuels examined.

Fuel 1:

Figure 6.11a shows a selection of material collected on stage 0 (D_{50} cutoff approximately 8.3 μm) of the cascade impactor. Much of the material is highly porous, suggesting that the particles did not melt. EDS was used to analyze a typical collection of particles on this stage, and is shown in Figure 6.11b. Note that the material analyzed is primarily calcium. Figure 6.11c shows that the majority of material collected in the impactor was collected on stage 0 and the preseparator. Since the melting temperature of pure CaO is high, it is not surprising there is limited evidence of melting.

Figure 6.12a shows the diverse assortment material collected on stage 1 of the cascade impactor. Stage 1 corresponds to a particle cutoff diameter of approximately 5.3 μm . These large size cuts (including stage 0 and the preseparator) tend to show a diverse assortment of material, with the majority of it appearing to be fragmented structures of the unmelted parent minerals. These are likely skeletal mineral structures left by the burnout of the carbon from the char. Also present are spheres, which appear to be minerals that have melted and coalesced. Although calcium is the dominant element on this stage, composition varies from particle to particle. For example, EDS of the particle in the upper right corner of photo is almost pure silicon, as shown in Figure 6.12b. Of the selected stages inspected, the fraction of molten/coalesced particles to unmelted porous structures increases as average size decreases.

Figure 6.12c shows the detail of the lacy, porous structure of material near the center of Figure 6.12a. Elemental analysis (Figure 6.12d) shows this to be about 80% calcium. In the absence of a fluxing agent, CaO is not expected to melt at the furnace temperature.

Figure 6.12e shows the mass contribution of this stage in relation to total mass collected on all stages. Figure 6.12f is the elemental analysis of a typical collection of particles on this stage. This EDS was conducted at 10 kV at 2000x. Composition remains predominantly calcium, as with the previous stage (see Figure 6.11b), but alkaline earth elements, silica, iron and phosphorous are more abundant.

Figure 6.13a shows material that has been collected on stage 4 (D_{50} of 1.7 μm) of the impactor. Note that the fraction of particles that have melted has increased. EDS analysis at 1500x and 10 kV indicates mostly calcium with a balance of alkaline earth elements, silica, iron and phosphorous, as was seen in a larger size cut (D_{50} of 5.3 μm , Figure 6.12f). Alkali elements sodium and potassium are not well represented.

Figure 6.14a shows ash collected on the final stage of the impactor, which is just prior to the borosilicate glass absolute filter. The particles are roughly spherical with low porosity and a D_{50} diameter of 0.4 μm . Closer inspection at higher magnification (Figure 6.14b) shows angularity to some of the particles (*i.e.*, a gravel-like appearance), as well as nodes on otherwise smooth spheres. This may be indicative of coagulation of aerosol alkali metals, or the sintering of the material rather than full melt. EDS results, shown in Figure 6.14c, indicate an increase in alkali metals potassium and sodium, as well as chlorine, presumably as an anion to the alkali metals. Figure 6.14d shows that this stage collects only a small fraction of the ash produced.

Inspection of the filter shows two remarkably different kinds of particles present. The surface of the filter is coated with particles that appear to be identical to the material collected on the 0.4 μm stage, shown in Figure 6.14a. A low power (250x) SEM photograph of the filter is shown in Figure 6.15a. In some areas, the fibers of the filter are visible through this collection of sub-micron particles. Inspection of the glass fibers themselves reveal (Figure 6.15b) that the fibers are collection surfaces for very fine material that is of the order of 0.05 μm . This suggests that the fine particles collected by the filter are made up of two modes. Scanning Electron Microscope techniques were unable to establish which of the two modes contributes the most mass.

Figure 6.15c shows the results of EDS analysis at low power (250x). This composition measurement requires careful interpretation. The EDS signal includes contributions from both the particles and the underlying borosilicate glass fiber filter. A semi-quantitative method of correction for the background elements composing the filter is presented later in this discussion (page 130). After correction, it appears that the material collected on the aerosol filter is primarily sodium and potassium, with chlorine as the primary anion.

Although the filter analysis is biased by the background composition of the filter itself, background elements are not a significant problem for SEM analysis of cascade impactor stages. Ash collected on the surface of aluminum foil impactor stage substrates was transferred to SEM stubs, which have a simple and known background signal.

Fuel 2:

Figure 6.16a is an elemental scan of a relatively dense collection of particles retained in the preseparator of the cascade impactor during testing of Fuel 2. The scan was performed at 750x and 10kV. Although no photo is available, SEM imaging verified that obvious plant

fiber structures were clearly visible in the preseparator. To illustrate composition diversity, an EDS scan of a char particle with a length scale of about 100 μm is shown in Figure 6.16b. What is particularly interesting about this particle is that it shows an intermediate char conversion extent between complete burnout (100% conversion) and the raw fuel, as discussed below. Analysis of this particle gives a semi-quantitative glimpse of ash morphology as a function of char conversion. Sodium, potassium, and chlorine are depleted compared to the parent fuel (see Figure 6.1, Fuel 2), resulting in an apparent “enrichment” of the lower volatility elements such as calcium, magnesium, silicon, iron. This indicates that alkali release begins early in the char conversion process. Work by Wornat *et al.* (1995) shows similar quantitative results for pine and switchgrass chars.

Figures 6.16d and 6.16e show the spectrum of the two scans shown in Figures 6.16a and 6.16b, respectively. The vertical axis is a count of photoelectrons, while the independent variable is the energy of the photoelectron. The background noise visible across all energies is known as a “carbon hump”, and is indicative of a carbon background or matrix. The scan shows evidence of the sputter coating, which is composed of gold and palladium. This is added during the SEM preparation to prevent surface charging. Note that the relative magnitude of gold and palladium to other detected elements is greater for scan 6.16e than for scan 6.16d. The implication is that much of the EDS energy is lost to a carbon background composed of incompletely burned fuel, and the particle analyzed in Figure 6.16b is indeed incompletely burned.

Figure 6.17a is material collected on stage 0 (D_{50} of 8.3 μm). Aggregates, spheres and porous structures are visible in this collection of particles. Composition varies significantly from particle to particle. Figure 6.17b is an EDS analysis of the uncommon 10 μm by 30 μm particle shown in the center of Figure 6.17a. It is predominantly Ca (Figure 6.17b), which is similar in composition to material found in the large size cuts of Fuel 1.

The EDS analysis of a more common structure is shown in Figure 6.17c. It is porous and predominantly calcium as well.

Figure 6.17d shows EDS results for a 1500x 10kV analysis of a collection of particles, considered typical of this stage. A photograph is not available. Note that calcium remains the dominant element.

Figure 6.17e illustrates the diversity of particles on this stage. The particle scanned was not photographed, but appeared to have a smooth surface, was oblong with a major axis of approximately 15 μm and a minor axis of 10 μm , and bulged slightly along the major axis. This particle was very unique in appearance compared to the majority of other material present. The high titanium content is indicative of foreign contamination.

Figure 6.18a and 6.19a show collections of particles on stage 4 (D_{50} of 1.7 μm). Like Fuel 1, stage 4 material is made of diverse particles. The lacy structure in the center of Figure 6.18a is shown in detail in Figure 6.18b, along with a general scan of the particle at 15,000x 10kV in Figure 6.18c. This size cut is part of a secondary mode of the ash size distribution, as shown in Figure 6.18e. A higher powered examination of the lacy particle at 100,000x (Figure 6.18d) indicates that composition not only can vary from particle to particle, but across the surface of the particle as well. The higher fraction of potassium and sodium, along with chlorine and sulfur, at the lower power examination tends to suggest that the particle has collected sub-micron aerosol particles during the combustion process, or is a condensation surface for vapor phase compounds. This will be examined in more detail later.

Figure 6.19b, a close-up view of a highlighted particle from Figure 6.19a, appears to be a calcium structure that has undergone some fluxing. Figure 6.19c is a close-up of a sphere also shown in Figure 6.19a. Three elemental analyses were conducted. Figure 6.19e is EDS was conducted at 100,000x 10kV, and included some nodes on the surface. Figure 6.19f was at 43,000x 10 kV, and focused on a single node only. Figure 6.19g focused on a smooth portion of the sphere. Compositional variation does not seem significant, which may indicate that the nodes were present during sphere formation rather than deposited by collision.

The aerosol filter of Fuel 2 was examined and is shown in Figure 6.20a. Material captured on and in the filter makes up about 30% of the total ash yield, as shown in Figure 6.20b. Like material collected on the Fuel 1 filter, the sub-micron particles have a granular appearance. Surface charging by the electron microscope resulted in the distortion line that runs left to right across the figure - *i.e.* it is not a true feature of the aerosol particles. EDS analysis conducted at 4000x and 10 kV (Figure 6.20c) shows significant quantities of chlorine and alkalis, implying that this sub-micron aerosol is primarily condensed salts.

Some large particles, on the order of 10 μm and larger, were also found on the filter. An example is shown in Figure 6.21a. These particles bypassed earlier stages, most likely by bouncing off the collection surfaces. EDS of three different particles (Figures 6.21b, c, and d) show high calcium, as is common for the larger particles, as well as alkalis and chlorine, which is common for smaller particles. This could be background signal from sub-micron particles, or impacted sub-micron particles collected by the large particle while sitting on the filter.

Fuel 3:

Figure 6.22a shows the aerosol filter surface recovered from firing Fuel 3. A significant number of large particles can be seen on the filter, most likely arriving at the filter by bouncing off earlier impactor stages. Figure 6.2 previously showed that unburned Fuel 3 has more oversized particles than unburned Fuel 1 and 2. This results in more large-diameter ash particles in the residual ash mode. The greater population of large ash particles leads to impactor overload and stage bounce, resulting in the appearance of more residual ash on the filter.

Examining Figure 6.22b, it is clear that sub-micron particles have adhered to the filter fibers themselves. This is very similar to the filter deposition mechanism observed for Fuel 1, Figure 6.15b. A notable difference is the lack of particles on the order of 0.4 μm . EDS analysis of the filter at 250x 10kV shows high silicon, calcium, and aluminum signals, part of which must be attributed to the filter material. Also present in significant quantities are potassium, sodium and sulfur which are likely attributable to the collected aerosol, as will be discussed later. Figure 6.22d shows the relative mass of the aerosol compared to the remainder. Although the aerosol yield is much less than the mass attributable to very large particles (8.3 μm D_{50} and greater), it is a significant fraction of the remaining mass.

Fuel 4:

Figure 6.23a is the Fuel 4 aerosol filter, showing that a substantial quantity of large particles bounced through to the aerosol filter. Closer examination of the filter fibers, as seen in Figure 6.23b, shows sub-micron particles adhered to the fibers. Figure 6.23c shows elemental analysis of the filter at low power, which includes large particles. This composition detected is not significantly different from the material analyzed at higher power, shown in Figure 6.23d.

One large (approximately 10 μm in diameter) particle on the surface of the filter was analyzed, as shown in Figure 6.23e, and found to have a higher calcium content than the overall filter surface. The composition of this particle is somewhat similar to the composition of particles found on the larger stage cuts of other fuels (*e.g.* Fuel 1, stage 1, Figure 6.12). Although no large stage cuts were analyzed for this fuel, it is logical to conclude that the composition of particles found there would be somewhat similar to this particle.

Figure 6.23f shows that Fuel 4 aerosol is a significant portion of the overall ash mass, similar in yield to Fuel 3.

Clean and Blank Filters:

The background elements present in the filter interfere with determining the composition of the material collected on the filter. For this reason, elemental analysis of clean (*i.e.* unused) and blank (*i.e.* used in the impactor/furnace, but with no solid fuel flow) filters were conducted. Figures 6.24a and 6.24b show EDS analysis at 15000x and 1000x respectively, which shows that the compositions of the two are essentially identical. The blank filter, Figure 6.24c, shows slightly more sulfur than the clean filter. This is possibly a result of trace amounts of sulfur in the natural gas (see Appendix D), or is band-width noise from the gold/palladium signal (sputter coating) adjacent to sulfur.

Figure 6.24d shows the blank filter at a magnification of 5000x and 10kV. Note that the image is distorted in the horizontal direction, which is caused by charging of the filter surface during scanning. As mentioned before, this is an instrument induced effect, manifest only in the photograph. During real-time observation, the fibers were shown to be of uniform diameter along their lengths, and relatively straight. The non-conductive nature of the blank filter is the primary cause of surface charging. The gold/palladium sputter coating has more difficulty reducing the effect here due to the tortuosity of the surface, which inhibits charge mobility.

6.2.3 Discussion of Screened Sawdust/sanderdust Results

Some general observations about this test series can be made, each worthy of discussion. These trends are illustrated with the aid of the results of Fuel 1 ash composition

measurements shown in Figure 6.25. These compositions are considered to be the most representative of the material collected on the indicated stage or filter. It is observed that:

- The largest size cut (8.3 μm) is almost entirely made of alkaline elements (calcium and magnesium).
- A second residual mode is centered near 2 μm . Particles in this mode are generally very diverse both physically and chemically. They remain primarily calcium and magnesium, like the largest size cut.
- The 0.4 μm size cut is essentially chemically identical to the 2 μm mode with the exception of the appearance of sodium, potassium, chlorine, and sulfur. This size cut is unique in that the particulate matter is physically uniform.
- The aerosol mode is high in alkali metals and anions. It appears to be composed of primarily sub-micron particulate matter that is formed via vaporization followed by nucleation and condensation.

These observations are discussed in detail below.

A clear trend drawn from the data is that calcium is the dominant element for all size cuts above the aerosol filter, as shown in Figure 6.25. Comparing the elemental composition of unburned Fuel 1 to the composition of all residual size fractions, it is clear that calcium and magnesium are enriched and sodium, potassium and chlorine are depleted in the residual ash. As expected, low volatility minerals remain with the residual fraction (the first four columns) while higher volatility alkalis and their anions escape (the right-most column), resulting in an apparent enrichment of the low volatility elements in the large residual mode. This general behavior is predicted by equilibrium calculations discussed in the Modeling chapter. These results are also similar to results seen by Wornat *et al.* (1995), where experiments with southern pine showed 80% of the original calcium and magnesium remained in the char particle after 95% char conversion of the particle to ash, and alkalis were depleted to 30% to 47% of their original content.

Residual Porous Ash:

The large calcium structures are generally very porous and do not appear to have gone through a molten stage. As discussed earlier (Chapter 2), calcium is typically found as a

component of the cell walls of the parent biofuel. It is proposed that the porous structure of these large residual particles is an artifact of the cell walls, resulting from the conversion and collapse of the original cellular structure, as organically bound calcium is converted to oxide form, and eventually carbonate form. Baxter *et al.* (1996), found that the calcium in biofuels they tested (wood/ straw/ shell mixes, paper, and other biofuels) is primarily in the form of ion-exchangeable and acid soluble compounds, and not in water soluble form or in an oxide form. The implication is that the calcium is in an organic form. Simple equilibrium (presented in the Modeling chapter) indicates the favored form of this calcium at elevated temperatures is as an oxide, in combination with silica oxide and/or magnesium oxide, until ultimately forming a carbonate around 1000 K. In the absence of fluxing agents, the melting temperature of oxide mixtures composed of primarily CaO is high, as illustrated in the phase diagram shown in Figure 6.26. Since the original cell walls of the parent wood fuel are calcium rich relative to other inorganics, and these inorganic are essentially atomically dispersed, it can be assumed that these solid phase structures will be formed without entering a melt phase.

Although there is a risk of oversimplifying with a simple two-oxide system as shown in Figure 6.26, it is useful for illustrative purposes for two reasons: 1): Although the addition of alkalis or other elements can lower eutectic temperatures and shift compositions, the basic behavior of the two oxide system is *generally* similar to the more complex system. Secondly, clean biomass fuel is much more likely to have well-dispersed inorganics rather than discrete mineral inclusions, as discussed previously. Therefore, the *locally* well-mixed organically-bound minerals and finely dispersed SiO₂ can form combined solid phases directly, with a melting temperature governed by the *local* composition. Hence, some information can be gained from solid/liquid phase diagrams, as long as kinetic limitations and their simplicity are recognized.

Returning to Figure 6.26, it is clear that a CaO rich system (+60% CaO, for example) will maintain a solid phase at higher temperatures than a system composed of 50% CaO and 50% SiO₂. Therefore a calcium-rich zone, such as a cell wall in the parent wood fuel, can generate porous particulate matter. It would be useful to determine the inorganics concentration by element in the parent wood fuel using SEM and EDS techniques, but that investigation is beyond the scope of the current study.

The highly porous calcium structures do not appear to have crystalline features, but instead appear to have undergone some surface softening. Some possible mechanisms for this phenomena are proposed. First, repeated formation and decomposition of metastable CaCO_3 , in a CO_2 environment, can result in catalyzed sintering of the CaO structure (Borgwardt *et al.*, 1989; Silcox *et al.*, 1989). This leads to an estimate of $0.25 \mu\text{m}$ for the minimum radius of curvature maintainable by a given CaO feature, as discussed in Chenevert *et al.* (1998). A second possibility is based on equilibrium and kinetic considerations. Below about 1000 K, simple equilibrium predicts for Fuel 1 that Ca_2SiO_4 (s) will be converted to CaCO_3 (s), and the CaMgO_2 (s) will be converted to $\text{Ca}_3\text{MgSi}_2\text{O}_8$, as shown in Figure 7.2 of the Modeling chapter. Of course, solid to solid phase reactions are not kinetically favored, so significant exchange of oxide metals is very unlikely. What is more likely is carbonate formation on the surface of existing solid phase calcium-based structures, which is ultimately diffusionally limited by CO_2 penetration into the oxide ash. Acting against the argument for carbonate formation is the fact that sampling for these tests occurred above 1000 K, and quench is fast after sampling.

A third possibility is alkali-catalyzed surface-melting of the existing structure. This is addressed in conjunction with addressing the diversity of composition and morphology in the $2 \mu\text{m}$ mode.

Residual Two Micron Mode:

The composition of the residual ash generally shows greater diversity, both morphological and chemically, as the particulate matter diameter decreases. This diversity is probably the result of many interacting processes, including inhomogeneity in the unburned fuel (meaning discrete mineral deposits), preferential combination of specific elements to form eutectic melts, fragmentation, and coalescence. These mechanisms are briefly addressed.

Inhomogeneity of the parent fuel is very common in coal, as discussed in the Mechanisms chapter. Discrete mineral inclusions of different composition are very likely to have different size distributions in the unburned fuel. For example, pyrite inclusions in Kentucky #11 unburned pulverized coal are generally 20 to $40 \mu\text{m}$ and larger, while most of the quartz is in the form of inclusions less than $20 \mu\text{m}$ (Boni *et al.*, and Figure 5.1). The size distribution of discrete mineral inclusions and extraneous material directly influences the ultimate size distribution and chemical composition of the resulting ash (*e.g.*, Boni *et*

al., 1990; Helble *et al.*, 1990; Kramlich and Newton, 1994b). The Random Coalescence Model presented by Barta *et al.* (1992) uses probability techniques to determine the ultimate size and composition of the residual ash based on the discrete mineral distribution in the parent fuel. Benson *et al.* (1993) presented a slagging/fouling model, also based on the discrete mineral composition of the unburned coal. The coal literature leaves no doubt that one should expect diversity in the residual mode, due to the diversity of the micro-inclusions in pulverized fuels.

Unlike coal, much of the ashing elements in biomass is finely, if not atomically, dispersed in the fuel. An exception is contamination, typically meaning the soil associated with the biomass source, which usually is in form of aluminosilicate clays. The sawdust/sanderdust fuels used here are low in aluminum and silica, so discrete minerals contamination from soil is not likely. However, these fuels are composed of waste from board-making facilities, so they do contain binding resins with some inorganic components. These resins surely modify the composition. Some fuel particles will likely have a resin coating rather than a uniformly distributed composition.

It is likely that some of the unique particles in the micron size range are the result of preferential combination of inorganic elements. In coal, the combination of alkali and alkaline elements with alumino-silicates is well studied. For example, Zygarlicke *et al.* (1992) performed artificial char experiments with Ca-Si-S and Na-Si-S systems. It was found that organically bound calcium reacted with quartz crystals to form a lower temperature eutectic. As the char particle surface recedes during burning, molten particles form on the char surface and eventually coalesce. Less research has been done with systems deficient in aluminum and silica. In a biomass system, switchgrass charring experiments conducted by Wornat *et al.* (1995) showed the formation of K-Si "beads" for a char conversion of 50%. At 94% conversion, beads on the surface of the char were primarily of Ca-Si. Shedding and fragmentation at the char surface (Helble, 1989) can liberate these non-homogeneous mineral melts. This results in a diverse mineral distribution in the smaller diameter range.

It is hypothesized that a significant factor in the physical and chemical diversity of the 2 μm mode particles is preferential combination of low-volatility elements interacting with alkalis to form melts. These melts are continuously transformed by temperature change, as well as by depletion of their alkali components. Sequestering of otherwise mobile

alkalies occurs when precipitates are formed, governed by phase equilibrium. Migration of molten combinations, catalyzed by alkalies, of otherwise immobile elements explains both the diversity of smaller particles, as well as the softening of some calcium-based structures. This hypothesis is illustrated by example using phase equilibrium of a simplified system as a guide.

As mentioned earlier, simple-system phase diagrams are useful for illustrating the *qualitative* behavior of the actual system. Figure 6.26 shows a phase diagram of a system composed of calcium oxide and silica oxide at one atmosphere. For now, other important inorganic components are not included. An example isopleth at 62% CaO is shown (dashed line). Following this line of constant composition from low temperature to high temperature, one would expect an atomically disperse mixture to form into a two phase system above 1464 C (indicated by point "A"). The solid phase consists of essentially solid Ca_2SiO_4 (point "B") and the liquid phase would consist of the eutectic composition of 55% CaO and 45% SiO_2 (point "C"). If the temperature is increased, more of the residual Ca_2SiO_4 (s) would be lost to form a CaO enriched liquid phase. Ultimately, all the solid phase is converted to the liquid phase (point "D"). For comparison, an isopleth is drawn to indicate the silicon and calcium concentration in Fuel 1 as determined by Atomic Absorption Spectroscopy. This corresponds to 73% CaO and 26% SiO_2 on a mass basis and is labeled "Fuel 1 by AAS".

Summarizing thus far: 1) If the system temperature does not reach the eutectic temperature, a two-phase system does not exist, and no molten minerals are liberated from the char matrix. In this case, the residual ash is porous because of burnout of organics, and spheroidal ash particulate matter is not present. 2) If the system temperature reaches the local eutectic temperature, a two phase system exists in which a fraction of the mineral matter is liquefied to form the eutectic composition. The remaining residual is porous as before, and the cooled ash is a mix of porous structures and spheroidal ash particles. 3) If the system reaches its ultimate melting temperature, all the mineral matter is molten. The residual will be essentially spheroidal.

Of course, the actual elemental distribution is not completely homogenous. Locally (*e.g.* in cell walls), the calcium concentration may be so high that very little of the local mineral matter enters the molten stage. For example, an isopleth at 20% SiO_2 and 80% CaO would

not form a partial melt until 2070 C. As discussed earlier, this is a likely mechanism for the residual porous structures dominating the larger size cuts.

The influence of alkali metals in this system is not trivial. It is generally well known by researchers that alkalis invariably lower the melting temperature of otherwise solid oxides. It is useful to review this phenomena by comparing the phase diagrams of a CaO-SiO₂ system and a CaO-SiO₂-Na₂O system. Figure 6.27 is a phase equilibrium diagram for a system composed of CaOSiO₂ and Na₂OSiO₂. The left edge of this figure shows the melting temperature of CaOSiO₂, which is 1544 C. On Figure 6.26, this same composition and melting temperature can be found in the middle of the figure at a CaO concentration of 48%. Returning to Figure 6.27, assume a local composition of ash that consists of 2Na₂O•CaO•3SiO₂ and is 1400 C, which is indicated by a letter "E". Note that above 1200 C, this mixture will be in liquid phase. In Figure 6.26, a mixture of CaO•3SiO₂ (which corresponds to 23% CaO) is indicated with the letter "E" at 1400 C. This composition is completely in solid form when sodium is not present. Hence, for this simple system it is clear that sodium depresses the melting temperature.

Going one step further, assume a system composed of 67% Na₂OSiO₂ and 23% CaOSiO₂ is very quickly lowered from 1400 C to the melting temperature. This is indicated by the line "E" to "F" on Figure 6.27. The solid Na₂O•2CaO•3SiO₂ (s) condenses out as the temperature is lowered. It is important to note that the bulk of the sodium that enters into this solid phase is essentially trapped by diffusional resistance from participating in further equilibrium driven reactions with other elements. Eventually (and ideally), the remaining liquid hits the peritectic temperature of about 1150 C, and completely condenses to 2Na₂O•CaO•3SiO₂ (s) by 1050 C. In this ideal system, the sodium in this system is completely captured by the solid phase.

In actuality, some sodium does escape the system. Equilibrium predicts alkalis to escape in the vapor phase at combustion conditions, either as chlorides (when available) or hydroxides, and experimental evidence verifies that most of the alkalis do escape. What is important to note is that a *fraction* of the sodium that does participate in a melt will be captured in the solid condensed phase, with that fraction dictated by phase equilibrium.

The fraction of sodium captured is influenced by the local composition. This is illuminated by the ternary diagram of CaO-SiO₂-Na₂O shown in Figure 6.28. This diagram has been modified with dotted lines indicating constant CaO:SiO₂ ratios. Following a dotted line from left to right is equivalent to a system which is uniformly being depleted of Na₂O while CaO and SiO₂ are held constant. For example, consider a system initially composed of 36% Na₂O, 50% SiO₂, and 14% CaO at a temperature of 1400 C, which is on the line of CaO:SiO₂ = 2:7 g/g. At a temperature above about 1150 C, this combination exists as a liquid. If the temperature is dropped before sodium can escape, the condensate will capture a fraction of the sodium as solid Na₂O•2CaO•3SiO₂. The amount captured is a function of sodium escape rate and the system temperature. Now assume that sodium is leaving the initial system (36% Na₂O, 50% SiO₂) at a rate such that the system temperature does not drop significantly prior to significant sodium depletion. The liquid will follow the dotted composition line from left to right as the sodium escapes, eventually condensing as Tridymite, a form of SiO₂. In a real system, the sodium will escape at a rate somewhere between these two extremes, resulting in some sodium capture, and some sodium release.

The example phase diagram systems discussed above focus on silica-based interactions. Silica system phase diagrams are relatively abundant because of their importance to the ceramics industry. Of course, other eutectics mixes are likely in the sawdust/sanderdust ash as well. For example, a CaO-Fe₂O₃ system has a eutectic at 1200 C, which is well below the melting point of CaO (2570 C) and pure Fe₂O₃ (about 1580 C). Investigation of all possible combinations is well beyond the scope of the current study, and would obviously include detailed chemical equilibrium in all phases.

Adding to this already complicated picture is the potential for locally reducing or stoichiometric combustion. Elevated temperatures and elimination of some otherwise stable oxide forms (e.g. CaO → Ca+O) can change the composition of the residual as well. This avenue of mineral matter transformation is usually discussed relative to vaporization and aerosol formation, but it is recognized that it may play a role in the residual mode.

Residual 0.4 Micron Mode:

The final residual size cut prior to the aerosol filter is made up of particulate matter with a gravel-like appearance and diverse composition. What makes it unique is its uniformity,

and the presence of alkalis and potential anions. Subsequent discussion in the Modeling chapter will suggest that the chlorine and sulfur are present because they are bonded with sodium and potassium. Thus, these four elements can probably be viewed as resulting from either (1) aerosol captured by the last impactor stage, possibly via coagulation with other particles, or (2) vaporized alkali that condense on the smallest existing particles. If Na, K, Cl, and S are removed from the 0.4 μm stage and the remaining elements are renormalized, the resulting composition is very similar to the 5.3 and 1.6 μm size cuts. This suggests that the 5.3, 1.6, and 0.4 μm materials are all the result of similar mechanisms, with the exception that the 0.4 μm stage is “contaminated” by the presence of alkali (either as aerosol or direct condensate).

The typical diameter of these particles (about .4 μm) is similar to the typical feature size making up the large, residual lacy calcium structures. For example, compare Figure 6.12c to Figure 6.14a. As discussed above, softening of the calcium structure and mobility of eutectic forming minerals is likely. It is proposed that these particles are formed from liberated subdivisions of the larger porous structures. This hypothesis is implicitly supported by the argument of a minimum maintainable radius of curvature of a CaO structure in a CO_2 catalyzed environment (Borgwardt *et al.*, 1986, Silcox *et al.*, 1989). That radius is estimated to be .25 μm for this system (Chenevert *et al.*, 1998). Examining the structure of the large porous particle in Figure 6.12c, it appears that the mode of further transformation of this structure is extensive fragmentation rather than coalescence.

Once liberated from the porous structure, yet still associated with fluxing elements, the sub-micron particles continue to soften. Since the particles remains primarily Ca (presumably CaO), the particles do not achieve full melt, but rather “relax” to its gravel-like appearance. Of course, all arguments for formation of eutectic melts, discussed earlier, apply.

Aerosol ash:

Composition analysis of material on collected by the aerosol filter presents a problem because the instrument signal comes from both the aerosol and the underlying filter substrate. An attempt was made to correct the raw filter concentrations using the blank filter response shown in Figure 6.25. The right-most column in Figure 6.25 presents this corrected composition and the column labeled “Aerosol Filter” is the uncorrected composition. To make the correction, it was assumed that all silicon detected on the Fuel 1 filter was from the filter itself (this is justified because Si is an inconsequential element in

these particular fuels, compared to other elements present). The filter composition based on EDS analysis of a filter used in the cascade impactor, but with no wood flow, is labeled “Blank Filter” in Figure 6.25. Using this as a scaling factor, the proportionate amount of other background elements were removed from the Fuel 1 filter elemental analysis, and the composition was normalized to 100%. Calcium, iron and phosphorous were set to zero, because the correction for these elements yielded slightly negative values.

The compositions shown in Figure 6.29 are the result of applying the normalizing procedure to EDS data for all four fuel aerosol filters. All four fuels show very high alkali content in the aerosol mode. Recalling that up to 30% of the total ash mass was accumulated on the filter stage, a significant portion of the total sodium and potassium must be in the aerosol size range.

Figure 6.29 indicates there is a large amount of chlorine present in the aerosol for Fuels 1 and 2. This is a reflection of the high chlorine content of the unburned fuel (see Table 6.1 and Figure 6.1). The analysis suggests that more than enough chlorine is present on the filter to tie all the sodium and potassium up as NaCl and KCl. Unburned Fuels 3 and 4 are deficient in chlorine on the filter, as seen in Table 6.1 and Figure 6.1, and the aerosol filter analysis reflects the deficiency. It appears that sodium and potassium are primarily bound as sulfates in these fuels.

Although sulfur content is similar in Fuels 1, 2, and 4, it does not appear that sulfate displaces the chloride ion for Fuels 1 and 2. This is obvious in Table 6.4, where the molar ratio of Cl to 2S is shown for the unburned fuels and the material collected on the aerosol filters. (Note that one mole of Cl captures one mole of Na as NaCl, and one mole of S captures two moles of Na as Na_2SO_4 , so the ratio Cl:2S is relevant.) It is clear that sulfur is under-represented in the aerosol mode when the parent fuel is rich in chlorine.

Equilibrium calculations, presented in the modeling chapter, indicate that sodium sulfate will form around 1250 K, prior to condensation of vapor phase KCl and NaCl around 900 K. The predominance of chlorine over sulfur indicates that the sulfur is unable to displace chlorine to form sulfate. This indicates that sulfate formation, which is essentially a $\text{SO}_2(\text{g})$ - alkali chloride(s) reaction in this system, is kinetically limited.

Potassium escapes the residual mode more effectively than sodium, as is seen in the ratio of Na to K in the fuels and aerosols in Table 6.4. The ratio of sodium to potassium is reduced

by half from the unburned fuel to the aerosol. A phase diagram of a $K_2O-Na_2O-SiO_2$ system, shown in Figure 6.30, suggests preferential capture of sodium by the residual ash. A dotted line representing a *molar* ratio of Na to K of 2.5 for Fuel 1 is shown as a dotted line in Figure 6.30. Note that the first condensed species along the length of this line is either a pure silicate, or a sodium silicate. Potassium (and some of the sodium) remains in the liquid phase, ultimately escaping, while a fraction of the sodium is bound in the solid form and becomes diffusionally immobile as the system cools. The quantitative fraction of sodium remaining with the residual ash is a function of system temperature history and other factors, as discussed earlier. Qualitatively, this simplified system indicates that the sodium will be preferentially captured over potassium. For comparison, a dotted line representing a Na to K molar ratio of 1:1 is also shown in Figure 6.30. It does overlap into a potassium-silica condensed phase, but only slightly. All for fuels tested lie in a region that favors sodium rather than potassium in the solid form.

Returning to Table 6.4, the cation to anion ratio indicates more than enough anions are available to capture the detected alkalis for Fuels 1, 2 and 3. The excess Cl and/or S may be related to the reduction in available Na due to residual capture. For Fuel 4, the molar ratio indicates that some of the alkali on the aerosol filter may be in the form other than chloride or sulfate, such as a carbonate. Equilibrium, discussed in the Modeling chapter, predicts some alkali carbonate formation for Fuel 4.

6.3 Milled Sawdust/sanderdust Experiments

6.3.1 Milled Sawdust/sanderdust Test Matrix and Conditions

Table 6.5 is a summary of milled sawdust/sanderdust experiments. The experiments were performed following the experimental procedures described in Section 4.5. In brief, the milled fuel was burned in the tunnel furnace and sampled isokinetically using the porous wall dilution probe. This diluted flue gas and particulate matter was passed through a cascade impactor to remove large particles, and then routed through a tank of a preselected volume. The tank volume controlled the residence time of the flue/aerosol prior to sizing of the remaining ash with an Electrical Aerosol Analyzer.

Table 6.5 is a summary of the test matrix for this series. The test number and fuel type are shown in the first two columns. Next, the sampling hardware configuration is shown. An

“x” in the Cascade Impactor column indicates that mass measurements of the cascade impactor stages were made. Although a cascade impactor was used for all EAA tests, not all cascade impactor ash collections were of interest. The next column indicates that an Electrical Aerosol Analyzer (EAA) was used for all tests, except for tests which were conducted solely to accurately measure the furnace temperature profile. Temperature profiling tests were performed with a High Velocity Thermocouple as described in Chapter 4.

The size of the delay tank (*i.e.* the residence time) between the cascade impactor and the EAA is a critical factor. Three tanks were used: a plastic tank (200 liters), a steel tank (199 liters), and a Plexiglas tank (21 liters). Some tests were also performed with no delay tank. The milled sawdust/sanderdust flow rate was also varied as shown in the next column in Table 6.5.

The tunnel furnace temperature was set by controlling the natural gas/air stoichiometry. The overall flow rate, the air to fuel ratio of the main burner, and the stoichiometry of the upper auxiliary burner are shown for each test. Also shown is the calculated dry oxygen content of the flue gas, with no solid fuel added. Note that the addition of solid fuel did not dramatically change the free oxygen content, as the wood fuel flow rate was about two orders of magnitude lower than the overall furnace flow rate.

Experiments were performed under three furnace conditions, and are grouped accordingly on Table 6.5. The first grouping are experiments conducted with the tunnel furnace main burner (natural gas fired) operated at the highest temperature. The high temperature furnace setting test was selected to be comparable to the screened sawdust/sanderdust series, and similar to an environment found in an industrial burner. The low temperature test series was performed in order to determine if vapor condensation prior to entering the sample probe affected the ultimate aerosol size distribution. This was a limited series with a lower furnace flow rate (*i.e.* longer furnace residence time) and a leaner stoichiometry. The auxiliary burner was run closer to stoichiometric in an attempt to maintain a constant temperature down the height of the furnace. The third grouping was conducted with a slightly leaner stoichiometry in the main and auxiliary burners, and about half the furnace mass flow rate of the first grouping.

Radial temperature profiles were obtained at every port in the furnace, as shown in Figures 6.31 through 6.33. These measurements were made using the High Velocity Thermocouple (HVTC) described in Chapter 4.

Figure 6.31 shows the radial temperature profile at a series of axial locations for the maximum furnace temperature and flow rate settings. Temperature fluctuations are quantified by the error bars accompanying each sample point. The tunnel furnace expands beginning near the point of fuel injection, and the temperature profiles at the first few ports (43 cm, 58 cm, and 74 cm) reflect the reduced tunnel diameter. From the top of the furnace to near the bottom, the temperature shows good radial uniformity. The obvious exception was at the last port of the furnace, which is located just above the inlet of the vertically positioned sampling probe at 185 cm from the point of fuel injection. The temperature dip noted on centerline was due to a backflow of air up the probe shaft, induced by the draw of furnace exhaust system. In normal operation the probe is independently aspirated and the temperature dip does not occur.

The temperature profiles also show a lower temperature near the furnace walls, which is the left-most point of each profile. Note that the temperature profile is flatter near the upper auxiliary burners where the tunnel is heated, as expected.

Figure 6.32 shows the temperature profiles for a slightly leaner main burner setting, but a richer upper auxiliary burner setting. Note that the temperature profiles in the upper region of the furnace, where the auxiliary burner is located, are tightly grouped. At the lower end of the furnace, the temperature drops more quickly since the lower auxiliary burners are not in use. Again, the influence of room-air entrainment up the sampling probe is seen in the 185 cm profile. The temperature at the 155 cm port and -5 cm from the centerline indicates a very localized temperature dip, which recovers by the 170 cm port. It is likely that a small crack is present in the refractory near this point, allowing a small amount of air from the idle auxiliary burner to enter. It appears to be a relatively small leak, judging from the temperature profile. This temperature series was chronologically the latest of the three milled sawdust/sanderdust temperature profile tests (*i.e.* Figures 6.31 and 6.33), so any leak is relatively new.

Figure 6.33 shows the temperature profiles for the leanest furnace setting. This profile set is very similar profiles describes with Figures 6.31 and 6.32. The temperature was

uniform radially, with the exception of the temperature dip discussed earlier at the lowest station.

Figure 6.34 summarizes the three temperature profiles. The axial temperature down the length of the furnace was calculated as the radial average of the temperature measured at each available port. These data are shown in tabular form on the lower portion of the figure. The average temperature measurements taken at the port nearest the inlet of the vertical sampling probe did not include data that were obviously influenced by the probe air entrainment, since it was an artifact of the inactive sampling probe.

The temperature profiles in Figure 6.34 are similar. The moderate temperature test was conducted with the upper auxiliary burners operating hotter than the other two tests, resulting in a flatter temperature profile near the top of the reactor.

The sample system modifications performed for the milled sawdust/ sanderdust experiments significantly changed the post-furnace environment experienced by the sampled flue gas and ash. Milled sawdust/sanderdust tests are characterized by longer furnace residence times (1 second for screened sawdust/sanderdust experiments versus 1.4 and 3.0 seconds for milled experiments), in-probe sample dilution, and a variable delay time prior to ash sizing.

Figure 6.35 shows the temperature/time history of the sampled gas, as well as a measure of the dilution of the sample with time. In the upper figure, three different furnace flow rates are illustrated. The 525 g/minute flow rate corresponds to the temperature profile versus time for the screened sawdust experiments discussed in Section 6.2. The steep temperature gradient near one second residence time is representative of quenching in the sampling probe. Recall that experiments conducted with the screened sawdust/ sanderdust were done with a simple water-cooled sampling probe rather than the dilution probe.

The temperature versus residence time for milled sawdust/sanderdust experiments at 525 g/minute furnace flow rate is indicated on Figure 6.35. The steep temperature gradient at about 1.4 seconds was the result of quenching inside the sampling probe. The dilution for this condition is indicated in the lower figure. Note that dilution in the sampling probe resulted in a significant temperature drop and an order of magnitude reduction in ash flow concentration prior to exiting the sample probe. The dilution ratio for the high temperature tests was about 25 to 1 on a mass basis. Following dilution and passage through the

cascade impactor, the sampled flue entered the delay tank. The delay tank residence time was controlled by tank volume: 239 seconds for a 199 liter tank, 25 seconds for a 21 liter tank, and no delay for no tank. The variable delay time provides an opportunity to observe the influence of “aging” on the aerosol generated by the primary flame.

The temperature profile indicated by a furnace flow rate of 305 g/minute in Figure 6.35 is based on test 112096T. It is typical of the other milled sawdust/ sanderdust experiments conducted. The probe dilution ratio for this furnace flow rate is about 25 parts dilution air to one part flue gas.

6.3.2 Milled Sawdust/sanderdust Results

Figures 6.36 through 6.42 are summaries of all Electrical Aerosol Analyzer (EAA) experiments conducted. Appendix F is a more detailed description of each individual test, with the practical limitations of listing all computer-collected data recognized. These figures are all shown in terms of $d(\text{volume})/d(\log \text{ diameter})$ versus particle diameter, where volume refers to the ash concentration expressed as μm^3 of aerosol per cm^3 of carrier gas. Like cascade impactor data expressed in this form, the area under the curve between two diameters is proportional to the mass in that diameter range.

A change in measuring procedures was incorporated early in this test series, in which the EAA was switched from hand-recorded measurements to computer controlled bin sizing and data acquisition. This allowed recording of up to 10 cycles through all particle diameter bin sizes (with high precision) in the same amount of time a researcher could record one cycle by hand. The large delay tank was changed from a plastic tank to a steel tank in this same time frame. In Figures 6.36 through 6.42, tests that include the symbol “m” refer to the method of data acquisition (manual) and a plastic delay tank, while tests that are identified with an “e” referring to electronic data acquisition and a steel delay tank.

The upper graph in Figure 6.36 shows those Fuel 1 tests conducted at the highest furnace temperature that used either the large plastic tank or the large steel tank. Both tanks had volumes of about 200 liters, which results in a delay time of 239 seconds. Each curve represents a different sawdust/sanderdust flow rate into the furnace. As one would expect, the aerosol decreases as wood flow rate decreases. In the upper graph of Figure 6.36, the cause of the difference between the 4.6 g/minute test with the steel tank and the two tests

with the plastic tank is not fully resolved, although it is clear there is significant variation associated with the manually collected size distributions.

The middle graph in Figure 6.36 shows all Fuel 1 experiments at the given furnace temperature when a delay tank of 21 liters was used. This is equivalent to a 25 second delay time, which is an order of magnitude shorter delay time than the tests shown in the upper graph. Immediately obvious is that the major aerosol mode peaks below $0.1 \mu\text{m}$, while the major mode with the longer delay tank time (above) peaks above $0.1 \mu\text{m}$.

Note also that there is now a size mode near $0.025 \mu\text{m}$ evident at all sanderdust/ sawdust flow rates. As the milled sawdust/ sanderdust flow rate decreases, both modes are attenuated, but the mode near $0.1 \mu\text{m}$ is decreased disproportionately more than the $0.025 \mu\text{m}$ mode.

The lower graph in Figure 6.36 shows aerosol size distribution from the Fuel 1 tests, at the same furnace conditions as above, but with no delay tank. The diluted sample was transported from the cascade impactor to the EAA with no delay other than residence time in the sampling line. In this graph, there is no obvious peak at $0.1 \mu\text{m}$. Below $0.1 \mu\text{m}$, the EAA becomes saturated at the highest flow rates, indicative of particle counts beyond the range of the instrument. Since mass is conserved, regardless of delay tank time, it is logical to conclude most of the mass was in the smaller size mode.

Similar trends for the other three sawdust/ sanderdust fuels are apparent in Figure 6.37 through Figure 6.39. Note that Fuels 3 and 4 appear to have enhanced $0.025 \mu\text{m}$ modes when compared to Fuels 1 and 2.

Figure 6.40 shows the results of testing at the intermediate furnace settings. Note that both Fuels 1 and 4 have no significant $0.025 \mu\text{m}$ mode, exhibit a $0.1 \mu\text{m}$ mode, and appear to show a possibly larger mode.

Figures 6.41 show all EAA tests at the lowest furnace temperature for Fuel 1. Interestingly, the $0.025 \mu\text{m}$ mode is not readily apparent in this series, except in the lowest sawdust/sanderdust flow rates.

Fuels 2, 3 and 4 test results at this furnace setting are shown in Figure 6.42. These profiles are very similar to results at the slightly hotter furnace settings shown in Figure 6.40.

Cascade impactor data for the milled sawdust/sanderdust is of secondary importance, but is given here for completeness. The cascade impactor was essentially a large particle filtering device for these tests, and as such it was operated above its standard operating volumetric flow rate of one cubic foot per minute. Ash size distributions are shown in Figures 6.43 through 6.45. Merging cascade impactor test data with the EAA data is a challenge, particularly since the cascade impactor is a mechanical integrator by nature (all ash is collected) and therefore includes all transient flow rates, while the EAA makes instantaneous measurements and does not directly measure mass.

6.3.3 Discussion of Milled Sawdust/sanderdust Results

Figure 6.46 shows three EAA tests with the independent variable being delay tank size (*i.e.* delay tank residence time). This particular test was conducted with Fuel 1, but all four fuels show similar behavior. The largest delay time (239 sec) results in the majority of the mass being centered near 0.1 μm . For a delay time of 25 seconds, mass is split between a 0.025 μm mode and 0.1 μm mode.

When testing with no delay time, number densities are beyond the range of the EAA for particle sizes below about 0.04 μm . Since total mass is conserved, regardless of residence time, it is logical to conclude that nearly all of the aerosol is below 0.04 μm for the test with no delay time.

Coagulation rate is the obvious mechanism controlling the size distribution in the size range measured by the EAA. Simple monodisperse coagulation theory, or Smoluchowski coagulation (see Hinds, 1992), argues that coagulation is governed by diffusion when particle diameter is on the order of the mean free path of molecules in the suspending medium. In this regime, large particles are formed by collisions between smaller particles that are under the influence of Brownian motion.

The practical limit of Brownian motion induced coagulation of aerosol particles is about 0.1 μm , and is demonstrated by the 239 second residence time test. The 25 second delay time

test shows that this time is insufficient for complete coagulation to the 0.1 μm mode. The test with no delay time shows that the elapsed time is insufficient for any significant coagulation to the 0.1 μm mode.

Figure 6.47 compares aerosol size distribution for Fuel 1 between a high furnace temperature test and a low furnace temperature test, with a delay time of 239 seconds. Note that the cooler furnace test shows nearly complete depopulation of the 0.025 μm mode, while the hotter furnace test indicates a small residual mode at 0.025 μm . The reason for this behavior is worthy of investigation, since the surface area of the 0.025 μm particles is a significant fraction of the total surface area available for downstream surface chemistry. This is explored in terms of coagulation theory and species equilibrium, as discussed below.

It is suggested that at the higher sampling temperature (*i.e.* hotter furnace) much of the condensation/ coagulation occurs within the dilution probe. Since this occurs under strongly diluted conditions, the coagulation rate is significantly reduced, yielding more fine particles. With the cooler test, the reduced sampling temperature moves the condensation/coagulation events into the undiluted furnace gas. Here, the accelerated coagulation rapidly depopulates the finer particle sizes.

This interpretation is supported by equilibrium calculations discussed in the Modeling chapter. Simple equilibrium shows that Na_2SO_4 is the first alkali species predicted to form a liquid or solid phase. This event is, however, accompanied by a reaction. This suggests that there may be a chemical kinetic barrier to rapid formation of this compound. Alternately, NaCl (s) and KCl (s) are formed directly from identical gas-phase species. This lowers the expected alkali condensation temperature to around 600 C. As mentioned above, this places the condensation event largely within the probe during high-temperature sampling and within the reactor free-stream for low-temperature sampling. Thus, the reduced coagulation rate (when the furnace gas is dilution quenched by high-temperature sampling) is the reason the fine particles remain for the higher temperature test, even with a 239 second delay time.

A qualitative extrapolation to practical systems indicates that while delay times are much less than those used in the present experiments, the initial number density is higher. This suggests that the dilution air location may have a significant influence on the final aerosol

particle size distribution, which in turn will affect both downstream impacts and collectability. Also, the presence of chlorine alters the condensation temperatures predicted at equilibrium. Thus, the behavior of the fuels that contain significant chlorine may be different than those that are chlorine poor.

To summarize:

- Testing with the EAA demonstrated that the size distribution in the sub-micron stage is bimodal, with one mode near 0.1 μm and the other near 0.025 μm . The relative proportion of mass in each size range is a function of the variables that influence coagulation rate. The influence of number density and residence time on size distribution was illustrated, shown that longer residence times led to increased coagulation.
- It is clear that depopulation of the 0.025 μm mode is affected by the composition of the vapor, in that species with high boiling temperatures will preferentially condense to form nucleate first. If the temperature is maintained just below the condensation temperature, and dilution is delayed, coagulation is fast.

Table 6.1: Analysis of As Received sanderdust and sawdust samples

		Fuel 1 sanderdust	Fuel 2 sanderdust	Fuel 3 sanderdust / board trim	Fuel 4, dryer fines/ board trim	Kentucky #11, sub- bit. coal*
Ultimate Analysis (% mass, Oven Dry Basis)	C	47.5	47.7	50.8	49.9	60.1
	N	5.2	3.4	0.19	0.10	1.2
	H	5.5	5.8	5.6	6.4	4.6
	S	.033	.030	.062	.038	4.4
	O by Δ	40.9	42.0	42.6	42.3	7.9
Moisture (% mass, as received)		4.2	4.1	5.2	4.2	3.8
Ash at 750C (% mass, OD Basis)		0.81	1.07	0.66	1.29	21.8
Major Mineral Components, (mg per kg raw fuel)	Ca	1640	2410	1120	3930	6589
	Na	1000	1500	480	870	466
	K	674	1020	454	1160	3827
	Mg	249	281	233	405	1137
	Mn	94	91	112	76	N/A
	Fe	198	43	308	75	29310
	P	65	80	57	118	183
	Si	403	263	241	200	45734
Total Halogens, (mg/kg raw fuel)		1215	2130	82	137	N/A
Mass (%) removed after sieving, doubled 1.6 x 1.6 mm screen		0	10	18	31	N/A

* Analysis of Kentucky #11 adapted from reference PSI. Additional components for Kentucky #11: Al: 21513 mg/kg, S: 4195 mg/kg, Ti: 1130 mg/kg.

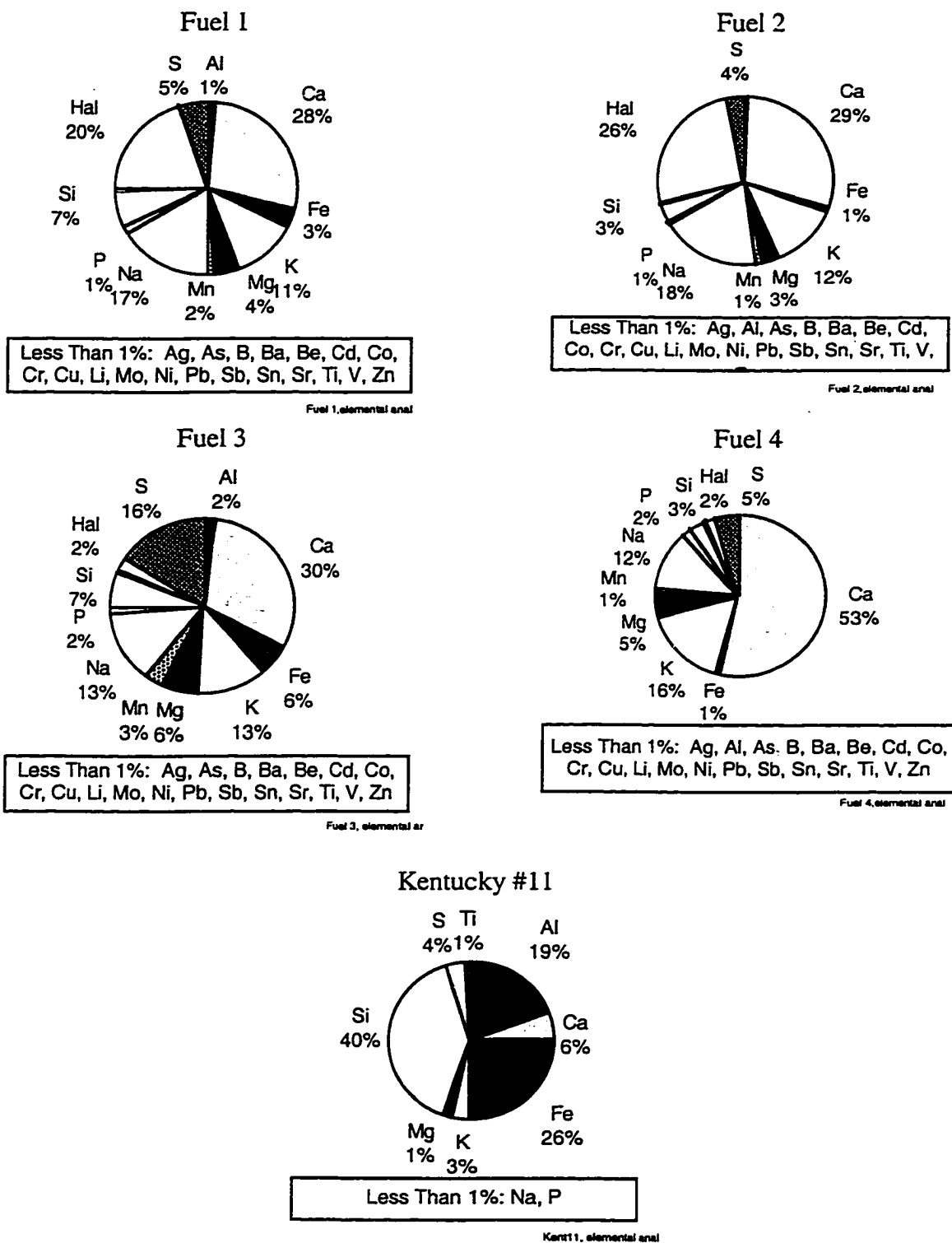


Figure 6.1: Atomic Absorption analysis of As-Received fuels

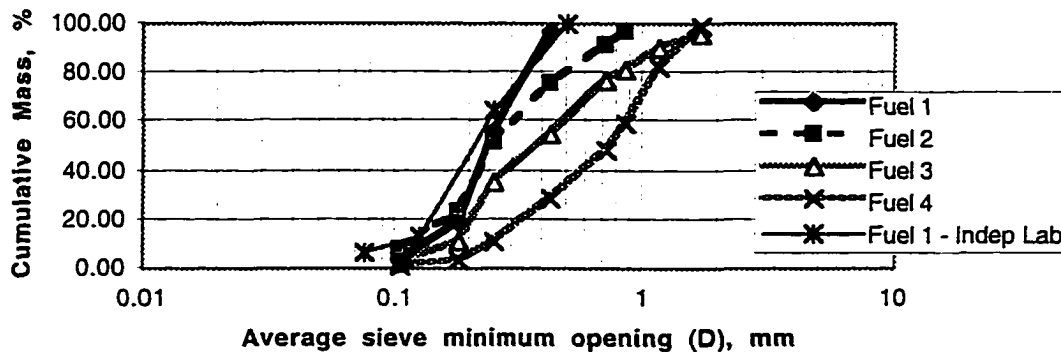


Figure 6.2: As-Received fuels size distribution by cumulative mass

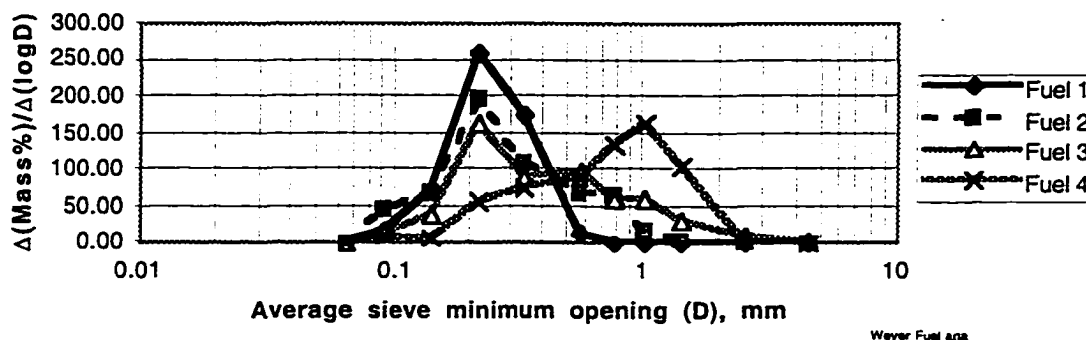


Figure 6.3: As-Received fuels size distribution

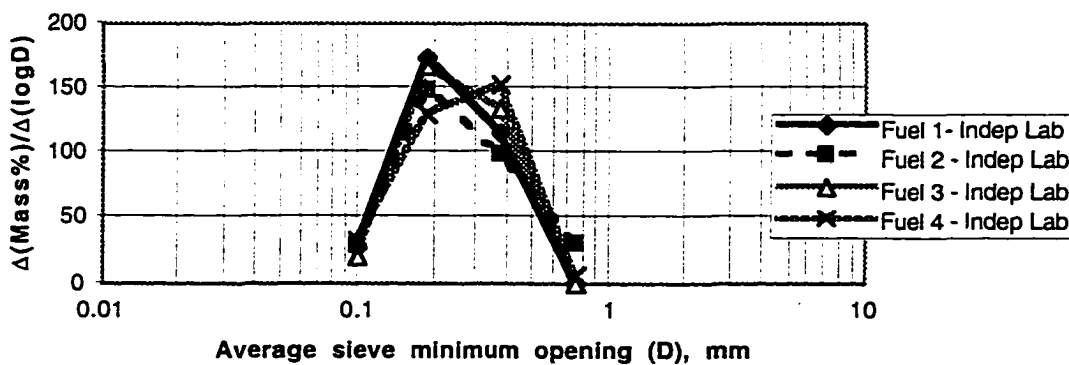


Figure 6.4: Milled fuel size distribution. Fuel 1 As-Received, Fuels 2, 3, and 4 milled to 0.5 mm diameter exit screen

Table 6.2: Screened sawdust/sanderdust test matrix

Test Number	Fuel	Fuel Flow rate, g/min	Sampling Time, min:sec	Total Ash collected, mg
08089501	Fuel 1	6.8	15:00	15.13
08099501	Fuel 1	6.8	5:00	4.34
08169501	Fuel 1	5.0	15:00	11.52
08169502	Fuel 1	5.0	15:00	10.59
08169503	Fuel 1	5.0	15:00	12.62
11099501	Fuel 1	5.1	10:00	N/A
10269501	Fuel 2	5.45	15:00	20.66
10269502	Fuel 2	5.45	10:00	14.75
10139501	Fuel 3	5.0	15:00	47.88
10319501	Fuel 3	5.0	15:00	51.69
11029501	Fuel 3	5.0	10:00	30.38
11079501	Fuel 4	5.22	10:00	63.22
11229501	Fuel 4	5.22	10:00	61.83
10169501	Temperature	0.0	--	--
10069401	Blank	0.0	15:00	0.26

Table 6.3: Test conditions for Screened sawdust/sanderdust experiments

	Average	Standard Deviation
Main Burner A/F Equivalence Ratio	1.57	0.02
Main Burner - Total mass flow including solid fuel entrainment air, g/min	524.1	12.6
Upper Aux Burner A/F Equivalence Ratio	1.65	0.01
Upper Aux Burner Mass Flow, g/min	545.2	3.0
Dry O2 No solid fuel injection, % by vol	9.1	0.4
Dry O2 solid fuel injection, % by vol	7.8	0.5
Residence Time - Solid fuel injection point to sample probe inlet, seconds	1.08	0.03

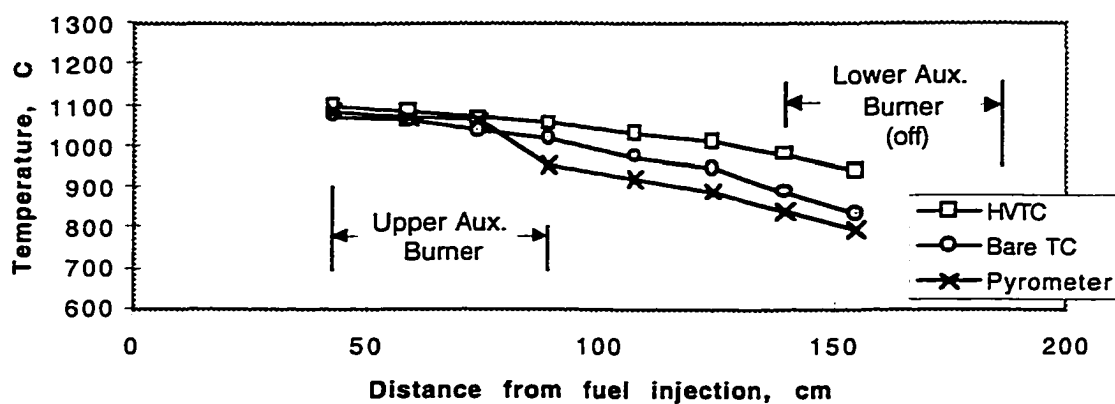


Figure 6.5: Temperature as a function of furnace height

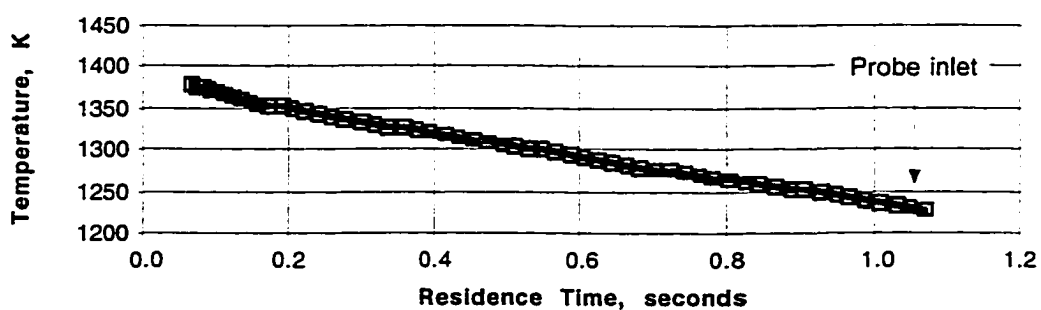


Figure 6.6: Temperature as a function of calculated residence time for Screened sawdust/sanderdust fuels, based on High Velocity Thermocouple measurements

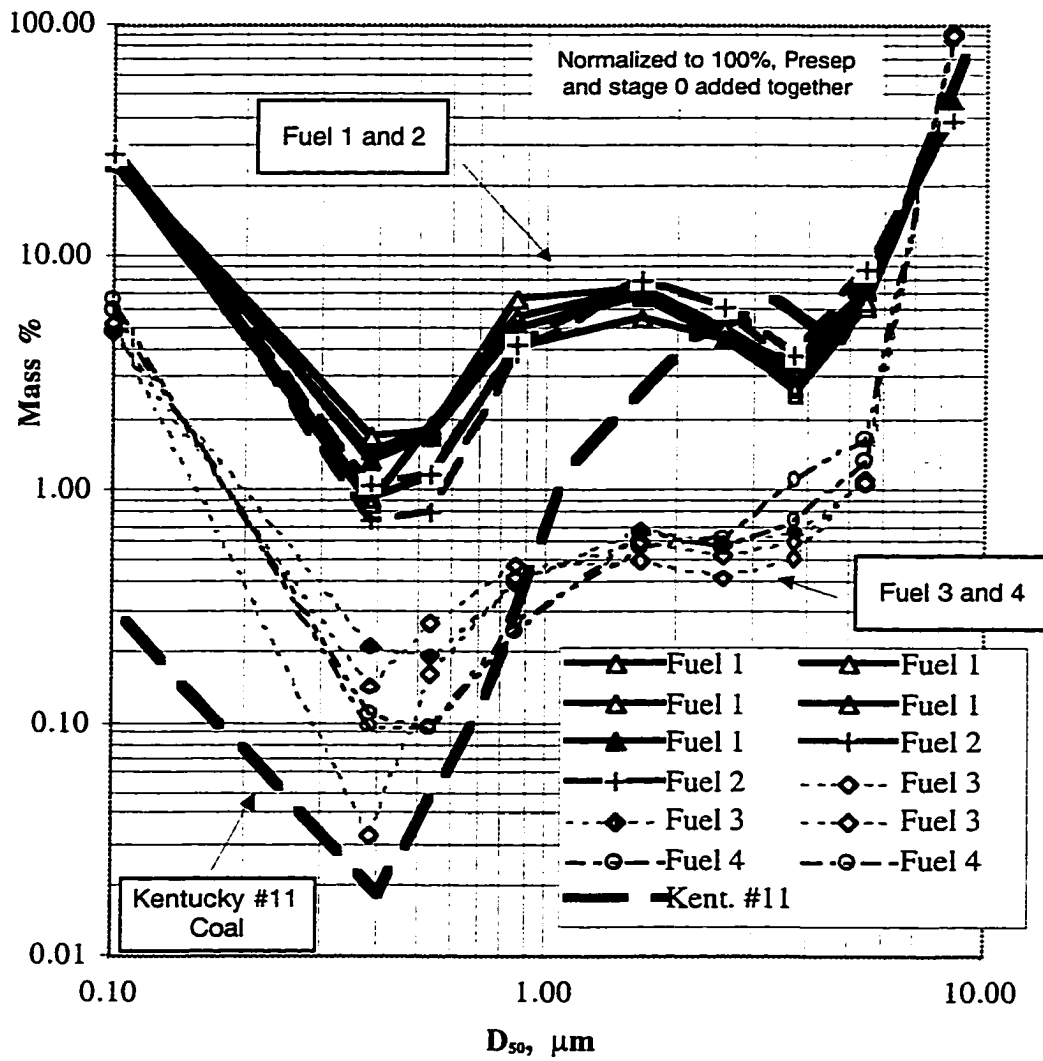


Figure 6.7: Screened sawdust/sanderdust ash size distribution as a function of impactor stage cutoff diameter.

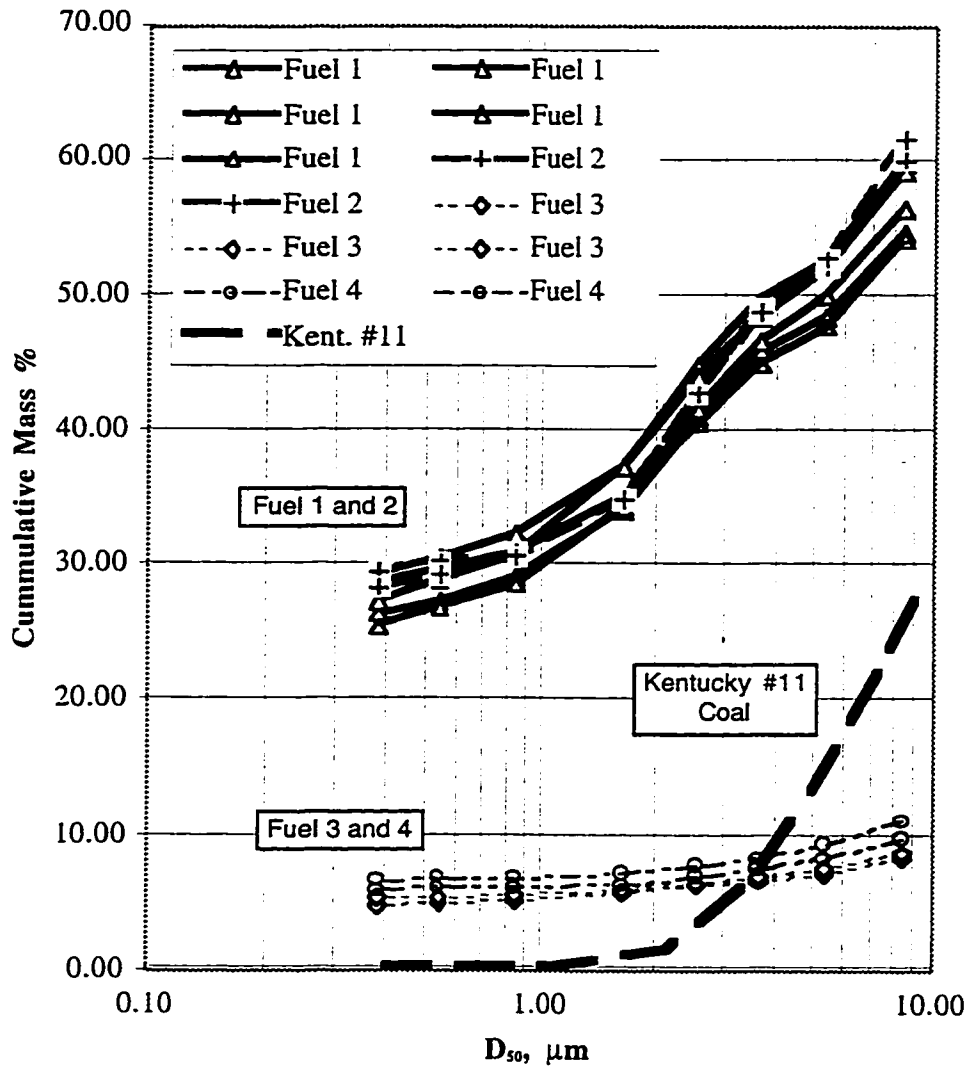


Figure 6.8: Screened sawdust/sanderdust ash size distribution as a function of cumulative mass

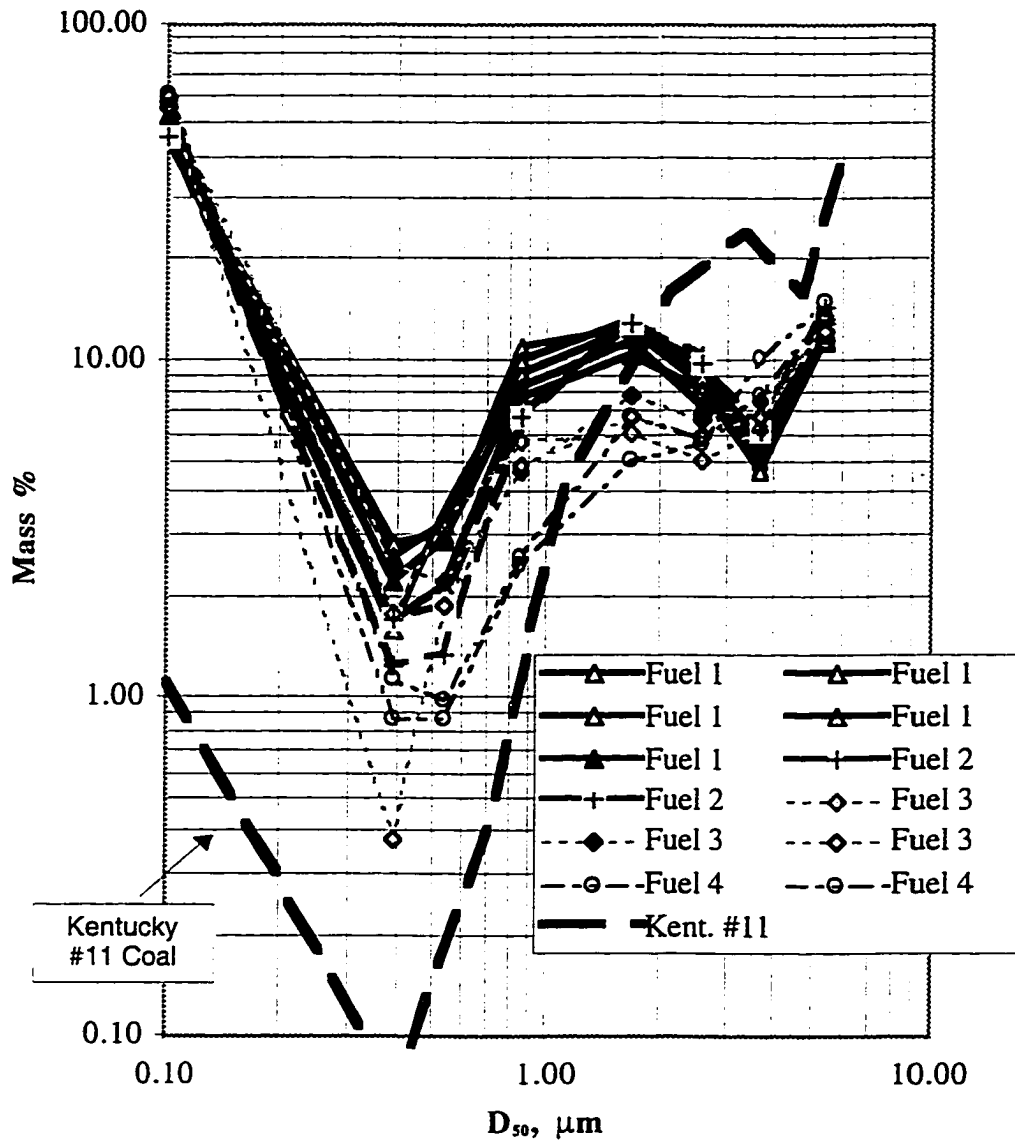


Figure 6.9: Screened sawdust/sanderdust ash size distribution as a function of impactor cutoff diameter, excluding ash of greater than 5 μm

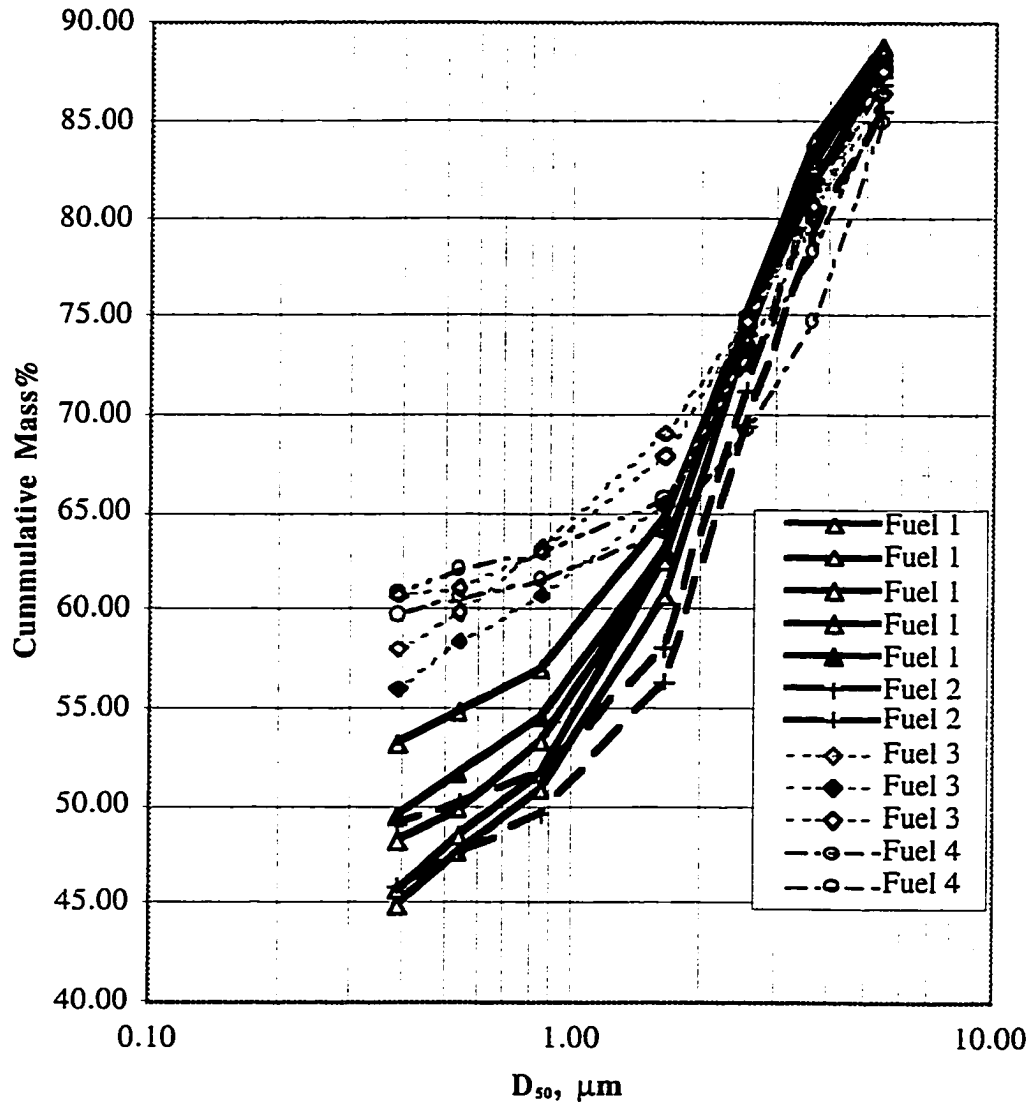
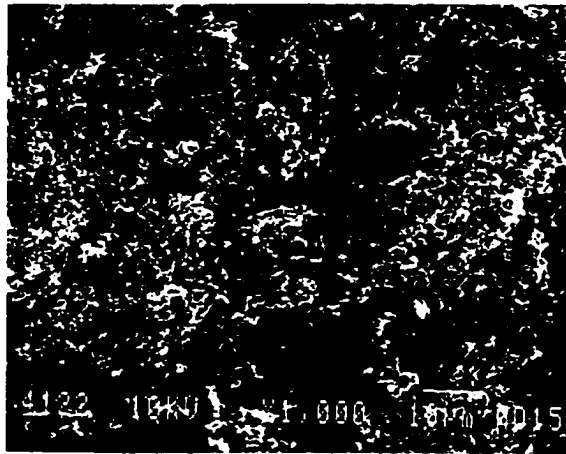


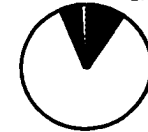
Figure 6.10: Screened sawdust/sanderdust ash size distribution as a function of cumulative mass, excluding particles of greater than 5 μm



(a) Typical ash material collected for Fuel 1, Stage 0

Fe, Na, P, S, Si 1%
Al, Cl, K, Ti <1%

Mn 2% Mg 8%

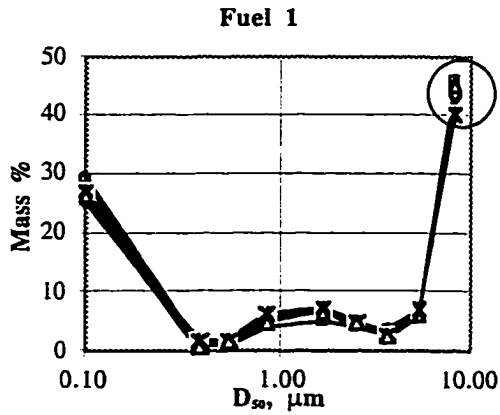


Ca 85%

% Mass

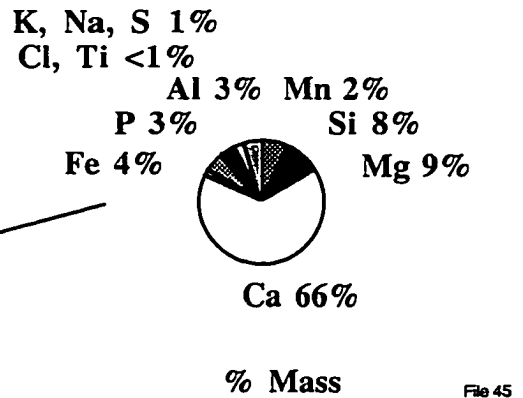
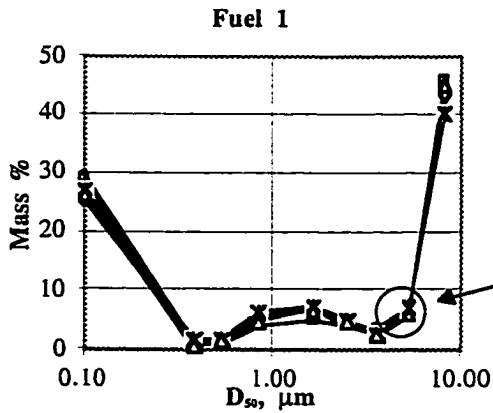
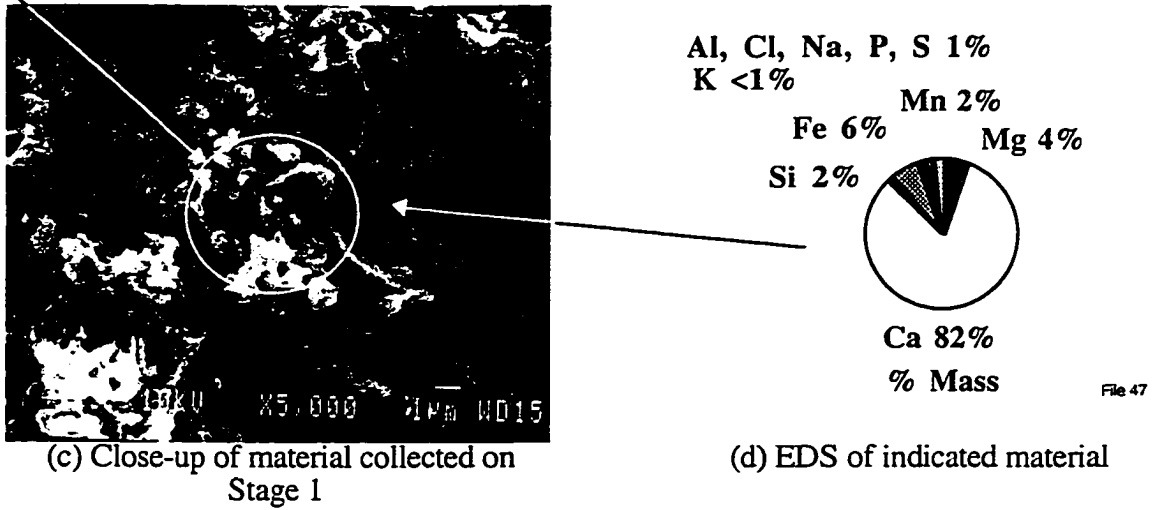
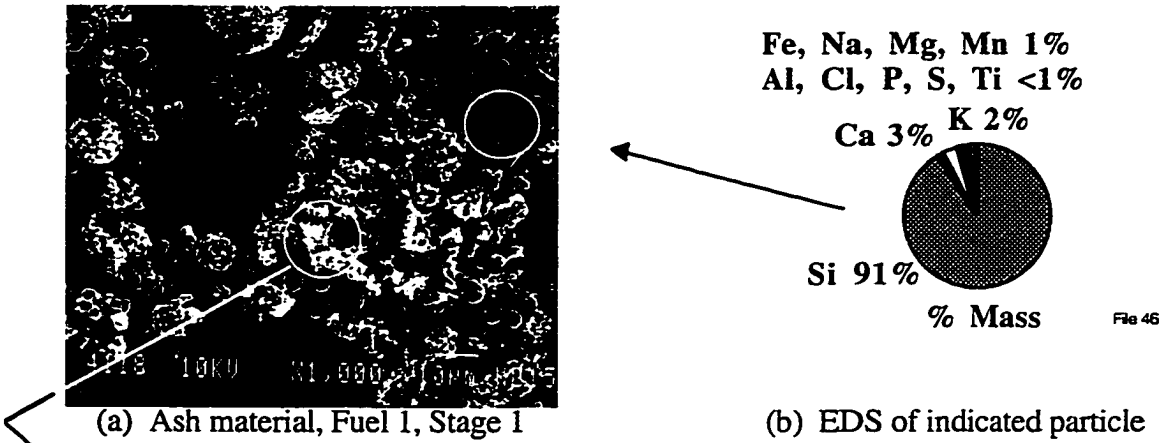
File 50

(b) EDS analysis of typical Fuel 1, Stage 0 ash, 1500x



(c) Ash mass distribution with area of interest highlighted

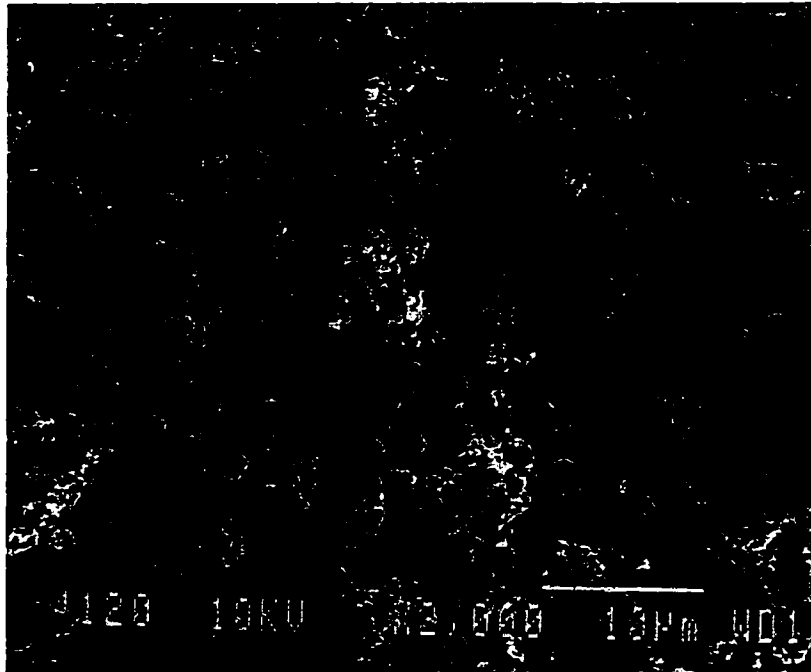
Figure 6.11: Fuel 1, Stage 0 Scanning Electron Microscope results



(e) Size distribution

(f) Typical Fuel 1, Stage 1 ash, 2000x

Figure 6.12: Fuel 1 Stage 1 Scanning Electron Microscope results



(a) Ash collected for Fuel 1, Stage 4

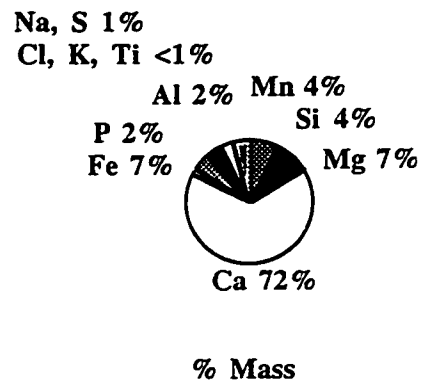
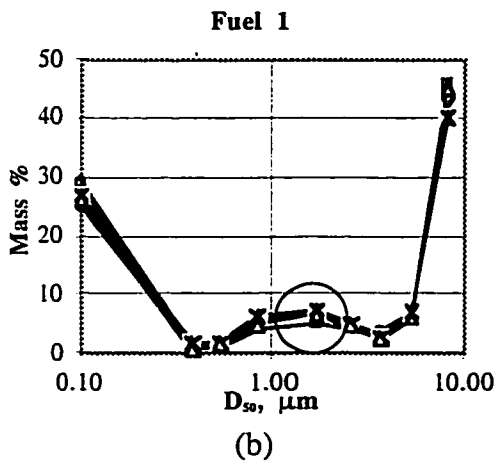
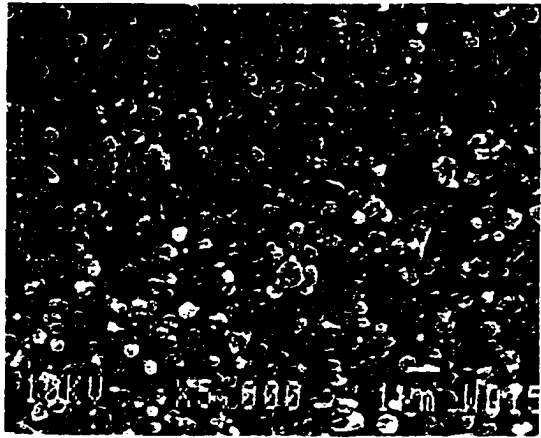
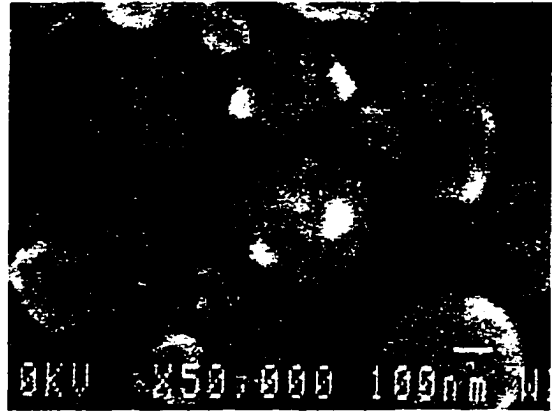


Figure 6.13: Fuel 1 Stage 4 Scanning Electron Microscope results

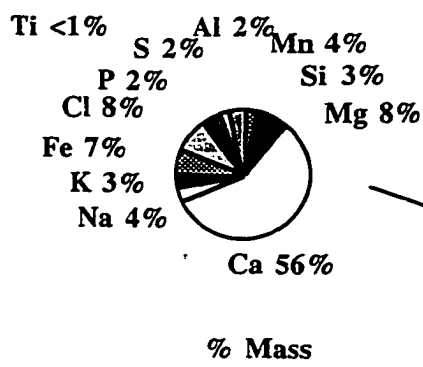
File 48



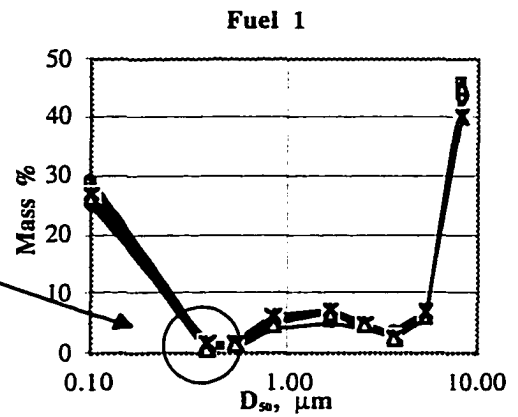
(a)



(b)



(c)



(d)

Figure 6.14: Fuel 1 Stage 7 Scanning Electron Microscope results

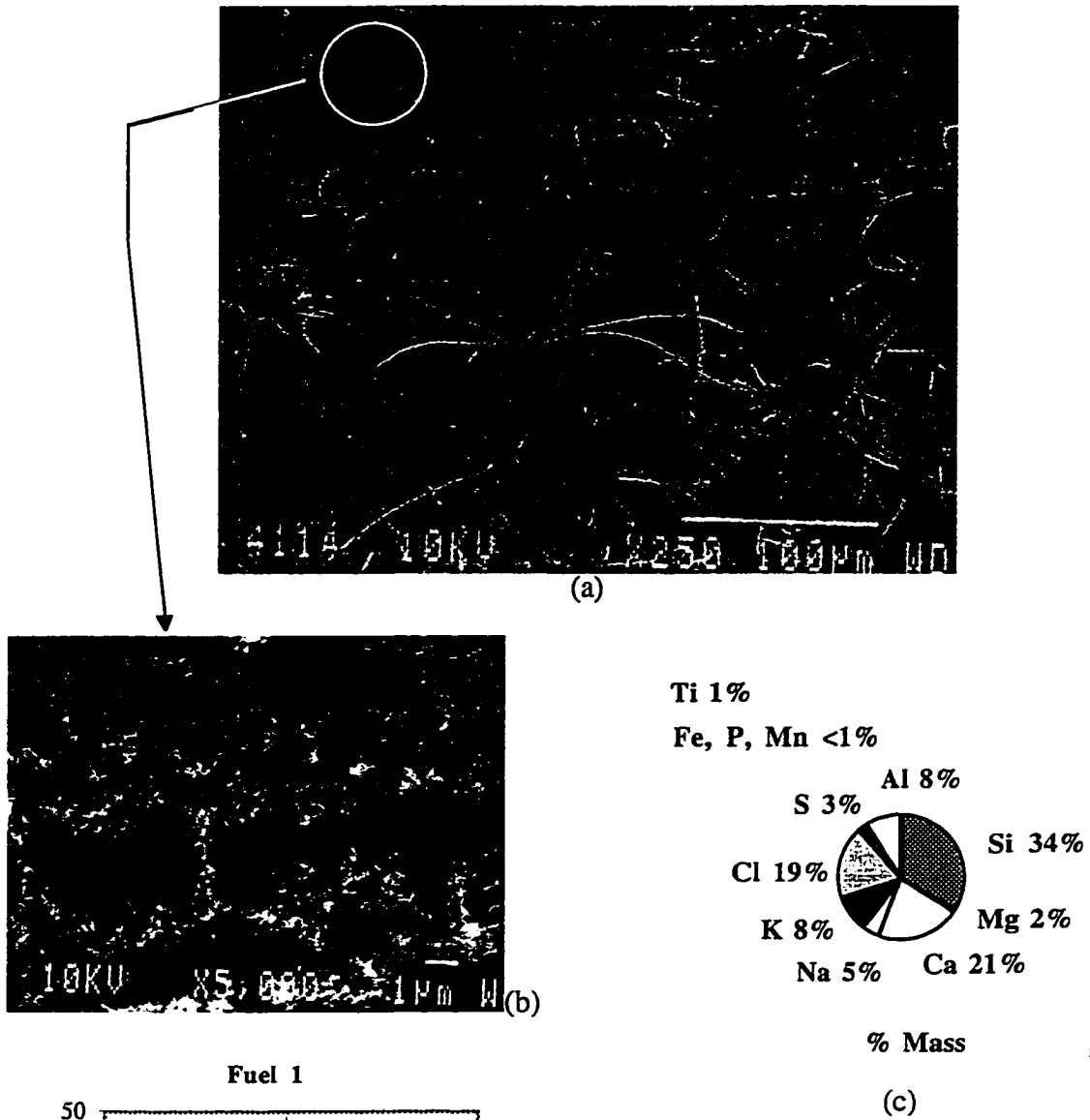
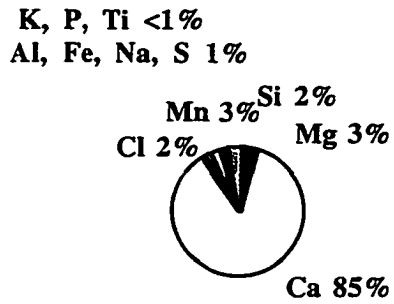


Figure 6.15: Fuel 1 aerosol filter

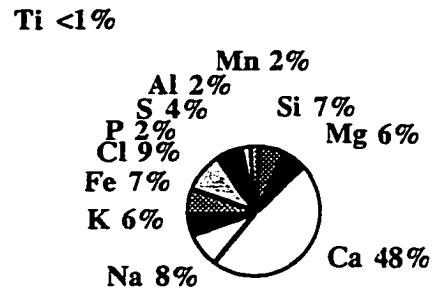
Fig 42



% Mass

File 38

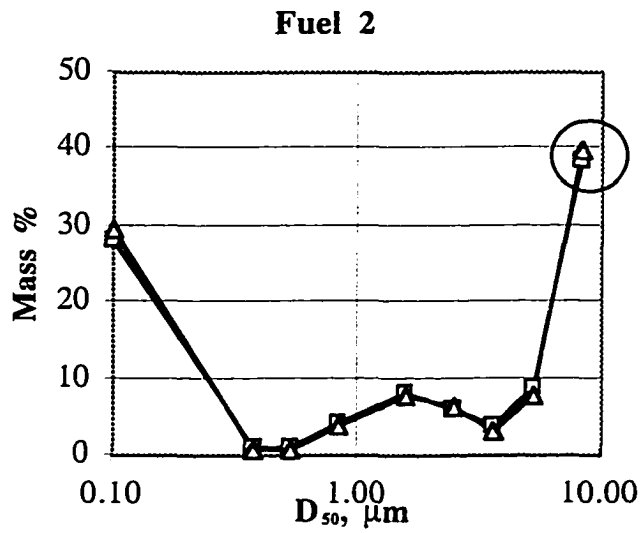
(a) 750x



% Mass

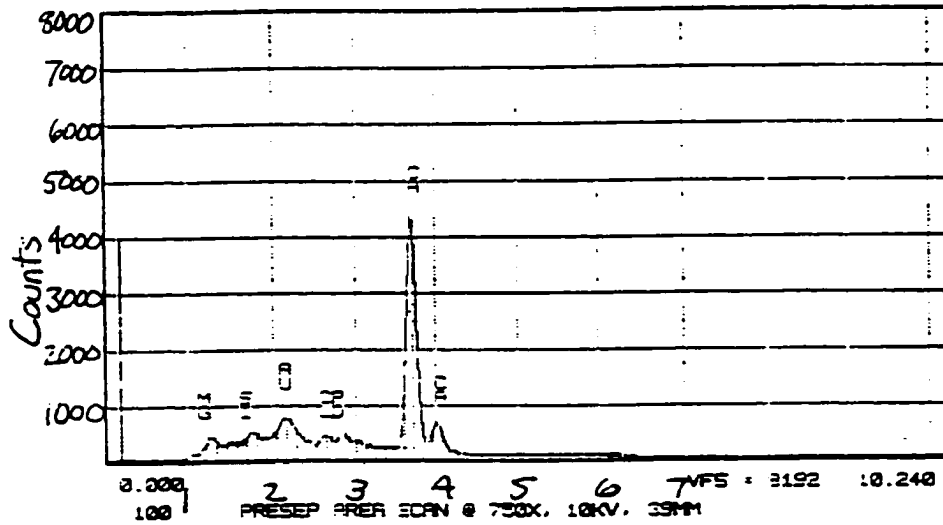
File 37

(b) Large particle with carbon background

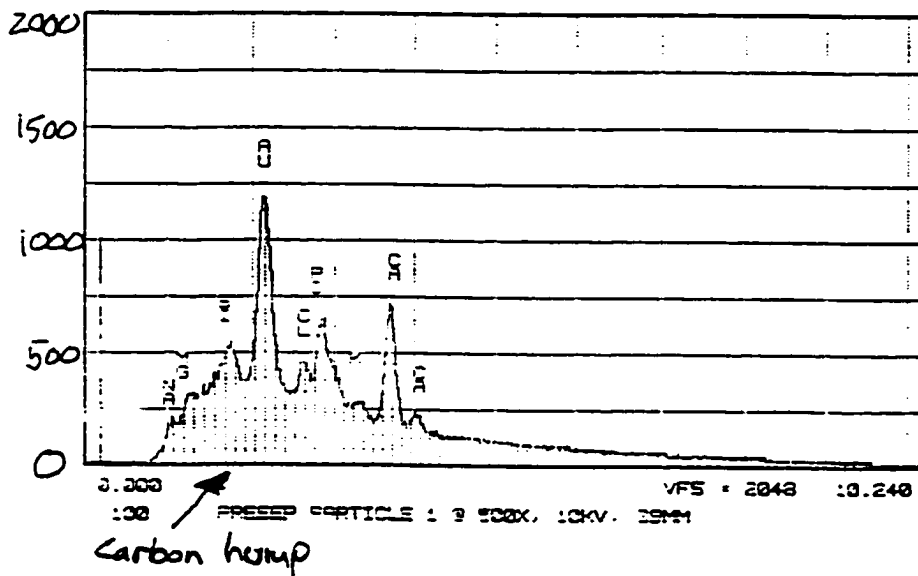


(c)

Figure 6.16: Fuel 2, ash from preseparator



(d) Unprocessed composition signal from EDS for 6.16(a)



(e) Unprocessed composition signal from EDS for 6.16(b)

Figure 6.16 (continued): Fuel 2. Preseparator

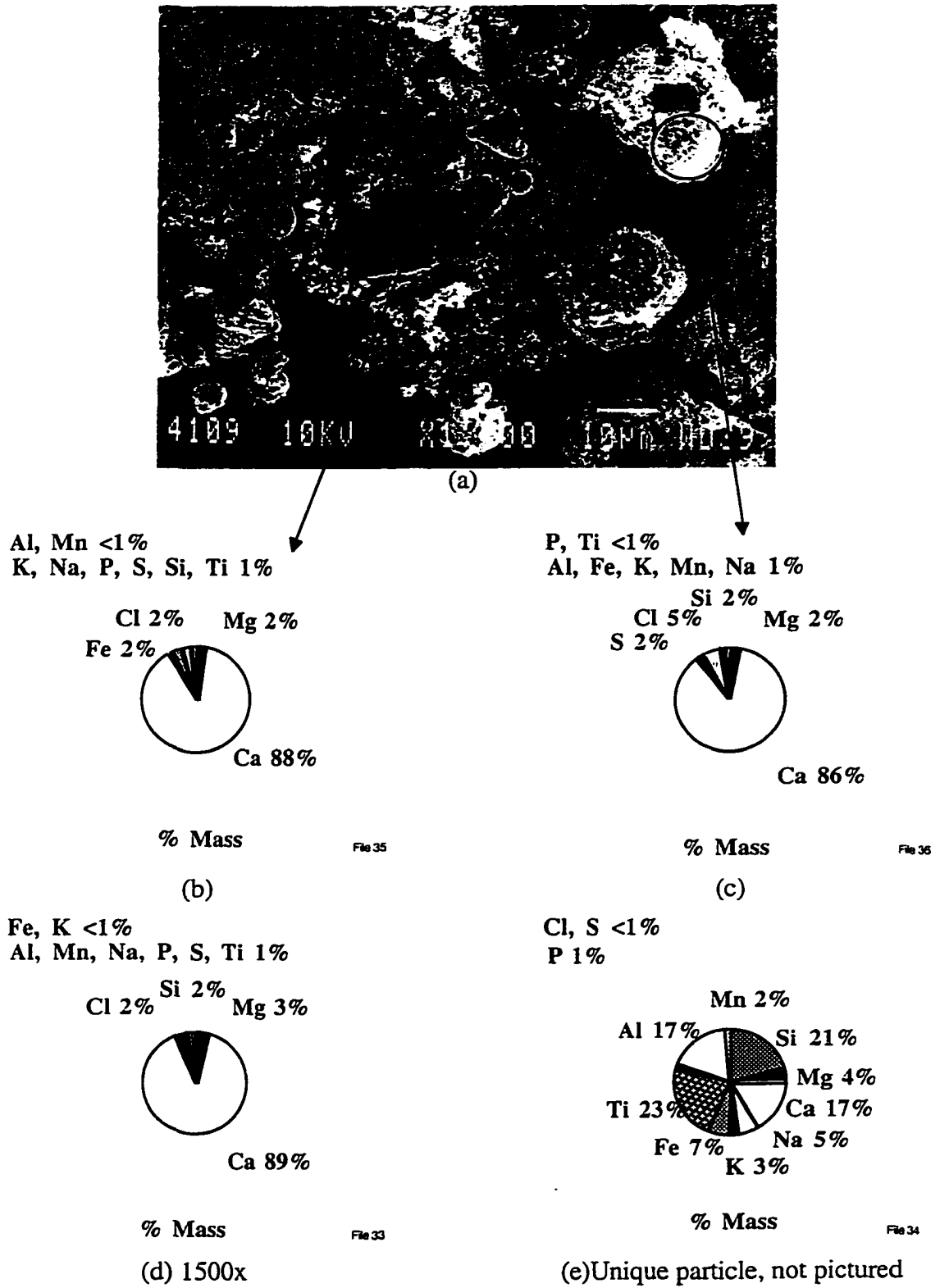
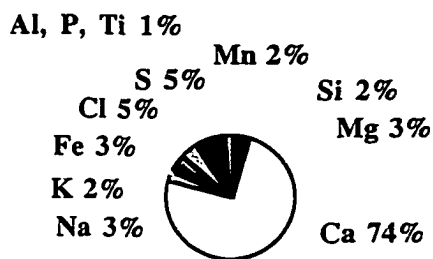
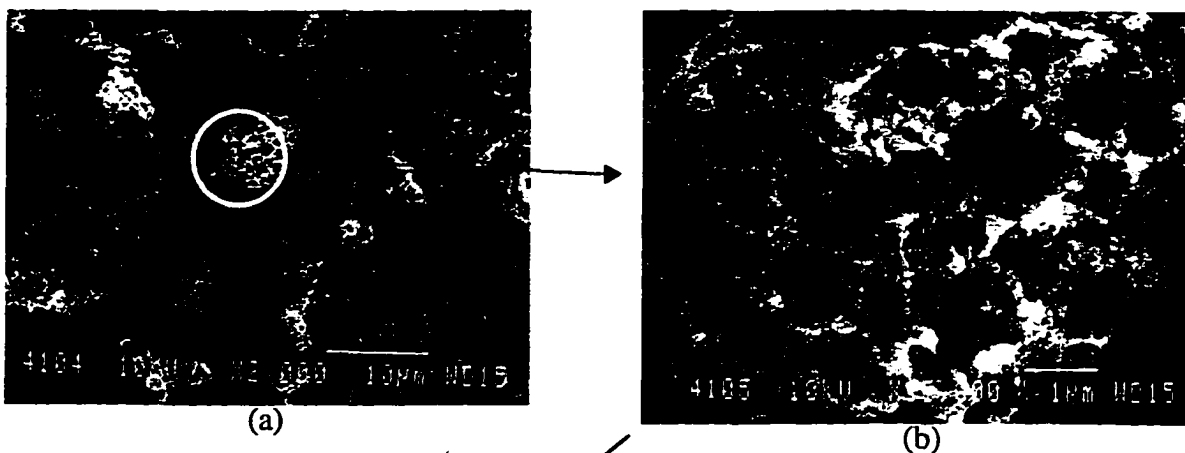


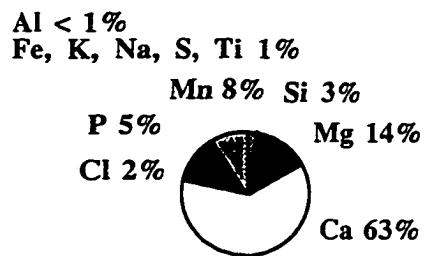
Figure 6.17: Fuel 2, Stage 0



% Mass

File 16

(c) EDS of lacy particle, 15K x



% Mass

File 15

(d) Lacy particle wall, 100K x

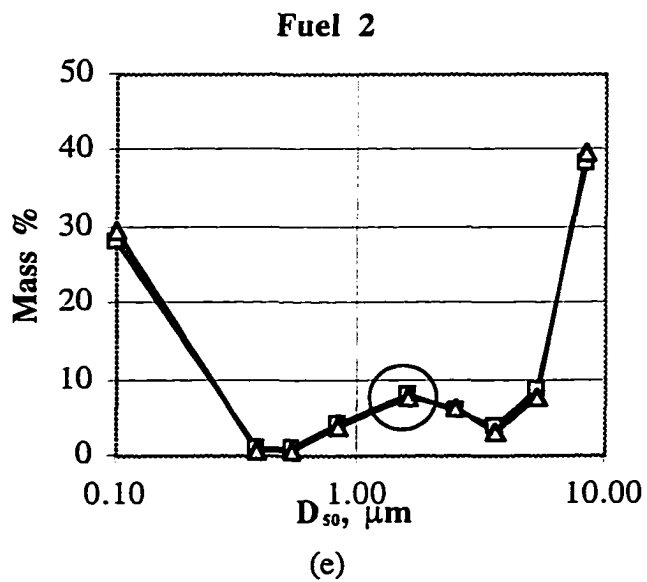


Figure 6.18: Fuel 2, Stage 4

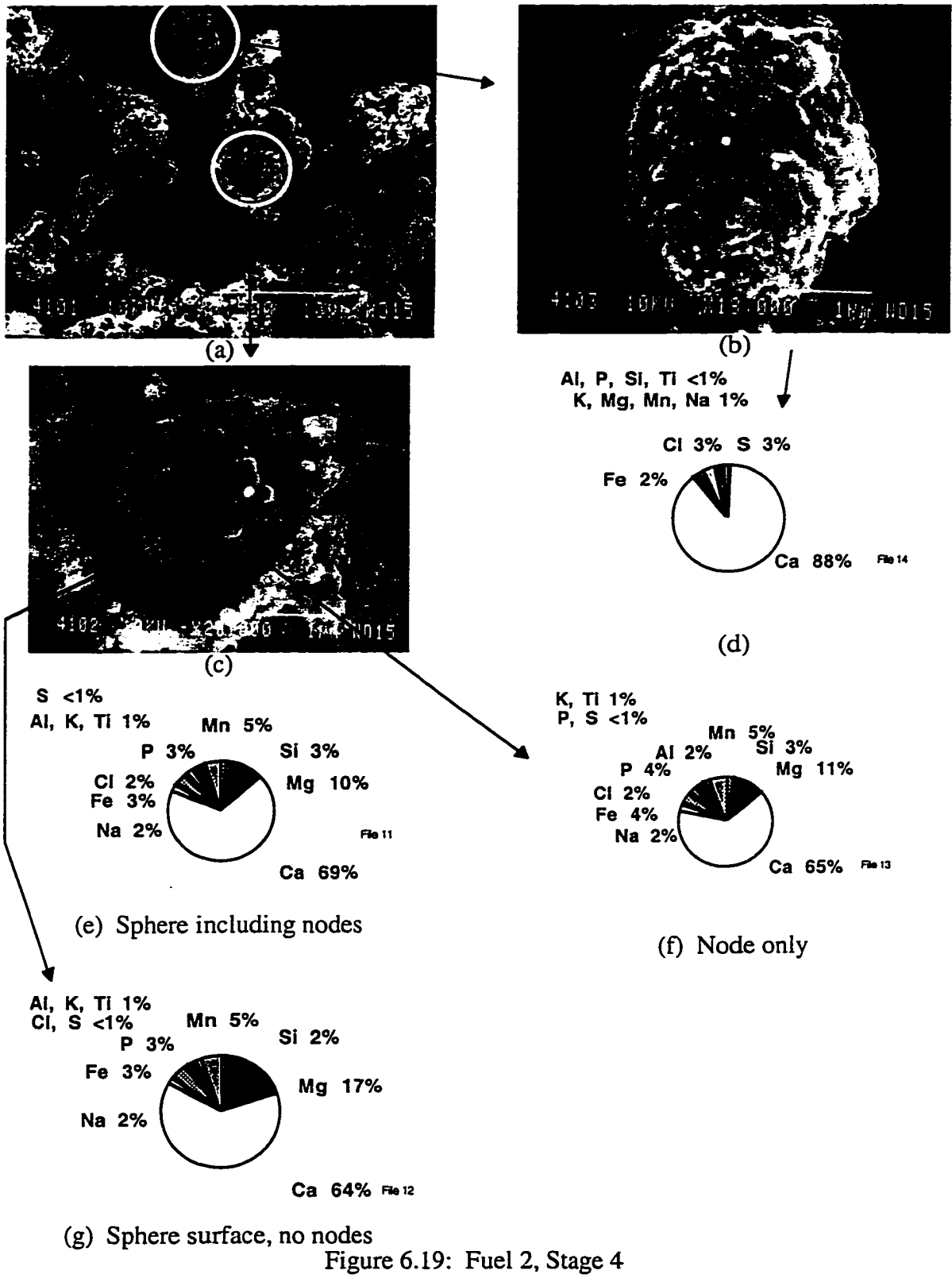
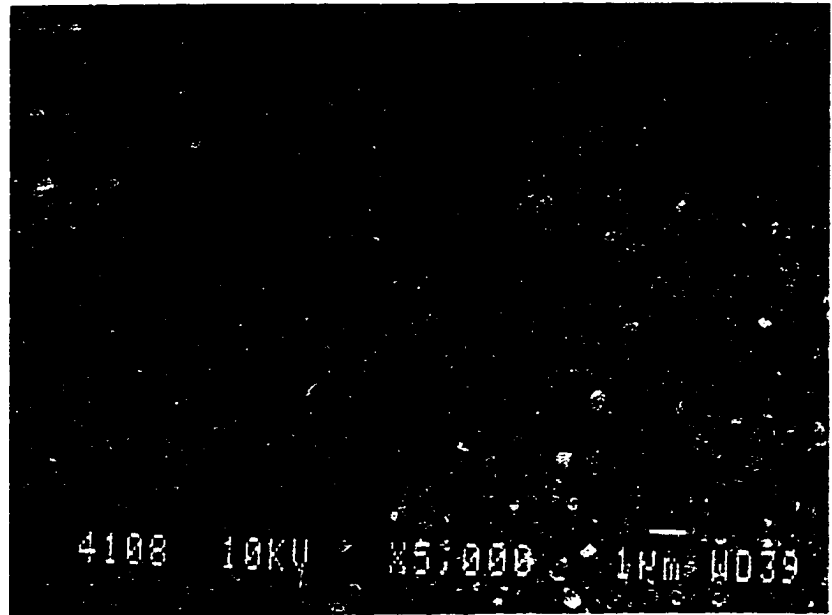
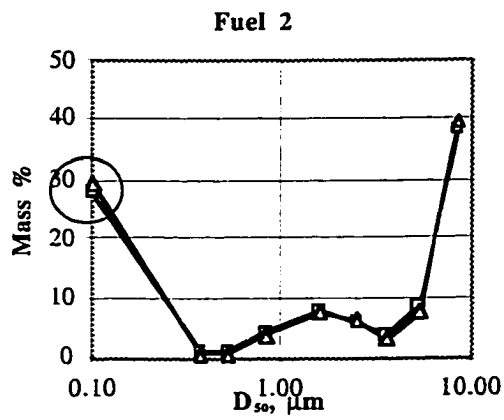


Figure 6.19: Fuel 2, Stage 4

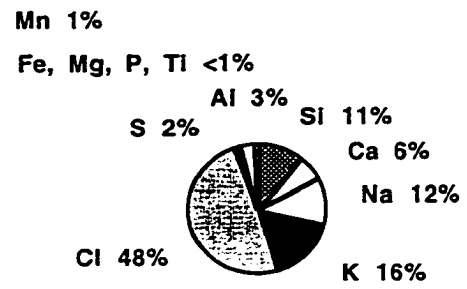
→
Distortion line -
instrument
artifact



(a)



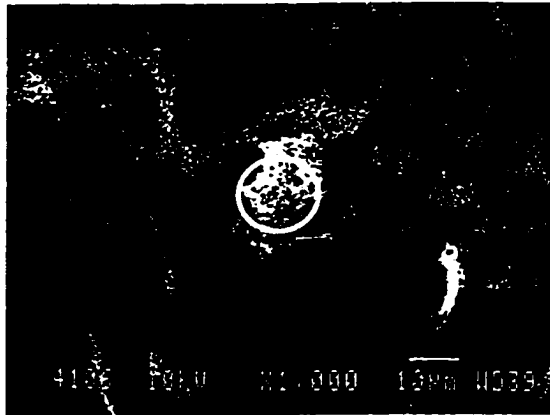
(b)



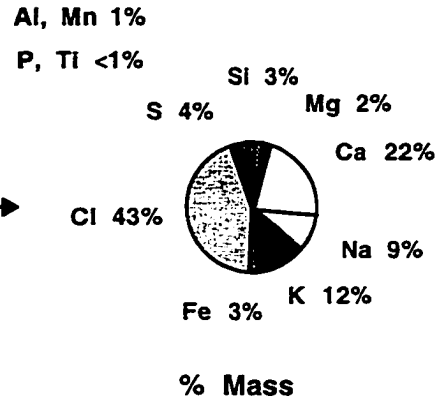
% Mass
(c)

File 17

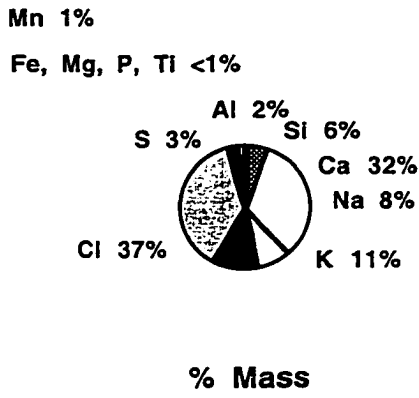
Figure 6.20: Fuel 2, aerosol filter



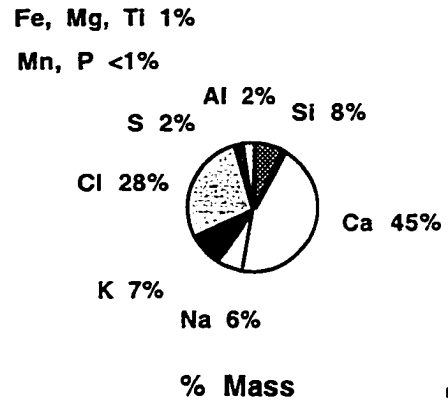
(a)



(b) Large particle on filter



(c) Particle on filter, not pictured



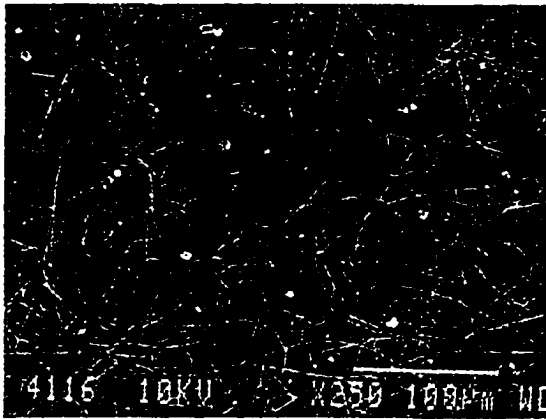
(d) Particle on filter, 10 μm dia, not pictured

Figure 6.21: Fuel 2 filter, oversize particles

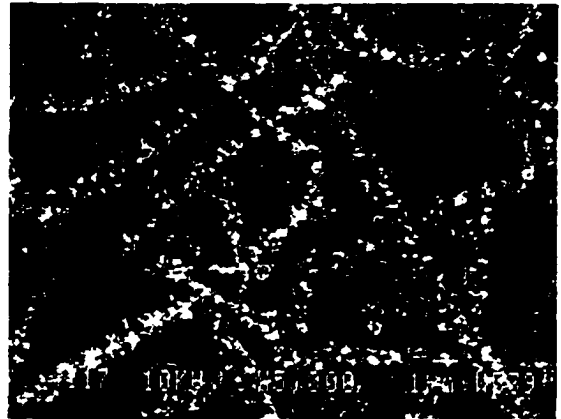
File 20

File 18

File 19



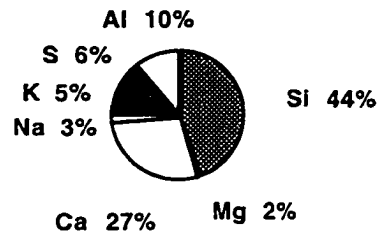
(a)



(b)

Cl, Mn, Ti 1%

Fe, P <1%

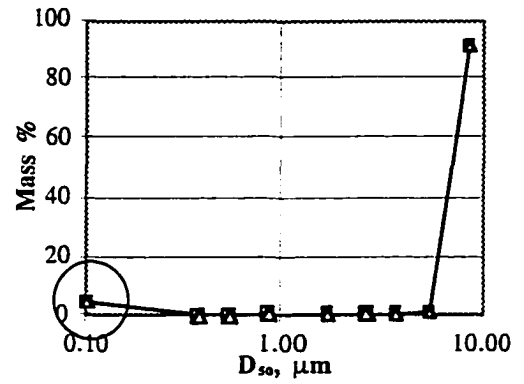


% Mass

File 43

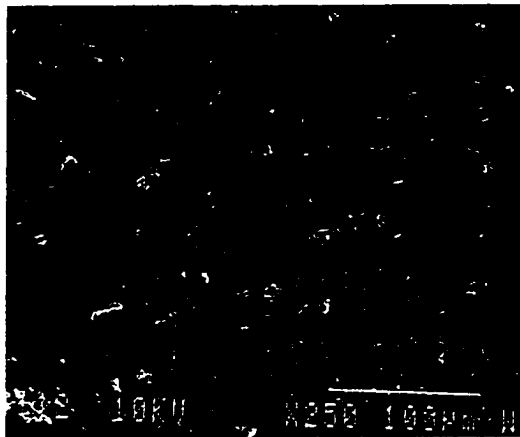
(c)

Fuel 3



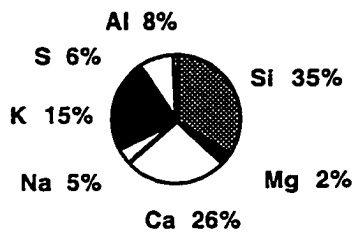
(d)

Figure 6.22: Fuel 3, aerosol filter



(a)

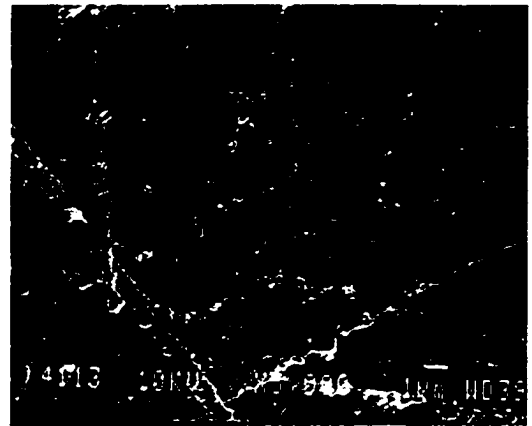
Cl, Mn 1%
Fe, P, Ti <1%



% Mass

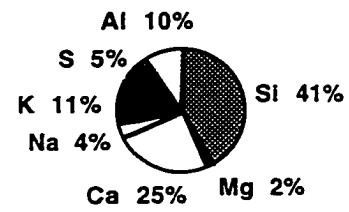
File 39

(c) Filter surface, low power (250 x)



(b)

Fe, Cl, Ti 1%
Mn, P <1%

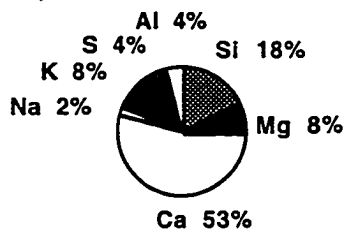


% Mass

File 41

(d) Filter surface, high power (5000x)

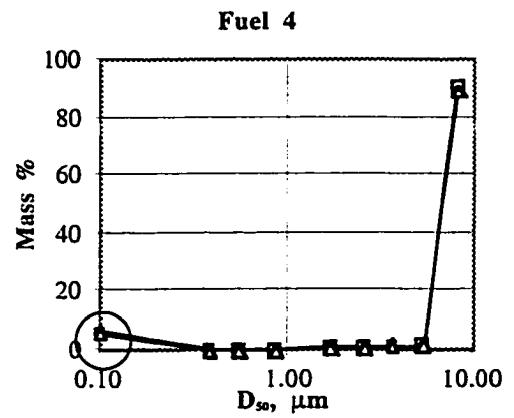
Cl, Fe, P 1%
Fe, Mn, Ti <1%



% Mass

File 40

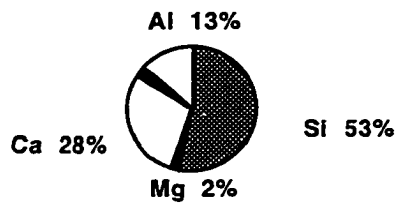
(e) 10 μm particle (not pictured)



(f)

Figure 6.23: Fuel 4, aerosol filter

Cl, K, Mn, P, S <1%
Fe, Na, Ti 1%

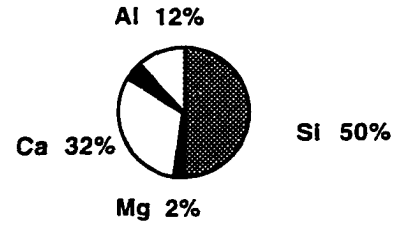


% Mass

File 30

(a) Clean filter, 15000 x

Cl, K, Mn, P <1%
Fe, Na, S, Ti 1%

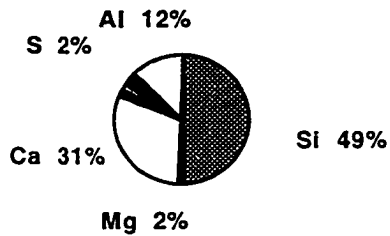


% Mass

File 31

(b) Clean filter, 1000 x

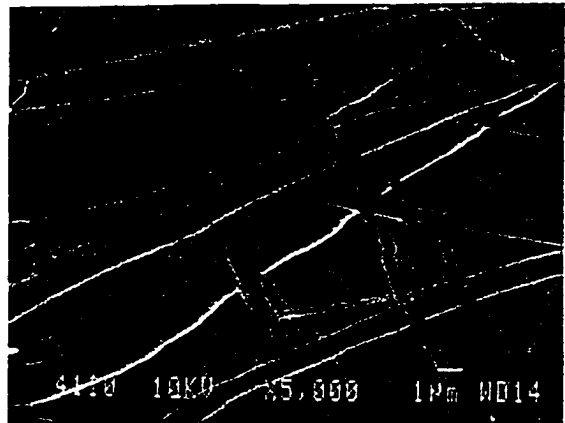
Cl, Mn, P <1%
Fe, Na, K, Ti 1%



% Mass

File 32

(c) Blank filter, 1000 x



(d) Blank filter, 1000 x,
(distortion of image from surface
charging)

Figure 6.24: Clean (unused) and blank (used) aerosol filters

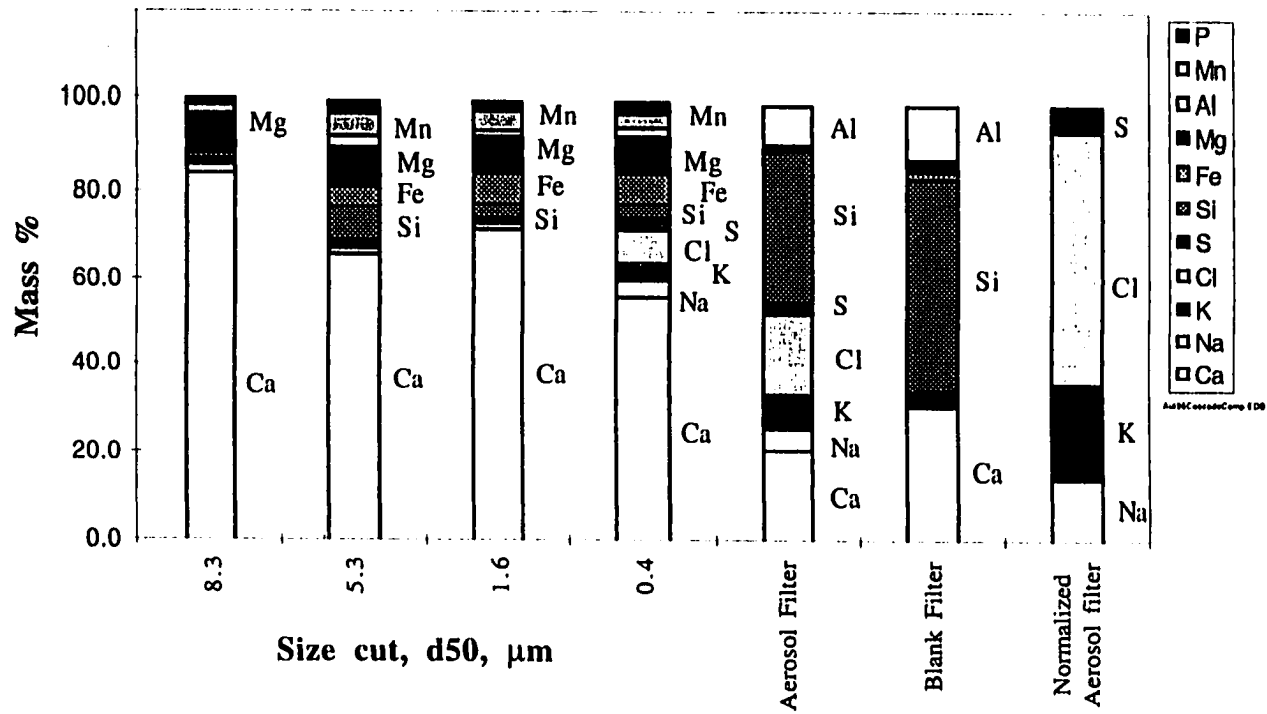


Figure 6.25: Fuel I ash elemental analysis by EDS, composition variation with particulate matter size

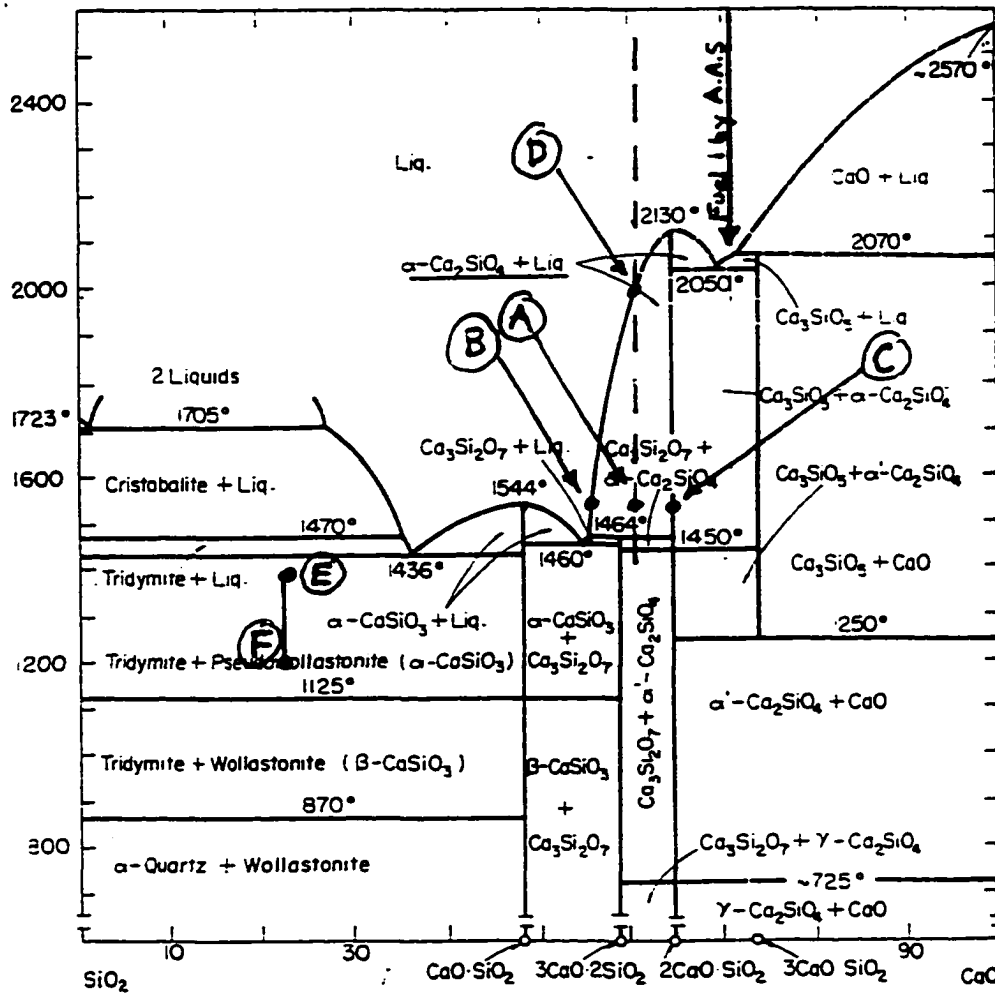


FIG. 237.—System CaO-SiO₂.

Bert Phillips and Arnulf Muan, *J. Am. Ceram. Soc.*, 42 [9] 414 (1959).

Based mainly on data of G. A. Rankin and F. E. Wright, *Am. J. Sci.* [4], 39, 5 (1915) and J. W. Greig, *Am. J. Sci.*, [5], 13, 1-44; [74] 133-54 (1927). Changes with respect to stability relations of tricalcium and dicalcium silicates based on data of D. M. Roy, *J. Am. Ceram. Soc.*, 41 [8] 293-99 (1958) and J. H. Welch and W. Gutt, *J. Am. Ceram. Soc.*, 42 [1] 11-15 (1959).

Figure 6.26: Phase diagram for CaO- SiO₂ system (American Ceramic Society, 1964)

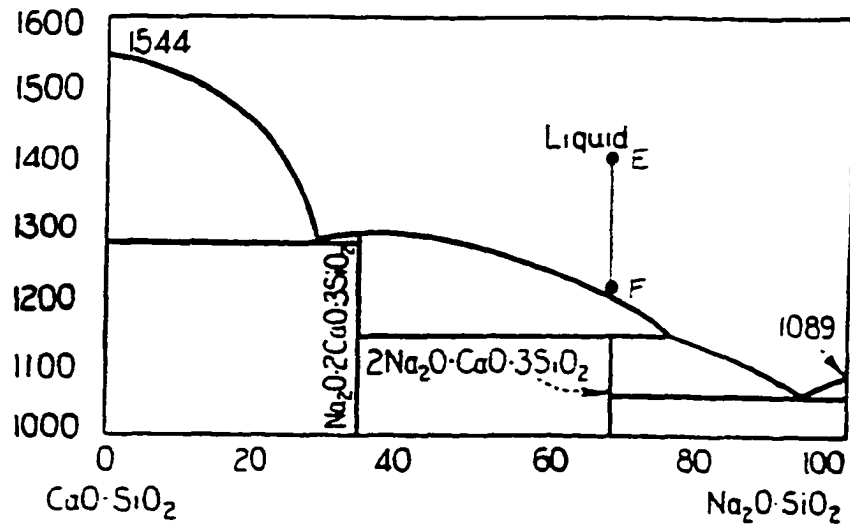


FIG. 484.—System $\text{Na}_2\text{O} \cdot \text{SiO}_2$ — $\text{CaO} \cdot \text{SiO}_2$.

G. W. Morey and N. L. Bowen, *J. Soc. Glass Technol.*, 9, 248 (1925); see also J. Spivak, *J. Geol.*, 52, 29 (1944).

Figure 6.27: Phase diagram for CaOSiO_2 - Na_2OSiO_2 system (American Ceramic Society, 1964)

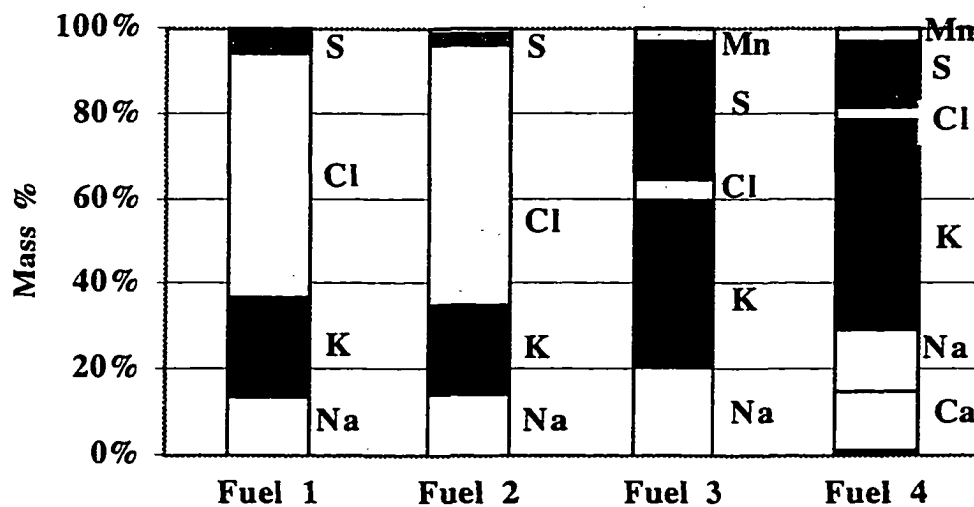


Figure 6.29: Composition of aerosol collected filters, determined by correcting EDS results for background signal from the filter substrate

Table 6.4: Comparison of alkali content to potential anion content in unburned fuels and aerosol ash

Molar Ratio	Fuel 1		Fuel 2		Fuel 3		Fuel 4	
	Unburned	Aerosol Filter Ash	Unburned	Aerosol Filter Ash	Unburned	Aerosol Filter Ash	Unburned	Aerosol Filter Ash
CL:2S, moles	1.7	6.0	3.3	14.2	0.1	0.1	0.2	0.1
Na:K, moles	2.5	1.1	2.5	1.2	1.8	0.9	1.3	0.5
Na+K:Cl+2S	1.1	0.6	1.2	0.6	0.8	0.9	2.5	1.8

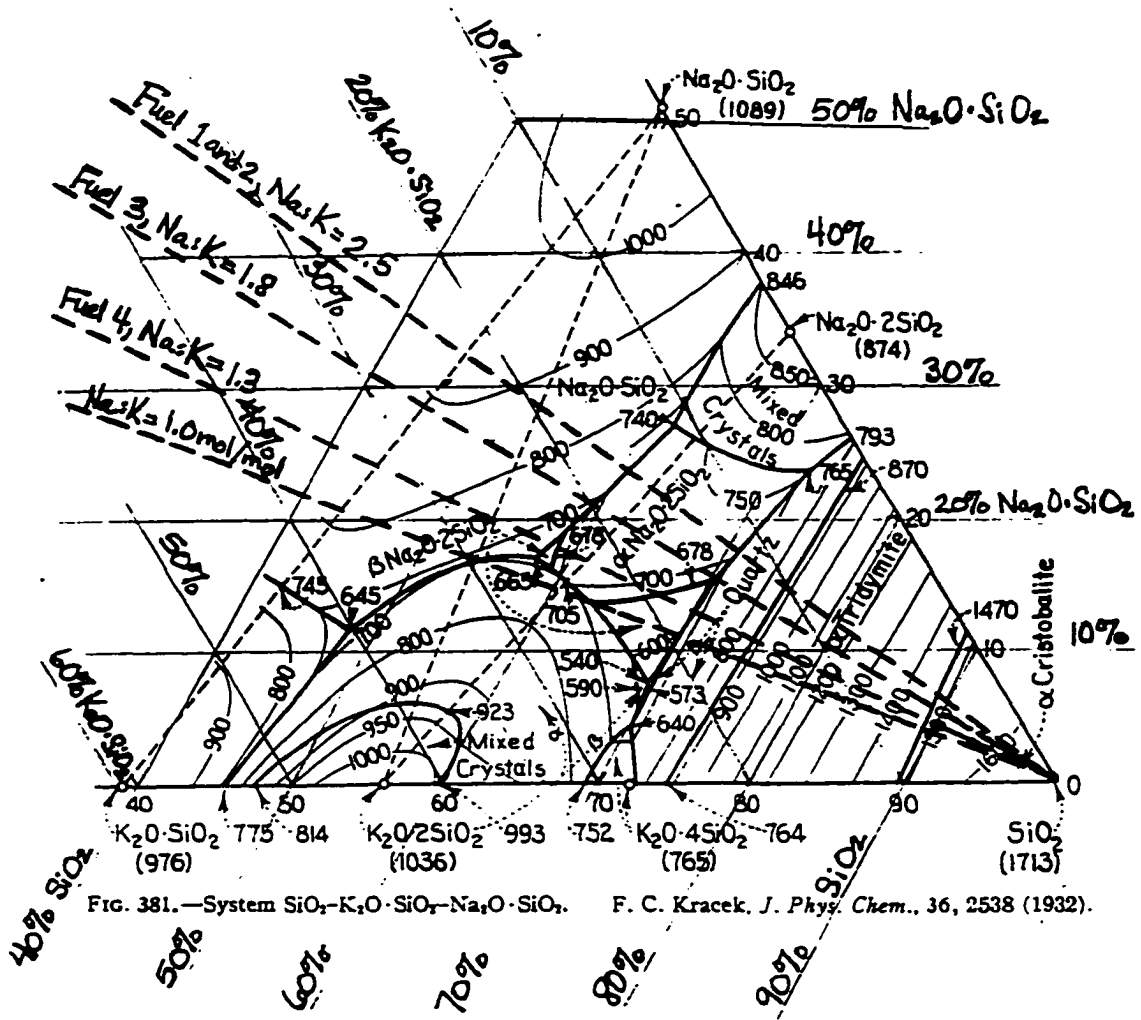


Figure 6.30: Ternary diagram for the high silica end of $\text{K}_2\text{O-Na}_2\text{O-SiO}_2$ system (American Ceramic Society, 1964)

Table 6.5: Milled sawdust/sanderdust test matrix

Test Number	Fuel	Cascade Impactor EAA Temperature	Plastic Tank (200 liter)	Steel Tank (199 liter)	Plexiglass Tank (21 liter) No Tank	Solid fuel flow rate, g/m	Furnace Flowrate, g/m (no solid fuel)	A/F, incl entrainment air, no solid fuel	Upper Aux A/F equiv	Dry O ₂ , no fuel, % vol	Dry O ₂ w/fuel, % vol
101796T		x					544.6	28.8	2.0	9.0	
10149601	Fuel 1	x x	x			4.6	547.1	29.3	2.0	9.3	8.2
10179602	Fuel 1	x x	x			4.6	544.6	28.8	2.0	9.0	8.0
10219601	Fuel 1	x x	x			4.6	543.0	28.7	2.1	9.0	7.9
11079601	Fuel 1	x		x		4.6 2.6 1.7 1.1	544.0	28.7	2.0	9.0	
11079602	Fuel 1	x		x		4.6 2.6 1.7 1.1 0.7	544.0	28.7	2.0	9.0	
11079603	Fuel 1	x		x		4.6 2.6 1.7 1.1 0.7	544.0	28.7	2.0	9.0	
11149601	Fuel 2	x x	x			3.8	548.0	28.9	1.9	9.1	8.3
11149602	Fuel 2	x x	x			3.8	548.7	29.1	2.0	9.2	8.3
11159601	Fuel 2	x		x		3.8 2.2 1.4 0.9 0.6	548.1	29.2	1.9	9.2	
11159602	Fuel 2	x		x		3.8 2.2 1.4 0.9 0.6	548.1	29.2	1.9	9.2	
11159603	Fuel 2	x		x		3.8 2.2 1.4 0.9 0.6	548.1	29.2	1.9	9.2	
11169601	Fuel 3	x x	x			4.4	538.7	28.6	2.0	9.0	7.9
11169602	Fuel 3	x x	x			4.4	545.9	29.1	1.9	9.2	8.1
11179601	Fuel 3	x		x		4.4 2.7 1.7 1.1 0.7	545.9	29.1	2.0	9.2	
11179602	Fuel 3	x		x		4.4 2.7 1.7 1.1 0.7	545.9	29.1	2.0	9.2	
11179603	Fuel 3	x		x		4.4 2.7 1.7 1.1 0.7	545.9	29.1	2.0	9.2	
11129601	Fuel 4	x x	x			3.4	546.5	28.9	2.0	9.1	8.2
10249601	Fuel 4	x x	x			3.4	544.6	28.8	2.0	9.0	8.2
11139601	Fuel 4	x		x		3.4 2.0 1.3 0.8 0.5	548.0	28.9	2.0	9.1	
11139602	Fuel 4	x		x		3.4 2.0 1.3 0.8 0.5	548.0	28.9	2.0	9.1	
11139603	Fuel 4	x		x		3.4 2.0 1.3	548.0	28.9	2.0	9.1	
Average:							545.9	28.9	2.0	9.1	
112596T		x					304.9	31.6	1.3	10.2	
11269601	Fuel 1	x x	x			4.6	307.1	31.2	1.3	10.0	8.2
11279601	Fuel 1	x x	x			4.6	305.3	30.9	1.3	9.9	8.0
11279602	Fuel 4	x x	x			3.4	305.9	31.0	1.3	10.0	8.5
11279603	Fuel 4	x x	x			3.4	302.8	30.7	1.3	9.9	8.3
Average:							305.3	31.0	1.3	9.9	
112096T		x					305.3	32.4	2.1	10.4	
11219601	Fuel 1	x x	x			4.6	303.1	32.2	2.0	10.4	8.5
11219602	Fuel 1	x x	x			4.6	302.9	31.9	2.0	10.3	8.4
11219603	Fuel 1	x		x		4.6 2.6 1.7 1.1 0.7	302.3	32.0	2.0	10.3	
11219604	Fuel 1	x		x		4.6 2.6 1.7 1.1 0.7	302.3	32.0	2.0	10.3	
11219605	Fuel 1	x		x		4.6 2.6 1.7 1.1 0.7	302.3	32.0	2.0	10.3	
11239602	Fuel 2	x x	x			3.8	303.7	32.6	1.9	10.5	9.0
11239603	Fuel 2	x x	x			3.8	303.3	32.7	2.0	10.6	9.0
11229601	Fuel 3	x x	x			4.4	302.8	32.1	2.0	10.4	8.5
11229602	Fuel 3	x x	x			4.4	307.7	32.6	2.0	10.5	8.7
11229603	Fuel 4	x x	x			3.4	302.9	31.9	2.0	10.3	8.8
11239601	Fuel 4	x x	x			3.4	303.5	32.5	2.0	10.5	9.0
11219606	Blank	x x					302.8	32.0	2.0	10.3	
Average:							303.5	32.2	2.0	10.4	

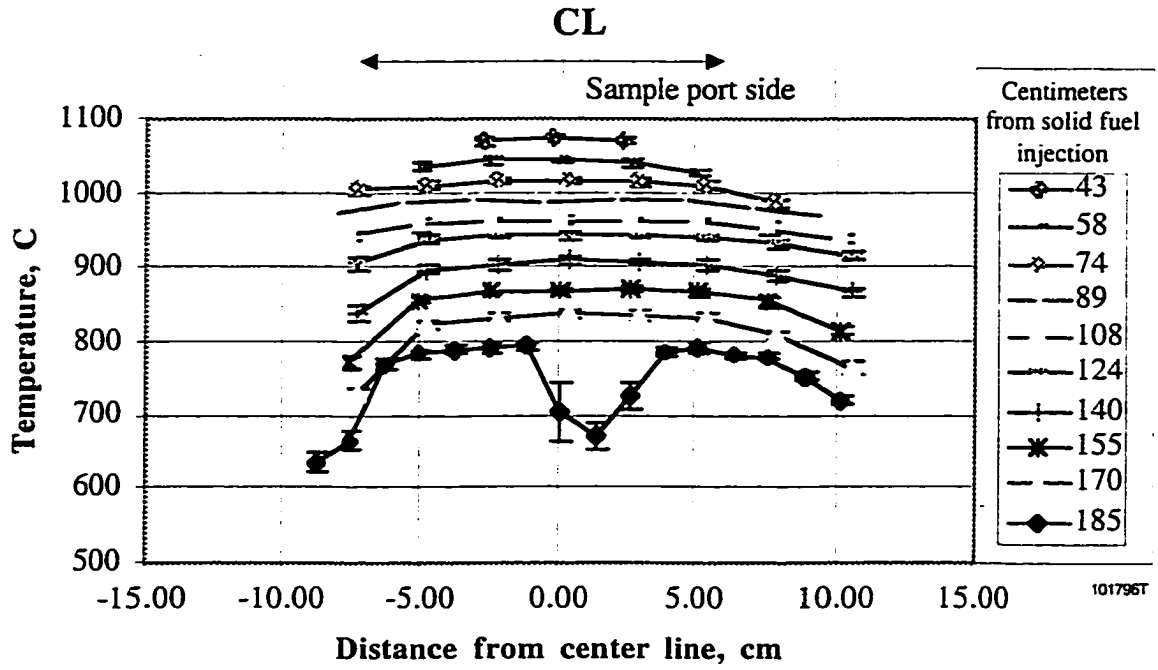


Figure 6.31: Transverse temperature profile by High Velocity Thermocouple at maximum temperature/flow rate settings, test number 101796T

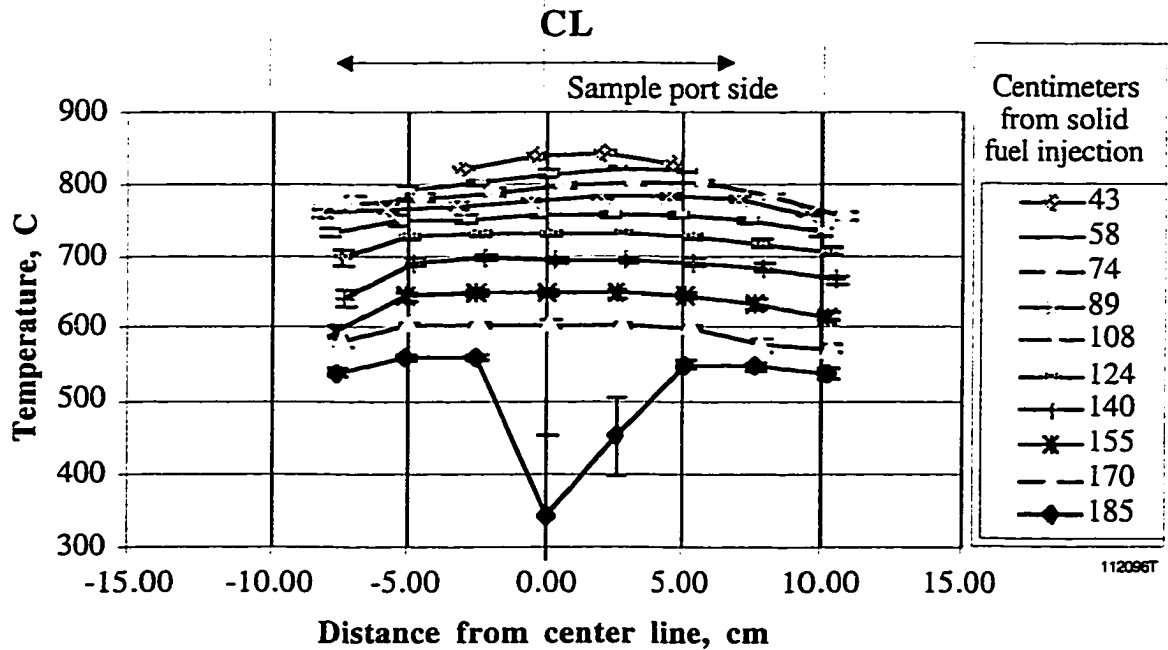


Figure 6.32: Transverse temperature profile by High Velocity Thermocouple at moderate temperature/flow rate settings, test number 112596T

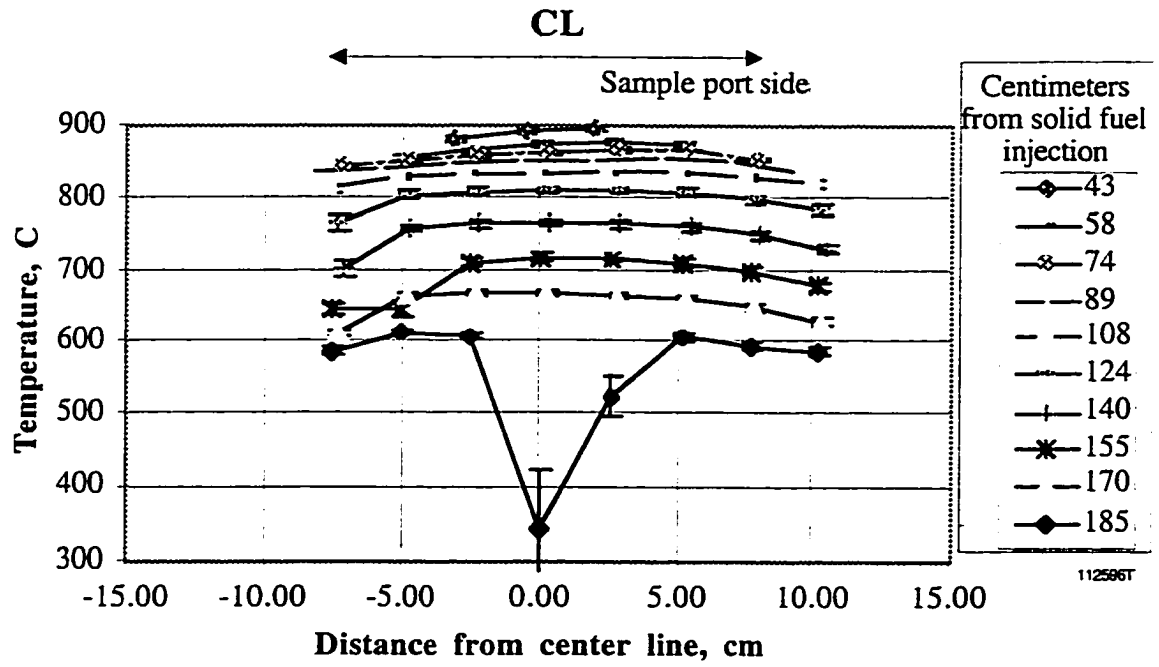
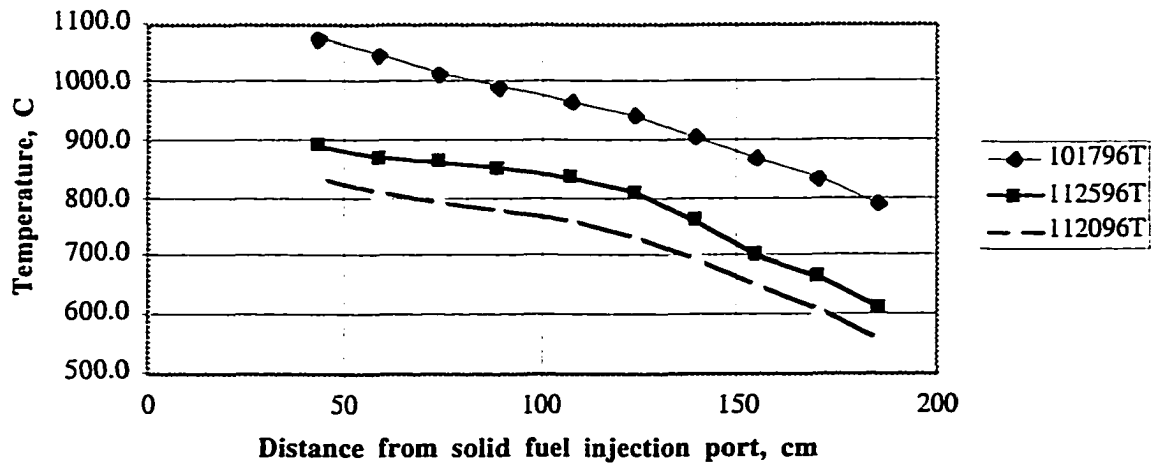


Figure 6.33: Transverse temperature profile by High Velocity Thermocouple at minimum temperature/flow rate settings, test number 112096T



	101796T	101796T	101796T	112596T	112596T	112096T	112096T
Port	cm from solid fuel injection	Average temperature, degC	Average dev. +/- K	Average temperature, degC	Average dev. +/- K	Average temperature, degC	Average dev. +/- K
k*	185	791.0	5.6	611.	4.6	559.	4.1
j	170	832.2	5.6	667.	3.7	609.	3.8
i	155	867.8	3.9	701.	5.8	650.	4.0
h	140	905.0	5.0	764.	4.6	696.	3.9
g	124	941.7	4.4	808.	4.7	733.	3.2
f	108	964.4	4.4	835.	3.3	758.	3.5
e	89	989.9	4.9	853.	3.1	780.	3.5
d	74	1013.3	4.4	862.	2.6	793.	4.4
c	58	1045.2	4.6	873.	3.3	815.	3.5
b	43	1073.0	3.7	889.	3.3	838.	3.3
Average temperature taken from -5 cm to +5 cm. relative to CL							
*Port K measurements from 0 to +2.5 cm disgarded							

Figure 6.34: Temperature profile as a function of distance from pulverized fuel injection for three different furnace settings

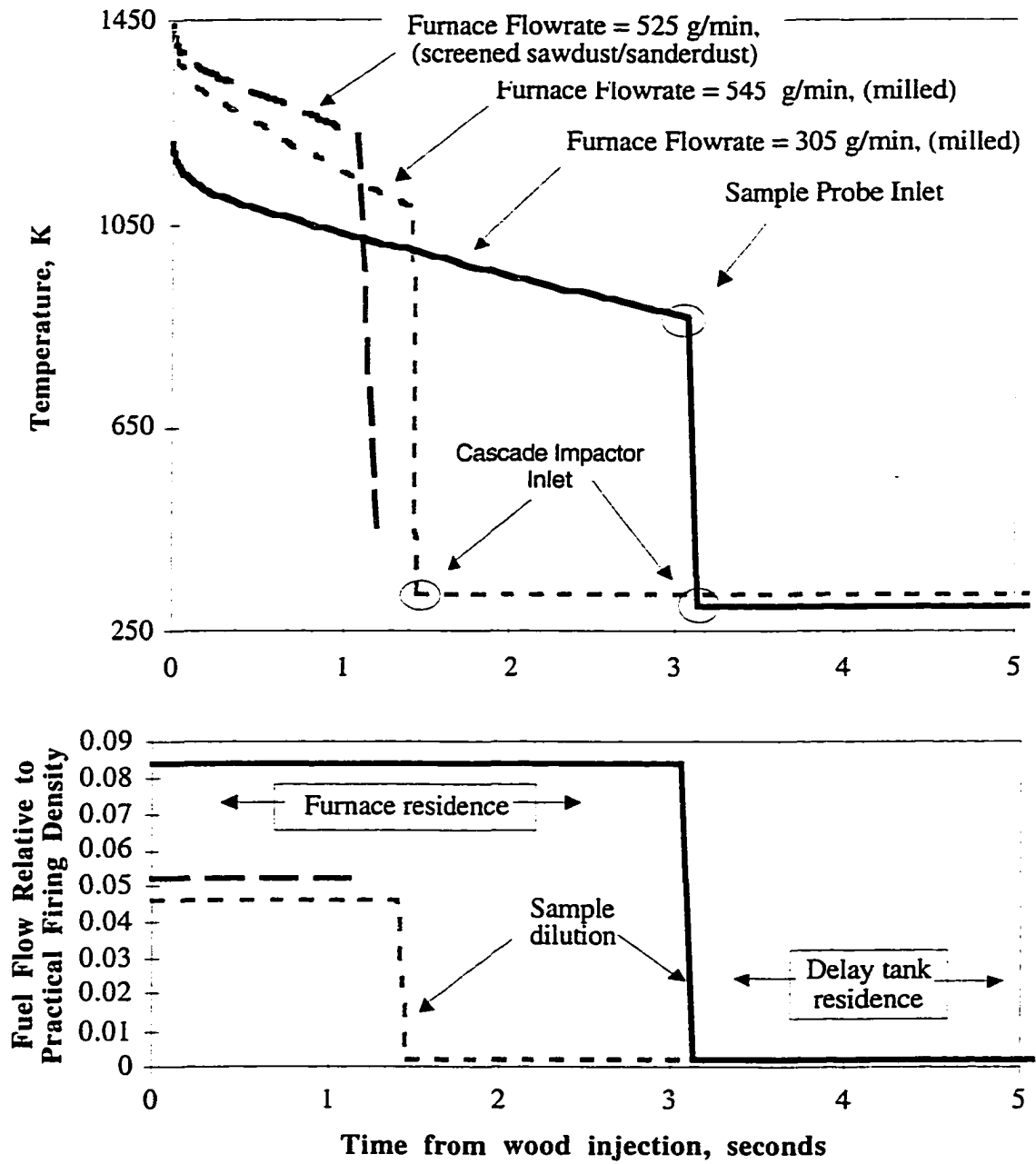


Figure 6.35: Temperature and dilution profiles for sawdust/sanderdust experiments

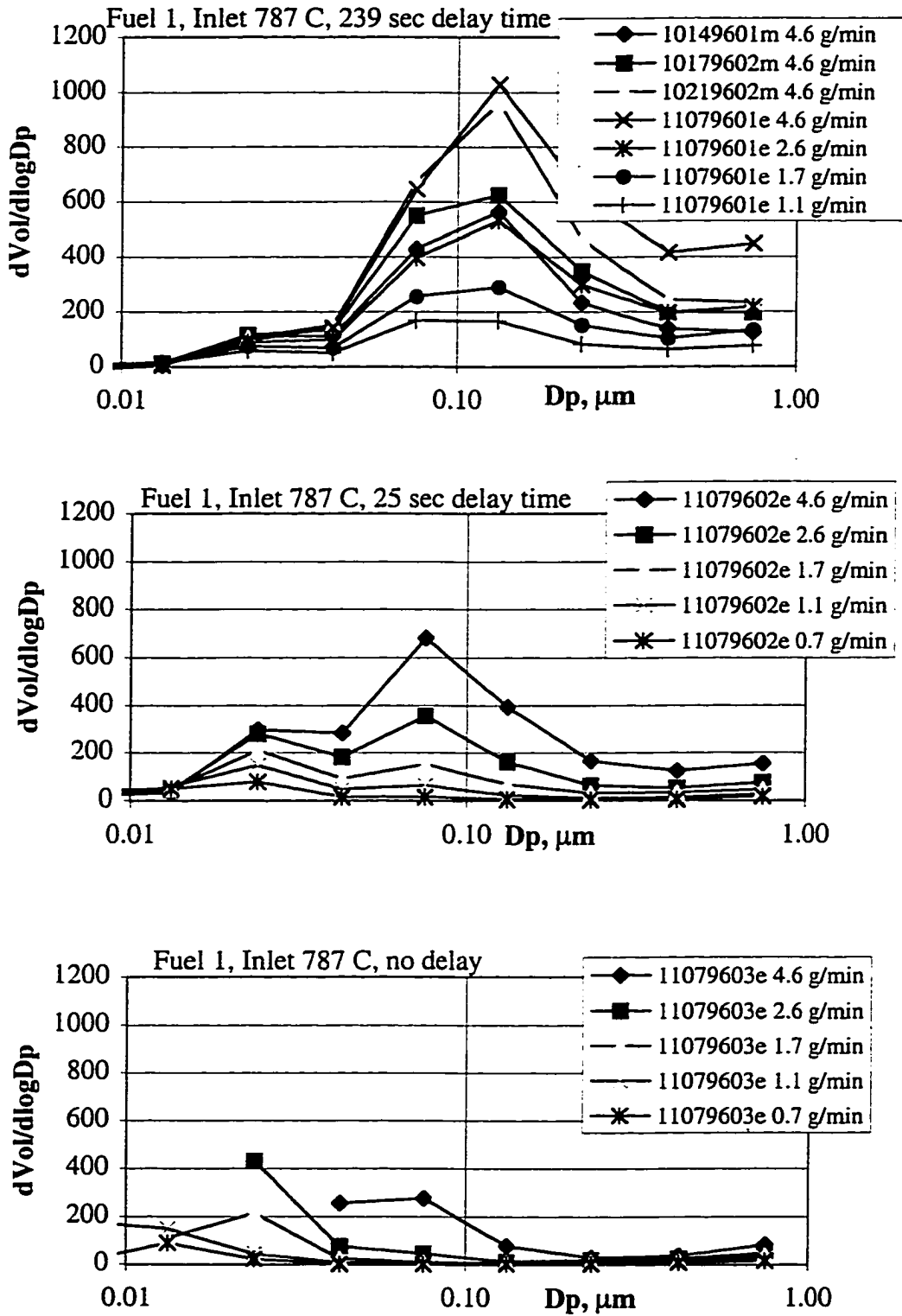


Figure 6.36: Fuel 1 EAA experiments at highest furnace temperature

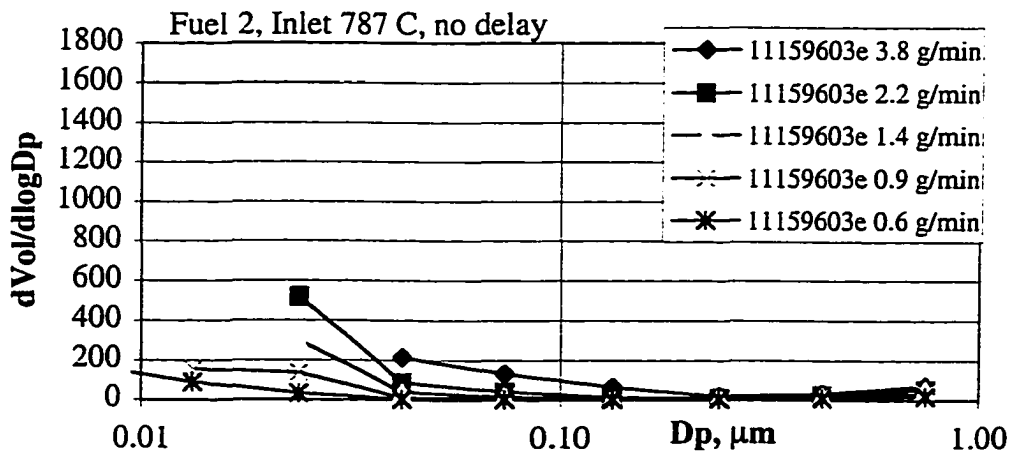
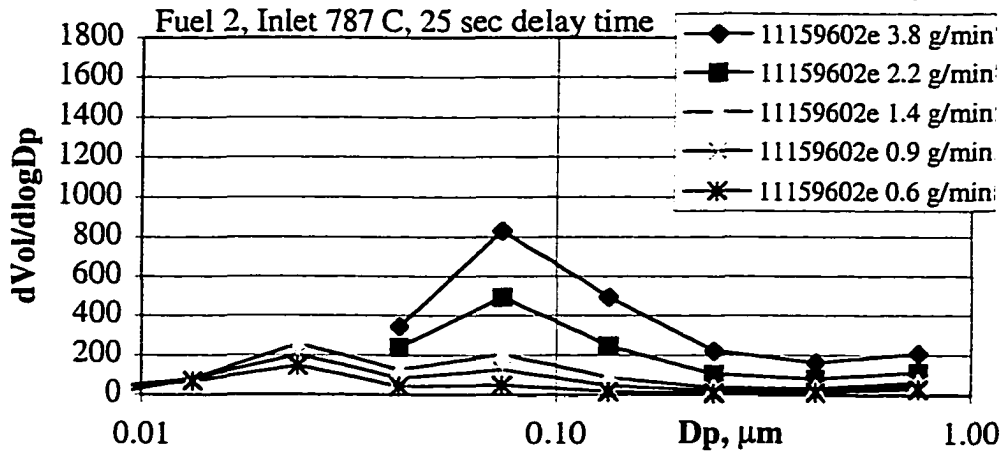
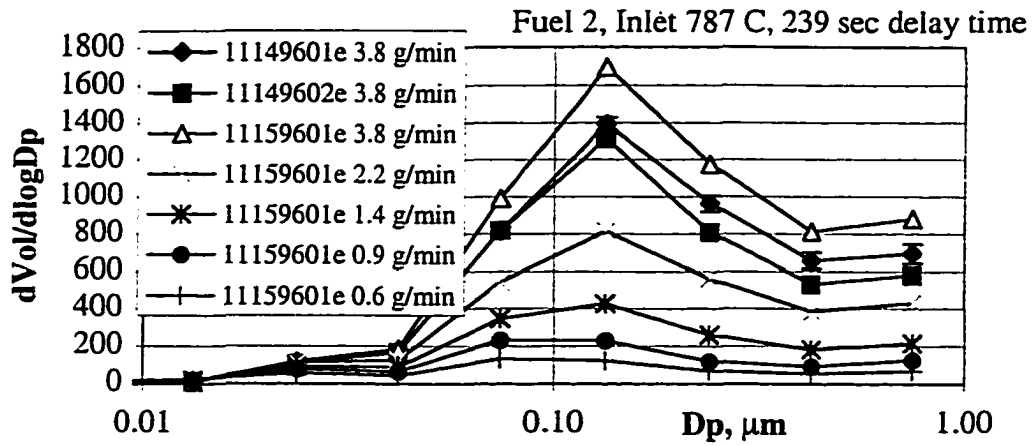


Figure 6.37: Fuel 2 EAA experiments at highest furnace temperature

EAA Summary

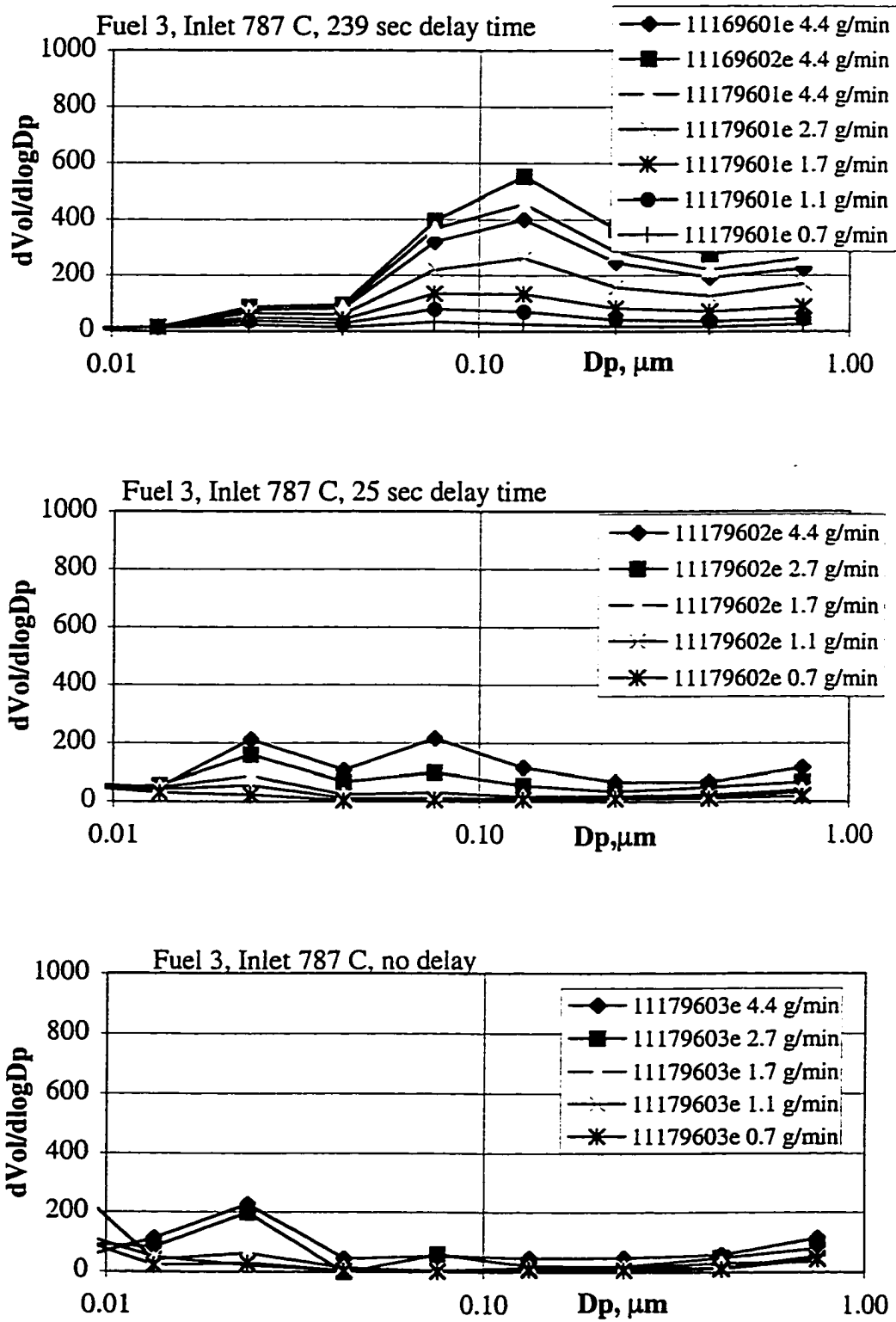


Figure 6.38: Fuel 3 EAA experiments at highest furnace temperature

EAA Summary

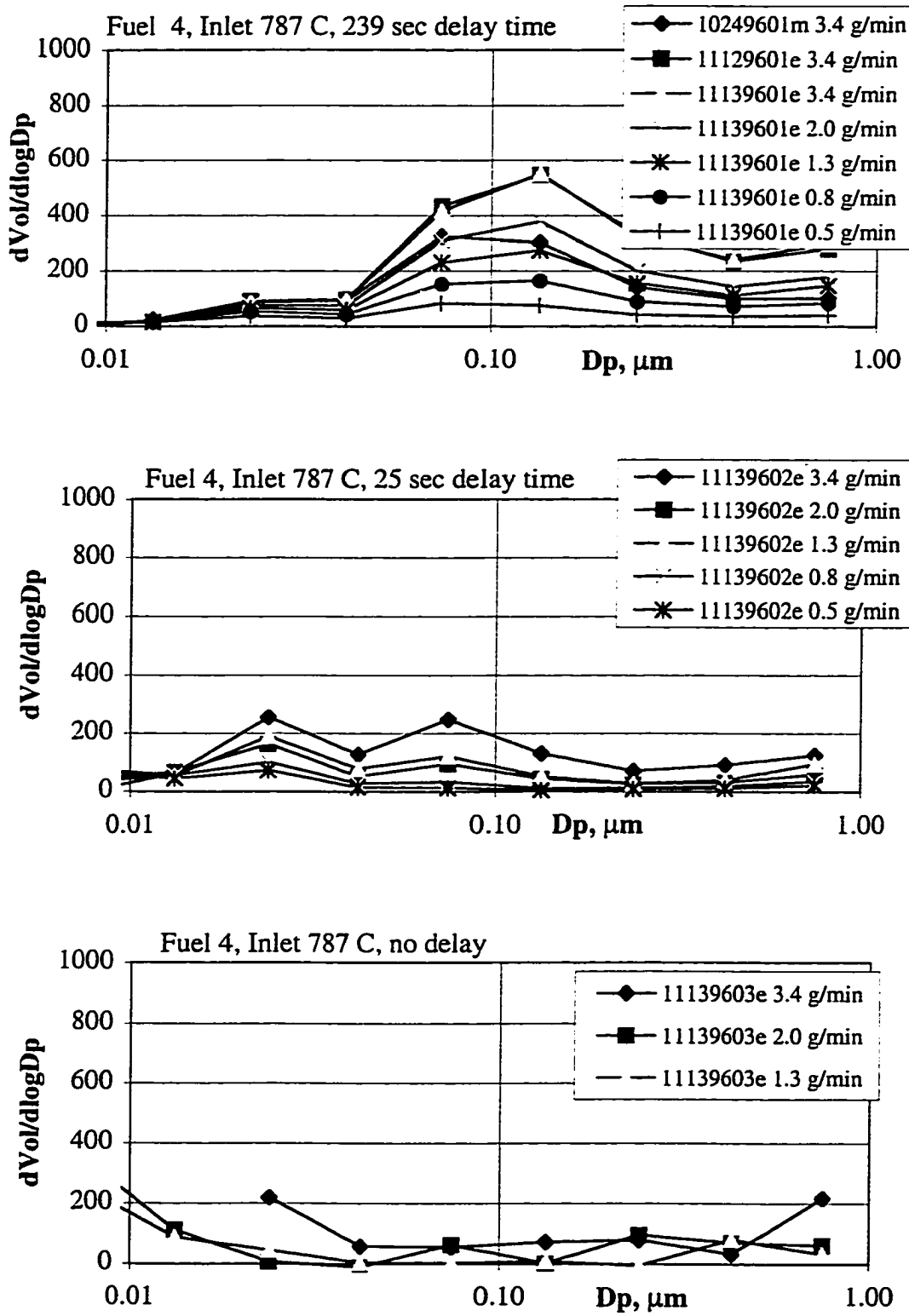


Figure 6.39: Fuel 4 EAA experiments at highest furnace temperature

EAA Summary

1

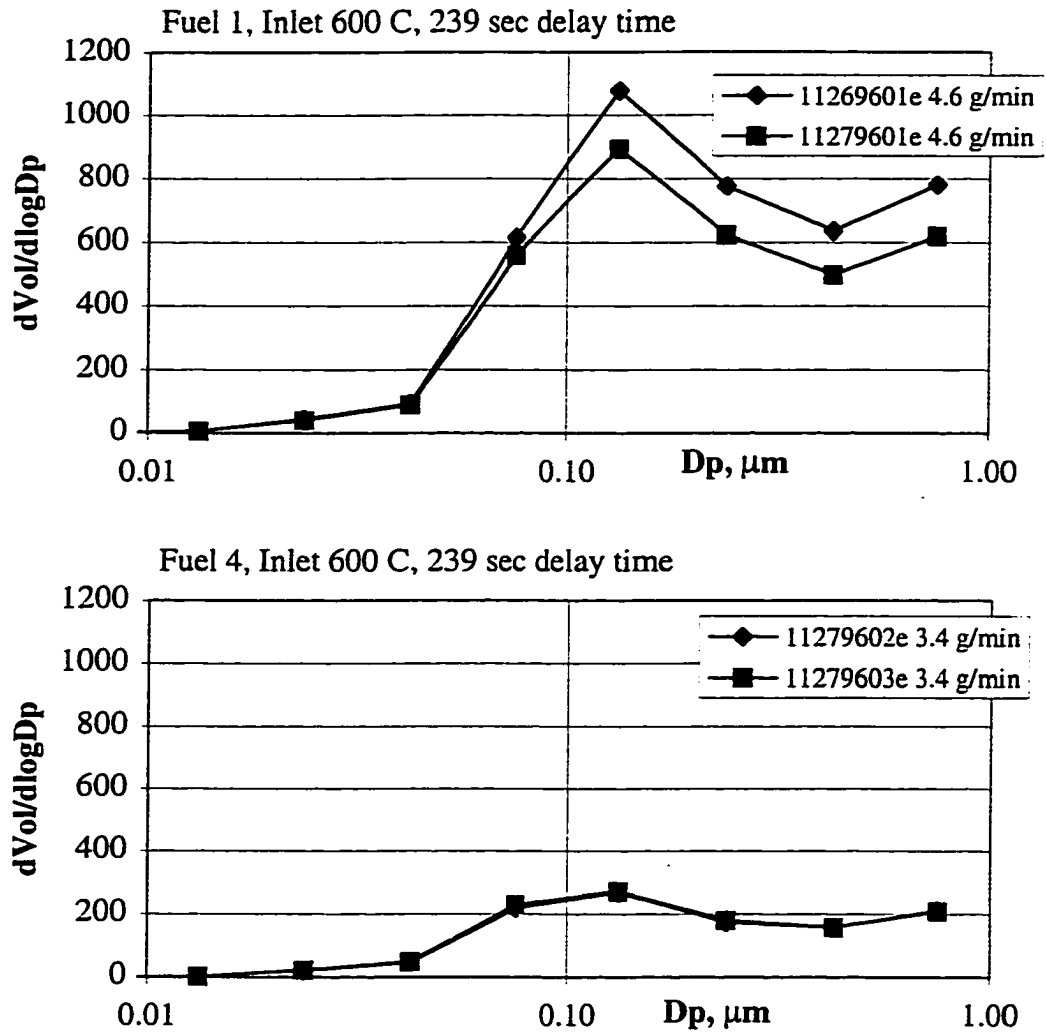


Figure 6.40: Fuel 1 and 4 EAA experiments at moderate temperature

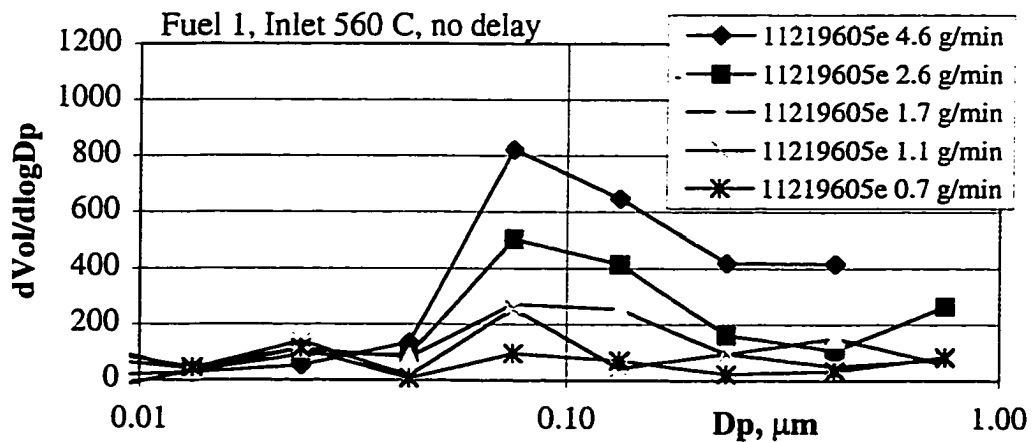
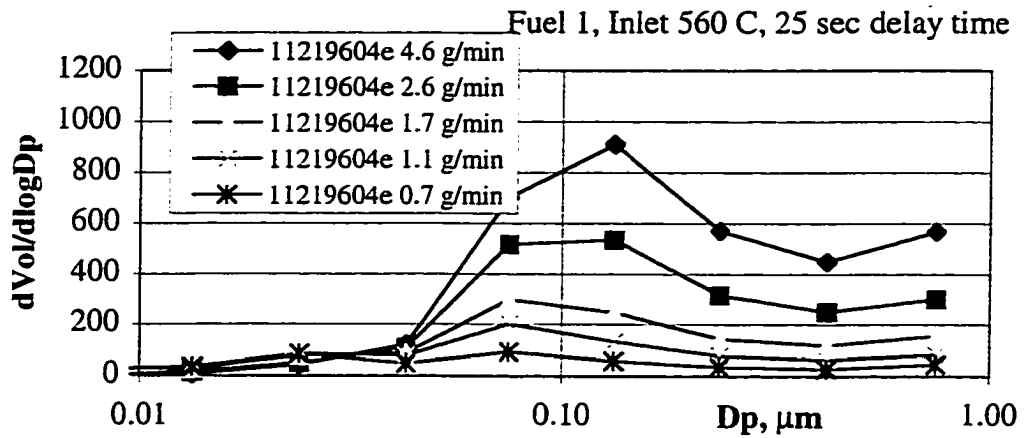
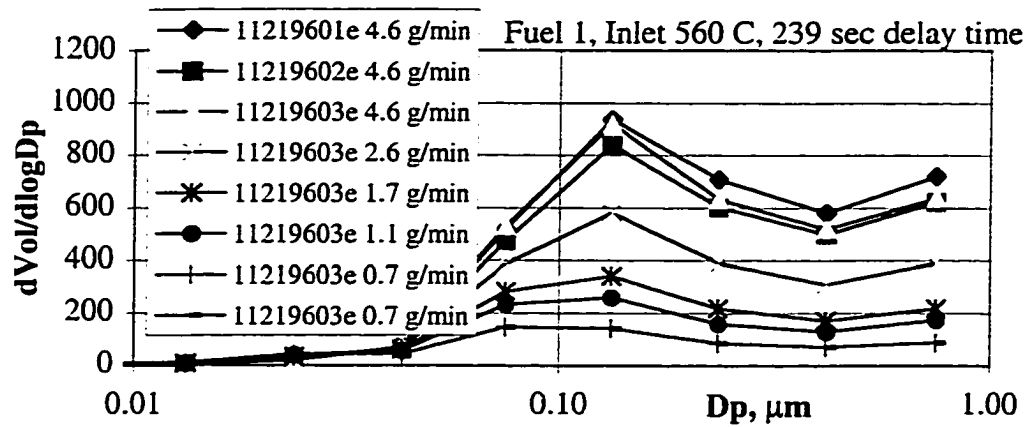


Figure 6.41: Fuel 1 EAA experiments at low furnace temperature

EAA Summary

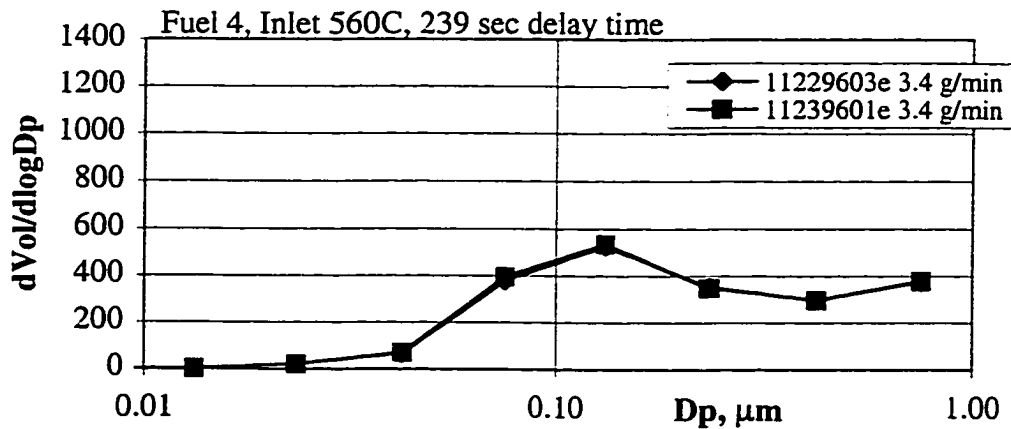
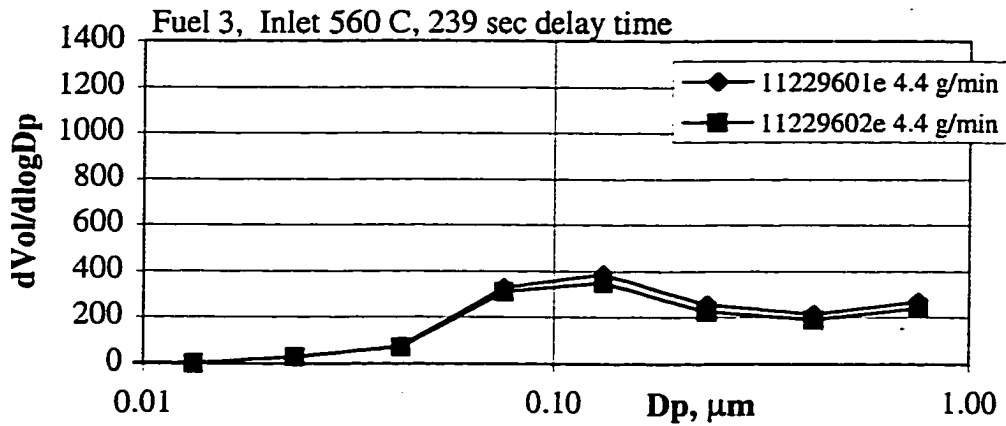
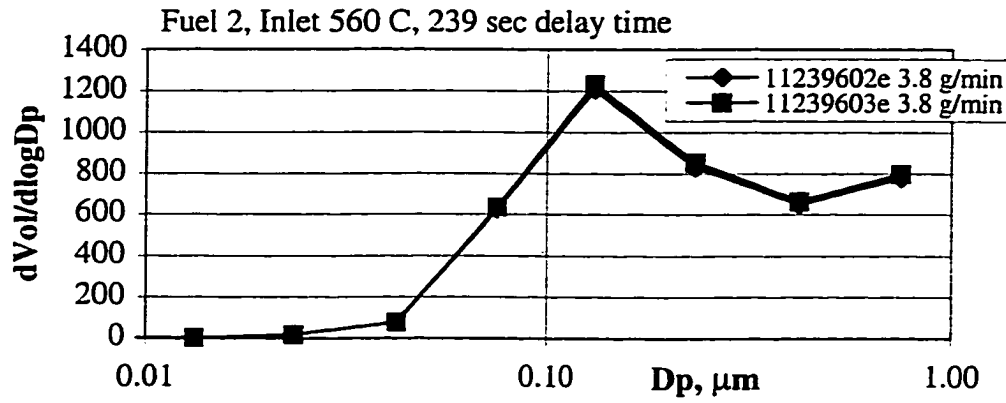


Figure 6.42: Fuels 2,3 and 4 EAA experiments at low furnace temperature

EAA Summary

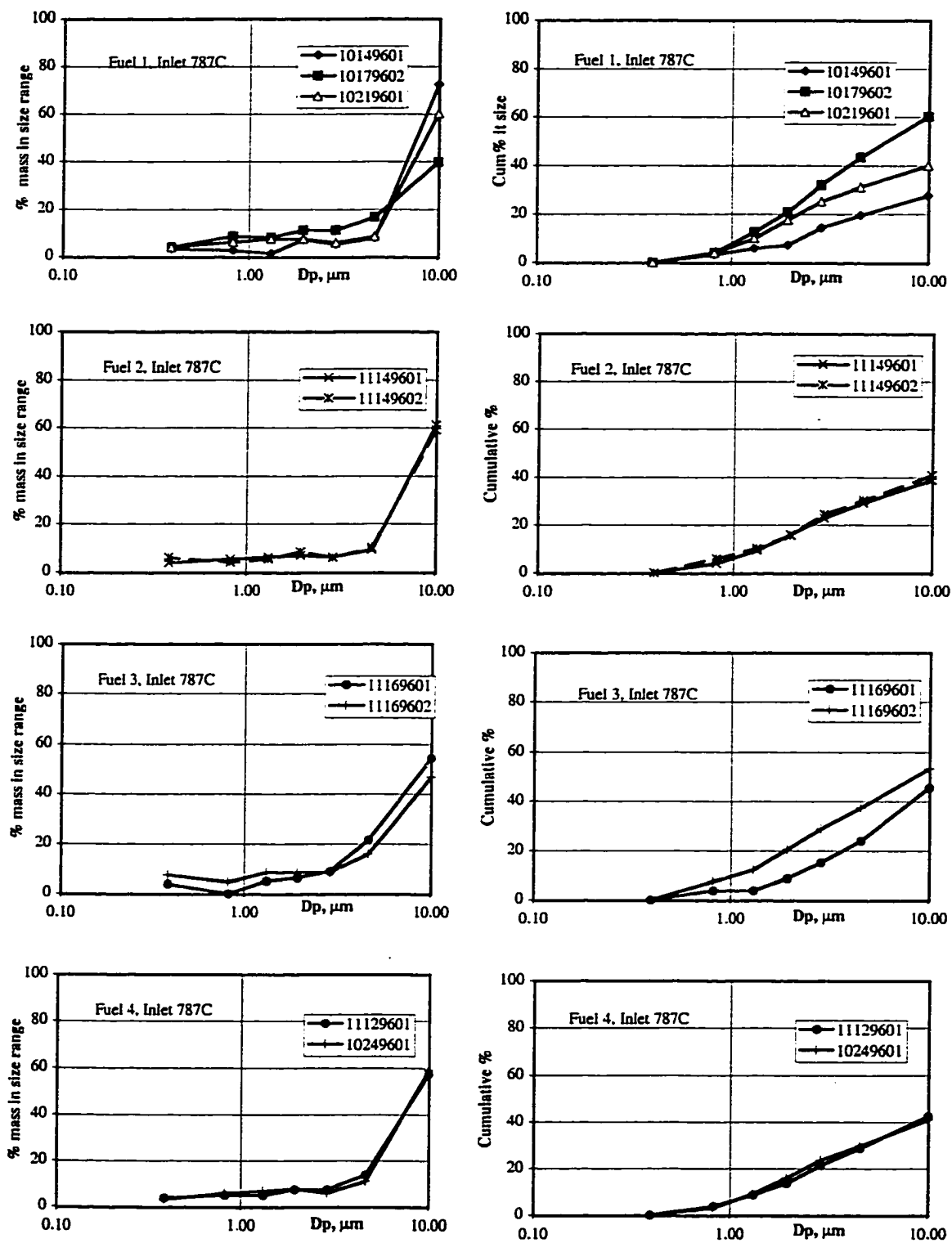


Figure 6.43: Fuels 1, 2, 3 and 4 cascade impactor data at highest furnace temperature

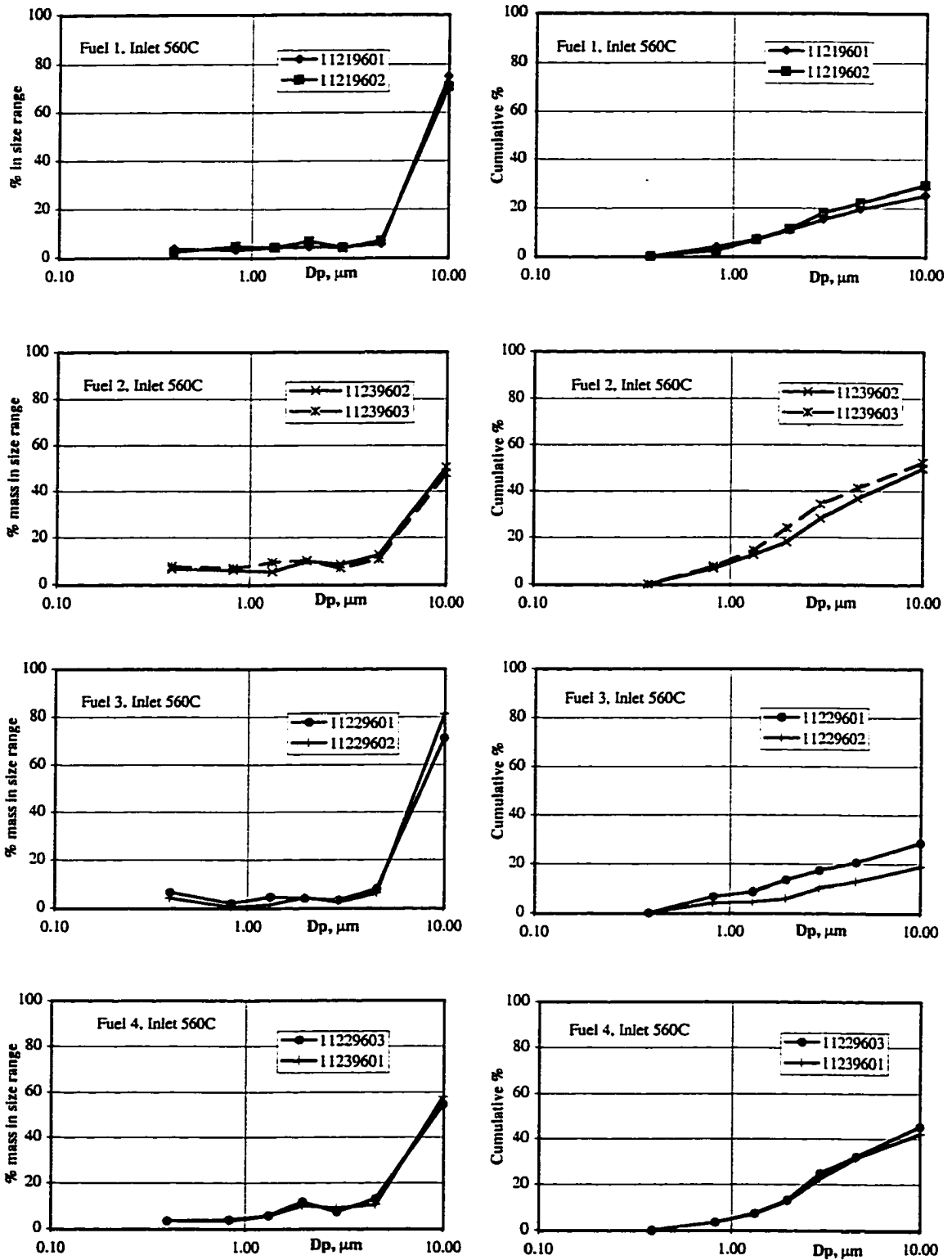


Figure 6.45: Fuels 1, 2, 3 and 4 cascade impactor data at low furnace temperature

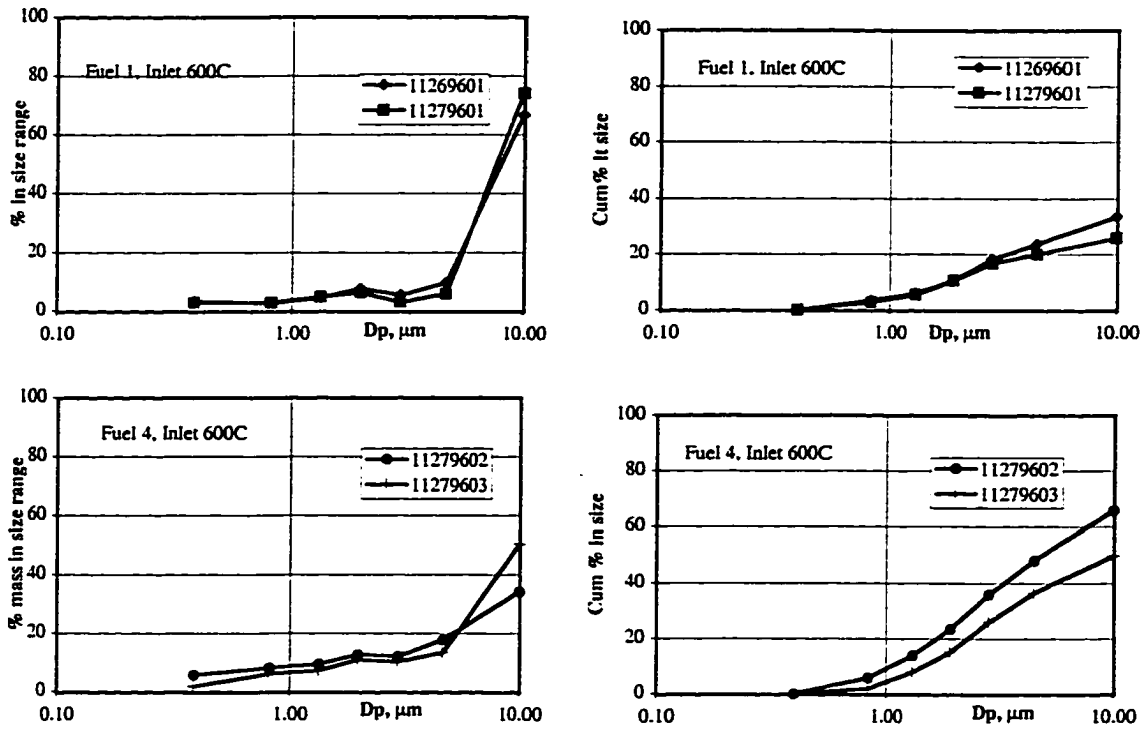


Figure 6.44: Fuels 1 and 4 cascade impactor data at moderate furnace temperature

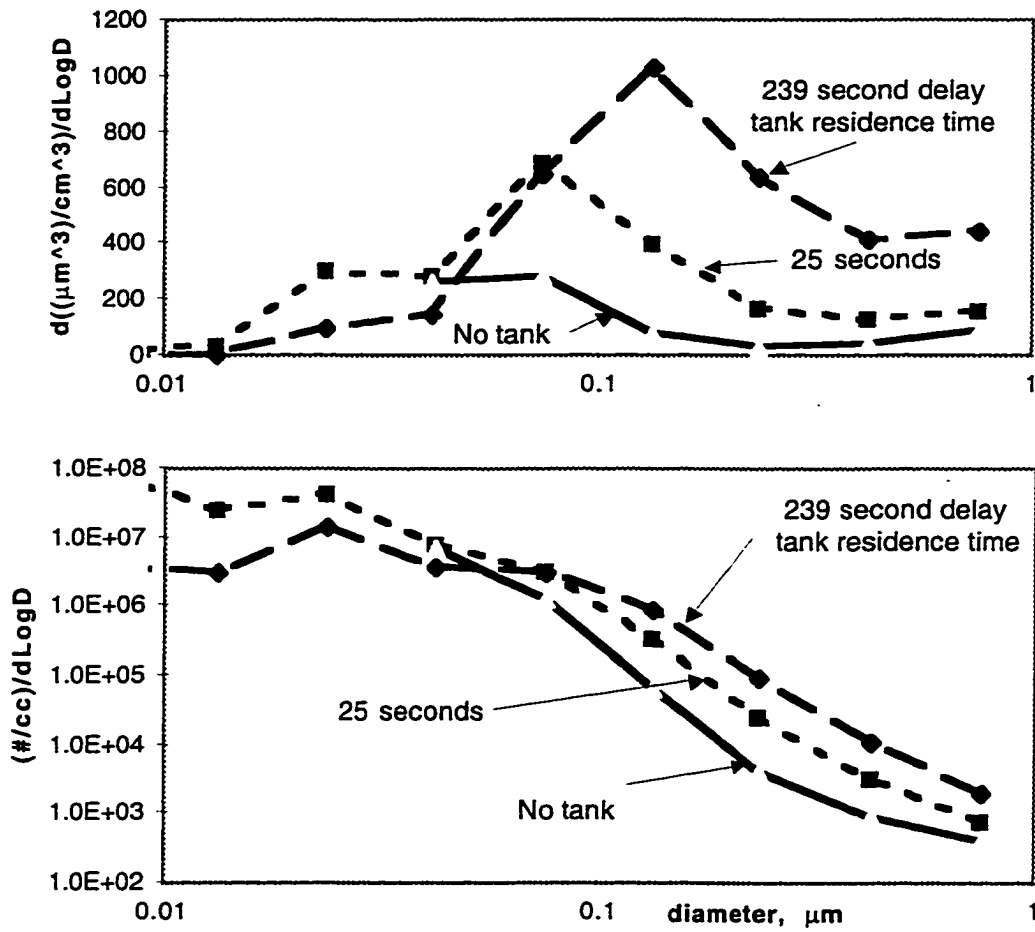


Figure 6.46: Fuel I tests with variable delay tank residence times

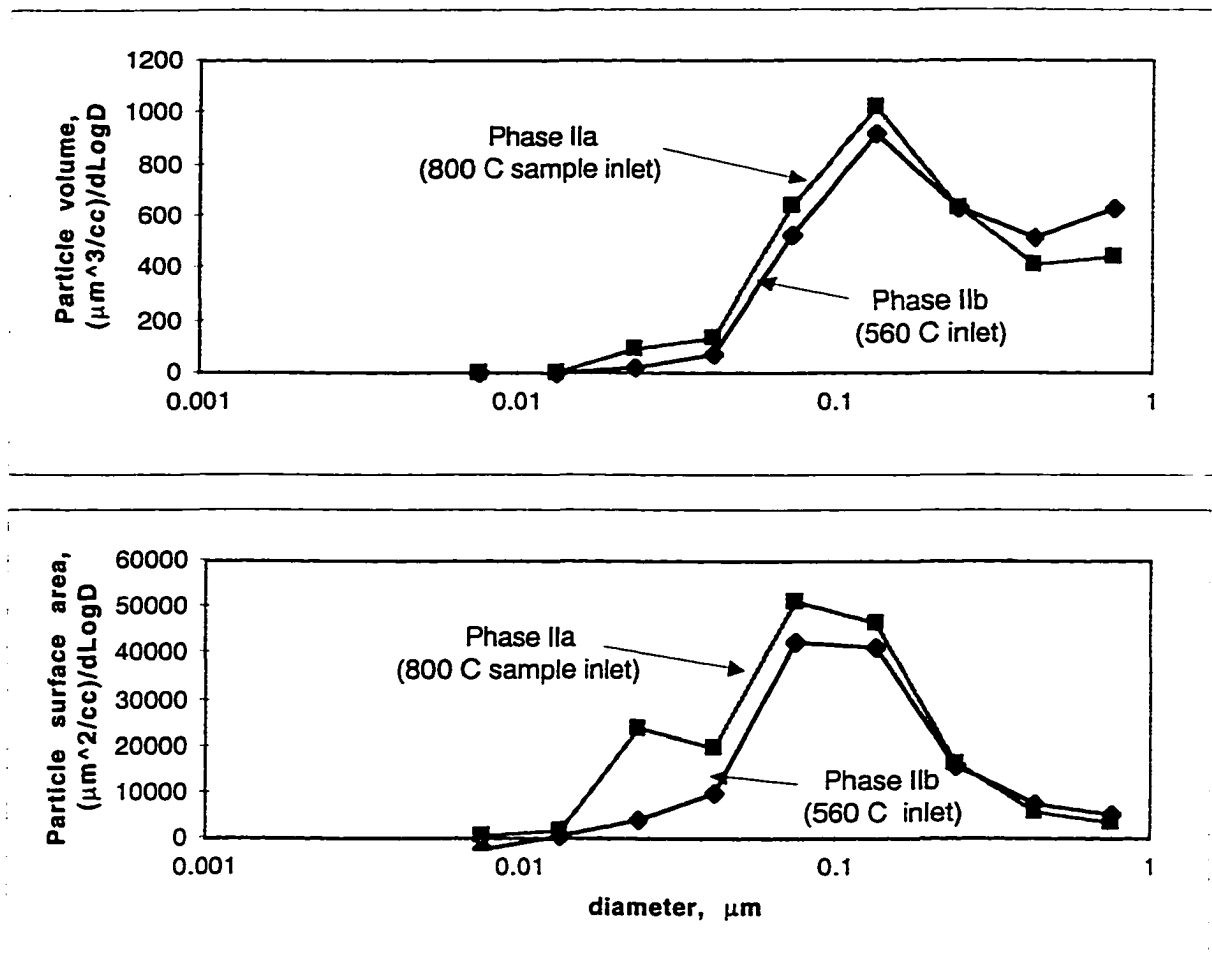


Figure 6.47: Fuel 1 EAA experiments showing the effect of sample inlet temperature on size distribution

MODELING

Modeling is used to examine the critical mechanisms that control ash transformations in the sub-micron particle size range. Although some industrial parameters can be duplicated at laboratory scale, it is clear that modeling plays an important role in bridging the gap between these conditions. The experimental results discussed earlier are used to anchor the model. The ultimate goal is to understand how the size distribution is developed, and how the mineral elements are partitioned into the various size classes.

7.1 Modeling Parameters

Modeling consists of three components: First, gas-phase and condensed phase mineral species favored by equilibrium are determined. Relatively high furnace temperatures and residence times suggest that equilibrium is a good model for gas-phase mineral transformations. Second, the fate of condensing mineral species is investigated by modeling the competition between *condensation* of vapor-phase mineral matter on existing particles, versus *homogeneous nucleation*. Third, the ultimate size distribution of condensed species is investigated by application of a coagulation model.

Modeling is investigated relative to the industrial application shown in schematic form in Figure 7.1. Sawdust/sanderdust is pneumatically injected tangential into the cylindrical primary combustor from a single port. Primary air is added tangential down the length of the burner through sized tuyures, which results in a variable mixture ratio. Overall, the primary combustion zone is operated with an excess air flow rate of 80% to 125%. Secondary air is added in the volume linking the suspension burner to the blend chamber. Blend air is added as required to obtain the desired mass flow rate and to limit the maximum dryer inlet temperature to 866K.

Table 7.1 compares typical combustion conditions in the laboratory tunnel furnace to conditions found in an industrial suspension burner fired with Fuel 4. The table shows that industrial furnace is operated in an overall lean mode, like the laboratory furnace. Facility engineers estimate a primary combustion zone temperature of 1750K to 1475K when operating with Fuel 4 and 80% to 125% excess air. If the primary combustion zone were perfectly premixed, this fuel to air ratio range would result in an adiabatic flame temperature

of 1452K to 1265K, based on the lower heating value of Fuel 4. The high temperature observed in the field is undoubtedly driven by the variable mixture ratio in the primary burner, in which air is added incrementally down the length of the burner.

Table 7.1 also shows the laboratory burner operates at an order of magnitude lower wood-fuel-flowrate-to-total-flowrate ratio than the industrial burner, although the dry oxygen content and exhaust gas temperature is similar. Recall that the laboratory tunnel furnace conditions are maintained with a natural gas and air flame, with sawdust/sanderdust added after primary combustion, while the industrial furnace is operated solely on sawdust and sanderdust. (Note that it was not the goal of the laboratory furnace experiments to match the industrial conditions. Instead, the goal of the dilute suspension firing was to maintain a known, controllable environment around each burning particle.)

The combustion zone residence time is based on plug flow estimates for both the laboratory and industrial systems. The highly-stirred nature of the suspension burner probably results in a variable particulate matter residence time. Incompletely burned sawdust/sanderdust particles have been observed entering the blend chamber from the secondary volume. Incomplete combustion is partly due to oversize fuel particles but is also due to the short residence time.

Table 7.2 shows a summary of idealized residual ash particle size distributions used for modeling alkali condensation onto existing residual particles. A idealized residual size distribution is used in modeling for two reasons: First, simplifying the input residual size distribution allows the user to analyze vapor capture by isolating a discrete particle diameter, rather than grouping vapor capture rates over a range of particle diameters. Secondly, residual ash size distributions are typically not characterized well enough to justify incorporating a detailed residual size input.

Appendix A details the method used for converting the discrete size distributions obtained from the experimental data set into the size distributions shown in Table 7.2. In summary, the residual particles are assumed to form two discrete modes, which are expressed as a Geometric Mass Mean Diameter and a Geometric Standard Deviation. For the heterogeneous vapor capture model, this is further simplified to a single particle size for each mode. It is assumed that these modes are made of a particulate matter with a solid

density of 3.25 g/cc (CaO). The particle number density for that mode is calculated assuming mass is conserved in that mode.

Since it was clear from the experimental results that Fuel 1 and Fuel 2 have similar experimental residual size distributions, their idealized size distributions are taken to be identical. Likewise, Fuel 3 and Fuel 4 idealized size distributions are taken to be identical.

7.2 Equilibrium

Equilibrium conditions were investigated using a derivative of the NASA chemical equilibrium code CET89 (Eddings). This code is very useful in particulate matter investigations because it includes metallic and alkali species in its equilibrium database and predicts equilibrium species in both the gas and condensed phase. Although the code considers condensed species, it does not treat interactions between these species (*e.g.*, the formation of solid solutions or eutectics). In other words, each condensed species is treated as an individual solid or liquid, in contact with the gas but not in contact with each other. For example, the code would not predict a suppression of sodium vapor pressure due to the complexing of the sodium with an aluminosilicate.

The products of combustion from the main burner (*i.e.* methane and air), and air used for pulverized fuel entrainment were included in the calculations. In general, elemental species considered are C, H, O, N, S, Al, Ca, Fe, Mg, Na, P, Si, and Cl. Concentrations of abundant common species (*e.g.*, H₂O, N₂, O₂, CO₂) and species not relevant to ash formation (*e.g.* CO, NO) are not presented here.

7.2.1 Fuel 1 Equilibrium at Laboratory Conditions

Figure 7.2 shows equilibrium conditions in the tunnel furnace for Fuel 1. Input composition is based on 4.64 grams/minute Fuel 1, 18.3 grams/minute natural gas, and 525 grams/minute air.

Equilibrium suggests that non-alkali solid phase minerals are favored at all reasonable flame temperatures of the reactor. It further suggests that solid phase chemistry will result in transformation into other solid species at lower temperatures (*e.g.*, the transformation of CaMgO₂ to Ca₃MgSi₂O₈ at 1000K). Of course, solid-to-solid transformation is not

kinetically favored on any reasonable time scale. It is more likely that solid mineral phases will evolve in a complex way, driven by very localized char composition and the local combustion environment. Mineral species already in close association or in a fuel rich environment may form preferentially over the global equilibrium species. In the absence of other mineral species, oxides are favored for non-alkali metals.

It is immediately clear in Figure 7.2 that vapor phase NaCl and KCl are stable at combustion temperatures. These are precursors to the condensed species formation. NaCl and KCl condense near 870K and 860K.

Sodium sulfate is expected by equilibrium to begin forming as a liquid near 1250K. This process is surely kinetically limited in a practical environment, since vapor-phase Na_2SO_4 is not a preferred species. At equilibrium, the formation mechanism is likely a NaOH reaction with SO_2 , but under kinetically controlled conditions it is more likely formed by sulfation of a condensed phase alkali. Formation of Na_2CO_3 begins at about 1050K, at the expense of the remaining vapor phase NaOH and some NaCl. However, a rapid quench rate may result in direct condensation of NaOH, without conversion to a carbonate. Although sodium carbonate is not a preferred vapor phase species, its formation may be assisted by the abundance of carbon species in the flue gas. HCl is formed during the conversion, but is converted back to alkali salts at a lower temperature. Kinetics probably favor direct condensation of the alkali salts without the HCl intermediary.

Figure 7.3 shows equilibrium conditions for only the alkali species in the laboratory furnace. Non-alkali solid phase minerals equilibrium values at 870K under these conditions are also shown for reference. Note that a rapid quench event through the condensation temperature will likely result in direct formation of solid phase from vapor phase NaCl and KCl. Although this fuel is much higher in chlorine than Fuels 3 and 4, it is an insufficient amount for complete capture of all alkali species. As discussed earlier (see Figure 7.2) Na_2SO_4 and Na_2CO_3 are probably not kinetically favored over condensed NaOH, in a rapid quench environment.

7.2.2 Fuel 1 Equilibrium at Industrial Conditions

Figure 7.4 shows equilibrium calculations for conditions in a commercial suspension burner operated at 80% excess air. The commercial burner is ideally fired with only air and

wood fuel, while the laboratory furnace hot gas environment is maintained by natural gas and air combustion. This results in an order of magnitude increase in ash concentration (per mole of combustion products) between the laboratory furnace and the commercial burner. The higher partial pressure of the mineral species drives the equilibrium condensation temperatures up. This is of little consequence for most non-alkali mineral species, since their condensation temperatures are higher than the commercial burner operating range of 1750 K to 1475K.

Sodium sulfate is formed at about 1400 K (compared to 1250 K for the laboratory furnace), but conversion is probably kinetically limited because vapor phase Na_2SO_4 does not exist, as stated earlier. Sodium carbonate is favored at about 1130 K (vs. 1080 K for the laboratory furnace), NaCl condenses from the vapor phase near 960K (vs. 880 K), and KCl condenses near 940 K (vs. 860 K). Higher condensation/formation temperatures promotes large particle formation via coagulation of the highly mobile sub-micron aerosol earlier in the time/temperature history of the combustion gases.

The preferential vapor-phase sodium species shifts from NaOH to NaCl near 1700 K, versus 1300 K for the laboratory furnace. This may result in a higher fraction of NaCl conversion to NaCl (s), and less conversion of NaOH to NaOH (l) in a rapid quench environment.

The calculated adiabatic temperature drops from 1630K to 1298K when combustion gases from the suspension burner mix with the air added in the secondary volume. It is possible that Na_2SO_4 can overcome the kinetic barrier and form in the secondary volume. This conversion is assumed to be negligible compared to other conversions events occurring downstream. In addition, dilution with secondary air lowers the partial pressure of all fuel-generated species. This results in a shift of solid and liquid-phase mineral formation toward slightly cooler temperatures, which is a detriment to Na_2SO_4 formation.

Figure 7.5 shows equilibrium calculations for the blend chamber. About five times the amount of air used during primary combustion is added in the blend chamber to reduce the dryer inlet temperature, as shown in Figure 7.1. This results in a significant dilution of the vapor phase species, and a drop in NaCl condensation temperature from about 950 K to 910K, and a drop in KCl from about 940K to 880K. Sodium sulfate and sodium carbonate equilibrium formation temperatures drop by about 60 K and 70K, respectively.

Equilibrium in the blend chamber was recalculated with sulfur and carbon excluded, with the purpose of excluding alkali species whose formation is most likely kinetically limited (*i.e.* Na_2CO_3 and Na_2SO_4). The major carbon species CO_2 was replaced with N_2 to preserve relative molar concentrations. The result is shown in the lower graph of Figure 7.5. Potassium has priority in chlorine capture over sodium, with the remaining sodium condensing to liquid NaOH.

Although the condensation scenario shown in the lower graph of Figure 7.5 is probably closer to the results expected from an industrial system, one obvious kinetic barrier exists. KOH in the vapor phase is predicted by equilibrium to capture chlorine from NaCl in order to completely convert to KCl (s). In reasonably rapid quench, NaCl, NaOH, and existing vapor phase KCl will likely homogeneously condense before this ion exchange is complete. Figure 7.6 gives insight to the fate of KOH, in the absence of S, C and Cl. Liquid phase KOH forms at a low temperature compared to other condensed alkalis. The high mobility of nucleated particulate (*e.g.* NaCl (s)) will probably aid in the conversion of KOH vapor to KCl (s) as a surface reaction. The large surface to volume ratio of these condensed species are a critical factor.

7.2.3 Fuel 2 Equilibrium

Fuel 2 is the highest in chlorine of the four fuels tested. Like Fuel 1, the chlorine combines with potassium and sodium to form salts in the vapor phase, as shown in Figure 7.7. Vapor phase NaCl and KCl eventually become condensed NaCl and KCl as the gas temperature is lowered. Sodium sulfate is favored by equilibrium starting at 1230 K, but its formation is limited by diffusion transport and residence time. Sulfation of NaCl(s) and NaCO_3 (s) will probably continue after exiting the primary and secondary combustion zones.

Interestingly, KCl (s) and Na_2SO_4 (s) exchange anions below 600 K. Although this solid-to-solid ion exchange will surely be rare in a practical combustion environment, surface sulfation of KCl particles by uncombined SO_2 seems reasonable.

Note that CaO (s) is directly formed at temperatures above 1070 K. This species is probably not kinetically limited as compared to more complex multi-metal species. The abundance of free oxygen surely favors direct oxidation of Ca. Further, direct oxidation of

other free minerals is more likely than formation of multi component minerals, unless these minerals are closely associated in the parent material prior to combustion. Carbon dioxide combining with CaO(s) beginning at 1100 K will likely be a surface reaction, limited by diffusion of CO₂ through the CaCO₃ product layer that grows on each CaO surface.

Figure 7.8 shows equilibrium results for the laboratory burner operated with Fuel 2 at 3.78 g/min. This is essentially a dilution limit case for the industrial burner, similar to conditions found in the blend chamber prior to entry into the dryer. The fuel-to-total-flow rate ratio is an order of magnitude lower than conditions found in the industrial primary combustion chamber. For reference, the predicted adiabatic temperatures through the industrial system is shown. Condensed NaCl and KCl are formed below about 900 K and 880 K, resulting in nucleated particles forming in the blend chamber. This is about 100 degrees cooler than NaCl and KCl condensation temperatures for the undiluted system shown in Figure 7.7.

7.2.4 Fuel 3 Equilibrium

Figure 7.9 shows Fuel 3 equilibrium for conditions in the industrial primary combustor. Fuel 3 is unique in that it contains nearly twice the sulfur of other fuels, and very low chlorine. Computational limitations of the equilibrium program require the removal of Ca, Mg, and Si species at 1600K. All species containing these elements are predicted to be in solid phase by this temperature, such that any additional transformation is probably limited by diffusion into the solid particle. Note that NaOH and KOH are the dominant forms of vapor phase alkalis above 1400K. In a rapid quench environment, it is reasonable to expect these vapors to homogeneously condense at a faster rate than diffusion transport allows Na₂SO₄ (s) and K₂SO₄ to form. Note that equilibrium predicts sulfated alkalis over KCl or NaCl when sulfur is present in excess.

Equilibrium calculations for the laboratory burner conditions, which is somewhat more dilute than conditions for the same fuel in the industrial burner blend chamber (*i.e.* a limit case), is shown in Figure 7.10. Sulfur is ideally tied up by Ca beginning at about 1270, and by sodium below 1260K. Since calcium is in the condensed phase prior to sulfation, CaSO₄ production is probably kinetically limited. Again, Na₂SO₄ is likely to be kinetically limited as well because of its lack of vapor phase. From a purely equilibrium standpoint, in

which excess sulfur is captured by CaSO_4 , potassium is expected to exchange ions to form KCl (s) around 650K.

When equilibrium is determined for Fuel 3 with sulfur and non-participating minerals excluded, alkali species (NaOH and KOH) form carbonates beginning around 1000 K. Condensation of NaOH and KOH is expected to occur near 975 K and 775 K, respectively, if only homogeneous nucleation and condensation are considered.

7.2.5 Fuel 4 Equilibrium

Figure 7.11 shows equilibrium for Fuel 4 at 80% excess air, which is a realistic condition for a commercial suspension burner. Calcium content is two to three times higher than the other three fuels. It is clear that significant amounts of CaO and CaCO_3 can be expected from this fuel.

Like Fuel 3, this fuel is an order of magnitude lower in chlorine than Fuels 1 and 2, and has about half the sulfur of Fuel 3. This low anion availability (Cl and sulfate) results in an interesting transition from Na_2SO_4 to K_2SO_4 around 1200 K under equilibrium conditions. This transition is kinetically unlikely. Formation of sodium carbonate is also indicated around 1200 K. Condensation of NaOH , followed by a CO_2 gas and $\text{NaOH}(\text{l})$ surface reaction may be more likely. This will be limited by CO_2 diffusion.

Figure 7.12 shows equilibrium for the limit case of laboratory burner conditions. This is similar to the fuel-to-total flow rate of the industrial configuration inside the Blend Chamber. The mineral KCl is the preferred chloride species above 820 K, and condensed species below 820K. Note that the quench rate in the temperature range of 1200K to 1000K plays an important role in the composition of the solid particulate matter. A very slow quench would allow alkali-sulfate formation, while a rapid quench favors direct condensation of alkali hydroxides followed by surface reactions.

7.2.6 Summary of Equilibrium Findings

RESIDUAL PARTICLES:

- Non-alkali metals and silicon form residual solids that are not expected to vaporize in at standard industrial furnace temperatures. Equilibrium predicts they will form complex

species that can recombine to form new species at cooler temperatures. In the absence of other mineral species, oxides are generally the favored form of non-alkali metals (*e.g.* MgO (s)). In practice, the composition is most likely driven by the very localized composition of the char particle and local combustion conditions (*i.e.* formation of eutectic mixtures, and reducing vs. oxidizing environment). Recombination of solids to form new solid species at lower temperatures is surely a phenomena limited to surface reactions between colliding residual particles.

- Equilibrium predicts formation of CaCO_3 and CaSO_4 through a solid/gas interaction. Sulfation of residual particles or combination with CO_2 is likely limited to surface interactions, assuming complete char burn-out. The kinetic limitation is SO_2 and CO_2 diffusion into the existing particle.

AEROSOL PARTICLES:

Figure 7.13 compares equilibrium results (at 700 K) to the material collected on the aerosol ash filters for the four sawdust/sanderdusts tested. For this comparison, the equilibrium column shows only species expected to form from gas phase species (*i.e.* no residual ash). These are alkali metals sodium and potassium, and potential anions chlorine and sulfur (as SO_2). Carbon and oxygen are not detectable by the method used to analyze the aerosol filter (EDS), so the anion CO_3 is not included in this system. However, the *alkali* associated with carbonate is included, since it is detectable by EDS. The elemental composition of the raw fuel as determined by Atomic Absorption is also shown.

In Figure 7.13, the raw fuel composition and the predicted equilibrium composition are essentially the same, reflecting the fact that sulfur and chlorine preferentially combine with the alkalies rather than with the residual ash. For Fuel 3, a small fraction of the available sulfur combines with calcium, so this sulfur is assumed to be part of the residual modes rather than the aerosol mode. Also, the chlorine in Fuel 3 remains in the vapor phase as HCl until about 650 K (Figure 7.11), so it is not included in the equilibrium balance at 700 K.

Immediately clear is that sodium is under-represented on all four aerosol filters in Figure 7.13. It is possible that sodium is preferentially captured over potassium by the residual ash prior to entering the gas phase, and therefore never enters the vapor phase. This is discussed at length in Chapter 6.

Figure 7.14 shows an under-representation of sulfur relative to chlorine on the aerosol filter for Fuels 1 and 2. This suggests there is resistance to sulfation when chlorine is present, even though sulfate formation is favored. If little chlorine is present (Fuels 3 and 4), then sulfate is formed. It is not clear when the sulfate is formed in Fuels 3 and 4. Neither equilibrium nor the experiments conducted can offer a definitive answer to this kinetics problem.

In summary, equilibrium relative to aerosol shows:

- Both potassium and sodium are predicted by equilibrium to escape the residual/char and enter the vapor phase. The preferred form of vapor phase sodium is chloride and hydroxide, in the range of typical combustion temperatures (about 1800K to 1400K). Vapor phase HCl is converted to NaCl and KCl as the combustion temperature is lowered, well above the condensation temperatures of NaCl and KCl. The vapor phase is exclusively hydroxide if chlorine is absent.
- Formation of Na_2SO_4 (liquid) from vapor phase sodium species (primarily NaOH) and SO_2 is predicted by equilibrium to occur near the adiabatic temperature of the Secondary Volume in the industrial burner. This formation is most likely kinetically limited in a practical quench environment, since this is a gas/gas interaction rather than a condensation event. Sulfation is will most likely occur in a practical combustor as a SO_2 gas reaction with condensed NaOH.
- Sulfur in excess of stoichiometric Na_2SO_4 and K_2SO_4 will prevent formation of solid phase NaCl and KCl, at equilibrium conditions. In a practical rapid quench environment, solid phase NaCl and KCl and liquid phase NaOH and KOH would likely be precursors to gas/particle sulfation.
- In a chlorine deficient environment, chlorine is preferentially complexed to solid form by potassium rather than sodium, until all chlorine is in solid phase. Since vapor phase NaCl condenses at a higher temperature than KCl, a rapid quench will likely lead to a significant NaCl formation.

7.3 Homogeneous and Heterogeneous Condensation Modeling

Equilibrium calculations indicate that alkali metals are vaporized during combustion. The metals enter a condensed state due to quench (by heat transfer from the system, addition of dilution air) or by chemical complexing. Neglecting vapor-phase chemical change (*e.g.* alkali sulfate formation), the super-saturated vapor will either self-nucleate and form homogeneous particles or it will diffuse to existing particles and condense (heterogeneous condensation). In a practical system, the condensation pathway will be a mixture of these two modes. The goal of the work described in this section is to resolve the relative importance of these two paths under the various experimental and practical conditions.

7.3.1 Homogeneous and Heterogeneous Modeling Method

Limit cases of homogeneous and heterogeneous condensation are illustrated in Figure 7.14. Homogeneous condensation tends to produce coagulated particles typically less than 0.1 μm in diameter with high number densities. Efficient filtering or electrical precipitation is usually required to remove these highly mobile homogeneous particles from industrial flue gas. In contrast, heterogeneous condensation on existing particles does not change the particle number density in the flue-gas. This typically means orders of magnitude lower number density and larger particle diameters. A significant fraction of these heterogeneous particles may be removed by centrifugal separators and/or cloth filtering.

Determining the ultimate fate of vapor phase alkalis requires resolving the relative contributions via these two different pathways. To that end, the critical controlling mechanisms are presented below and incorporated into a computational model. The model is applied to data from laboratory and industrial sources.

Kelvin Effect

Condensation on a flat material surface occurs when the vapor pressure of the material exceeds the saturation pressure. If the material surface is curved, molecules are less tightly bound at the surface because there are less adjacent molecules sharing Van der Waal forces. Hence, the saturation pressure of material in equilibrium with its curved surface is greater than the saturation pressure over a flat surface of the same material. This relationship between the plane-surface saturation pressure, p_{sat} , and the saturation pressure over a curved surface, p_d , is given by:

$$\ln\left(\frac{P_d}{P_{sat}}\right) = \frac{4\bar{v}\sigma}{d_p \tilde{R}T} \quad (\text{eq 7.1})$$

and is known as the Kelvin effect (for example, see Hinds, 1982). The Kelvin relationship dictates that a supersaturated ($s=p_{vap}/p_{sat} > 1$) condition will result in a condensation event only if the system contains condensation nuclei with diameters greater than a critical diameter. In a system lacking foreign nuclei, homogeneous condensation occurs when the saturation ratio is high enough for molecular clusters to initiate nucleation. In a system with foreign particles present (*i.e.* larger diameter nuclei), the supersaturation will be partially or fully relieved by heterogeneous condensation on the foreign particles, as summarized in Table 7.3. The remainder of this section presents relations to quantify s_{het} and s_{crit} , and explores the rate of condensation for these two modes as a function of known variables.

Homogeneous nucleation and condensation

Friedlander (1977) derived a relationship for the rate of droplet formation as a function of saturation ratio, based on homogeneous nucleation initiated by molecular clusters.

$$I = \left[\frac{P_1}{(2\pi mkT)^{1/2}} \right] * (n_1 v_m^{2/3}) * \left[\frac{\sigma v_m^{2/3}}{kT} \right]^{1/2} \exp\left[-\frac{16\pi\sigma^3 v_m^2}{3(kT)^3 (\ln S)^2} \right] \quad (\text{eq. 7.2})$$

Friedlander defines the critical saturation ratio (S_{crit}) as the ratio at which droplets are formed at a rate of one drop/cm³/sec, which is considered a formation rate that can be conveniently observed experimentally.

For modeling, it is assumed that reaching the critical saturation ratio will result in rapid relief of the supersaturation by homogeneous condensation. This is a reasonable assumption for three reasons: The high surface-area-to-volume ratio of the newly formed nuclei represent a significant increase in available condensation surface area. Secondly, the high number density of the nuclei limits gas transport resistance for NaCl (v) to the particle surface. Third, as the newly-formed particles grow, the Kelvin effect relaxes. Hence, all remaining vapor is assumed to be converted to homogeneously condensed particulate matter.

Heterogeneous Condensation

Within the heterogeneous condensation regime, the rate of vapor deposition on the particle surface is strongly driven by the particle diameter relative to the mean free path in the carrier gas. For a particle with a diameter much greater than the gas mean free path (Knudsen number, $Kn = \lambda/d \ll 1$) in an infinite medium, continuum gas dynamics applies. It can be shown that diffusion results in a growth law ($d\text{molecules}/d\text{time}$) proportional to particle diameter (Friedlander, 1977).

$$\frac{d\#}{dt} = \frac{2\pi D d_p (p_1 - p_d)}{kT} \quad \text{for } Kn \ll 1 \quad (\text{eq. 7.3})$$

For particles with diameters much smaller than the gas mean free path ($Kn \gg 1$), molecular bombardment is the governing conversion mode and particle growth rate is proportional to the particle diameter squared (Friedlander, 1997).

$$\frac{d\#}{dt} = \frac{\alpha \pi d_p^2 (p_1 - p_d)}{(2\pi m k T)^{1/2}} \quad \text{for } Kn \gg 1 \quad (\text{eq. 7.4})$$

For the modeling approach, the transition region of $Kn \approx 1$ is of particular interest. Experimental size distributions of the residual ash showed that a foreign particle diameter in the range of $0.3 \mu\text{m}$ to $10 \mu\text{m}$ is likely, which is near the mean free path of the combustion gas (about $0.3 \mu\text{m}$ at 1000 K). Hence, the approximate interpolation formula proposed by Fuchs and Stutugin (1971) is used:

$$\frac{d\#}{dt} = \frac{2\pi D d_p (p_1 - p_d)}{kT} * \left\{ \frac{1 + Kn}{1 + 1.71Kn + 1.333Kn^2} \right\} \quad \text{for all } Kn \quad (\text{eq 7.5})$$

The Fuchs/Stutugin equation reduces to equation 7.3 for $Kn \ll 1$, and about 1.2 times the value of equation 7.4 for $Kn \gg 1$ (Friedlander, 1977).

Modeling Approach

Some assumptions are made for modeling the condensation rate of vapor on existing particle surfaces. They are:

- No spacial temperature gradient. The particle is at the same temperature as the freestream fluid. The heat of vaporization (endothermic condensation) is dissipated quickly compared to the condensation rate on the particle.
- No convective mass transfer to the particle surface. The particle travels with the fluid.
- The density gradient to the particle surface is negligible (no diffusion induced secondary convection term).
- Surface wetting properties of the nucleate are identical to the condensing material.
- The mineral NaCl is the vaporized/condensing species. When present in a fuel, it is favored in the vapor phase at combustion temperatures, and is predicted to condense to solid phase by equilibrium. Kinetic arguments also favor its formation in a rapid quench environment. It is in high abundance in two of the four sawdust/sanderdusts investigated, and it is expected to closely match the behavior of KCl under similar conditions. Under rapid quench conditions that are present in an industrial dryer, this model is likely to simulate NaOH or KOH condensation mechanisms as well.

The computer code is written using Mathematica, and is described in detail in Appendix I. In summary, the model is composed of the following steps:

1. The properties of the vapor phase species and hot gas are calculated.
2. Condensation rate equations are defined. For heterogeneous particulate matter formation, the equation of Fuchs and Stutugin (1971) is used, as described above. The relation for critical saturation ratio defines the region dominated by homogeneous condensation.
3. The foreign particle number density, foreign particle diameter, initial vapor phase partial pressure and quench rate are supplied. The model allows two foreign particle diameters and corresponding particle number densities.
4. The temperature at which heterogeneous condensation is initiated is calculated, based on the Kelvin effect and vapor properties. The temperature at which homogeneous

condensation (in the absence of foreign particles) occurs is calculated, based on the input conditions and critical saturation ratio.

5. Beginning at the temperature of heterogeneous condensation initiation, the vapor collection rate on the surface of heterogeneous nuclei is calculated.
6. The time step is incremented. The mass of vapor captured over the incremental time step is calculated.
7. The partial pressure and saturation ratio of the free vapor is recalculated. This is done with respect to the vapor captured by the heterogeneous particulate matter and the system temperature at the end of the incremental time step.
8. The critical saturation ratio for homogeneous nucleation is calculated.
9. If the new saturation ratio calculated in step 7 is greater than the critical saturation ratio calculated in step 8, then homogeneous nucleation occurs and the remaining vapor phase is assumed to form homogeneous condensate. If the saturation ratio is less than the critical saturation ratio, steps 6 through 8 are repeated until all vapor is captured heterogeneously, or homogeneous nucleation occurs.

7.3.2 Homogeneous and Heterogeneous Condensation Model Results

Figure 7.15 shows predicted condensation regimes for a combustor with an initial NaCl vapor pressure of 14 Pa. This approximately corresponds to the partial pressure of all alkali species (mainly NaCl and KCl, and NaOH and KOH) present in an industrial suspension burner operated on Fuel 1 with 80% excess air. Three heterogeneous particle sizes are also assumed to be present, as an example. As the flue gas temperature is decreased with time (*i.e.* a Lagrangian coordinate system), the gas volume will go through three condensation regimes. Between 1030 K and 1022 K, the system saturation ratio ($S = P_{\text{vapor}}/P_{\text{sat}}$) is less than one, which dictates that only vapor phase alkali species are present. At 1022 K, the radius of curvature of a particle with a diameter of 7.16 μm is adequate for condensation of vapor phase, and the vapor phase will begin to be depleted by condensation on particles of this size and larger. Note that this saturation ratio is very close to unity, which is indicative that the Kelvin effect is of little consequence for a particle of relatively large diameter.

The second largest particle in the hypothetical system becomes a collection surface around 1014 K. Although this particle is 3 orders of magnitude smaller (in terms of mass) than the largest particle, the two condensation temperatures are separated by only 8 K.

As the temperature is reduced further, and assuming the system has not been appreciably depleted of vapor phase alkali, the cross-over of point at which individual molecular clusters act as nuclei is reached around 994 K. This corresponds to a particle diameter of about .00222 μm in this system. Below this temperature, the supersaturation is quickly relieved by condensation on these particles.

Note that the condensation temperature becomes very sensitive to the particle diameter between .00222 μm and .00669 μm - diameters which are only separated by a factor of 3. This is a manifestation of the Kelvin effect. Examining equation 7.5, for condensation to occur:

$$(p_1 - p_d) > 0 \quad (\text{eq. 7.6}).$$

Substituting in Kelvin's relation for p_d yields;

$$\left(p_1 - p_{\text{sat}} * e^{\left[\frac{4\bar{v}\sigma}{d_p RT} \right]} \right) > 0 \quad (\text{eq. 7.7}).$$

From this relation, it is clear that the exponential term is near unity for large values of d_p , and rapidly increases for very small values of d_p . Note that this relationship also implies that pure particles with diameters below a critical size (for a given temperature and partial pressure) have a negative condensation rate, and will vaporize.

The following modeling results focus primarily on Fuel 1. The residual size distribution for Fuel 2 is essentially identical to Fuel 1, as discussed relative to Table 7.2, such that presentation of Fuel 2 modeling is redundant.

Figure 7.16 demonstrates the effect of quench rate assuming a system composed of Fuel 1 in an 80% excess air environment. The initial vapor pressure shown here is the sum of the NaCl and KCl vapor predicted by equilibrium prior to condensation. Condensation on heterogeneous particles, with diameters of 7.16 μm and .669 μm , begins at 1008 K. These particle diameters are large enough that the Kelvin effect is relatively small and the

temperature at which heterogeneous condensation commences is essentially the flat-surface condensation temperature.

The topmost curve shows the depletion of alkali vapor pressure a very rapid quench rate of 10,000 K/sec. Less than 3% of the available alkali vapor is captured by the heterogeneous particles by the time the point of homogeneous nucleation is reached, at 974 K. Recall that reaching the homogeneous nucleation state results in a rapid depletion of the system via condensation on the newly-formed high surface area to volume nucleates. Hence, the remaining 97% of the NaCl is depleted homogeneously. For a very slow quench, vapor capture by heterogeneous particles will be much greater, as is illustrated by the 400 K/sec curve in Figure 7.16. The heterogeneous particles are able to deplete the vapor reservoir at a rate fast enough for the saturation ratio to remain below the critical pressure ratio for homogeneous nucleation, until 818 K. All of the vapor is collected by the heterogeneous particles, leaving none for conversion to homogeneous particles.

The lower graph in Figure 7.16 shows some practical limitations of aerosol control through quench rate. As the vapor concentration is reduced, the rate of vapor capture decreases, as can be seen in the flattening of the 400 K/sec quench curve with residence time. Note also that a high quench rate correlates to a faster capture rate, which can be seen by comparing the slope of the 400 K/sec curve the 700 K/sec curve around 0.1 seconds. It is clear that the capture rate is faster for the 700 K/sec quench, but the duration of the 400 K/sec quench ultimately results in greater heterogeneous capture.

Figure 7.17 shows a series of graphs for six different quench rates. Each graph shows eleven separate initial vapor pressures separated by increments of 1.5 Pascal. Examining the upper left graph as an example, the temperature at which heterogeneous condensation is initiated can be very low for a low initial concentration. As the initial concentration is increased, the temperature for heterogeneous condensation becomes less sensitive to initial concentration. The practical implication is that a system with a high initial concentration of NaCl requires a slow quench at a higher temperature for conversion to hetero-particles. A slow quench beginning below the critical saturation temperature for that partial pressure is of no value.

The partial pressures at the bottom of Figure 7.18 give an indication of the alkali-species vapor pressure for Fuel 1 combusted in an industrial suspension burner. The first vapor

pressure is based on the NaCl content of Fuel 1. The second combines the NaCl and KCl of Fuel 1 and approximates it as all NaCl. The third combines the NaCl, KCl, NaOH, and KOH in Fuel 1 and approximates it as all NaCl. This is meant to give an idea of condensable vapor available in a high alkali fuel. Note that for a given quench rate, the absolute mass captured by heterogeneous particles increases as partial pressure increases. Regardless of initial concentration, the fraction of vapor converted to heterogeneous particulate is about the same.

The top plot in Figure 7.18 shows NaCl vapor pressure as predicted in an industrial blend chamber, in which the industrial burner hot gas illustrated in Figure 7.17 has been diluted by a factor of 5.4. Note that the conversion to heterogeneous particles is very low, even for an extremely slow quench rate of 200 K/sec. It is clear that quenching after dilution results in poor vapor capture. The mechanism for this is primarily a reduction in the total hetero-particle surface area per volume of hot gas. Dilution greatly increases the gas volume, but, of course, leaves total hetero-particle surface area unchanged.

The lower plot in Figure 7.18 shows NaCl vapor pressure for the laboratory furnace configuration. Condensation on the heterogeneous particles is very low, regardless of quench rate. Almost all of the NaCl and KCl present in the fuel was found on the aerosol filter, which is indicative of homogeneous condensation. The quench rate in the undiluted sampling probe is calculated to be about 5400 K/sec, based on measured probe inlet temperature and estimated exit temperature.

The modeling results for Fuel 1 are summarized in Figure 7.19. The mass fraction captured by heterogeneous condensation relative to the initial NaCl in the system is shown, as a function of quench rate. The “Industrial Burner” grouping shows the conversion for eleven initial vapor pressures. It is clear that the initial vapor pressure only weakly drives the conversion efficiency, while the quench rate is critical. This observation is the same for the grouping labeled “Industrial Blend Chamber” and the “Laboratory Furnace” grouping.

Comparing the groupings in Figure 7.19, it is obvious that the change in quench rate for a given capture efficiency is directly proportional to the dilution ratio. Diluting the industrial burner hot gas by a factor of ten requires a reduction in a quench rate (for the same conversion efficiency) by a factor of ten, which is essentially shown by the laboratory

furnace data. This is intuitively reasonable, since dilution by an order of magnitude reduces the heterogeneous particle number density by an order of magnitude in the system.

If heterogeneous capture of the vapor is desirable, as one would expect in an industrial application, quenching prior to dilution is critical. For example, a quench rate of 1000 K/sec will convert about 40% of the alkali vapor to heterogeneous particulate in the industrial burner, but only about 5% will be converted for the same quench rate after the hot gas has been diluted by a factor of 5.4 in the blend chamber.

It was found in Fuel 1 modeling that less than 3% of the heterogeneously captured vapor was deposited in the large particle mode. Although the capture rate for a single 7.16 μm particle is approximately an order of magnitude greater than the capture rate of a .669 μm particle, the small particle number density is three orders of magnitude greater than the large particle mode. Hence, the heterogeneous capture process is dominated by the smaller diameter particles. Fuel 3 and Fuel 4 have residual modes composed primarily of large (8 μm) particles, as was shown in Table 7.2. It is clear that only a very small fraction of vapor will be captured at any reasonable quench rate for Fuel 3 and Fuel 4.

7.3.3 Summary of Homogeneous and Heterogeneous Modeling Findings

- The critical temperature range for condensing alkali vapor onto existing residual particles is dictated by the diameter of the existing residual particles (upper bound), and the vapor pressure of the condensable alkali vapor (lower bound). The time/temperature history of the flue gas outside of this temperature range does not effect the conversion efficiency.
- The conversion efficiency of vapor phase alkali to heterogeneous particles is a logarithmic function of the quench rate between the temperature at which heterogeneous condensation starts, and the temperature at which homogeneous nucleation starts. Therefore conversion efficiency can be modified significantly with small changes in quench rate, in a slow quench environment.
- For a fixed quench rate, the initial vapor pressure of the condensing species does significantly change the conversion efficiency.

- Dilution of a condensing system requires a directly proportional increase in quench rate in order to achieve the same conversion efficiency. Dilution of the flue gas reduces the conversion efficiency primarily through reduction of the foreign particle number density.
- In order to obtain the highest conversion efficiency in an industrial dryer application, the undiluted flue gas should be quenched through the temperature range of conversion prior to dilution. This may be best accomplished by staged dilution in an industrial application, in which only enough dilution air is added to lower the system temperature into the heterogeneous condensation temperature range. Additional dilution air may be added downstream of an insulated volume (*i.e.* a slow quench zone), in order to obtain the desired dryer inlet temperature and volumetric flow rate.

7.4 Coagulation Modeling

The MAEROS2 code (Gelbard, 1996) is used to determine the influence of coagulation on the ultimate aerosol size distribution. The code is a numerical method based on resolving the diameter distribution into discrete bins and enforcing conservation of mass for each component (Gelbard, 1996). Coagulation rate can be calculated with Brownian motion, gravity and turbulence terms. For the purposes of this work, only Brownian motion is considered.

The program calculates the size distribution of aerosol as a function of time for an enclosed volume (*i.e.* Eulerian coordinate system). By coordinate transformation, the code also applies to a moving volume (*i.e.* Lagrangian coordinate system). The input parameters are initial mass concentration with a mean particle diameter and geometric standard deviation, condensable vapor source rate, aerosol source rate, volume, temperature, and system pressure.

7.4.1 Coagulation Modeling for Fuel 1 Ash

It is clear that the ultimate size distribution is a function of many variables. A major factor with a condensing aerosol species is the initial particle size, number concentration, and residence time for coagulation. This is investigated by modeling the expected conditions in

an industrial suspension burner used for drying of wood chips. Some assumptions are necessary in order to examine the fundamental coagulation process:

- Non-alkali minerals form particles with an initial size distribution similar to the residual particle size distribution found during laboratory-scale experiments. This is approximated as two log-normal size distributions, which are described by a geometric mean diameter and geometric standard deviation. Calculation of these parameters are described in Appendix A. It is assumed that all non-alkali species are part of this size distribution.
- Alkali species condense as chlorides when chlorine is available, and hydroxides otherwise. The initial mass of self-nucleated particulate matter is therefore set by the alkali content of the as-received fuel. The initial diameter of the nucleated particulate matter is assumed to be the critical diameter of nucleation for NaCl in the reactor. The calculation for initial aerosol mass and diameter is shown in Appendix A.
- Turbulence is not included, although it surely increases the coagulation rate. Incorporating fluid dynamic effects into this phase of the modeling is beyond the scope of the current investigation.
- Every collision results in a larger particle.
- A uniform particulate matter density is required for all input size distributions. The appropriate density for each example is noted as necessary.

Figures 7.20 through 7.23 show coagulation results for Fuel 1 in for an idealized industrial burner shown in Figure 7.1. For this series, it was assumed that three initial size distributions were present: 1) An aerosol mode composed of all the aerosol-forming material, assuming to have a diameter of $1.9 \times 10^{-3} \mu\text{m}$, 2) a residual mode (labeled Zone 2), corresponding to a residual mode with a geometric mean diameter of $1.7 \mu\text{m}$, and 3) A residual mode (labeled Zone 3), corresponding to the largest residual mode with a geometric mean diameter of $7.8 \mu\text{m}$. (Note that a geometric mean diameters are required by MAEROS2 rather than count mean diameters.) The ash concentration is based on the expected concentration in the blend chamber shown in Figure 7.1, with an initial combustion conditions of 80% excess air. The temperature in the blend chamber is

approximated to be 800 K, for modeling purposes. All particulate matter is assumed to have a uniform density of 2.7 g/cc.

These three initial modes are shown in Figure 7.20. A sum of the modes is also shown by the curve-fit line. In Figure 7.21 and 7.22 the aerosol mode very quickly coagulates through Brownian motion and marches toward the larger size distributions. The advance slows as the mean diameter increases, as shown in Figure 7.23. It is clear from Figure 7.24 that the residual modes do not significantly participate at any reasonable time scale because of low mobility. Note that the aerosol mode is predicted to eventually stabilize at about 0.05 μm .

Figure 7.25 compares two conditions - "aging" of initial aerosol in a plug flow condition and aging in a perfectly mixed chamber. In the perfectly mixed condition (taken as the estimated volume of an industrial-scale blend chamber), freshly nucleated particulate matter interacts with older aerosol to form a wider size distribution. The plug flow condition is the limit case of the industrial blend chamber with no mixing. No fresh nucleated particulate matter is available, hence the size distribution is determined by the coagulation of the initial aerosol, and the peak is narrower.

Figure 7.26 are MAEROS2 results for a conditions similar to coagulation conditions in the delay tanks used for the milled sawdust/sanderdust experiments. For this comparison, the density of the aerosol was assumed to be 1 g/cc. Hence, the axis is the aerodynamic diameter of the particulate, which is equivalent to the diameter as determined by the EAA.

Comparing Figure 7.26 to experimental results shown in Figure 7.27, the fundamental behavior of the coagulating aerosol is clear: The mean diameter is driven by the coagulation of the nucleated aerosol. In the experimental results, a secondary mode is present, possibly related to unaccounted pre-existing modes. This is possibly an artifact of non-uniform nucleation, for example NaCl, and KCl do have condensation temperatures higher than NaOH and KOH. Other possible nucleate sources can include (but are not limited to) reduction/oxidation-formed aerosols of CaO, 0.4 μm range aerosol not captured by the impactor, or soot.

7.4.2 Summary of Coagulation Modeling

- Coagulation modeling of the industrial burner blend chamber demonstrated that coagulation changes the ash size distribution only below 1 μm range. The coagulating aerosol is expected to converge to about .05 μm under typical conditions for an industrial burner. Residual modes above 1 μm are not expected to change, due to low Brownian mobility.
- Coagulation modeling suggests that the *major* mode diameter of sub-micron aerosol may be reasonably predicted by assuming the aerosol is composed of the alkali components of the parent fuel, in the form of alkali chlorides and alkali hydroxides. More extensive characterization of initial aerosol components is required to model detailed coagulation.

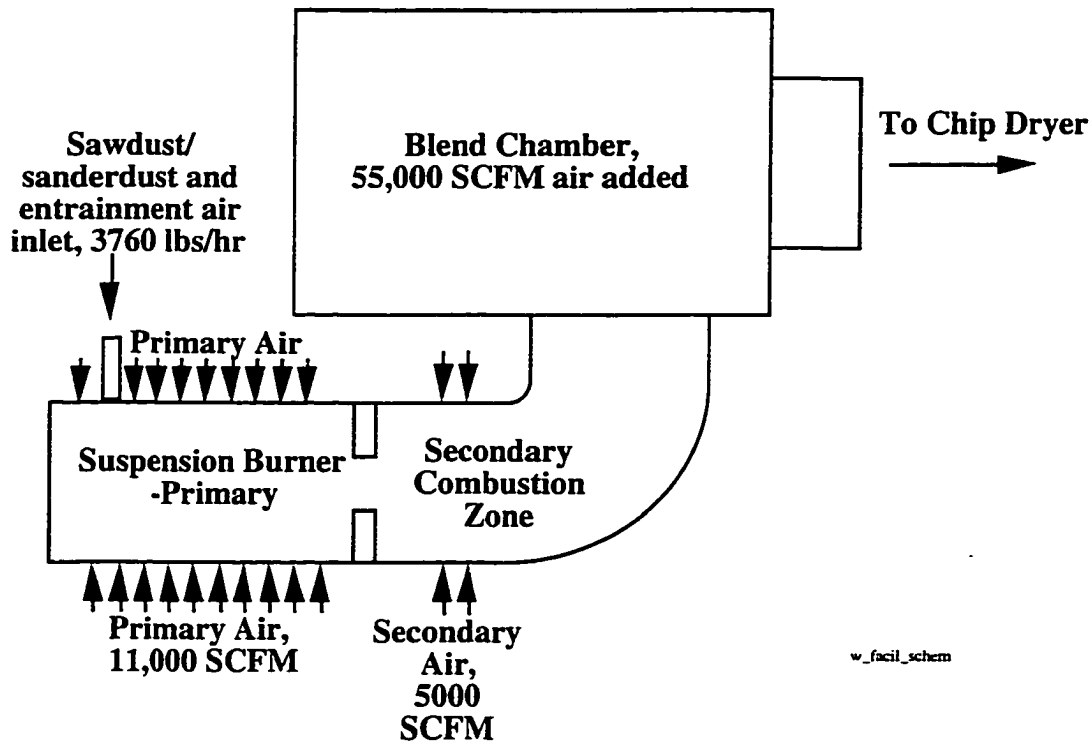


Figure 7.1: Example configuration of a sawdust/sanderdust burner used for wood chip drying in a strand board production facility

Table 7.1 Comparison of typical laboratory conditions to typical industrial burner conditions

Parameter	Laboratory Tunnel Furnace	Industrial Suspension Burner*
Dry Oxygen Post-Combustion, Percent by Volume	7.3% to 9.0%	9.4% to 11.7% (primary)
Typical Maximum Operating Temperature	1450K	1750K to 1475K
Wood Fuel Flowrate over Total Flowrate, kg/kg	.006 to .009 (main) .00024 to .00032 (in dilution probe)	.07 to .09 (primary) .05 to .06 (secondary) .012 to .016 (blend)
Combustion Zone Residence Time	1.0 to 1.3 seconds	.08 seconds primary .16 seconds secondary

*Industrial conditions estimated for Fuel 4, based on information supplied by site engineers

Table 7.2: Simplified residual particle size distributions used for modeling

	Hetero-particle Diameter 1, μm	Diameter 1, number density, $\#/(kg \text{ Fuel})$	Hetero-particle Diameter 2, μm	Diameter 2, number density, $\#/(kg \text{ Fuel})$
Fuel 1 and 2	7.16	$4.74 \cdot 10^9$.669	$2.64 \cdot 10^{12}$
Fuel 3 and 4	8.21	$7.43 \cdot 10^9$.689	$3.35 \cdot 10^{11}$

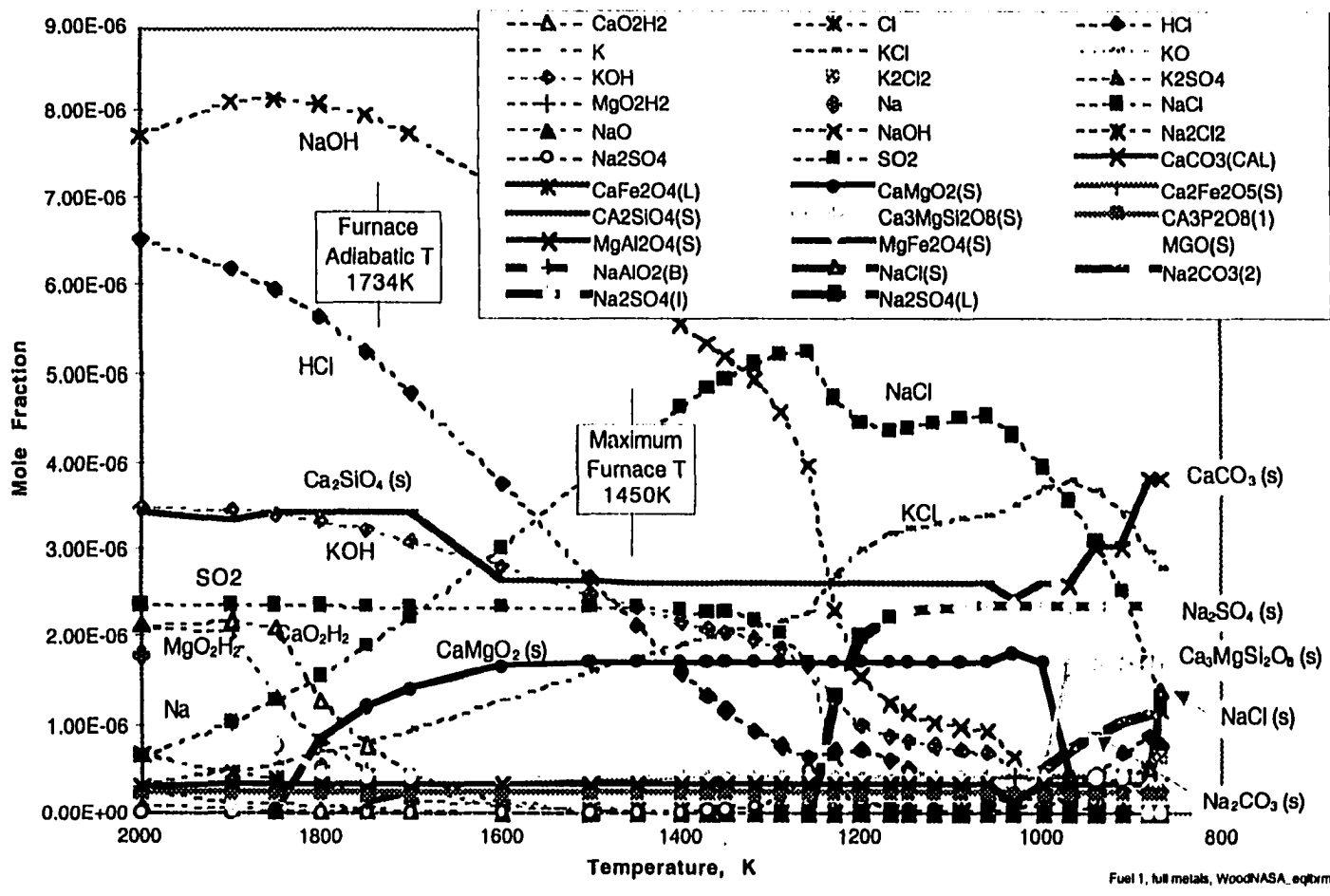


Figure 7.2: Fuel 1 equilibrium calculations for tunnel furnace conditions. Excess oxygen is 7.9% by dry volume, $(\text{Fuel 1 flowrate})/(\text{Total flowrate}) = 0.0085$.

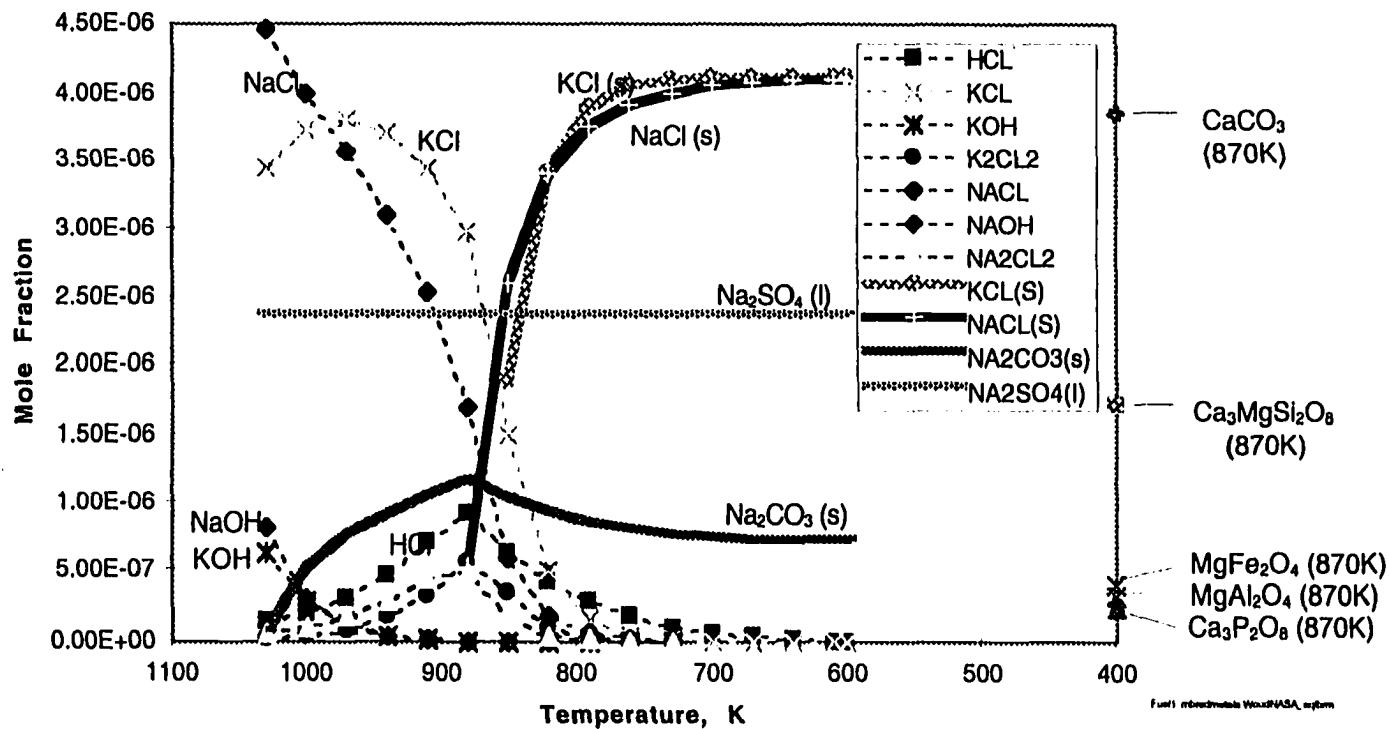


Figure 7.3: Fuel 1 equilibrium calculations for tunnel furnace conditions, alkali species only. Excess oxygen is 7.9% by dry volume, (Fuel 1 flowrate)/(Total flowrate) = 0.0085.

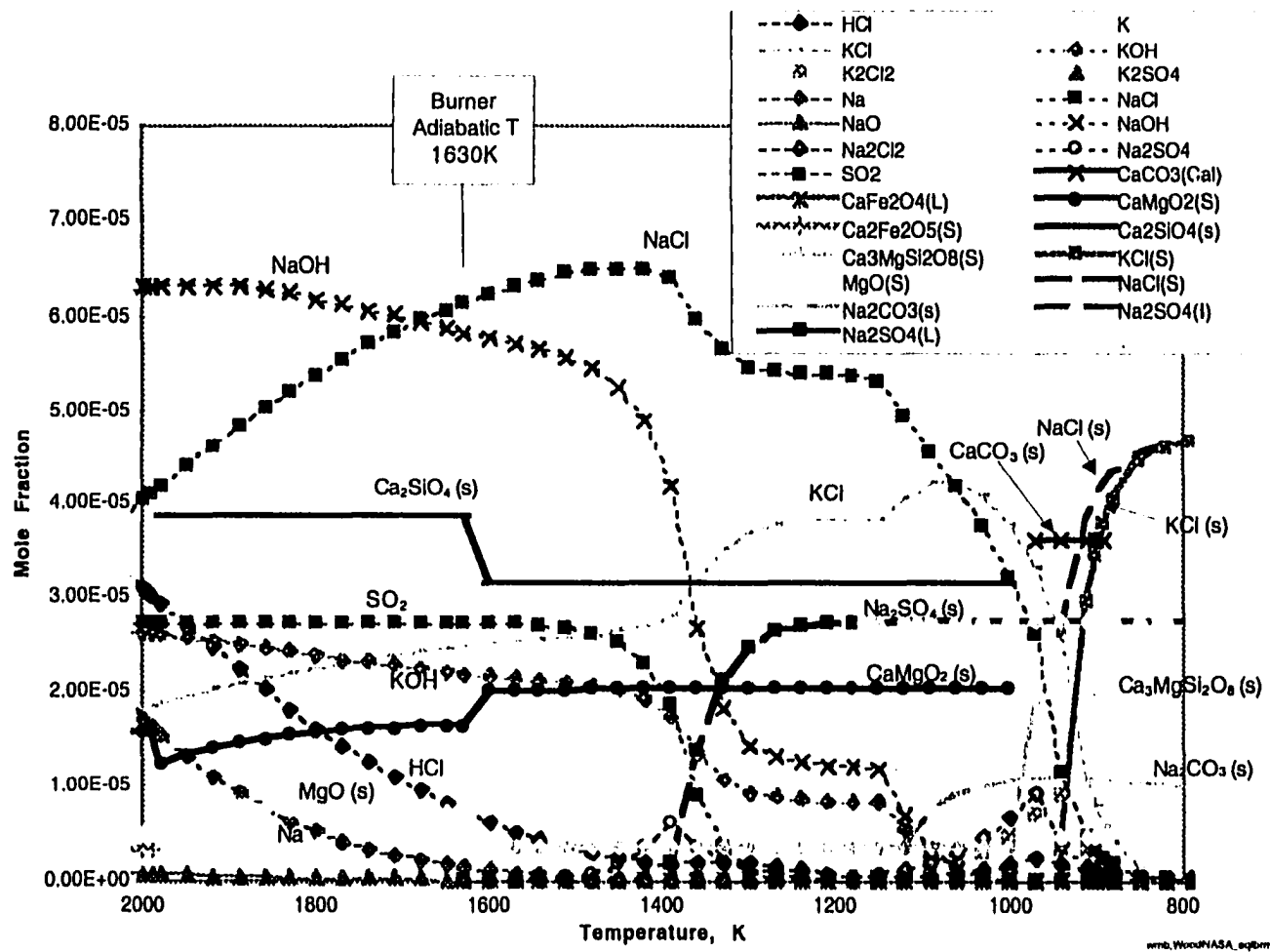


Figure 7.4: Fuel 1 equilibrium calculations for industrial burner conditions. Excess oxygen is 9.3% by dry volume, $(\text{Fuel 1 flowrate})/(\text{Total flowrate}) = 0.094$

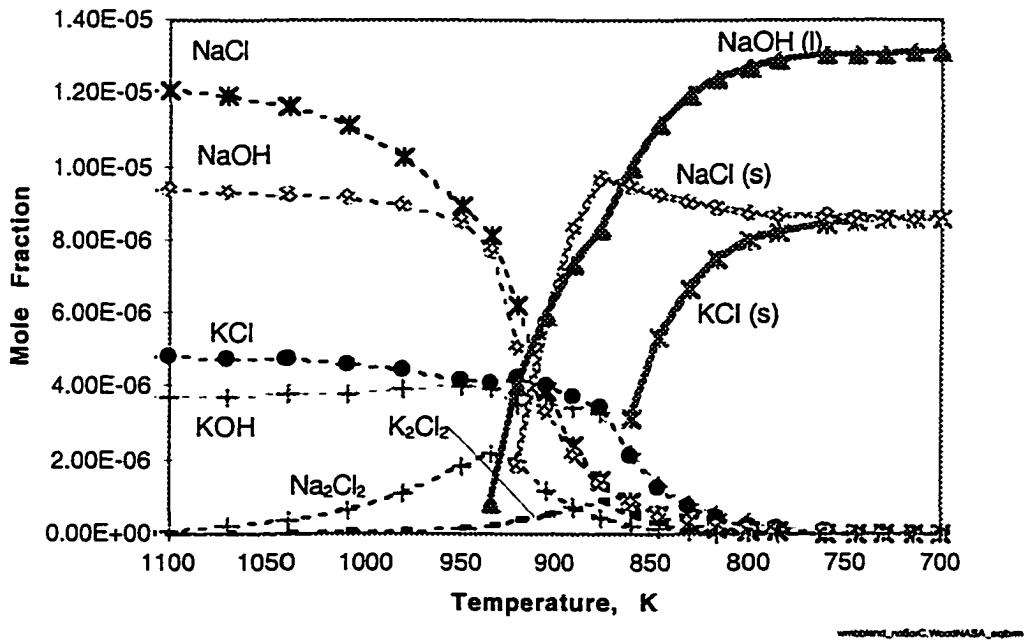
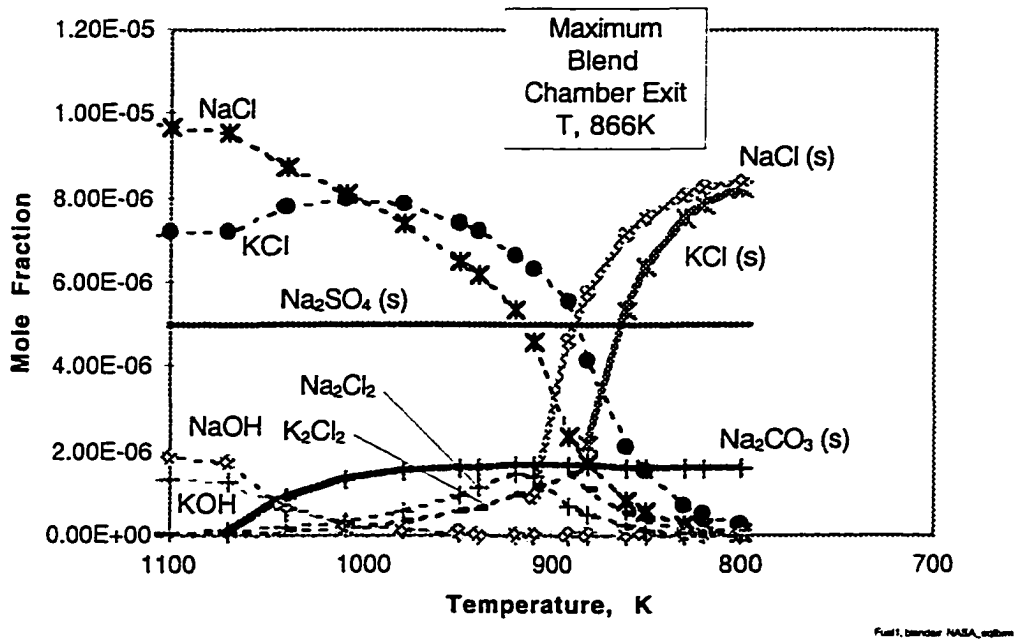


Figure 7.5: Fuel 1 equilibrium calculations for industrial burner conditions in Blend Chamber, with sulfur and carbon included, and with sulfur and carbon not included, (Fuel 1 flowrate)/(Total flowrate) = 0.017

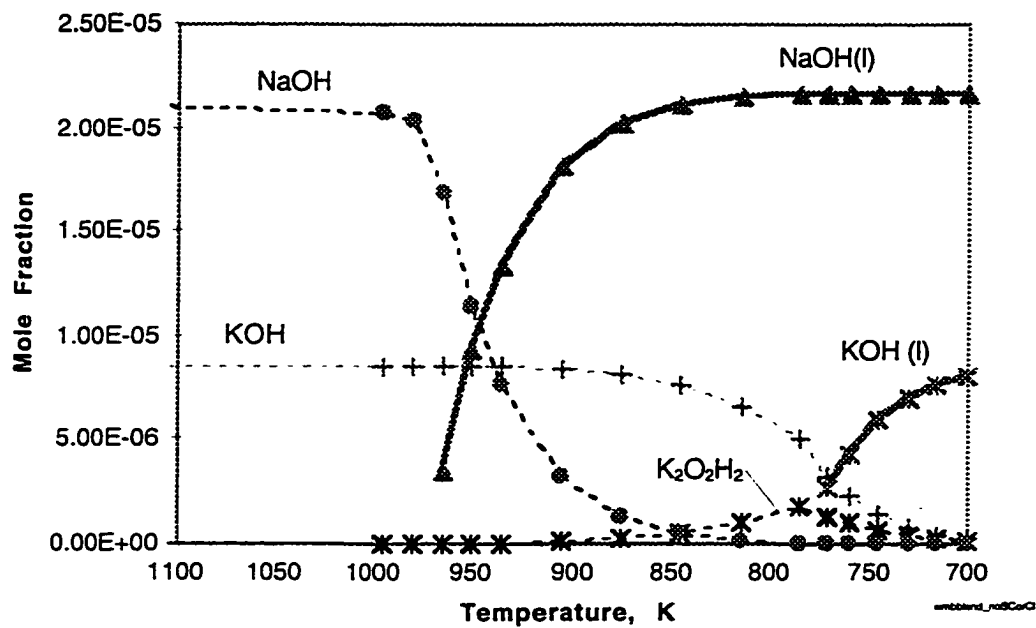


Figure 7.6: Fuel 1 equilibrium calculations for industrial burner conditions in Blend Chamber; sulfur, carbon and chlorine not included, (Fuel 1 flowrate)/(Total flowrate) = 0.017

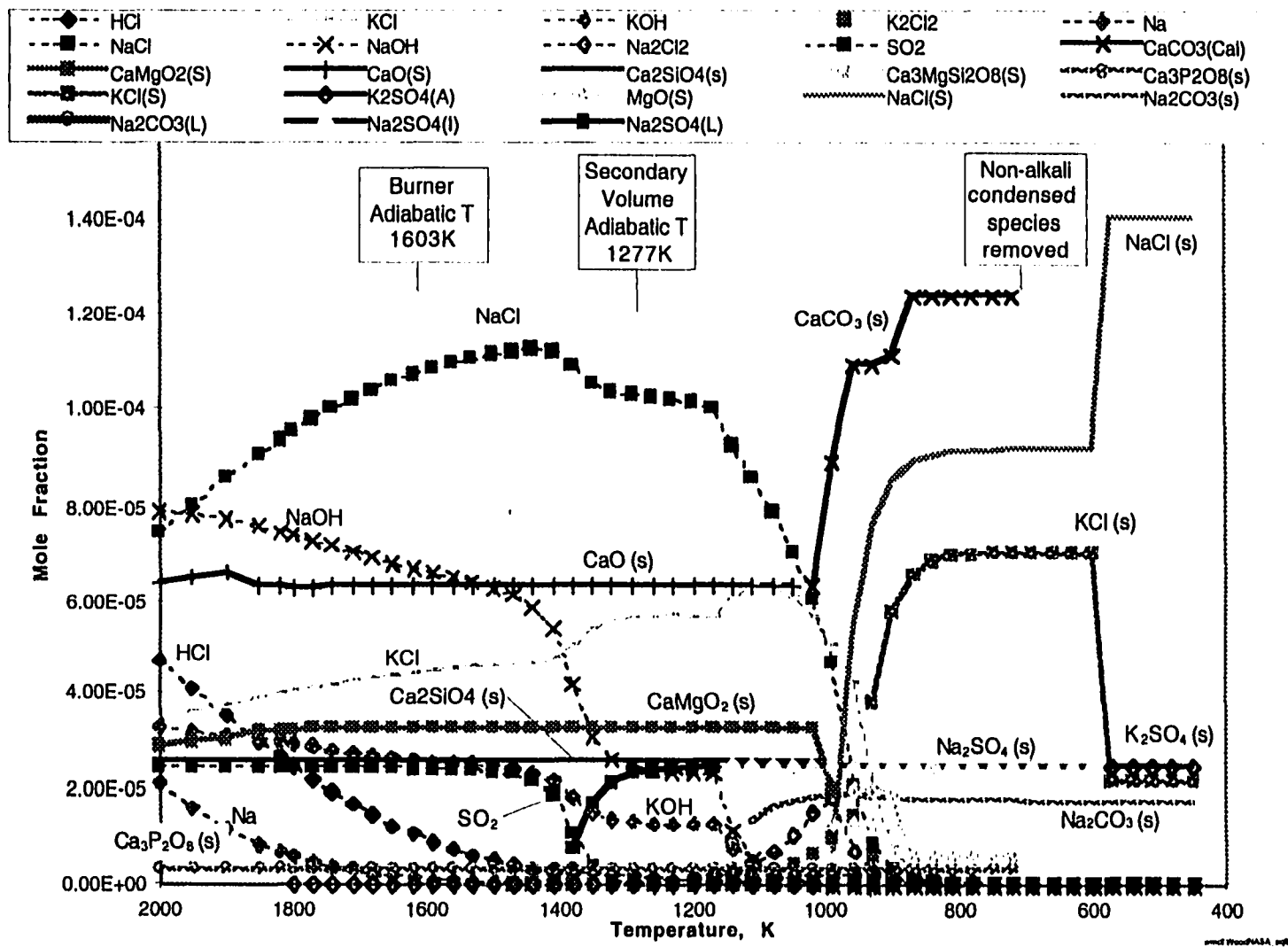


Figure 7.7: Fuel 2 equilibrium calculations for industrial burner conditions, (Fuel 2 flowrate)/(Total flowrate) = 0.093

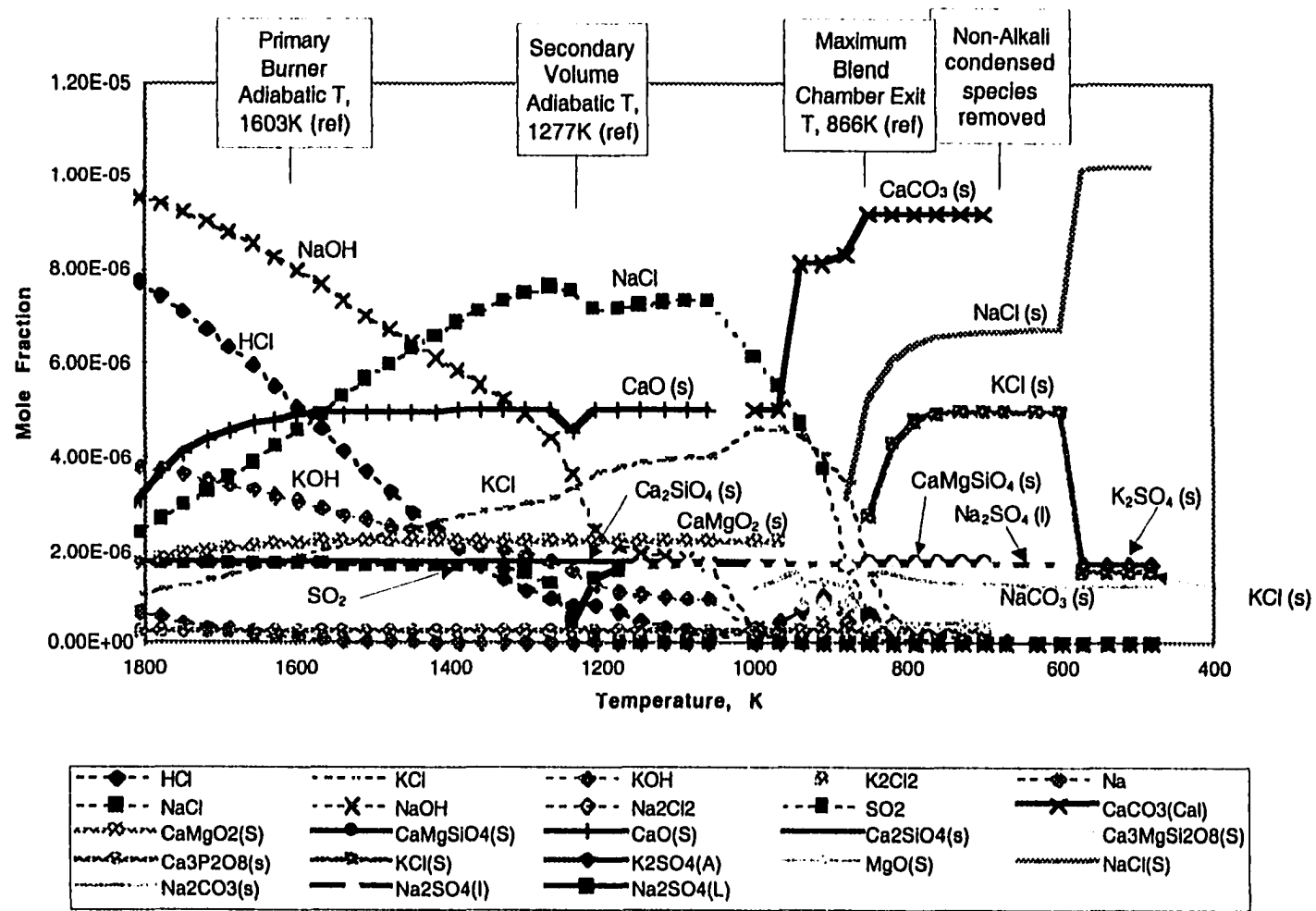


Figure 7.8: Fuel 2 equilibrium calculations for laboratory burner conditions, (Fuel 2 flowrate)/(Total flowrate) = 0.0068

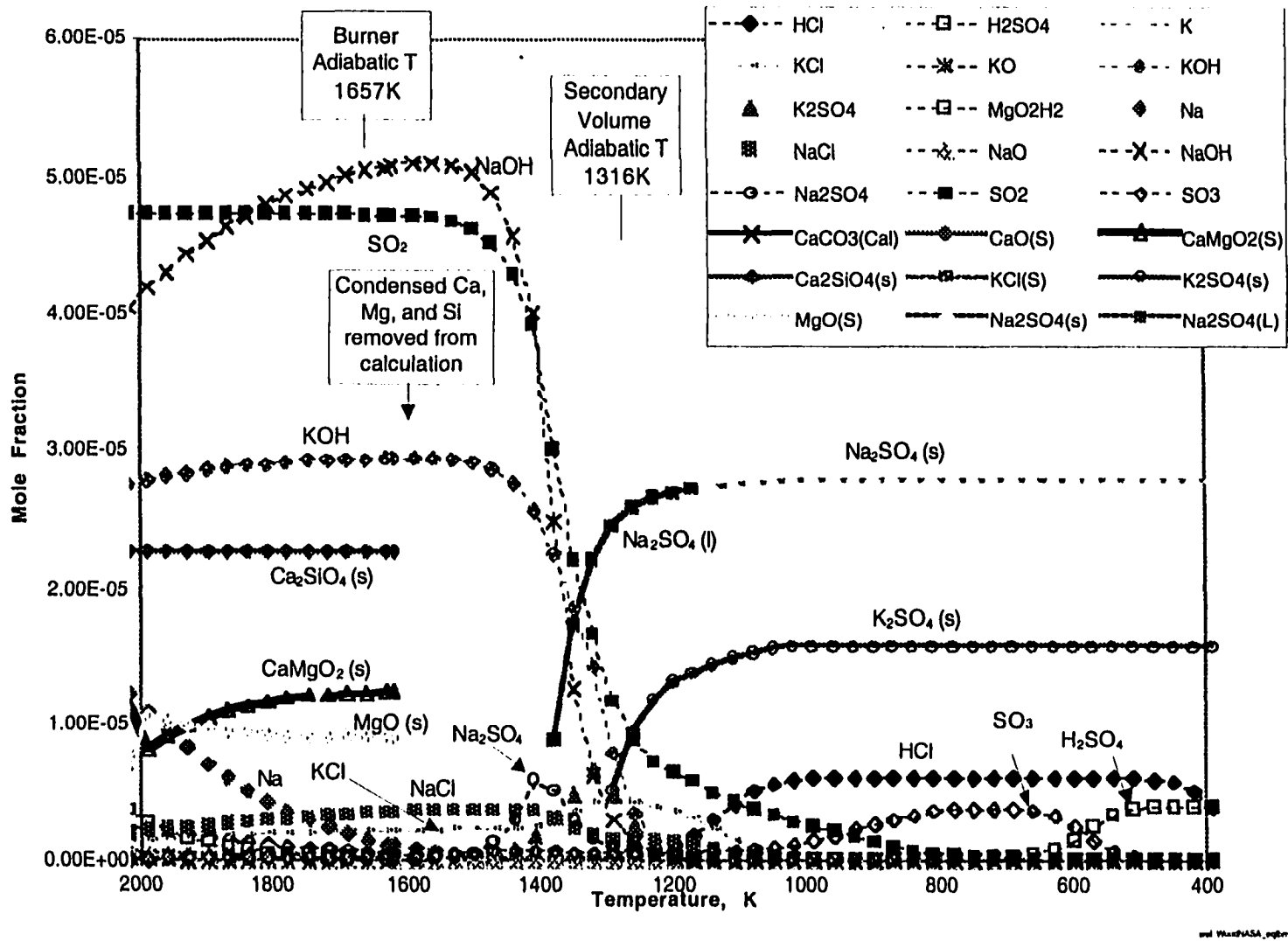


Figure 7.9: Fuel 3 equilibrium calculations for industrial burner conditions, (Fuel 3 flowrate)/(Total flowrate) = 0.090

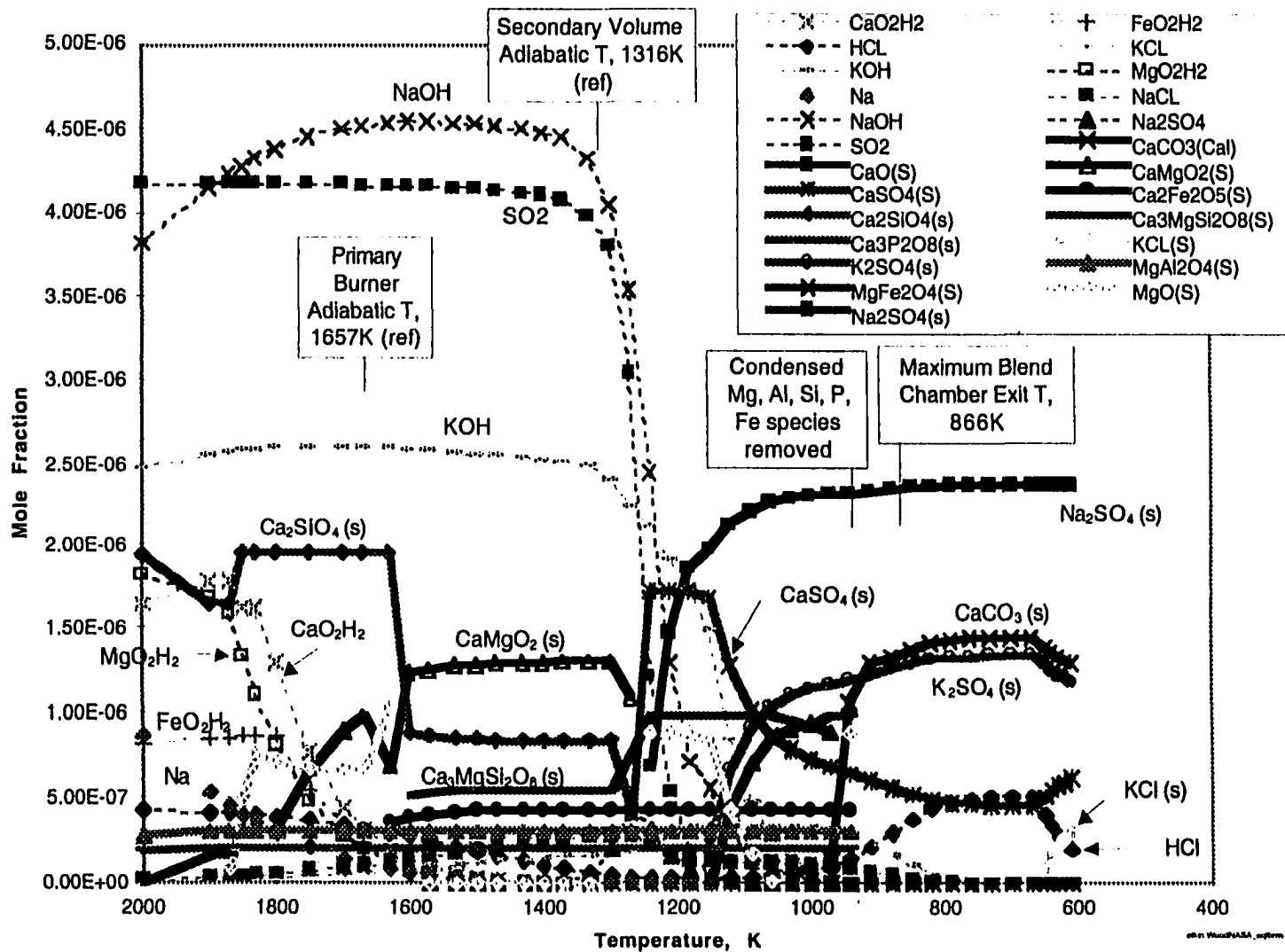


Figure 7.10: Fuel 3 equilibrium calculations for laboratory burner conditions, (Fuel 3 flowrate)/(Total flowrate) = 0.0081

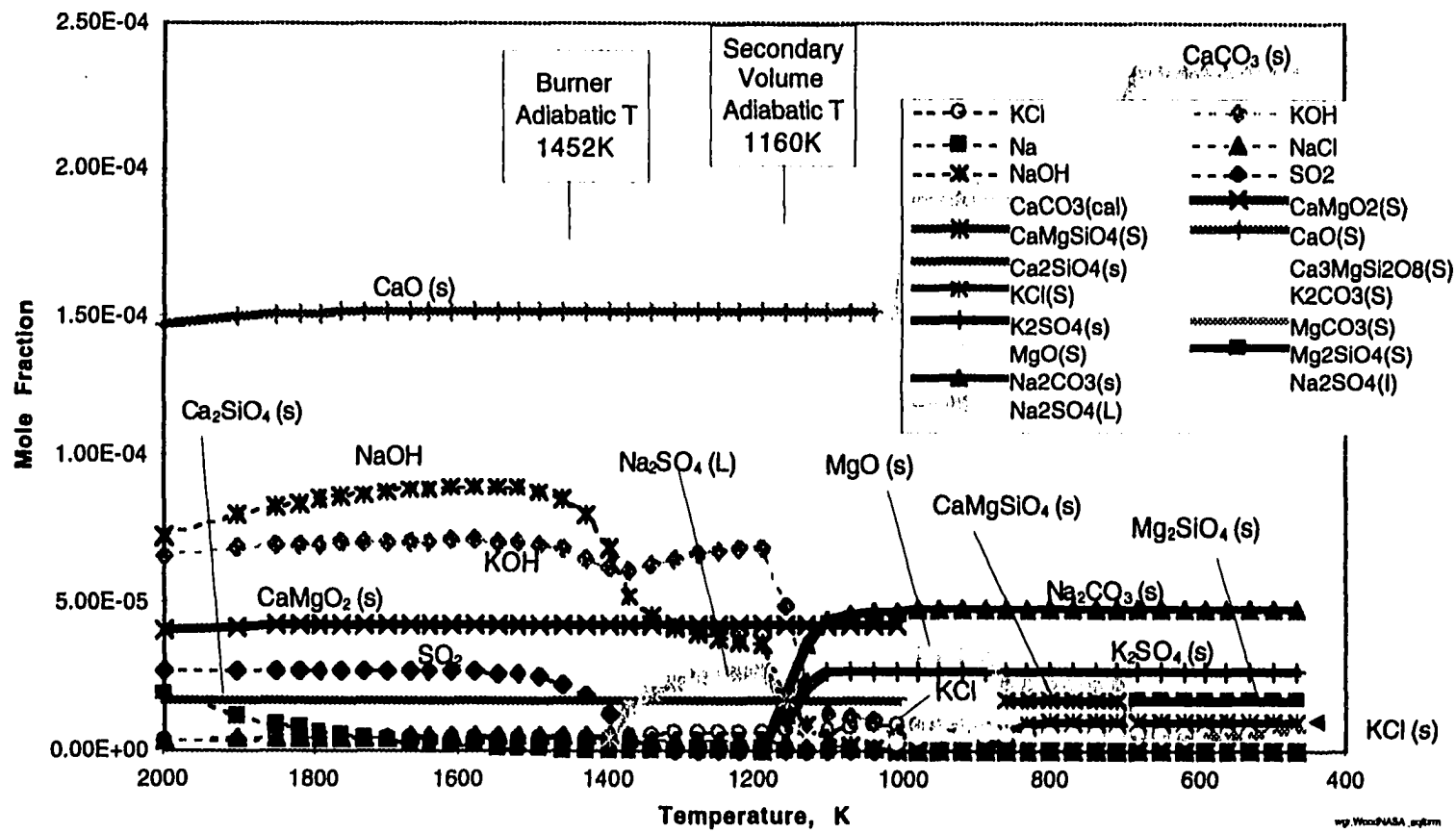


Figure 7.11: Fuel 4 equilibrium calculations for industrial burner conditions, (Fuel 4 flowrate)/(Total flowrate) = 0.087

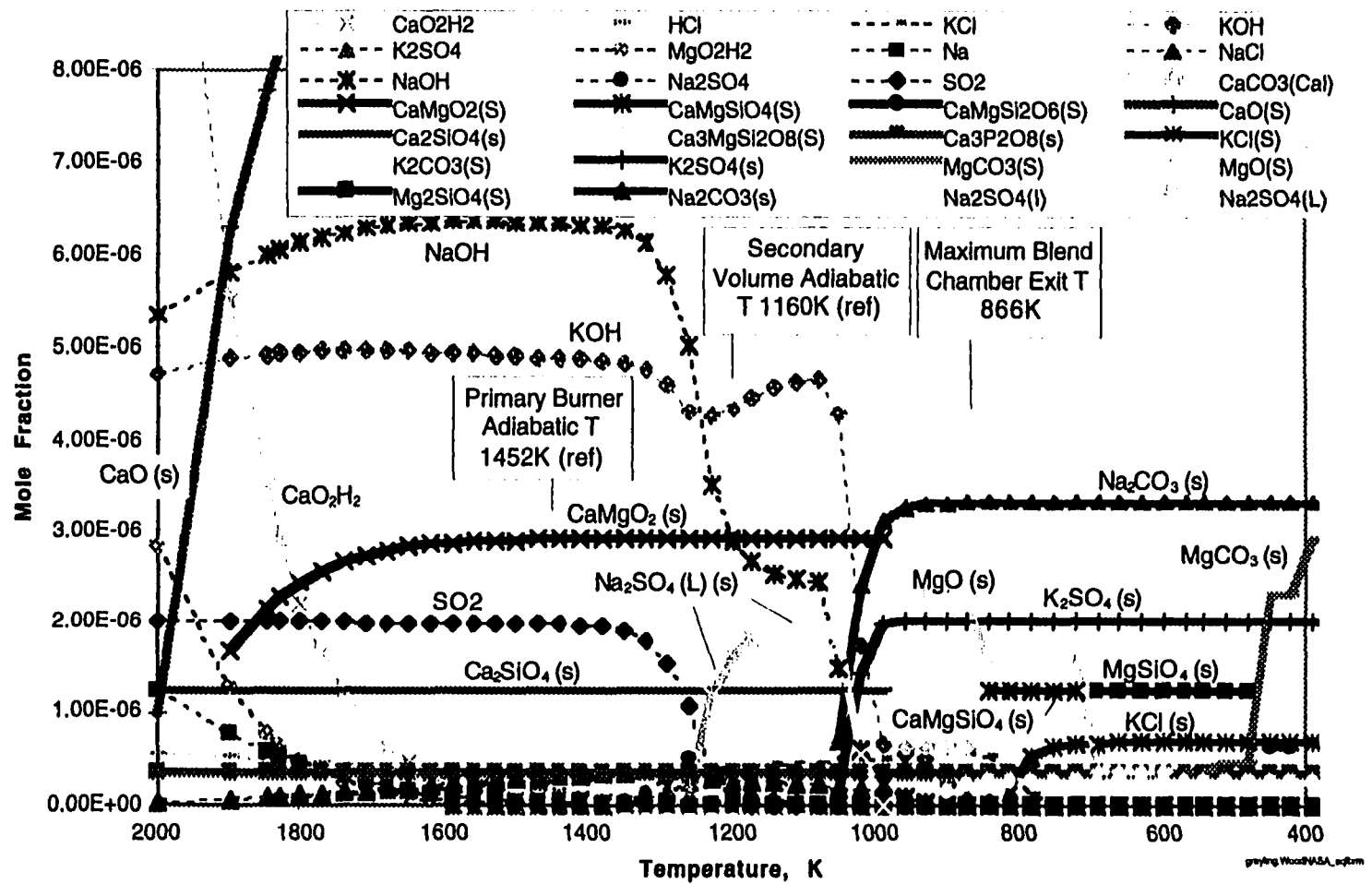


Figure 7.12: Fuel 4 equilibrium calculations for laboratory burner conditions, (Fuel 4 flowrate)/(Total flowrate) = 0.0062

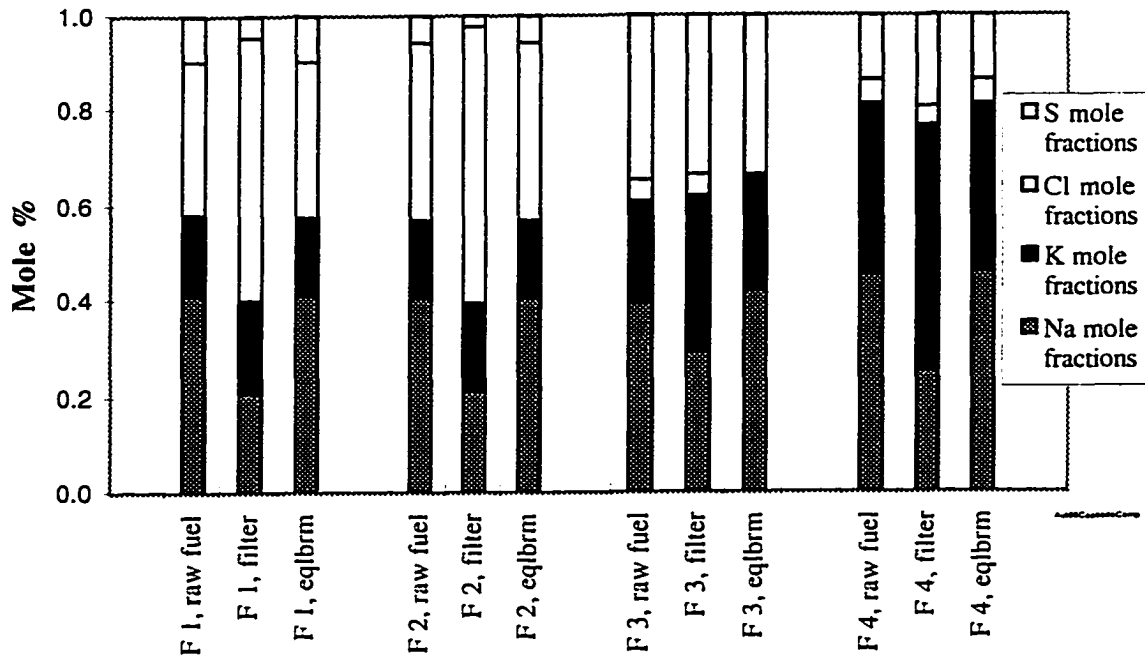


Figure 7.13: Predicted aerosol composition vs. measured aerosol composition. A comparison based on raw fuel composition, aerosol ash composition and equilibrium composition.

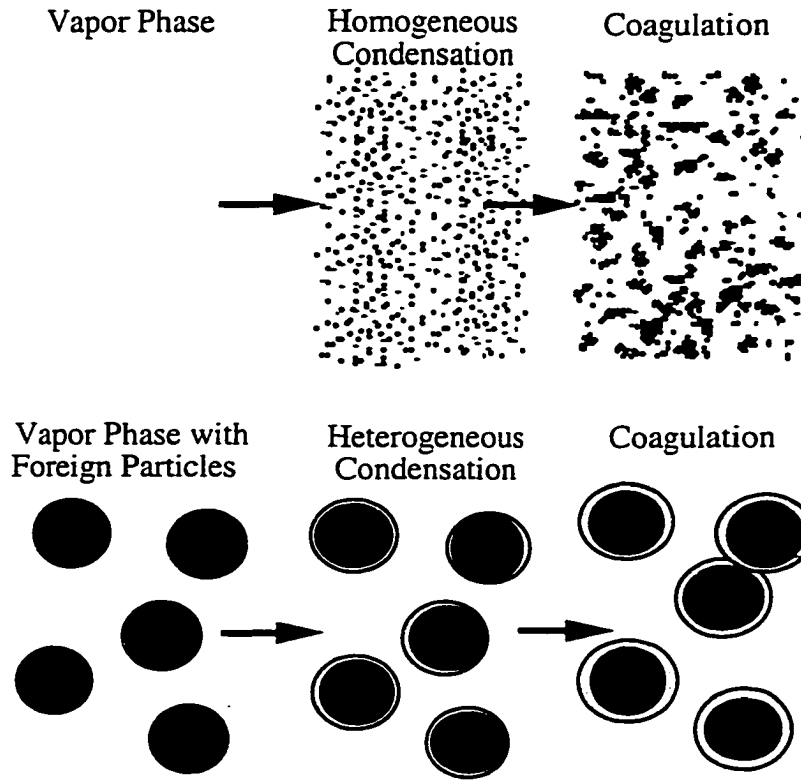


Figure 7.14: Limit cases of homogeneous condensation and heterogeneous condensation in a super saturated environment.

Table 7.3: Saturation Ratio ($S=P_{vap}/P_{sat}$) condensation regimes for systems containing only vapor phase, and systems containing foreign particles.

Saturation Ratio S_{crit} = homogeneous condensation S_{het} = heterogeneous condensation	Vapor Phase with no Foreign Particles	Vapor Phase with Foreign Particles
$S < 1$	No Condensation	No Condensation
$S_{het} < S < S_{crit}$	No Condensation	Heterogeneous Condensation only
$S_{het} < S_{crit} < S$	Homogeneous Condensation	Homogeneous and Heterogeneous Condensation Competition

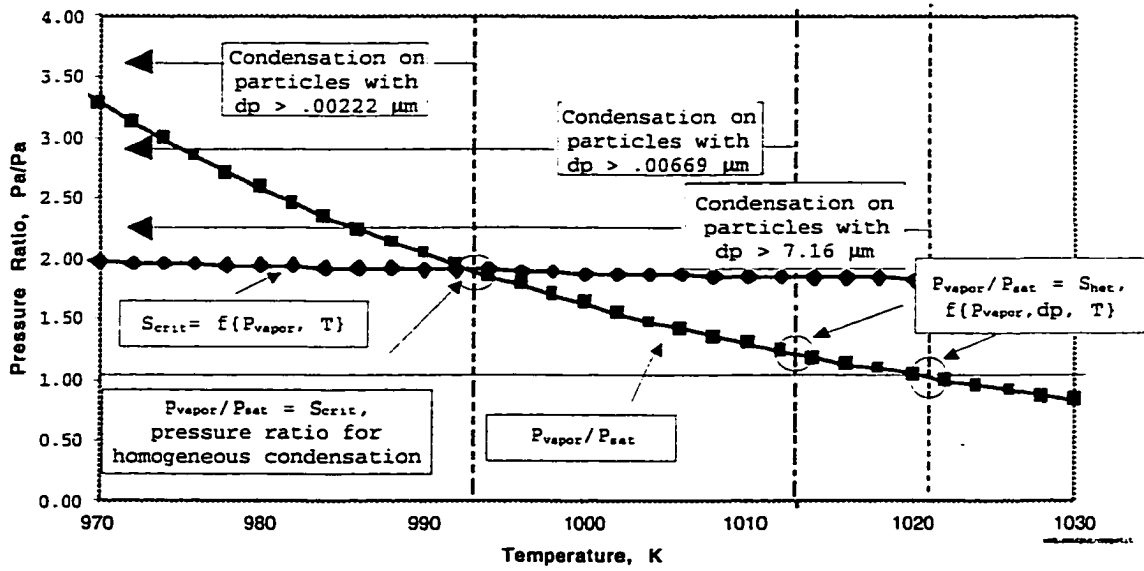


Figure 7.15: Condensation regimes for a system containing NaCl vapor at 14 Pa partial pressure.

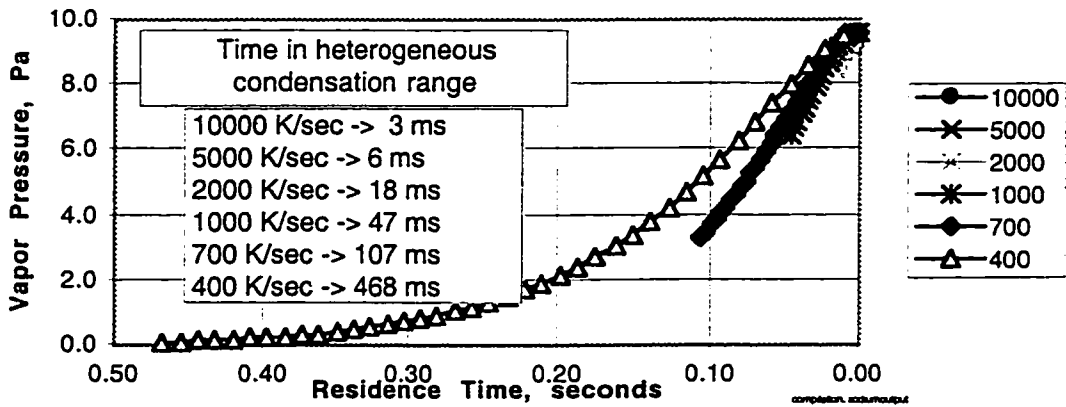
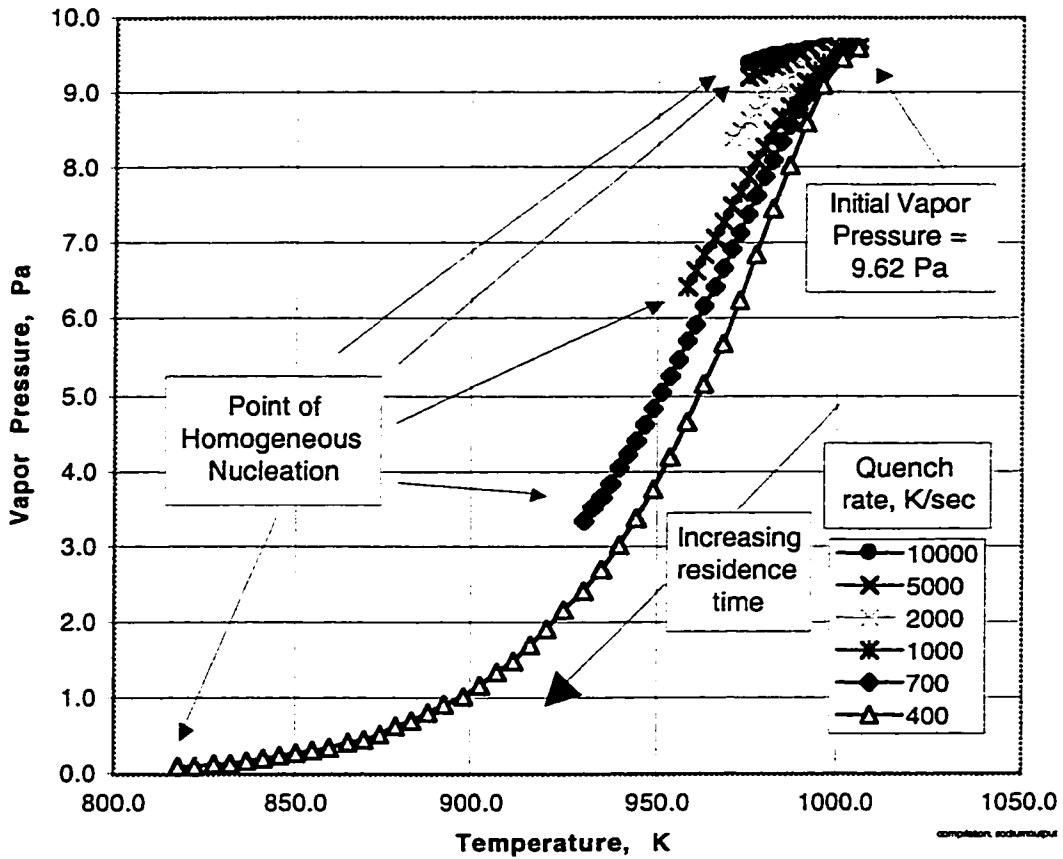


Figure 7.16: Alkali vapor capture by heterogeneous particles as a function of system quench rate for an initial vapor pressure of 9.62 Pa, Fuel/Total Mass = .094. Heterogeneous particle size and number densities: $dp_1 = 7.16 \mu\text{m}$, $4.74e9 \text{ \#/kgFuel}$; $dp_2 = .669 \mu\text{m}$, $2.64e12 \text{ \#/kgFuel}$

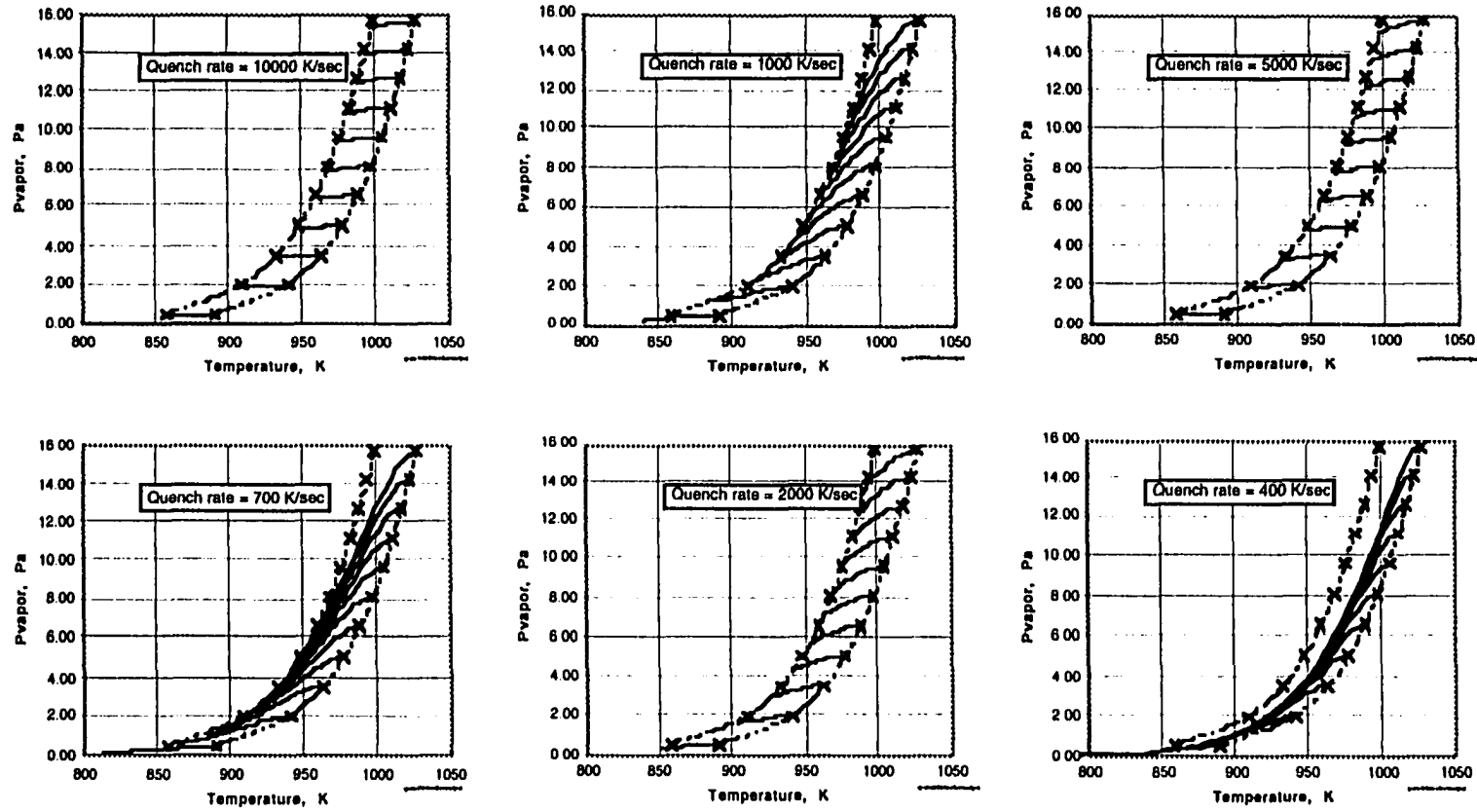
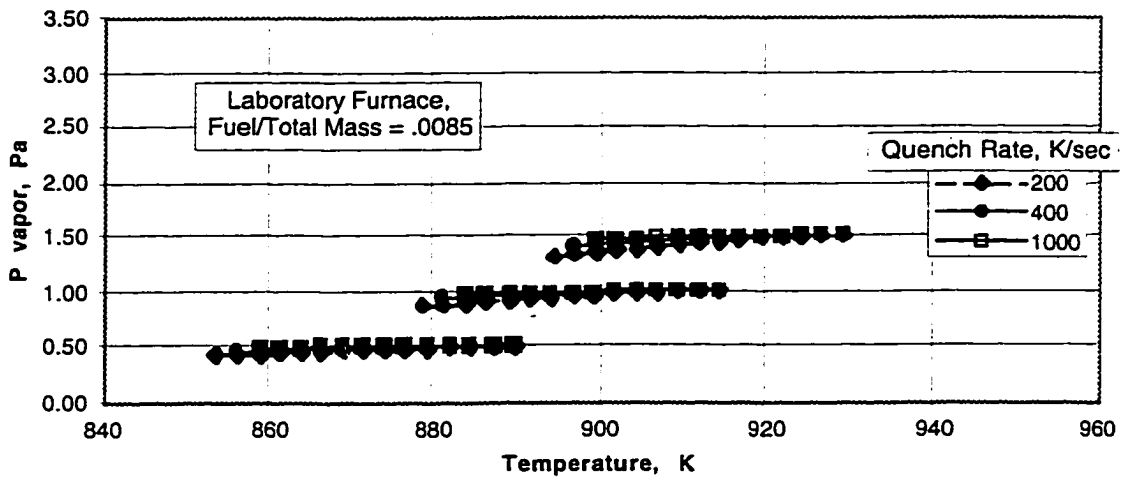
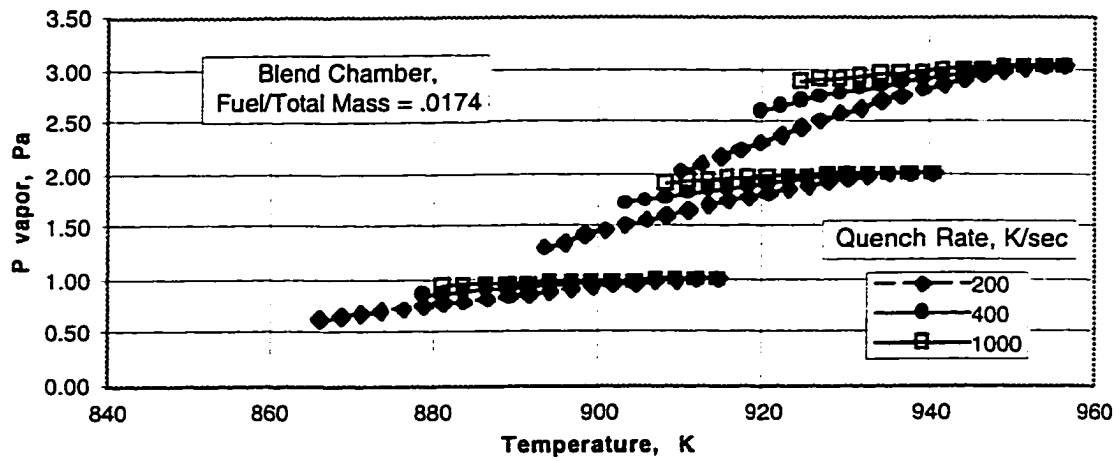


Figure 7.17: Vapor capture by heterogeneous particles as a function of quench rate for Fuel 1, Fuel/Total Mass = .094. Heterogeneous particle size and number densities: $dp_1 = 7.16 \mu\text{m}$, $4.74e9 \text{ \#/kgFuel}$; $dp_2 = .669 \mu\text{m}$, $2.64e12 \text{ \#/kgFuel}$.



Example Alkali Loading	Industrial Burner Blend Chamber	Laboratory Burner
Fuel 1 NaCl	1.1 Pa	0.5 Pa
Fuel 1 NaCl x 1.4	1.7 Pa	0.7 Pa
Fuel 1 NaCl x 2.4	2.7 Pa	1.3 Pa

Figure 7.18: Change in Alkali vapor pressure with quench rate, for Fuel 1 in Industrial Blend Chamber and Laboratory Furnace. Heterogeneous particle size and number densities: $dp_1 = 7.16 \mu\text{m}$, $4.74e9 \text{ \#/kgFuel}$; $dp_2 = .669 \mu\text{m}$, $2.64e12 \text{ \#/kgFuel}$.

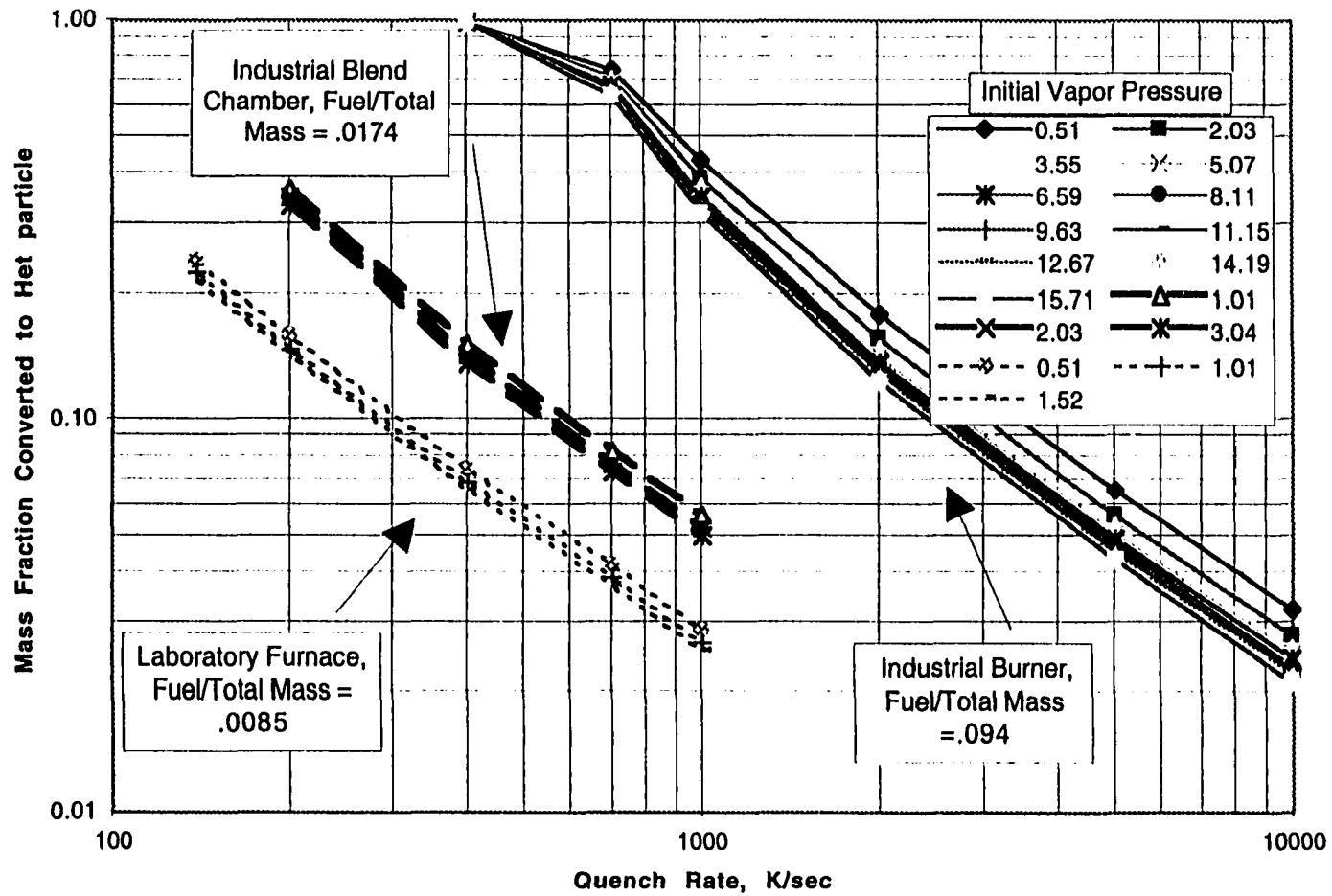


Figure 7.19: Comparison of heterogeneous collection efficiency as a function of Quench Rate and dilution ratio for Fuel 1. Heterogeneous particle size and number densities: $dp1 = 7.16 \mu\text{m}$, $4.74e9 \text{ \#/kgFuel}$; $dp2 = .669 \mu\text{m}$, $2.64e12 \text{ \#/kgFuel}$.

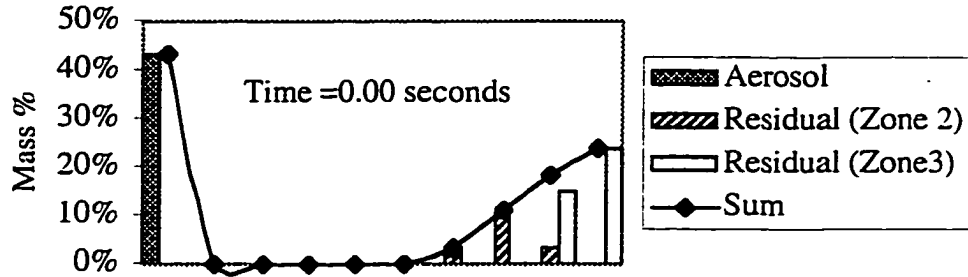


Figure 7.20: Fuel 1 aerosol coagulation in industrial blend chamber at initial conditions

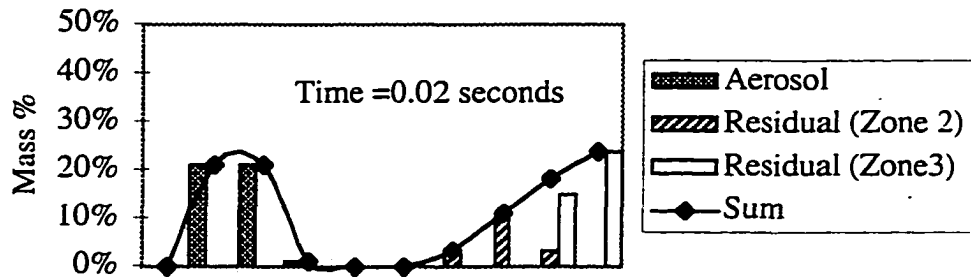


Figure 7.21: Fuel 1 aerosol coagulation in industrial blend chamber at 0.02 seconds

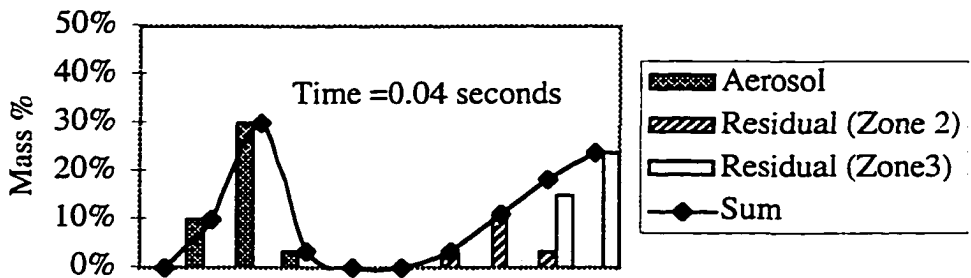


Figure 7.22: Fuel 1 aerosol coagulation in industrial blend chamber at 0.04 seconds

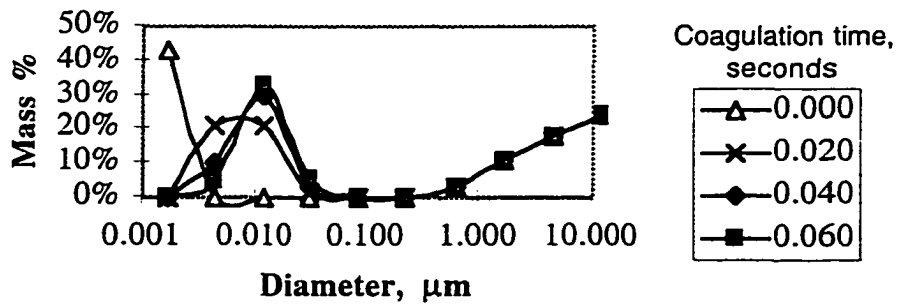


Figure 7.23: Fuel 1 aerosol coagulation in industrial blend chamber as a function of time

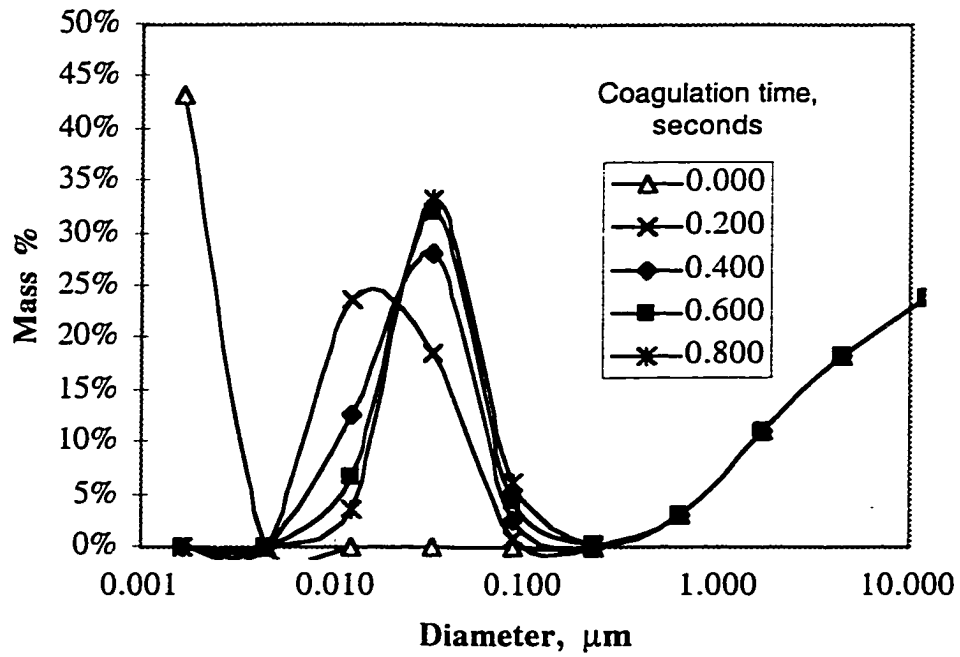


Figure 7.24: Fuel 1 aerosol coagulation in industrial blend chamber for long residence

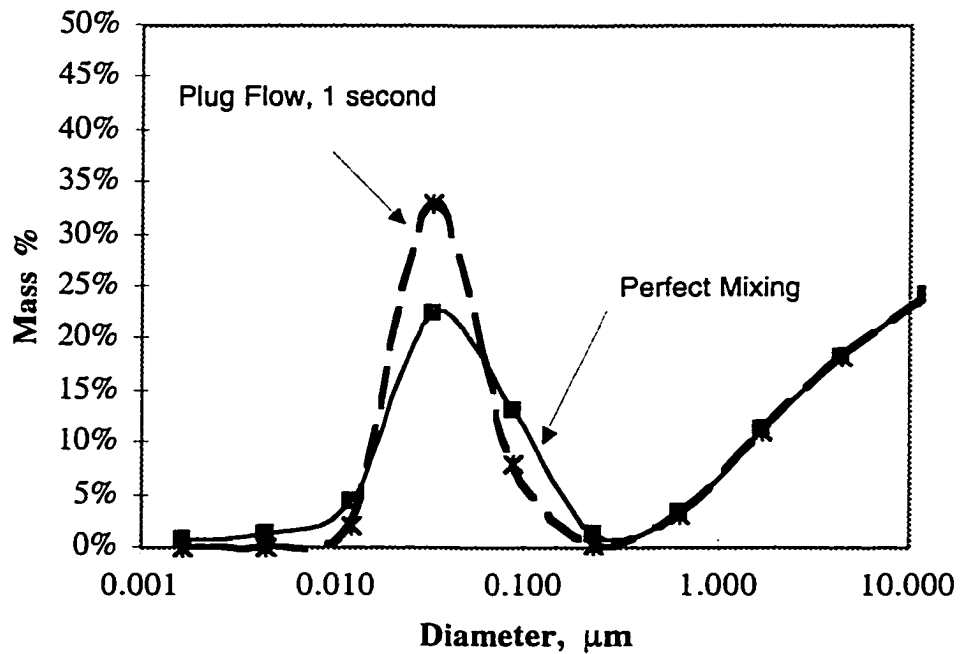


Figure 7.25: Fuel 1 aerosol coagulation in industrial blend chamber, comparing limit cases of plug flow versus perfect mixing

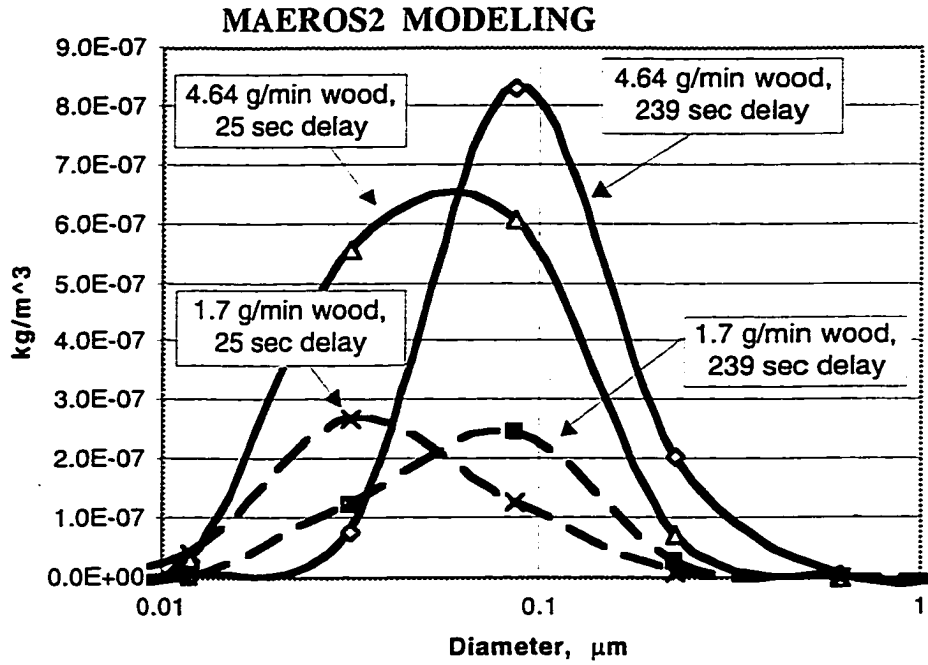


Figure 7.26: Fuel 1 aerosol coagulation in the EAA delay tank as calculated by MAEROS2

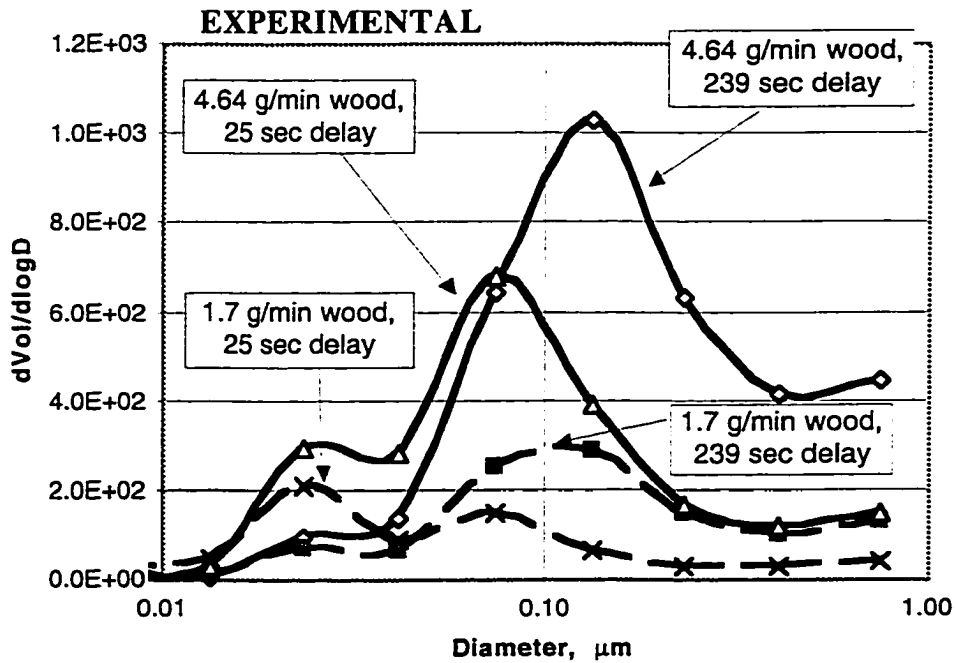


Figure 7.27 Fuel 1 aerosol coagulation in the EAA delay tank as measured experimentally

CONCLUSIONS AND SUMMARY

Understanding and predicting residual and aerosol ash properties of biomass and coal fuels is of paramount importance to the industrial community. Potential for excessive slagging, fouling, corrosion, and/or aerosol escape continues to separate viable fuel sources from unusable fuel sources. Development of reliable prediction methods and libraries of ashing characteristics for pulverized fuels significantly aids in the design of cost effective industrial facilities.

The body of work presented here is an investigation into the ash characteristics of industrially significant sawdust/sanderdust fuels. The two primary objectives are: 1) Accurately characterize the morphology and composition of the residual and aerosol ash, and 2) Develop a modeling methodology useful for predicting the characteristics of the ash formed by sawdust/sanderdust combustion, with particular focus on the aerosol mode.

Like many clean biomass-derived fuels, the fuels tested are high in alkali and low in clay minerals compared to coal. High alkali fuels have presented challenges to industry. They typically generate highly mobile sub-micron aerosol ash via a vaporization/condensation mechanism. This sub-micron particulate matter often leads to fouling in the convective pass of industrial boilers. Sub-micron ash that is not retained by the furnace must be efficiently cleaned from the flue gas for health and environmental reasons, reasons which are enforced with federal regulations. Generally, efficient aerosol capture requires expensive pollution control equipment. Alkalies can also combine with clay minerals to form low melting eutectics. These are capable of forming glass-like slags, as well as producing “sticky” surfaces for accelerated fouling. Hence, the study of these high alkali fuels is an important step in cataloging behavior and developing useful predictive models.

A secondary objective of this work is to present an investigation of ash morphology for a well-characterized set of research coals and artificial chars. This database serves as a source of comparison for the sawdust/sanderdust experiments and explores variables affecting coal aerosol yield.

Sawdust/sanderdust Results

Ash size distributions as determined by the cascade impactor showed three mass modes. Scanning Electron Microscopy (SEM) and Energy Dispersive X-ray Spectroscopy (EDS) were used to investigate these distinct modes. In brief, the modes can be described as:

- *A residual mode composed of large particulate matter, on the order of 8 μm and larger.* This mode contains the bulk of residual ash and is dominated by calcium-based porous structures. It is hypothesized that the porous nature of these structures is related to the distribution of calcium in the cell walls of the parent fuel. Organically bound calcium is converted to oxide or carbonate as the cell walls collapse, with little fluxing. Magnesium, the other alkaline earth element in the fuel, is also present. All other elements are less well represented.

EDS showed little complexing or surface deposition of alkali metals in the large residual mode. Low mobility of the large residual mode and low fluxing due to high Ca concentrations is the likely reason for the lack of alkali metals.

- *A secondary residual mode near 2 μm .* This mode is more chemically and morphologically diverse than the large residual mode. Both spherical particles (indicating full melting) and porous structures are present. It is suggested that the melts are evidence of eutectic formation, with alkali metals being the active fluxing agents. These eutectic melts are mobile compared to unmelted structures, and therefore are susceptible to separation from the parent ash particle. The average size of a single melt particle is governed by the *local* combustion conditions and the *local* mineral matter composition. Hence, the magnitude and the location of this size mode may be the result of natural segregation of the eutectic material.

The high volatility of the alkali allows most of the alkali to escape, but a fraction is captured by solidifying melts as they enter a two-phase region. Smaller particles near 0.4 μm show more alkali content and a very uniform size. Fluxing appears to be driven by alkalis here as well, but deposition via condensation is also likely.

- *An aerosol mode near 0.1 μm .* This mode is composed primarily of alkali chlorides when chlorine is available, and sulfates when chlorine is not available. These conclusions are based on EDS measurements modified to remove the background signal of the filter substrate. Although simple equilibrium predicts condensed sulfate to form prior to condensation of vapor phase alkali chlorides, sulfur does not appear to displace chlorine on the aerosol particles. Sodium appears to be under-represented in the aerosol mode relative to potassium. Preferential complexing of sodium with the limited amount of silicates available is suggested.

Cascade Impactor and SEM work suggests that the aerosol may be composed of particulate matter of more than one size mode. Determination of the magnitudes of these individual modes was investigated with an isokinetic sampling probe, a delay tank to control coagulation time, and an Electrical Aerosol Analyzer. It was found that the aerosol size distribution is a function of the variables that influence coagulation, specifically the initial aerosol density (mass/volume) and time.

Tests with no delay tank, a 25 second delay tank, and a 239 second delay tank demonstrated that the 0.1 μm peak is formed over time by coagulation of much smaller particulate matter. The maximum mode diameter migrates from less than 0.01 μm to about 0.1 μm as coagulation time increases. Long coagulation times (239 seconds) leads to an aerosol peak near 0.1 μm for all sawdust/sanderdust fuels.

Sampling vapor-phase alkalies and quenching by dilution results in a low initial number density of nucleated alkalies. This low initial number density results in slow coagulation. Sampling and diluting *after* initial nucleation results in high number densities and very fast coagulation prior to entering the probe. After entering the probe, coagulation continues as before, but much of the coagulation process is already accomplished.

It is concluded from the EAA tests that aerosol is formed via homogeneous nucleation/condensation. This particulate matter is initially less than 0.01 μm in diameter but quickly coagulates to a larger diameter. The ultimate diameter of the particulate matter can be modified, with dilution and coagulation time being the control variables.

Modeling Results

Modeling was approached in a modular form. By splitting the process into three elements, the role and importance of each modeling element is isolated. These elements are: 1) Equilibrium calculations to investigate the preferred species of alkali metals and the residual elements, 2) Condensation modeling to determine the partitioning of alkali metal vapor between homogenous particulate formation (self-nucleation) and deposition on existing residual particles, and 3) Coagulation modeling to determine the ultimate diameter of nucleated aerosol particulate matter.

Equilibrium:

A simple equilibrium model, which includes condensed phase species but does not incorporate eutectic formation, predicts an aerosol mode driven by alkali vaporization and condensation. Alkalies are expected to vaporize to form alkali chlorides, when chlorine is present, as well as hydroxides. No significant alkali sulfates in vapor phase are expected. As the gases cool, sulfates are favored by equilibrium to form a condensed phase, followed by condensation of vapor phase alkali chlorides. However, it is clear from the present experiments that sulfate formation is limited relative to the rapid condensation of vapor phase chlorides. This illustrates the limitations on conclusions drawn from equilibrium predictions. In particular, condensation events accompanied by a change in composition requires a reaction. This imposes a kinetic limitation that might not be overcome in reality. The data show this for Fuels 1 and 2. Here, the predominant aerosol anion is chlorine, even though sulfates are the favored equilibrium product and sulfur is present in abundance. It is clear that the sulfur cannot displace the chlorine as an anion. Whether this is due to a pure chemical kinetic constraint, or a transport limitation (*e.g.*, the resistance of a thin product layer of sulfate on alkali chloride particles to the diffusion of sulfur to the chloride substrate) is not known.

Complexing of the alkali species with silicates is also not predicted, since this is a eutectic formation process that is beyond the capabilities of the NASA CET89 program. Additionally, this complexing is a *local* mineral matter concentration phenomena rather than an *overall* composition phenomena, so system equilibrium calculations are not appropriate tools to investigate this. Low mobility of liquid and solid phases to form equilibrium compounds is an obvious limitation.

Equilibrium shows that non-alkali metals and silicon form residual solids that are not expected to vaporize at standard industrial furnace temperatures. Equilibrium predicts they will form complex species that can recombine to form new species at cooler temperatures. In the absence of other mineral species, oxides are generally the favored form of non-alkali metals (*e.g.* MgO (s)). Recombination of solids to form new solid species at lower temperatures is surely a phenomena limited to very minor surface reactions between colliding residual particles.

Condensation Modeling:

A modeling program was written to determine the fate of alkali chlorides that enter the vapor phase. One pathway is self-nucleation (at the critical saturation ratio) to form highly mobile particles, which ultimately coagulate. The other pathway is heterogeneous condensation on particles in the residual mode, which results in a low number density and little coagulation. This model is based on diffusion-driven vapor transport (both continuum and free molecule modes considered) for heterogeneous condensation, and the critical saturation ratio (*i.e.* diameter) for homogeneous condensation. The Kelvin effect, accounting for the influence of particle curvature on vapor pressure, is also included.

This model showed that the critical temperature range for condensing alkali vapor onto existing residual particles is dictated by the diameter of the existing residual particles (upper bound), and the vapor pressure of the condensable alkali vapor (lower bound). For a given heterogeneous particle diameter and alkali vapor pressure, there exists a temperature at which condensation on the particle surface will occur. Maintaining a temperature below this temperature, yet above the self-nucleation temperature, promotes heterogeneous condensation.

The conversion efficiency of vapor phase alkali to heterogeneous particles is a logarithmic function of the quench rate between the temperature at which heterogeneous condensation starts, and the temperature at which homogeneous nucleation starts. Therefore, conversion efficiency can be modified significantly with small changes in quench rate, as long as the quench environment is relatively gentle.

A finding of practical significance is that dilution ratio is an important control parameter. In order to obtain the highest conversion efficiency to the larger, more easily removed heterogeneous particles in an industrial dryer application, the undiluted flue gas should be quenched through the temperature range of conversion prior to dilution. This may be best

accomplished by staged dilution. Additional dilution air may be added downstream of an insulated volume (*i.e.* a slow quench zone), in order to obtain the desired dryer inlet temperature and volumetric flow rate.

Coagulation Modeling:

Coagulation modeling of the industrial burner blend chamber demonstrated that coagulation changes the ash size distribution only below $\approx 1 \mu\text{m}$. The coagulating aerosol is expected to converge to about $.05 \mu\text{m}$ under typical conditions for an industrial burner. Residual modes above $1 \mu\text{m}$ are not expected to change, due to low Brownian mobility. Results suggests that the *major* mode diameter of sub-micron aerosol may be reasonably predicted by assuming the aerosol is composed of the alkali components of the parent fuel, in the form of alkali chlorides and alkali hydroxides.

Pulverized Coal and Artificial Char Results

Investigations with these fuels was limited to mass distribution measurements obtained using the tunnel furnace, water-cooled probe, and cascade impactor.

Experiments with unmodified coals show similar ash size distributions for all three coals tested: A sub-micron aerosol mode, a $3 \mu\text{m}$ mode, and a $> 9 \mu\text{m}$ mode. The aerosol is most likely formed from condensed and coagulated vapors, while the $3 \mu\text{m}$ and $\geq 9 \mu\text{m}$ modes are fragmented and coalesced residual ash.

The sum of aerosol from individually burned aerodynamically-sized coal fractions is greater than the aerosol yield of the whole coal. This is demonstrated with Upper Freeport coal, in which the aerosol yield was about 0.25% of the total ash for the whole coal, compared to 0.75% of the total ash for the summed coal fractions. This lends support to the conclusion that alkali vapor release is attenuated by close association of mineral inclusions, since this close association is disturbed by the aerodynamic sizing process.

The ash size distribution is not identical for all aerodynamically-sized coal fractions. Sized Upper Freeport of $< 18 \mu\text{m}$ contributes as much mass to the $4 \mu\text{m}$ mode as all other size cuts combined. Ash from size cuts greater than $18 \mu\text{m}$ are predominantly greater than $9 \mu\text{m}$ in diameter. If the $4 \mu\text{m}$ mode is assumed to be formed by the surface shedding of fine

particles during char combustion, then the finer coal cut should have a higher yield since it exposes the most surface area per unit mass.

The experiments with bentonite-doped artificial char show that aerosol yield generally decreases with increasing bentonite, although the affect of incomplete burnout and experimental uncertainty cannot be ignored. Suppression of aerosol fraction is most likely alkali metal absorption by bentonite inclusions as the surface of the char particle recedes during combustion, as has been noted by other researchers

Experiments with calcite chars show that calcite fragmentation is limited, with most mass remaining in the large ($>9 \mu\text{m}$) particle range. This results in very little surface area for sodium interaction. Sodium and calcite interaction is also probably limited because of the high melting temperature of CaO , which is the favored species above 900°C . This limits the opportunity for chemical interaction between sodium and calcium.

Pyrite minerals exhibited significant fragmentation, as has been observed by other researchers. Like bentonite, the pyrite generally shows a reduction in aerosol yield with increased mineral content, although it remains to be determined if this is a result of sodium/pyrite interaction, or is too small observe relative to the experimental uncertainty.

Suggested Future Investigations

Past investigations by other researchers into the mechanisms of ash transformations have always left room future research. The complexity of ash formation mechanisms dictate that the current investigation is no exception. Hence, this research may be the starting point for the following future investigations:

- Benefication of coal to reduce mineral content has shown some success, but potentially increases the sub-micron aerosol yield. An area worthy of further investigation is benefication of high-alkali fuels by leaching. Some work has been done in this area with naturally leached rice straw (Jenkins *et al.*, 1997). Modifying the current sawdust/sawdust samples by a simple water leach process may yield results of practical significance to the industrial community.

- Doping of the current fuel with finely dispersed clays might also be of interest. This may be done concurrently with the leaching process mentioned above, by leaching the fuel with clay in a water suspension as a final rinse. Ideally, surface tension would hold the suspended clay onto the fuel particles during evaporative drying. The clay would act as an alkali sink as vapor attempted to leave the particle during combustion, and as a deposition surface during the condensation phase. Critical parameters are uniform distribution of the char surface, and clay particle size, respectively. Of course, potential for slagging must be recognized.
- A unified model of aerosol and residual ash transformations would be useful to the biomass combustion industry. The evolution of the current investigation verified that this is no simple matter. It is obvious that a unified model requires incorporation of discrete mineral sizes and dispersions in the parent fuel, temperature/time histories in the combustor and flue, accurate determination of local stoichiometry, incorporation of fluid dynamics, and more. This type of aggressive modeling (Barta, *et al.*, 1992) and experimental research (Boni, *et al.*, 1990) has been initiated by coal investigators. The growing importance of biomass combustion in industry warrants its inclusion in this important work.

BIBLIOGRAPHY

- Allen, M. D., Raabe, O. G., Slip Correction Measurements of Spherical Solid Aerosol Particles in an Improved Millikan Apparatus, Aerosol Science and Technology, Vol 4, pp 269-286, 1985
- American Ceramic Society, Inc, Phase Diagrams for Ceramists, compiled by E. M. Levin, C. R. Robbins and H. F. McMurdie, American Ceramic Society, Inc, Columbus, OH, 1964
- American Society for Testing Materials, D 388, 1966
- Andersen Instruments, Inc., Operating Manual for Andersen 1 ACFM Non-Viable Ambient Particle Sizing Samplers, Andersen Instruments, Inc. 1985
- Anthony, D. B., Howard, J. B., Coal Devolatilization and Hydrogasification, *American Institute of Chemical Engineering Journal*, Vol. 22, No. 4, 1976
- Babcock and Wilcox Company, Steam: Its Generation and Use , 40th Ed., Shultz, S. C., Kitto, J. B. (editors), pp 40:13 to 40:15, Babcock and Wilcox Company, Barberton, OH, 1992
- Baxter, L. L., Ash Deposition During Biomass and Coal Combustion: A Mechanistic Approach, *Biomass and Bioenergy*, Vol. 4, No. 2, pp 85-102, 1993
- Baxter, L. L., The Evolution of Mineral Particle Size Distributions During Early Stages of Coal Combustion, *Progress in Energy and Combustion Science*, Vol. 16, pp 261-266, 1990
- Baxter, L. L., Miles, T. R., Miles, T. R. Jr., Jenkins, B. M., Dayton, D. C., Milne, T. A., Bryers, R. W., Oden, L. L., Alkali Deposits found in Biomass Power Plants, National Renewable Energy Laboratory, *Document No. TP-433-8142*, Vol. II, 1996

- Beeley, T., Crelling, J., Gibbins, J., Hurt, R., Lunden, M., Man, C., Williamson, J., Yang, N., Transient High-Temperature Thermal Deactivation of Monomaceral-Rich Coal Chars, *Twenty-Sixth Symposium (International) on Combustion/ The Combustion Institute*, pp 3103, 1996
- Benson, S. A., Hurley, J. P., Zygarlicke, C. J., Steadman, E. N., Erickson, T. A., Predicting Ash Behavior in Utility Boilers, *Energy and Fuels*, Vol. 7, pp 746 - 754, 1993
- Berkowitz, N., An Introduction to Coal Technology, 2nd ed., Academic Press, Inc., San Diego, California, 1994
- Boni, A. A., Beer, J. M., Bryers, R. W., Flagan, R. C., Helble, J. J., Huffman, G. P., Huggins, F. E., Peterson, T. W. , Sarofim, A. F., Srinivasachar, S., Wendt, J. O. L., (Principle Investigators), Transformations of Inorganic Coal Constituents in Combustion Systems. Phase I Final Report, U.S. Department of Energy, *Contract No. DE-AC22-86PC90751*, March, 1990
- Borgwardt, R. H., Roache, N. F., Bruce, K. R., Method for Variation of Grain Size in Studies of Gas-Solid Reactions Involving CaO, *Industrial Engineering Chemistry Fundamentals*, Vol. 25, pp 165-169, 1986
- Brockman, J. E., "Sampling and Transport of Aerosols", in Aerosol Measurements: Principles, Techniques and Applications, edited by Klaus Willeke and Paul A. Baron, Van Nostrand Reinhold, New York, NY, Chpt. 6, 1993
- Bryers, R. W., Fireside Slagging, Fouling, and High-Temperature Corrosion of Heat-Transfer Surface Due to Impurities in Steam-Raising Fuels, *Progress in Energy and Combustion Science*, Vol 22, pp 29 -120, 1996
- Burchard, J. K., The Significance of Particle Emissions, *Journal of the Air Pollution Control Association*, Vol 24, no. 12, p 114, 1974
- Calkins, W. H., The Chemical Forms of Sulfur in Coal: A Review, *Fuel*, Vol. 73, No. 4, pp 475-484. 1994

- Chenevert, B. C., Kramlich, J. C., Nichols, K. M., Ash Characteristics of High Alkali Sawdust and Sanderdust Biomass Fuels, *Twenty-Seventh Symposium (International) on Combustion/The Combustion Institute*, Paper No. 2C03 (in press), 1998
- Damle, A. S., Ensor, D. S., Ranade, M. B., Coal Combustion Aerosol Formation Mechanisms: A Review, *Aerosol Science and Technology*, No. 1, pp 119 - 133, 1982
- Dana, J. D., Manual of Mineralogy, 17th edition, revised by Hurlbut, C. S. Jr., Wiley, New York, 1959
- Eddings, E. G., modified CET89, Reaction Engineering International; Original code documented in Gordon, S., McBride, B.J., Computer Program for Calculation of Complex Chemical Equilibrium Compositions, Rocket Performance Incident and Reflected Shocks and Chapman-Jouguet Detonations, National Aeronautics and Space Administration, *Document NASA SP-273*, 1973
- Energy Information Administration, Demonstrated Reserve Base of Coal in the United States on January 1, 1980, U.S. Department of Energy, *Document DOE/EIA-0280 (80)*, 1982
- Environmental Protection Agency, Code of Federal Regulations, Title 40, Chapter I, Sub-Chapter C, part 50, 1997
- Essenhigh, R. H., "Fundamentals of Coal Combustion" in Chemistry of Coal Utilization, 2nd Supplementary Volume, Elliott, M. A. (ed.), Wiley, New York, 1981
- Flagan, R. C., Friedlander, S. K., "Particle Formation in Pulverized Coal Combustion, - A Review" in Recent Developments in Aerosol Science, Shaw, D. T., (ed.), Wiley, New York, 1978
- Friedlander, S. K., Smoke, Dust and Haze, John Wiley & Sons, Inc., New York, 1977
- Gallagher, N. B., Alkali Metal Partitioning in a Pulverized Coal Combustion Environment, Ph. D. Dissertation, University of Arizona, 1992

- Gallagher, N. B., Peterson, T. W., Wendt, J. O. L., Sodium Partitioning in a Pulverized Coal Combustion Environment, *Twenty-Sixth Symposium (International) on Combustion/The Combustion Institute*, pp 3197-3204, 1996
- Gelbard, F., MAEROS2 (aerosol coagulation code), October 1996 version, written by Gelbard, Sandia National Laboratories, Albuquerque, NM, 97185-0834, 1996
- Glasser, W. G., "Lignin" in Fundamentals of Thermochemical Biomass Conversion, Overend, R.P, Milne, T. A., Mudge, L. K. (editors), Elsevier Applied Science Publishing Co., Inc., New York, 1982
- Glassman, I., Combustion, 2nd edition, Academic Press, Inc, San Diego, CA, 1987
- Helble, J. J., Srinivasachar, S., Boni, A. A., Factors Influencing the Transformation of Minerals During Pulverized Coal Combustion, *Progress in Energy and Combustion Science*, Vol. 16, pp 267-279, 1990
- Hinds, W. C., Aerosol Technology: Properties, Behavior, and Measurement of Airborne Particles, John Wiley & Sons, New York, NY, 1982 x
- Hoffman, D. A., The Design, Construction and Testing of a Fine Ash Formation Furnace, Master of Science in Mechanical Engineering Thesis, University of Washington, 1994
- Howard, J. B., "Fundamentals of Coal Pyrolysis and Hydrolysis" in Chemistry of Coal Utilization, 2nd supplementary volume, Elliott, M. A. (ed.), Wiley, New York, 1981
- Kramlich, J. C., Newton, G. H., Influence of Coal Properties and Pretreatment on Ash Aerosol Yield, *Fuel*, Vol. 73, No. 3, pp 455 - 462, 1994(a)
- Kramlich, J. C., Newton, G. H., Influence of Coal Rank and Pretreatment on Residual Ash Particle Size, *Fuel Processing Technology*, Vol. 37, pp 143 - 161, 1994(b)
- Kramlich, J. C., Chenevert, B. C., Park, J., Hoffman, D. A., Butcher, E. K., Suppression of Fine Ash Formation in Pulverized Coal Flames, Final Technical Report, U.S. Department of Energy, *DOE Grant No. DE-FG22-92PC92548*, July, 1996

- Lide, D. R. (Editor-in-Chief), Handbook of Chemistry and Physics, 75th edition, CRC Press, Inc., Boca Raton, Florida, 1994
- Lindner, E. R., Wall, T. F., Sodium Ash Reactions During Combustion of Pulverized Coal, *Twenty-Third Symposium (International) on Combustion/ The Combustion Institute*, pp 1313-1321, 1990
- Liu, B. Y. H., Pui, D. Y. H., On the Performance of the Electrical Aerosol Analyzer, *Aerosol Science*, Vol. 6, pp 249 - 264, 1975 x
- Liu, B. Y. H., Whitby, K. T., Pui, D. Y. H., A Portable Electrical Analyzer for Size Distribution Measurement of Submicron Aerosols, *Journal of the Air Pollution Control Association*, Vol 24, no. 11, pp 1067 - 1072, 1974 x
- Liu, B. Y. H., Zhang, Z. Q., Kuehn, T. H., A Numerical Study of Inertial Errors in Anisokinetic Sampling, *Journal of Aerosol Science*, Vol. 20, No. 3, pp 367-380, 1989
- McCain, J. D., Gooch, J. P., Smith, W. B., Results of Field Measurements of Industrial Particulate Sources and Electrostatic Precipitator Performance, *Journal of the Air Pollution Control Association*, Vol. 25, pp 117-121, 1975
- Miccio, F., Salatino, P., Monte-Carlo Simulation of Combustion-Induced Percolative Fragmentation of Carbons, *Twenty-Fourth Symposium (International) on Combustion/The Combustion Institute*, pp 1145 - 1151, 1992
- Miles, T. R., Personal Communication- email regarding alkali-induced slagging in MDF resinated sawdust burners, Technical Consultants, Inc; Portland, OR, August 18, 1998
- Mitchell, R. E., Akanetuk, A. E. J., The Impact of Fragmentation on Char Conversion During Pulverized Coal Combustion, *Twenty-Sixth Symposium (International) on Combustion/The Combustion Institute*, pp 3137-3144, 1996
- Mitchell, R. E., McLean, W. J., *Nineteenth Symposium (International) on Combustion/The Combustion Institute*, pp 1113-1122, 1982
- Morrow, P. E., *American Ind. Hyg. Assoc. Journal*, Vol. 25, p 213, 1964

- Mulcahy and Smith, Kinetics of Combustion of Pulverized Fuel: A Review of Theory and Experiment, *Reviews of Pure and Applied Chemistry*, Vol. 19, pp 81-108, 1969
- Neville, M., Quann, R. J., Haynes, B. S., Sarofim, A. F., Vaporization and Condensation of Mineral Matter during Pulverized Coal Combustion, *Eighteenth Symposium (International) on Combustion/The Combustion Institute*, pp 1267 - 1274, 1981
- Neville, M., Sarofim, A. F., The Fate of Sodium During Pulverized Coal Combustion, *Fuel*, Vol. 64, March, pp 384 - 390, 1985
- Niksa, S., Predicting the Evolution of Fuel Nitrogen from Various Coals, *Twenty-Fifth Symposium (International) on Combustion/The Combustion Institute*, pp 537 - 544, 1996
- Osman, E. A., Goss, J. R., Ash Chemical Composition, Deformation and Fusion Temperatures for Wood and Agricultural Residues, *American Society of Agricultural Engineers Winter Meeting*, paper 83-3549, held in Chicago, Illinois, 1983
- Park, J., Development of Artificial Char for Coal Mineral Transformation Studies, Master of Science in Mechanical Engineering Thesis, University of Washington, 1995
- Quann, R. J., Sarofim, A. F., Vaporization of Refractory Oxides During Pulverized Coal Combustion, *Nineteenth Symposium (International) on Combustion/The Combustion Institute*, pp 1429 - 1440, 1982
- Raask, E., Mineral Impurities in Coal Combustion, Hemisphere Publishing Corporation, Washington, 1985
- Riley, P., (Washington Natural Gas), Average natural gas composition from January 1996 to December 1996 for Seattle area customers, personal communication, May 1997
- Sarofim, A. F., Howard, J. B., Padia, A. S., The Physical Transformation of the Mineral Matter in Pulverized Coal Under Simulated Combustion Conditions, *Combustion Science and Technology*, Vol. 16, pp 187-204, 1977

- Saxena, S. C., Devolatilization and Combustion Characteristics of Coal Particles, *Progress in Energy and Combustion Science*, Vol. 16, pp 55-94, 1990
- Senior, C. L., Flagen, R. C., Ash Vaporization and Condensation During Combustion of a Suspended Coal Particle, *Aerosol Science and Technology*, Vol. 1, pp 371-383, 1982
- Shaw, D. W., Essenhigh, R. H., Temperature Fluctuations in Pulverized Coal (P.C.) Flames, *Combustion and Flame*, Vol 86, pp 333-346, 1991
- Silcox, G. D., Kramlich, J. C., Pershing, D. W., Mathematical Model for the Flash Calcination of Dispersed CaCO_3 and $\text{Ca}(\text{OH})_2$ Particles, *Industrial Engineering Chemical Research*, Vol. 28, pp 155-160, 1989
- Smith, K. L., Smoot, L. D., Characteristics of Commonly Used U.S. Coals. Towards a Set of Standard Research Coals, *Progress in Energy and Combustion Science*, Vol. 16, pp 1-53, 1990
- Srinivasachar, S., Helble, J. J., Boni, A. A., Mineral Behavior During Coal Combustion: 1. Pyrite Transformations, *Progress in Energy and Combustion Science*, Vol. 16, pp 281 - 292, 1990 (a)
- Srinivasachar, S., Helble, J. J., Ham, D. O., Domazetis, G. , A Kinetic Description of Vapor Phase Alkali Transformations in Combustion Systems, *Progress in Energy and Combustion Science*, Vol. 16, pp 303 - 309, 1990 (b)
- Stach, E., Taylor, G. H., Mackowsky, M.-T., Chandra, D., Teichmüller, M., and Teichmüller, R., Stach's Textbook of Coal Petrology, 3rd ed., Gebrüder Borntraeger, Berlin, Germany, 1982
- Theander, O., "Cellulose, Hemicellulose, and Extractives" in Fundamentals of Thermochemical Biomass Conversion, Overend, R.P, Milne, T. A., Mudge, L. K. (editors), Elsevier Applied Science Publishing Co., Inc., New York, 1982
- Thermo-Systems Incorporated, Operating and Service Manual - Model 3030 Electrical Aerosol Size Analyzer, St. Paul, MN, undated

- Wall, T. F., Mineral Matter Transformations and Ash Deposition in Pulverized Coal Combustion, *Twenty-Fourth Symposium (International) on Combustion/The Combustion Institute*, pp 1119-1126, 1992
- Wark, K., Warner, C. F., Air Pollution: Its Origin and Control, 2nd edition, HarperCollins, Publishers, Inc., New York, New York, 1981
- Wibberley, L. J., Wall, T. F., Alkali-Ash Reactions and Deposit Formation in Pulverized-Coal-Fired Boilers; The Thermodynamic Aspects Involving Silica, Sodium, Sulphur, and Chlorine, *Fuel*, Vol. 61, pp 87-92, 1982 (a)
- Wibberley, L. J., Wall, T. F., Alkali-Ash Reactions and Deposit Formation in Pulverized-Coal-Fired Boilers; Experimental Aspects of Sodium Silicate Formation and the Formation of Deposits, *Fuel*, Vol. 61, pp 93-99, 1982 (b)
- Willeke, K., Temperature Dependence of Particle Slip in a Gaseous Medium, *Journal of Aerosol Science*, Vol. 7, pp 381-387, 1976
- Wornat, M. J., Hurt, R. H., Yang, N. Y. C., Headley, T. J., Structural and Compositional Transformations of Biomass Chars during Combustion, *Combustion and Flame*, Vol. 100, pp 131-143, 1995
- Zhang, Z. Q., Liu, B. Y. H., On The Empirical Fitting Equations for Aspiration Coefficients for Thin-Walled Sampling Probes, *Journal of Aerosol Science*, Vol. 20, No. 6, pp 713-720, 1989
- Zygarlicke, C. J., McCollor, D. P., Benson, S. A., Ash Particle Size and Composition Evolution During Combustion of Synthetic Coal and Inorganic Mixtures, *Twenty-Fourth Symposium (International) on Combustion/The Combustion Institute*, pp 1171-1177, 1992

APPENDIX A: SIMPLIFIED RESIDUAL SIZE DISTRIBUTION

Calculation of simplified residual size distribution for Fuel 1 and Fuel 2, and Fuel 3 and 4:

Residual size distributions for Fuel 1 and Fuel 2 are very similar, as are distributions for Fuel 3 and 4. Hence, a simplified size distribution is made based on an average of Fuel 1 and 2, and another simplified size distribution is made with Fuel 3 and 4. These consist of two modes per residual size distribution, with a corresponding Geometric Mass Mean Diameter and a Geometric Standard Deviation. Some parameters are more appropriately estimated without averaging, such as chemical composition. In this case, Fuel 1 is considered the primary fuel when Fuel 1 and 2 are not averaged. Fuel 4 is considered the primary fuel when Fuel 3 and 4 are not averaged.

Assume an industrial burner wood flow rate of 3760 lbs/hr, per site information from Fuel 4 facility.

$$3760 \text{ lbs/hr} * .4536 \text{ kg/lb} * 1\text{hr}/3600 \text{ sec} = \underline{47376 \text{ kg/sec}}$$

Assume 80% excess air. This assumption based on the maximum firing rate of the Fuel 4 facility.

According to equilibrium calculations, and assuming complete combustion, the air to fuel ratio and adiabatic flame temperature is:

Fuel 1 and 2:

9.60 (kg Air)/(kg Fuel 1), T adiabatic = 1630 K.

Fuel 3 and 4:

10.49 (kgAir)/kg Fuel 4), T adiabatic = 1452 K

This adiabatic temperature is lower than the estimated temperature for the Fuel 4 combustion in the industrial facility, as provided by facility personnel (they estimate 1755 K). This is probably a result of variable stoichiometry in the main burner under non-ideal conditions.

NASA equilibrium predicts non-alkali species existing as solids for temperatures of 1600K and below. Primary species are:

Fuel 1:

Ca_2SiO_4 (s) -> 3.14e-5 moles/(moles total)

CaMgO_2 (s) -> 2.01e-5 moles/(moles total)

$\text{Ca}_3\text{MgSiO}_8$ (s) -> 3.60e-6 moles/(moles total)

Fuel 4:

CaO (s) -> 1.51e-4 moles/(moles total)

CaMgO_2 (s) -> 4.31e-5 moles/(moles total)

Ca_2SiO_4 (s) -> 1.80e-5 moles/(moles total)

All non-alkali minerals go to an oxide form. These may recombine to form complex species as above, but they are essentially (and by formula) oxides. So, it is assumed these form the residual size distribution. Based on the ICP analysis of Fuel 1 and Fuel 4 conducted by an independent industrial laboratory, the mass of the ash in oxide form is (as calculated by spread sheet WoodNASA_eqibrm/ RawFuel atomic spec):

Fuel 1 = 4308.9 (mg ash)/(kg as-received wood), not including K, Cl, Na, or S
Fuel 4 = 7177.5 (mg ash)/(kg as-received wood), not including K, Cl, Na, or S

Assuming this is all ash that is residually formed (i.e. never enters a vapor phase), the size distribution of residual ash found during laboratory scale testing is assumed to be reasonably accurate.

In the primary industrial combustor, alkali species are expected to be in vapor phase, based on NASA equilibrium calculations. Species are: NaOH, NaCl, KOH, KCl, HCl. In the secondary chamber, the temperature (adiabatic T = 1298K for Fuel 1) is cool enough for Na₂SO₄ formation, but is probably not kinetically favored. KCl and NaCl are the primary vapor phase alkalis. It is assumed that aerosol coagulation begins in the blend chamber in such a way that NaOH and KCl form nucleated particles in tandem with NaCl. Therefore, NaCl KCl and NaOH form nucleated particles simultaneously, and the initial size distribution of these particles is similar to self-nucleated NaCl at the partial pressure of the sum of NaCl, KCl and NaOH. Na₂SO₄ is assumed not to be formed as an initial species.

If all the alkalies form chlorides or hydroxides from the vapor phase, an estimate of the initial aerosol size distribution can be determined.

Fuel 1 = 3277.3 (mg aerosol ash)/(kg as-received wood), with K and Na as hydroxides and chlorides
Fuel 4 = 3121.7 (mg ash)/(kg as-received wood), with K and Na as hydroxides and chlorides

In order to use this information, the laboratory-determined size distribution was broken down into 3 zones, as shown in the figures at the end of this section:

Zone 1: Particles .4 μm and smaller. It is assumed that all ash in this zone is from the vaporization/nucleation/condensation formation mechanism. This is stage 7 (.39 μm) and the filter (~.1 μm).

Zone 2: A residual mode formed by breakup of the parent particles, assumed to be stages 2 (3.66 μm) to stage 6 (.54 μm).

Zone 3: A residual mode formed by conglomerated and unfragmented particles. Stages 0 (8.33 μm) and 1 (5.33 μm) and the preseperator. The ash in the preseperator was assumed to be 8.33 μm like stage 0.

The average mass on each stage is shown in Table A.1. In terms of zones, this yields:

Fuel 1&2 Zone 1 = 29.22% ash
 Fuel 1&2 Zone 2 = 22.06% ash
 Fuel 1&2 Zone 3 = 48.73% ash

Fuel 3&4 Zone 1 = 5.74% ash
 Fuel 3&4 Zone 2 = 2.43% ash
 Fuel 3&4 Zone 3 = 91.83% ash

Calculating the mass and average initial diameter of the aerosol requires assumptions. It should be recognized that the aerosol mass as collected on the aerosol filter may under represent amount of aerosol-forming material in the fuel. Incomplete combustion of the fuel may have left some alkali in the fuel, and much of it may be complexed with the residual. Additionally, some coagulation/deposition into the larger size modes may have occurred prior to size sorting in the impactor. For modeling purposes, it seems more reasonable to estimate that the mass in the aerosol mode based on the total alkali as chlorides and hydroxides. Using this approximation, the mass of aerosol relative to the mass of residual is:

For Fuel 1, this is:

$$\frac{\text{Alkali as chlorides/hydroxides}}{\text{Alkali as chlorides/hydroxides} * \text{metals as oxides}} = \frac{3277.3}{3277.3 * 4308.9} = 43\% \text{ aerosol}$$

This compared to 48.73% based on experimental results. Hence, this assumption is of little consequence.

For Fuel 4, this is:

$$\frac{\text{Alkali as chlorides/hydroxides}}{\text{Alkali as chlorides/hydroxides} * \text{metals as oxides}} = \frac{3121.7}{3121.7 * 7177.5} = 30\% \text{ aerosol}$$

This compared to 5.7% based on experimental results. The reason this aerosol estimate is higher than experimental results is probably related to incomplete burnout of the residual ash. For modeling purposes, using the 30% aerosol seems to be a more appropriate value to use.

It is assumed that the *residual* modes will be formed with mass proportional to the ash collected in each residual zone (i.e. zones 2 and 3), as discussed above. Based on this assumption, our three-zone ash distribution is:

For Fuels 1 and 2, the mass divided between Zones 2 and 3 is:

$$\text{Zone 2} \rightarrow 22.06\% / (22.06\% + 48.73\%) = 31.2\%$$

Percent mass of ash in Zone 2, relative to the total ash in Zones 2 and 3.

$$\text{Zone 3} \rightarrow 48.73\% / (48.73\% + 22.06\%) = 68.8\%$$

Percent mass of ash in Zone 3, relative to the total ash in Zones 2 and 3.

For Fuels 3 and 4, the mass divided between Zones 2 and 3 is:

$$\text{Zone 2} \rightarrow \frac{2.43\%}{(2.43\% + 91.83\%)} = 2.58\%$$

Percent mass of ash in Zone 2, relative to the total ash in Zones 2 and 3.

$$\text{Zone 3} \rightarrow \frac{91.83\%}{(2.43\% + 91.83\%)} = 97.4\%$$

Percent mass of ash in Zone 3, relative to the total ash in Zones 2 and 3.

Calculate the ash per second in each zone:

Fuel 1&2:

$$\text{Zone 3: } .688 * .004309 \text{ (kg oxide ash/kgFuel)} * .47376 \text{ (kgFuel/sec)} =$$

$$\underline{.001404 \text{ kgAsh/sec}}$$

$$\text{Zone 2: } .312 * .004309 \text{ (kg oxide ash/ kgFuel)} * .47376 \text{ (kgFuel/sec)} =$$

$$\underline{.0006369 \text{ kgAsh/sec}}$$

$$\text{Zone 1: } .003277 \text{ (kg aerosol ash/kgFuel)} * .47376 \text{ (kgFuel/sec)} =$$

$$\underline{.0015525 \text{ kgAsh/sec}}$$

Fuel 3&4:

$$\text{Zone 3: } .974 * .007178 \text{ (kg oxide ash/ kgFuel)} * .47376 \text{ (kgFuel/sec)} =$$

$$\underline{.003312 \text{ kgAsh/sec}}$$

$$\text{Zone 2: } .026 * .007178 \text{ (kg oxide ash/ kgFuel)} * .47376 \text{ (kgFuel/sec)} =$$

$$\underline{.00008842 \text{ kgAsh/sec}}$$

$$\text{Zone 1: } .003122 \text{ (kg aerosol ash/kgFuel)} * .47376 \text{ (kgFuel/sec)} =$$

$$\underline{.001479 \text{ kgAsh/sec}}$$

Assuming that each zone forms a log-normal distribution, the zone Geometric Mass Mean Diameter and Geometric Standard Deviation is calculated. The GMMD and GSD are calculated on a separate spreadsheet (Aut95CascadeComp/Compilation). This was facilitated by assuming that all mass on a stage is made of particles of the stage cut-off diameter. The preseparator was assumed to be all 8.33 μm particles, like stage 0.

Fuel 1&2

Zone 3:

GMMD: 7.77 μm

GSD: 1.18

Mass Fraction: 68.8%

Fuel 3&4

Zone 3:

GMMD: 8.27 μm

GSD: 1.05

Mass Fraction: 97.4%

Fuel 1&2

Zone 2:

GMMD: 1.68 μm

GSD: 1.74

Mass Fraction: 31.2%

Fuel 3&4

Zone 2:

GMMD: 1.98 μm

GSD: 1.81

Mass Fraction: 2.6%

These distributions are shown in Figures A.1 and Figure A.2. An aerosol mode is also shown, based on the *experimental* size distribution. As discussed earlier, this distribution

is misleading if one is attempting coagulation calculations. The initial aerosol distribution used for modeling is discussed next.

For the aerosol, the initial particulate diameter is estimated based on the critical saturation ratio (discussed in the modeling chapter) for a system composed of NaCl with an initial vapor pressure of .8 Pa. This results in a critical diameter of:

All Fuels:

Zone 1: Initial diameter: 1.9×10^{-9} meters

This is also the calculated critical diameter for a system with an initial vapor pressure from 1.22 Pa to 0.4 Pa, within 2 %.

Note that for modeling purposes (in particular, the MAEROS2 code), a uniform material density must be assumed for the residual and aerosol modes. For convenience, this density is chosen to be 2733 kg/m^3 , which is the density of CaCO_3 . This is more than NaCl, KCl, NaOH, and KOH (1980 to 2170 kg/m^3), but less than the oxide CaO (3300 kg/m^3). It is a compromise between the estimated aerosol density and residual density.

Surface Area Estimate:

Estimate the particulate surface area, assuming a density of CaO (3.25 g/cc):
 $(3.25 \text{ gCaO/cc}) * (100^3 \text{ (cm}^3\text{)/(m}^3\text{)}) * (1\text{kg}/1000\text{g}) = 3250 \text{ kg/m}^3$

Fuel 1&2:

Volume of Zone 3 ash:

$$((1/3250) \text{ m}^3/\text{kg}) * (.001404 \text{ kgAsh/sec}) = \underline{4.32e-7 \text{ m}^3/\text{sec}}$$

Volume of Zone 2 ash:

$$((1/3250) \text{ m}^3/\text{kg}) * (.0006369 \text{ kgAsh/sec}) = \underline{1.9596e-7 \text{ m}^3/\text{sec}}$$

Fuel 3&4:

Volume of Zone 3 ash:

$$((1/3250) \text{ m}^3/\text{kg}) * (.003312 \text{ kgAsh/sec}) = \underline{1.020e-6 \text{ m}^3/\text{sec}}$$

Volume of Zone 2 ash:

$$((1/3250) \text{ m}^3/\text{kg}) * (.00008842 \text{ kgAsh/sec}) = \underline{2.72e-8 \text{ m}^3/\text{sec}}$$

To solve for the number density, it is assumed that the Count Mean Diameter is the critical parameter rather than the Geometric Mass Mean Diameter. Since the absolute mass collected from the vapor phase is a strong function of available surface area, it is assumed that conserving the residual particle surface area (for a fixed mass) is important. Hence, the GMMD is converted to CMD:

Fuel 1&2:

$$\underline{\text{Zone 3: CMD} = \text{GMMD}/(\text{Exp}(3\ln^2\text{GSD})) = 7.16 \text{ } \mu\text{m}}$$

$$\underline{\text{Zone 2: CMD} = \text{GMMD}/(\text{Exp}(3\ln^2\text{GSD})) = .669 \text{ } \mu\text{m}}$$

Fuel 3&4:

$$\underline{\text{Zone 3: CMD} = \text{GMMD}/(\text{Exp}(3\ln^2\text{GSD})) = 8.21 \text{ } \mu\text{m}}$$

$$\underline{\text{Zone 2: CMD} = \text{GMMD}/(\text{Exp}(3\ln^2\text{GSD})) = .689 \text{ } \mu\text{m}}$$

Note that the CMD is somewhat smaller than the GMMD, especially for Zone 2. Using the CMD, the significant surface area of the smaller size particles is included.

Converting the particle diameter and ash volumes to particle number densities:

$N \cdot \frac{4}{3} \pi r^3 = \text{volume/time}$
Solving for N, particles per sec:

Fuel 1&2:

$$\begin{aligned} \text{For Zone 3: } N &= \frac{(3 \cdot 8)}{(4 \cdot \pi \cdot (7.16e-6)^3)} \cdot (4.32e-7) = \underline{2.248e9 \text{ particles/sec}} \\ \text{For Zone 2: } N &= \frac{(3 \cdot 8)}{(4 \cdot \pi \cdot (.669e-6)^3)} \cdot (1.96e-7) = \underline{1.25e12 \text{ particles/sec}} \\ \text{Zone 2 surface area over Zone 3 surface area} &= 4.8 \end{aligned}$$

Fuel 3&4:

$$\begin{aligned} \text{For Zone 3: } N &= \frac{(3 \cdot 8)}{(4 \cdot \pi \cdot (8.21e-6)^3)} \cdot (1.02e-6) = \underline{3.520e9 \text{ particles/sec}} \\ \text{For Zone 2: } N &= \frac{(3 \cdot 8)}{(4 \cdot \pi \cdot (.689e-6)^3)} \cdot (2.72e-8) = \underline{1.588e11 \text{ particles/sec}} \\ \text{Zone 2 surface area over Zone 3 surface area} &= 1.8e-4 \end{aligned}$$

Note that very little of the surface area is in Zone 2 for Fuel 3 and 4, since the particle count is very low compared to all other zones.

It is informative to also calculate the total surface area in a volume of hot gas in the blend chamber for Fuel 1, as provided by the hetero- particles. Assuming the density in the blend chamber is the density of the hot gas system at 800K, equilibrium shows the hot gas density to be .441 kg/m³ for Fuel 1. The total flow rate for this system is 27.18 kg/sec, for a wood flowrate of .47376 kg/sec and air to fuel ratio of 56.37 kgAir/kgFuel.

Volumetric flowrate at 800K for Fuel 1 is $(1/.441)(\text{m}^3/\text{kg}) \cdot 27.18 \text{ kg/sec} = 61.63 \text{ m}^3/\text{sec}$. This seems very high, but is probably reasonably accurate based on the scale of an industrial-size wood chip dryer.

The particle number density and surface-area/volume for Fuel 1 and 2 in Zone 3 is:
 $(2.248e9 \text{ particles/sec}) / (61.63 \text{ kg/m}^3) = \underline{3.6346e7 \text{ particles/m}^3}$ at 800K in Blend Chamber

$(.3260 \text{ m}^2/\text{sec}) / (61.63 \text{ kg/m}^3) = \underline{5.874e-3 \text{ m}^2/\text{m}^3}$ at 800K in Blend Chamber, which is a very small surface area for condensation

The particle number density and surface-area/volume for Fuel 1 and 2 Zone 2 is:
 $(1.2496e12 \text{ particles/sec}) / (61.63 \text{ kg/m}^3) = \underline{2.028e10 \text{ particles/m}^3}$ at 800K in Blend Chamber

$(1.757 \text{ m}^2/\text{sec}) / (61.63 \text{ kg/m}^3) = \underline{.02851 \text{ m}^2/\text{m}^3}$ at 800K in Blend Chamber, which is a very small surface area for condensation.

Table A.1: Averages of mass collected on stages for screened sawdust/sanderdust experiments

Stage number	Dia, μm	Fuel 1 and 2 mass % on stage (averages)	Fuel 3 and 4 mass % on stage (averages)
Presep and 0	8.32	41.19	90.54
1	5.33	7.54	1.29
2	3.66	3.27	.77
3	2.53	5.42	.55
4	1.64	7.39	.60
5	.85	4.65	.35
6	.54	1.33	.15
7	.39	1.08	.12
Filter	.10	28.14	5.62

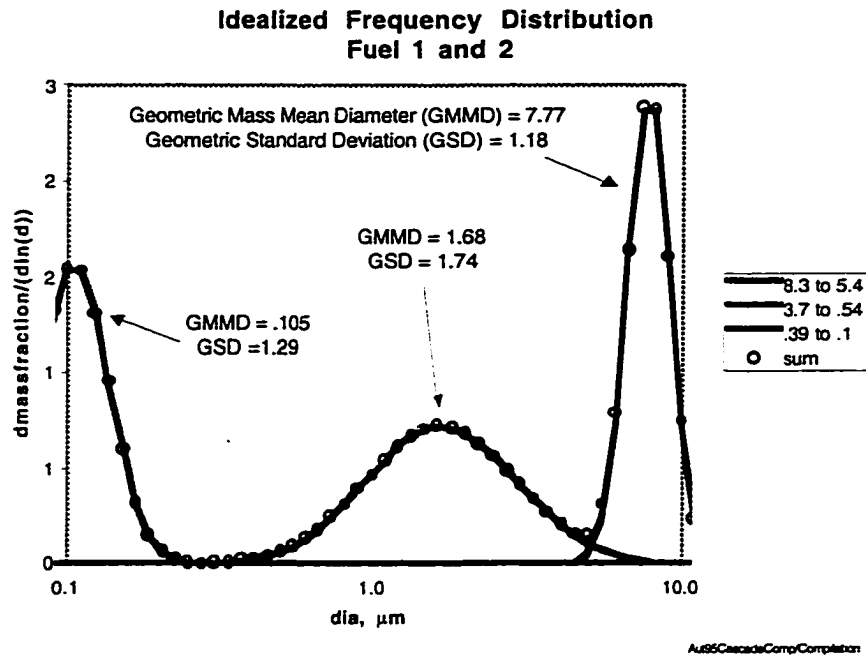


Figure A.1: Approximated mass/size distribution of Fuel 1 and Fuel 2 based on experimentally determined size distributions

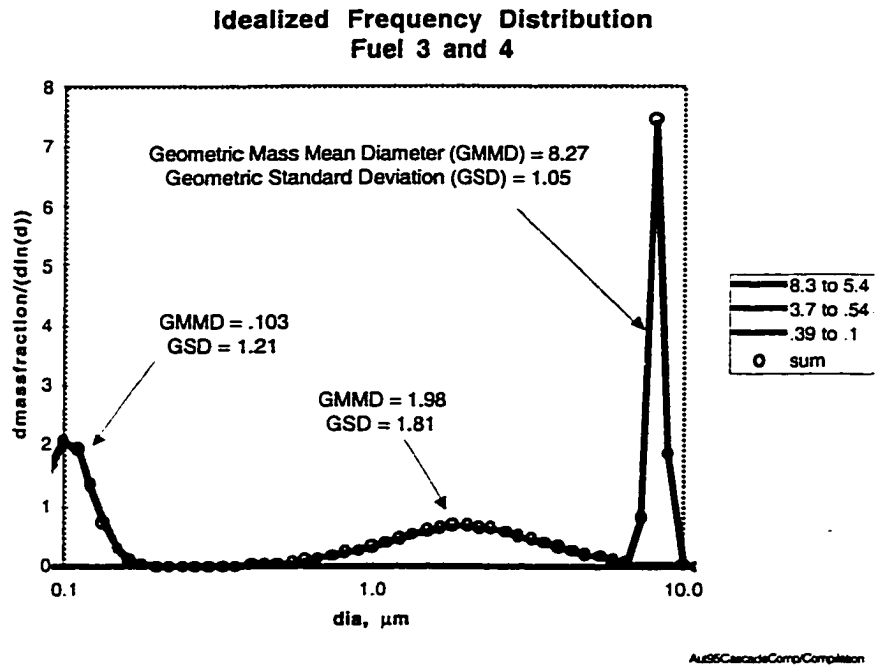


Figure A.2: Approximated mass/size distribution of Fuel 3 and Fuel 4 based on experimentally determined size distributions

APPENDIX B: AIR, WATER AND NATURAL GAS SCHEMATICS, AND SUMMARY OF LABORATORY MODIFICATIONS

During experimental testing, extensive modifications were made to the furnace and laboratory. Significant modifications included:

- Addition of two high volume exhaust systems to aid in laboratory cooling (laboratory ambient temperature was known to reach 95 F in summer months).
- Redesign of the main burner mounting system to greatly improve heat transfer to the gas stream. Casting of main burner interface. Plugs for inactive main ports were also cast. Modification of flame detector mounts to prevent heat damage, and condensation buildup.
- Backfire burner modifications to prevent sooting.
- Replumbing of the air supply system to decouple valving. An additional air source was also added to supply air for ancillary equipment
- Replumbing of the water supply system, including adding an additional source, and filtration and settling traps.
- Extensive exhaust system modifications, including water atomizer redesign, a dilution control, and condensate drain systems. Eventual corrosion of the existing stainless steel exhaust ducting required a major redesign and rebuild of the exhaust system. This included modification to the upper backfire burners exit ports.
- Addition of internal and external exhaust duct coolant coils.
- Redesign and construction of the pulverized fuel feed system, including redesign of the water cooled injector spike.
- Exhaust duct insulation to rooms B6 and G4.
- Redesign and construction of horizontal sample port mount, vertical sample port mount, pulverized fuel injector mount and furnace packing.

Figures B-1, B-2, and B-3 show configurations of the air, natural gas, and water supply systems for the tunnel furnace and ancillary devices.

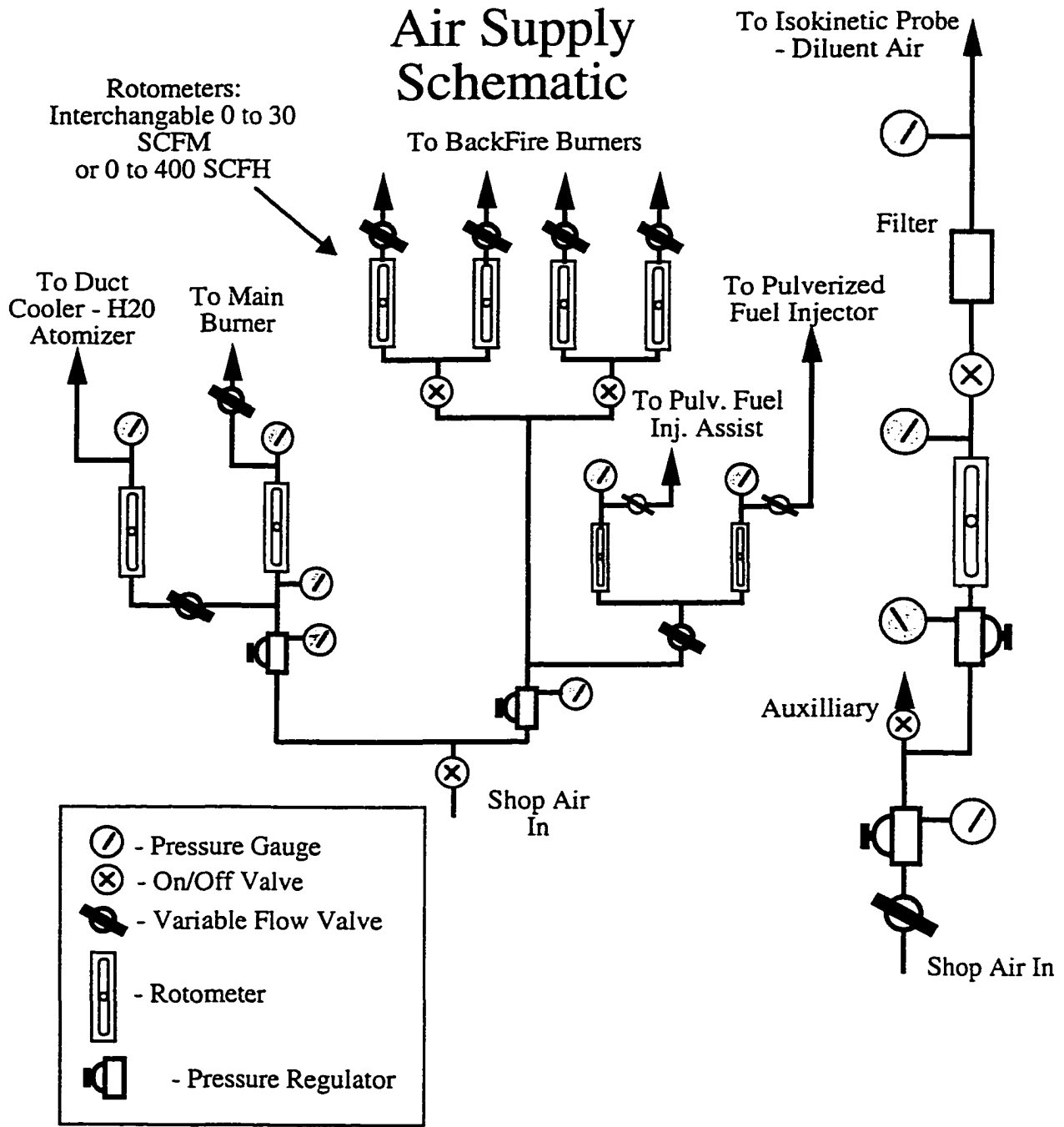


Figure B-1: Air Supply Schematic

Natural Gas Supply Schematic

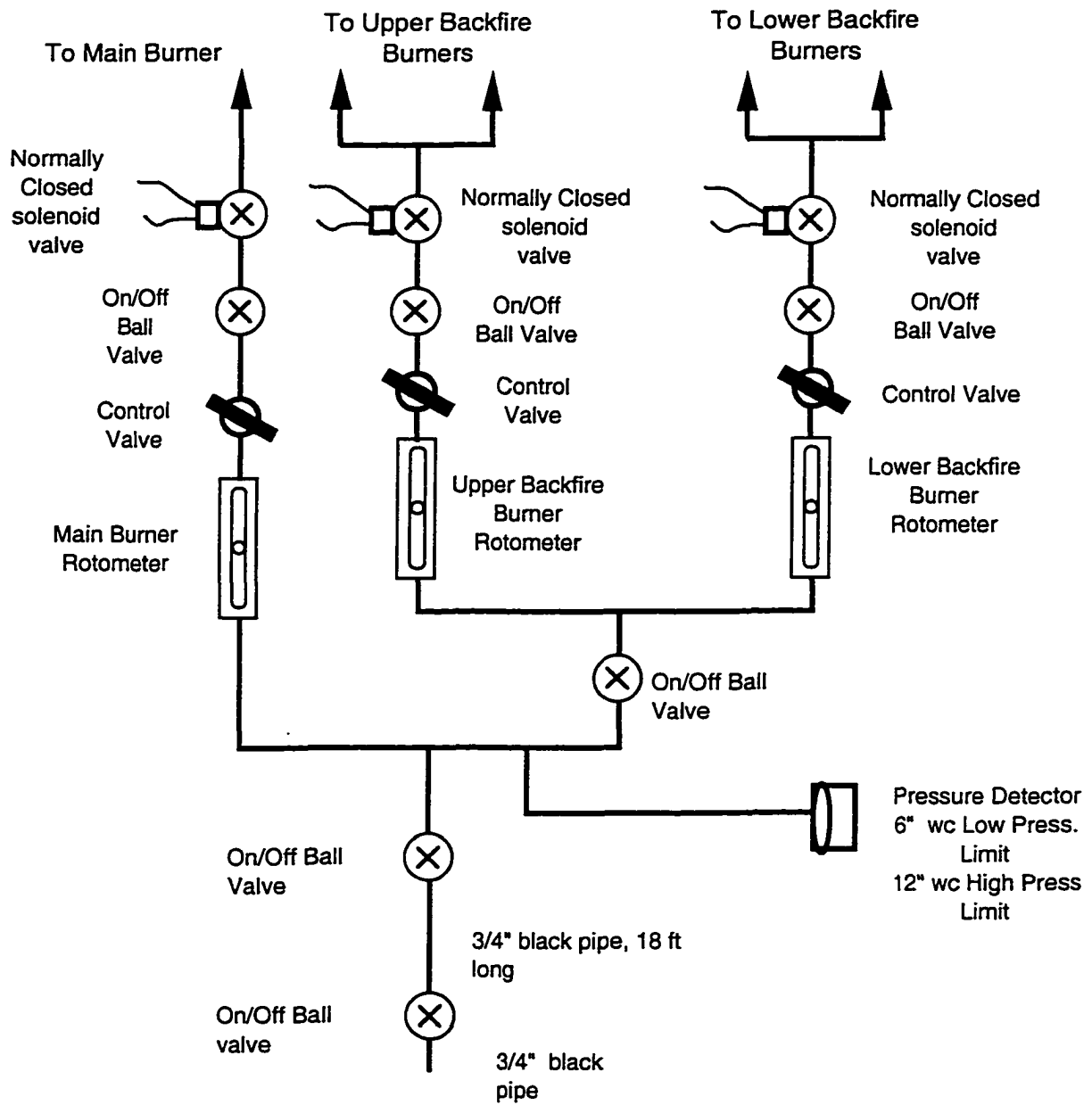


Figure B-2: Natural Gas Supply Schematic

Water Supply Schematic

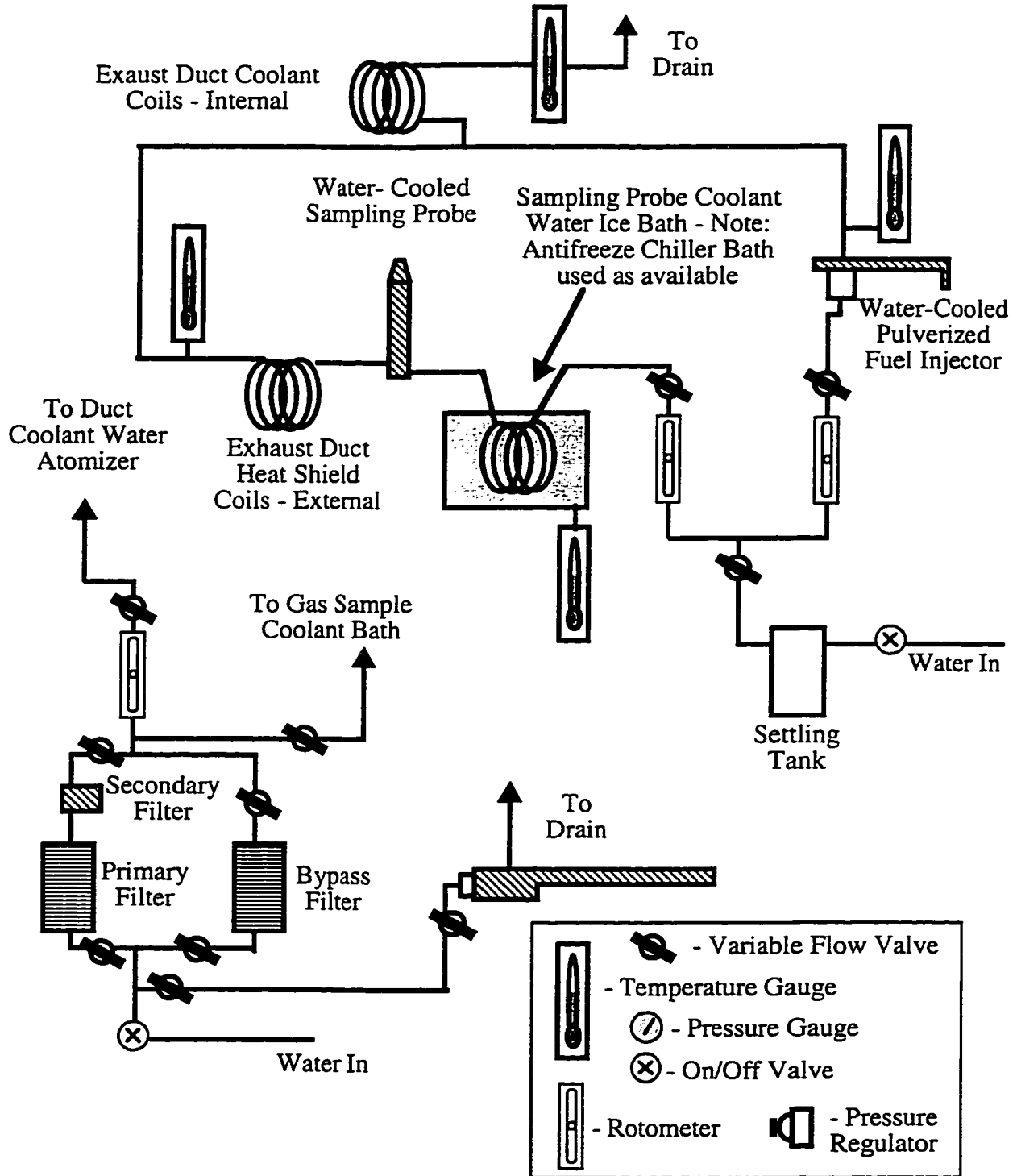


Figure B-3: Water Supply Schematic

APPENDIX C: SAMPLING EFFICIENCY USING A SIMPLE WATER-COOLED PROBE AT NON-ISOKINETIC CONDITIONS

Practical constraints on the maximum inner diameter of the simple water cooled sampling probe required that sampling be conducted at non-isokinetic conditions. This was remedied when the porous-walled isokinetic sampling probe was designed and constructed. Since the research presented here is primarily concerned with particulate matter in the micron and sub-micron range (i.e. low stokes number), and sampling velocity mismatch is less of a factor as stokes number decreases, this sampling bias was determined to be acceptable. What follows is an estimate of sampling error, based on the general procedure presented by Brockman (1993), and also Hinds (1982). Corrections for probe misalignment and inlet wall thickness are considered to be negligible.

Sampling a particle-laden gas stream at a faster flow rate than the bulk velocity of the gas stream is termed super-isokinetic sampling. Large particles that have sufficient momentum will deviate from the gas flow lines, resulting in a fraction of these particles missing the probe inlet. Hence, the large particulate will be under-represented in the captured flue gas. A numerical correlation determined by Liu, Zhang, and Kuehn (1989) and Zhang and Lui (1989) is recommended by Brockman (1993) to estimate the sampling efficiency:

$$\eta_{asp} = 1 + \frac{\left(\frac{U_o}{U} - 1\right)}{\left[1 + \frac{\left(0.506\left(\frac{U_o}{U}\right)^5\right)}{Stk}\right]}$$

$$0.01 \leq Stk \leq 100$$

$$0.1 \leq \frac{U_o}{U} \leq 1$$

where:

$$Stk = \frac{\tau * U_o}{d}, \text{ Stokes number}$$

$$\tau = \frac{\rho_p * d_p^2 * C_c}{18 * \eta}, \text{ relaxation time, sec}$$

$$\rho_p = \text{particle density, kg/m}^3$$

d_p = particle diameter, m

C_c = Cunningham Slip Coefficient

η = dynamic gas viscosity, Pa * sec

U_o = freestream velocity, m/sec

U = probe inlet velocity, m/sec

d = probe diameter, m

Cunningham Slip Coefficient is based on an empirical fit derived from air data (Allen and Raabe, 1985) as interpreted by Brockman (1993):

$$C_o = 1 + Kn \left[\alpha + \beta * e^{\frac{-\gamma}{Kn}} \right]$$

$$\alpha = 1.142$$

$$\beta = 0.558$$

$$\gamma = 0.999$$

The dynamic gas viscosity is calculated by (Brockman, 1993):

$$\eta = \eta_{ref} \left(\frac{T_{ref} + S}{T + S} \right) \left(\frac{T}{T_{ref}} \right)^{1.5}$$

η_{ref} = reference viscosity, $18.203 * 10^{-6}$ Pa * s

S = Sutherland Interpolation constant for air, 110.4 K

T_{ref} = reference temperature, 293.15 K

T = hot gas temperature, K

Calculation of the Knudsen number at elevated temperatures is based on the mean free path calculation by Willeke (1976):

$$Kn = \frac{2\lambda}{d_p}$$

$$\lambda = \lambda_{ref} \left(\frac{P_{ref}}{P} \right) \left(\frac{T}{T_{ref}} \right) \left(\frac{1 + \frac{S}{T_{ref}}}{1 + \frac{S}{T}} \right)$$

λ_{ref} = reference gas mean free path, = $.0665 * 10^{-6}$ meters

P_{ref} = reference pressure, = 101325 Pa

An estimate of sampling efficiency for a representative Screened sawdust/ sanderdust test (08169501) is shown in Figure C-1. Relevant input data is:

Gas inlet temperature = 1114.15 K
 Probe inlet diameter = .01427 m (9/16 inch)
 Freestream velocity = .85 m/s
 Probe inlet velocity = 6.01 m/s
 Particle density = 2700 kg/m³ (calcium carbonate density)

Below 10 μm the sampling efficiency is 90% or greater. The size distribution below this diameter is not strongly biased by non-isokinetic conditions. Above 10 μm , the capture efficiency begins to asymptote to the oversampling ratio, meaning that only the particles with straight trajectories into the probe inlet will enter, as expected. The absolute magnitude of the particulate matter above 10 μm is of little consequence to this study.

The sampling efficiency for the isokinetic probe is also estimated. Isokinetic conditions are maintained to the tolerance of the sampling system. Errors may be introduced by calibration drift of the CO₂ meter, rotometer errors, or other measurement errors. Assuming that flow velocities are inadvertently mismatched by 20%, the sampling efficiency is calculated. Input variables are:

Gas inlet temperature = 1061 K
 Probe inlet diameter = .01427 m (9/16 inch)
 Freestream velocity = .874 m/s
 Probe inlet velocity = (.874 * 1.2) m/s
 Particle density = 2700 kg/m³ (calcium carbonate density)

The results are shown in Figure C-2. It is clear that worst-case sampling error for the isokinetic probe is negligible over the range of particle diameters of interest.

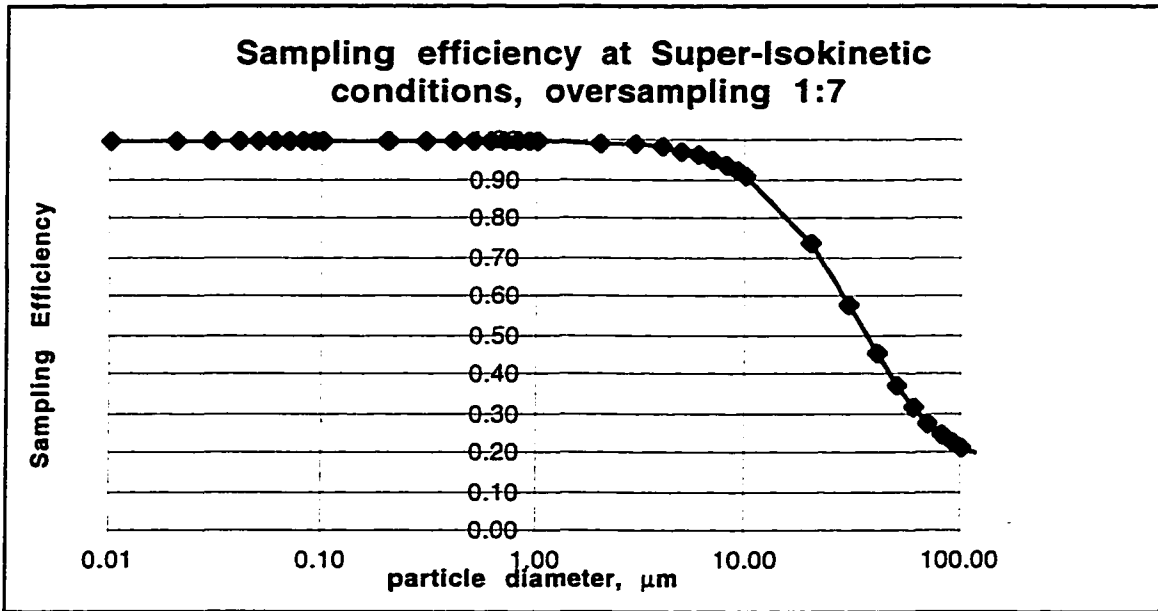


Figure C.1: Super-Isokinetic sampling efficiency

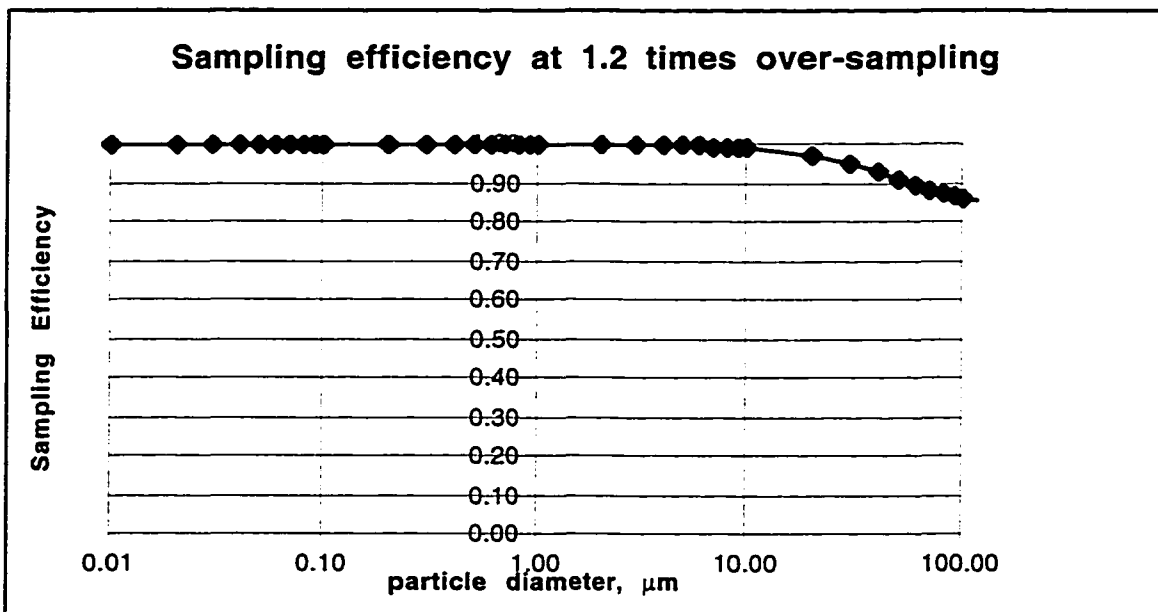


Figure C.2: Isokinetic sampling efficiency with instrument error included

APPENDIX D: NATURAL GAS COMPOSITION

Personal Communication with Paul Riley, Process Lead, Gas Measurement, Washington Natural Gas, 206-224-2369

Average Gas Composition for January 1996 to December 1996:

Species	Formula	Btu/ft ³	Mass %
Methane	CH ₄	1012.0	95.66%
Ethane	C ₂ H ₆	1773.7	02.74%
Propane	C ₃ H ₈	2522.1	00.56%
N Butane	C ₄ H ₁₀	3270.1	00.07%
I Butane	C ₄ H ₁₀	3260.5	00.11%
Pentane	C ₅ H ₁₂	4014.6	00.02%
Hexane	C ₆ H ₁₄	5141.2	00.01%
Carbon Dioxide	CO ₂	0000.0	00.11%
Nitrogen	N ₂	0000.0	00.70%
Average Btu/ft ³		1041.0	

Avg Specific Gravity = .5811

WNG Sulphur System Average = 0.02987 Grains H₂S / 100 ft³

Average H₂O Content = 0.2 gallons / Mmcf

End of Personal Communication with Paul Riley

Calculation of sulphur fraction from furnace operation in a typical pulverized wood test:

.02987 grains of H₂S per 100 ft³ of Natural Gas = 1.9355 mg H₂S/100ft³

Mass of S in H₂S = 32.066 / (32.066 + 2*1.0079) = .94008 S/H₂S

Density of methane = 101325 Pa / ((8314.4 J/kmol*K)*300K) / 16 kmol/kg CH₄) = .64 kg/m³

Mass flowrate of NG during typical test = 18 grams/minute

Mass flowrate of S during typical test:

(1.9355 mg H₂S/100ft³) * .94008 S/H₂S * 35.314 ft³/m³ * (1/.64995)*(m³/kg) * .018 kg/min = .0178 mg S per minute from natural gas.

Mass flowrate of S from pulverized wood during typical test:

Fuel 1 at 4.64 grams/minute => S = 4.6 * 10⁻⁵
moles/minute = 1.475 mg/minute from wood fuel

About 80 times more sulphur comes from the wood fuel than from the natural gas. Coal contains an order of magnitude more S than the wood fuels used. Hence, S from natural gas is not of concern in this system.

APPENDIX E: SCREENED SAWDUST/SANDERDUST CASCADE IMPACTOR TEST SUMMARIES

The spreadsheets that follow summarize the detailed measurements and calculations required to determine the size distribution of ash for four pulverized wood fuels. These experiments were conducted with a natural-gas fired furnace. Ash samples were collected with a simple water cooled sampling probe and size-sorted with a Mark II cascade impactor.

Table E.2: Test 08099501

Item	Value	Units	Notes
Test Code	08099501	08099501	
Test loc	6.00	min	
Test dur	3.00	min	
Coal Properties			
grain	17.49	g/min	
UL Ana	448.845	g/min	
Carbon	24.743	g/h	
Hydrogen	1.091	mass/min	
Chlorine	2.192	mass/min	
Hydrogen (monatomic)	12.787	mass/min	
Chlorine	1.218	mass/min	
Chlorine (monatomic)	22.841	g/min	
Hydrogen	0.197	mass/min	
Chlorine (monatomic)	0.828	mass/min	
Hydrogen	8.719	mass/min	
Chlorine (monatomic)	5.971	mass/min	
Hydrogen	1.327	mass/min	
Chlorine (monatomic)	2.399	mass/min	
Hydrogen	13.487	mass/min	
Chlorine (monatomic)	9.000	mass/min	
Hydrogen	1.114	mass/min	
Chlorine (monatomic)	7.010	mass/min	
Hydrogen	0.094	mass/min	
Chlorine (monatomic)	28.112	g/min	
Hydrogen	307.634	g/min	
Chlorine (monatomic)	513.949	g/min	
Hydrogen	51.537	mass/min	
Chlorine (monatomic)	2.818	mass/min	
Hydrogen	919.842	g/min	
Chlorine (monatomic)	28.937	g/min	
Hydrogen	1097.829	g/min	
Chlorine (monatomic)	1.475	g/min	
Hydrogen	28.78843	g/min	
Chlorine (monatomic)	18.343	g/min	
Hydrogen	17.836	g/min	
Chlorine (monatomic)	9.029	g/min	
Hydrogen	1.032	g/min	
Chlorine (monatomic)	361.800	g/min	
Hydrogen	19.783	g/min	
Chlorine (monatomic)	1.935	g/min	
Hydrogen	9.955	g/min	
Chlorine (monatomic)	0.026	g/min	
Hydrogen	7.020	g/min	
Chlorine (monatomic)	1.22	g/min	

Table E.5: 08169503

Rate	Fuel 1	8/16/98	Monday	MT	Main NO	81.5 %	Probe ch 1	168 F	Imp Inlet diam	9/16	MAIN BURNER	17 317	CH4AA only
Coal	MS	08169503	medium	BF/NO	Main Air	35.0 %	Probe ch 2	99 mm	inches	0.618	main CH4	466.848	CH4AA only
bed inc	18.00	minutes	BF/NO	BF/NO	Coal bed	44.0 %	Probe ch 3	25 units	inches	0.38	main Air	1.871	CH4AA only
bed dur			BF/NO	BF/NO	Coal bed	4.0	Probe ch 4	5 gpm	fraction	43.0	main Air	28.568	CH4AA only
Coal Properties	(Ref. cont)		BF/NO	BF/NO	Coal bed	4.0	Probe ch 5	3.0	in lb	20 %	main Air	0.187	CH4AA only
grams	normal/100g		BF/NO	BF/NO	Coal bed	4.0	Probe ch 6	136 mm	inches	49	main Air	0.187	CH4AA only
	Carbon	3.76	BF/NO	BF/NO	Coal bed	20 %	Probe ch 7	90 F	inches	49	main Air	0.187	CH4AA only
	Hydrogen	6.87	BF/NO	BF/NO	Coal bed	49	Probe ch 8	101 F	inches	49	main Air	0.187	CH4AA only
	Oxygen	2.48	BF/NO	BF/NO	Coal bed	49	Probe ch 9	0 °C	inches	49	main Air	0.187	CH4AA only
	Nitrogen	0.36	BF/NO	BF/NO	Coal bed	49	Probe ch 10	0 °C	inches	49	main Air	0.187	CH4AA only
	Ash	0.00	BF/NO	BF/NO	Coal bed	49	Probe ch 11	0 °C	inches	49	main Air	0.187	CH4AA only
	Total	0.81	BF/NO	BF/NO	Coal bed	49	Probe ch 12	0 °C	inches	49	main Air	0.187	CH4AA only
		0.21	BF/NO	BF/NO	Coal bed	49	Probe ch 13	0 °C	inches	49	main Air	0.187	CH4AA only
		100.07698	BF/NO	BF/NO	Coal bed	49	Probe ch 14	0 °C	inches	49	main Air	0.187	CH4AA only
Shape	Initial (g)	Final (g)	Heard	Heard	% in size range	Com. %	Size Range	Temp. C.	Fuel comp on Elemental level	3.78E-02	Carbon (monatomic)	1.279	total
Densities	0.3274	0.3250	0.0056	0.0056	49.10	49.00	10.00 10.00 L-up	941 g/cm	Hydrogen (monatomic)	6.87E-02	Hydrogen (monatomic)	2.327	total
	0.29758	0.29856	0.00098	0.00098	5.39	54.52	8.29 9.0 L-up	899 g/cm	Oxygen (monatomic)	2.48E-02	Oxygen (monatomic)	13.224	total
	0.29787	0.29864	0.00077	0.00077	6.10	48.45	5.24 6.0 L-up	899 g/cm	Nitrogen (monatomic)	0.36E-02	Nitrogen (monatomic)	0.600	total
	0.32967	0.32700	0.00033	0.00033	7.81	45.80	3.46 4.7 L-up	899 g/cm	Sulfur (monatomic)	0.00E-02	Sulfur (monatomic)	1.293	total
	0.32728	0.32773	0.00081	0.00081	4.83	40.97	2.54 3.3 L-up	899 g/cm	vacuum photo	0.187	vacuum photo	7.599	total
	0.32946	0.32773	0.00087	0.00087	9.89	34.07	1.85 2.1 L-up	899 g/cm	vacuum photo	0.187	vacuum photo	0.982	total
	0.32946	0.32749	0.00093	0.00093	4.99	29.08	0.85 1.1 L-up	899 g/cm	coal flow rate	16	coal flow rate	28.105	total
	0.32946	0.32719	0.00024	0.00024	1.90	27.18	0.54 0.7 L-up	899 g/cm	BACKFIRE BURNERS		BACKFIRE BURNERS	307.484	total
	0.32916	0.32836	0.00011	0.00011	0.87	26.31	0.39 0.4 L-up	899 g/cm	moderately CH4		moderately CH4	513.093	total
	0.33181	0.33493	0.00332	0.00332	26.31	0.00	0.10 0.3 L-up	899 g/cm	moderately Air		moderately Air	51.368	total
	total mass:		0.01782						moderately Air		moderately Air	2.608	total
									moderately Air		moderately Air	819.843	total
									moderately Air		moderately Air	28.681	total
									moderately Air		moderately Air	1095.174	total
									moderately Air		moderately Air	1.49E-02	total
									moderately Air		moderately Air	2.25E-01	total
									moderately Air		moderately Air	19.293	total
									moderately Air		moderately Air	72.754	total
									moderately Air		moderately Air	9.029	total
									moderately Air		moderately Air	1.528	total
									moderately Air		moderately Air	349.888	total
									moderately Air		moderately Air	19.463	total
									moderately Air		moderately Air	1.42E-01	total
									moderately Air		moderately Air	2.19E-01	total
									moderately Air		moderately Air	0.038	total
									moderately Air		moderately Air	7.000	total
									moderately Air		moderately Air	48.396	total
									moderately Air		moderately Air		total

Table E.6: Test 10139501

Date:	10/19/90	Main No.:	60.6 %	Probe Set I:	189 F	Probe Set II:	195 F	Probe Set III:	195 F	Probe Set IV:	195 F	Probe Set V:	195 F	Probe Set VI:	195 F	Probe Set VII:	195 F	Probe Set VIII:	195 F	Probe Set IX:	195 F	Probe Set X:	195 F	Probe Set XI:	195 F	Probe Set XII:	195 F	Probe Set XIII:	195 F	Probe Set XIV:	195 F	Probe Set XV:	195 F	Probe Set XVI:	195 F	Probe Set XVII:	195 F	Probe Set XVIII:	195 F	Probe Set XIX:	195 F	Probe Set XX:	195 F	Probe Set XXI:	195 F	Probe Set XXII:	195 F	Probe Set XXIII:	195 F	Probe Set XXIV:	195 F	Probe Set XXV:	195 F	Probe Set XXVI:	195 F	Probe Set XXVII:	195 F	Probe Set XXVIII:	195 F	Probe Set XXIX:	195 F	Probe Set XXX:	195 F
Coal	10139501	10139501	60.6 %	Probe Set I:	189 F	Probe Set II:	195 F	Probe Set III:	195 F	Probe Set IV:	195 F	Probe Set V:	195 F	Probe Set VI:	195 F	Probe Set VII:	195 F	Probe Set VIII:	195 F	Probe Set IX:	195 F	Probe Set X:	195 F	Probe Set XI:	195 F	Probe Set XII:	195 F	Probe Set XIII:	195 F	Probe Set XIV:	195 F	Probe Set XV:	195 F	Probe Set XVI:	195 F	Probe Set XVII:	195 F	Probe Set XVIII:	195 F	Probe Set XIX:	195 F	Probe Set XX:	195 F	Probe Set XXI:	195 F	Probe Set XXII:	195 F	Probe Set XXIII:	195 F	Probe Set XXIV:	195 F	Probe Set XXV:	195 F	Probe Set XXVI:	195 F	Probe Set XXVII:	195 F	Probe Set XXVIII:	195 F	Probe Set XXIX:	195 F	Probe Set XXX:	195 F
Main No.:	10139501	10139501	60.6 %	Probe Set I:	189 F	Probe Set II:	195 F	Probe Set III:	195 F	Probe Set IV:	195 F	Probe Set V:	195 F	Probe Set VI:	195 F	Probe Set VII:	195 F	Probe Set VIII:	195 F	Probe Set IX:	195 F	Probe Set X:	195 F	Probe Set XI:	195 F	Probe Set XII:	195 F	Probe Set XIII:	195 F	Probe Set XIV:	195 F	Probe Set XV:	195 F	Probe Set XVI:	195 F	Probe Set XVII:	195 F	Probe Set XVIII:	195 F	Probe Set XIX:	195 F	Probe Set XX:	195 F	Probe Set XXI:	195 F	Probe Set XXII:	195 F	Probe Set XXIII:	195 F	Probe Set XXIV:	195 F	Probe Set XXV:	195 F	Probe Set XXVI:	195 F	Probe Set XXVII:	195 F	Probe Set XXVIII:	195 F	Probe Set XXIX:	195 F	Probe Set XXX:	195 F
Coal Process:	10139501	10139501	60.6 %	Probe Set I:	189 F	Probe Set II:	195 F	Probe Set III:	195 F	Probe Set IV:	195 F	Probe Set V:	195 F	Probe Set VI:	195 F	Probe Set VII:	195 F	Probe Set VIII:	195 F	Probe Set IX:	195 F	Probe Set X:	195 F	Probe Set XI:	195 F	Probe Set XII:	195 F	Probe Set XIII:	195 F	Probe Set XIV:	195 F	Probe Set XV:	195 F	Probe Set XVI:	195 F	Probe Set XVII:	195 F	Probe Set XVIII:	195 F	Probe Set XIX:	195 F	Probe Set XX:	195 F	Probe Set XXI:	195 F	Probe Set XXII:	195 F	Probe Set XXIII:	195 F	Probe Set XXIV:	195 F	Probe Set XXV:	195 F	Probe Set XXVI:	195 F	Probe Set XXVII:	195 F	Probe Set XXVIII:	195 F	Probe Set XXIX:	195 F	Probe Set XXX:	195 F

Table E.7: Test 10169501T

Date:	10/16/95	mo/day/yr	Main NG:	60.0 %		Probe ckt T:	187 F												
Coal:	None	source	Main Air:	34.0 %		Probe ckt Rr:	110												
		process		43.0 psig		Comb prg p:													
test no:	10169501	m/W/num	BF1NG:	45.0 %		Coal feed:		imp inlt diam	97.8	inches									
test dur:		minutes	BF1Ar:	4.0 %	units, front	Coal feed conv:		Mainduct rad	4	inches									
Coal Properties: (Ref. only)				4.0 %	units, back	Vacuum Rator:		Main Gas Rot	0.6	fraction									
grams	stromer/100g		BF2NG:		%	Vacuum Rator:		Main Air Rot	0.34	fraction									
			BF2Ar:		units, front			Main Air Roto	43.0	psig									
		Ult. Ana:			units, back	atomizer air:		Inj. Air Roto	40	%									
		Carbon:				atomizer air:		Inj. Air Roto	48	psig									
		Hydrogen:				atomizer H ₂ O:													
		Oxygen:																	
		Nitrogen:				over burn T:	112	F											
		Sulfur:				entr bypass:	0	'actm'											
		Ash:				inj exit T:	118	F											
		Moisture:																	
		Total:																	

Stage	Initial(g)	Final(g)	Net(g)	% in size range	Cum. % R. size range	D50 calc.	Size Range micrometers (default)	T/C Port	Temp. C.										
Preseparator	0		0.00000				10.0 A up	B											
	1		0.00000				9.0 - 10.0	C											
	2		0.00000				6.8 - 9.0	D											
	3		0.00000				4.7 - 6.8	E											
	4		0.00000				3.3 - 4.7	F											
	5		0.00000				2.3 - 3.3	G											
	6		0.00000				1.1 - 2.3	H											
	7		0.00000				0.7 - 1.1	I											
Backup Filter			0.00000				0.4 - 0.7	J											
			total mass:	0.00000			0 - 0.4	K											

Notes:																			
Temp measurement with High velocity TC																			
Procedure:	Started at port H., went through up to B, then did 'I' test. Water valves full open, shop air on, full closed sample valve. inserted HVTC to center line. Let warm up about 15 seconds. Slowly opened suction valve until at 15 in Hg. Let set for about 30 seconds for temp stabilization. Closed suction valve. Slowly removed HVTC and inserted in next port ASAP. Open ports as needed. Didn't leave open during sampling.																		

Test 10169501 - Main NG @ 60%, Main Air @ 34%/43psig, BF1 @ 45% and 4/4 units, Inj air at 40%/4psig																			
Port	Dist. from Inj.	Dist from thro	Pyrrometer	Bare TC	HVTC	d7/dume	268.128	quench rate											
b	43.18	18	1085	1075	1098														
c	58.42	21	1068	1058	1088														
d	73.86	27	1063	1037	1047														
e	88.9	33	950	1016	1052														
f	107.95	40.5	919	979	1032														
g	124.48	47	891	945	1010														
h	130.7	53	837	887	980														
i	154.04	59	795	832	928														
j		65																	
k		71																	

MAIN BURNER		
mdot CH ₄	18.884	g/min
mdot Main Air	453.509	g/min
phi	1.554	Air Fuel by mass
mdot/ndotF	29.844	g/g
CO ₂	1.058	moles/min
H ₂ O	2.112	moles/min
N ₂	12.421	moles/min
O ₂	1.192	moles/min
mdot air inj	45.882	g/min
O ₂	0.334	moles/min
N ₂	1.257	moles/min
Dry O ₂ w/inj	0.385	vol%
Dry O ₂ w/o inj	0.124	vol%
CO ₂	1.058	moles/min
H ₂ O	2.112	moles/min
N ₂	13.678	moles/min
SO ₂	0.000	moles/min
O ₂	1.528	moles/min
Dry O ₂	0.385	vol%
H ₂ O w	0.074	mass fraction
mol wt wet	28.102	g/mol
dens @ inj	297.430	g/m ³
mdot duct	619.283	g/min
vdot	91.785	m ³ /min
vdot	2.830	ft ³ /sec
dens @ imp inj	810.478	g/m ³
rho=(P/R^2 T)		
mol wt dry	29.414	g/mol
dens @ roto	1211.037	g/m ³
rho=(P/R^2 T)		
vol/water/roto	0.00E+00	m ³ /min
vol/water/croto	0.00E+00	m ³ /min
mdot/roto	0.000	g/min
mdot/lmp	0.000	g/min
vol/wt/lmp	0.000	m ³ /min
vol/wt/lmp	0.000	m ³ /min
vol/wt/lmp	0.000	m ³ /min
vol/wt/lmp	0.000	m ³ /min
mdot ash	0.00E+00	g/min
expected ash	0.00E+00	g
volume rate	0.000	vol in/vol tot
velocity rate	0.000	Vel in/Vol duct
%Dry ash	#DIV/0!	%
based on act		

BACKFIRE BURNERS

mdot BF1 CH ₄	18.7677071
mdot BF1 Ar	529.177954
phi	1.640
mdot/ndotF	28.1429133

ACTUAL ASH: 0 g

Gas Temperature Profile

Temperature, C	1200
	1150
	1100
	1050
	1000
	950
	900
	850

Table E.12: Test I1079501

Date:	11/7/96	mod/nyr	Main NG:	60.6 %	170 F																					
Coal:	Double Sixed	process	Main Air:	36.0 %	97 mm																					
test no:	11079501	mod/nyr	BF Inq:	43.0 %	350 units																					
test air:	10.00	mod/nyr	BF Air:	45.0 %	5.22 gms																					
Coal Properties: (Ref. only)			BF2 Air:	4.0 units front	33.0 %																					
Stems	48,752	stem/100g	BF2 NG:	0.0 %																						
	6,644	Carbon	BF2 Air:	0.0 units front																						
	41,124	Hydrogen	In Rate:	40 %																						
	0,418	Strontium	In Rate:	49 %																						
	2,036	0.03 Hydrogen	Imp in temp:	288 C (est)																						
	0	0.03 Sulfur	Imp temp biased on:	90 C (est)																						
	100,044	0.22 Sulfur	Imp in temp	90 C (est)																						
		0.22 Sulfur	% sp. ash	2.7 units (est)																						
Stage		Final(d)	Heated	% in size range		170 F	Temp, C																			
Preprocessor	0	0.32152	0.37496	0.05883	84.83																					
1	0.28532	0.29670	0.29827	0.00521	5.49																					
2	0.19609	0.20459	0.20094	0.00084	1.33																					
3	0.11999	0.11819	0.00048	0.78	7.69																					
4	0.35296	0.32437	0.00036	0.00036	0.57																					
5	0.35186	0.32185	0.00016	0.35	6.10																					
6	0.35549	0.35556	0.00006	0.09	6.01																					
7	0.32490	0.32407	0.00007	0.11	5.90																					
Backup Filter	0.33133	0.33500	0.00373	6.80	0.00																					
		Total mass:		0.04322																						

APPENDIX F: MILLED SAWDUST/SANDERDUST ELECTRICAL AEROSOL ANALYZER TEST SUMMARIES

The spreadsheets that follow summarize the detailed measurements and calculations required to determine the size distribution in the sub-micron range of ash for four pulverized wood fuels. These experiments were conducted with a natural-gas fired furnace. Ash samples were collected with an isokinetic, water-cooled, sampling probe. Particulate matter approximately 0.4 μm and larger were removed with a Mark II cascade impactor, and the remaining aerosol size distribution was determined with an Electrical Aerosol Analyzer (EAA). Coagulation time at ambient conditions for the aerosol was controlled by the size of delay tank between the cascade impactor and the EAA. EAA data was collected electronically, and is presented in graphical form in the body of the dissertation. Furnace operating conditions, sampling conditions and test notes are summarized here.

Table F.1: Test Log for Milled Sawdust/sanderdust Experiments

Master copy	Test Number	Fuel	Fuel No.	Spread sheet used	1-Stage 2-Stage 3-Stage 4-Stage	400 600 800 1000 1200 1400 1600 1800 2000	50 100 200 400 600 800 1000 1200 1400 1600 1800 2000	10 Flour Flour	Wood Flour	Main NO. Gross	Total Amountment Gr. (No Fuel)	Total Amountment Gr. (No Fuel)	AF, Test Amountment Gr. (No Fuel)	Upper Air AF Equiv	Upper Air Gr. (No Fuel)	Upper Air Mo. (No Fuel)	Upper Air Mo. (No Fuel)	Dry Gr. No Fuel (By Vol)	Dry Gr. No Fuel (By Vol)	Sample Fuel Temp. (C)
1	08019601	Fuel 1	0.00		0					17.9	466.2	22.1	27.8	1.23	105.3	5.9	5.9	9.6	9.6	0.0
2	08029601	Fuel 1	0.00		0					17.9	459.2	43.5	28.0	1.20	103.2	5.9	5.9	9.1	9.1	0.0
3	08129601	Fuel 1	0.00		0					17.7	465.8	43.5	28.8	1.20	103.2	5.9	5.9	9.1	9.1	0.0
4	08149601	Fuel 1	0.00		0					17.7	465.8	43.5	28.9	1.97	196.1	4.6	4.6	9.4	9.4	900.0
5	08099601	Fuel 1	0.00		0					17.7	465.8	56.2	29.5	2.19	199.9	5.0	5.0	9.3	9.3	0.0
6	08099601	Fuel 1	0.00		0					17.9	466.0	50.2	29.5	1.97	199.9	5.0	5.0	9.3	9.3	0.0
7	10099601	Fuel 1	0.00		0					17.9	466.0	50.2	29.8	2.03	174.4	5.0	5.0	9.5	9.5	0.0
8	10149601	Fuel 1	0.00		0					18.1	464.1	53.6	29.8	2.03	174.4	5.0	5.0	9.5	9.5	0.0
9	10179602	Temperature			0					18.3	464.1	53.6	29.8	2.00	172.1	5.0	5.0	9.0	9.0	0.0
10	10179602	Fuel 1	0.00		0					18.3	464.1	53.6	29.8	1.98	169.2	5.0	5.0	9.0	9.0	0.0
11	10219601	Fuel 1	0.00		0					18.3	464.1	53.6	29.8	2.05	176.1	5.0	5.0	9.0	9.0	0.0
12	10229601	Fuel 4	0.00		0					18.3	463.2	54.5	29.7	2.05	176.1	5.0	5.0	9.0	9.0	0.0
13	10249601	Fuel 4	0.00		0					18.2	464.1	54.5	29.8	2.00	171.9	5.0	5.0	9.0	9.0	0.0
14	10299601	Fuel 1	0.00		0					18.3	464.1	53.6	29.8	2.01	173.0	5.0	5.0	9.0	9.0	0.0
15	10299601	Fuel 1	0.00		0					18.3	464.1	53.6	29.8	2.01	173.0	5.0	5.0	9.0	9.0	0.0
16	10299601	Fuel 1	0.00		0					18.3	464.1	53.6	29.8	2.01	173.0	5.0	5.0	9.0	9.0	0.0
17	10299601	Fuel 1	0.00		0					18.3	464.1	53.6	29.8	2.01	173.0	5.0	5.0	9.0	9.0	0.0
18	11079601	Fuel 1	0.00		0					18.3	462.2	53.9	29.7	2.05	176.1	5.0	5.0	9.0	9.0	0.0
19	11079602	Fuel 1	0.00		0					18.3	462.2	53.9	29.7	2.03	174.5	5.0	5.0	9.0	9.0	0.0
20	11079602	Fuel 1	0.00		0					18.3	462.2	53.9	29.7	2.03	174.5	5.0	5.0	9.0	9.0	0.0
21	11179601	Fuel 4	0.00		0					18.3	462.2	53.9	29.7	2.03	174.5	5.0	5.0	9.0	9.0	0.0
22	11199601	Fuel 4	0.00		0					18.3	462.2	53.9	29.7	2.03	174.5	5.0	5.0	9.0	9.0	0.0
23	11299602	Fuel 4	0.00		0					18.3	462.2	53.9	29.7	2.03	174.5	5.0	5.0	9.0	9.0	0.0
24	11299602	Fuel 4	0.00		0					18.3	462.2	53.9	29.7	2.03	174.5	5.0	5.0	9.0	9.0	0.0
25	11299602	Fuel 4	0.00		0					18.3	462.2	53.9	29.7	2.03	174.5	5.0	5.0	9.0	9.0	0.0
26	11299602	Fuel 2	0.00		0					18.3	462.2	53.9	29.7	1.97	169.2	5.0	5.0	9.1	9.1	0.0
27	11299602	Fuel 2	0.00		0					18.3	462.2	53.9	29.7	1.97	169.2	5.0	5.0	9.1	9.1	0.0
28	11299602	Fuel 2	0.00		0					18.3	462.2	53.9	29.7	1.97	169.2	5.0	5.0	9.1	9.1	0.0
29	11299602	Fuel 2	0.00		0					18.3	462.2	53.9	29.7	1.97	169.2	5.0	5.0	9.1	9.1	0.0
30	11299602	Fuel 2	0.00		0					18.3	462.2	53.9	29.7	1.97	169.2	5.0	5.0	9.1	9.1	0.0
31	11299602	Fuel 3	0.00		0					18.3	462.2	53.9	29.7	1.97	169.2	5.0	5.0	9.1	9.1	0.0
32	11299602	Fuel 3	0.00		0					18.3	462.2	53.9	29.7	1.97	169.2	5.0	5.0	9.1	9.1	0.0
33	11299602	Fuel 3	0.00		0					18.3	462.2	53.9	29.7	1.97	169.2	5.0	5.0	9.1	9.1	0.0
34	11299602	Fuel 3	0.00		0					18.3	462.2	53.9	29.7	1.97	169.2	5.0	5.0	9.1	9.1	0.0
Average of all Non-temperature Tests																				
35	112996T	Temperature			0					18.2	462.2	53.9	29.7	2.07	170.0	4.9	4.9	10.4	10.4	0.0
36	11219601	Fuel 1	0.00		0					18.2	462.2	53.9	29.7	1.99	167.0	4.9	4.9	10.4	10.4	0.0
37	11219602	Fuel 1	0.00		0					18.2	462.2	53.9	29.7	2.00	171.5	5.0	5.0	10.3	10.3	0.0
38	11219603	Fuel 1	0.00		0					18.2	462.2	53.9	29.7	1.97	169.2	5.0	5.0	10.3	10.3	0.0
39	11219604	Fuel 1	0.00		0					18.2	462.2	53.9	29.7	1.97	169.2	5.0	5.0	10.3	10.3	0.0
40	11219605	Fuel 1	0.00		0					18.2	462.2	53.9	29.7	1.97	169.2	5.0	5.0	10.3	10.3	0.0
41	11219606	Blank	0.00		0					18.2	462.2	53.9	29.7	1.97	169.2	5.0	5.0	10.3	10.3	0.0
42	11299601	Fuel 3	0.00		0					18.2	462.2	53.9	29.7	1.97	169.2	5.0	5.0	10.3	10.3	0.0
43	11299602	Fuel 3	0.00		0					18.2	462.2	53.9	29.7	1.97	169.2	5.0	5.0	10.3	10.3	0.0
44	11299603	Fuel 4	0.00		0					18.2	462.2	53.9	29.7	1.97	169.2	5.0	5.0	10.3	10.3	0.0
45	11299604	Fuel 4	0.00		0					18.2	462.2	53.9	29.7	1.97	169.2	5.0	5.0	10.3	10.3	0.0
46	11299605	Fuel 2	0.00		0					18.2	462.2	53.9	29.7	1.97	169.2	5.0	5.0	10.3	10.3	0.0
47	11299605	Fuel 2	0.00		0					18.2	462.2	53.9	29.7	1.97	169.2	5.0	5.0	10.3	10.3	0.0
Average of all Non-temperature Tests																				
48	112596T	Temperature			0					18.2	462.2	53.9	29.7	2.0	160.0	5.0	5.0	10.1	10.1	0.0
49	11259601	Fuel 1	0.00		0					18.2	462.2	53.9	29.7	1.97	169.2	5.0	5.0	10.1	10.1	0.0
50	11279601	Fuel 1	0.00		0					18.2	462.2	53.9	29.7	1.97	169.2	5.0	5.0	10.1	10.1	0.0
51	11279602	Fuel 4	0.00		0					18.2	462.2	53.9	29.7	1.97	169.2	5.0	5.0	10.1	10.1	0.0
52	11279603	Fuel 4	0.00		0					18.2	462.2	53.9	29.7	1.97	169.2	5.0	5.0	10.1	10.1	0.0
Average of all Non-temperature Tests																				

Table F.2: Test 0819601

1	2	3	4	5	6	7	8	9	10	11	12	13	14	15	16	17	18	19	20	21	22	23	24	25	26	27	28	29	30	31	32	33	34	35	36	37	38	39	40	41	42	43	44	45	46	47	48	49	50	51	52	53	54	55	56	57	58	59	60	61	62	63	64	65	66	67	68	69	70	71	72	73	74	75	76	77	78	79	80	81	82	83	84	85	86	87	88	89	90	91	92	93	94	95	96	97	98	99	100
1	2	3	4	5	6	7	8	9	10	11	12	13	14	15	16	17	18	19	20	21	22	23	24	25	26	27	28	29	30	31	32	33	34	35	36	37	38	39	40	41	42	43	44	45	46	47	48	49	50	51	52	53	54	55	56	57	58	59	60	61	62	63	64	65	66	67	68	69	70	71	72	73	74	75	76	77	78	79	80	81	82	83	84	85	86	87	88	89	90	91	92	93	94	95	96	97	98	99	100

Table F.3: Test 08069601

Item No.	Item Description	Unit	Quantity	Unit Price	Total Price	Comments
1
2
3
4
5
6
7
8
9
10
11
12
13
14
15
16
17
18
19
20
21
22
23
24
25
26
27
28
29
30
31
32
33
34
35
36
37
38
39
40
41
42
43
44
45
46
47
48
49
50

Table F.4: Test 08129601

1	2	3	4	5	6	7	8	9	10	11	12	13	14	15	16	17	18	19	20	21	22	23	24	25	26	27	28	29	30	31	32	33	34	35	36	37	38	39	40	41	42	43	44	45	46	47	48	49	50	51	52	53	54	55	56	57	58	59	60	61	62	63	64	65	66	67	68	69	70	71	72	73	74	75	76	77	78	79	80	81	82	83	84	85	86	87	88	89	90	91	92	93	94	95	96	97	98	99	100																																																																																																																																																																																																																																																																																																																																																																																																																																																																																																																																																																																																																																																																																																																																																																																																																																
0100	0101	0102	0103	0104	0105	0106	0107	0108	0109	0110	0111	0112	0113	0114	0115	0116	0117	0118	0119	0120	0121	0122	0123	0124	0125	0126	0127	0128	0129	0130	0131	0132	0133	0134	0135	0136	0137	0138	0139	0140	0141	0142	0143	0144	0145	0146	0147	0148	0149	0150	0151	0152	0153	0154	0155	0156	0157	0158	0159	0160	0161	0162	0163	0164	0165	0166	0167	0168	0169	0170	0171	0172	0173	0174	0175	0176	0177	0178	0179	0180	0181	0182	0183	0184	0185	0186	0187	0188	0189	0190	0191	0192	0193	0194	0195	0196	0197	0198	0199	0200	0201	0202	0203	0204	0205	0206	0207	0208	0209	0210	0211	0212	0213	0214	0215	0216	0217	0218	0219	0220	0221	0222	0223	0224	0225	0226	0227	0228	0229	0230	0231	0232	0233	0234	0235	0236	0237	0238	0239	0240	0241	0242	0243	0244	0245	0246	0247	0248	0249	0250	0251	0252	0253	0254	0255	0256	0257	0258	0259	0260	0261	0262	0263	0264	0265	0266	0267	0268	0269	0270	0271	0272	0273	0274	0275	0276	0277	0278	0279	0280	0281	0282	0283	0284	0285	0286	0287	0288	0289	0290	0291	0292	0293	0294	0295	0296	0297	0298	0299	0300	0301	0302	0303	0304	0305	0306	0307	0308	0309	0310	0311	0312	0313	0314	0315	0316	0317	0318	0319	0320	0321	0322	0323	0324	0325	0326	0327	0328	0329	0330	0331	0332	0333	0334	0335	0336	0337	0338	0339	0340	0341	0342	0343	0344	0345	0346	0347	0348	0349	0350	0351	0352	0353	0354	0355	0356	0357	0358	0359	0360	0361	0362	0363	0364	0365	0366	0367	0368	0369	0370	0371	0372	0373	0374	0375	0376	0377	0378	0379	0380	0381	0382	0383	0384	0385	0386	0387	0388	0389	0390	0391	0392	0393	0394	0395	0396	0397	0398	0399	0400	0401	0402	0403	0404	0405	0406	0407	0408	0409	0410	0411	0412	0413	0414	0415	0416	0417	0418	0419	0420	0421	0422	0423	0424	0425	0426	0427	0428	0429	0430	0431	0432	0433	0434	0435	0436	0437	0438	0439	0440	0441	0442	0443	0444	0445	0446	0447	0448	0449	0450	0451	0452	0453	0454	0455	0456	0457	0458	0459	0460	0461	0462	0463	0464	0465	0466	0467	0468	0469	0470	0471	0472	0473	0474	0475	0476	0477	0478	0479	0480	0481	0482	0483	0484	0485	0486	0487	0488	0489	0490	0491	0492	0493	0494	0495	0496	0497	0498	0499	0500	0501	0502	0503	0504	0505	0506	0507	0508	0509	0510	0511	0512	0513	0514	0515	0516	0517	0518	0519	0520	0521	0522	0523	0524	0525	0526	0527	0528	0529	0530	0531	0532	0533	0534	0535	0536	0537	0538	0539	0540	0541	0542	0543	0544	0545	0546	0547	0548	0549	0550	0551	0552	0553	0554	0555	0556	0557	0558	0559	0560	0561	0562	0563	0564	0565	0566	0567	0568	0569	0570	0571	0572	0573	0574	0575	0576	0577	0578	0579	0580	0581	0582	0583	0584	0585	0586	0587	0588	0589	0590	0591	0592	0593	0594	0595	0596	0597	0598	0599	0600	0601	0602	0603	0604	0605	0606	0607	0608	0609	0610	0611	0612	0613	0614	0615	0616	0617	0618	0619	0620	0621	0622	0623	0624	0625	0626	0627	0628	0629	0630	0631	0632	0633	0634	0635	0636	0637	0638	0639	0640	0641	0642	0643	0644	0645	0646	0647	0648	0649	0650	0651	0652	0653	0654	0655	0656	0657	0658	0659	0660	0661	0662	0663	0664	0665	0666	0667	0668	0669	0670	0671	0672	0673	0674	0675	0676	0677	0678	0679	0680	0681	0682	0683	0684	0685	0686	0687	0688	0689	0690	0691	0692	0693	0694	0695	0696	0697	0698	0699	0700	0701	0702	0703	0704	0705	0706	0707	0708	0709	0710	0711	0712	0713	0714	0715	0716	0717	0718	0719	0720	0721	0722	0723	0724	0725	0726	0727	0728	0729	0730	0731	0732	0733	0734	0735	0736	0737	0738	0739	0740	0741	0742	0743	0744	0745	0746	0747	0748	0749	0750	0751	0752	0753	0754	0755	0756	0757	0758	0759	0760	0761	0762	0763	0764	0765	0766	0767	0768	0769	0770	0771	0772	0773	0774	0775	0776	0777	0778	0779	0780	0781	0782	0783	0784	0785	0786	0787	0788	0789	0790	0791	0792	0793	0794	0795	0796	0797	0798	0799	0800	0801	0802	0803	0804	0805	0806	0807	0808	0809	0810	0811	0812	0813	0814	0815	0816	0817	0818	0819	0820	0821	0822	0823	0824	0825	0826	0827	0828	0829	0830	0831	0832	0833	0834	0835	0836	0837	0838	0839	0840	0841	0842	0843	0844	0845	0846	0847	0848	0849	0850	0851	0852	0853	0854	0855	0856	0857	0858	0859	0860	0861	0862	0863	0864	0865	0866	0867	0868	0869	0870	0871	0872	0873	0874	0875	0876	0877	0878	0879	0880	0881	0882	0883	0884	0885	0886	0887	0888	0889	0890	0891	0892	0893	0894	0895	0896	0897	0898	0899	0900	0901	0902	0903	0904	0905	0906	0907	0908	0909	0910	0911	0912	0913	0914	0915	0916	0917	0918	0919	0920	0921	0922	0923	0924	0925	0926	0927	0928	0929	0930	0931	0932	0933	0934	0935	0936	0937	0938	0939	0940	0941	0942	0943	0944	0945	0946	0947	0948	0949	0950	0951	0952	0953	0954	0955	0956	0957	0958	0959	0960	0961	0962	0963	0964	0965	0966	0967	0968	0969	0970	0971	0972	0973	0974	0975	0976	0977	0978	0979	0980	0981	0982	0983	0984	0985	0986	0987	0988	0989	0990	0991	0992	0993	0994	0995	0996	0997	0998	0999

Table F.5: Test 08149601

1	2	3	4	5	6	7	8	9	10	11	12	13	14	15	16	17	18	19	20	21	22	23	24	25	26	27	28	29	30	31	32	33	34	35	36	37	38	39	40	41	42	43	44	45	46	47	48	49	50	51	52	53	54	55	56	57	58	59	60	61	62	63	64	65	66	67	68	69	70	71	72	73	74	75	76	77	78	79	80	81	82	83	84	85	86	87	88	89	90	91	92	93	94	95	96	97	98	99	100
1	2	3	4	5	6	7	8	9	10	11	12	13	14	15	16	17	18	19	20	21	22	23	24	25	26	27	28	29	30	31	32	33	34	35	36	37	38	39	40	41	42	43	44	45	46	47	48	49	50	51	52	53	54	55	56	57	58	59	60	61	62	63	64	65	66	67	68	69	70	71	72	73	74	75	76	77	78	79	80	81	82	83	84	85	86	87	88	89	90	91	92	93	94	95	96	97	98	99	100

Table F.6: Test 09039601

Item	1	2	3	4	5	6	7	8	9	10	11	12	13	14	15	16	17	18	19	20	21	22	23	24	25	26	27	28	29	30	31	32	33	34	35	36	37	38	39	40	41	42	43	44	45	46	47	48	49	50	51	52	53	54	55	56	57	58	59	60	61	62	63	64	65	66	67	68	69	70	71	72	73	74	75	76	77	78	79	80	81	82	83	84	85	86	87	88	89	90	91	92	93	94	95	96	97	98	99	100
1	2	3	4	5	6	7	8	9	10	11	12	13	14	15	16	17	18	19	20	21	22	23	24	25	26	27	28	29	30	31	32	33	34	35	36	37	38	39	40	41	42	43	44	45	46	47	48	49	50	51	52	53	54	55	56	57	58	59	60	61	62	63	64	65	66	67	68	69	70	71	72	73	74	75	76	77	78	79	80	81	82	83	84	85	86	87	88	89	90	91	92	93	94	95	96	97	98	99	100	

Table F.7: Test 09099601

1	2	3	4	5	6	7	8	9	10	11	12	13	14	15	16	17	18	19	20	21	22	23	24	25	26	27	28	29	30	31	32	33	34	35	36	37	38	39	40	41	42	43	44	45	46	47	48	49	50	51	52	53	54	55	56	57	58	59	60	61	62	63	64	65	66	67	68	69	70	71	72	73	74	75	76	77	78	79	80	81	82	83	84	85	86	87	88	89	90	91	92	93	94	95	96	97	98	99	100
001	002	003	004	005	006	007	008	009	010	011	012	013	014	015	016	017	018	019	020	021	022	023	024	025	026	027	028	029	030	031	032	033	034	035	036	037	038	039	040	041	042	043	044	045	046	047	048	049	050	051	052	053	054	055	056	057	058	059	060	061	062	063	064	065	066	067	068	069	070	071	072	073	074	075	076	077	078	079	080	081	082	083	084	085	086	087	088	089	090	091	092	093	094	095	096	097	098	099	100

Table F.8: Test 10089601

Line	Code	Quantity	Unit	Material	Notes	Unit Price	Amount	Material	Unit Price	Amount	Material	Unit Price	Amount	Material	Unit Price	Amount	Material	Unit Price	Amount
1	10089601	1	EA

Table F.9: Test I0149601

Run	1	2	3	4	5	6	7	8	9	10	11	12	13	14	15	16	17	18	19	20	21	22	23	24	25	26	27	28	29	30	31	32	33	34	35	36	37	38	39	40	41	42	43	44	45	46	47	48	49	50	51	52	53	54	55	56	57	58	59	60	61	62	63	64	65	66	67	68	69	70	71	72	73	74	75	76	77	78	79	80	81	82	83	84	85	86	87	88	89	90	91	92	93	94	95	96	97	98	99	100
1	101	102	103	104	105	106	107	108	109	110	111	112	113	114	115	116	117	118	119	120	121	122	123	124	125	126	127	128	129	130	131	132	133	134	135	136	137	138	139	140	141	142	143	144	145	146	147	148	149	150	151	152	153	154	155	156	157	158	159	160	161	162	163	164	165	166	167	168	169	170	171	172	173	174	175	176	177	178	179	180	181	182	183	184	185	186	187	188	189	190	191	192	193	194	195	196	197	198	199	200

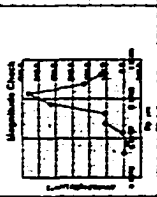


Table F.12: Test 10219601

1	2	3	4	5	6	7	8	9	10	11	12	13	14	15	16	17	18	19	20	21	22	23	24	25	
10219601	10219601	10219601	10219601	10219601	10219601	10219601	10219601	10219601	10219601	10219601	10219601	10219601	10219601	10219601	10219601	10219601	10219601	10219601	10219601	10219601	10219601	10219601	10219601	10219601	10219601
...



Table F.13: Test 10229601

Item	5	6	7	8	9	10	11	12	13	14	15	16	17	18	19	20	21	22	23	24	25
1	0.05	0.05	0.05	0.05	0.05	0.05	0.05	0.05	0.05	0.05	0.05	0.05	0.05	0.05	0.05	0.05	0.05	0.05	0.05	0.05	0.05
2	0.10	0.10	0.10	0.10	0.10	0.10	0.10	0.10	0.10	0.10	0.10	0.10	0.10	0.10	0.10	0.10	0.10	0.10	0.10	0.10	0.10
3	0.15	0.15	0.15	0.15	0.15	0.15	0.15	0.15	0.15	0.15	0.15	0.15	0.15	0.15	0.15	0.15	0.15	0.15	0.15	0.15	0.15
4	0.20	0.20	0.20	0.20	0.20	0.20	0.20	0.20	0.20	0.20	0.20	0.20	0.20	0.20	0.20	0.20	0.20	0.20	0.20	0.20	0.20
5	0.25	0.25	0.25	0.25	0.25	0.25	0.25	0.25	0.25	0.25	0.25	0.25	0.25	0.25	0.25	0.25	0.25	0.25	0.25	0.25	0.25
6	0.30	0.30	0.30	0.30	0.30	0.30	0.30	0.30	0.30	0.30	0.30	0.30	0.30	0.30	0.30	0.30	0.30	0.30	0.30	0.30	0.30
7	0.35	0.35	0.35	0.35	0.35	0.35	0.35	0.35	0.35	0.35	0.35	0.35	0.35	0.35	0.35	0.35	0.35	0.35	0.35	0.35	0.35
8	0.40	0.40	0.40	0.40	0.40	0.40	0.40	0.40	0.40	0.40	0.40	0.40	0.40	0.40	0.40	0.40	0.40	0.40	0.40	0.40	0.40
9	0.45	0.45	0.45	0.45	0.45	0.45	0.45	0.45	0.45	0.45	0.45	0.45	0.45	0.45	0.45	0.45	0.45	0.45	0.45	0.45	0.45
10	0.50	0.50	0.50	0.50	0.50	0.50	0.50	0.50	0.50	0.50	0.50	0.50	0.50	0.50	0.50	0.50	0.50	0.50	0.50	0.50	0.50
11	0.55	0.55	0.55	0.55	0.55	0.55	0.55	0.55	0.55	0.55	0.55	0.55	0.55	0.55	0.55	0.55	0.55	0.55	0.55	0.55	0.55
12	0.60	0.60	0.60	0.60	0.60	0.60	0.60	0.60	0.60	0.60	0.60	0.60	0.60	0.60	0.60	0.60	0.60	0.60	0.60	0.60	0.60
13	0.65	0.65	0.65	0.65	0.65	0.65	0.65	0.65	0.65	0.65	0.65	0.65	0.65	0.65	0.65	0.65	0.65	0.65	0.65	0.65	0.65
14	0.70	0.70	0.70	0.70	0.70	0.70	0.70	0.70	0.70	0.70	0.70	0.70	0.70	0.70	0.70	0.70	0.70	0.70	0.70	0.70	0.70
15	0.75	0.75	0.75	0.75	0.75	0.75	0.75	0.75	0.75	0.75	0.75	0.75	0.75	0.75	0.75	0.75	0.75	0.75	0.75	0.75	0.75
16	0.80	0.80	0.80	0.80	0.80	0.80	0.80	0.80	0.80	0.80	0.80	0.80	0.80	0.80	0.80	0.80	0.80	0.80	0.80	0.80	0.80
17	0.85	0.85	0.85	0.85	0.85	0.85	0.85	0.85	0.85	0.85	0.85	0.85	0.85	0.85	0.85	0.85	0.85	0.85	0.85	0.85	0.85
18	0.90	0.90	0.90	0.90	0.90	0.90	0.90	0.90	0.90	0.90	0.90	0.90	0.90	0.90	0.90	0.90	0.90	0.90	0.90	0.90	0.90
19	0.95	0.95	0.95	0.95	0.95	0.95	0.95	0.95	0.95	0.95	0.95	0.95	0.95	0.95	0.95	0.95	0.95	0.95	0.95	0.95	0.95
20	1.00	1.00	1.00	1.00	1.00	1.00	1.00	1.00	1.00	1.00	1.00	1.00	1.00	1.00	1.00	1.00	1.00	1.00	1.00	1.00	1.00
21	1.05	1.05	1.05	1.05	1.05	1.05	1.05	1.05	1.05	1.05	1.05	1.05	1.05	1.05	1.05	1.05	1.05	1.05	1.05	1.05	1.05
22	1.10	1.10	1.10	1.10	1.10	1.10	1.10	1.10	1.10	1.10	1.10	1.10	1.10	1.10	1.10	1.10	1.10	1.10	1.10	1.10	1.10
23	1.15	1.15	1.15	1.15	1.15	1.15	1.15	1.15	1.15	1.15	1.15	1.15	1.15	1.15	1.15	1.15	1.15	1.15	1.15	1.15	1.15
24	1.20	1.20	1.20	1.20	1.20	1.20	1.20	1.20	1.20	1.20	1.20	1.20	1.20	1.20	1.20	1.20	1.20	1.20	1.20	1.20	1.20
25	1.25	1.25	1.25	1.25	1.25	1.25	1.25	1.25	1.25	1.25	1.25	1.25	1.25	1.25	1.25	1.25	1.25	1.25	1.25	1.25	1.25

Table F.14: Test 10249601

1	2	3	4	5	6	7	8	9	10	11	12	13	14	15	16	17	18	19	20	21	22	23	24	25	26	27	28	29	30	31	32	33	34	35	36	37	38	39	40	41	42	43	44	45	46	47	48	49	50	51	52	53	54	55	56	57	58	59	60	61	62	63	64	65	66	67	68	69	70	71	72	73	74	75	76	77	78	79	80	81	82	83	84	85	86	87	88	89	90	91	92	93	94	95	96	97	98	99	100
1	2	3	4	5	6	7	8	9	10	11	12	13	14	15	16	17	18	19	20	21	22	23	24	25	26	27	28	29	30	31	32	33	34	35	36	37	38	39	40	41	42	43	44	45	46	47	48	49	50	51	52	53	54	55	56	57	58	59	60	61	62	63	64	65	66	67	68	69	70	71	72	73	74	75	76	77	78	79	80	81	82	83	84	85	86	87	88	89	90	91	92	93	94	95	96	97	98	99	100

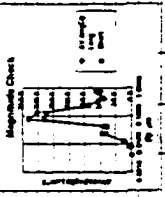


Table F.19: Test I1149602

Item	1	2	3	4	5	6	7	8	9	10	11	12	13	14	15	16	17	18	19	20	21	22	23	24	25	26	27	28	29	30	31	32	33	34	35				
1	11111111	11111111	11111111	11111111	11111111	11111111	11111111	11111111	11111111	11111111	11111111	11111111	11111111	11111111	11111111	11111111	11111111	11111111	11111111	11111111	11111111	11111111	11111111	11111111	11111111	11111111	11111111	11111111	11111111	11111111	11111111	11111111	11111111	11111111	11111111	11111111	11111111		
2	11111111	11111111	11111111	11111111	11111111	11111111	11111111	11111111	11111111	11111111	11111111	11111111	11111111	11111111	11111111	11111111	11111111	11111111	11111111	11111111	11111111	11111111	11111111	11111111	11111111	11111111	11111111	11111111	11111111	11111111	11111111	11111111	11111111	11111111	11111111	11111111	11111111	11111111	
3	11111111	11111111	11111111	11111111	11111111	11111111	11111111	11111111	11111111	11111111	11111111	11111111	11111111	11111111	11111111	11111111	11111111	11111111	11111111	11111111	11111111	11111111	11111111	11111111	11111111	11111111	11111111	11111111	11111111	11111111	11111111	11111111	11111111	11111111	11111111	11111111	11111111	11111111	11111111
4	11111111	11111111	11111111	11111111	11111111	11111111	11111111	11111111	11111111	11111111	11111111	11111111	11111111	11111111	11111111	11111111	11111111	11111111	11111111	11111111	11111111	11111111	11111111	11111111	11111111	11111111	11111111	11111111	11111111	11111111	11111111	11111111	11111111	11111111	11111111	11111111	11111111	11111111	11111111
5	11111111	11111111	11111111	11111111	11111111	11111111	11111111	11111111	11111111	11111111	11111111	11111111	11111111	11111111	11111111	11111111	11111111	11111111	11111111	11111111	11111111	11111111	11111111	11111111	11111111	11111111	11111111	11111111	11111111	11111111	11111111	11111111	11111111	11111111	11111111	11111111	11111111	11111111	11111111

Table F.20: Test 11159601

Line No.	Item No.	Part No.	Part Description	QTY	UNIT PRICE	TOTAL PRICE	Notes
1	1	11159601	11159601	1	11159601	11159601	
2	2	11159601	11159601	1	11159601	11159601	
3	3	11159601	11159601	1	11159601	11159601	
4	4	11159601	11159601	1	11159601	11159601	
5	5	11159601	11159601	1	11159601	11159601	
6	6	11159601	11159601	1	11159601	11159601	
7	7	11159601	11159601	1	11159601	11159601	
8	8	11159601	11159601	1	11159601	11159601	
9	9	11159601	11159601	1	11159601	11159601	
10	10	11159601	11159601	1	11159601	11159601	
11	11	11159601	11159601	1	11159601	11159601	
12	12	11159601	11159601	1	11159601	11159601	
13	13	11159601	11159601	1	11159601	11159601	
14	14	11159601	11159601	1	11159601	11159601	
15	15	11159601	11159601	1	11159601	11159601	
16	16	11159601	11159601	1	11159601	11159601	
17	17	11159601	11159601	1	11159601	11159601	
18	18	11159601	11159601	1	11159601	11159601	
19	19	11159601	11159601	1	11159601	11159601	
20	20	11159601	11159601	1	11159601	11159601	
21	21	11159601	11159601	1	11159601	11159601	
22	22	11159601	11159601	1	11159601	11159601	
23	23	11159601	11159601	1	11159601	11159601	
24	24	11159601	11159601	1	11159601	11159601	
25	25	11159601	11159601	1	11159601	11159601	
26	26	11159601	11159601	1	11159601	11159601	
27	27	11159601	11159601	1	11159601	11159601	
28	28	11159601	11159601	1	11159601	11159601	
29	29	11159601	11159601	1	11159601	11159601	
30	30	11159601	11159601	1	11159601	11159601	
31	31	11159601	11159601	1	11159601	11159601	
32	32	11159601	11159601	1	11159601	11159601	
33	33	11159601	11159601	1	11159601	11159601	
34	34	11159601	11159601	1	11159601	11159601	
35	35	11159601	11159601	1	11159601	11159601	
36	36	11159601	11159601	1	11159601	11159601	
37	37	11159601	11159601	1	11159601	11159601	
38	38	11159601	11159601	1	11159601	11159601	
39	39	11159601	11159601	1	11159601	11159601	
40	40	11159601	11159601	1	11159601	11159601	
41	41	11159601	11159601	1	11159601	11159601	
42	42	11159601	11159601	1	11159601	11159601	
43	43	11159601	11159601	1	11159601	11159601	
44	44	11159601	11159601	1	11159601	11159601	
45	45	11159601	11159601	1	11159601	11159601	
46	46	11159601	11159601	1	11159601	11159601	
47	47	11159601	11159601	1	11159601	11159601	
48	48	11159601	11159601	1	11159601	11159601	
49	49	11159601	11159601	1	11159601	11159601	
50	50	11159601	11159601	1	11159601	11159601	

Table F.24(cont.): Test 112096T

Run	Time	Temp	Humidity	Pressure	Wind	Direction	1	2	3	4	5	6	7	8	9	10	11	12	13	14	15	16	17	18	19	20	21	22	23	24	25	26	27	28	29	30	31	32	33	34	35	36	37	38	39	40	41	42	43	44	45	46	47	48	49	50																																																																																																																																																																																												
112096T	11:00	1000	6	1020	1.020	10	1110	10	1120	10	1130	10	1140	10	1150	10	1200	10	1210	10	1220	10	1230	10	1240	10	1250	10	1300	10	1310	10	1320	10	1330	10	1340	10	1350	10	1400	10	1410	10	1420	10	1430	10	1440	10	1450	10	1500	10	1510	10	1520	10	1530	10	1540	10	1550	10	1600	10	1610	10	1620	10	1630	10	1640	10	1650	10	1700	10	1710	10	1720	10	1730	10	1740	10	1750	10	1800	10	1810	10	1820	10	1830	10	1840	10	1850	10	1900	10	1910	10	1920	10	1930	10	1940	10	1950	10	2000	10	2010	10	2020	10	2030	10	2040	10	2050	10	2100	10	2110	10	2120	10	2130	10	2140	10	2150	10	2200	10	2210	10	2220	10	2230	10	2240	10	2250	10	2300	10	2310	10	2320	10	2330	10	2340	10	2350	10	2400	10	2410	10	2420	10	2430	10	2440	10	2450	10	2500	10	2510	10	2520	10	2530	10	2540	10	2550	10	2600	10	2610	10	2620	10	2630	10	2640	10	2650	10	2700	10	2710	10	2720	10	2730	10	2740	10	2750	10	2800	10	2810	10	2820	10	2830	10	2840	10	2850	10	2900	10	2910	10	2920	10	2930	10	2940	10	2950	10	3000	10	3010	10	3020	10	3030	10	3040	10	3050	10

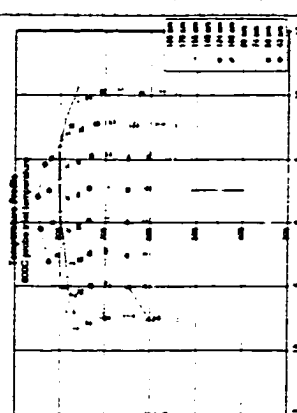
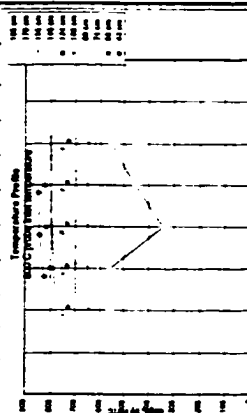


Table F.25: Test 11219601

Test No.	Category	Specimen	Depth (ft)	Weight (lb)	Volume (cc)	Grain Size (mm)	Grain Size (%)	Grain Size (in)	Grain Size (cm)	Grain Size (m)
11219601-1	1	11219601-1	0.5	100	100	0.1	100	0.001	0.001	0.001
11219601-2	1	11219601-2	0.5	100	100	0.1	100	0.001	0.001	0.001
11219601-3	1	11219601-3	0.5	100	100	0.1	100	0.001	0.001	0.001
11219601-4	1	11219601-4	0.5	100	100	0.1	100	0.001	0.001	0.001
11219601-5	1	11219601-5	0.5	100	100	0.1	100	0.001	0.001	0.001
11219601-6	1	11219601-6	0.5	100	100	0.1	100	0.001	0.001	0.001
11219601-7	1	11219601-7	0.5	100	100	0.1	100	0.001	0.001	0.001
11219601-8	1	11219601-8	0.5	100	100	0.1	100	0.001	0.001	0.001
11219601-9	1	11219601-9	0.5	100	100	0.1	100	0.001	0.001	0.001
11219601-10	1	11219601-10	0.5	100	100	0.1	100	0.001	0.001	0.001
11219601-11	1	11219601-11	0.5	100	100	0.1	100	0.001	0.001	0.001
11219601-12	1	11219601-12	0.5	100	100	0.1	100	0.001	0.001	0.001
11219601-13	1	11219601-13	0.5	100	100	0.1	100	0.001	0.001	0.001
11219601-14	1	11219601-14	0.5	100	100	0.1	100	0.001	0.001	0.001
11219601-15	1	11219601-15	0.5	100	100	0.1	100	0.001	0.001	0.001
11219601-16	1	11219601-16	0.5	100	100	0.1	100	0.001	0.001	0.001
11219601-17	1	11219601-17	0.5	100	100	0.1	100	0.001	0.001	0.001
11219601-18	1	11219601-18	0.5	100	100	0.1	100	0.001	0.001	0.001
11219601-19	1	11219601-19	0.5	100	100	0.1	100	0.001	0.001	0.001
11219601-20	1	11219601-20	0.5	100	100	0.1	100	0.001	0.001	0.001
11219601-21	1	11219601-21	0.5	100	100	0.1	100	0.001	0.001	0.001
11219601-22	1	11219601-22	0.5	100	100	0.1	100	0.001	0.001	0.001
11219601-23	1	11219601-23	0.5	100	100	0.1	100	0.001	0.001	0.001
11219601-24	1	11219601-24	0.5	100	100	0.1	100	0.001	0.001	0.001
11219601-25	1	11219601-25	0.5	100	100	0.1	100	0.001	0.001	0.001
11219601-26	1	11219601-26	0.5	100	100	0.1	100	0.001	0.001	0.001
11219601-27	1	11219601-27	0.5	100	100	0.1	100	0.001	0.001	0.001
11219601-28	1	11219601-28	0.5	100	100	0.1	100	0.001	0.001	0.001
11219601-29	1	11219601-29	0.5	100	100	0.1	100	0.001	0.001	0.001
11219601-30	1	11219601-30	0.5	100	100	0.1	100	0.001	0.001	0.001
11219601-31	1	11219601-31	0.5	100	100	0.1	100	0.001	0.001	0.001
11219601-32	1	11219601-32	0.5	100	100	0.1	100	0.001	0.001	0.001
11219601-33	1	11219601-33	0.5	100	100	0.1	100	0.001	0.001	0.001
11219601-34	1	11219601-34	0.5	100	100	0.1	100	0.001	0.001	0.001
11219601-35	1	11219601-35	0.5	100	100	0.1	100	0.001	0.001	0.001
11219601-36	1	11219601-36	0.5	100	100	0.1	100	0.001	0.001	0.001
11219601-37	1	11219601-37	0.5	100	100	0.1	100	0.001	0.001	0.001
11219601-38	1	11219601-38	0.5	100	100	0.1	100	0.001	0.001	0.001
11219601-39	1	11219601-39	0.5	100	100	0.1	100	0.001	0.001	0.001
11219601-40	1	11219601-40	0.5	100	100	0.1	100	0.001	0.001	0.001
11219601-41	1	11219601-41	0.5	100	100	0.1	100	0.001	0.001	0.001
11219601-42	1	11219601-42	0.5	100	100	0.1	100	0.001	0.001	0.001
11219601-43	1	11219601-43	0.5	100	100	0.1	100	0.001	0.001	0.001
11219601-44	1	11219601-44	0.5	100	100	0.1	100	0.001	0.001	0.001
11219601-45	1	11219601-45	0.5	100	100	0.1	100	0.001	0.001	0.001
11219601-46	1	11219601-46	0.5	100	100	0.1	100	0.001	0.001	0.001
11219601-47	1	11219601-47	0.5	100	100	0.1	100	0.001	0.001	0.001
11219601-48	1	11219601-48	0.5	100	100	0.1	100	0.001	0.001	0.001
11219601-49	1	11219601-49	0.5	100	100	0.1	100	0.001	0.001	0.001
11219601-50	1	11219601-50	0.5	100	100	0.1	100	0.001	0.001	0.001

Table F.29: Test 11229601

NO	CH	TEST	CONV	UNIT	TIME	WIND	TEMP	REL	HUMID	WIND	VELOCITY	TIME	TIME	TIME	TIME	TIME	TIME	TIME	TIME	TIME
1		11229601																		
2	102																			
3	103																			
4	104																			
5	105																			
6	106																			
7	107																			
8	108																			
9	109																			
10	110																			
11	111																			
12	112																			
13	113																			
14	114																			
15	115																			
16	116																			
17	117																			
18	118																			
19	119																			
20	120																			
21	121																			
22	122																			
23	123																			
24	124																			
25	125																			
26	126																			
27	127																			
28	128																			
29	129																			
30	130																			
31	131																			
32	132																			
33	133																			
34	134																			
35	135																			
36	136																			
37	137																			
38	138																			
39	139																			
40	140																			
41	141																			
42	142																			
43	143																			
44	144																			
45	145																			
46	146																			
47	147																			
48	148																			
49	149																			
50	150																			

Table F.33: Test 11239602

1	2	3	4	5	6	7	8	9	10	11	12	13	14	15	16	17
1	2	3	4	5	6	7	8	9	10	11	12	13	14	15	16	17
1	2	3	4	5	6	7	8	9	10	11	12	13	14	15	16	17

Table F.34: Test 11239603

Run No.	Time	Pressure	Flow	Temp	Humidity	Altitude	Speed	Direction	Weather	Remarks	Other	1st	2nd	3rd	4th	5th	6th	7th	8th	9th	10th	11th	12th	13th	14th	15th	16th	17th	18th	19th	20th	21st	22nd	23rd	24th	25th	26th	27th	28th	29th	30th
1	11:23:00	91.0	0.13	31.5	78.5	11239603	0.0	0	0	0	0	0	0	0	0	0	0	0	0	0	0	0	0	0	0	0	0	0	0	0	0	0	0	0	0	0	0	0	0		
PUEL INJECTION		PUEL INJECTION		PUEL INJECTION		PUEL INJECTION		PUEL INJECTION		PUEL INJECTION		PUEL INJECTION		PUEL INJECTION		PUEL INJECTION		PUEL INJECTION		PUEL INJECTION		PUEL INJECTION		PUEL INJECTION		PUEL INJECTION		PUEL INJECTION		PUEL INJECTION		PUEL INJECTION		PUEL INJECTION		PUEL INJECTION		PUEL INJECTION		PUEL INJECTION	
1	11:23:00	91.0	0.13	31.5	78.5	11239603	0.0	0	0	0	0	0	0	0	0	0	0	0	0	0	0	0	0	0	0	0	0	0	0	0	0	0	0	0	0	0	0	0	0		

Table F.35: Test 112596T

A		B		C		D		E		F		G		H		I		J		K		L		M		N		O		P		Q		R		S		T																							
1	2	3	4	5	6	7	8	9	10	11	12	13	14	15	16	17	18	19	20	21	22	23	24	25	26	27	28	29	30	31	32	33	34	35	36	37	38	39	40	41	42	43	44	45	46	47	48	49	50												
11/25/88	11/25/88	11/25/88	11/25/88	11/25/88	11/25/88	11/25/88	11/25/88	11/25/88	11/25/88	11/25/88	11/25/88	11/25/88	11/25/88	11/25/88	11/25/88	11/25/88	11/25/88	11/25/88	11/25/88	11/25/88	11/25/88	11/25/88	11/25/88	11/25/88	11/25/88	11/25/88	11/25/88	11/25/88	11/25/88	11/25/88	11/25/88	11/25/88	11/25/88	11/25/88	11/25/88	11/25/88	11/25/88	11/25/88	11/25/88	11/25/88	11/25/88	11/25/88	11/25/88	11/25/88	11/25/88	11/25/88	11/25/88	11/25/88	11/25/88	11/25/88	11/25/88	11/25/88	11/25/88	11/25/88	11/25/88						
Date	Time	Temp	Temp	Temp	Temp	Temp	Temp	Temp	Temp	Temp	Temp	Temp	Temp	Temp	Temp	Temp	Temp	Temp	Temp	Temp	Temp	Temp	Temp	Temp	Temp	Temp	Temp	Temp	Temp	Temp	Temp	Temp	Temp	Temp	Temp	Temp	Temp	Temp	Temp	Temp	Temp	Temp	Temp	Temp	Temp	Temp	Temp	Temp	Temp	Temp	Temp	Temp	Temp	Temp	Temp	Temp	Temp	Temp	Temp	Temp	Temp

Table F.36: Test 11269601

Run	3	4	5	6	7	8	9	10	11	12	13	14	15	16	17	18	19	20	21	22	23	24	25
001	0000	0000	0000	0000	0000	0000	0000	0000	0000	0000	0000	0000	0000	0000	0000	0000	0000	0000	0000	0000	0000	0000	0000
REMARKS		REMARKS		REMARKS		REMARKS		REMARKS		REMARKS		REMARKS		REMARKS		REMARKS		REMARKS		REMARKS		REMARKS	
01		02		03		04		05		06		07		08		09		10		11		12	
13		14		15		16		17		18		19		20		21		22		23		24	
25		26		27		28		29		30		31		32		33		34		35		36	
37		38		39		40		41		42		43		44		45		46		47		48	
49		50		51		52		53		54		55		56		57		58		59		60	
61		62		63		64		65		66		67		68		69		70		71		72	
73		74		75		76		77		78		79		80		81		82		83		84	
85		86		87		88		89		90		91		92		93		94		95		96	
97		98		99		00		01		02		03		04		05		06		07		08	
09		10		11		12		13		14		15		16		17		18		19		20	
21		22		23		24		25		26		27		28		29		30		31		32	
33		34		35		36		37		38		39		40		41		42		43		44	
45		46		47		48		49		50		51		52		53		54		55		56	
57		58		59		60		61		62		63		64		65		66		67		68	
69		70		71		72		73		74		75		76		77		78		79		80	
81		82		83		84		85		86		87		88		89		90		91		92	
93		94		95		96		97		98		99		00		01		02		03		04	

APPENDIX G: PULVERIZED COAL CASCADE IMPACTOR TEST SUMMARIES

The spreadsheets that follow summarize the detailed measurements and calculations required to determine the size distribution of ash for pulverized coal fuels. These experiments were conducted with a natural-gas fired furnace. Ash samples were collected with a simple water cooled sampling probe and size-sorted with a Mark II cascade impactor.

Table G.1: Test log for pulverized coal experiments

Test Number	Fuel	Solid Fuel Modification	Furnace Flowrate, g/m (no solid fuel)	A/F equiv	Upper Aux A/F equiv	Dry O2%, no fuel	Dry O2%, w/fuel	Upper Temp, C	Lower Temp, C	Sample Temp, C	Sample Time, min
Horizontal Probe Tests											
05219401	Upper Freeport	raw	489.0	1.7	1.6	9.2	8.8	1058	621	350	15
05239401	Upper Freeport	raw	492.3	1.7	1.5	9.2	8.8	1057	625	325	15
05249401	Upper Freeport	raw	492.3	1.7	1.5	9.2	8.8	1045	624	325	15
05269401	Upper Freeport	cleaned	492.0	1.7	1.6	9.4	9.0	1063	628	360	15
05269402	Upper Freeport	cleaned	492.0	1.7	1.5	9.4	9.0	1058	623	365	15
05279401	Upper Freeport	cleaned	483.5	1.7	1.6	9.2	8.7	1075	623	350	15
06019401	Upper Freeport	37 - 85 μ m	492.1	1.7	1.5	9.3	9.3	1058	642	330	15
05049401	Kentucky #11	raw	494.7	1.7	1.6	9.5	9.1	1060	612	308	15
05059401	Kentucky #11	raw	494.7	1.7	1.6	9.5	9.5	1060	612	308	15
05069401	Kentucky #11	raw	494.7	1.7	1.0	9.5	9.5	1060	688	375	15
06029401	Kentucky #11	37 - 85 μ m	492.0	1.7	Off	9.4	9.0	1068	637	350	15
05109401	Illinois #6	raw	488.9	1.7	1.6	9.3	8.9	1058	603	325	15
05119401	Illinois #6	raw	483.0	1.7	1.6	9.2	8.8	1050	634	350	15
05129401	Illinois #6	raw	494.7	1.7	1.6	9.5	9.1	1063	632	350	15
05139401	Illinois #6	raw	488.9	1.7	1.6	9.3	8.9	1050	632	350	15
05209401	Illinois #6	raw	494.8	1.7	1.6	9.4	9.0	1065	623	372	15
05319401	Illinois #6	37 - 85 μ m	492.0	1.7	1.5	9.4	9.0	1068	630	330	15
Vertical Probe Tests											
09159401	Upper Freeport	raw	507.6	1.8	1.7	9.8	9.4	1190	575	700	15
09169401	Upper Freeport	raw	516.2	1.8	1.7	10.0	9.6	1180	575	700	15
10169401	Upper Freeport	raw	517.6	1.7	1.7	9.0	8.6	1245	660	813	15
10219401	Upper Freeport	raw	519.2	1.7	1.7	9.1	8.7	1243	662	807	15
10259401	Upper Freeport	raw	519.8	1.7	1.7	9.0	8.6	1245	663	805	15
11149401	Upper Freeport	< 18 μ m	518.9	1.7	1.7	9.2	8.8	1246	649	798	15
11149402	Upper Freeport	< 18 μ m	518.9	1.7	1.7	9.2	8.8	1246	649	798	15
11169401	Upper Freeport	< 18 μ m	519.1	1.7	1.7	9.1	8.7	1238	633	777	5
11219401	Upper Freeport	< 18 μ m	519.1	1.7	1.7	9.1	8.7	1244	646	798	5
11079401	Upper Freeport	18 - 37 μ m	518.7	1.7	1.7	9.0	8.6	1243	650	798	15
11109401	Upper Freeport	18 - 37 μ m	521.7	1.7	1.7	9.1	8.7	1250	656	800	15
11119401	Upper Freeport	18 - 37 μ m	519.2	1.7	1.7	9.1	8.7	1239	649	798	15
11039401	Upper Freeport	37 - 85 μ m	517.5	1.7	1.7	9.1	8.7	1254	650	800	15
11049401	Upper Freeport	37 - 85 μ m	519.2	1.7	1.7	9.0	8.6	1245	661	800	15
11289401	Upper Freeport	> 85 μ m	517.6	1.7	1.7	9.0	8.6	1249	646	795	5
12029401	Upper Freeport	> 85 μ m	520.5	1.7	1.7	9.0	8.5	1245	647	791	5
12079401	Upper Freeport	> 85 μ m	519.3	1.7	1.6	9.0	8.6	1250	648	793	1
10139401	Kentucky #11	raw	519.2	1.7	1.7	9.0	8.6	1249	663	813	15
10149401	Kentucky #11	raw	519.8	1.7	1.7	9.0	8.7	1250	662	817	15
09089401	Kentucky #11	raw	517.8	1.8	1.6	10.1	9.7	1190	560	655	15
09099401	Kentucky #11	raw	516.2	1.8	1.6	10.0	9.6	1180	560	680	15
10079401	Kentucky #11	raw	514.7	2.0	1.7	11.1	10.8	1125	628	759	15
10119401	Kentucky #11	raw	514.5	2.0	1.7	11.2	10.9	1118	623	744	15
09219401	Illinois #6	raw	516.4	1.8	1.7	9.9	9.5	1180	580	700	15
09239401	Illinois #6	raw	516.4	1.8	1.7	9.9	9.5	1185	595	725	15
10069401	Blank	--	512.9	1.9	1.7	10.5	10.5	1173	635	770	15

Table G.8: Test 05139401

Date	Unit	5/13/89	me/day/yr	Mean NO	Mean AQ	57.0%	Upper T	1050 g	399 g (est)
Coal	lb/dry	process	970	970	970	970	970	970	970
		05139401	15.00						
Coal Properties		(Ref. only)							
Element #									
1									
2									
3									
4									
5									
6									
7									
Stack									
Parameter									
1									
2									
3									
4									
5									
6									
7									
Backup Effect									
Notes									
1.1) STAGE 7 AND STAGE 8 STACKED IN WORKING ORDER DATA FROM 7 AND 8 ARE NOT ACCURATE									

Table G.9: Test 05209401

Date	5170/94	mo/d/yr	Main NG	% in air	Cum. %	Upper I	1085 g	Upper I	Upper I	372 g	Upper I	Upper I	Upper I	Upper I	Upper I	Upper I	Upper I	Upper I	Upper I	Upper I				
Coal																								
test no.																								
test dur.																								
Coal Properties																								
Minerals																								
grams																								
State																								
Preparator																								
Notes																								
Observations																								

Table G.19: Test 09089401

Date	9/8/94	me/day/yr	Mean NO _x	57.0 %	Upper I	1180 g	Imp wt clean	0.5823	inches	mod CH ₄	18.036 g/min	CH ₄ AA only
Coal	Kentucky #11	process	Mean Air	31.8 ratio	Lower I	955 g	Maindust R ₁	0.57	fracton	mod. Main d	199.228 g/min	CH ₄ AA only
lead no	09089401	mid/yr num	BE/NO	4.5 units, base	Coal feed	820 units	Maindust R ₂	0.41	fracton	mod. Main d	1.728 units	CH ₄ AA only
lead Air	16.00	mid/yr num	BE/Air	0.0 units, iron	Vacuum Pool	11.0 g/min	Maindust R ₃	0.37	fracton	mod. Main d	1.933	CH ₄ AA only
Coal Process	(Ref. arb.)	mid/yr num	BE/NO	0.0 units, iron	Vacuum Pool	82.0 g/min	Maindust R ₄	0.29	fracton	mod. Main d	1.903	CH ₄ AA only
Kentucky #11		mid/yr num	BE/Air	0.0 units, base	Vacuum Pool	10.9 in Hg	Maindust R ₅	0.19	fracton	mod. Main d	1.903	CH ₄ AA only
grams	67.23	stem/100g	IR RNO	0.0 units, base	Steamer RNO	180 g/min	IR Air Flow	39.295	fracton	mod. Main d	1.903	CH ₄ AA only
grams	4.42	stem/100g	IR RNO	0.0 units, base	Steamer RNO	180 g/min	IR Air Flow	39.295	fracton	mod. Main d	1.903	CH ₄ AA only
grams	7.45	stem/100g	IR RNO	0.0 units, base	Steamer RNO	180 g/min	IR Air Flow	39.295	fracton	mod. Main d	1.903	CH ₄ AA only
grams	1.22	stem/100g	IR RNO	0.0 units, base	Steamer RNO	180 g/min	IR Air Flow	39.295	fracton	mod. Main d	1.903	CH ₄ AA only
grams	4.22	stem/100g	IR RNO	0.0 units, base	Steamer RNO	180 g/min	IR Air Flow	39.295	fracton	mod. Main d	1.903	CH ₄ AA only
grams	3.85	stem/100g	IR RNO	0.0 units, base	Steamer RNO	180 g/min	IR Air Flow	39.295	fracton	mod. Main d	1.903	CH ₄ AA only
grams	100.1	stem/100g	IR RNO	0.0 units, base	Steamer RNO	180 g/min	IR Air Flow	39.295	fracton	mod. Main d	1.903	CH ₄ AA only
Stage	Initial (g)	Final (g)	Net (g)	% in size range	Size Range	EDD	Coal Composition on Elemental level					
Preseparator	0.30328	0.32553	0.02195	41.47	10.0 A.W.P.	10	Carbon	4.81	meas/100g	NO	1.876	meas/100g
0	0.27818	0.28240	0.01422	16.92	40.0 I.R.O. -10.0	9	Hydrogen	4.42	meas/100g	CO	2.508	meas/100g
1	0.27784	0.28920	0.01136	14.86	26.35 S.S. -8.0	8	Oxygen	0.48	meas/100g	CO ₂	13.446	meas/100g
2	0.30404	0.30881	0.00487	9.34	19.01 A.T. -5.9	7	Nitrogen	0.99	meas/100g	N ₂	0.672	meas/100g
3	0.30383	0.31083	0.00710	8.24	9.77 S.S. -4.7	6	Sulfur	0.13	meas/100g	Dry O ₂ w/in	10.037	wt%
4	0.30388	0.30885	0.00528	6.89	2.89 I. -2.3	5	Ash	20.96	g/100g	Dry O ₂ w/in	8.800	wt%
5	0.30449	0.30638	0.00191	2.49	0.40 I. -2.1	4	190	0.21	meas/100g	Dry O ₂ w/in	0.011	meas/100g
6	0.30484	0.30499	0.00015	0.20	0.21 O.T. -1.1	3	mod coal	1.1	g/min	CO	1.936	meas/100g
7	0.30480	0.30450	0.00000	0.00	0.21 O.T. -0.7	2	Proba Inlet	688	degC	NO ₂	2.033	meas/100g
Backup Filter	0.33158	0.33174	0.00016	0.21	0.00 0. -0.4	1	Vacuum Pool	100	degC (cell)	SO ₂	13.744	meas/100g
							Vacuum Pool	23	degC (cell)	SO ₂	0.9915	meas/100g
							Vacuum Pool	97	degC (cell)	SO ₂	1.695	meas/100g
							Vacuum Pool	16	min	Equv. Ratio	0.071	mass fracton
							coal flow air	18	min	mod wt wet	28.181	g/mol
										dens @ inlet	359.815	g/m ³
										mod. dust	618.889	g/min
										voluct	43.250	meas/100g
										NO ₂ (H ₂ O)	2.360	meas/100g
										dens @ I.R.O.	370.979	g/m ³
										mod. dust	27.221	g/min
										voluct @ I.R.O.	598.129	g/m ³
										voluct @ I.R.O.	0.925	me ² /min
										voluct @ I.R.O.	0.857	l ² -2/min
										mod. dust	18.533	g/min
										mod. dust	20.808	g/min
										voluct @ I.R.O.	0.023	me ² /min
										voluct @ I.R.O.	0.799	l ² -2/min
										voluct @ I.R.O.	350.814	me ² /min
										voluct @ I.R.O.	19.188	me ² /min
										mod. dust	0.09828	g/min
										mod. dust	0.1387	g
										exp. dust	0.632	% of ash
												based on actual

Table G.27: Test 10119401

Date	10/11/94	10/11/94	10/11/94	10/11/94	10/11/94	10/11/94	10/11/94	10/11/94	10/11/94	10/11/94	10/11/94	10/11/94	10/11/94	10/11/94	10/11/94	10/11/94	10/11/94	10/11/94	10/11/94	10/11/94	10/11/94	10/11/94	10/11/94
Coal	Kentucky #11	process	main AQ	Main AQ	41.0 %	Upper J	1118 g	imp pit dum	0.625 inches														
test no	10119401	mid/runum	BF1AQ	BF1AQ	31.5 ppm	Lower T	829 g	Manufact r/c	4 inches														
test dur	15.00	minutes	BF1AQ	BF1AQ	4.6 %	Coal feed	1.1 g/m	Main Gas R/c	0.51 fraction														
Coal Properties	Kentucky #11	BF2AQ	BF2AQ	BF2AQ	0.0 %	Vacuum Bag	48.0 %	Main Air R/c	0.41 fraction														
grams	57.23	4.81	BF2AQ	BF2AQ	0.0 %	atomizer air	8.0	in AQ R/c	31.6 ppm														
	4.42	0.49	in Ratio	in Ratio	1.0 %	atomizer HSC	318 ppm	in AQ R/c	0.10 %														
	7.64	0.49	in Ratio	in Ratio	3.9 ppm	str. len. T	197 F	in AQ R/c	3.9 ppm														
	4.23	0.13																					
	20.86	20.86																					
	3.84	0.21																					
	100.1																						
Stage																							
Preprocessor	0	0.30208																					
1	0.27685	0.28803																					
2	0.27785	0.29044																					
3	0.30080	0.30735																					
4	0.30328	0.31099																					
5	0.30460	0.30753																					
6	0.30390	0.30405																					
7	0.30442	0.30446																					
Backup Filter	0.32788	0.32830																					
Notes	Plenty of black particles above the 0 stage offsets. The prep. looked good and brown. The 0 stage is very synchronized. Neal piles of brown ash with black particles on edges and mid in equivalent areas between brown ash piles. Same with stage 1, but only a small amount of black particles. The stages get cleaner as they go down. The brown piles are almost 100% of particles by stages 4 or 5. The filter, all before last test, has hundreds of black particles > 10microns. Turning up main NG post test to 92%. Oct. 11, 4.12pm. Injected some ash of stage 0 when loading (c1%).																						

Table G.28: Test 10139401

Date	10/13/04	10/13/04	10/13/04	10/13/04	12/8/04	12/8/04	12/8/04	12/8/04	12/8/04	12/8/04	12/8/04	12/8/04	12/8/04	12/8/04	12/8/04	12/8/04	12/8/04	12/8/04		
Coal	Kentucky #11	Kentucky #11	Mean Air	Mean Air	Upper I	Upper I	Upper I	Upper I	Upper I	Upper I	Upper I	Upper I	Upper I	Upper I	Upper I	Upper I	Upper I	Upper I		
test no	10139401	10139401	BF7KO	BF7KO	BF7KO	BF7KO	BF7KO	BF7KO	BF7KO	BF7KO	BF7KO	BF7KO	BF7KO	BF7KO	BF7KO	BF7KO	BF7KO	BF7KO		
test desc	Coal Processing	Coal Processing	Coal Processing	Coal Processing	Coal Processing	Coal Processing	Coal Processing	Coal Processing	Coal Processing	Coal Processing	Coal Processing	Coal Processing	Coal Processing	Coal Processing	Coal Processing	Coal Processing	Coal Processing	Coal Processing		
test date	10/13/04	10/13/04	10/13/04	10/13/04	10/13/04	10/13/04	10/13/04	10/13/04	10/13/04	10/13/04	10/13/04	10/13/04	10/13/04	10/13/04	10/13/04	10/13/04	10/13/04	10/13/04		
1	0.30144	0.28327	0.08213	0.08213	0.4139	41.81	10.0	4.16	41.81	0.9525	inches	0.9525	inches	0.9525	inches	0.9525	inches	0.9525		
2	0.27503	0.28003	0.01500	0.01500	14.10	27.52	10.0	10.0	27.52	0.83	inches	0.83	inches	0.83	inches	0.83	inches	0.83	inches	
3	0.30145	0.30904	0.00461	0.00461	19.44	17.08	8.0	8.0	17.08	0.08	fraction	0.08	fraction	0.08	fraction	0.08	fraction	0.08	fraction	
4	0.30045	0.30752	0.00797	0.00797	4.33	12.74	7.8	4.7	12.74	0.41	fraction	0.41	fraction	0.41	fraction	0.41	fraction	0.41	fraction	
5	0.30113	0.30510	0.00476	0.00476	4.47	6.19	3.3	3.3	6.19	0.32	pa/g	0.32	pa/g	0.32	pa/g	0.32	pa/g	0.32	pa/g	
6	0.30187	0.30738	0.00176	0.00176	1.18	0.44	1.1	1.1	0.44	0.91	mol/mol	0.91	mol/mol	0.91	mol/mol	0.91	mol/mol	0.91	mol/mol	
7	0.30310	0.30189	0.00092	0.00092	0.11	0.33	0.7	0.7	0.33	0.91	mol/mol	0.91	mol/mol	0.91	mol/mol	0.91	mol/mol	0.91	mol/mol	
Backup Filter	0.32762	0.32785	0.00033	0.00033	0.31	0.00	0.4	0.4	0.00	0.91	mol/mol	0.91	mol/mol	0.91	mol/mol	0.91	mol/mol	0.91	mol/mol	
		total mass	0.10841							1202.10	g/m ³	1202.10	g/m ³	1202.10	g/m ³	1202.10	g/m ³	1202.10	g/m ³	
Notes:	Stack particles above stage 0																			
		Stage 0 slightly overloaded. Stage 1 loaded very good. Very slight overheat																		
		Bottomed stage 2 while unloading. Lost some air, maybe up to 5%.																		
		Some black particles on filter. Not clear as bed as could have. May be 50 to 100 particles visible.																		
		I washed the particles from Stage 1 and Stage 2, office plates plus separator cup.																		

Table G.30: Test 10169401

Date	10/16/94			mol/day/yr	Main NG	62.0%	Upper T	1245 e										
Coal	Upper Freeport			source	Main Air	41.0%	Sample T	813 e										
test no	10169401			mid/yr	BF1 NG	45.0%	Lower T	890 e										
test dur	15.00			minutes	BF1 Air	4.7	units, front	Coal feed	920	units	imp inlet diam	0.5625	inches					
Coal Properties (Rel only)					BF2 NG		units, back	Coal feed cor	1.1	g/min	Manduct rad	4	inches					
Upper Freeport	grams				BF2 Air		units, front	Vacuum Rate	87.0	%	Main Gas Flo	0.67	fraction	mdot CH4	17.458	g/min		
64.57	8.39						units, back	Vacuum Rate	8.0	in hg	Main Air Flo	0.41	fraction	mdot Main A	489.352	g/min		
4.97	4.97							atomizer air		full open	Main Air Flo	31.6	psig	phi	1.834	units		
3.92	0.25							atomizer air		psig	Inj Air Flo	1.9	%	mole fract	1.091			
1.63	0.12							atomizer H2O	250	mm	Inj Air Flo	39	psig	CO2	1.091	mole/min	CH4 Air only	
2.07	0.06							exh duct T	90	F				H2O	2.182	mole/min	CH4 Air only	
23.23	23.23							over furn T	108	F	Coal Composition on Elemental level				N2	13.493	mole/min	CH4 Air only
0.51	0.03										Carbon (mon)	5.38	mole%/100g	O2	1.982	mole/min	CH4 Air only	
100											Hydrogen (r)	4.07	mole%/100g	mdot air inj	10.831	g/min		
											Oxygen (mo)	0.25	mole%/100g	O2	0.079	mole/min	Inj Air only	
											Nitrogen (m)	0.12	mole%/100g	N2	0.287	mole/min	Inj Air only	
											Sulfur (mon)	0.05	mole%/100g	Dry O2 w/in	8.892	vol%	tot. w/o coal	
											Ash	23.23	g/100g	Dry O2 w/o r	8.707	vol%	L w/o coal (n)	
											H2O	0.03	mole%/100g	Coal Fraction	0.011	mdot coal/100g		
														CO2	1.150	mole/min	total	
														H2O	2.205	mole/min	total	
														NO	13.700	mole/min	total	
														SO2	0.007	mole/min	total	
														O2	1.392	mole/min	total	
														Dry O2	8.867	vol%		
														H2O w	0.077	mass fraction		
														CFH				
														Equip. Ratio	1.670	w/in, no solid	level	
														mol. wt. wet	28.104	g/mol		
														dens @ inlet	315.393	g/m^3		
														mdot duct	518.485	g/min	minus ash	
														educt	50.693	meters/min		
														educt	2.768	l/see		
														dens @ STP	1202.10	g/m^3		
														BACKFIRE BURNERS				
														mol. wt. dry	29.477	g/mol		
														dens @ mole	898.345	g/m^3		
														mdot BF1 CH4	16.767	g/min	vol/liters	
														mdot BF1 Air	552.639	g/min	vol/liters	
														phi	1.717	A/F equiv ratio		
														mdot AmdotF	29.450	g/min		
														mdot BF2 CH4	0	g/min	vol/liters	
														mdot BF2 Air	0	g/min	vol/liters	
														phi	0	A/F equiv ratio		
														#DIV/0!		vol/inlet	518.010	
														#DIV/0!		vol/inlet	28.325	
																mdot coal	0.01291	
																expected ash	0.1936	
																%Diff. ash	-104.237	%
																		based on actual

Table G.33: Test 11039401

Date	11/19/04	mol/dt/yr	Man No.	61.5 %	Upper 1	1264	e/Neat	e/cpl	Sample	0.625	inches	mol/dt	g/min	CH4/air only
Coal	Upper	37-45 cm	Man/Air	41.0 %	Sample 1	800	f	CH4/air only	0.625	inches	mol/dt	g/min	CH4/air only	
test no.	11039401	mol/dt/yr	BFMS	45.0 %	Upper 1	800	f	CH4/air only	0.625	inches	mol/dt	g/min	CH4/air only	
Coal	BFMS	15.00	BFMS	4.7 %	Coal feed	1	g/min	CO	0.619	inches	mol/dt	g/min	CH4/air only	
Upper	BFMS	mol/dt	BFMS	4.7 %	Vacuum Res.	1	g/min	CO	0.619	inches	mol/dt	g/min	CH4/air only	
Sample	BFMS	mol/dt	BFMS	4.7 %	Vacuum Res.	1	g/min	CO	0.619	inches	mol/dt	g/min	CH4/air only	
BFMS	BFMS	mol/dt	BFMS	4.7 %	Vacuum Res.	1	g/min	CO	0.619	inches	mol/dt	g/min	CH4/air only	
BFMS	BFMS	mol/dt	BFMS	4.7 %	Vacuum Res.	1	g/min	CO	0.619	inches	mol/dt	g/min	CH4/air only	
BFMS	BFMS	mol/dt	BFMS	4.7 %	Vacuum Res.	1	g/min	CO	0.619	inches	mol/dt	g/min	CH4/air only	
BFMS	BFMS	mol/dt	BFMS	4.7 %	Vacuum Res.	1	g/min	CO	0.619	inches	mol/dt	g/min	CH4/air only	
BFMS	BFMS	mol/dt	BFMS	4.7 %	Vacuum Res.	1	g/min	CO	0.619	inches	mol/dt	g/min	CH4/air only	
0.01	0.01	0.01	0.01	0.01	0.01	0.01	0.01	0.01	0.01	0.01	0.01	0.01	0.01	0.01
0.02	0.02	0.02	0.02	0.02	0.02	0.02	0.02	0.02	0.02	0.02	0.02	0.02	0.02	0.02
0.03	0.03	0.03	0.03	0.03	0.03	0.03	0.03	0.03	0.03	0.03	0.03	0.03	0.03	0.03
0.04	0.04	0.04	0.04	0.04	0.04	0.04	0.04	0.04	0.04	0.04	0.04	0.04	0.04	0.04
0.05	0.05	0.05	0.05	0.05	0.05	0.05	0.05	0.05	0.05	0.05	0.05	0.05	0.05	0.05
0.06	0.06	0.06	0.06	0.06	0.06	0.06	0.06	0.06	0.06	0.06	0.06	0.06	0.06	0.06
0.07	0.07	0.07	0.07	0.07	0.07	0.07	0.07	0.07	0.07	0.07	0.07	0.07	0.07	0.07
0.08	0.08	0.08	0.08	0.08	0.08	0.08	0.08	0.08	0.08	0.08	0.08	0.08	0.08	0.08
0.09	0.09	0.09	0.09	0.09	0.09	0.09	0.09	0.09	0.09	0.09	0.09	0.09	0.09	0.09
0.10	0.10	0.10	0.10	0.10	0.10	0.10	0.10	0.10	0.10	0.10	0.10	0.10	0.10	0.10

Table G.35: Test 11079401

Date	11/27/94	Moisture (%)	Mean NO	62.0 %	Upper I	1243 g	Flow rate	1.233 g	Flow rate	1243 g	Flow rate	1.233 g	Flow rate	1.233 g	Flow rate	1.233 g	Flow rate	1.233 g	Flow rate	1.233 g	Flow rate	1.233 g	Flow rate	1.233 g	Flow rate	1.233 g	Flow rate		
Cell	Upper Friction source	19.37	1.07	0.01	0.01	0.01	0.01	0.01	0.01	0.01	0.01	0.01	0.01	0.01	0.01	0.01	0.01	0.01	0.01	0.01	0.01	0.01	0.01	0.01	0.01	0.01	0.01	0.01	0.01
Cell	Upper Friction (Cell only)	19.37	1.07	0.01	0.01	0.01	0.01	0.01	0.01	0.01	0.01	0.01	0.01	0.01	0.01	0.01	0.01	0.01	0.01	0.01	0.01	0.01	0.01	0.01	0.01	0.01	0.01	0.01	0.01
Cell	Upper Friction (Cell only)	19.37	1.07	0.01	0.01	0.01	0.01	0.01	0.01	0.01	0.01	0.01	0.01	0.01	0.01	0.01	0.01	0.01	0.01	0.01	0.01	0.01	0.01	0.01	0.01	0.01	0.01	0.01	0.01
Cell	Upper Friction (Cell only)	19.37	1.07	0.01	0.01	0.01	0.01	0.01	0.01	0.01	0.01	0.01	0.01	0.01	0.01	0.01	0.01	0.01	0.01	0.01	0.01	0.01	0.01	0.01	0.01	0.01	0.01	0.01	0.01
Cell	Upper Friction (Cell only)	19.37	1.07	0.01	0.01	0.01	0.01	0.01	0.01	0.01	0.01	0.01	0.01	0.01	0.01	0.01	0.01	0.01	0.01	0.01	0.01	0.01	0.01	0.01	0.01	0.01	0.01	0.01	0.01

Table G.36: Test I1109401

Date	11/10/84	mol/day/yr	Mean NO _x	Mean NO _x	Upper I	1250 g	mp wt disc	0.5625	inches	mod CH ₄	17.458	CH ₄ only
Coal	Upper Finest	source	Main Air	Main Air	Sample 1	558 g	Method 1A	0.93	inches	mod CH ₄	492.225	CH ₄ only
lead no	11109401	mg/dry num	BE/NO	BE/NO	Coal feed cor	820 units	Main Air	0.17	inches	mod CH ₄	1.547	CH ₄ only
lead Air	15.00	minutes	BE/Air	BE/Air	Coal feed cor	1.1 g/m	Main Air	0.17	inches	mod CH ₄	1.547	CH ₄ only
Coal Process	(Ref. ent)				Vacuum Pk	91.0 %	Main Air	0.17	inches	mod CH ₄	1.547	CH ₄ only
Upper Finest					Vacuum Pk	8.9 in lb	Main Air	0.17	inches	mod CH ₄	1.547	CH ₄ only
grams	mol/day/100g				diometer air	1.1 g/m	Main Air	0.17	inches	mod CH ₄	1.547	CH ₄ only
41.67	2.39				diometer air	1.1 g/m	Main Air	0.17	inches	mod CH ₄	1.547	CH ₄ only
4.07	0.23				diometer air	1.1 g/m	Main Air	0.17	inches	mod CH ₄	1.547	CH ₄ only
3.82	0.12				diometer air	1.1 g/m	Main Air	0.17	inches	mod CH ₄	1.547	CH ₄ only
1.93	0.08				diometer air	1.1 g/m	Main Air	0.17	inches	mod CH ₄	1.547	CH ₄ only
2.07	0.09				diometer air	1.1 g/m	Main Air	0.17	inches	mod CH ₄	1.547	CH ₄ only
23.23	23.23				diometer air	1.1 g/m	Main Air	0.17	inches	mod CH ₄	1.547	CH ₄ only
0.51	0.03				diometer air	1.1 g/m	Main Air	0.17	inches	mod CH ₄	1.547	CH ₄ only
100					diometer air	1.1 g/m	Main Air	0.17	inches	mod CH ₄	1.547	CH ₄ only
Shape	(mol/day)	(mol/day)	(mol/day)	(mol/day)	(mol/day)	(mol/day)	(mol/day)	(mol/day)	(mol/day)	(mol/day)	(mol/day)	(mol/day)
Preparator	0.32820	0.42799	0.19279	0.19279	Size Range	600	mod coal	1.1	g/min	H ₂ O	1.190	mol/day/min total
1	0.28727	0.31896	0.02078	0.02078	Probe Inlet	10	Probe Inlet	809	degC	N ₂	2.205	mol/day/min total
2	0.28705	0.30748	0.01083	0.01083	Imposed Inlet	9	Imposed Inlet	100	degC	SO ₂	0.0007	mol/day/min total
3	0.33539	0.35442	0.00000	0.00000	Vacuum Pk	9.9	Vacuum Pk	8	in Hg	O ₂	1.42	mol/day/min total
4	0.33013	0.33442	0.00429	0.00429	Vacuum Pk	4.7	Vacuum Pk	23	degC	O ₂	6.873	mol/day/min total
5	0.35069	0.33201	0.00165	0.00165	Vacuum Pk	3.3	Vacuum Pk	69	CFM	Eqw. Ratio	0.078	mass fraction
6	0.35069	0.33201	0.00165	0.00165	Coal flow in	2.1	Coal flow in	13	min	mol wt wet	28.11	g/mol
7	0.32877	0.32340	0.00013	0.00013		1.1				den@100	318.276	g/m ³
Backup Filter	0.32877	0.32878	0.00001	0.00001		0.7				mod. feed	522.817	mol/day
	0.33117	0.33158	0.00041	0.00041		0.4				Moist	50.469	mol/day/min
										Value	2.725	mol/day
										Sample Wt	212.559	g/m ³
										mod wt dry	28.372	g/mol
										ventilation	892.182	g/m ³
										ventilation	0.528	m ³ /min
										ventilation	0.375	ft ³ /min
										mod@100	24.843	g/min
										moisture	26.560	g/min
										ventilation	0.522	m ³ /min
										ventilation	1.52	ft ³ /min
										AF equiv	918.871	mol/min
										ventil	28.372	mol/day
										mod@100	0.01789	g/min
										expected	0.1848	g
										%Del eth	31.977	%
												based on actual

Table G.37: Test I1119401

Date:	11/11/94 (mols/day)	1339 (gross)	Upper 1		1339 (gross)														
Coal	Upper Feed	Lower	Upper 1	Upper 2	Upper 3	Upper 4	Upper 5	Upper 6	Upper 7	Upper 8	Upper 9	Upper 10	Upper 11	Upper 12	Upper 13	Upper 14	Upper 15	Upper 16	Upper 17
Coal no.	18-37	18-37	18-37	18-37	18-37	18-37	18-37	18-37	18-37	18-37	18-37	18-37	18-37	18-37	18-37	18-37	18-37	18-37	18-37
Coal Process	BE/NO	BE/NO	BE/NO	BE/NO	BE/NO	BE/NO	BE/NO	BE/NO	BE/NO	BE/NO	BE/NO	BE/NO	BE/NO	BE/NO	BE/NO	BE/NO	BE/NO	BE/NO	BE/NO
Upper Feed	11119401	11119401	11119401	11119401	11119401	11119401	11119401	11119401	11119401	11119401	11119401	11119401	11119401	11119401	11119401	11119401	11119401	11119401	11119401
Upper 1	4.0%	4.0%	4.0%	4.0%	4.0%	4.0%	4.0%	4.0%	4.0%	4.0%	4.0%	4.0%	4.0%	4.0%	4.0%	4.0%	4.0%	4.0%	4.0%
Upper 2	2.1%	2.1%	2.1%	2.1%	2.1%	2.1%	2.1%	2.1%	2.1%	2.1%	2.1%	2.1%	2.1%	2.1%	2.1%	2.1%	2.1%	2.1%	2.1%
Upper 3	4.7%	4.7%	4.7%	4.7%	4.7%	4.7%	4.7%	4.7%	4.7%	4.7%	4.7%	4.7%	4.7%	4.7%	4.7%	4.7%	4.7%	4.7%	4.7%
Upper 4	2.3%	2.3%	2.3%	2.3%	2.3%	2.3%	2.3%	2.3%	2.3%	2.3%	2.3%	2.3%	2.3%	2.3%	2.3%	2.3%	2.3%	2.3%	2.3%
Upper 5	1.1%	1.1%	1.1%	1.1%	1.1%	1.1%	1.1%	1.1%	1.1%	1.1%	1.1%	1.1%	1.1%	1.1%	1.1%	1.1%	1.1%	1.1%	1.1%
Upper 6	0.51%	0.51%	0.51%	0.51%	0.51%	0.51%	0.51%	0.51%	0.51%	0.51%	0.51%	0.51%	0.51%	0.51%	0.51%	0.51%	0.51%	0.51%	0.51%
Upper 7	0.100	0.100	0.100	0.100	0.100	0.100	0.100	0.100	0.100	0.100	0.100	0.100	0.100	0.100	0.100	0.100	0.100	0.100	0.100
Upper 8	0.21345	0.21345	0.21345	0.21345	0.21345	0.21345	0.21345	0.21345	0.21345	0.21345	0.21345	0.21345	0.21345	0.21345	0.21345	0.21345	0.21345	0.21345	0.21345
Upper 9	0.27392	0.27392	0.27392	0.27392	0.27392	0.27392	0.27392	0.27392	0.27392	0.27392	0.27392	0.27392	0.27392	0.27392	0.27392	0.27392	0.27392	0.27392	0.27392
Upper 10	0.27464	0.27464	0.27464	0.27464	0.27464	0.27464	0.27464	0.27464	0.27464	0.27464	0.27464	0.27464	0.27464	0.27464	0.27464	0.27464	0.27464	0.27464	0.27464
Upper 11	0.32821	0.32821	0.32821	0.32821	0.32821	0.32821	0.32821	0.32821	0.32821	0.32821	0.32821	0.32821	0.32821	0.32821	0.32821	0.32821	0.32821	0.32821	0.32821
Upper 12	0.32709	0.32709	0.32709	0.32709	0.32709	0.32709	0.32709	0.32709	0.32709	0.32709	0.32709	0.32709	0.32709	0.32709	0.32709	0.32709	0.32709	0.32709	0.32709
Upper 13	0.32864	0.32864	0.32864	0.32864	0.32864	0.32864	0.32864	0.32864	0.32864	0.32864	0.32864	0.32864	0.32864	0.32864	0.32864	0.32864	0.32864	0.32864	0.32864
Upper 14	0.32865	0.32865	0.32865	0.32865	0.32865	0.32865	0.32865	0.32865	0.32865	0.32865	0.32865	0.32865	0.32865	0.32865	0.32865	0.32865	0.32865	0.32865	0.32865
Upper 15	0.32723	0.32723	0.32723	0.32723	0.32723	0.32723	0.32723	0.32723	0.32723	0.32723	0.32723	0.32723	0.32723	0.32723	0.32723	0.32723	0.32723	0.32723	0.32723
Upper 16	0.21384	0.21384	0.21384	0.21384	0.21384	0.21384	0.21384	0.21384	0.21384	0.21384	0.21384	0.21384	0.21384	0.21384	0.21384	0.21384	0.21384	0.21384	0.21384
Upper 17	0.32850	0.32850	0.32850	0.32850	0.32850	0.32850	0.32850	0.32850	0.32850	0.32850	0.32850	0.32850	0.32850	0.32850	0.32850	0.32850	0.32850	0.32850	0.32850
Upper 18	0.14992	0.14992	0.14992	0.14992	0.14992	0.14992	0.14992	0.14992	0.14992	0.14992	0.14992	0.14992	0.14992	0.14992	0.14992	0.14992	0.14992	0.14992	0.14992
Upper 19	0.32889	0.32889	0.32889	0.32889	0.32889	0.32889	0.32889	0.32889	0.32889	0.32889	0.32889	0.32889	0.32889	0.32889	0.32889	0.32889	0.32889	0.32889	0.32889
Upper 20	0.32950	0.32950	0.32950	0.32950	0.32950	0.32950	0.32950	0.32950	0.32950	0.32950	0.32950	0.32950	0.32950	0.32950	0.32950	0.32950	0.32950	0.32950	0.32950
Upper 21	0.14992	0.14992	0.14992	0.14992	0.14992	0.14992	0.14992	0.14992	0.14992	0.14992	0.14992	0.14992	0.14992	0.14992	0.14992	0.14992	0.14992	0.14992	0.14992

Table G.42: Test 11289401

Date	11/28/24	mol/dry/ft	Mean NO _x	62.0 %	Upper I	1219.0	mg. H ₂ O	0.8823	inches	mol CH ₄	17.488	CH ₄ AA only
Coal	11289401	mol/dry/ft	Mean PM ₁₀	4.1 %	Sample 1	282.6	Wetted	0.32	friction	mol/dry/ft	492.882	CH ₄ AA only
Unit no.	11289401	mol/dry/ft	BEFNO	45.5 %	Coal feed	833.6	Wetted	0.32	friction	mol/dry/ft	1.934	CH ₄ AA only
Coal type	5.00	mol/dry/ft	BEFAR	4.0 %	Coal feeder	819.0	Wetted	0.32	friction	mol/dry/ft	1.981	CH ₄ AA only
Coal type	5.00	mol/dry/ft	BEFAR	4.0 %	Vacuum Pk	819.0	Wetted	0.32	friction	mol/dry/ft	1.981	CH ₄ AA only
Upper Freeport	mol/dry/ft	mol/dry/ft	BEFNO	1.0 %	Vacuum Pk	119.0	Wetted	0.32	friction	mol/dry/ft	2.192	CH ₄ AA only
grains	5.39	mol/dry/ft	BEFAR	1.0 %	atomizer air	119.0	Wetted	0.32	friction	mol/dry/ft	2.192	CH ₄ AA only
	4.07	mol/dry/ft	BEFAR	1.0 %	atomizer H ₂ O	119.0	Wetted	0.32	friction	mol/dry/ft	2.192	CH ₄ AA only
	3.92	mol/dry/ft	BEFAR	1.0 %	atomizer H ₂ O	119.0	Wetted	0.32	friction	mol/dry/ft	2.192	CH ₄ AA only
	1.43	mol/dry/ft	BEFAR	1.0 %	over, 1/2 in.	119.0	Wetted	0.32	friction	mol/dry/ft	2.192	CH ₄ AA only
	2.07	mol/dry/ft	BEFAR	1.0 %	over, 1/2 in.	119.0	Wetted	0.32	friction	mol/dry/ft	2.192	CH ₄ AA only
	23.23	mol/dry/ft	BEFAR	1.0 %	over, 1/2 in.	119.0	Wetted	0.32	friction	mol/dry/ft	2.192	CH ₄ AA only
	0.51	mol/dry/ft	BEFAR	1.0 %	over, 1/2 in.	119.0	Wetted	0.32	friction	mol/dry/ft	2.192	CH ₄ AA only
	100	mol/dry/ft	BEFAR	1.0 %	over, 1/2 in.	119.0	Wetted	0.32	friction	mol/dry/ft	2.192	CH ₄ AA only
Stage	Initial (g)	Final (g)	Net (g)	% in size range	Size Range	ESD	mol coal	0.03	inches	mol/dry/ft	8.707	CH ₄ AA only
	0.32851	0.35086	0.02215	73.76	10.0-10.0	10	Probe inlet	1.1	g/min	mol/dry/ft	1.150	CH ₄ AA only
	0.32883	0.30284	0.04111	13.69	12.5-10.0	10	Probe inlet	7.65	decC	mol/dry/ft	2.703	CH ₄ AA only
	0.30156	0.30284	0.00125	4.16	8.0-5.0	8.0	Probe inlet	100	decC	mol/dry/ft	13.700	CH ₄ AA only
	0.32680	0.32774	0.00094	3.13	5.0-4.7	4.7	Vacuum Pk	7.5	in H ₂ O	mol/dry/ft	0.0007	CH ₄ AA only
	0.32755	0.32781	0.00026	1.00	4.0-3.3	3.3	Vacuum Pk	23	decC	mol/dry/ft	1.392	CH ₄ AA only
	0.32240	0.32270	0.00030	1.00	3.0-2.1	2.1	Vacuum Pk	47	CFH	mol/dry/ft	0.497	CH ₄ AA only
	0.32677	0.32687	0.00010	0.67	2.4-1.1	1.1	coal filter	5	mm	mol/dry/ft	0.077	CH ₄ AA only
	0.33110	0.33115	0.00005	0.17	2.4-0.7	0.7	coal filter	5	mm	mol/dry/ft	1.610	CH ₄ AA only
	0.33171	0.33174	0.00003	0.19	2.19-0.4	0.4	coal filter	5	mm	mol/dry/ft	28.108	CH ₄ AA only
	0.32740	0.32804	0.00064	2.19	0.0-0.4	0	coal filter	5	mm	mol/dry/ft	310.728	CH ₄ AA only
Backup Filter			total mass				coal filter	5	mm	mol/dry/ft	2.726	CH ₄ AA only
							coal filter	5	mm	mol/dry/ft	918.274	CH ₄ AA only
							coal filter	5	mm	mol/dry/ft	29.477	CH ₄ AA only
							coal filter	5	mm	mol/dry/ft	809.619	CH ₄ AA only
							coal filter	5	mm	mol/dry/ft	0.028	CH ₄ AA only
							coal filter	5	mm	mol/dry/ft	0.021	CH ₄ AA only
							coal filter	5	mm	mol/dry/ft	25.020	CH ₄ AA only
							coal filter	5	mm	mol/dry/ft	27.084	CH ₄ AA only
							coal filter	5	mm	mol/dry/ft	0.030	CH ₄ AA only
							coal filter	5	mm	mol/dry/ft	1.044	CH ₄ AA only
							coal filter	5	mm	mol/dry/ft	626.937	CH ₄ AA only
							coal filter	5	mm	mol/dry/ft	28.813	CH ₄ AA only
							coal filter	5	mm	mol/dry/ft	0.01339	CH ₄ AA only
							coal filter	5	mm	mol/dry/ft	0.0668	CH ₄ AA only
							coal filter	5	mm	mol/dry/ft	122.326	CH ₄ AA only
							coal filter	5	mm	mol/dry/ft	122.326	CH ₄ AA only

Table G.44: Test 12079401

Date	12/27/84	mo/d/yr	Mean NO	62.2 %	Upper T	1250 g (mass)	any oil down													
Coal	Upper Frappos	process	Mean Air	41.0 %	Sampler T	783 g (mass)	Manufact red	0.6895	noles/m	CH4/Air only										
test no	12079401	mid/hyrum	BE/AV	45.0 %	Lower T	948 g (mass)	Mach Das Pas	0.922	noles/m	CH4/Air only										
test dur	1.00	min/hrs	BE/AV	4.9	Coal feed cor	870 units	Main Air Rct	0.41	noles/m	CH4/Air only										
Coal Proportion	(Ref. only)		BE/AV	4.9	vacuum rate	87.0 %	Main Air Rct	31.9	noles/m	CH4/Air only										
Upper Frappos			BE/AV	1.0	vacuum rate	7.5 in hd	Main Air Rct	10.1	noles/m	CH4/Air only										
grams	64.67	moles/100g	BE/AV	39.8	atomizer air	183 mm	In Air Rate	38.6	noles/m	CH4/Air only										
	4.07	4.07	In Rate	1.0	atomizer H ₂ O	113 F	In Air Rate	10.1	noles/m	CH4/Air only										
	3.92	0.23	In Rate	1.0	oil dust T	120 F	In Air Rate	10.1	noles/m	CH4/Air only										
	1.63	0.12			graze lvm T	120 F	Coal Composition on Elemental level													
	2.07	0.08					Carbon content	5.39	moles/100g											
	23.23	23.23					Hydrogen in	4.07	moles/100g											
	0.81	0.03					Nitrogen in	0.25	moles/100g											
	100						Sulfur (max)	0.08	moles/100g											
							Ash	23.23	g/100g											
Stage	Initial(g)	Final(g)	Net(g)	% in size	µm	Size Range	ECD	µm	moles/100g											
Pressorator	0.32791	0.32353	0.00438	81.21	18.78	10.0 & up	10	µm	0.1154	noles/m										
0	0.24972	0.30041	0.05069	9.97	8.82	9.0-10.0	9	µm	2.242	noles/m										
1	0.24983	0.30009	0.00016	2.31	6.50	9.0-9.0	8	µm	13.745	noles/m										
2	0.32880	0.32695	0.00015	2.17	4.34	7.5-8.8	4.7	µm	0.0507	noles/m										
3	0.32814	0.32620	0.00006	0.97	3.47	5.5-6.7	3.3	µm	1.386	noles/m										
4	0.32872	0.32874	0.00002	0.28	2.18	3.3-4.7	2.1	µm	8.689	noles/m										
5	0.32817	0.32819	0.00002	0.29	1.60	1.1-2.1	1.1	µm	0.077	mass fraction										
6	0.32840	0.32840	0.00000	0.00	2.89	1.1-2.1	1.1	µm	28.109	wt/m										
7	0.32718	0.32717	0.00001	0.14	2.89	1.1-2.1	1.1	µm	321.309	g/m ³										
Backup Filter	0.32168	0.32167	0.000019	2.75	0.00	0-0.4	0	µm	49.822	noles/m										
		total mass							2.724	µg/m ³										
									0.99992	g										
Notes:	Plated note - Since previous test of 9 minutes was suspended, I'm going to do a 1 minute																			
	* 1.9 microns with wet coal																			
	* The separator had a really tight (visual weight estimate)																			
	* Stage 2 again had theory dry ash on the 1st slide. 3/2 bars off to the slide. Stage 3																			
	looks about clean, but with Borden anyway. Stage 2 only has a visible pile in the																			
	center. Stage 3 has no visible ash. These stages look just like the 9 minute test.																			
	(12079401), for ex. 1, but Borden is cleaner. Stage 3 has this traditional visible piles,																			
	while stage 4 only had extremely thin piles showing. Stage 6 has very thin piles in																			
	retropect, all these piles are very thin, including stage 7. Five looks the most loaded,																			
	but not much.																			
	* The later again has visible particles, on the order of 10 um.																			
	* I dropped stage 6 like down, but I don't think it hurt. No hose ash, and I dropped it a																			
	short distance onto clean cotton. Little of this the two surfaces collected.																			
	* Temperature was measured about 8 hours after test. No reason to suspect it to change																			
	over that time period.																			

APPENDIX H: ARTIFICIAL CHAR CASCADE IMPACTOR TEST SUMMARIES

The spreadsheets that follow summarize the detailed measurements and calculations required to determine the size distribution of ash for artificial char fuels. The series was conducted in association with Park (1995), using a natural-gas fired furnace. Ash samples were collected with a simple water cooled sampling probe and size-sorted with a Mark II cascade impactor.

Table H.1: Test log for artificial char experiments

Test Number	Char Name	A/F Equiv. (w/o char)	Furnace Flow Rate, grams	Dry O ₂ , % (w/o char)
03019501	Ben 1.25 g	1.47	634	7.7
03139501	Ben 1.25 g	1.47	631	7.8
03029501	Ben 2.50 g	1.45	621	7.5
03149501	Ben 2.50 g	1.47	627	7.8
03039501	Ben 3.75 g	1.44	625	7.5
03149502	Ben 3.75 g	1.48	627	7.9
02279501	Ben 5.00 g	1.44	621	7.4
03149503	Ben 5.00 g	1.46	628	7.7
03129501	Cal 0.25 g	1.46	630	7.7
03079502	Cal 0.50 g	1.45	629	7.6
03079501	Cal 0.75 g	1.46	631	7.7
03069502	Cal 1.00 g	1.46	630	7.7
02219501	Pyr 0.93 g	1.44	625	7.5
03179502	Pyr 0.93 g	1.42	617	7.3
03039502	Pyr 1.85 g	1.44	625	7.5
03179501	Pyr 1.85 g	1.46	628	7.7
03069501	Pyr 2.78 g	1.46	630	7.7
03169501	Pyr 2.78 g	1.47	631	7.8
03169504	Pyr 3.70 g	1.47	627	7.8
02239501	Pyr 3.70 g	1.44	622	7.5
02149501	Suc50/C50	1.42	617	7.3
03129502	Suc50/C50	1.43	618	7.4
02069501	Suc50/C50	1.63	521	8.9
02179501	Suc75/C25	1.44	622	7.5
03169503	Suc75/C25	1.45	628	7.6

Table H.4: Test 02149501

Item	2/14/98	2/14/98	2/14/98	2/14/98	2/14/98	2/14/98	2/14/98	2/14/98	2/14/98	2/14/98	2/14/98	2/14/98	2/14/98	2/14/98	2/14/98	2/14/98	2/14/98	2/14/98	2/14/98	2/14/98	2/14/98			
Unit	mg/kg	mg/kg	mg/kg	mg/kg	mg/kg	mg/kg	mg/kg	mg/kg	mg/kg	mg/kg	mg/kg	mg/kg	mg/kg	mg/kg	mg/kg	mg/kg	mg/kg	mg/kg	mg/kg	mg/kg	mg/kg			
1st Air	15.90	18.30	19.00	20.00	21.00	22.00	23.00	24.00	25.00	26.00	27.00	28.00	29.00	30.00	31.00	32.00	33.00	34.00	35.00	36.00	37.00	38.00	39.00	40.00
2nd Air	15.90	18.30	19.00	20.00	21.00	22.00	23.00	24.00	25.00	26.00	27.00	28.00	29.00	30.00	31.00	32.00	33.00	34.00	35.00	36.00	37.00	38.00	39.00	40.00
3rd Air	15.90	18.30	19.00	20.00	21.00	22.00	23.00	24.00	25.00	26.00	27.00	28.00	29.00	30.00	31.00	32.00	33.00	34.00	35.00	36.00	37.00	38.00	39.00	40.00
4th Air	15.90	18.30	19.00	20.00	21.00	22.00	23.00	24.00	25.00	26.00	27.00	28.00	29.00	30.00	31.00	32.00	33.00	34.00	35.00	36.00	37.00	38.00	39.00	40.00
5th Air	15.90	18.30	19.00	20.00	21.00	22.00	23.00	24.00	25.00	26.00	27.00	28.00	29.00	30.00	31.00	32.00	33.00	34.00	35.00	36.00	37.00	38.00	39.00	40.00
6th Air	15.90	18.30	19.00	20.00	21.00	22.00	23.00	24.00	25.00	26.00	27.00	28.00	29.00	30.00	31.00	32.00	33.00	34.00	35.00	36.00	37.00	38.00	39.00	40.00
7th Air	15.90	18.30	19.00	20.00	21.00	22.00	23.00	24.00	25.00	26.00	27.00	28.00	29.00	30.00	31.00	32.00	33.00	34.00	35.00	36.00	37.00	38.00	39.00	40.00
Total	15.90	18.30	19.00	20.00	21.00	22.00	23.00	24.00	25.00	26.00	27.00	28.00	29.00	30.00	31.00	32.00	33.00	34.00	35.00	36.00	37.00	38.00	39.00	40.00
Procedural	0.2218	0.2211	0.2211	0.2211	0.2211	0.2211	0.2211	0.2211	0.2211	0.2211	0.2211	0.2211	0.2211	0.2211	0.2211	0.2211	0.2211	0.2211	0.2211	0.2211	0.2211	0.2211	0.2211	0.2211
1	0.4894	0.4879	0.4879	0.4879	0.4879	0.4879	0.4879	0.4879	0.4879	0.4879	0.4879	0.4879	0.4879	0.4879	0.4879	0.4879	0.4879	0.4879	0.4879	0.4879	0.4879	0.4879	0.4879	0.4879
2	0.2270	0.2274	0.2274	0.2274	0.2274	0.2274	0.2274	0.2274	0.2274	0.2274	0.2274	0.2274	0.2274	0.2274	0.2274	0.2274	0.2274	0.2274	0.2274	0.2274	0.2274	0.2274	0.2274	0.2274
3	0.2268	0.2274	0.2274	0.2274	0.2274	0.2274	0.2274	0.2274	0.2274	0.2274	0.2274	0.2274	0.2274	0.2274	0.2274	0.2274	0.2274	0.2274	0.2274	0.2274	0.2274	0.2274	0.2274	0.2274
4	0.2264	0.2268	0.2268	0.2268	0.2268	0.2268	0.2268	0.2268	0.2268	0.2268	0.2268	0.2268	0.2268	0.2268	0.2268	0.2268	0.2268	0.2268	0.2268	0.2268	0.2268	0.2268	0.2268	0.2268
5	0.2275	0.2275	0.2275	0.2275	0.2275	0.2275	0.2275	0.2275	0.2275	0.2275	0.2275	0.2275	0.2275	0.2275	0.2275	0.2275	0.2275	0.2275	0.2275	0.2275	0.2275	0.2275	0.2275	0.2275
6	0.2264	0.2264	0.2264	0.2264	0.2264	0.2264	0.2264	0.2264	0.2264	0.2264	0.2264	0.2264	0.2264	0.2264	0.2264	0.2264	0.2264	0.2264	0.2264	0.2264	0.2264	0.2264	0.2264	0.2264
7	0.2268	0.2268	0.2268	0.2268	0.2268	0.2268	0.2268	0.2268	0.2268	0.2268	0.2268	0.2268	0.2268	0.2268	0.2268	0.2268	0.2268	0.2268	0.2268	0.2268	0.2268	0.2268	0.2268	0.2268
Backup Error	0.2270	0.2270	0.2270	0.2270	0.2270	0.2270	0.2270	0.2270	0.2270	0.2270	0.2270	0.2270	0.2270	0.2270	0.2270	0.2270	0.2270	0.2270	0.2270	0.2270	0.2270	0.2270	0.2270	0.2270
Total mass	0.2270	0.2270	0.2270	0.2270	0.2270	0.2270	0.2270	0.2270	0.2270	0.2270	0.2270	0.2270	0.2270	0.2270	0.2270	0.2270	0.2270	0.2270	0.2270	0.2270	0.2270	0.2270	0.2270	0.2270
Notes	1) (C.J. measurement is about 1% off collection of sample. Spelling on labels checked off. Also due to this it is on sample. The coal collector stated with a grain of salt that the amount of ash because I opened the ribs too fast. Effect unknown. Coal seems to be from the bottom of the drum. 2) Samples were collected by means of the number 10. Probably for about one or two feet into the drums were past and of this (i.e. with of test). 3) Probably for about one or two feet into the drums were past. 4) Samples 5 and 6 look completely clean. Perhaps they are relatively pure amount of ash in 1. 5) Samples 5 and 6 look completely clean. Perhaps they are relatively pure amount of ash in 1. 6) Samples 5 and 6 look completely clean. Perhaps they are relatively pure amount of ash in 1. 7) Samples 5 and 6 look completely clean. Perhaps they are relatively pure amount of ash in 1. 8) Samples 5 and 6 look completely clean. Perhaps they are relatively pure amount of ash in 1. 9) Samples 5 and 6 look completely clean. Perhaps they are relatively pure amount of ash in 1. 10) Samples 5 and 6 look completely clean. Perhaps they are relatively pure amount of ash in 1. 11) Samples 5 and 6 look completely clean. Perhaps they are relatively pure amount of ash in 1. 12) Samples 5 and 6 look completely clean. Perhaps they are relatively pure amount of ash in 1. 13) Samples 5 and 6 look completely clean. Perhaps they are relatively pure amount of ash in 1. 14) Samples 5 and 6 look completely clean. Perhaps they are relatively pure amount of ash in 1. 15) Samples 5 and 6 look completely clean. Perhaps they are relatively pure amount of ash in 1. 16) Samples 5 and 6 look completely clean. Perhaps they are relatively pure amount of ash in 1. 17) Samples 5 and 6 look completely clean. Perhaps they are relatively pure amount of ash in 1. 18) Samples 5 and 6 look completely clean. Perhaps they are relatively pure amount of ash in 1. 19) Samples 5 and 6 look completely clean. Perhaps they are relatively pure amount of ash in 1. 20) Samples 5 and 6 look completely clean. Perhaps they are relatively pure amount of ash in 1. 21) Samples 5 and 6 look completely clean. Perhaps they are relatively pure amount of ash in 1. 22) Samples 5 and 6 look completely clean. Perhaps they are relatively pure amount of ash in 1.																							

Table H.5: Test 02179501

Date:	2/17/95	AC #2	Svz/C2B	Source	Mean Air	Mean NG	Mean Air	Flow Rate	145 F	Probe exit I:	1.60	Temp, C:	110	Probe exit II:	1.60	Temp, C:	110
Test no:	02179501	Process	BFMS	Flow Rate	44.0 %	Flow Rate	44.0 %	Flow Rate	110 F	Flow Rate	44.0 %	Flow Rate	110 F	Flow Rate	44.0 %	Flow Rate	110 F
Test date:	15-87	Mineral	BFMS	Flow Rate	44.0 %	Flow Rate	44.0 %	Flow Rate	110 F	Flow Rate	44.0 %	Flow Rate	110 F	Flow Rate	44.0 %	Flow Rate	110 F
Coal Properties (Ref. test):		Flow Rate	BFMS	Flow Rate	44.0 %	Flow Rate	44.0 %	Flow Rate	110 F	Flow Rate	44.0 %	Flow Rate	110 F	Flow Rate	44.0 %	Flow Rate	110 F
GRMB:		Flow Rate	BFMS	Flow Rate	44.0 %	Flow Rate	44.0 %	Flow Rate	110 F	Flow Rate	44.0 %	Flow Rate	110 F	Flow Rate	44.0 %	Flow Rate	110 F
Scale:		Flow Rate	BFMS	Flow Rate	44.0 %	Flow Rate	44.0 %	Flow Rate	110 F	Flow Rate	44.0 %	Flow Rate	110 F	Flow Rate	44.0 %	Flow Rate	110 F
Stage:	Initial	Final	Net	Flow Rate	44.0 %	Flow Rate	44.0 %	Flow Rate	110 F	Flow Rate	44.0 %	Flow Rate	110 F	Flow Rate	44.0 %	Flow Rate	110 F
Preseparator	0	0.33066	0.33235	0.00170	30.44	0.00170	0.00170	0.00170	110	0.00170	30.44	0.00170	110	0.00170	30.44	0.00170	110
	1	0.30112	0.29923	0.00039	6.33	0.00039	0.00039	0.00039	110	0.00039	6.33	0.00039	110	0.00039	6.33	0.00039	110
	2	0.32716	0.32742	0.00027	4.69	0.00027	0.00027	0.00027	110	0.00027	4.69	0.00027	110	0.00027	4.69	0.00027	110
	3	0.33180	0.33232	0.00052	5.44	0.00052	0.00052	0.00052	110	0.00052	5.44	0.00052	110	0.00052	5.44	0.00052	110
	4	0.33093	0.33117	0.00024	2.88	0.00024	0.00024	0.00024	110	0.00024	2.88	0.00024	110	0.00024	2.88	0.00024	110
	5	0.34093	0.34099	0.00006	0.17	0.00006	0.00006	0.00006	110	0.00006	0.17	0.00006	110	0.00006	0.17	0.00006	110
	6	0.33178	0.33366	0.00187	31.80	0.00187	0.00187	0.00187	110	0.00187	31.80	0.00187	110	0.00187	31.80	0.00187	110
Residue Flow		Total mass															
Notes:																	

Table H.13: Test 03069501

Date:		3/18/85	mo/day/yr	Main INCL																			
Coal:	AC 86		source	Main Akr.																			
Test no:	Prf 276 g	03069501	mg/day/mum	BFING																			
Test dir:	13.28	min/day		BEIAR																			
Coal Prospector:	(Red. con)																						
ANAL:		Element/100g	Unit Ana	in Rnde																			
				Carbon																			
				Hydrogen																			
				Nitrogen																			
				Sulfur																			
				Ash																			
				Moisture																			
				Total																			
Stage	Initial(g)	Final(g)	(Net(g))																				
Preparation	0	0.33090	0.33485	0.00405																			
	1	0.33041	0.33856	0.00815																			
	2	0.33084	0.34642	0.00878																			
	3	0.33021	0.33230	0.00198																			
	4	0.32685	0.32785	0.00110																			
	5	0.32744	0.32806	0.00082																			
	6	0.32720	0.32842	0.00082																			
	7	0.32654	0.32862	0.00086																			
Rechar Effic.	0.33184	0.33302	0.00118																				
		Total mass		0.01118																			
Notes:																							

Table H.17: Test 03129501

Date: Coal:	AQ #14 CH4.0.25 g 03129501 14.20 Coal Processor (B&E only)	Imp/26817/1 source process M/d/Y/Min 14.20 minutes	Mean NOx		Mean SO2		Procs stat T:		T/C Port Temp, C	CO2		CO2 fraction	CO2 flow	CO2 flow/1000 lbs	CO2 flow/1000 lbs	
			Mean NOx ppm BF/NOx	Mean SO2 ppm BF/SO2	99.9 % 48.2 % 33.0 % 44.0 % 3.8 %	% in size over 10µm	Size Range µm range	141 F 160 mm 7 ppm 15 ppm 67/m		141 F 160 mm 7 ppm 15 ppm 67/m	141 F 160 mm 7 ppm 15 ppm 67/m					141 F 160 mm 7 ppm 15 ppm 67/m
0																
1																
2																
3																
4																
5																
6																
7																
Back-up Filter																
Preprocessor																
1																
2																
3																
4																
5																
6																
7																
Back-up Filter																
Preprocessor																
1																
2																
3																
4																
5																
6																
7																
Back-up Filter																
Preprocessor																
1																
2																
3																
4																
5																
6																
7																
Back-up Filter																

Table H.27: Test 03179502

Step	Initial	Final	Net	% In sig range	Count	Size Range	T/C Perf	Temp, C	Flow Rate	Flow Rate	Flow Rate	Flow Rate	Flow Rate	Flow Rate	Flow Rate	Flow Rate	Flow Rate	Flow Rate	Flow Rate	Flow Rate	Flow Rate			
Preseparator	0	0.32558	0.32802	0.00236	37.24	82.86	10.0 a up	B	1807	Probe Heat T														
	1	0.48272	0.48730	0.00458	8.54	54.11	8.0-10.0	C	1186	Investor Inlet														
	2	0.48272	0.48730	0.00458	9.66	47.47	5.8-9.0	D	1164	Vacuum Roto														
	3	0.32558	0.32787	0.00038	9.01	41.49	4.7-5.8	E	1144	Vacuum Roto														
	4	0.32558	0.32638	0.00044	9.99	24.49	3.3-4.7	F	1107	Vacuum Roto														
	5	0.32558	0.32676	0.00047	7.44	27.09	2.1-3.3	G	1088	Coal flow line														
	6	0.32558	0.32872	0.00035	8.64	21.62	1.1-2.1	H	1033															
	7	0.32558	0.32643	0.00012	1.90	19.68	0.7-1.1	I	989															
	8	0.32558	0.32722	0.00013	2.08	17.68	0.4-0.7	J	888															
	9	0.32558	0.32811	0.00011	17.68	0.00	0-0.4	K	821															
	Becham Filter			0.33100	0.33211																			
	Total mass			0.00832																				
	Notes: . Let the filter in the imbedded for an extra 15 minutes (beyond the nominal 20 minutes). Shouldn't be a big deal. . Filter has some ash, but not alot. Filter is pretty dirty.																							

APPENDIX I: HOMOGENEOUS AND HETEROGENEOUS CONDENSATION COMPETITION MODEL

(* This code predicts the fate of vapor phase condensing species in a hot gas environment containing foreign particles. The heterogeneous condensation rate is assumed to be driven exclusively by diffusion to the particle surface. The rate is approximated for the entire range of Kn by the Fuchs and Stutugin (1971) relation. The freestream vapor pressure is incrementally recalculated as condensation depletes the system. Homogeneous nucleation and condensation is assumed to collect all remaining vapor phase material when/if the critical saturation ratio is achieved *)

Off[General::spell1]

Clear[nmolwt, dif, nliqdens, n σ , n, λ , km, k, s, m, i, del, time, d]

(* **Universal constants** *)

k = 1.380⁻²³; (* \sim Boltzmann constant, N m/K *)

n_{av} = 6.023²⁶; (* \sim Avogadro, molecules/kmol *)

gasconst = k * n_{av} / (* $\frac{\text{J}}{\text{kmol}\cdot\text{K}}$ *)

(* **NaCl properties** *)

(* Properties compiled from Physical and Thermodynamic Properties of Pure Chemicals Data Compilation, T.E Daubert and R.P. Danner, editors *)

```

mmolwt = 58.443; (* -NaCl molecular wt, kg/kmol *)
nbp = 1738.15; (* -NaCl normal boiling point, K *)
m = mmolwt / nav; (* -NaCl molecule weight, kg/molecule*)
nliqdens[τ_] := .40073 / (.10591(1+(1-τ/3400)-1.7527));
(* -NaCl liquid density for 1073 K < T < 3400 K, kmol/m3 *)

mmolvol = 1 / nliqdens[nbp];
(*-NaCl molal volume at boiling point, m3/kmol*)
ncoldia = (1.18 * 10-9) * mmolvol1/3;
(* -NaCl collision diameter,
meters. Estimate based on method presented in Perry's
Chemical Engineer's Handbook, 4th ed. McGraw-Hill, 1963 *)

psat[τ_] :=
Exp[56.543 - (2.6153**4) / τ - 4.2034 * Log[τ] + (7.9833**^-4) * τ];
(* -NaCl saturated vapor press,
1074 K < T < 1738 K, Pa. Extrapolation to lower temperatures is
similar to saturation pressure from NASA equilibrium code.*)

nσ[τ_] := .20133 * (1 - τ / 3400)1.4978;
(* -NaCl surface tension for 1074 K < T < 1738 K, N/m *)

bdl = 2.667**^-10; (* NaCl bond length,
meters. CRC Handbook of Chemistry and Physics, 75th Ed. *)
va =  $\frac{4}{3} \pi$  (ncoldia / 2)3; (* -NaCl molecule volume, estimate, m3 *)

```

(* Other properties of the system *)

amolwt = 28.84; (* -Air molecular wt, kg/kmol *)
psys = 101325; (* -system pressure, Pa *)

(* NaCl diffusivity *)

(* prediction
 method from Perry's Chemical Engineers handbook*)

acoldia = 3.617 * 10⁻¹⁰; (* -air collisional diameter, meters *)

id = .48; (* -collision integral for diffusion,
 f(k*T/energy-of-molec-interaction), from Perry's, # *)

coldia = (acoldia + ncoldia) / 2;

bee = $\left(10.7 - 2.46 * \left(\frac{1}{\text{amolwt}} + \frac{1}{\text{amolwt}} \right)^{.5} \right) * 10^{-4} + 1.01325 * 10^{-19};$

(* -term in diffusivity equation,
 from Perry's, $\left((\text{Pa} * \text{m}^2 * \left(\frac{\text{kg}}{\text{kmol}} \right)^{.5}) / (\text{K}^{1/2}) \right) * \left(\frac{\text{m}^2}{\text{sec}} \right)$ *)

diff[tau_] := $\frac{\text{bee} * \tau^{1/2} * \left(\frac{1}{\text{amolwt}} + \frac{1}{\text{amolwt}} \right)^{.5}}{\text{psys} * \text{coldia}^2 * \text{id}}$ (* (m²)/sec*);

(* -diffusivity, mks units on all variables *)

(* Hot gas property functions *)

n[tau_] := psys / (gasconst * tau); (* -Total molar density, kmol/m³ *)

lambda[tau_] := 1 / ($\sqrt{2} * \pi * n[\tau] * n_{av} * (3.385 * 10^{-10})^2$); (* -Mean free path, meters *)

kn[tau_, dia_] := lambda[tau] / dia; (* Knudsen number, heteroparticle *)

(* Define condensation functions *)

```
current = 1**6; (* droplet current, defines scrit,  $\frac{i}{m^3 \text{ sec}}$  *)

het[tau_, pinf_, dia_] :=
  (2 * pi * dia * dif[tau] (pinf - psat[tau] + Exp[ $\frac{4 n\sigma[\tau] v_n}{dia + k \tau}$ ]) / (k * tau)) *
  ((1 + km[tau, dia]) / (1 + 1.71 * km[tau, dia] + 1.333 * (km[tau, dia])2));
  (* -diffusion rate to het particle,
  including Fuchs and Stutugin (1971) approximation, molecules/sec *)
```

```
scrit[tau_, p_] := Exp[ $\left( \left( -\frac{(16 \pi (n\sigma[\tau])^3 v_n^2)}{3 (k \tau)^3} \right) / \right.$ 
   $\left. \left( \text{Log}[current / \left( 2 * \left( \frac{p}{(2 \pi m k \tau)^{-5}} \right) * \left( \left( \frac{p}{k \tau} \right) v_n^{(2/3)} \right) * \right.$ 
   $\left. \left. \left( \frac{n\sigma[\tau] v_n^{2/3}}{k \tau} \right)^{-5} \right) \right] \right) \right]^{.5}$ ;
  (* -saturation ratio at which homogeneous condensation starts,
  adapted from Friedlander (1977) *)
```

```
dcrit[tau_, p_] :=  $\frac{4 * n\sigma[\tau] * v_n}{k * \tau * \text{Log}[s_{crit}[\tau, p]]}$ ;
```

```
i[tau_, p_, s_] := 2 *  $\left( \frac{p}{(2 \pi m k \tau)^{-5}} \right) * \left( \left( \frac{p}{k \tau} \right) v_n^{(2/3)} \right) * \left( \frac{n\sigma[\tau] v_n^{2/3}}{k \tau} \right)^{-5} * \text{Exp}\left[ \left( -\frac{(16 \pi (n\sigma[\tau])^3 v_n^2)}{3 (k \tau)^3 (\text{Log}[s])^2} \right) \right]$ ; (* droplet current
calculated from saturation ratio,  $\frac{i}{m^3 \text{ sec}}$ , Friedlander (1977) *)
```

(* "Do" loop to examine vapor fate as a function of multiple input variables *)

```
docount = 0; (* Initialize counter of times through loop *)
ClearAll[para, delmass, sal]; (* clear output variables *)
para = {"docount", "dpo", "dpt", "aeta o", "aeta t", "pinit", "theto", "thett", "tscrit", "delmass", "grate"};
AppendTo[para, {"num", "m", "m", "num", "num", "Pa", "K", "K", "K", "fract", "K/sec"}];
sal = {"", "", "", "", "", "", "", "", "", "", ""};
(* label output variables *)
```

```
Do[docount = docount + 1; (* start "Do" loop with independent variable *)
```

(* Heteroparticle properties and quench rate*)

```
mr = 117.03; (* kgAir/kgWood, mixture ratio *)
```

```
kgwood = .47376; (* kg wood in system *)
```

```
kgair = mr * kgwood; (* kg air in sytem *)
```

```
kmoltot = (kgwood + kgair) / amolwt; (* kmols in system *)
```

```
dpo = 7.16 * 10-6; (* large heteroparticle diameter, meter *)
```

```
no = 2.248 * 109; (* # of large hetero particles *)
```

```
dpt = .669 * 10-6; (* small heteroparticle diameter, meter *)
```

```
nt = 1.2496 * 1012; (* # of small hetero particles *)
```

```
qrates = 1000; (* quench rate, K/sec *)
```

**(* Find the temperature at which hetero
and homogeneous condensation starts *)**

```
Off[FindRoot::frmp]; (* suppress machine precision warning *)
```

```
theto = temp /.
```

```
FindRoot[het[temp, pinit, dpo] == 0, {temp, 900}, AccuracyGoal -> 0];
```

```
(* calculate temperature at which  
heterogeneous condensation starts for large particles *)
```

```
thett = temp /.
```

```
FindRoot[het[temp, pinit, dpt] == 0, {temp, 900}, AccuracyGoal -> 0];
```

```
(* calculate temperature at which  
heterogeneous condensation starts for smaller particles *)
```

```
tscrit = temp /. FindRoot[pinit / psat[temp] - scrit[temp, pinit] == 0,  
{temp, 750}, AccuracyGoal -> 3];
```

```
(* calculate temperature at which homogeneous condensation starts *)
```

```
On[FindRoot::frmp]; (* reactivate machine precision warning *)
```

```
tf = (theto - tscrit) / qrates; (* time to go from thet to tscrit, sec *)
```

```
del = tf / 100; (* timestep -
```

```
100 steps over estimated time in condensation zone, seconds *)
```

**(* Loop to determine mass fraction
captured by heterogeneous condensation *)**

```
For[time = 0; count = 0; pored = 0; ptred = 0;
```

```
step = 1; scr = scrit[tscrit, pinit]; ssys = pinit / psat[theto];
```

```
τ = theto; kmols = (pinit / psys) * kmoltot; pres = pinit; Clear[sol];
```

```
sol = {"s,sys", "s,cr", "pres", "tau", "time", "kmols", "lrgfrac"};}
```

```
AppendTo[
```

```
sol, {"s,sys", "s,cr", "pres", "tau", "time", "kmols", "lrgfrac"}],
```

```
(* set initial conditions: time counter,
```

```
times through For loop counter,
```

```

large particle partial pressure counter,
small particle partial pressure counter,
step counter (for print subroutine),
homogeneous and heterogeneous saturation ratios, temperature,
molar density, NaCl partial pressure, clear storage variable,
and give header names to output variables *)

scr > ssys && pres ≥ pinit*.01,
(* test: continue iteration until the calculated system saturation
ratio is greater than critical saturation ratio or the
partial pressure drops to 1/100 th of the initial value *)

time += del, (* step: increment time step. Time
is incremented after execution of body loop, below. *)

count = count + 1; (* count times through loop *)

τ = theto - qrate * (time + del / 2);
(* average temperature during time increment *)

hetmecho = NIntegrate [ ηo *
    het [theto - qrate * tyme, pres, dpo]  $\frac{1}{n_{av}}$ , {tyme, time, time + del} ];
(* kmols collected by large
particle het mechanism during time increment, kmols *)
If [ τ ≤ thett,
    hetmecht = NIntegrate [ ηt * het [theto - qrate * tyme, pres, dpt]  $\frac{1}{n_{av}}$ ,
        {tyme, time, time + del} ], hetmecht = 0 ];
(* kmols collected by small
particle het mechanism during time increment, kmols *)

kmols = kmols - hetmecho - hetmecht; (* calculate
reduction in freestream vapor mass after time increment *)
pored = hetmecho + pored;
(* cumulative kmols collected by large particles *)
ptred = hetmecht + ptred;
(* cumulative kmols collected by small particles *)
lrgfrac = pored / (pored + ptred);
(* fraction of kmols collected
by the large het particles vs all het particles *)

pres = (kmols / kmoltot) * psys; (* new vapor pressure, Pa *)
ssys = N [ pres / psat [τ] ];
scr = scrit [τ, pres]; (* calculate vapor pressure,
new saturation ratio, and new critical saturation ratio *)
AppendTo [sol, {ssys, scr, pres, τ, time, kmols, lrgfrac}];
(* save new variable values *)

```

```

If[step == count, AppendTo[sal,
  {ssys, scc, pres, τ, time, kmols, lrgfrac}]; step = count + 8];
(* save every 8th new variable value to a variable "sal". Limit
  output so that file is of manageable size *) (* end of "For" loop *)

delmass =  $\left( \frac{pinit}{psys} + kmoltot - kmols \right) / \left( \frac{pinit}{psys} + kmoltot \right);$ 
(* Calculate
  fraction of NaCl mass that condenses on het particles *)

AppendTo[para, {docount, dpo, dpt,
  ηo, ηt, pinit, theto, thett, tscrit, delmass, grate}];
(* save output values to variables for later examination *)

dur[docount] = ListPlot[Table[{sol[[i, 4]], sol[[i, 3]]}, {i, 2, count}],
  DisplayFunction -> Identity];
(* save output data to graphics variable*)

duh[docount] = ListPlot[Table[{sol[[i, 4]], sol[[i, 2]]}, {i, 2, count}],
  DisplayFunction -> Identity];
(* save output data to graphics variable*)

{pinit, (5-6)*psys, (15-6)*psys, (5-6)*psys}];
(* End of "do" loop. The initial
  partial pressure of the condensing vapor is incremented. *)

```

**(* Export results
to external file for further data analysis *)**

```

Clear[stmp]
stmp = OpenWrite["out1", PageWidth -> 200];
Write[stmp,
  OutputForm[NumberForm[TableForm[{"mr=", mr}, TableSpacing -> {0, 2}],
    {7, 4}, ExponentFunction -> (If[0 < # < 0, Null, #]&),
    NumberFormat -> (SequenceForm[#1, "e", #3]&)]]];

Write[stmp,
  OutputForm[NumberForm[TableForm[N[para], TableSpacing -> {0, 2}],
    {7, 4}, ExponentFunction -> (If[0 < # < 0, Null, #]&),
    NumberFormat -> (SequenceForm[#1, "e", #3]&)]]];

Write[
  stmp, OutputForm[NumberForm[TableForm[sal, TableSpacing -> {0, 2}],
    {7, 4}, ExponentFunction -> (If[0 < # < 0, Null, #]&),
    NumberFormat -> (SequenceForm[#1, "e", #3]&)]]];
(* save para=
  {docount, dpo, dpt, ηo, ηt, pinit, theto, thett, tscrit, delmass, grate}
  and sal to an output file named out1. This file can
  be imported by Microsoft Excel for data analysis. *)
Close[stmp];

```

(* Graphics routines and curve fits for run-time display of output *)

```

afit = Fit[Table[{para[[i, 7]], para[[i, 6]]},
  {i, 3, docount + 2}], {1, tp, tp2, tp3, tp4}, tp]
afitp = Plot[afit, {tp, para[[docount + 2, 7]], para[[3, 7]]},
  DisplayFunction -> Identity];
a = ListPlot[Table[{para[[i, 7]], para[[i, 6]]}, {i, 3, docount + 2}],
  PlotJoined -> False, DisplayFunction -> Identity]
bfit = Fit[Table[{para[[i, 9]], para[[i, 6]]},
  {i, 3, docount + 2}], {1, tp, tp2, tp3, tp4}, tp]
bfitp = Plot[bfit,
  {tp, para[[docount + 2, 9]], para[[3, 9]]}, DisplayFunction -> Identity];

b = ListPlot[Table[{para[[i, 9]], para[[i, 6]]}, {i, 3, docount + 2}],
  PlotJoined -> False, DisplayFunction -> Identity]

d = Show[Table[dur[dummy], {dummy, 1, docount}],
  PlotJoined -> True, DisplayFunction -> Identity]
Show[a, b, d, afitp, bfitp, DisplayFunction -> $DisplayFunction,
  GridLines -> Automatic, Frame -> True, RotateLabel -> True,
  FrameLabel -> {"Temperature, K", "Vapor Pressure, Pa", " ", " "}]

Show[Table[duh[dummy], {dummy, 1, docount}],
  DisplayFunction -> $DisplayFunction,
  GridLines -> Automatic, Frame -> True, RotateLabel -> True,
  FrameLabel -> {"Temperature, K", "Scrit, Pvpap/Psat", " ", " "}]

1.74138 10-9 + 8.24909 10-7 tp + 0.000250491 tp2 - 5.76697 10-7 tp3 + 3.
-Graphics-

1.85534 10-9 + 7.95427 10-7 tp + 0.000233106 tp2 - 5.57819 10-7 tp3 + 3.
-Graphics-

-Graphics-

```


**(* Subprogram to illustrate the regions of
heterogeneous and homogeneous condensation*)**

```

dpo = 7.16*10-6; (* large heteroparticle diameter, meter *)
no = 3.6346*107; (* # of large hetero particles per m3 of gas *)
dpt = .669*10-6; (* small heteroparticle diameter, meter *)
nt = 2.028*1010; (* # of small hetero particles per m3 of gas *)
pvapor = 14; (* Pa *)

Plot[{scrit[temp, pvapor],  $\frac{pvapor}{psat[temp]}$ , het[temp, pvapor, dpo],
      het[temp, pvapor, dpt], 1}, {temp, 940, 1030}, PlotRange -> {0, 4}]

regions =
Table[{temp, scrit[temp, pvapor],  $\frac{pvapor}{psat[temp]}$ , het[temp, pvapor, dpo],
      het[temp, pvapor, dpt], dcrit[temp, pvapor]}, {temp, 940, 1030, 2}];

PrependTo[regions, {"temp", "scrit",
  "pvap/psat", "het f[dpo]", "het f[dpt]", "dcrit"}];

TableForm[regions];

simp = OpenWrite["competit", PageWidth -> 200];

Write[simp, OutputForm[
  NumberForm[TableForm[{"dpo", dpo}, {"dpt", dpt},
    {"pvapor", pvapor}], TableSpacing -> {0, 2}],
  {7, 4}, NumberFormat -> {SequenceForm[#1, "e", #3]&}]];

Write[simp,
  OutputForm[NumberForm[TableForm[N[regions], TableSpacing -> {0, 2}],
    {7, 4}, NumberFormat -> {SequenceForm[#1, "e", #3]&}]];

Close[simp];

```

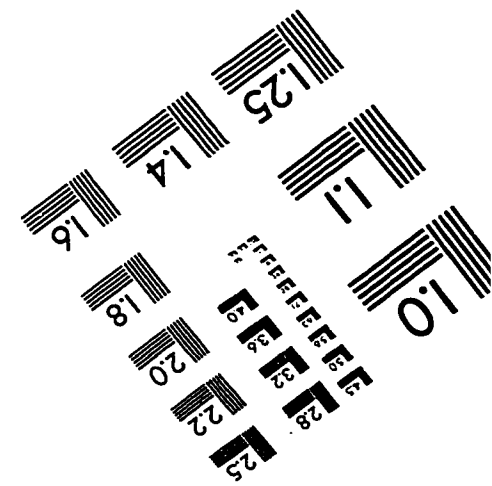
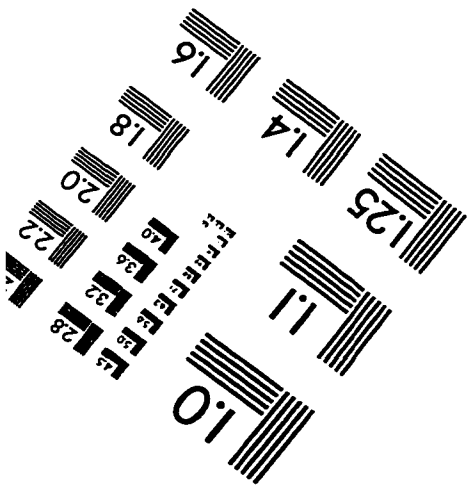
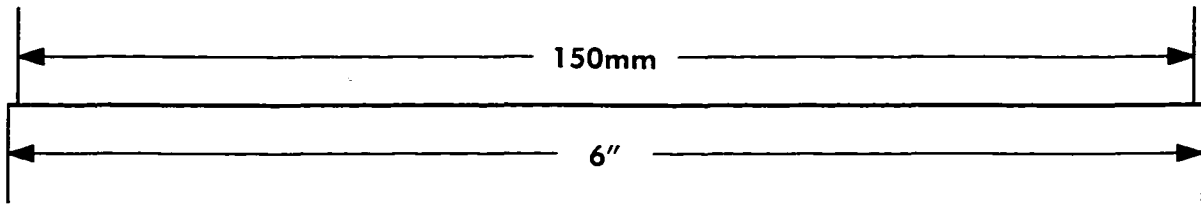
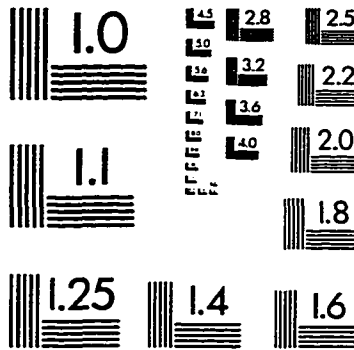
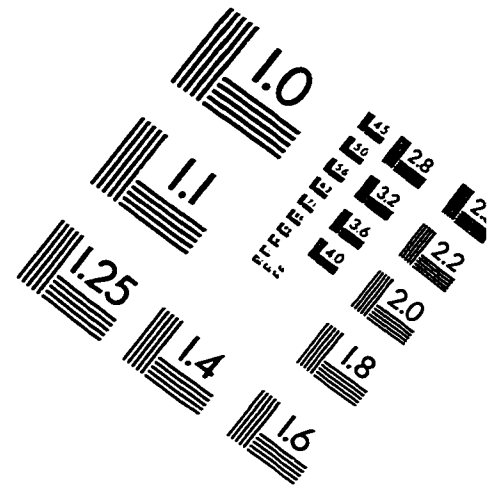
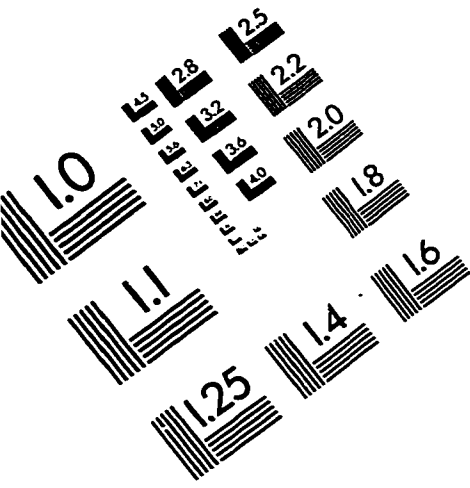
VITA

Blake Charles Chenevert

Master of Science, Mechanical Engineering, University of Washington, 1992

Doctor of Philosophy, Mechanical Engineering, University of Washington, 1998

IMAGE EVALUATION TEST TARGET (QA-3)



APPLIED IMAGE, Inc
 1653 East Main Street
 Rochester, NY 14609 USA
 Phone: 716/482-0300
 Fax: 716/288-5989

© 1993, Applied Image, Inc., All Rights Reserved